CARPAL KINEMATICS

IN THE NORMAL, SCAPHOLUNATE DEFICIENT AND SURGICALLY RECONSTRUCTED WRIST

Xin Zhang
(ORCID 0000-0002-8395-0479)

Submitted in total fulfilment of the requirements of the degree of Doctor of Philosophy

December, 2020

Department of Biomedical Engineering
Melbourne School of Engineering
The University of Melbourne

Abstract

Normal wrist function is ensured by a delicate interplay between bony architecture and soft-tissue constraints. Disruptions of this balance may alter carpal kinematics and joint contact, impairing the normal wrist physiology and biomechanics. The scapholunate interosseous ligament (SLIL), whose integrity is pivotal to normal scapholunate motion and that of the entire wrist, has been recognised as the most commonly injured carpal ligament. If left untreated, prolonged exposure to the altered joint motion may induce attrition of the secondary soft-tissue stabilisers, setting the stage for degenerative osteoarthritis. However, the exact role of these ligamentous stabilisers in maintaining normal scapholunate motion remains poorly understood. At present, many surgical procedures have been developed to treat scapholunate instability, but very few of them have been experimentally validated for their efficacy. Hence the aim of this investigation was twofold. Firstly, to evaluate the effects of different stages of scapholunate instability on wrist kinematics, and establish the relative contribution of various secondary scapholunate stabilisers to scapholunate motion and; secondly, to biomechanically evaluate the outcome of two reconstructive surgeries in treating scapholunate instability.

As these experiments were highly invasive, a novel cadaveric wrist testing platform (CWTP), consisting of a computer-controlled dynamic wrist cadaver simulation apparatus (DWSA) and a biplane X-ray fluoroscopy system, was developed. A comprehensive set of validation experiments were carried out to assess the performance of the CWTP in carrying out *in-vitro* wrist simulations. It was shown that the DWSA was capable of achieving

highly accurate and repeatable wrist movements, with robust control performance maintained even in the presence of severe ligament injuries to the wrist. The measurement accuracy and precision of the custom-built biplane X-ray fluoroscopy system were also evaluated. And the results demonstrated that the system was capable of resolving rigid body motion to a sub-degree and sub-millimetre accuracy.

Dynamic wrist simulations, including flexion-extension (FEM), radial-ulnar deviation (RUD) and the dart-thrower's motion (DTM), were then performed in seven cadaveric wrist specimens. A four-stage ligament division protocol was developed based on a previous study that correlated specific anatomic lesions of the scapholunate supporting ligaments with different Geissler grades of scapholunate instability, as well as the widely-accepted injury mechanism of hyperextension, ulnar deviation and intercarpal supination. This included sequentially dividing the volar (v-) and the membranous (m-) SLIL in Stage I; the dorsal (d-) SLIL in Stage II; the radioscaphocapitate (RSC) and the long radiolunate (LRL) ligaments in Stage III; and the dorsal intercarpal (DIC) ligament, the scaphotrapeziotrapezoid (STT) ligament, and about 40% of the dorsal radiocarpal (DRC) ligament in Stage IV. Reconstructive surgeries were then performed with the goal of re-stabilising the severely disrupted scapholunate joint. Two different techniques, including a novel dorsal transarticular loop tenodesis (DTLT) procedure and the widely-used three-ligament tenodesis (3LT) procedure, were assessed for their efficacy in restoring the normal scapholunate biomechanics.

With incremental ligament division, the scaphoid became progressively more flexed, ulnarly deviated, pronated and radially translated. The largest and the second-largest changes in the scaphoid kinematics were observed after the Stage II and IV ligament divisions, respectively. The motion of the dissociated scaphoid is likely to be primarily dictated by the bony geometry. Dividing the v- and m-SLIL, or the RSC and LRL ligaments, however, did not induce appreciable alterations. The lunate was found to be progressively more extended, supinated, and translated towards the volar and ulnar aspect of the radius. The most considerable changes in the lunate kinematics

were noted after the complete division of the SLIL in Stage II. Its dissociation from the scaphoid was immediately evident, as the lunate rotation in the sagittal plane was observed to be significantly attenuated. Dividing the volar extrinsic ligaments in Stage III caused the lunate to pronate instead of rotating into further supination, as well as to become ulnarly translated. In comparison, apart from causing the lunate to become statistically more supinated, dividing the dorsal carpal ligaments and the STT ligament in Stage IV induced no noticeable alterations in the lunate kinematics.

The DTLT resulted in a slightly insufficient reduction of the scaphoid in both the sagittal and transverse planes. And the procedure was found to induce a substantial amount of unphysiological volar translation of the scaphoid during ulnar deviation of the wrist. In contrast, the 3LT resulted in a much better correction of the scaphoid flexion; however, the scaphoid still appeared malrotated in pronation in the transverse plane. Furthermore, the pathological scaphoid supination was still present during wrist extension after the 3LT procedure, suggesting that the reconstruction was not capable in preventing the volar opening of the scapholunate interval. For the lunate, poor results were obtained after the 3LT, as the lunate remained collapsed in significant extension and supination. And since the tendon graft was tightened towards the ulnar side of the wrist, the 3LT not only did not correct the ulnar translation of the carpus, the condition was exacerbated by the procedure. The DTLT, on the other hand, led to a successful reduction of the dorsally collapsed lunate, which in turn restored its dynamic extension. The abnormal lunate supination was also corrected. However, cases of overcorrections were observed in these two planes.

The results suggested that apart from the SLIL, the dorsal carpal and the STT ligaments might have a vital contribution to the scaphoid stability, and the volar extrinsic ligaments are essential in preventing ulnar translation of the carpus. For the DTLT procedure, a complementary dorsal capsulodesis might be beneficial in correcting the residual scaphoid flexion. And the non-physiological volar translation of the scaphoid during wrist ulnar deviation might be due to the passive stretching of the radially situated ECR-B

graft used by the procedure, pronating the scaphoid and lunate as a unit towards the volar aspect of the radius. For the 3LT procedure, its inefficacy in preventing the volar opening of the scapholunate interval might be attributed to the ulnar and dorsal directed pull of the tendon graft, which might not be adequate for counteracting the supination tendency experienced by the scaphoid during wrist extension. Therefore it may be beneficial for a volar reconstruction of the scapholunate joint to be carried out in conjunction with the 3LT procedure. Furthermore, given the unsuccessful reduction of the lunate after 3LT, a transosseous passage of the tendon graft might be considered, instead of simply attaching it to the dorsum of the lunate.

In summary, this study advances the understanding of normal and pathological wrist function, and provide a foundation for improved clinical practice in the surgical treatment of scapholunate injuries of the wrist.

Declaration

This is to certify that:

(i) the thesis comprises only my original work towards the PhD except where indicated in the Preface,

(ii) due acknowledgement has been made in the text to all other material used,

(iii) the thesis is less than 100,000 words in length, exclusive of tables, maps, bibliographies, appendices and footnotes.

Xin Zhang *21 December 2020*

Acknowledgements

First and foremost, I would like to thank my principal supervisor A/Prof. David Ackland, who enthusiastically and patiently guided me through the work involved in this project. I sincerely express my gratitude for the hard work and invaluable input that he has provided over the years.

I am deeply thankful to my external supervisor Mr. Stephen Tham, whom I am incredibly fortunate to know and to work with, and profoundly indebted to. I would never be able to complete this study without his insightful guidance and trust.

I am grateful to Prof. Peter Lee and Dr. Vijay Rajigopal for serving on my Ph.D. Advisory Committee and for their support and unique insight into my project. I am also grateful to A/Prof. Eugene Ek, A/Prof. David McCombe and Mr. Kemble Wang for their clincal insights and constructive comments in the conceptualisation of this study. I would like to acknowledge Mr. Bruno Crepaldi, for his expertise and assistance in performing the dissections and the surgeries. I will never forget those late nights and early mornings we have spent together in that lab, as well as the torture we have been through in finding the optimal marker placement for those tiny bones of the wrist. I would also like to thank Ms. Susie Kerby and Ms. Namrata Phan from the anatomy department for the help they have kindly provided me in acquiring the specimens for this study. I also thank Mr. Rob Willams from Melbourne Brain Centre Imaging Unit for his assistance with the CT scan.

To all my peers in the Biomechanics group, past and present, thank you so much for your constant friendship and the memorable experience we have shared over the years. In particular, I would like to thank my good friends, Mahdi Pourdanial, Yanqi Wu, Arman Namver, Wei Wang, Kwongming Tse, Qilin Yu, Shaktivesh, Azadeh Kian. I am truly privileged to have you on my side, and you have all played such an important role in my life. Thanks also to Shanyuanye Guan, Dale Robinson, Wei Gu, and Wen Wu, for all your assistance and knowledgable insight into my study.

I am eternally indebted to my parents, Xiaofang Zhang and Yazhen Weng, for your endless love and enduring support. For me being thousands of miles away from home for so many years, I know it must be hard for you. I thank you wholeheartedly, for giving me the strength and courage to pursue my dreams. I would also like to thank my girlfriend, Shan Xu, for your love, care, and companion during the difficult times in the year 2020. You brightened my life.

Contents

List of Figures **xvii**

List of Tables **xxvi**

List of Abbreviations **xxxi**

1 Background **1**

1.1 Anatomy of the Wrist . . . 3

1.1.1 Osseous Anatomy . . . 4

1.1.1.1 Distal Radius and Ulna . . . 4

1.1.1.2 Proximal Carpal Row . . . 5

1.1.1.3 Distal Carpal Row . . . 7

1.1.2 Ligamentous Anatomy . . . 11

1.1.2.1 Extrinsic Ligaments . . . 12

1.1.2.2 Intrinsic Ligaments . . . 15

1.1.3 Musculature . . . 22

1.2 Motion of the Wrist . . . 28

1.2.1 Definition of the Joint Coordinate Systems . . . 30

1.2.1.1 Global Wrist . . . 30

1.2.1.2 Carpal Bones . . . 34

1.2.2 Range of Global Wrist Motion . . . 34

1.3 Biomechanics of the Wrist . . . 37

1.3.1 Carpal Kinematics . . . 37

1.3.2 Theories of Carpal Motion 40
1.3.3 Carpal Contact Characteristics 45
1.4 SLIL Injury and Scapholunate Instability 51
1.4.1 Overview 51
1.4.2 Clinical Classification 52
1.4.3 Effect on Carpal Kinematics 56
1.4.4 Effect on Carpal Contact 67
1.4.5 Management of Scapholunate Instability 71
1.4.5.1 Diagnosis 71
1.4.5.2 Treatment Options 75
1.5 Experimental Methods Employed For Studying Wrist Biomechanics 92
1.5.0.1 *In-vitro* Wrist Simulation 92
1.5.0.2 Techniques Used to Study Carpal Kinematics 100
1.5.0.3 Techniques Used to Characterise Articular Contact 109

2 Cadaveric Wrist Testing Platform 119
2.1 Introduction 120
2.2 Dynamic Wrist Simulation Apparatus 123
2.2.1 Structural Design 123
2.2.1.1 Apparatus Framework 123
2.2.1.2 Forearm Mounting Fixture 125
2.2.1.3 Tendon-Actuator Connection 128
2.2.2 Electromechanical Design 131
2.2.2.1 Wrist Position Measurement System 131
2.2.2.2 Tendon Force Measurement System 139
2.2.2.3 Motion Synthesis System 141
2.2.3 Motion Control Algorithm 145
2.2.4 Software Implementation 159

2.3 Subsidiary Measurement Systems . . . 163
2.3.1 Biplane X-ray Fluoroscopy System . . . 163
2.3.1.1 Hardware Setup . . . 164
2.3.1.2 Software and Control System . . . 168
2.3.2 Marker-Based Kinematic Analysis . . . 173
2.3.3 Pressure Measurement System . . . 183
2.3.3.1 Synchronisation . . . 184
2.4 Summary . . . 186

3 Validation of the Testing Apparatuses 191
3.1 Introduction . . . 192
3.2 Validation of the DWSA . . . 193
3.2.1 Global Wrist Motion . . . 197
3.2.2 Muscle Forces . . . 207
3.3 Validation of the Biplane X-Ray Fluoroscopy System . . . 217
3.3.1 Inter-Marker Distances . . . 219
3.3.2 Rigid Body Kinematics . . . 225
3.4 Joint System Validation of the CWTP . . . 233
3.5 Summary . . . 239

4 Wrist Biomechanics 241
4.1 Carpal Kinematics . . . 242
4.1.1 Materials and Methods . . . 243
4.1.1.1 Specimen Acquisition . . . 243
4.1.1.2 Specimen Preparation . . . 244
4.1.1.3 System Calibration and Preparation . . . 251
4.1.1.4 Testing Protocol and Data Collection . . . 254
4.1.1.5 Sequential Ligament Resection . . . 256
4.1.1.6 Scapholunate Ligament Reconstruction . . . 260
4.1.1.7 Data Analysis . . . 265

4.1.2 Results . . . 267
4.1.2.1 Normal Carpal Kinematics . . . 267
4.1.2.2 Carpal Pathokinematics Following Ligament Resection . . . 276
4.1.2.3 Carpal Kinematics Following Reconstructive Surgery . . . 304
4.1.3 Discussion . . . 310
4.1.3.1 Normal Carpal Kinematics . . . 310
4.1.3.2 Carpal Pathokinematics . . . 327
4.1.3.3 Carpal Kinematics Following Reconstructive Surgery . . . 346
4.1.3.4 Limitation . . . 356
4.2 Radiocarpal Contacts . . . 361
4.2.1 Materials and Methods . . . 362
4.2.1.1 Pressure Sensor Measurement . . . 362
4.2.1.2 Joint Proximity Measurement . . . 368
4.2.2 Results and Discussion . . . 372

5 Conclusions **399**

References **464**

Appendices **469**

A Specifications of Key Components Comprising the CWTP **469**
A.1 Vicon Motion Capture Camera . . . 470
A.2 Uniaxial Load Cell . . . 471
A.3 Analogue Data Acquisition Device . . . 472
A.4 Stepper Motor . . . 480
A.5 Motor Drive . . . 482
A.6 Motion Controller . . . 484
A.7 C-arm Fluoroscopy Units . . . 488

A.8 Machine Vision Camera 490
A.9 C-mount Lenses 492
A.10 Tekscan Pressure Mapping System 494
A.11 Validation Plate 496

B Intercarpal Kinematics **497**
B.1 Normal Physiological Wrist 498
B.2 After Ligament Divisions and Reconstructive Surgeries 501

List of Figures

1.1 Bones and joints comprising the wrist . . . 3
1.2 Ulnar and volar tilt of the distal radius . . . 4
1.3 Anatomy of the radiocarpal joint . . . 5
1.4 Anatomy of the midcarpal joint . . . 8
1.5 Photograph showing the helicoidal articular surface of the hamate . . . 10
1.6 Architecture of the extrinsic ligaments of the wrist. . . . 12
1.7 Extrinsic ligaments of the wrist . . . 13
1.8 Architecture of the intrinsic ligaments of the wrist. . . . 16
1.9 Intrinsic ligaments of the wrist . . . 17
1.10 The scapholunate interosseous ligament. . . . 19
1.11 "Scissoring" of the dorsal ligamentous "V" during global wrist flexion and extension. . . . 21
1.12 Muscles of the wrist. . . . 23
1.13 Relative positions and moment arms of the wrist muscles. . . . 24
1.14 Schematics showing two primary degrees of freedom of wrist motion. . . . 28
1.15 Pronation-supination of the forearm. . . . 29
1.16 Schematics of wrist circumduction and dart-thrower's motion . 29
1.17 Schematics of a right radius with its local coordinate system defined . . . 31
1.18 Schematics of a right third metacarpal with its local coordinate system defined . . . 33

1.19 An example showing the definition of the carpal bone coordinate systems. 35
1.20 Scaphoid hypothesised as the key in preventing a "zigzag" collapse of the carpus 41
1.21 The column theory 42
1.22 The oval-ring theory 43
1.23 Progressive stages of SLAC 55
1.24 Watson's scaphoid shift test 71
1.25 An example of the radiographic presentations of scapholunate dissociation 73
1.26 Imaginary axes and tangents drawn to evaluate carpal alignment 74
1.27 Direct repair of the SLIL. 75
1.28 Schematics of Blatt dorsal capsulodesis. 77
1.29 Various tenodesis techniques described previously in the literature 81
1.30 Schematics of the scapholunate axis method described by Lee et al. (2014). 83
1.31 Schematics of the arthroscopic ligamentoplasty described by Corella et al. (2013). 84
1.32 Schematics of the "dynodesis" and the RASL techniques . . . 85
1.33 Scaphocapitate and scaphotrapeziotrapezoid arthrodeses . . . 88
1.34 An illustration and a case example of the RSL arthrodesis technique 88
1.35 Schematics and case example of a proximal row carpectomy performed in concert with a radial styloidectomy 89
1.36 Four-corner fusion performed in concert with a scaphoidectomy 90
1.37 An example of total wrist arthroplasty 91
1.38 An example of total wrist fusion 91
1.39 An example of the motion constraining apparatus used for passive wrist simulations 93
1.40 Passive wrist simulation facilitated by a Stuart platform . . . 94
1.41 Static wrist testing apparatus developed at Mayo Clinic 95

1.42 Dynamic wrist motion simulator originally developed by Tong (1985) and later improved by Werner et al. (1996) 97

1.43 Dynamic wrist simulator developed by Iglesias (2015) 99

1.44 An experimental setup where sonic digitisers were employed in concert with a motion constraining device to study wrist kinematics 101

1.45 An experimental setup where electromagnetic motion trackers were employed to study carpal kinematics 102

1.46 Various types of electromagnetic motion tracking sensors . . . 103

1.47 An experimental setup in which a video motion capture system was used to track the hand and wrist movement of a pianist during music performance. 104

1.48 An experimental setup developed to take biplanar radiographs of cadaveric wrist specimens 106

1.49 An example experimental setup used in CT-based *in-vivo* carpal kinematics studies 108

1.50 An experimental setup where load cells were used to measure the forces transmitted by the radius and ulna 109

1.51 Working principle and application of Fuji Pressure-sensitive films 110

1.52 Schematics showing the construction of a Tekscan pressure sensor 113

1.53 General principle of the RBSM 117

2.1 Photograph of the Cadaveric Wrist Testing Platform 122

2.2 CAD model of DWSA's structural framework 124

2.3 Rotation mechanism of the DWSA. 125

2.4 CAD model of the forearm mounting fixture 126

2.5 Photograph of a dissected cadaveric wrist specimen with its muscle tendons trapped using custom-made wire-woven sleeves 128

2.6 CAD model of the DWSA featuring the primary and secondary pulley systems 129

2.7 Photograph of the Vicon video motion capture system 132

2.8 An example demonstrating the use of Vicon DataStream SDK 134
2.9 A screenshot showing spheres being fitted by Geomagic to models of the retro-reflective markers. 135
2.10 Schematics visualising the flexion-extension angle, α, and the radial-ulnar deviation angle, β 137
2.11 Schematics visualising the pronation-supination angle, γ. . . . 138
2.12 Mechanical connection of the uniaxial load cell 139
2.13 Photograph of two bridge input modules and the carrier chassis 140
2.14 CAD model of the stepper motor and its adjustable mounting 141
2.15 Photograph of the electrical cabinet 144
2.16 Control architecture of the DWSA 148
2.17 An example of the trajectories used in simulating wrist DTM . 150
2.18 Schematics showing the distal insertion and proximal passage sites identified for each muscle tendon 155
2.19 Schematic drawing of the force control problem 157
2.20 LabVIEW block diagram of DWSA's main control VI 161
2.21 Front panel GUI of the DWSA's LabVIEW control console . . 162
2.22 Beam configuration of the two C-arm X-ray fluoroscopy units . 164
2.23 An example of the biplanar radiographs taken by the two C-arm units 165
2.24 Photograph and exploded CAD model of the camera assembly 166
2.25 Timing chart of the image acquisition process 168
2.26 USB development board used to generate the pulse signal . . . 169
2.27 Custom X-ray Exposure control console 170
2.28 Front panel of the top-level LabVIEW VI 172
2.29 Distortion correction grids being mounted next to the XRIIs of the two C-arm fluoroscopy units 174
2.30 Original and distortion corrected radiograph of the grid 175
2.31 Calibration phantom manufactured for the biplane fluoroscopy system 176

2.32 Matlab program developed for digitising and tracking the radio-opaque markers . . . 178
2.33 A simple illustration of the triangulation process . . . 179
2.34 Photograph of the I-scan pressure measurement system . . . 183
2.35 Signal pathway of the CWTP . . . 189

3.1 Examples showing the small position control error achieved in simulating wrist FEM and DTM . . . 197
3.2 An example of the DTM trajectory being plotted in the FEM-RUD plane . . . 198
3.3 An example showing the angular discrepancy, ϵ, between the reference and the actual directions of the 3MC during simulated wrist DTM . . . 199
3.4 An example of the control time delay, δt, exhibited by the DWSA during dynamic wrist simulation. . . . 199
3.5 An example of normalising time into % Movement Cycle . . . 200
3.6 An example of the repeatability assessment, the raw data points and the 95% confidence interval were plotted (insect) to show the scattering of the position control performance between different cycles . . . 201
3.7 RMS position control error achieved in seven cadaveric wrist specimens . . . 204
3.8 Average total muscle forces recorded during FEM, RUD and DTM for seven cadaveric wrist specimens . . . 209
3.9 Percentage contribution of individual muscles during dynamic wrist motion simulations performed in seven wrists before and after ligament disruptions . . . 214
3.10 Schematics illustrating the marker triangulation process and the concept of inter-marker distance . . . 219
3.11 Photograph of the validation plate and CAD model of the validation gimbal . . . 220
3.12 Sample radiographs of the validation plate and gimbal assembly 221
3.13 Histograms of the inter-marker distance errors recorded for each cadaver . . . 223

3.14 A GMM being fitted to the combined error histogram 226
3.15 Schematics of the mock-up wrist model used in the simulation 227
3.16 Process flow of the computer simulation 228
3.17 Histogram of the errors in estimating the rotational and translational rigid body kinematics 231
3.18 An example of the carpal bone motion repeatability. Unfiltered carpal bone kinematics, recorded during three consecutive cycles of DTM of a single specimen, was wrapped and normalised to 0 to 100% of movement cycle and plotted together. The 95% confidence interval were also plotted for each kinematic parameter to show their scattering. 235

4.1 An example of the plain radiograph taken for one of the cadaveric wrist specimens 244
4.2 Photograph showing the tendon of ECR-B being split along the fibres. The resultant tendon strip was necessary for later SL reconstructions. 245
4.3 Schematics of the ligament-sparing dorsal capsulotomy developed by Berger et al. (1995) 247
4.4 Photograph of a dissected and prepared cadaveric wrist specimen before CT scan. The specimen was not yet cemented to the metallic potting block at this stage to avoid significant artifact under CT. 248
4.5 Photograph of a cadaveric wrist specimen mounted to the DWSA 250
4.6 An example of the "calibrated" CT data 253
4.7 Sequence and designated stages of ligament severing 257
4.8 Schematics of the novel dorsal transarticular loop tenodesis procedure 261
4.9 Schematics of the three-ligament tenodesis procedure 263
4.10 An example of different data visualisation incorporated to assist interpretation 277
4.11 Scaphoid kinematics (w.r.t the radius) measured during FEM following incremental ligament resections and two reconstructive surgeries 279

4.12 Scaphoid kinematics (w.r.t the radius) measured during RUD following incremental ligament resections and two reconstructive surgeries . . . 280

4.13 Scaphoid kinematics (w.r.t the radius) measured during DTM following incremental ligament resections and two reconstructive surgeries . . . 281

4.14 Lunate kinematics (w.r.t the radius) measured during FEM following incremental ligament resections and two reconstructive surgeries . . . 282

4.15 Lunate kinematics (w.r.t the radius) measured during RUD following incremental ligament resections and two reconstructive surgeries . . . 283

4.16 Lunate kinematics (w.r.t the radius) measured during DTM following incremental ligament resections and two reconstructive surgeries . . . 284

4.17 Capitate kinematics (w.r.t the radius) measured during FEM following incremental ligament resections and two reconstructive surgeries . . . 285

4.18 Capitate kinematics (w.r.t the radius) measured during RUD following incremental ligament resections and two reconstructive surgeries . . . 286

4.19 Capitate kinematics (w.r.t the radius) measured during DTM following incremental ligament resections and two reconstructive surgeries . . . 287

4.20 Dynamic rotation exhibited by the Scaphoid and Lunate in the sagittal plane during global wrist FEM . . . 336

4.21 Dynamic rotation exhibited by the scaphoid in the sagittal plane during global wrist RUD . . . 337

4.22 Recruitment of the RSC and LRL ligaments during wrist ulnar deviation and extension . . . 339

4.23 Dynamic rotation exhibited by the lunate in the sagittal plane during wrist RUD and FEM . . . 341

4.24 Recruitment of the DRC and DIC ligaments during wrist ulnar flexion . . . 343

4.25 Dynamic rotation exhibited by the scaphoid in the coronal plane and the sagittal plane during wrist RUD 344

4.26 Dynamic rotation exhibited by the scaphoid in the sagittal plane during wrist RUD following the DTLT and the 3LT procedures. 349

4.27 Photograph of an unprepared Tekscan Medical 4000 pressure sensor 363

4.28 Calibration of the pressure sensor 364

4.29 An example of the calibration curve and the resultant calibration error 365

4.30 Photograph of a prepared pressure sensor 366

4.31 Photograph showing the pressure sensor being anchored to three screws drilled volarly into the radius and ulna 367

4.32 Precise location of the pressure sensor was found using CT scan 367

4.33 Bone surface models used for joint proximity calculation . . . 368

4.34 Schematics showing the proximity calculation process for one facet located on the distal radius 369

4.35 Maps showing joint proximities and pressure measurements at wrist neutral position 378

4.36 Maps showing joint proximities and pressure measurements at wrist neutral position (continued). 379

4.37 Maps showing joint proximities and pressure measurements at 30 degrees of global wrist flexion 380

4.38 Maps showing joint proximities and pressure measurements at 30 degrees of global wrist flexion (continued) 381

4.39 Maps showing joint proximities and pressure measurements at 30 degrees of global wrist extension 382

4.40 Maps showing joint proximities and pressure measurements at 30 degrees of global wrist extension (continued) 383

4.41 Maps showing joint proximities and pressure measurements at 20 degrees of global wrist ulnar deviation 384

4.42 Maps showing joint proximities and pressure measurements at 20 degrees of global wrist ulnar deviation (continued) 385

4.43 Maps showing joint proximities and pressure measurements at 20 degrees of global wrist radial deviation 386

4.44 Maps showing joint proximities and pressure measurements at 20 degrees of global wrist radial deviation (continued) 387

4.45 Maps showing joint proximities and pressure measurements at 30 degrees of global wrist flexion combined with 20 degrees of wrist ulnar deviation 388

4.46 Maps showing joint proximities and pressure measurements at 30 degrees of global wrist flexion combined with 20 degrees of wrist ulnar deviation (continued) 389

4.47 Maps showing joint proximities and pressure measurements at 30 degrees of global wrist extension combined with 20 degrees of wrist radial deviation 390

4.48 Maps showing joint proximities and pressure measurements at 30 degrees of global wrist extension combined with 20 degrees of wrist radial deviation (continued) 391

4.49 Photograph of a Tekscan Model 6900 pressure sensor with three of its measuring figures being taped together. 394

5.1 Pilot studies concerning other surgical methods 412

B.1 Scaphoid kinematics (w.r.t the Lunate) measured during FEM following incremental ligament resection and two different SLIL reconstructions. 502

B.2 Scaphoid kinematics (w.r.t the Lunate) measured during RUD following incremental ligament resection and two different SLIL reconstructions. 503

B.3 Scaphoid kinematics (w.r.t the Lunate) measured during DTM following incremental ligament resection and two different SLIL reconstructions. 504

B.4 Capitate kinematics (w.r.t the Lunate) measured during FEM following incremental ligament resection and two different SLIL reconstructions. 505

B.5 Capitate kinematics (w.r.t the Lunate) measured during RUD following incremental ligament resection and two different SLIL reconstructions. 506

B.6 Capitate kinematics (w.r.t the Lunate) measured during DTM following incremental ligament resection and two different SLIL reconstructions. 507

List of Tables

1.1 Extreme range of global wrist motion 34

1.2 Functional range of global wrist motion 36

1.3 Summary of previously reported force transmission ratios in different regions of the radioulnocarpal joint, when the wrist is placed in its neutral position 47

1.4 Summary of previously reported peak articular pressures in different regions of the radioulnocarpal joint, when the wrist is placed in its neutral position 48

1.5 Percentage change in articular contact pressure at different wrist positions 50

1.6 Geissler arthroscopic grades of scapholunate interosseous ligament injuries with suggested management options 52

1.7 Stages of scapholunate instability 54

1.8 Summary of literature on the effect induced by disruptions to various scapholunate supporting ligaments on kinematics or static alignments of the carpus 57

1.9 A review on the retrospective follow-up/prospective cohort studies conducted for various modifications of the Brunelli's tenodesis technique in treating both the dynamic and static scapholunate instabilities 80

3.1 Position control accuracy achieved by the DWSA on cadaveric wrist specimens in both healthy and injured state during three different types wrist motion simulations 205

3.2 Time delay of the DWSA's position control, calculated for all three types of motion simulations performed in both healthy and ligament deficient cadaveric wrist specimens 205

3.3 Position control repeatability achieved by the DWSA during three different types wrist motion simulations in cadaveric wrist specimens before and after ligament disruptions 206

3.4 Combined force control accuracy (average deviation from Λ) achieved by the DWSA in both healthy and ligament deficient cadaveric wrist specimens 208

3.5 Repeatability achieved for controlling the force in each wrist muscles for cadaveric wrist specimens in both healthy and injured states, during all three types of wrist motion simulations 212

3.6 Accuracy and precision of the present biplane fluoroscopy system as characterised by the *in-situ* and stand-alone validation experiments 224

3.7 Carpal bone level kinematic repeatability achieved by the DWSA in both healthy and ligament deficient cadaveric wrist specimens 238

4.1 Information on the human cadavers used in the present study 243

4.2 Stages of the incremental resection of the SL supporting ligaments 256

4.3 Mean and standard deviation of the scaphoid kinematics measured relative to the radius 273

4.4 Mean and standard deviation of the lunate kinematics measured relative to the radius 274

4.5 Mean and standard deviation of the capitate kinematics measured relative to the radius 275

4.6 Carpal kinematics measured during global wrist flexion and extension compared with the values reported previously by a selection of studies 316

4.7 Results of the present thesis compared with those previously reported in the literature values for radiocarpal and scapholunate angles, and percentage contribution of the radioscaphoid, radiolunate and capitolunate articulation in the sagittal plane during global wrist flexion and extension 318

4.8 Carpal kinematics measured during global wrist radial and ulnar deviation compared with the values reported previously by a selection of studies 321

4.9 Results of the present thesis compared with those previously reported in the literature for radiocarpal and scapholunate angles, and percentage contribution of the radioscaphoid, radiolunate and capitolunate articulation in the sagittal plane during global wrist radial and ulnar deviation 323

4.10 Angular attitude of the scaphoid and lunate at neutral wrist position, flexion of 30°, and extension of 20°, reported in the present study and compared with data in the literature 335

4.11 Angular attitude of the scaphoid and lunate at ulnar deviation of 15° and radial deviation of 5°, reported in the present study and compared with data in the literature 335

B.1 Mean and standard deviation of the scaphoid kinematics measured relative to the lunate 499

B.2 Mean and standard deviation of the capitate kinematics measured relative to the lunate 500

List of Abbreviations

3LT . . . . . three-ligament tenodesis
4CF . . . . . four-corner fusion
ACL . . . . . anterior cruciate ligament
ADC . . . . . analogue-to-digital converter
AP . . . . . anteroposterior
APL . . . . . abductor pollicis longus
BC . . . . . Blatt's capsulodesis
CH . . . . . capitohamate
CMM . . . . . coordinate measurement machine
CNC . . . . . computer-numerical-control
CRPS . . . . . complex regional pain syndrome
CT . . . . . computed tomography
CWTP . . . . . cadaveric wrist testing platform
DIC . . . . . dorsal intercarpal
DISI . . . . . dorsal intercalated segment instability
DJD . . . . . degenerative joint disease
DOF . . . . . degree-of-freedom
DTLT . . . . . dorsal transarticular loop tenodesis
DTM . . . . . dart thrower's motion
DWSA . . . . . dynamic wrist simulation apparatus
ECR-B . . . . . extensor carpi radialis brevis
ECR-L . . . . . extensor carpi radialis longus
ECU . . . . . extensor carpi ulnaris
EMG . . . . . electromyography
EMI . . . . . electromagnetic interference
EPB . . . . . extensor pollicis brevis
FCR . . . . . flexor carpi radialis

FCU . . . . . flexor carpi ulnaris
FEM . . . . . flexion-extension motion
FIFO . . . . . first-in-first-out
FOOSH . . . . . fall on an outstretched hand
GPIO . . . . . general-purpose input/output
GPO . . . . . general power outlets
GUI . . . . . graphical user interface
ISB . . . . . International Society of Biomechanics
IWIW . . . . . International Wrist Investigators Workshop
JCS . . . . . joint coordinate system
LCS . . . . . local coordinate system
LRL . . . . . long Radiolunate
LTIL . . . . . lunotriquetral interosseous ligament
MBT . . . . . modified Brunelli tenodesis
MRAC . . . . . Model Reference Adaptive Control
NP . . . . . normal physiological
PA . . . . . posteroanterior
PCSA . . . . . physiological cross-sectional area
PD . . . . . proportional-derivative
PID . . . . . proportionalintegralderivative
PRC . . . . . proximal row carpectomy
PV . . . . . position-velocity
PVA . . . . . position-velocity-acceleration
RASL . . . . . reduction and association of the scaphoid and lunate
RBSM . . . . . rigid body spring modelling
RMS . . . . . root-mean-squared
ROM . . . . . range of motion
RSA . . . . . Röentgen stereo-photogrammetry analysis
RSC . . . . . radioscaphocapitate
RSL . . . . . radioscapholunate
RUD . . . . . radial-ulnar deviation
SC . . . . . scaphocapitate
SDK . . . . . software development kit
SL . . . . . scapholunate

SLAC . . . . . scapholunate advanced collapse
SLAM . . . . . scapholunate axis method
SLIL . . . . . scapholunate interosseous ligament
SLTT . . . . . scapholunotriquetral tenodesis
SRL . . . . . short Radiolunate
STT . . . . . scaphotrapeziotrapezoid
SVD . . . . . singular value decomposition
TC . . . . . triquetrocapitate
TFCC . . . . . triangular fibrocartilage complex
TH . . . . . triquetrohamate
TT . . . . . triquetrohamate
UC . . . . . ulnocapitate
UL . . . . . ulnolunate
UT . . . . . ulnotriquetral
VAS . . . . . Visual Analogue Score
VI . . . . . virtual instrument
VISI . . . . . volar intercalated segment instability
XRII . . . . . X-ray image intensifier

1

Background

Contents

1.1 Anatomy of the Wrist 3
1.1.1 Osseous Anatomy 4
1.1.2 Ligamentous Anatomy 11
1.1.3 Musculature 22
1.2 Motion of the Wrist 28
1.2.1 Definition of the Joint Coordinate Systems 30
1.2.2 Range of Global Wrist Motion 34
1.3 Biomechanics of the Wrist 37
1.3.1 Carpal Kinematics 37
1.3.2 Theories of Carpal Motion 40
1.3.3 Carpal Contact Characteristics 45
1.4 SLIL Injury and Scapholunate Instability 51
1.4.1 Overview 51
1.4.2 Clinical Classification 52
1.4.3 Effect on Carpal Kinematics 56
1.4.4 Effect on Carpal Contact 67
1.4.5 Management of Scapholunate Instability 71
1.5 Experimental Methods Employed For Studying Wrist Biomechanics 92

This chapter provides a brief background of this dissertation. This includes the anatomy and biomechanics of the wrist, the pathophysiology of the destabilising SLIL injury, and the surgical measures currently employed to manage this type of injury. Previous studies concerning both the normal and the pathological wrist biomechanics are reviewed. Furthermore, experimental methods used to investigate the carpal kinematics and joint contact characteristics are also briefly surveyed.

1.1 Anatomy of the Wrist

The wrist, as a result of million years of evolutionary adaptation, is arguably the most sophisticated "joint" in the human body, empowering human beings with flexibility and stability in use of their hands. However, it is rather imprecise to simply depict the wrist as one of those joints in conventional terms, as it is composed by a collection of articulations formed by its bony constituents. And the macroscopic wrist motion is really the net result of the interactions happening between these articulations, guided by an intricate network of soft-tissue constraints.

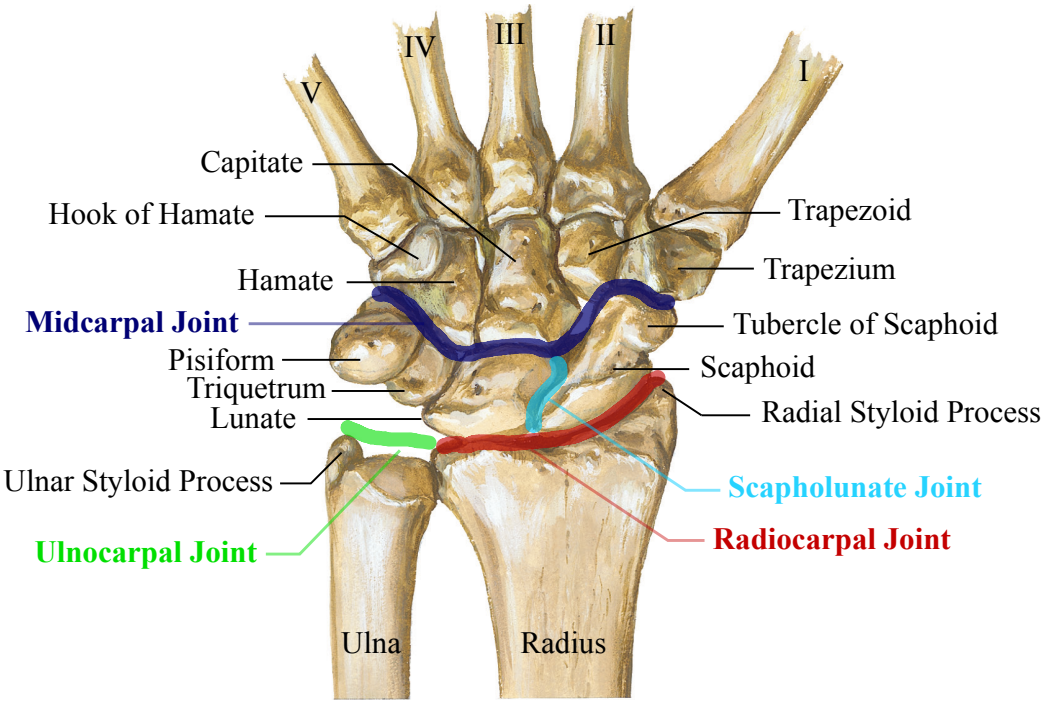

Figure 1.1: Bones and joints comprising the wrist. The scapholunate joint is shown as an example of the intercarpal joint of the wrist. Modified from Netter (2014), with permission from Elsevier.

From a anatomical-functional stand point, the wrist (Fig. 1.1) is considered to be primarily comprised of the radiocarpal and the midcarpal joints (Austin, 2005). The distal radioulnar joint, despite its presence in the proximity and its functional involvement in the wrist motion, is commonly re-

garded as a part of the forearm rather than a constituent articulation of the wrist complex (Hagert, 1992; Souza, 2001). While the articulation formed between adjacent carpal bones is usually termed as the intercarpal joint. The articulation formed between the scaphoid and lunate, or the scapholunate joint, is a typical example of the intercarpal joints of the wrist.

1.1.1 Osseous Anatomy

The osseous structures comprising the wrist complex are the eight irregularly shaped and interlocking carpal bones, distributed between the distal ends of both the radius and ulna and the bases of the metacarpals.

1.1.1.1 Distal Radius and Ulna

The concave articulating surfaces of the distal radius presents an ulnar inclination of 15 to 25 degrees (Fig. 1.2A), and has a volar tilt of 10 to 15 degrees (Fig. 1.2B) (Berger, 1996a). It is partitioned sagittally into two fossae to accept the scaphoid and lunate by a fibro-cartilaginous ridge, known as the interfacet prominence (Fig. 1.3a).

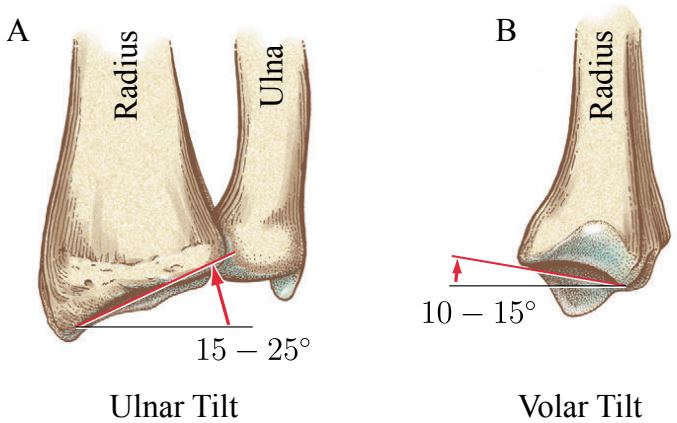

Figure 1.2: **(A)** Anterior view and **(B)** medial view of the distal radius and ulna, showing the ulnar and the volar tilt of the distal radius. Adapted from Neumann (2010), with permission from Elsevier.

The distal ulna, however, does not articulate directly with the carpus, but through a collection of ligamentous and cartilaginous structures known as the triangular fibrocartilage complex (TFCC). The TFCC is found to arise from the ulnar aspect of the lunate fossa and span ulnarward to insert onto the ulnar styloid process (Fig. 1.3b). It is believed to provide support and cushions the lunate and triquetrum, and its appearance in substitution of an ulnocarpal articulation is postulated to have allowed brachiation and ultimately promoted the development of the hand (Palmer and Werner, 1981).

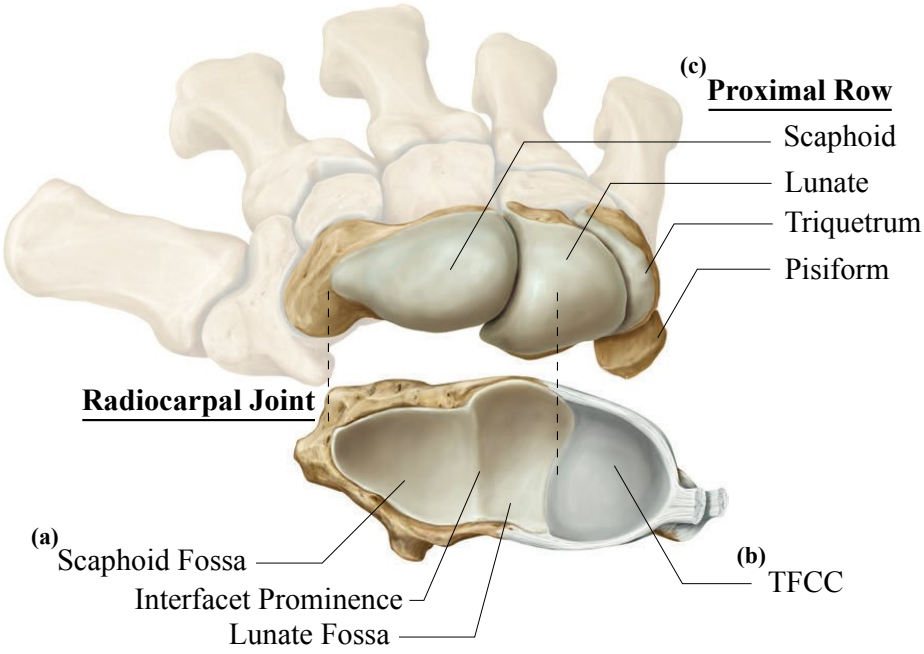

Figure 1.3: Anatomy of the radiocarpal joint, with the articular surfaces of the distal radius and ulnar (lower) viewed distally, and those formed collectively by the proximal carpal row (upper) viewed proximally. Adapted from Schünke et al. (2006), with permission from Thime.

1.1.1.2 Proximal Carpal Row

Based on their proximity to the distal radius and ulna, the eight small carpal bones are often grouped anatomically into two rows, namely the proximal

and the distal carpal rows. Starting from the radial side, the proximal carpal row incorporates the scaphoid, lunate, triquetrum and pisiform (Fig. 1.3c). Together with the distal radius and the TFCC, they form the articulation of the radiocarpal and the ulnocarpal joint. Furthermore, except for the insertion of the flexor carpi ulnaris on the pisiform, the proximal row is lack of any direct tendinous attachments, and is therefore commonly referred to as the "intercalated segment" between the distal radius and the distal carpal row (Taleisnik, 1988; Gould et al., 2015).

Scaphoid

The scaphoid bone has a boat-like shape and is the second largest carpal bone in the wrist complex. It can be visually partitioned into three regions, namely the proximal pole, the waist and the distal pole. It interposes between the distal radius and the trapezium with a large convex and dorsally extending radial facet for articulating with the radius proximally and a convex distal pole for the trapezium and trapezoid. On the palmar surface near the distal pole, a round bony projection to which the transverse flexor retinaculum is attached, can be readily identified and is commonly referred as the scaphoid tuberosity (Berger, 2010). The scaphoid articulates with the neighbouring lunate with a flat semilunar medial facet, while interfacing with the distally and medially situated capitate with the large concavity at its waist.

Lunate

As the name suggest, the shape of the lunate resembles a crescent moon. It has a convex proximal facet for articulating with the radius and a distal concavity for interlocking with the head of the capitate. In the mediolateral direction, the lunate has a triangular proximomedial facet for interfacing with the triquetrum and a semilunar proximolateral facet for articulating with the neighbouring scaphoid.

Triquetrum

The pyramidal-shaped triquetrum is the most medially located bone in the proximal carpal row. Palmarly, it articulates with the pisiform through a flat oval-shaped palmar facet and radially with the lunate through a square radial facet. Distally, it articulates with the hamate with a uniquely concavo-convex distal facet, which, according to previous studies, has been described as spiral or helicoidal in shape (Taleisnik, 1976; Weber, 1984; Berger, 1996a). By virtue of this contact geometry, the triquetrum-hamate joint is believed to exhibit a "screw-like" rotatory engagement during wrist ulnar deviation, directing the triquetrum to rotate into an extended and volarly translated posture (Kauer, 1986). However, the role and kinematic implication of such a joint configuration is still under debated (Moritomo et al., 2003), and the discussion will be expanded in later sections.

Pisiform

The pea-shaped pisiform is the smallest carpal bone and only articulates with the triquetrum through its flat and slightly elevated dorsal facet. As it is often found to be completely enveloped by the fibres of the abductor digiti minimi and the tendinous insertion of the flexor carpi ulnaris (FCU) (Pevny et al., 1995), it is considered more of a sesamoid bone that enhances the moment arm of the FCU than functionally as a part of the proximal carpal row (Youm et al., 1978; Volz et al., 1980; Panchal-Kildare and Malone, 2013). Furthermore, the pisiform also provides the medial attachment for the flexor retinaculum (Berger, 2010).

1.1.1.3 Distal Carpal Row

The distal carpal row, on the other hand, is comprised of the trapezium, trapezoid, capitate and hamate. Distally, it articulates with the bases of the five metacarpals, forming the carpometacarpal joint. Proximally, it articulates with the proximal carpal row, forming the midcarpal joint. The

midcarpal joint can be divided descriptively into medial and lateral joint compartments (Fig. 1.4). The medial compartment is composed by the convexity of the head of the capitate and the apex of the hamate combined and the deep concave recess formed collectively by the distal articular surfaces of the scaphoid, lunate and triquetrum (Fig. 1.4a). The smaller lateral compartment is formed between the distal pole of the scaphoid proximally and the concavity of the trapezium and trapezoid distally (Fig. 1.4b).

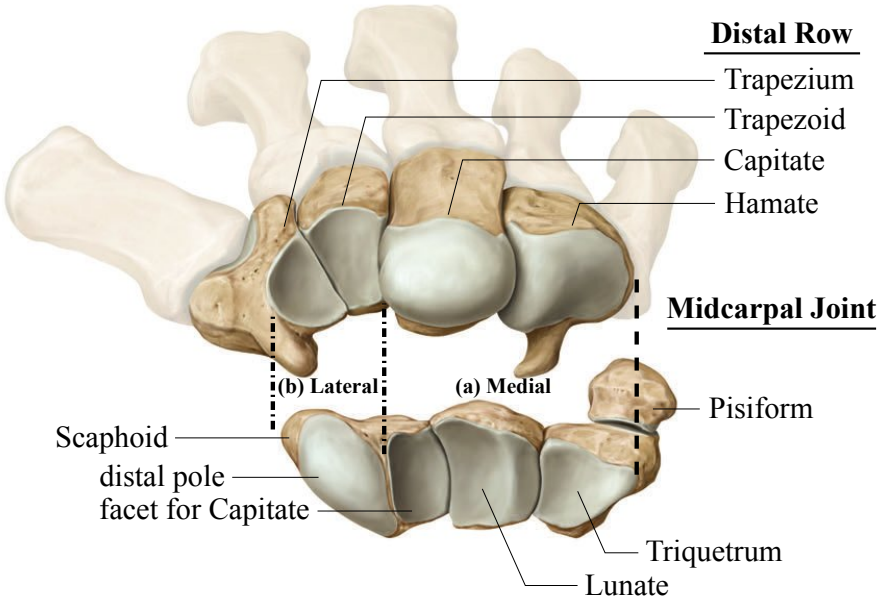

Figure 1.4: Anatomy of the midcarpal joint, showing both its (a) medial and (b) lateral compartments. The distal articular surface formed collectively by the proximal carpal row (lower) is viewed distally and the proximal articular surface formed collectively by the distal carpal row (upper) is viewed proximally. Adapted from Schünke et al. (2006), with permission from Thime.

Trapezium

The trapezium is an irregularly shaped and the most laterally situated carpal bone within the distal carpal row. It has a saddle-shaped distal surface for

interfacing with the first metacarpal and a slightly concave facet for articulating with the distal scaphoid. On the palmar side of the trapezium, a proximodistally elongated crest known as the trapezial ridge, provides an attachment site for the flexor retinaculum (White et al., 2012). The trapezial groove, which is located just medial to the trapezial ridge, allows passage of the tendon of the flexor carpi radialis (FCR) (Bishop et al., 1994).

Trapezoid

The trapezoid is the smallest bone in the distal carpal row and bears a faint resemblance to a boot. Its triangular distal facet enables the articulation with the second metacarpal, while the other three, from medial to lateral, facilitate the articulation with the neighbouring capitate, scaphoid and trapezium.

Capitate

The capitate is the largest carpal bone that occupies the centre of the carpus. As the name suggests, its prominent proximal surface is rounded and largely convex, known as the head of the capitate. Proximally, it fits comfortably into the deep recess formed by the scaphoid and lunate. Distally, it articulates primarily with the base of the third metacarpal, but is also found to be in contact with the second and forth metacarpals at the slightly angled lateral and medial edges of its distal facet. Furthermore, in contrast to the head of the capitate, which is covered entirely by cartilage and free of any ligamentous attachments, both the palmar and dorsal body of the capitate is completely embedded within the surrounding soft-tissue structures.

Hamate

The hamate is a wedge-shaped bone that bears a hamulus or a hook-like projection on its palmar surface. Its location defines the ulnar boundary of the distal carpal row. Similar to that of the capitate, the proximal pole of the hamate is entirely covered with articular cartilage, but with the hamulus

completely buried within the surrounding ligamentous attachments (Berger, 1996a). At the apex of the hamulus, the flexor retinaculum is attached, completing its four attachment sites within the carpus (Cobb et al., 1993). Its distal surface is separated by a faint anteroposterior ridge into two facets for articulating with the bases of the fourth and fifth metacarpals. It narrows proximally to become "wedged" into a space enclosed mediolaterally by the triquetrum and capitate and proximally by the lunate. Medially, its articular surface is concordant with that of the triquetrum, forming a helicoidal joint. Laterally, it articulate with the capitate through an elongated and flattened lateral facet. Proximally, the hamate articulates with the lunate in wrist ulnar deviation via a narrow facet borne by its convex margin (Standring and Gray, 2008).

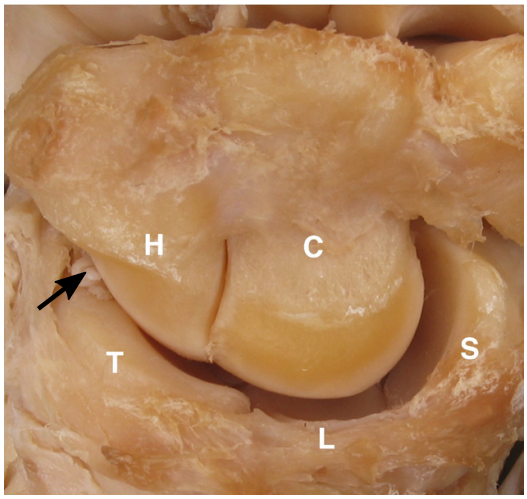

Figure 1.5: Photograph of a specimen with its midcarpal joint dissected, showing the helicoidal articular surface of the hamate (black arrow). H, hamate; C, capitate; T, triquetrum; L, lunate; S, scaphoid. Reproduced from McLean et al. (2009), with permission from Elsevier.

1.1.2 Ligamentous Anatomy

The ligamentous structures of the wrist play a vital role in guiding, stabilizing and constraining the intricate interactions of the carpal bones during wrist motion. The importance of the wrist ligaments can be better appreciated if one examines the proximal carpal row, which, as described previously, has been commonly referred to as the intercalated segment. Due to the lack of tendinous insertions, the motion of this intercalated segment is entirely modulated by the mechanical forces in the surrounding environment. Complex yet stable motion of the wrist would not be possible if there was not such a sophisticated network of carpal ligaments to guide and balance this inherently unstable intercalated segment.

Therefore, basic knowledge of the ligamentous anatomy of the wrist may be beneficial for a better understanding of the wrist biomechanics. A selection of carpal ligaments that were deemed most important and most relevant to the present study was examined in the following sections in detail. And since variable nomenclatures have been adopted in the literature (Brown et al., 1998; Buijze et al., 2011), the carpal ligaments described hereafter were in accordance to the standardisation formulated by the International Wrist Investigators' Workshop (IWIW) Terminology Committee (Gilula et al., 2002).

The carpal ligaments can be categorized in several ways based on different grouping criteria. Histologically, the majority of the carpal ligaments can be described as either intra-capsular, namely those being entirely incorporated into the joint capsule, or intra-articular, namely those being found within the joint space (Berger and Garcia-Elias, 1991; Pulos and Bozentka, 2015). Both types of ligaments are formed by fascicle bundles made of densely packed collagen fibres. These fascicles are aligned with the gross orientation of the ligaments and are tightly encircled by perifascicular spaces, which are composed by loose areolar connective tissue containing neurovascular triads (Berger and Blair, 1984; Berger, 2001). But unlike the intra-articular ligaments which are wrapped solely within a synovial lining, an additional fibrous lamina is found on the most superficial aspect of the intra-capsular

ligaments (Berger, 1996a).

Although other grouping strategies are also available, the following sections was built upon the commonly-accepted intrinsic-extrinsic division, proposed by Taleisnik (1976). As the name suggests, the division is decided on whether the carpal ligament originates and inserts within boundaries of the carpus. In other words, the extrinsic ligaments are those arise outside the carpus, for example from the distal radius and ulnar, whereas the intrinsic ligaments are those whose origins and insertions are encapsulated entirely within bounds of the carpus.

1.1.2.1 Extrinsic Ligaments

According to their anatomical locations, the extrinsic carpal ligaments can be further categorised as palmar radiocarpal, palmar ulnocarpal and dorsal radiocarpal ligaments (Fig. 1.6 and 1.7).

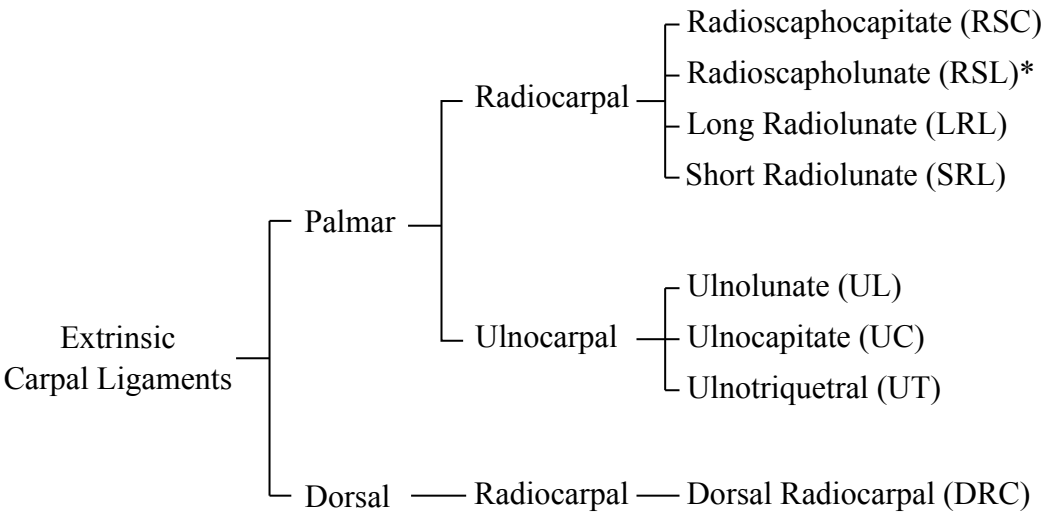

Figure 1.6: Architecture of the extrinsic ligaments of the wrist. *Note: the radioscapholunate (RSL) ligament (or the ligament of Testut) has been proven to be primarily a neurovascular vinculum (Berger and Blair, 1984).

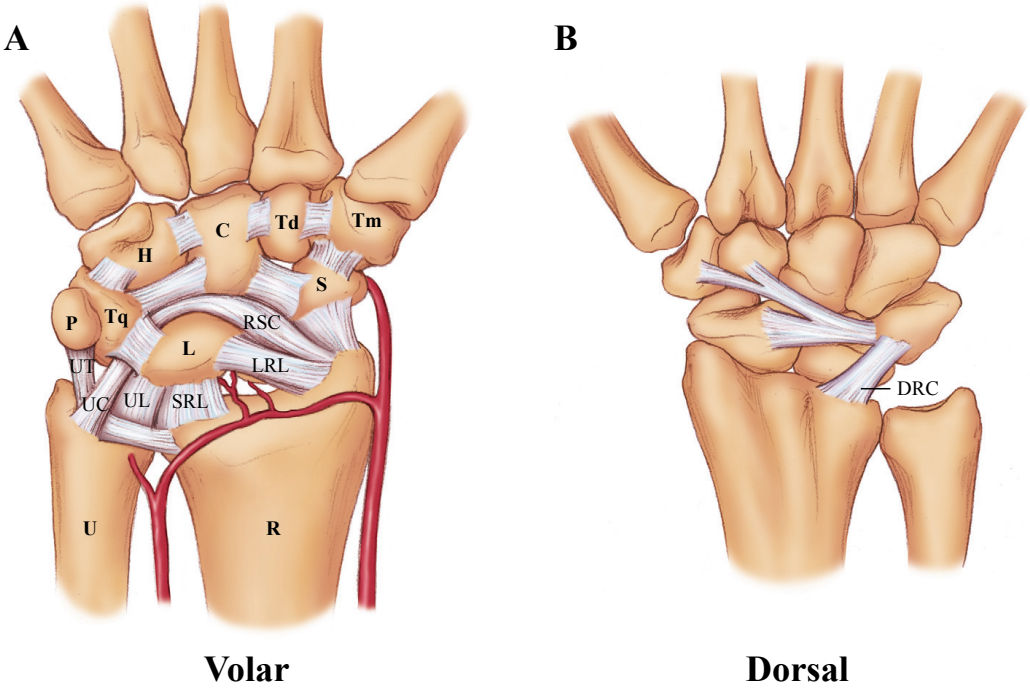

Figure 1.7: The extrinsic ligaments of the wrist. **(A)** On the volar side from radial to ulnar, these include the radioscaphocapitate (RSC),long radiolunate (LRL), short radiolunate (SRL), ulnolunate (UL), ulnocapitate (UC), and ulnotriquetral (UT) ligaments. **(B)** On the dorsal side, there is only one extrinsic ligament, namely the dorsal radiocarpal (DRC) ligament. Bones: R, radius; U, ulna; S, scaphoid; L, lunate; Tq, triquetrum; P, pisiform; Tm, trapezium; Td, trapezoid; C, capitate; H, hamate. Reproduced from Whitty and Moran (2009), with permission from Elsevier.

Radioscaphocapitate Ligament

The radioscaphocapitate (RSC) ligament is the most radially situated ligament in the palmar radiocarpal ligament group. It can be found in the radial most region of the palmar rim of the distal radius and attaches proximally to the radial styloid process. Three major components can be identified for this ligament: a large radiocapitate band, a radioscaphoid band and a portion analogous to a radial collateral ligament (Berger and Landsmeer, 1990). The RSC ligament coalesces ulnarly with fibres of the ulnocapitate (UC) ligament, forming the ulnar limb of the arcuate ligament. This par-

ticular configuration of the ligaments is likened to a "sling", supporting the midcarpal region, and in particular, preventing palmar subluxation of the capitate during wrist extension (Berger and Garcia-Elias, 1991). Since the RSC runs in a groove on the waist of the scaphoid, it is also thought to act as a "fulcrum" or a "seatbelt" around which the scaphoid rotates (Watts et al., 2011). Furthermore, as one of the radiocarpal ligaments, the RSC is believed to provide restraint to passive radiocarpal pronation (Ritt et al., 1995), and helps in preventing the carpus from translating dorsally (Berger, 1997), and ulnarly (Rayhack et al., 1987; Viegas et al., 1995).

Long radiolunate Ligament

The long radiolunate (LRL) ligament arises from the volar edge of the scaphoid fossa, just ulnar to the origin of the RSC ligament. Being partially overlayed by the RSC ligament proximally, the LRL ligament traverses distally and ulnarly towards the lunate. It inserts broadly onto the palmar horn of the lunate, covering the volar portion of the scapholunate interosseous ligament (v-SLIL). Together with the short radiolunate ligament (SRL), which is the ligament located immediately ulnar to the LRL, they are believed to function as important restraints to ulnar and distal translocation of the lunate (Taleisnik, 1976; Kijima and Viegas, 2009). Furthermore, the LRL is parted from the RSC ligaments by an interligamentous sulcus, rendering the palmar aspect of the proximal lunocapitate articulation devoid of any ligamentous support (Berger and Blair, 1984). This region of capsular vulnerability is often called *the space of Poirier*, and is thought to be opened and ultimately allows the lunate to dislocate volarly in the advanced stage of perilunate instability (Mayfield et al., 1980; Redjal and Rafijah, 2009).

Dorsal Radiocarpal Ligament

The dorsal radiocarpal ligament (DRC) is the only extrinsic ligament on the dorsal aspect of the wrist. It arises from the dorsodistal rim of the

radius, distal and slightly ulnar to the Lister's tubercle, and courses obliquely towards the ulnar aspect of the lunate and to finally insert onto the dorsal tubercle of the triquetrum (Berger, 2010). And along with the adjacent dorsal intercarpal ligament (DIC), form a lateral V-shaped configuration. The fibre orientation of the DRC ligament has made researchers to speculate if it has a role in preventing passive supination (Ritt et al., 1995), and ulnar translation of the carpus (Mizuseki and Ikuta, 1989; Viegas et al., 1995; Berger, 1997).

1.1.2.2 Intrinsic Ligaments

The intrinsic ligaments of the wrist are those both originate and insert within the carpus. They are mainly responsible for either binding the adjacent bones within each carpal row or linking up the two carpal rows.

The original grouping scheme, as devised by Taleisnik (1976), further divided the intrinsic ligaments into three categories: short, long and intermediate. However, since this grouping strategy is entirely based on the morphology of the ligaments, it might be difficult for those who lack a systematic understanding to visualise the general architecture of the carpal ligaments. Hence, a location-oriented grouping, similar to the one adopted for the extrinsic ligaments, is employed for the intrinsic ligaments of the wrist (Fig. 1.8 and 1.9).

It is worth noticing that apart from the extrinsic ligaments described previously in detail, there are three key intrinsic ligaments, including the the scapholunate interosseous ligament (SLIL), the scaphotrapeziotrapezoid (STT) ligament, and the dorsal intercarpal (DIC) ligament, that cross or directly attach to the scaphoid or the lunate (Short et al., 2007). These ligaments are therefore deemed more relevant to the present study and described in detail.

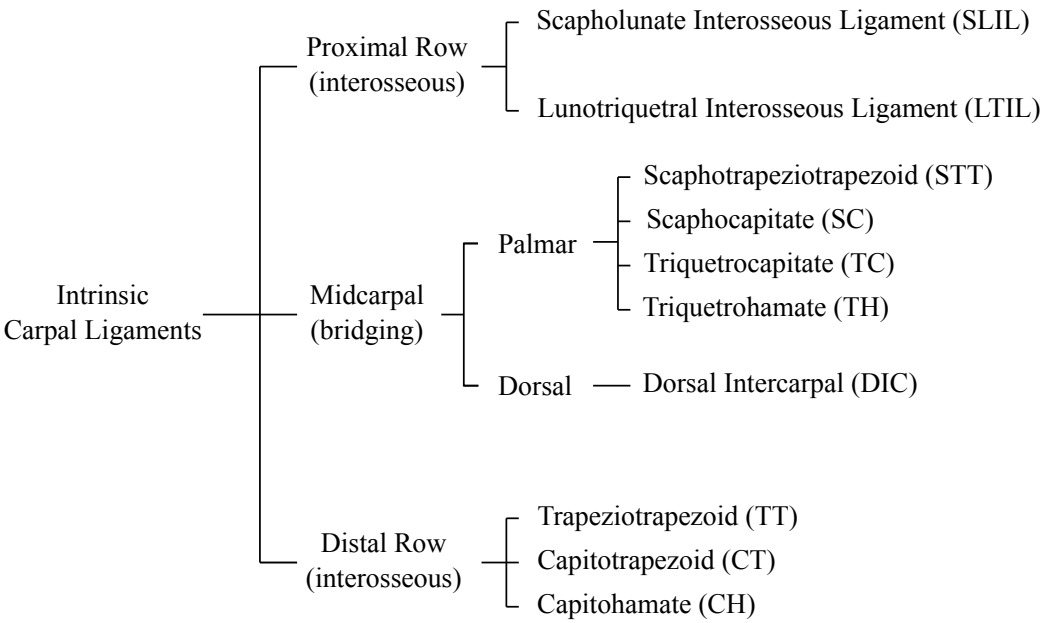

Figure 1.8: Architecture of the intrinsic ligaments of the wrist.

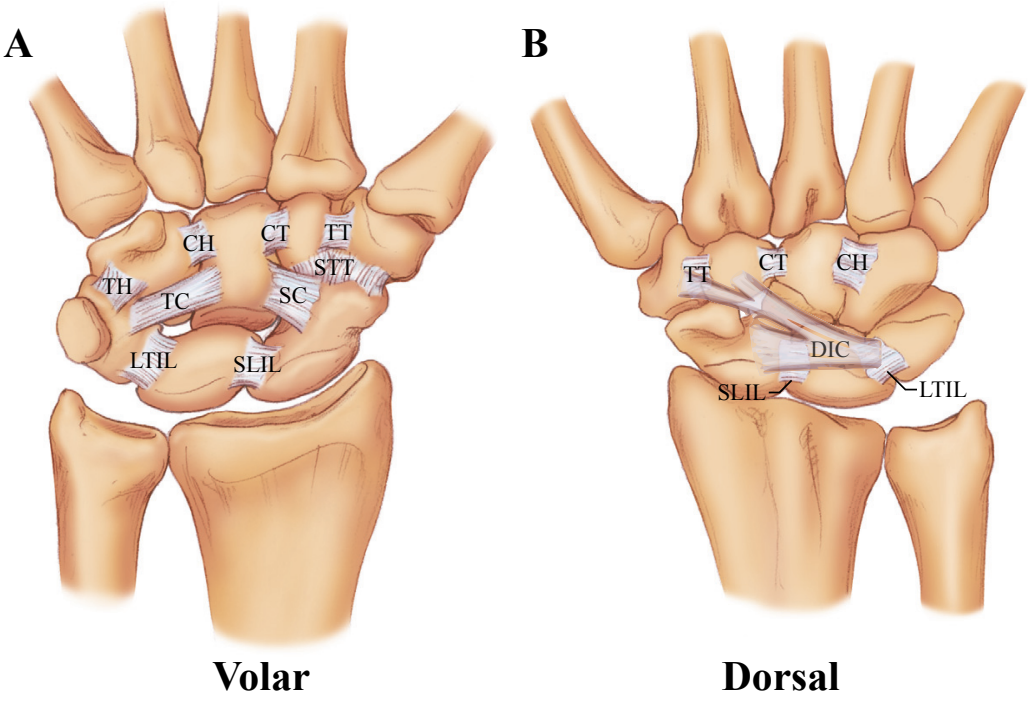

Figure 1.9: The intrinsic ligaments of the wrist. **(A)** On the volar side, these include the scapholunate interosseous ligament (SLIL), lunotriquetral interosseous ligament (LTIL), scaphocapitate (SC), triquetrocapitate (TC), scaphotrapeziotrapezoid (STT), trapeziotrapezoid (TT), capitotrapezoid (CT), capitohamate (CH), and triquetrohamate (TH) ligaments. **(B)** On the dorsal side, apart from the dorsal components of the SLIL, LTIL, TT, CT and CH ligaments, there is only one dorsal intrinsic ligament, namely the dorsal intercarpal (DIC) ligament (transparent). Modified from Whitty and Moran (2009), with permission from Elsevier.

Scapholunate Interosseous Ligament

The scapholunate interosseous ligament (SLIL) is a C-shaped ligament that connects the scaphoid and lunate. Namely, the SLIL attaches only to the dorsal, proximal and palmar margins of the articulating surface of the scapholunate joint, leaving the distal edge of the articulation uncovered and in communication with the midcarpal joint. It has been widely accepted that the SLIL can be divided into three histologically distinct subregions (Fig. 1.10), including the dorsal (d-), the proximal membranous (m-), and the volar (v-) subregions (Sokolow and Saffar, 2001).

The d-SLIL is a typical articular ligament, composed of stout and transversely oriented collagen fascicles (Berger, 1996b). It measures 5-6 mm in length (proximodistal), 3-5 mm in width (mediolateral), and 2-4 mm in thickness (Battistella, 2009; Apergis, 2013). It blends into the dorsal capsule distally and merges with the dorsal intercarpal (DIC) ligament proximally (Buijze et al., 2011). The d-SLIL is found to be capable of withstanding a distraction force up to 260 N, being the strongest among all three subregions and is recognised as the most crucial stabiliser to the scapholunate articulation (Berger, 1997; Kitay and Wolfe, 2012). The d-SLIL is joined proximally by the fibrocartilaginous m-SLIL. This membranous subregion is about 4 mm in length, 11 mm in width and 1 mm in thickness (Nagao et al., 2005), and is shown to possess a mechanical strength as low as 63 N (Berger et al., 1999). Therefore, the m-SLIL is commonly considered as having minimal contribution to the scapholunate stability (Kitay and Wolfe, 2012). The v-SLIL is histologically comparable to the d-SLIL but is composed by collagen fibres that are more obliquely oriented (Berger, 1996b). It measures approximately 3-5 mm in length, 4-7 mm in width and 1 mm in thickness (Apergis, 2013), and is shown to have a diminished mechanical strength of approximately 118 N, comparing to the d-SLIL (Berger et al., 1999). However, an *ex-vivo* study has suggested that the v-SLIL might serve to provide important rotational restraint to the scapholunate joint (Berger et al., 1999). Furthermore, despite the lack of biomechanical evidence on its actual efficacy, the concept of making the conventional d-SLIL reconstruction more anatomical

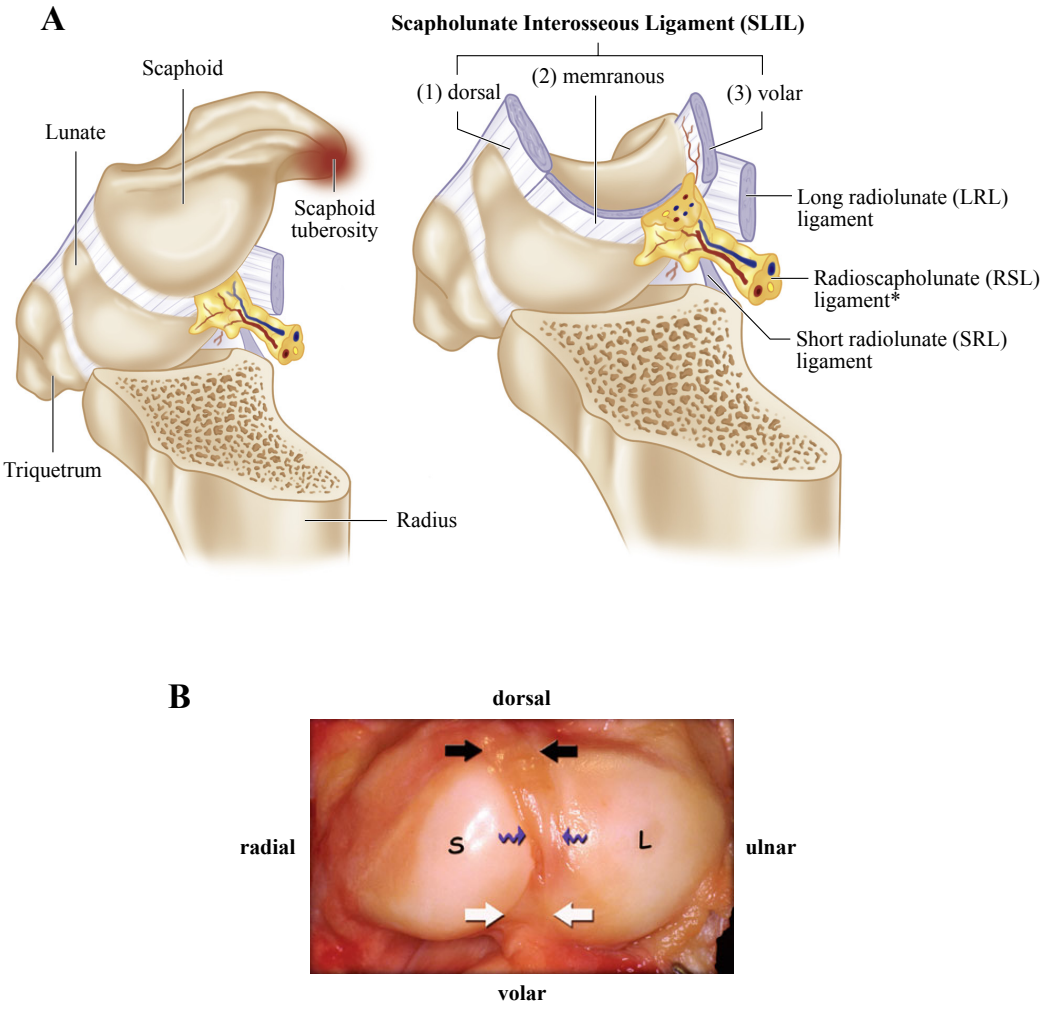

Figure 1.10: The scapholunate interosseous ligament. **(A)** An illustration of the SLIL from a radial and dorsal perspective. The radial styloid region of the distal radius (image on the the *left*) and the scaphoid (*right*) have been excised/hidden for clarity. Adapted from Michelotti and Chung (2018), with permission from Elsevier. **(B)** A photograph of the SLIL as viewed proximally from the radiocarpal joint. Note the three different subregions of the SLIL: the d- (black arrows), m- (blue wavy arrows), and v-SLIL (white arrows). (Adapted from Apergis (2013), with permission from Springer Nature.

by complementing it with a concurrent v-SLIL reconstruction has gained increasing popularity among hand surgeons (Corella et al., 2013; Ho et al., 2015; Kang et al., 2018).

In addition, it has been shown that the lunotriquetral interosseous ligament (LTIL) is also of C-shaped, consisting of the dorsal, proximal and volar subregions (Ritt et al., 1998; Standring and Gray, 2008). However, instead of having the thickest and strongest subregion being dorsal as in the SLIL, that of the LTIL is located on the volar aspect. This differential thickening of the interosseous ligaments seems to be in support of the theory that the lunate is balanced between the flexing torque exerted by the scaphoid and the extending torque exerted by the triquetrum (Kauer, 1974, 1980).

Scaphotrapeziotrapezoid Ligament

The Scaphotrapeziotrapezoid (STT) ligament is a stout ligament complex that lies palmarly in the lateral compartment of the midcarpal joint. It originates from the radial and volar aspect of the distal scaphoid pole and branches into two while extending distally. The radial (scaphotrapezium) band is fan-shaped and inserts broadly onto the radial and proximal aspect of the trapezium, whereas the ulnar (scaphotrapezoid) band inserts onto the proximal edge of the trapezoid (Drewniany et al., 1985; Moritomo et al., 2000b; Kijima and Viegas, 2009). It has been shown to be able to withstand a load up to 150 N (Nowak, 1991), and is believed to be a prominent stabiliser to the STT joint (Drewniany et al., 1985). Owing to its attachment to the distal scaphoid, the STT ligament complex is also believed to serve as an important restraint to prevent the scaphoid from collapsing into excessive flexion (Boabighi et al., 1993).

Dorsal Intercarpal Ligament

The dorsal intercarpal ligament (DIC) is a major row-crossing ligament. It arises dorsally from the radial and distal aspect of the triquetrum and branches into two while traversing distally and radially. It is frequently

classified as an extrinsic ligament in the literature, despite the definition of extrinsic ligaments being the ones connecting to bones outside the carpus (this ligament is regarded as intrinsic to the carpus in the present thesis based on its anatomy, strictly adhering to the definition to avoid confusion).

The thicker branch of the DIC attaches to the distal horn of the lunate to insert dorsally onto both the groove of the scaphoid and the proximal margin of the trapezium, whereas the distally situated thinner branch inserts onto the proximal aspect of the capitate and trapezoid (Berger, 2010). As mentioned previously, it is arranged in an unique lateral "V" configuration with the DRC ligament (Fig. 1.7B). Some researchers have hypothesised that through "scissoring" of the two arms composing the lateral "V", the dorsal aspect of the scaphoid is kept stable throughout the entire range of wrist motion, and the same level of scaphoid stability would be difficult to achieve without compromising the flexibility of wrist motion if this particular construct was replaced by a single ligament crossing proximodistally above the scaphoid (Viegas et al., 1999).

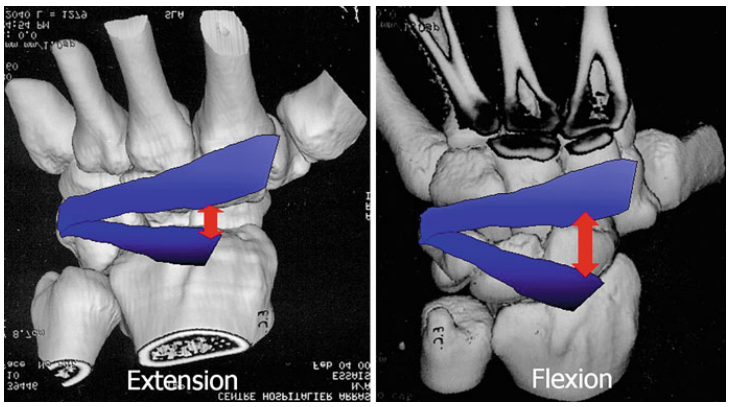

Figure 1.11: "Scissoring" of the dorsal ligamentous "V" during global wrist flexion and extension. Reprinted from Camus (2013), with permission from Springer Nature.

1.1.3 Musculature

There are around twenty-four muscles whose tendons extend across the wrist, and all of them can be regarded as having certain contribution in the synthesis of wrist motion. However, only five of them are considered as dedicated wrist motor muscles. This includes the flexor carpi ulnaris (FCU) and radialis (FCR), the extensor carpi ulnaris (ECU), and the extensor carpi radialis longus (ECR-L) and brevis (ECR-B) (Horii et al., 1993; Loren et al., 1996). Moreover, despite being a prominent abductor of the thumb, the abductor pollicis longus (APL) is also recognised as a strong radial deviator of the wrist and is often included in muscle-driven *in-vitro* simulation of the wrist (Werner et al., 1996; Kobayashi et al., 1997b; Erhart et al., 2012; Iglesias, 2015), owing to its "collateral" arrangement to the carpus and a large moment arm about the axis of wrist radioulnar deviation (Kauer, 1980; Brand, 1985; Gonzalez et al., 1997). In this section, a brief description was provided for each of these muscles.

Flexor Carpi Ulnaris

The flexor carpi ulnaris (FCU) muscle is the most medially situated wrist muscle and lies superficially to the forearm. As the name suggests, it is the primary flexor of the wrist and a synergist to wrist ulnar deviation. It arises by two heads: the smaller humeral head arises from the common flexor tendon attached to the medial epicondyle of the humerus, and the larger ulnar head arises from the medial margin of the olecranon of the ulna, respectively (Standring and Gray, 2008). It runs slightly anteriorly along the ulna and sends its tendon distally to completely envelop the pisiform, making the FCU the only wrist muscle inserting within bounds of the carpus. But since the pisiform is only loosely connected to the triquetrum, the FCU is believed to act mostly on the hamate and the base of the fifth metacarpal through the pisohamate and pisometacarpal ligament (Pevny et al., 1995). In terms of its force generation capabilities, the FCU is believed to be the strongest among all wrist motors, benefiting from its large physiological cross-sectional area

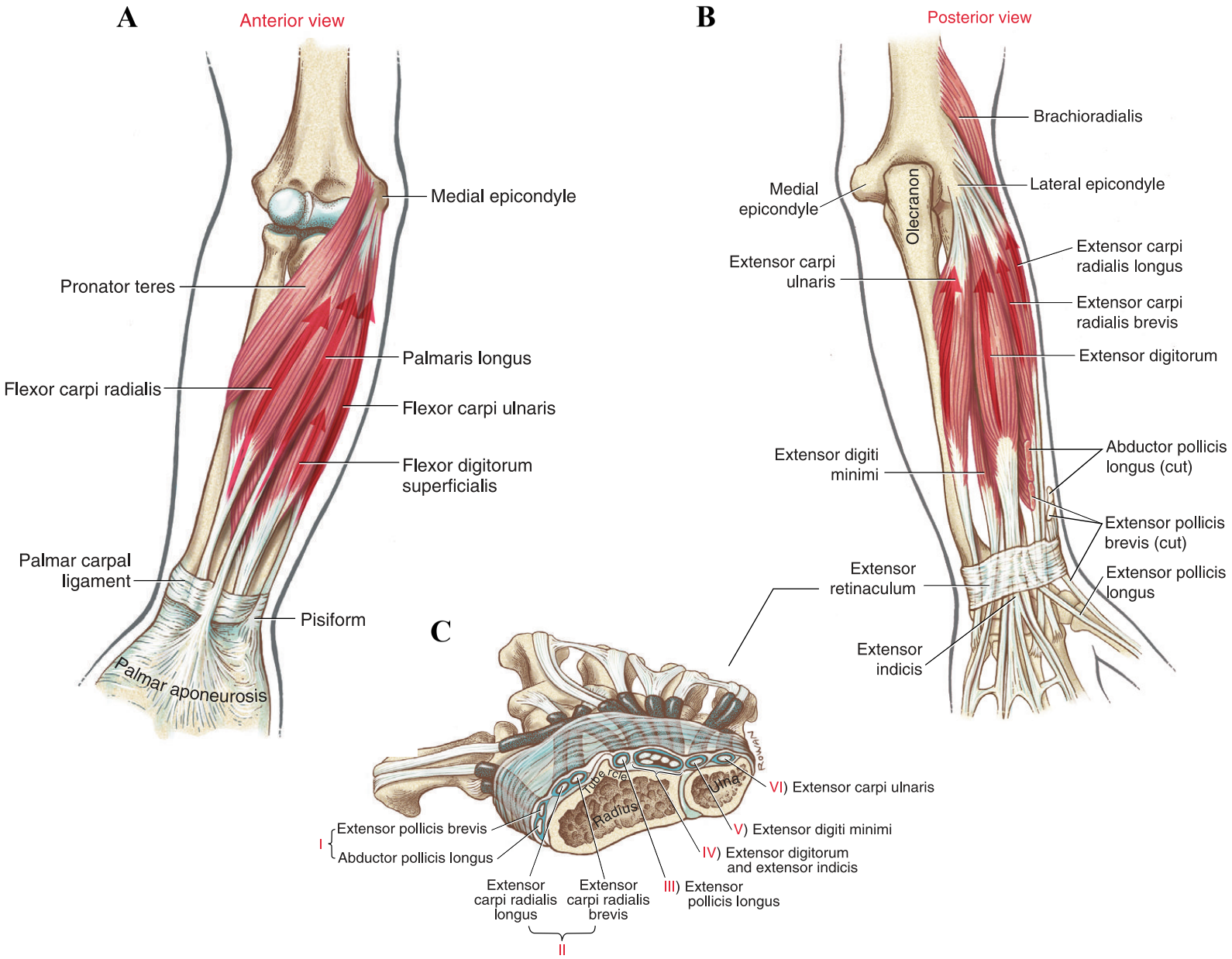

Figure 1.12: **(A)** An anterior and **(B)** a posterior view of the right forearm, depicting the wrist prime movers. **(C)** The extensor retinaculum as viewed obliquely from the dorsal and proximal aspect, showing the six (indicated using Roman numerals) fibro-osseous extensor compartments. Reprinted from Neumann (2010), with permission from Elsevier.

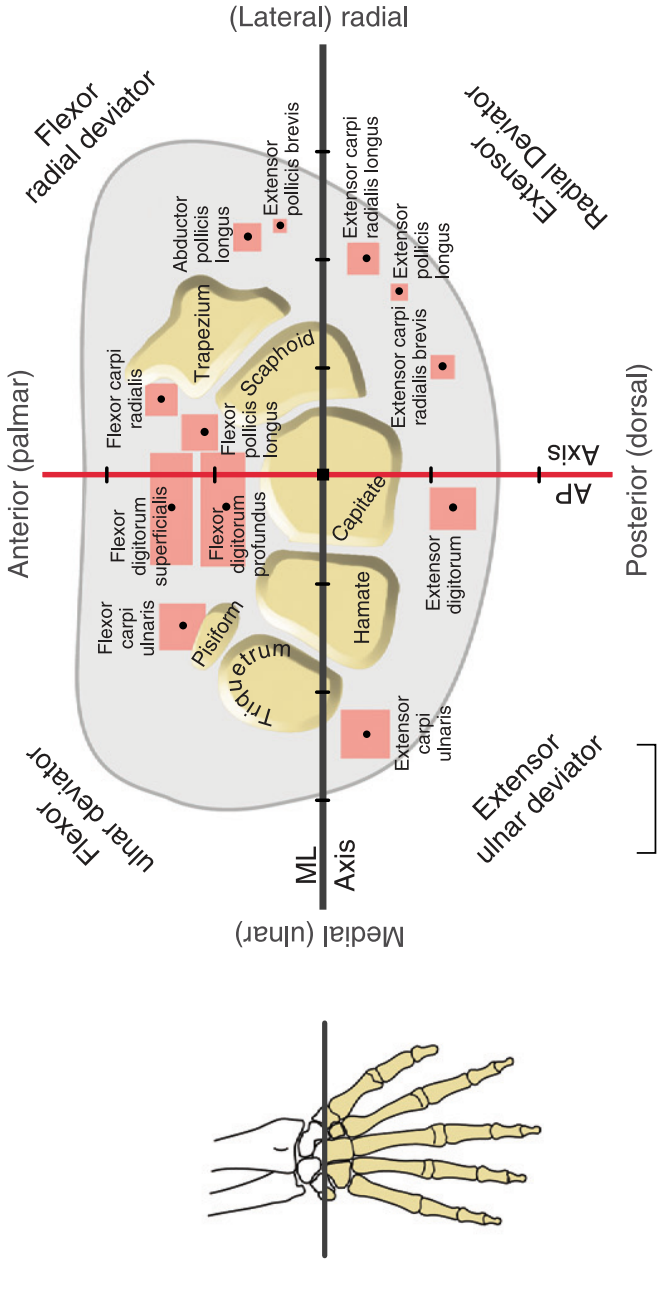

Figure 1.13: A cross-sectional view looking distally through the carpal tunnel of a right wrist, depicting the relative position, cross-sectional area, and length of the moment arm for various muscles that cross the wrist at the level of the head of the capitate. Reprinted from Neumann (2010), with permission from Elsevier.

(PCSA) (Loren and Lieber, 1995; Holzbaur et al., 2007).

Flexor Carpi Radialis

The flexor carpi radialis (FCR) muscle is also a superficially situated flexor but lies anteriorly to the forearm and laterally to the FCU. It arises from the medial epicondyle of the humerus via the common flexor tendon. It has a small muscle belly that ends approximately halfway along the radius, sending a slender tendon distally through a canal formed inferiorly by a grove on the trapezium and superiorly by the flexor retinaculum (Standring and Gray, 2008). The tendon of the FCR continues to traverse distally, passing over the scaphoid tuberosity to supposedly gain increased mechanical advantage, to finally insert on the bases of the second and third metacarpal. Based on its close relationship with the scaphoid, some postulated that the FCR might act as a 'dynamic stabiliser': when the muscle contracts, its volar passage over the scaphoid tuberosity might allow it to exert a dorsally directed force on the scaphoid, prevent it from flexing excessively (Jantea et al., 1994; Linscheid and Dobyns, 2002). However, a more recent study has showed that the FCR actually flexes the scaphoid, and it is the supinating moment induced by this muscle that helps to close the scapholunate interval in SLIL-deficient wrists (Salvà-Coll et al., 2011).

Extensor Carpi Ulnaris

The extensor carpi ulnaris (ECU) lies on the posterior side of the forearm and originates from the lateral epicondyle of the distal humerus via the common extensor tendon. The ECU routes distally towards the ulnar head and ends in a tendon before leaving the forearm. The tendon of the ECU slides in a groove located dorsally near the ulnar styloid process and is kept secure by its subsheath, buried deep within the supratendinous layer of the extensor retinaculum (Taleisnik et al., 1984; Gupta et al., 2018). This fibro-osseous tunnel, dedicated to the ECU tendon, is often referred to as the sixth extensor compartment (Standring and Gray, 2008). But owing to this anchorage on

the distal ulnar, the force generation capability of the ECU will be affected by the forearm rotation, unlike other wrist motor muscles (Campbell et al., 2013). And it has already been shown that the ECU has a diminished contribution to wrist extension when the forearm is pronated (Horii et al., 1993). Furthermore, the ECU has been considered as a scapholunate-destabilising muscle for SLIL-deficient wrists, as contracting this muscle would provoke strong pronation of the wrist, separating the scaphoid further away from the lunate (Salvà-Coll et al., 2012).

Extensor Carpi Radialis Longus

The extensor carpi radialis longus (ECR-L) muscle, while being termed as an extensor of the wrist, is actually a prominent wrist abductor, owing to its longer moment arm in the radial direction (Loren et al., 1996). It arises from the lateral supracondylar ridge of the humerus and runs distally on the lateral border of the radius. At about proximal one-third of the dorsal radius, its muscle belly terminates into a flat tendon, running underneath the abductor pollicis longus (APL) and extensor pollicis brevis (EPB) muscles. Together with the extensor carpi radialis brevis (ECR-B) muscle, it extends into the second extensor compartment, laying in a groove located immediately lateral to the Lister's tubercle (Standring and Gray, 2008). Finally, it inserts radially onto the dorsal aspect of the base of the second metacarpal.

Extensor Carpi Radialis Brevis

The extensor carpi radialis brevis (ECR-B) muscle is the smaller muscle located just ulnar to the ECR-L. The ECR-B is more effective in extending the wrist rather than abducting it, unlike the ECR-L (Loren et al., 1996). It arises mainly from the lateral epicondyle of the humerus via the common extensor tendon. Its muscle belly ends into a flat tendon around the midpoint of the forearm and shares the second extensor compartment with the that of the ECR-L upon leaving the forearm. Its tendon ultimately inserts on the dorsal and radial aspect of the base of the third metacarpal, and occasionally

sends a slip to the second metacarpal or exchanging tendinous fibres with that of the ECR-L (Standring and Gray, 2008).

Abductor Pollicis Longus

The abductor pollicis longus (APL) muscle, together with the extensor pollicis brevis (EPB) muscle, are two of the muscles that possess a sustainable moment arm for wrist radial deviation. But since the PCSA of the EPB is significantly less small (Brand, 1985; Gonzalez et al., 1997), the APL muscle is therefore considered as one of the most competent wrist abductor. Unlike other wrist motors, the APL arises dorsally from the mid-lateral surface of the ulna, the adjoining interosseous membrane, and a region at mid-radius distal to the origin of supinator (Standring and Gray, 2008). It runs obliquely along the deep posterior surface of the radius then rises to become superficial upon crossing the wrist. Closely accompanied by the EPB, its tendon extend into the first extensor compartment, which is embedded in a groove located on the lateral side of the distal radius. Finally, it inserts radially onto the trapezium and the base of the first metacarpal.

1.2 Motion of the Wrist

The wrist is categorised as a condyloid joint and exhibits a biaxial movement with respect to the forearm: flexion-extension motion (FEM), occurs in the sagittal plane about an axis directed mediolaterally (Fig. 1.14A), and abduction-adduction or radial-ulnar deviation (RUD), occurs in the coronal plane about an anteroposteriorly directed axis (Fig. 1.14B) (Muscolino, 2011). Since the apparent or the macroscopic wrist motion is a net result of the complex three-dimensional motion and interactions occurring between carpal bones, the term 'global wrist motion' is often used to avoid confusion with the motion of individual carpal bones (Werner et al., 1997a).

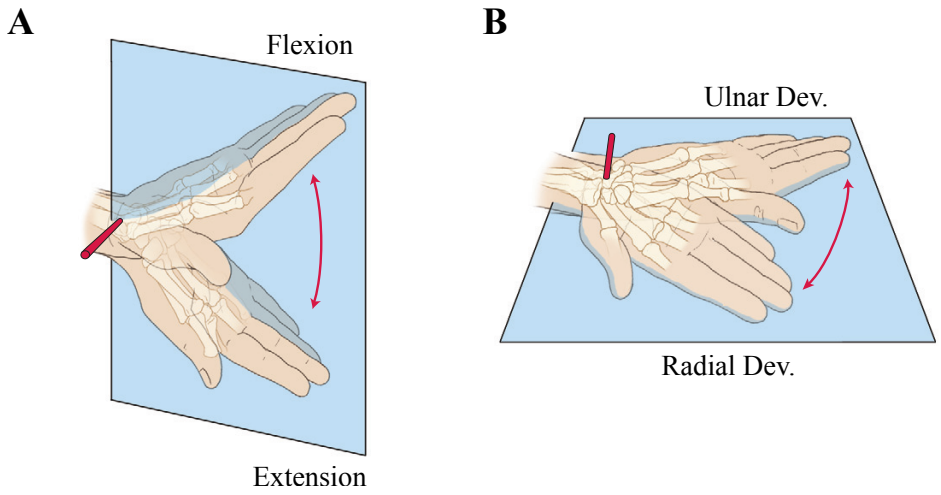

Figure 1.14: Schematics showing two primary degrees of freedom of wrist motion: (**A**) flexion-extension motion and (**B**) radial-ulnar deviation. Adapted from Muscolino (2011), with permission from Elsevier.

Additionally, it is commonly accepted that the internal-external rotation of the hand and wrist, or pronation-supination, is caused by motion occurs within the forearm at the radioulnar joint (Fig. 1.15), and is therefore not recognised as a degree of wrist motion (Neumann, 2010; Muscolino, 2011).

Furthermore, out-of-plane motion of the wrist, such as circumduction (Fig. 1.16A) and the so-called "dart-thrower's motion" (DTM, Fig. 1.16B), which occurs in an oblique path and is considered fundamental to many daily

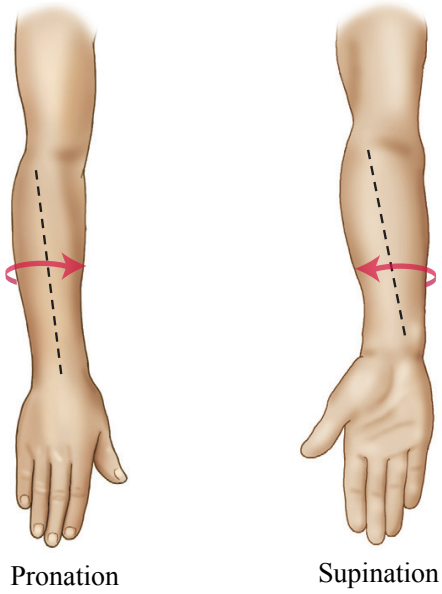

Figure 1.15: Pronation-supination of the forearm, with the approximate axis of rotation shown by the dashed line. Adapted from Muscolino (2011), with permission from Elsevier.

activities such as pitching a ball, hammering a nail, swing a club or combing hairs (Palmer et al., 1985; Saffar and Semaan, 1994; Brigstocke et al., 2014; Garg et al., 2014), is nothing but a superposition of the aforementioned FEM and RUD, not a distinct degree-of-freedom of the wrist (Neumann, 2010).

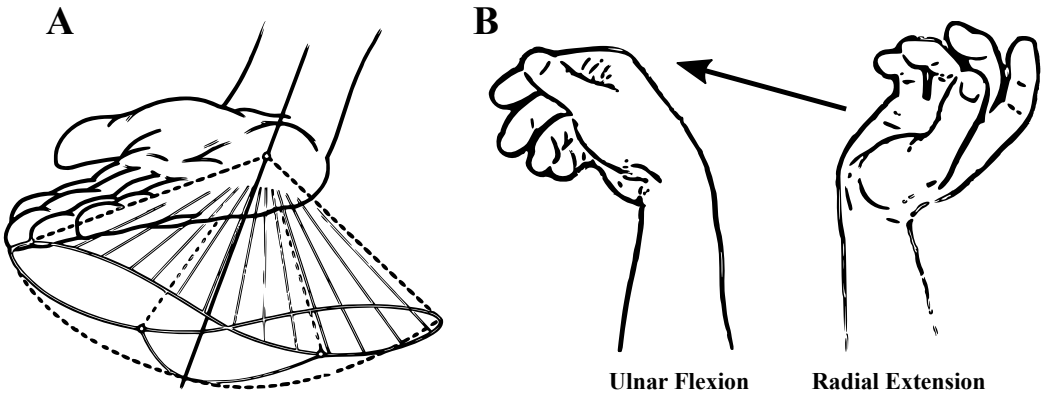

Figure 1.16: Schematics of (**A**) Wrist circumduction and (**B**) Dart-thrower's motion (DTM), which occurs obliquely from a combined posture of radial extension towards ulnar flexion.

1.2.1 Definition of the Joint Coordinate Systems

A set of joint coordinate systems (JCS) must be defined for the wrist before both its macroscopic motion and microscopic carpal bone motion can be quantitatively analysed. Although the choice of joint coordinate systems may be entirely arbitrary in principle and varies throughout the literature, the one set by the Standardisation and Terminology Committee of the International Society of Biomechanics (ISB) was adhered to in the present study to allow for ease of communication and uniformity of languages in the field (Wu et al., 2005).

1.2.1.1 Global Wrist

Global wrist motion is defined as the motion of the third metacarpal (3MC) with respect to the radius (Wu et al., 2005). In other words, the global wrist motion at any instant in time may be described using the relative attitude of the 3MC as observed in reference to the radius. Local coordinate systems (LCS) are therefore defined for both the radius and 3MC based on their respective anatomical landmarks, in order to allow their configurations to be described in space.

Radius

The LCS of the radius (Fig. 1.17), or the radial coordinate system, $\mathcal{R}_{Rad}$, has its origin, O_r, defined midway on the line connecting the midpoint of the interfacet prominence distally and the centre of the depression in the radial head proximally. In addition, the origin should also coincide with the approximate centre of the shaft of the radius in the transverse plane. The Y-axis of $\mathcal{R}_{Rad}$, Y_r, is defined by drawing a line parallel to the long shaft of the radius from O_r to intersect the midpoint of the interfacet prominence on the distal radius. For a right wrist, Y_r is defined to be pointing proximally. The Z-axis of $\mathcal{R}_{Rad}$, Z_r, is defined to be both perpendicular to Y_r and lies in a plane defined approximately coronal by the tip of the radial styolid process,

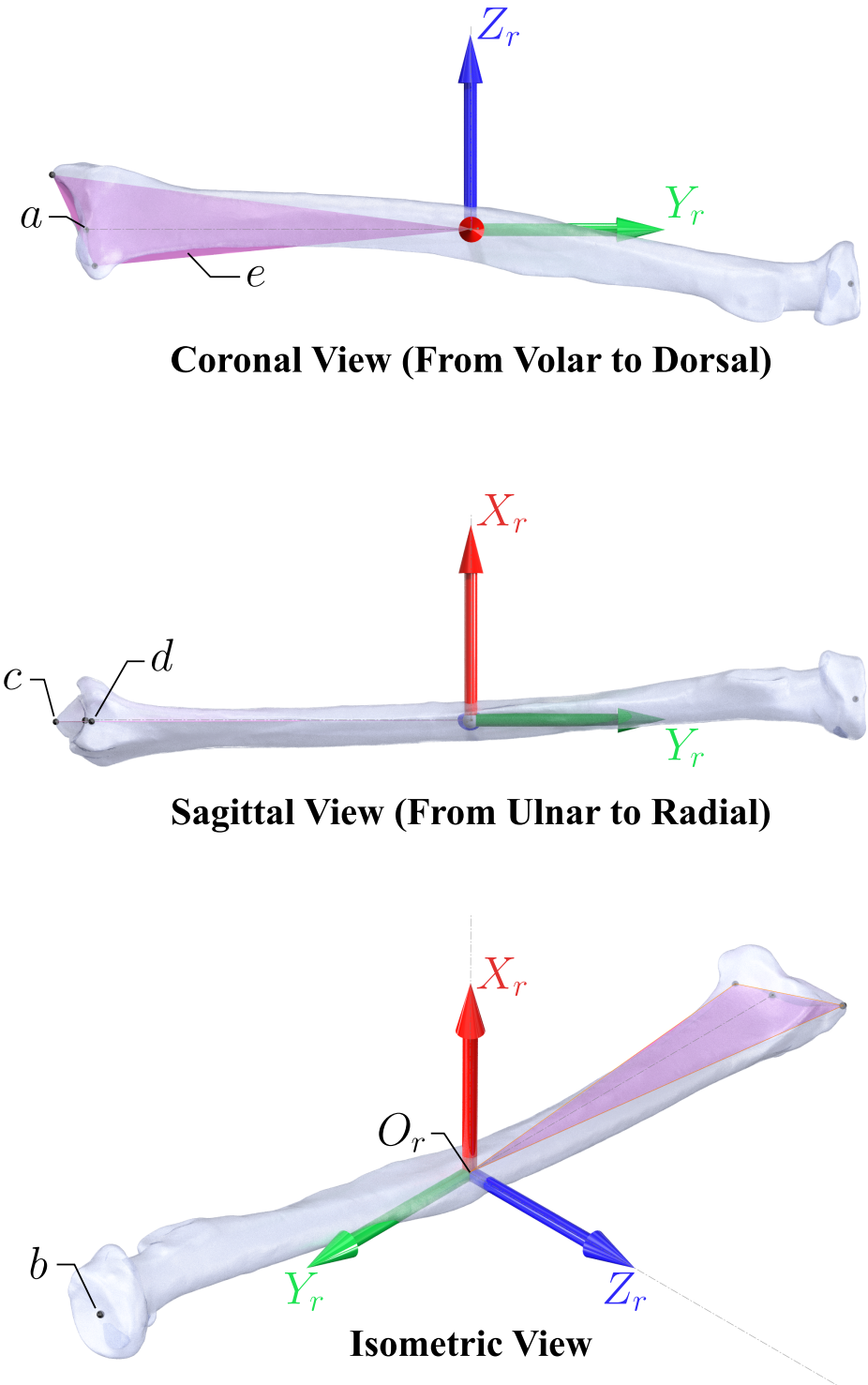

Figure 1.17: Schematics of a right radius with its local coordinate system defined. a) the interfacet prominence, b) the centre of the depression in the radial head, c) the radial styloid process, d) the base of the sigmoid notch, and e) the plane (purple) defined by c, d and O_r.

the base of the sigmoid notch, and O_r. Z_r is defined to be pointing radially for a right wrist. Finally, the X-axis, X_r, its direction can be derived as the cross-product of the two vectors defining axes Z_r and Y_r. X_r is defined to be pointing volarly for a right wrist. For a left wrist, the directions of all three axes are completely opposite to those defined for a right wrist, namely Y_r, Z_r and X_r is distal, ulnar and dorsal, respectively.

The Third Metacarpal

The LCS of the 3MC (Fig. 1.18), $\mathcal{R}_{3MC}$, has its origin, O_{3mc}, defined midway between the base and head of the 3MC. Similarly, the origin defined should be coincident with the approximate centre of the tubular bone in the transverse plane.

The Y-axis of $\mathcal{R}_{3MC}$, Y_{3mc}, is defined by the line connecting the centre of the 3MC's distal head to that of its base. The X-axis, X_{3mc}, is defined such that it forms a plane with Y_{3mc} that splits the 3MC sagittally into two roughly symmetrical parts. The Z-axis, Z_{3mc}, is again derived according to the right-hand rule using the previous two axes defined. For a right wrist, Y_{3mc}, Z_{3mc} and X_{3mc} is proximal, radial and volar, respectively. And these are completely the opposite for a left wrist.

Global Wrist Motion

For describing the global wrist motion, the methods developed by Grood and Suntay (1983) involving the use of "floating axis", are suggested by the ISB (Wu et al., 2005). Flexion-extension, α, is measured as the rotation around the Z-axis fixed to the proximal segment, namely Z_r of the radius. Pronation-supination, γ, is measured as the rotation around the Y-axis fixed to the distal segment, namely Y_{3mc} of the 3MC. The radial-ulnar deviation, β, is measured around the floating axis which needs to be constantly updated according to the configuration of the 3MC with respect to the radius and is defined as the common axis perpendicular to both Y_{3mc} and Z_r. Caution needs to be exercised when determining the third floating axis as it should always form

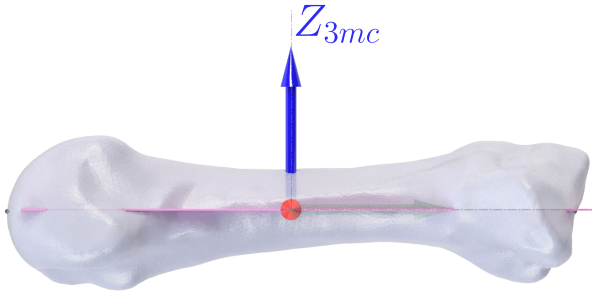

Coronal View (From Volar to Dorsal)

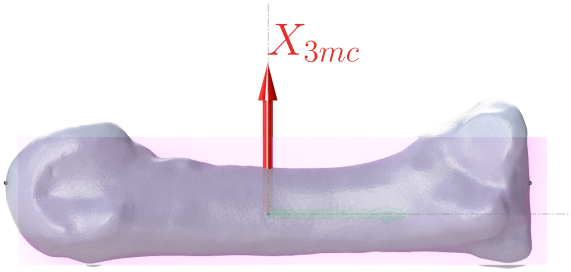

Sagittal View (From Ulnar to Radial)

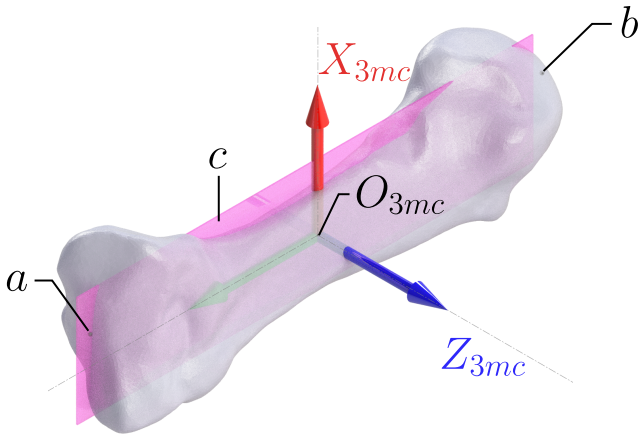

Isometric View

Figure 1.18: Schematics of a right third metacarpal with its local coordinate system defined. a) the base and b) the head of the 3MC, c) the plane (purple) approximately splits the 3MC into two mirror images.

a right-handed coordinate system with the other two. The neutral wrist position is defined as the position in which the wrist is in neutral flexion-extension and radial-ulnar deviation at the same time (Wu et al., 2005). In other words, it is the position in which the 3MC is aligned with the radius in both the sagittal and coronal plane.

1.2.1.2 Carpal Bones

Unlike the radius and the 3MC, the LCS for each of the irregularly shaped carpal bones is difficult to define using palpable anatomical landmarks. According to the ISB (Wu et al., 2005), since the majority of researchers tend to measure carpal motion relative to the radius, the LCS for each carpal bone is defined to be in parallel with that of the radius when the wrist is placed in its neutral position (Fig. 1.19). And the origin of the LCS is defined to be coincident with the volumetric centroid of that bone.

1.2.2 Range of Global Wrist Motion

The extreme range of global wrist motion have been investigated by many researchers (Table 1.1). A slightly greater amount of excursion can be achieved

Table 1.1: Extreme range of global wrist motion

Study	**Extreme Range of Motion** (degree)			
	Flexion	Extension	Ulnar Dev.	Radial Dev.
AAOS (1965)	73	75	33	19
Brumfield et al. (1966)	73♂ / 82♀	64♂ / 65♀	-	-
Sarrafian et al. (1977)	66	55	-	-
Boone and Azen (1979)	76	75	36	22
Volz et al. (1980)	-	-	35	15
Youm and Flatt (1984)	80	70	55♂	25♂
Ryu et al. (1991)	79	59	37	21

AAOS: American Academy of Orthopaedic Surgeons

for wrist flexion than extension, and for wrist ulnar deviation than radial deviation. The former is believed to be attributed to the volar tilt of the distal

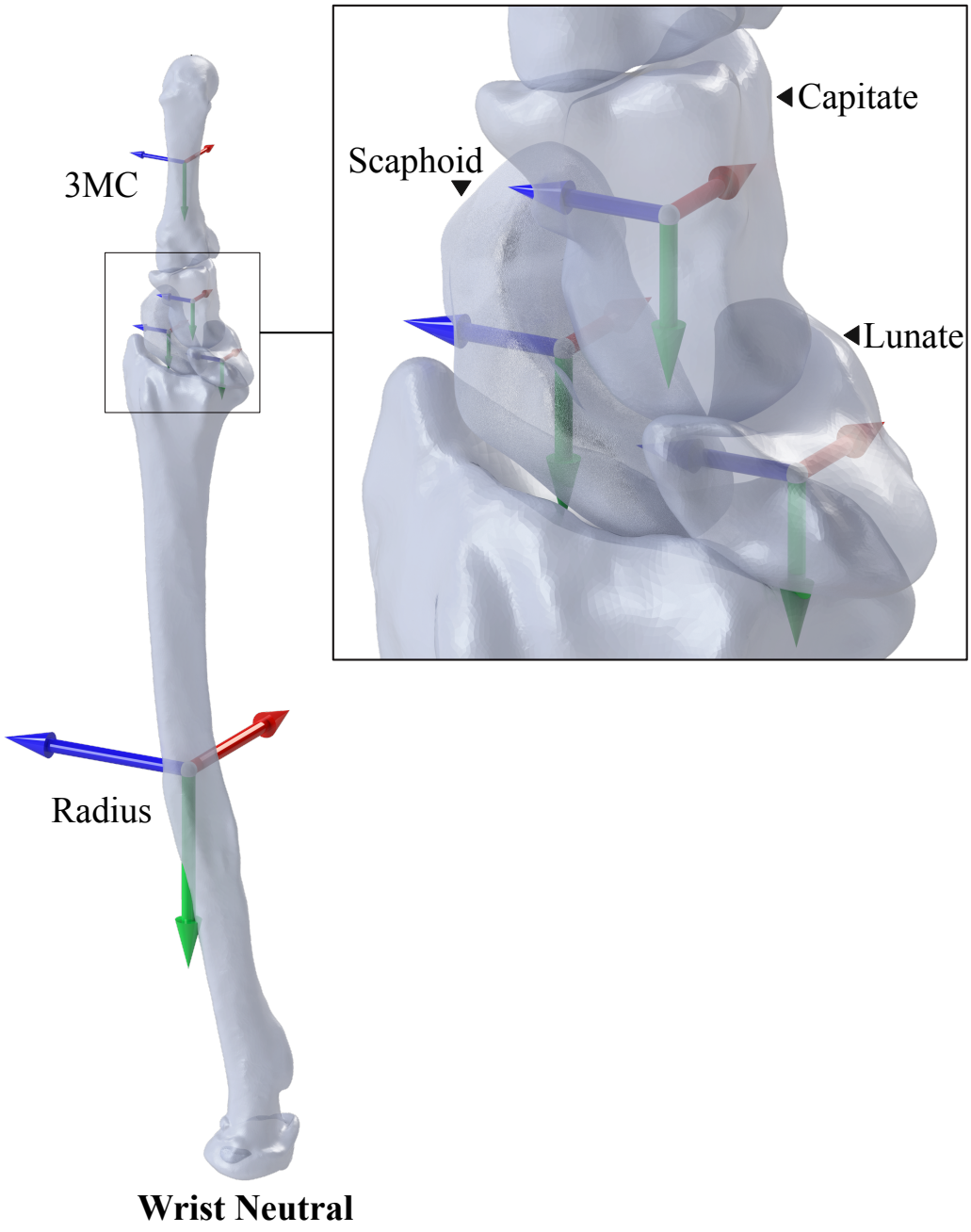

Figure 1.19: An example showing the definition of the carpal bone coordinate systems. The radius, 3MC, scaphoid, lunate, and capitate of a right wrist is shown from a dorsal-medial perspective. The LCS of the carpal bones are defined at their volumetric centroids, and are in parallel with that of the radius when the wrist is placed in the neutral position.

radius as well as the thicker volar radiocarpal ligaments, the latter asymmetry is thought to be a consequence of the presence of the radial styloid process, which effectively blocks the wrist in end-range of radial deviation (Volz et al., 1980; Neumann, 2010).

Table 1.2: Functional range of global wrist motion

Study	**Functional Range of Motion** (degree)			
	Flexion	Extension	Ulnar Dev.	Radial Dev.
Brumfield and Champoux (1984)	10	35	-	-
Porter and Stockley (1984)	30	45	15	15
Palmer et al. (1985)	5	30	15	10
Ryu et al. (1991)	40	40	30	10
Nelson et al. (1994)	50	51	40	12

The functional range of global wrist motion, on the other hand, provides knowledge of the minimal wrist motion requirement in performing activities of daily living and therefore serves as an important benchmark for evaluating the efficacy of surgical procedures and rehabilitation protocols. In contrast to the asymmetry towards flexion and ulnar deviation in extreme range of global wrist motion, it is clear that a slightly extended while ulnarly deviated posture is preferred during functional tasks (Table 1.2). Some believe this bias is related to the fact that a more powerful grip can be achieved with such a posture of the wrist (Palmer et al., 1985).

1.3 Biomechanics of the Wrist

A brief review of literature is presented focusing on two major aspects of the wrist biomechanics: carpal kinematics and the contact characteristics of the radiocarpal joint of the wrist.

1.3.1 Carpal Kinematics

As mentioned, the eight carpal bones can be descriptively grouped into two rows. And aside from the FCU, which attaches to the pisiform, all other prime movers of the wrist only insert distally on the bases of the metacarpals, leaving the proximal carpal row without any direct tendinous attachments. Thus, the proximal carpal row is often considered as an intercalated segment whose motion is mostly dictated by the mechanical signals in the surrounding. In a nutshell, the moment generated by muscle activation transmits proximally through the semi-rigid carpometacarpal joint to cause motion of the distal carpal row. This is subsequently "felt" by the proximal row as soon as the compressive force transmitted through the midcarpal joint and the tightness of the ligamentous constraints linking the two carpal rows reach a certain level, producing the final macroscopic wrist motion (Werner, 2010).

Flexion-Extension

Wrist flexion is initiated primarily by the tendinous pull of the prime wrist flexors, namely the FCR and FCU, causing the bones in the distal carpal row, which are firmly held to one another by their dense interosseous ligaments, to rotate synergistically into a flexed and slightly ulnarly deviated posture (Ruby et al., 1988; Horii et al., 1991). The proximal row follows the distal row into a similar position, but since the bones are less tightly bound, they do not exhibit three-dimensional motion to the same degree and in the same direction (de Lange et al., 1985; Kobayashi et al., 1997a; Moojen et al., 2002). Despite the substantial controversy in regards to the small conjoined

out-of-plane motion of those carpal bones, it is well documented that the lunate exhibits the least in-plane excursion, followed by the triquetrum and the scaphoid (Berger, 1996a).

Wrist extension is initiated by the pull of prime wrist extensors, namely the ECR-B and -L, and ECU. Similarly, the motion starts at the midcarpal joint with the distal row rotating into extension with slight radial deviation (Ruby et al., 1988; Horii et al., 1991). The proximal row follows the distal row into extension, but again with appreciable intercarpal motion occurring between the constituent carpal bones (de Lange et al., 1985; Kobayashi et al., 1997a; Moojen et al., 2002). Interestingly, the scaphoid has been shown to exhibit a large in-plane excursion comparable to the arc of global wrist extension, making it to be considered functionally as a part of the distal carpal row by some researchers (Sarrafian et al., 1977).

Furthermore, it has also been noticed that the radiocarpal and midcarpal joints might have contributed differently during wrist flexion and extension. However, there have been disagreements in regards to how the global wrist motion is apportioned between the two joints. Gellman et al. (1988) found the radiocarpal joint to be more important, accounting for 63% and 53% of the global wrist flexion and extension, respectively. Garcia-Elias et al. (1994), however, reported the global wrist flexion occurred predominately at the midcarpal joint, while wrist extension was mostly facilitated by the radiocarpal joint. Besides, as pointed out by the authors, this difference was only seen in about two-thirds of the population, and the global wrist motion was equally divided between the radiocarpal and midcarpal joints for the remaining one-third.

Radial-Ulnar Deviation

Wrist radial and ulnar deviations are facilitated by coordinated contractions of the prime wrist abductors and adductors, located on both the anterior and posterior sides of the forearm, respectively. For the bones in the distal carpal row, they rotate synergistically to become mostly radially deviated

with combined supination during radial deviation of the wrist, whereas the opposite is observed during wrist ulnar deviation (Kobayashi et al., 1997a; Ritt et al., 1998; Moojen et al., 2002). In regards to their conjoined motion in the sagittal plane, however, disagreements exist among these investigators.

For the bones in the proximal carpal row, despite also being observed to follow the global wrist into radial or ulnar deviation, they rotate primarily in the sagittal plane: they collectively flex during wrist radial deviation, and extend during ulnar deviation (Kobayashi et al., 1997a; Ritt et al., 1998; Moojen et al., 2002; Kaufmann et al., 2005). This adaptive behaviour of the proximal carpal row is thought to be of critical importance to the normal wrist motion in the coronal plane: when the wrist is brought to radial deviation, the distance on the radial side of the carpus shortens due to the engagement of the scaphotrapeziotrapezoid joint; this change is reversed when the wrist is brought into ulnar deviation, and the scaphoid is pulled upright to maintain joint congruency (Volz et al., 1980; Linscheid, 1986; Garcia-Elias et al., 1989). Furthermore, the two carpal rows have been shown to traverse in a reciprocal pattern in the coronal plane, namely the distal row translate in the same direction radially or ulnarly as the global wrist motion, whereas the proximal row translates in the opposite direction (Ruby et al., 1988; Kobayashi et al., 1997a).

In addition, despite the variation in the values reported, it is generally agreed that radial deviation of the wrist is facilitated predominately at the midcarpal level, accounting for approximately 70-80% of the global wrist motion, whereas ulnar deviation of the wrist is almost evenly contributed by both the radiocarpal and midcarpal joint (de Lange et al., 1985; Ritt et al., 1998; Kobayashi et al., 1997a; Ishikawa et al., 1999; Goto et al., 2005).

1.3.2 Theories of Carpal Motion

As there is no unanimity among investigators on the functional anatomy of the carpus, various theories have been proposed in an attempt to explain the intricate yet stable motion of the carpus, and to unveil the myth behind the impressive weight-bearing capability of the joint formed by a humble group of eight tiny carpal bones.

In earlier published accounts, the row concept, borrowed directly from on the arrangement of the carpal bones, has been used to elucidate the carpal motion. The proximal and distal carpal rows were thought to be closely adapted to one another as rigid functional groups, with each rotating around fixed axes during both sagittal and coronal plane wrist motion (Güenther, 1850; Humphry, 1858; Henke, 1859). But after examining the radiographies of his own wrist, Bryce (1896) found the two rows were not entirely locked into each other and the bony articulations formed between and within the carpal rows were adapted to the motion of the carpus. In particular, he was perhaps the first to notice differential motion between the scaphoid and lunate. Johnston (1907) suggested that flexion and extension of the wrist occurred primarily at the midcarpal joint, and radial and ulnar deviation was facilitated through the scaphoid sliding down the slope on the distal radius. However primitive and simplistic they might seem, early versions of the row concept have laid the cornerstone for further investigation of the carpus.

Built on the ideas of Destot (1926), Gilford et al. (1943) took a step further to realise that the two carpal rows were essentially linked together by the scaphoid, acting as an intermediary supporting rod to prevent the carpus from collapsing. And the famous "slider-crank" analogy of the scaphoid proposed later by Linscheid et al. (1972), is basically a refinement of this idea. In essence, when subjected to axial loading, the wrist exhibits a strong tendency to collapse into a zigzag configuration with the lunate abnormally extended and the capitate dorsally translated, bearing some resemblance to a concertina (Landsmeer, 1961; Fisk, 1970); the scaphoid, however, counteracts

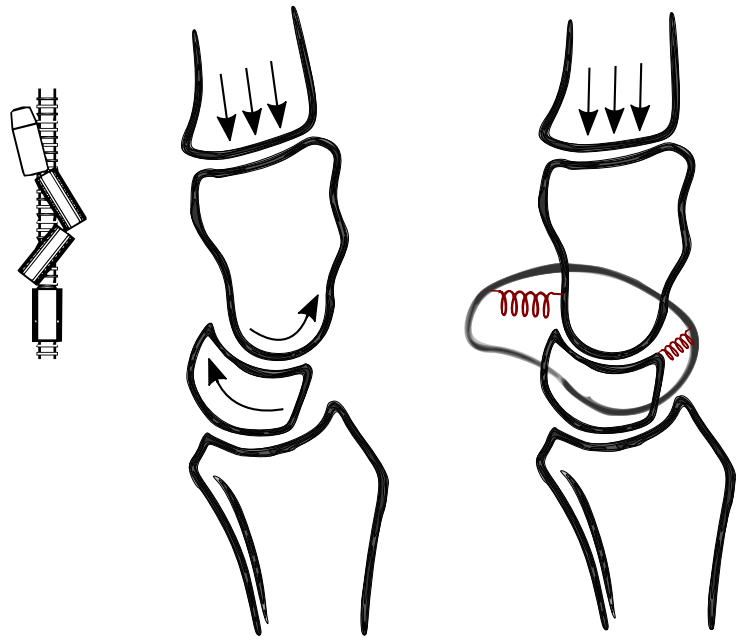

Figure 1.20: The scaphoid was hypothesised as the key in preventing a "zigzag" collapse of the carpus (*left*), as long as the dorsal scapholunate and the palmar scaphocapitate ligamentous links (*right*, red springs) are intact.

this movement potential dorsally and volarly through the scapholunate and scaphocapitate ligamentous connections (Gilford et al., 1943).

Based predominately on phylogenetic studies of birds, Navarro (1921) put forward an entirely different interpretation of the carpal function. In his view, the wrist complex can be considered both anatomically and functionally as comprised of three independent columns (Fig. 1.21A): the central column, formed by the lunate, capitate and hamate, controls flexion and extension of the wrist and provides mechanical strength against axial loading; the lateral column, comprised of the scaphoid, trapezium and trapezoid as a 'mobile linkage column'; and the medial column, formed by the triquetrum and pisiform, acts as a pivot for carpal rotation. Taleisnik (1976) revised this concept to exclude the pisiform due to its negligible contribution towards the carpal motion (Fig. 1.21B). And the entire distal row was consolidated into the central column, as minimal intercarpal motion could be found between bones in the distal row. As remarked by Garcia-Elias (2013a), one of the major

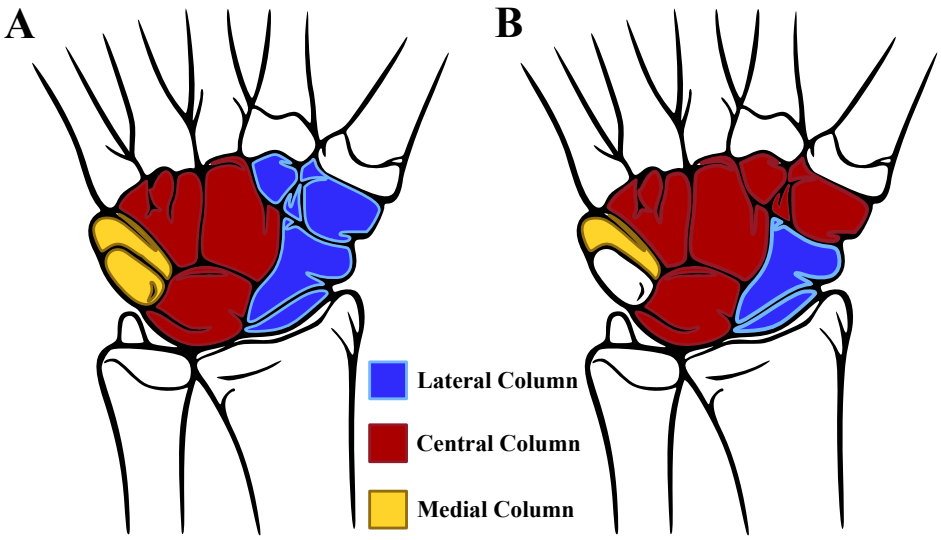

Figure 1.21: The column theory (**A**) as originally proposed by Navarro (1921) and (**B**) after being revised by Taleisnik (1976).

significances of the columnar carpal concept is that it guides the investigators to realise that motion of the central column is not only modulated by the scaphoid laterally, but also by the triquetrum medially. By incorporating the force transmission into the abstract analysis focused solely on the carpal kinematics, Weber (1980) further advanced this concept. He believed that the stability of the intercalated system of the carpus was ensured not only by the ligaments, but also by the control and constraint provided through contact surfaces, specifically, via those of the helicoidal triquetrohamate joint. He envisioned that the engagement of this joint would induce an extension moment on the lunate, counteracting the flexion moment exerted laterally by the scaphoid. This concept was later reintroduced as the 'Self-Stabilizing Spring Theory' (Garcia-Elias, 2013a; Kamal et al., 2016). However, the results obtained in a loading experiment conducted by Kobayashi et al. (1997b) did not lend enough support to this theory.

Lichtman et al. (1981) argued that it was misleading to consider the lunate as a part of the central flexion-extension column, as they believed the lunate possessed a considerable amount of bi-planar mobility relative to the capitate. The authors also perceived that a columnar view of the carpus

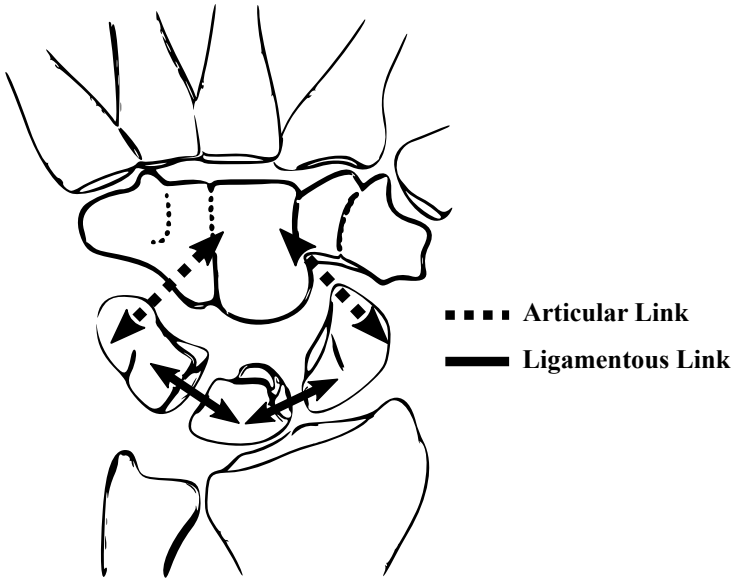

Figure 1.22: The oval-ring theory proposed by Lichtman et al. (1981).

would struggle in providing a universal explanation that accounts for a broad spectrum of clinically observed carpal instabilities. This was especially the case for those occurred in a transverse direction within the same column, such as the midcarpal instability. They then formulated the "oval-ring" theory, in which the carpus was modelled as comprised of four segments, including the distal carpal row as a functional unit and each of the bones in the proximal carpal row. The four segments are linked together via either bony articulations or ligamentous connections to form a complete ring (Fig. 1.22), whose integrity is thought of critical importance in maintaining the physiological carpal motion. The bony articulations of the scaphotrapeziotrapezoid and triquetrohamate joints are modelled as two 'mobile links' that permits the normal reciprocal motion between the proximal and distal carpal rows during wrist radial-ulnar deviation, whereas the ligamentous links represented by the scapholunate and the lunotriquetral interosseous ligaments ensure the carpus does not manifest a dorsal (DISI) or a volar intercalated segment instability (VISI).

In contrast to most of the existing theories, which were proposed based on qualitative observations of the carpal motion and thus remained largely

speculative, Sandow et al. (2014) formulated the 'Stable Central Column Theory' through the use a novel computational method. In simple terms, the authors estimated the dynamic relationships between bones of the carpus according to the so-called isometric constraints, which were essentially the pairs of points located on the surfaces of different carpal bones and the radius whose distance stayed constant throughout the range of wrist motion. They suggested that the lunate and the distal row function as a stable central column, which was supported laterally by the scaphoid, functioning in a manner analogous to a 'two gear four-bar linkage' mechanically. The triquetrum was believed to act primarily as a restraint, preventing ulnar translation of the carpus, while also providing control over lunate flexion. Surprisingly, the authors did not find any fixed relationship between the triquetrum and hamate, which challenged the importance of the triquetrohamate joint as perceived in many existing theories (Rainbow et al., 2016).

However, it is not without doubt as to whether there exists a universal theory that could adequately model the carpal motion. After studying the static radiographs of 52 volunteers, Craigen and Stanley (1995) found there was significant variation in the radiographic appearance of the scaphoid during wrist radial-ulnar deviation between male and female subjects. They showed that there were substantially more sagittal plane rotation and less coronal plane translations of the scaphoid in women, and subsequently hypothesised that wrists of female subjects were more likely to function in a column-like pattern. In a similar study involved 60 volunteers, Garcia-Elias et al. (1995) found the scaphoids in wrists suffered from a higher degree of joint laxity tended to exhibit more rotation in the sagittal plane during wrist radial-ulnar deviation, whereas those in less lax wrist demonstrated more coronal plane rotation, further adding to the contention that human wrists display a spectrum of both row-like and column-like carpal motion.

1.3.3 Carpal Contact Characteristics

In order to support stable hand function, the wrist must withstand a considerable amount of force transmitted through the carpometacarpal joint (Garcia-Elias and Lluch, 2017). Therefore it might be beneficial to have some basic knowledge on the joint contacts and force transmissions within the carpus before the normal biomechanics of the wrist and the pathomechanics of related injuries can be better understood.

Midcarpal Joint

Only a handful of studies have experimentally examined the contact characteristics of the midcarpal joint, presumably due to the limited space available and the anatomical complexity within the region. Viegas et al. (1993) loaded five cadaveric specimens with four different levels of force, ranging from 143 N to 525 N. Based on the imprint of the pressure-sensitive film placed inside the midcarpal joint, he found the contact was made mainly through the scaphotrapeziotrapezoid, scaphocapitate, lunocapitate, and triquetrohamate articulations, with a force transmission ratio of 23%, 28%, 29% and 20%, respectively. The total contact area, however, was found to account for less than 40% of the available joint surface, even at the highest level of loading. The centroids of contact area were found to be less variable in different wrist positions, which concurred with the notion that the distal carpal row functions as an integral unit with minimal intercarpal motion. However, since the placement of the pressure-sensitive film required excision of the dorsal capsule and surrounding ligaments, the authors flagged that the results obtained in that cadaver model might not be exactly reflective of those in the physiological condition.

Majima et al. (2008) studied force transmission within the carpus *in-vivo* in seven subjects. Based on computed tomography (CT) scans of the wrist, patient-specific three-dimensional rigid body spring models (3D-RBSM) were developed. The authors found a force transmission ratio of 13%, 16%, 31%, 28%, and 12%, for the scaphotrapezium,

scaphotrapezoid, scaphocapitate, lunocapitate and triquetrohamate articulations, respectively, for wrists placed in the neutral position with a total of 140 N force applied through their metacarpals. These values are in good agreement with those obtained experimentally, and those reported previous by using a two-dimensional version of the RBSM (Schuind et al., 1995). Furthermore, it is also obvious that the distal surface of the scaphoid and lunate are significantly loaded by the capitate, taking up almost 60% of the force transmitting within the carpus.

Radioulnocarpal Joint

In contrast to the midcarpal joint, the force transmission ratios in different regions of the radioulnocarpal joint have been studied extensively using a variety of methods (Table 1.3). In general, when the wrist is in the neutral position, over 50% of the force is transmitted through the radioscaphoid articulation, while the rest transmits through the radiolunate articulation and the TFCC to the ulna, accounting for approximately 35% and 15% of the total force, respectively (Garcia-Elias and Lluch, 2017).

The articular pressures in different regions of the radioulnocarpal joint are often reported as their peak values in the literature (Table 1.4). Despite the fact that those measurements cover a wide range, it is evident that the peak pressure transmitted across the radioscaphoid articulation is about 20%-50% higher than that across the radiolunate articulation, when the wrist is placed in the neutral position. However, the average pressure borne by the scaphoid and the lunate has been shown to be comparable. A value of 1.16 and 1.02 MPa have been reported by Blevens et al. (1989), with a load of 178 N distributed across the tendons of the wrist prime movers. With a total load of 200 N, Tang et al. (2009) similarly found an average pressure of 1.4 and 1.3 MPa for the radioscaphoid and radiolunate contact, respectively.

Collectively, the area of the radioulnocarpal contact accounts for less than a quarter of the total articular surface available (Tencer et al., 1988; Blevens et al., 1989; Guo et al., 2009). Individually, based on the imprint of

Table 1.3: Summary of previously reported force transmission ratios in different regions of the radioulnocarpal joint, when the wrist is placed in its neutral position

Study	**Method**	**Applied Load (N)**	**Force Transmission Ratio (%)**		
			Radius		Ulna
			Scaphoid Fossa	Lunate Fossa	TFCC
Trumble et al. (1987)	Load Cell	98.1	83		17
Werner et al. (1992)		NM	83		17
Blevens et al. (1989)	Fuji Film	178	34	26	40
Short et al. (1992)		89*	50	29	21
Hara et al. (1992)	Conductive Rubber	98	50	35	15
Horii et al. (1990)	RBSM	143	46	32	22
Watanabe et al. (1993)		210	41	46	13
Schuind et al. (1995)		131†	55	35	10
Iwasaki et al. (1998)	3D-RBSM	143‡	44	31	25
Genda and Horii (2000)		140	48	40	12
Majima et al. (2008)		140	52	42	6
Matsuki et al. (2009)		140	47	39	14
Mrquez-Florez et al. (2016)		142§	51	35	14§§
Guo et al. (2009)	FEA	100|	55		45
Gislason et al. (2009)		1473‖	88‖		12‖
Bajuri et al. (2012)		NM¶	90		10

* 5 lb (22.2 N) applied to in total of four wrist flexors and extensors.
† each carpometacarpal joint transmit a mean of 26.2 N of force.
‡ 22.5, 33.0, 42.2, 25.6, 19.7 N of force were applied to the 1st through the 5th digits, respectively.
§ 21.5, 34.3, 42.2, 25.9, 18.1 N of force were applied to the 1st through the 5th digits, respectively.
§§ summation of the results for the ulnolunate and ulnotriquetrum contact
| forces were applied through the 2nd and 3rd metacarpals only.
‖ average of the results reported for three subjects.
¶ 0.2, 0.16, 0.13, 0.15, 0.09 MPa of load were applied to the 1st through the 5th metacarpals, respectively.
RBSM: rigid body spring model; FEA: finite element analysis; NM: not mentioned.

Table 1.4: Summary of previously reported peak articular pressures in different regions of the radioulnocarpal joint, when the wrist is placed in its neutral position

Study	Appied Load (N)	Peak Pressure (MPa)		
		RS	RL	TFCC
Palmer and Werner (1984)	89*	3.3	3	1.4
Tencer et al. (1988)	103		3.17§	
Kazuki et al. (1991)	100	2.8	2.7	0.2
Hara et al. (1992)	98	2.4	1.5	1.1
Iwasaki et al. (1998)	143	3.7	2.7	2.2
Genda and Horii (2000)	140	4.5	3.4	
Carrigan et al. (2003)	15†	1.9-2.6‡		
Guo et al. (2009)	100	5.2	2.9	
Fischer et al. (2011)	110	1.7[a]	1.6[a]	
		1.9[b]	1.3[b]	
		2.3[c]	1.9[c]	
Daly et al. (2018)	406	6.7	6.2	

* 5 lb (22.2 N) applied to in total of four wrist flexors and extensors.
§ the entire radioulnocarpal articulation.
† applied to the capitate.
‡ 5 or 10 MPa cartilage modulus, fixed or unconstrained scaphoid.
[a] pressure-sensitive film, [b] Tekscan, and [c] predicted by a MRI-based model.
RS: radioscaphoid, RL: radiolunate

the pressure-sensitive film, Short et al. (1992) reported that the contact in the scaphoid fossa, lunate fossa and the TFCC accounts for only about 9%, 6% and 8% of the available articular surface, respectively.

Furthermore, the contact characteristics of the radioulnocarpal joint have been found to be a function of the global wrist position. However, conflicting results have been reported by different researchers. For instance, Tencer et al. (1988) tested five cadaveric wrist specimens, with each of them loaded statically in thirty-six different positions. They noted that the centroids of both radioscaphoid and radiolunate contact translated towards the volar aspect of the distal radius when the wrist was moved from 20 flexion to 20 extension. But with the wrist moving into further extension, the authors observed that both contact centroids translated in the opposite

direction towards the dorsal aspect of the radius. However, the authors did not find any significant movement of both contact centroids in either radial or ulnar deviation of the wrist.

In contrast, after examining the pressure imprints obtained in twelve cadaver wrists with each loaded and balanced in six different static postures, Blevens et al. (1989) reported that both of the radioscaphoid and radiolunate contact centroids translated monotonically radially during wrist flexion and ulnarly during extension. In wrist ulnar deviation, the authors reported that the centroid of radioscaphoid contact translated significantly volarly, and that of the radiolunate contact translated dorsally. In wrist radial deviation, the centroid of radioscaphoid contact translated primarily radially, whereas that of the radiolunate contact translated significantly towards the volar aspect of the radius.

In four cadaver wrists, Kazuki et al. (1991) found the contact centroid of radiolunate articulation moved dorsally in flexion and towards the volar side of the radius in extension. They also observed that the contact centroid of radioscaphoid articulation translated towards the dorsal side of the radius as the wrist moved into ulnar deviation.

These are again in direct contradiction with the observations reported in a more recent study performed by Tang et al. (2009), who tested six cadaveric wrist specimens in neutral, 45° of flexion and 45° of extension with a total load of 200 N. They suggested that the centroid of radioscaphoid contact moved significantly towards the dorsal and ulnar aspect of the radius in wrist flexion and moved volarly and radially in extension, whereas the centroid of radiolunate contact moved consistently towards the dorsal and radial aspect of the radius during both wrist flexion and extension.

In terms of the changes in articular contact pressure, based on the available data in the literature, it is evident that disagreements mainly exist over those measured for both wrist flexion and extension (Table 1.5).

Table 1.5: Percentage change (with respect to the values measured in the neutral position) in articular contact pressure at different wrist positions

Study	**Flexion**		**Extension**		**Ulnar Dev.**		**Radial Dev.**	
	RS	RL	RS	RL	RS	RL	RS	RL
Blevens et al. (1989)	-16.5%	-8.3%	-6.0%	-9.7%	-20.3%	+10.8%	+2.8%	-18.7%
Hara et al. (1992)*	+20.8%	+60.0%	-4.2%†	+80.0%†	-12.5%	+93.3%	+8.3%	-26.7%

* mean peak pressure
† values measured at 20° of wrist extension.
† at 40° of wrist extension, these changed to -41.7% and +46.7% for RS and RL, respectively.
RS: radioscaphoid, RL: radiolunate

1.4 SLIL Injury and Scapholunate Instability

In this section, the pathophysiology of the scapholunate interosseous ligament injury and the so-called scapholunate instability, which often ensues after the injury, is briefly reviewed. Knowledge on the injury-induced alterations of the carpal kinematics and contact are summarised to-date. Diagnostic methods and treatment options for managing different stages of scapholunate instability are also surveyed.

1.4.1 Overview

The scapholunate joint is arguably one of the keystones for normal carpal function. It has been recognised that the stability of this joint is ensured primarily by the scapholunate interosseous ligament (SLIL), and supported by several other ligamentous structures presented in the vicinity, providing secondary stability (Kitay and Wolfe, 2012). However, as biomechanically important as the anterior cruciate ligament (ACL) is to the knee, the SLIL also suffers a very high rate of injury.

Whilst exceptions may exist, disruption of the SLIL and the adjacent secondary stabilisers often leads to scapholunate instability (Boabighi et al., 1993; Chennagiri and Lindau, 2013; Mugnai et al., 2016). Patients who suffer from this disabling instability often find their wrists incapable of bearing mechanical loads and exhibit abnormal kinematics with sudden shifts and audible "clunks" during wrist motion (Garcia-Elias, 1999). Forced movement of the scaphoid and lunate during a traumatic event, such as a fall on an outstretched hand (FOOSH), typically with the wrist hyperextended, ulnarly deviated, and coupled with intercarpal supination, is believed to be the major cause of this injury (Mayfield et al., 1980). It has also been recognised that instead of being an "all-or-none" type of condition, scapholunate instability represents a spectrum of injuries, dependant upon both the severity and

chronicity of the ligamentous disruption (Linscheid et al., 1972; Mayfield, 1984; Watson et al., 1993; Nathan and Blatt, 2000). Furthermore, if the initial, isolated injury to the SLIL is mistakenly dismissed and left untreated, prolonged exposure to the altered kinematics and articular contact is likely to inflict further damage such as straining of the secondary stabilisers and attrition of the cartilage, which may subsequently result in irreversible postural changes of the carpal bones and ultimately degenerative osteoarthritis (Linscheid et al., 1983; Watson et al., 1997; Garcia-Elias et al., 2006). Scapholunate instability is, therefore, believed to be a progressive pathology, and many classification systems have been developed to better describe the different stages of its clinical manifestation, guiding the diagnostics and the following treatments.

1.4.2 Clinical Classification

Geissler et al. (1996) advocated that the articular spaces of both radiocarpal and midcarpal joints needed to be examined during wrist arthroscopy to increase the sensitivity for detecting ligament lesions in the scapholunate interval. Based on the arthroscopic findings, the authors classified the extent of SLIL injuries into four distinctive grades (Table 1.6).

Table 1.6: Geissler arthroscopic grades of scapholunate interosseous ligament injuries with suggested management options (modified from Geissler et al. (1996) and Geissler (2015)).

Geissler Grade	Description	Management
I	Attenuation/hemorrhage of SLIL as seen from the RC joint. No incongruency of carpal alignment in the midcarpal space.	Immobilization
II	Attenuation/hemorrhage of SLIL as seen from the RC joint. Incongruency/step-off as seen from midcarpal space. A slight gap (> width of a probe) may be present in the SL interval.	Arthroscopic reduction and pinning
III	Incongruency/step-off of carpal alignment is seen in both the RC and MC spaces. The probe may be passed through the gap in the SL interval.	Arthroscopic/open reduction and pinning
IV	Incongruency/step-off of carpal alignment is seen in both the RC and MC spaces. A 2.7 mm arthroscope may be passed through the gap. Gross instability with manipulation.	Open reduction and repair

RC: radiocarpal; MC: midcarpal; SL: scapholunate; SLIL: scapholunate interosseous ligament

Despite being widely quoted, this classification scheme has not yet been validated *in-vivo* for its intra- and interobserver reliability (Izadpanah and Kakar, 2016). Furthermore, since this classification scheme is based solely on the arthroscopic appearances of the scapholunate interval and does not explicitly correlate the pathoanatomy with different stages of scapholunate instability, its diagnostic use is therefore relatively limited (Rimington et al., 2010; Messina et al., 2013).

Wolfe (2001) classified scapholunate instability into five different stages, based on the severity and the constancy of the pathology. For each stage, quantitative radiographic indications, along with the ligaments that were likely to have become attenuated, as well as the treatment option deemed most suitable, were formulated (Table 1.7).

In *occult* scapholunate instability, the SLIL is believed to have only suffered a partial attenuation, but without having its dorsal component compromised. Carpal bones in the affected wrist may not exhibit postural changes that are visible radiographically (Yin and Gilula, 2001), and the arthroscopic examination may report Geissler Grade I-II findings without gross instability (Garcia-Elias, 2011). Wrist dysfunction may be reported in mechanically demanding activities, and accompanied by local synovitis and pain in some cases (Watson et al., 1993).

The next stage is *dynamic* scapholunate instability. It is characterised by the complete disruption of the SLIL, including its dorsal component. Malalignment of the carpal bones may still be absent under routine static radiography, but traces of unusual kinematics and abnormal widening of the scapholunate gap may be unveiled using the so-called stress films, in which the wrist is loaded and imaged in specific postures (Mayfield et al., 1980).

With additional attenuation of one or more secondary stabilisers of the scapholunate joint, the stage known as *scapholunate dissociation* may be reached. Although the exact ligamentous lesion responsible for producing this pathologic pattern remains unclear, many researchers have highlighted the importance of the RSC, STT and DIC ligaments (Drewniany et al., 1985; Mitsuyasu et al., 2004; Short et al., 2007; Messina et al., 2013). In this

Table 1.7: Stages of scapholunate instability (modified from Wolfe (2001) and Kitay and Wolfe (2012)).

Stage	I. Occult	II. Dynamic	III. Scapholunate Dissociation	IV. DISI	V. SLAC
Speculated Ligament Injury	Partial SLIL	Complete SLIL deficiency; Partial disruptions of the volar extrinsics	Complete SLIL deficiency; Volar or dorsal extrinsics	Complete SLIL deficiency; Secondary changes in RL, ST, DIC	As in stage IV
Radiographic Appearance	Normal plain XR; Abnormal fluoroscopy	Usually normal plain XR; Abnormal stress XR	SL gap$\geq$ 3 mm RS angle $\geq 60°$ Grossly abnormal stress XR	SL gap$\geq$ 3 mm SL angle$\geq 70°$ RL angle$\geq 15°$ CL angle$\geq 15°$	1. Styloid DJD 2. RS DJD 3. CL DJD 4. Pancarpal DJD
Proposed Treatment	Pinning or Capsulodesis	SLIL repair with capsulodesis	Repair or Reconstruction	Reducible: reconstruction Static: intercarpal fusion	Intercarpal fusion or PRC

SLIL: scapholunate interosseous ligament; SL: scapholunate; RS: radioscaphoid; RL: radiolunate; CL: capitolunate; DISI: dorsal intercalated segment instability. SLAC: scapholunate advanced collapse; DJD: degenerative joint disease; PRC: proximal row carpectomy; XR: X-ray.

stage, the unison between the scaphoid and lunate is lost, and an usual widening of the scapholunate interval is observable on static radiograph. Furthermore, the scaphoid is likely to appear as abnormally flexed in this stage. With passage of time, a deformity termed *dorsal intercalated segment instability* (DISI) may develop under the carpal mechanics which has already been disrupted. This deformity is characterised by the abnormal extension of the lunate, with the dorsal migration of the capitate (Linscheid et al., 1972). Short et al. (2007) believed that the attenuation of the volar radiolunate ligaments might be the key to the pathogenesis of this stage.

Eventually, the presented malalignment becomes irreducible, attributed to secondary changes in the region such as fibrosis (Garcia-Elias, 2011). Permanent postural changes of the carpal bones may result in a constant joint incongruence which exacerbates cartilage wearing and ultimately results in degenerative joint disease (DJD) (Tischler et al., 2014). This stage has been commonly refereed to as *scapholunate advanced collapse* (SLAC) and four distinctive phases have been identified to depict its progression from the radial-most portion of the radioscaphoid joint (Stage 1. styloid DJD), across the entire radioscaphoid joint (Stage 2. RS DJD), to arrive at the capitolunate joint (Stage 3. CL DJD), and finally to involve both the radiocarpal and midcarpal joints, and even the distal radioulnar joint as well (Stage 4. Pancarpal DJD) (Watson and Ryu, 1986; Imbriglia, 2004; Weiss and Rodner, 2007).

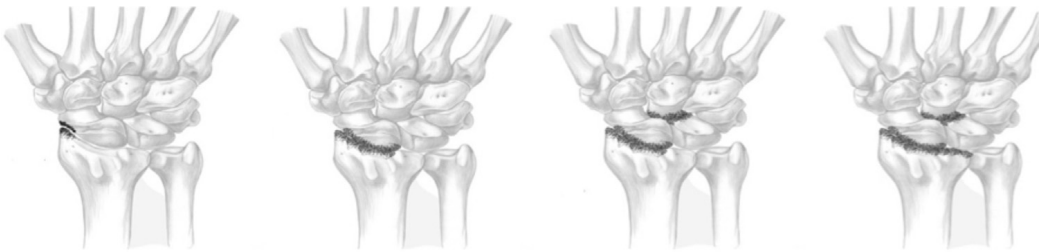

Figure 1.23: Progressive stages of SLAC. Reprint from Belhaouane et al. (2016), with permission from Elsevier.

1.4.3 Effect on Carpal Kinematics

Published accounts on the effect induced by injuries to various scapholunate supporting ligaments on the kinematics or normal alignments of the carpus are reviewed to-date (Table 1.8).

In summary, apart from the SLIL, which has now been recognised as the primary stabiliser of the scapholunate joint, no consensus has been reached on which ligaments provide the most important secondary stability and are therefore the key in preventing the progression of scapholunate instability.

Furthermore, there have been a limited number of studies that have presented the full three-dimensional picture of the pathological carpal motion resultant from each stage of ligament division during dynamic wrist motion. Rotational behaviours of the carpal bones are often reported in the same plane as the global wrist motion (Crisco et al., 2003; Stoesser et al., 2016), or without looking at that in the transverse plane (Berdia et al., 2006; Waters et al., 2016). And changes in the carpal translations after the ligamentous disruptions are frequently overlooked, as it was deemed "difficult to analyse ... in a comparative and quantitative way", according to Short et al. (2002a). In addition, the existing studies focused primarily on the "apparent" alterations in the carpal kinematics, namely, these analyses did not differentiate injury-induced changes that were entirely static and postural from those that were dynamic and behavioural, affecting the way carpal bone moves during global wrist motion.

Table 1.8: Summary of literature on the effect induced by disruptions to various scapholunate supporting ligaments on kinematics or static alignments of the carpus

Study	n	Methods	Order of Lig. Division or Lig. Studied	Key Findings
Mayfield et al. (1976)	28 + 19	28 were dissected and anatomically analysed for the descriptive and functional implications of the ligaments. 19 were subjected to impact test with weights (8.6-19.5 kg) dropped from predetermined heights (38-110 cm). Specimens were then dissected for visual examination of ligamentous injuries.	Volar extrinsic ligaments (not explicitly specified)	In wrist hyperextension, the radioscapholunate ligament (referred to as the radioscaphoid ligament in the original text) was thought to be under maximum tension, and rupture of this ligament was believed to allow separation of the scaphoid from the lunate. Rupture of the radioscaphocapitate (referred to as the radiocapitate ligament in the original text) was believed to destabilise the distal carpal row and allow separation of the two rows.
Berger et al. (1982a)	8	The specimens were secured in a holding device with a pin drilled into their 3MC. The wrist motion was constrained in the coronal plane, and a protractor was used to measure the global wrist position. Tendons of the wrist prime movers were quasistatically loaded. An array of sonic digitisers or spark gaps were used to track the scaphoid and lunate kinematics.	SLIL	The scaphoid and lunate kinematics were found to be minimally affected and continued to track well relative to each other. The authors concluded that an isolated disruption of the SLIL would not result in major disturbances to the normal scapholunate motion.
Ruby et al. (1987)	4	The specimens were positioned in F15° w/ UD10° (a posture thought to stress the SLIL) by balancing the load applied to the wrist tendons via calibrated springs. The scaphoid, lunate, triquetrum and capitate were marked using metal staples, and static biplanar radiography was used to track their position in space. In addition, the dorsal capsule of the cadaveric wrist specimen was left open.	SLIL	The disruption of the d-SLIL caused a significant change in the normal scapholunate relationship. The scaphoid collapsed in flexion and pronation, and the capitate was found to be also flexed but supinated. Minimal changes were found for the lunate position with respect to the radius. The gap between the proximal pole of the scaphoid and the lunate measured up to 3 mm, but the total scaphoid translation was found to be small, around 0.2 mm.

Table 1.8 continued from previous page

Meade et al. (1990)	6	The specimens were radiographically evaluated (SL angle and gap) before and after each stage of ligament division. Stress films were also obtained with the wrist subjected to 13.5 kg of axial load, and the distance between the radius and the scaphoid was measured.	RSL, v- and d-SLIL, RSC (referred to as the radiocapitate ligament in the original text)	Sequential sectioning of the RSL, v-SLIL, d-SLIL and RSC resulted in consecutive increases in the scapholunate angle by 4.8°, 3.7°, 4.5°, 14°, respectively. Moreover, sectioning of the v-SLIL, the entire SLIL, and the RSC increased the scapholunate gap by 0.5, 0.5, and 1.5 mm, respectively. The RSC was, therefore speculated to be important in maintaining the normal scapholunate relationship. Furthermore, the authors believed the RSL and RSC provided restraint against the ulnar translation of the scaphoid. In addition, the authors claimed that the standard radiographic thresholds used in diagnosing scapholunate instability (a scapholunate angle of 70°with a gap of 3 mm) were not sensitive enough as they were not exceeded until significant ligamentous disruptions, involving the RSL, SLIL, and RSC ligaments had occurred.
Ritt et al. (1995)	14	The specimens were disarticulated at the carpometacarpal joints, with the forearm amputated just proximal to the radiocarpal joint. K-wires were inserted to create carpal arthrodesis as well as to fix the forearm. The prepared specimens were potted both proximally and distally in metal blocks and subjected to a supination-pronation torque at a rate of 180°/min. Torque-displacement curves were recorded following each stage of sequential ligament division.	Extrinsic ligaments, including UT, UL, SRL, LRL, RSC and DRC	The RSC was found to serve as the primary constraint against intercarpal pronation, whereas the LRL and SRL were shown to provide moderate resistance against pronation and have similar characteristics. Intercarpal supination was shown to be checked by the DRC as well as the UL ligaments.

Table 1.8 continued from previous page

Short et al. (1995)	6	The dynamic wrist motion simulator described by Werner et al. (1996) was used. Protruding electromagnetic sensors were attached to the third metacarpal and the radius to measure the global wrist position, as well as to the scaphoid and lunate to monitor their angular motions. Three to four 1 × 1.5 cm Tekscan sensors were tapped together and inserted into the radioulnocarpal joint to provide simultaneous articular pressure measurements. FEM (E30°-F30° and E30°-F50°) as well as RUD (RD10°-UD10°) were simulated.	SLIL	Sectioning the SLIL caused the scaphoid to flex (as much as 3.6°) and pronate, and the lunate to extend (as much as 5.4°) during both wrist FEM and RUD. A trend for the articular pressure to shift from the radioscaphoid fossa to the radiolunate fossa was observed after dividing the SLIL.
Short et al. (2002b)	8	Same as above. The effect of a dorsal capsulotomy that sectioned the DRC ligament or the insertion of a pressure sensor into the radioulnocarpal joint on the scapholunate kinematics was investigated.	DRC	The scapholunate motion was found to be statistically affected by both a dorsal capsulotomy through the DRC and insertion of the pressure sensor. The lunate was found to extend less (by 5°-8°) during wrist extension after insertion of the sensor, and exhibit less ulnar deviation (by about 4°) during wrist flexion after both the dorsal capsulotomy and sensor insertion. The scaphoid kinematics was not affected by the dorsal capsulotomy alone, but the sensor insertion caused it to extend less (by 5°) during extension. Furthermore, both the dorsal capsulotomy and sensor insertion increased the supination experienced by the scaphoid and lunate during flexion ($\leq$ 2°). During RUD, the scaphoid was found to flex and supinate more, whereas the lunate was shown to flex, supinate and radially deviate more following the dorsal capsulotomy or sensor insertion.

Short et al. (2002a) Part I of a series of studies on SL supporting ligaments	8	Tendon-driven FEM (E30°-F50°) and RUD (RD10°-UD20°) were simulated using the wrist motion simulator developed by Werner et al. (1996). The entire SLIL, the STT and RSC were sectioned sequentially, and the scaphoid and lunate kinematics were recorded and analysed after each stage of ligament division. After all three ligaments were sectioned, the wrist was moved through 1,000 cycles of FEM (E30°-F30°) to mimic repetitive use of the wrist after sustaining ligamentous injuries, and the changes in the scaphoid and lunate kinematics were also recorded. And based on the obtained kinematics, the minimum distance between the scaphoid and lunate was also determined.	SLIL, STT, and RSC	During FEM, a statistically significant increase in scaphoid ulnar deviation and lunate extension was observed with sectioning of the SLIL. However, sectioning the STT and RSC, as well as 1,000 cycles of motion, did not cause further changes in either scaphoid ulnar deviation or lunate extension. Statistical increases in scaphoid flexion were not observed until all three ligaments were sectioned, and a further increase was observed following repetitive cycling. During RUD, sectioning SLIL did not cause statistically significant changes to be observed in scaphoid or lunate motion. Increase in scaphoid ulnar deviation and lunate extension was observed with further sectioning of the STT ligament. After incremental sectioning of the RSC and 1,000 repetitive cycles of wrist motion, a further increase in lunate extension was observed. A statistical increase in the minimum distance between the scaphoid and lunate was observed when all three ligaments were sectioned, with or without being repetitively cycled.
Short et al. (2005) Part II	8×3	Same as above, but with three groups of 8 specimens, all other permutations of the ligament sectioning sequence apart from the one adopted in the previous study were attempted.	RSC, SLIL, STT (group 1) STT, RSC, SLIL (group 2) SLIL, RSC, STT (group 3)	Sectioning only the STT or the RSC ligament resulted in minimal changes in the rotational motion of the scaphoid and lunate. Sectioning of the SLIL initiated a significant increase in scaphoid flexion and ulnar deviation, as well as in lunate extension. Most of the time, radial or ulnar deviation of the lunate was not affected by the ligament division. Additional changes in the scaphoid and lunate kinematics were seen with all three ligaments sectioned and the wrist subjected to repetitive motion cycles. Furthermore, the division of the SLIL resulted in the most significant change in the minimum distance between the scaphoid and lunate. No significant changes were seen after the division of either the STT or the RSC ligament or both.

Table 1.8 continued from previous page

Short et al. (2007) Part III	8×3	Similar to Part I and II of the study. Three sets of 8 specimens were used to investigate the effect of sectioning the DRC, DIC, SLIL, RSC, and STT ligaments in three different combinations.	STT, SLIL, RSC (group 1) DRC, DIC, SLIL (group 2) DIC, SLIL, DRC (group 3)	Sectioning only the DIC or the STT ligament resulted in minimal changes in the rotational motion of the scaphoid and lunate. Sectioning the DRC in isolation caused the lunate to deviate slightly radially. The change in the scaphoid and lunate motion caused by sectioning the dorsal ligaments (group 2 and 3) was found to be larger than sectioning the volar ligaments (group 1). Furthermore, the coronal plane motion of the lunate was the least affected by sequential ligament divisions. In addition, apart from those involved with a SLIL divison, sectioning the DIC in isolation also caused a statistically significant but slight increase in the minimum distance between the scaphoid and lunate.
Crisco et al. (2003)	8*	Neutral carpal postures, as well as the carpal kinematics during FEM (4 static positions: F and E of 30° and 60°) of both wrist in 8 patients who suffered unilateral SLIL tears, were compared with those of 10 uninjured volunteers. CT scans were obtained, and markerless bone registration technique was employed.	SLIL	The scaphoid and lunate were found to be significantly more extended compared to those in normal patients. However, abnormalities were also found in the contralateral uninjured wrists, as the lunate extension and scaphoid flexion in both wrists of injured patients were found to be not different from each other. Therefore the authors were unable to attribute altered carpal kinematics to SLIL injuries.
Mitsuyasu et al. (2004)	5	The specimens were loaded in a static loading jig in the neutral wrist position. An axial load of 5 kg was applied the second and the third metacarpals. Six stages of ligament division were carried out, and the carpal alignment was examined before and after each stage. Radiographs were taken, and the SL angle and gap, RS and RL angles were measured both manually (goniometer) as well as photogrammetrically by digitising the coordinates of the screws placed inside the carpal bones.	Dorsal capsule, v- and m-SLIL, DIC (detached from the scaphoid and trapezium), d-SLIL and DIC (detached from the lunate and DRC)	The complete distribution of the SLIL did not lead to a static collapse of the lunate. Further detaching the DIC from the scaphoid lead to abnormal flexion of the scaphoid and the formation of the scapholunate diastasis. Detaching the DIC from the lunate lead to DISI deformity in both loaded and unloaded conditions. The authors, therefore, believed that the DIC might be critical in stabilising the scaphoid and lunate and suggested that this ligament needed to be repaired or reconstructed in clinical settings.

**in-vivo* study

Table 1.8 continued from previous page

Elsaidi et al. (2004)	14	The specimen was loaded at the neutral position by a static weight of 30 lb (133.45 N) applied through a traction bow. Anteroposterior and lateral radiographs were taken before and after each stage of ligament division. Scapholunate angle, gap and capitolunate angle were measured.	Volar extrinsic ligaments (RSC, LRL, RSL, SRL), plus the m-, v- and d-SLIL, DIC, and DRC	No scapholunate diastasis or significant increases in the scapholunate angle were observed after dividing the volar extrinsic ligaments and the SLIL. The additional release of the DIC and the dorsal capsule from the scaphoid led to rotatory subluxation of the scaphoid with an increase in the scapholunate angle. Sectioning the DRC further resulted in static DISI deformity. The authors, therefore, concluded that the DIC might be an important stabiliser for the scaphoid, and the DRC might be important for preserving the normal posture of the lunate.
Berdia et al. (2006)	8	The setup was similar to that described in Short et al. (2002a). FEM (E30°-F50°) and RUD (RD10°-UD10°) were simulated. Effect of hysteresis in carpal motion was analysed for the intact stage as well as after each stage of sequentially sectioning the SLIL, STT and RSC ligament. And the amount of motion hysteresis was quantified by computing the area between the two curves representing a reciprocating wrist motion.	STT, STT and RSC	For FEM, the area representing the hysteresis effect of both the scaphoid and lunate motion was found to be significantly increased only after all three ligaments were divided. For RUD, the scaphoid hysteresis was shown to be statistically increased as soon as the SLIL was sectioned, and this increasing trend was also observed in the following stages of ligament division. The lunate hysteresis, however, was found to be decreasing with sequential ligament sectioning in a subset of 4 specimens that were deemed to be laxer. The authors speculated that this divergent behaviour might explain why patients who suffered scapholunate instability sometimes did not develop a static DISI deformity.

Table 1.8 continued from previous page

Werner et al. (2007)	8	Similar to that described in Short et al. (2002a). Scapholunate instability was created by sectioning the SLIL, RSC, and the STT ligaments. And the level of the resultant instability was quantified and subsequently correlated with morphological measurements of the distal radius and the scaphoid. These measurements included the depth, the volar and ulnar tilt of the radioscaphoid fossa, as well as the curvature measurements of both the distal radius and the proximal scaphoid. The force required to dislocate the scaphoid was also calculated via rigid-body dynamics simulation.	SLIL, RSC, and STT	After ligament division, the scaphoid was found to be more flexed and translated dorsally and radially to ride on the dorsal rim of the radius. Sudden "clunk" of the scaphoid was observed during extension in some specimens, as the subluxed scaphoid was reduced back into the radioscaphoid joint. The author also found the curvatures of the radioscaphoid fossa and the proximal scaphoid were larger in those specimens which sustained ligamentous injuries but did not exhibit gross scapholunate instability. Furthermore, they suggested a deeper radioscaphoid fossa and a larger volar tilt might also provide more resistance against the dorsal dislocation of the scaphoid.
Werner et al. (2011)	37	Similar as above. Wrist FEM (E30°-F50°), RUD (RD10°-UD20°), and DTM (E30°R10°-F30°U10°) were simulated, and the changes in scaphoid and lunate translations after sectioning the SLIL along with either two volar or dorsal ligaments were investigated.	SLIL, w/ STT and RSC (the volar group), or w/ DIC and DRC (the dorsal group)	After sectioning the SLIL with the two dorsal ligaments (dorsal group), the scaphoid moved radially, and the lunate moved ulnarly during FEM, and especially in wrist flexion. During RUD, releasing the dorsal group ligaments caused the lunate to translate statistically more volarly, especially during wrist ulnar deviation. Sectioning the SLIL along with the ligaments in the volar group resulted in similar changes, but with the lunate exhibiting statistically different translations in the distal-proximal direction during FEM. Furthermore, after dividing either the volar or dorsal group ligaments and with 1,000 cycles of repetitive wrist motion, there was a statistical increase in the minimal distance between the scaphoid and lunate.

Table 1.8 continued from previous page

Omori et al. (2013)	6+6[a]	Centroid locations of each carpal bone and postures of the scaphoid and lunate were calculated based on the CT scan with the subject's wrist placed in the neutral position. The joint proximity was also calculated for the radiocarpal and midcarpal articulations.	SLIL and other SL stabilisers (not explicitly specified)	The scaphoid was shown to rotate in flexion and pronation and translate dorsally and radially, whereas the lunate was extended and supinated in patients with stage IV scapholunate instability. The entire distal row translated dorsally. The radioscaphoid contact was shown to be translated significantly radially and dorsally, owing to subluxation of the scaphoid. However, joint contact congruity was found to be retained in the radiolunate, lunocapitate and STT articulations.
Garcia-Elias et al. (2014)	6+6[b]	The patients were instructed to move their wrist from their maximal available radial-extension to ulnar-flexion twice within 15 seconds, and the wrist motion was captured using 4D CT. Geometric measurements, including the lateromedial displacement of the scaphoid and the lunate along the coronal plane, as well as the scaphotrapezial angle in the plane of motion, were taken based on the reconstructed motion series.	SLIL and other SL stabilisers (not explicitly specified)	The authors found the scaphoid and lunate in normal patients did not flex or extend, but translated in the coronal plane by approximately 5 to 6 mm during DTM. However, in patients with a torn SLIL, the scaphoid was found to translated considerably more radially than the lunate, measured 12.8 mm and 4.8 mm, respectively, inducing a scapholunate gap. Therefore, the authors warned about the use of DTM in rehabilitation exercises.
Eschweiler et al. (2016b)	8	Passive wrist motion was simulated under the effect of gravity of the hand and the weights (0.5 kg applied to each of five wrist muscles). A pin was inserted into the third metacarpal, and protractor-like apparatus was used to confine the wrist motion in FEM (E30°-F30°) and RUD (UD20°-RD15°) planes. Small electromagnetic sensors were embedded into all carpal bones except for the pisiform to track their motion.	SLIL	The distal row bones were not affected by the isolated disruption of the SLIL, and the changes in the kinematics of the proximal row bones were also small. As compared to the intact state, the rotational behaviour of the scaphoid showed a mean difference of 2° for FEM and 1° for RUD. Moreover, those of the lunate and triquetrum only showed a marginal difference ($< 1°$) for wrist motion in both planes. The translational behaviour of the scaphoid was found to be altered during FEM, as it showed an increased dorsal translation (2.5 mm) in wrist flexion. The lunate showed increased proximal (up to 3.0 mm) and ulnar (up to 2.0 mm) translations during both wrist flexion and radial deviation.

[a] *in-vivo* study with 6 (Stage IV scapholunate instability: complete SLIL tear with DISI) + 6 (normal control)
[b] *in-vivo* study with 6 (unilateral SL instability) + 6 (normal control)

Table 1.8 continued from previous page

Waters et al. (2016)	16	Similar to Werner et al. (2011).	v- and d-SLIL	The author found sectioning of the d-SLIL accounted for 37%, 72%, and 68% of the increase in scaphoid flexion in FEM, RUD, and DTM, respectively, whereas, sectioning the v-SLIL accounted for only 7%, 6%, and 14% of the increase. Sectioning of the d-SLIL also induced 53%, 77%, and 32% of the increase in scaphoid ulnar deviation, as well as 55%, 57%, and 58% of the increase in lunate extension in FEM, RUD, and DTM, respectively. The authors concluded that the d-SLIL provided more stability to the scapholunate joint than the v-SLIL.
Stoesser et al. (2016) & Padmore et al. (2019)	8	Tendon-driven FEM (F45°-E45°) and RUD (RD10°-UD20°) were simulated using the wrist motion simulator developed by Iglesias (2015). The scaphoid and lunate kinematics were tracked using protruding optical markers rigidly attached to the bones.	SLIL, STT, and RSC	During wrist flexion, sectioning of the d-SLIL in isolation did not cause a statistically significant increase in scaphoid flexion. Completely sectioning the SLIL caused an increase of 3.5° in scaphoid flexion comparing to that in the intact state but was shown to be statistically insignificant (p=0.08). Sectioning the STT and RSC further did not result in significant alterations in scaphoid kinematics. The lunate was not statistically extended until the entire SILI was sectioned, the increase in lunate extension was found to be 4.7° compared to that in the intact state. No statistical changes were observed in subsequent stages of ligament sectionings. During wrist extension, sequential sectioning of those scapholunate supporting ligaments did not result in significant alterations in scaphoid kinematics. And again, the increase in lunate extension was not statistically significant until the entire SLIL was sectioned. This was found to be 4° comparing to that in the intact state. Furthermore, sectioning the RSC in addition to the SLIL and the STT ligament caused another statistical increase of 0.9°. During RUD, sequential ligament sectioning did not result in statistical changes in scaphoid kinematics. For the lunate, sectioning the entire SLIL caused a mean increase of 3.5°in its extension. Sequentially sectioning the STT and RSC caused a consecutive increase of 0.5° and 1.8° in lunate extension, respectively.

Table 1.8 continued from previous page

Werner and Short (2018)	22 + 15	Similar to Werner et al. (2011). In 22 specimens, the SLIL and two volar ligaments (STT, RSC) were sectioned, whereas, in 15 specimens, the SLIL was sectioned along with two dorsal ligaments (DIC, DRC). In order to see whether a higher amount of ECU force was required to achieve the same global wrist motion, changes in its contribution (ratio of the ECU force to the total muscle force) before and after ligament division were also analysed.	SLIL, w/ STT and RSC (the volar group), or w/ DIC and DRC (the dorsal group)	Sectioning the SLIL with either the volar or the dorsal ligament group caused a statistically significant increase in scaphoid pronation and lunate supination during FEM, RUD, and DTM. Sectioning the dorsal group of ligaments induced statistically more lunate supination than sectioning the volar group. But sectioning both groups of ligaments produced a similar amount of scaphoid pronation. Furthermore, a greater ECU force was recorded after dividing either group of ligaments in order to allow for the same global wrist motion to be achieved. But no statistically significant difference in the increment of ECU force was found between the two sectioning groups.
Pérez et al. (2019)	30	Specimens were randomised into five groups to study the effect of sectioning the SLIL, LRL, STT and DIC in different orders. In addition, the DIC's attachment to the lunate (DIC^{L}) and the scaphoid (DIC^{S}) were studied separately. Each specimen was loaded by 71 N distributed among tendons of five wrist muscles. The outcome of each stage of ligament division was assessed based on radiographic measurements, including SL angle and gap, RL angle and dorsal scaphoid translation.	SLIL w/ DIC^{L}, -^{S}, STT, LRL (group 1) DIC^{L}, -^{S}, LRL, STT (group 2) STT, LRL, DIC^{L}, -^{S} (group 3) LRL, STT, DIC^{L}, -^{S} (group 4) LRL, DIC^{L}, -^{S}, STT (group 5)	Isolated disruption of the SLIL did not increase the RL angle. Sectioning the SLIL along with the LRL or the DIC^{L} resulted in a significant increase in RL angle, but did not lead to an immediate DISI deformity. The deformity was evident after sectioning the SLIL with either the STT (considered as a vital scaphoid stabiliser by the authors), or the DIC^{L+S} (a critical lunate stabiliser).

1.4.4 Effect on Carpal Contact

To date, there have been very few studies that have evaluated the change in carpal contact biomechanics induced by disruptions of the scapholunate supporting ligaments.

Burgess (1987) studied the effect of rotatory subluxation of the scaphoid on radioscaphoid contact area in eight cadaver wrists. Black chalk dust was applied to the proximal articulating surface of the scaphoid to allow the radioscaphoid contact to be traced and outlined on the distal radius. The authors found rotatory subluxation of the scaphoid rendered a more dorsally located radioscaphoid contact, and with 20° of scaphoid rotation, a dramatic 77% decrease in its contact area was observed.

Viegas et al. (1987b) evaluated the changes in the radiocarpal contact characteristics following Stage I to III of the progressive perilunate instability described by Mayfield et al. (1980). In five cadaver writs, the instability patterns were simulated by sequentially sectioning the SLIL (Stage I), the RSC (referred to as the radiocapitate ligament in the original text) and RSL ligament (Stage II), and the LRL ligament (referred to as the radiotriquetral ligament in the original text) and the LTIL (Stage III). Pressure-sensitive films (Fuji films) were placed into the radiocarpal joint to record the articular contact imprints. With increasing instability of the proximal carpal row, the authors found the radioscaphoid contact area decreased but the contact pressure significantly increased. In addition, the centroid of radioscaphoid contact was observed to be shifted significantly towards the dorsal and ulnar aspect of the distal radius, whereas that of the radiolunate contact was found to be shifted volarly and ulnarly with progression of the instability.

Blevens et al. (1989) examined the effect of incrementally sectioning the SLIL, STT, as well as the RSC, RSL, LRL ligaments (referred to collectively as the palmar intra-capsular radiocarpal ligaments in the original text) in different combinations and permutations in twelve cadaver wrists. Pressure-sensitive films were again placed into the radiocarpal articulation through a dorsal capsulotomy to record changes in the joint contact area,

force and pressure. The wrist was loaded in five different postures, with a total of 178 N distributed across the tendons of five wrist prime movers. After analysing the imprints of the pressure-sensitive films, the authors found a complete disruption of the SLIL led to the separation of the radioscaphoid and radiolunate contact areas. The centroid of radioscaphoid contact was found to translate dorsally and radially, directly challenging the findings reported by Viegas et al. (1987b). The shape of the radioscaphoid contact was shown to change dramatically from a congruent circular pattern, concentric with the articulating radioscaphoid fossa, to a narrow ellipse outlining the dorsal rim of the distal radius, resulting in a significant decrease in the radioscaphoid contact area. In return, this caused a significant 37% increase in the radioscaphoid contact pressure, as the force transmitted through the radioscaphoid articulation was found to be roughly unaffected. The radiolunate contact was shown to exhibit a 20% increase in pressure, but with its contact area remained relatively large and concentric with the articulating fossa. In contrast, except for an almost one-third decrease in the radioscaphoid contact area and force after sectioning the STT ligament, isolated disruptions of the secondary ligamentous stabilisers were shown to induce minimal alterations in both the radioscaphoiod and radiolunate contact characteristics. After sectioning all selected ligaments, the proximal pole of the scaphoid was found to be subluxated, and both the radioscaphoid contact force and pressure were found to be decreased considerably. And this load was believed to be subsequently borne by the lunate, as the contact force and pressure within the radiolunate articulation were found to be increased. Furthermore, the centroid of radiolunate contact was found to translated volarly and ulnarly. The authors concluded that periscaphoid ligament disruptions tended to decouple the scaphoid from the force transmission column of the wrist, and partial scaphoid instability was deemed more detrimental to the radioscaphoid joint than a complete destabilisation of the scaphoid (such as in its rotatory subluxation), as it was shown to induce the highest pressure within the articulation.

Short et al. (1995) qualitatively evaluated the effect of sectioning the SLIL on the pressure distribution within the radioulnocarpal joint in a group of six cadaver wrists. Three to four flexible piezoresistive pressure sensors (Tekscan sensors) were taped together to provide adequate coverage over the entire articular surface. After sectioning the SLIL, the authors observed a trend for high articular contact pressure to shift from the radioscaphoid fossa to the radiolunate fossa.

Johnson et al. (2013) studied *in-vivo* radiocarpal contact mechanics in ten patients with unilateral scapholunate ligament injury using a novel MRI-based surface contact modelling technique. Compared with their uninjured side, wrists with a torn SLIL demonstrated significantly higher contact force and peak contact pressure in both the radioscaphoid and radiolunate articulation. In addition, they found the distance between the centroids of radioscaphoid and radiolunate contact was increased in SLIL-deficient wrists. In one subject, they showed that the radiocarpal contact was changed from mid-dorsal to dorsoradial, and the radiolunate contact was found to be shifted volarly on the distal radius, concurring with those reported previously. However, they suggested that the contact area of the radioscaphoid articulation was substantially larger on the injured side, contradicting with the findings in most studies.

Omori et al. (2013) also investigated the *in-vivo* radiocarpal contact in six patients suffering complete tears of the SLIL with an established DISI deformity using an imaging-based joint proximity mapping (inter-bone distance) approach. They qualitatively evaluated the proximity maps of the radioscaphoid and radiolunate articulations and found subluxation of the scaphoid rendered an incongruent and dorsoradially shifted contact with the radius. In contrast, joint congruency was found to be preserved in the radiolunate articulation even with DISI, but the joint proximity map indicated that the contact was made primarily through the dorsal aspect of the distal radius.

In summary, out of the limited published investigations on this topic, there have not been any studies that systematically evaluated the change in

radioulnocarpal contacts as a result of each stage of scapholunate instability. Furthermore, presumably owing to the use of pressure-sensitive films, the loading experiments were conducted mostly in a static fashion, commonly with the cadaveric wrist specimen placed in a collection of selected postures with dead weights attached to the tendons to simulate physiological muscle loadings. In the dynamic test conducted by Short et al. (1995), the applied muscle loads seemed to be arbitrary as their wrist joint simulator was developed with a position control algorithm (Werner et al., 1996). Additionally, in their study, the total load applied to the cadaveric wrist specimen was not kept constant between wrist positions at which the radioulnocarpal pressure was compared, creating ambiguity as to whether the observed difference was indeed a result of the simulated ligamentous injury.

1.4.5 Management of Scapholunate Instability

1.4.5.1 Diagnosis

Although SLIL injuries and scapholunate instability are very common, their diagnoses are often delayed or even missed, especially when the ligamentous disruption is isolated and the instability is still at its early stages, owing to the subtlety of their clinical presentations. Moreover, the signs or symptoms might be concealed by other more obvious problems at present, for instance, some distal radius fractures are often complicated by a various degrees of ligamentous disruptions (Geissler et al., 1996; Ogawa et al., 2013), further obstructing the diagnosis of scapholunate instability.

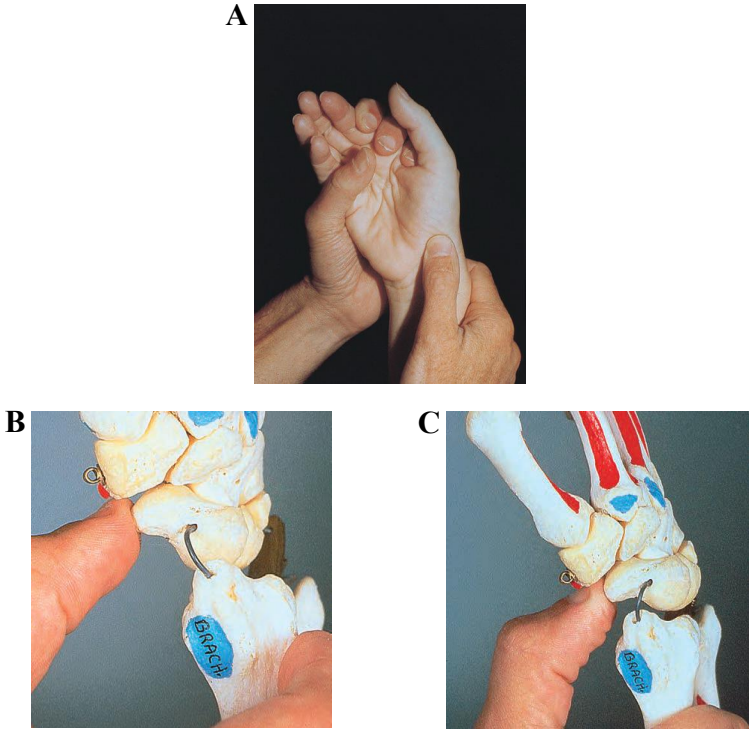

Figure 1.24: **(A)** A photograph of the Scaphoid Shift Test developed by Watson et al. (1993) being performed by a physician. **(B)** An illustration of the examiner's hand placement in relation to the scaphoid tubercle. **(C)** The scaphoid tends to displace out of the scaphoid fossa during the manoeuvre in SLIL-deficient wrists. Reprint from Goldfarb and Gelberman (2010) and Viegas (2010), with permission from Wolters Kluwer Health.

A provocative manoeuvre, known as 'the Scaphoid Shift Test', has been proposed to diagnose scapholunate instability (Watson et al., 1993). It also allows the otherwise indescribable discomfort experienced by the patient during wrist motion to be reproduced to aid the diagnostic process. In short, dorsally directed pressure is applied to the scaphoid tuberosity on the palmar aspect, while the patient's wrist is passively brought from ulnar to radial deviation by the clinician (Fig. 1.24B). If the SLIL is disrupted, the proximal pole of the scaphoid is likely to be forced out of the radioscaphoid fossa and subluxate dorsally onto the dorsal rim of the distal radius, causing pain to perceived at the radial and dorsal aspect of the wrist (Fig. 1.24C). Furthermore, since the externally applied pressure will prevent the extended scaphoid from going into flexion as the wrist radially deviate, a characteristic "clunk", as a result of the spontaneous reduction of the scaphoid, will be heard as soon as the thumb pressure is released. Although cases of false positive test results have been reported due to ligamentous hyperlaxity (Easterling and Wolfe, 1994), the Scaphoid Shift Test has been shown to have a mean positive likelihood ratio of 2.76 and has been highly recommended for diagnosing scaphoid instability (Valdes and LaStayo, 2013).

Radiographic examinations of the wrist are essential once scapholunate instability is suspected. Standard posteroanterior (PA) and lateral views of the carpus are commonly obtained. Additional projections with the wrist "stressed" in specific postures or with a clenched fist have also been suggested and proven useful, especially in diagnosing dynamic scapholunate instability (Mayfield et al., 1980; Lawand and Foulkes, 2003; Sikora et al., 2019).

On PA radiographs, scapholunate dissociation may be suspected if an asymmetric and widened scapholunate interval (scapholunate diastasis) is observed (Fig. 1.25) (Gilula and Weeks, 1978; Tischler et al., 2014). This radiographic presentation is frequently referred to as the 'Terry-Thomas sign', which is an analogy to the person's dental diastema (Frankel, 1977). Foreshortening of the scaphoid with its tuberosity superimposed onto its waist, or radiographically a 'signet ring sign', can be observed on the PA projection when the scaphoid has collapsed into rotatory subluxation in advanced stages

of scapholunate instability (Cautilli and Wehb, 1991).



Figure 1.25: An example of the radiographic presentations of scapholunate dissociation: the Terry-Thomas sign (white double arrow) and the signet ring sign (black arrow heads). Reprint from Garcia-Elias and Lluch (2017), with permission from Elsevier.

On lateral radiographs, intercarpal angles defined between imaginary tangents or axes drawn for the carpal bones, are often used in the clinical assessment of the carpal alignment (Fig. 1.26). Despite the choice of diagnostic thresholds may vary between physicians, a radioscaphoid angle $> 60°$ is generally indicative of rotatory subluxation of the scaphoid (Gilula et al., 2002). And a DISI deformity is considered, when an increased radiolunate angle $> 10°$, a capitolunate angle $> 30°$, and a scapholunate angle $> 80°$ are observed (Zanetti et al., 1998).

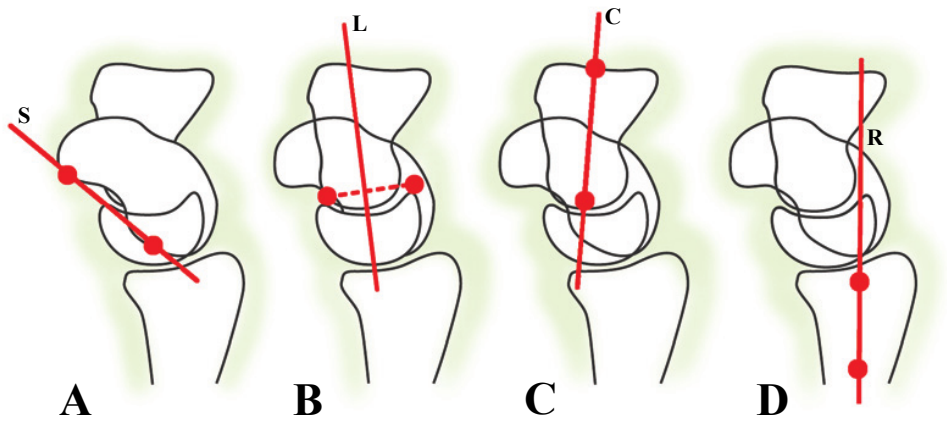

Figure 1.26: Imaginary axes and tangents drawn to the carpal contours are commonly used as bases for clinically measuring intercarpal angles on lateral radiographs. They include the **(A)** scaphoid tangent, **(B)** lunate tangent (dashed line, connecting the two distal horns of the lunate), and the lunate axis (solid line, perpendicular to the lunate tangent), **(C)** capitate axis, **(D)** the axis of the radius. Reprint from Garcia-Elias and Lluch (2017), with permission from Elsevier.

1.4.5.2 Treatment Options

The optimal treatment for SLIL injury and scapholunate instability is heavily debated and remains an unsolved problem in the field of wrist surgery. In most literature, the choice of treatment strategy is often based upon factors including the extent as well as the chronicity of the injury, reducibility of the carpal derangement, and whether there are secondary arthritic changes in the joint (Kitay and Wolfe, 2012; Chennagiri and Lindau, 2013; Konopka and Chim, 2018).

Acute Injuries

Open surgeries are typically not recommended when the SLIL is only partially attenuated and the injury is diagnosed acutely within two to three weeks (Pappou et al., 2013). Instead, arthroscopic debridement (Weiss et al., 1997), electrothermal shrinkage with percutaneous pinning (Darlis et al., 2005), or physiotherapy that re-educates the FCR muscle (Salvà-Coll et al., 2011; Kitay and Wolfe, 2012; Andersson, 2017), have been suggested for managing this type of injury. When the injury is acute but involves the complete disruption of the SLIL, open reduction with a direct repair of the SLIL, specifically its dorsal component, is often suggested (Kitay and Wolfe, 2012).

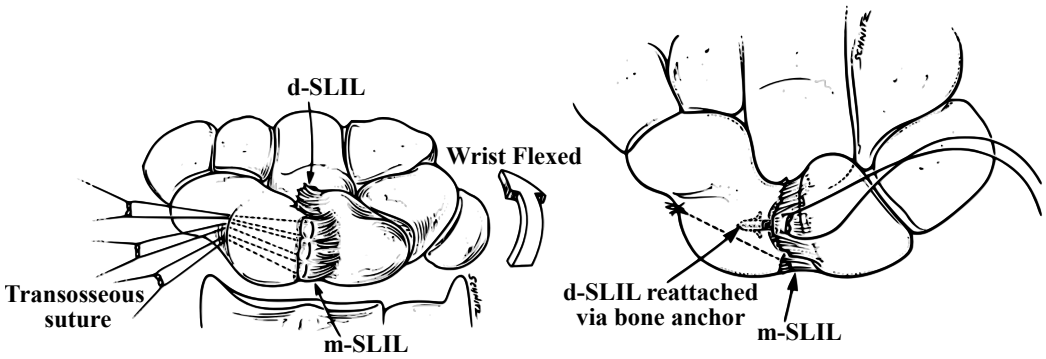

Figure 1.27: Schematics showing direct repair of the SLIL. Reproduced from Wolfe (2001), with permission from Elsevier.

Since the d-SLIL is avulsed laterally from the scaphoid in most cases (Andersson and Garcia-Elias, 2013), primary repair of this ligament often involves reattaching the ligament remnant to the scaphoid, by means of transosseous sutures (Palmer et al., 1978; Linscheid and Dobyns, 1992a), or bone anchors (Beredjiklian et al., 1998; Bickert et al., 2000; Rosati et al., 2010). The repair is then supplemented by temporary fixation of the scapholunate and scaphocapitate joints for up to eight weeks. In addition, some authors have also advocated for a dorsal capsulodesis to be carried out in conjunction to the direct ligament repair, so that stability of the scapholunate joint can be restored not only in the coronal plane but also in the sagittal plane (Cohen and Taleisnik, 1998; Wyrick et al., 1998; Minami et al., 2003; Szabo, 2008).

Chronic Injuries without Static Malalignment

Since the diagnosis of SLIL injuries is often delayed and the devascularised ligament remnants degenerate fairly rapidly, a direct repair of the SLIL in the sub-acute or chronic setting can be not only difficult to perform, but also ineffective, given the considerable amount of tension and torsional loads it has to sustain during normal scapholunate motion (Garcia-Elias, 2011; Andersson, 2017). Although many surgical techniques have been proposed, the most appropriate treatment for chronic SLIL injuries remains the subject of debate. For patients presenting with an irreparable d-SLIL but undisrupted secondary scapholunate stabilisers such that there is no significant carpal malalignment, dorsal capsulodesis (Lavernia et al., 1992; Deshmukh et al., 1999; Moran et al., 2005), and ligamentoplasties with locally-sourced tissues or bone-ligament-bone autografts (Svoboda et al., 1995; Weiss, 1998; Harvey et al., 2007), have been attempted.

Apart from the variations in the way the technique has been modified and implemented between different authors, dorsal capsulodesis generally describes a surgical procedure in which the abnormally flexed and pronated scaphoid is reduced and held in place by means of a checkrein made of a distal flap of the dorsal capsule (Blatt, 1987), or a portion of the DIC ligament (Szabo et al., 2002). Retrospective reviews on the outcomes of this type

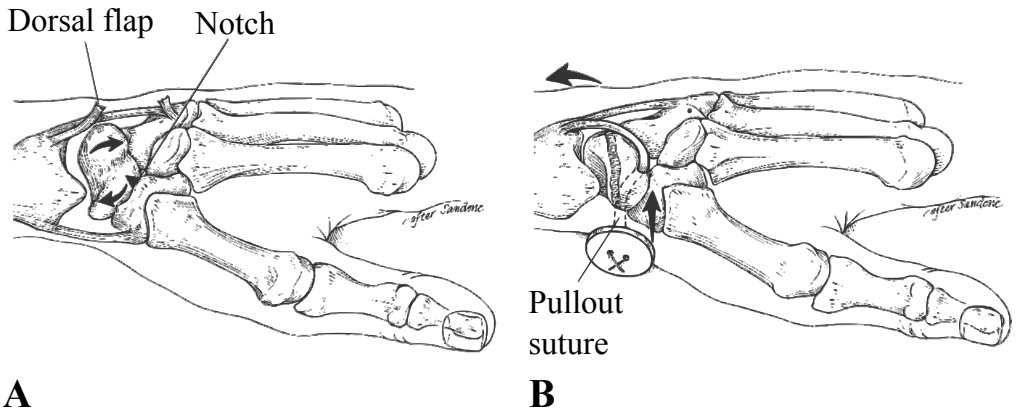

Figure 1.28: Schematics of Blatt dorsal capsulodesis. **(A)** Distally based capsular flap is attached to the abnormally flexed scaphoid. **(B)** Tightening of the capsulodesis extends the distal scaphoid (arrows), creating a passive dorsal restraint to abnormal scaphoid flexion. Reprint from Walsh et al. (2002), with permission from Wolters Kluwer Health.

of procedures have been mixed. Satisfactory results have been reported in the short-term (Lavernia et al., 1992; Wintman et al., 1995; Szabo et al., 2002); in contrast, significant loss in range of wrist motion, inadequate outcome in pain relief, and deteriorations in the maintenance of scapholunate relationship in the long-term have also been noted (Deshmukh et al., 1999; Moran et al., 2005; Gajendran et al., 2007).

The efficacy of dorsal capsulodesis in treating scapholunate instability have also been evaluated biomechanically. Slater et al. (1999) measured the amount of improvement in scapholunate angle and diastasis in cadaveric wrist specimens underwent both types of dorsal capsulodeses, following complete division of the SLIL. The authors found the scapholunate gap was reduced in both cases, but with Szabo's DIC capsulodesis being more effective. Surprisingly, no statistically significant improvements in the scapholunate angle were observed after both types of procedures. By means of a dynamic wrist motion simulator, Short et al. (2009) specifically evaluated the efficacy of Szabo's capsulodesis in a cadaver model. Instead of using conventional radiographic indicators such as the scapholunate angle, the authors reported the alterations in the rotational behaviours of the scaphoid and lunate. Following

the DIC capsulodesis, recurrence of the scapholunate diastasis with gross instability was observed only after a few cycles of dynamic wrist motion, lending support to the gradual deterioration in radiographic carpal alignment as seen clinically in the long-term.

Chronic Injuries with Reducible Static Malalignment

After prolonged exposure to the altered carpal kinematics, the secondary ligamentous stabilisers may become attenuated as a result of the constant attritional wear, static but reducible carpal malalignment may be present. For these patients, it is highly advisable to have the SLIL reconstructed with more robust tissues than local ligaments or capsules (Garcia-Elias, 2011; Konopka and Chim, 2018). And the use of tendon grafts with a procedure called "tenodesis" has been a popular choice in the surgical reconstruction of the SLIL since its introduction in the 1970s (Palmer et al., 1978). Despite the fact that new tenodesis procedures are being proposed continuously for better outcomes, the technique generally involves passing a tendon graft through pre-drilled tunnels in the scaphoid and lunate, and by tightly looping the graft around the two, the disrupted scapholunate joint may be re-associated, thus mimicking a SLIL functionally. Among the early attempts (Almquist et al., 1991; Linscheid and Dobyns, 1992b), the tenodesis procedure proposed by Brunelli and Brunelli (1995) is arguably the most popular and gives rise to many later derivatives. Since this technique required the remnant FCR graft to be tethered on the dorsal aspect of the distal radius, it was then modified by Van Den Abbeele et al. (1998), who suggested the graft should not be set to cross the radiocarpal joint, but to be anchored dorsally on the lunate or tightened around the DRC ligament. Garcia-Elias et al. (2006) further refined the technique by considering an oblique volar-distal to dorsal-proximal passage of the FCR graft through the scaphoid, and was given the name *three-ligament tenodesis*, as it was believed to simultaneously replicate the action of the STT, d-SLIL, and the DRC ligament (a detailed description of the surgical procedures can be found later in Section 4.1.1.6).

The original Brunelli's technique and its derivatives have been practised clinically without prior laboratory validations. Based primarily on the improvements in radiographic parameters, namely the scapholunate angle and gap measured pre-operatively and at the time of follow-up, many have retrospectively reviewed the efficacy of these procedures in treating chronic scapholunate instability (Table 1.9).

Table 1.9: A review on the retrospective follow-up/prospective cohort studies conducted for various modifications of the Brunelli's tenodesis technique in treating both the dynamic and static scapholunate instabilities

Study	Patients	Age	Severity of SL Instability	Tenodesis Procedure	Follow-up Time (mo.)	Pain (VAS)		DASH Score		Grip (kg)		SL Gap (mm)			SL Angle (degree)			Complications
						pre	post	pre	post	pre	post	pre	early	final	pre	early	final	
Moran et al. (2006)	15	39	Dynamic (9) Static (6)	VDA	36 (24-84)						37* (14-65)	2 (1-3) 4.3 (2-8)		2 (1-4) 3 (2-6)	49 (45-60) 82 (70-95)		52 (35-75) 57 (35-95)	2 OA
Talwalkar et al. (2006)	55	38.1 (20-63)	Dynamic (32) Static (23)	VDA	47 (11-101)		6 5.8				22.6 (6-72) 29.9 (15-72)							4 persist pain 3 neuroma 2 ulnar symp. 1 CPRS
Chabas et al. (2008)	19	43 (23-57)	Dynamic (12) Static (7)	VDA	37 (12-60)	7.5* (3-10)	2.5 3.9				37 31	2.8*	2 3	1.8 3.2	61*	52 54	62 62	2 CPRS 1 OA 1 neuroma
Links et al. (2008)	44	29.5 (19-44)	Static	4BTW (23) VDA + RASL (21)	29 (23-39)	6.7 6.9	3.4 2	67.5 77.9	45.1 25.1	30 30	34 41	3.7 3.9		3 2.2	61 61		53 46	3 scarring
Nienstedt (2013)	8	40 (28-54)	Static	VDA	166 (144-180)				9 (2-38)			5.1 (4-7)	2.4 (1-3)	2.8 (2-4)	72 (60-100)	46 (30-58)	63 (55-75)	1 OA 1 CRPS
Pauchard et al. (2013)	19	42.8 (22-56)	Dynamic (8) Static (11)	3LT	25 (12-46)	$3.2^a/6.3^b$ $3.3^a/6.5^b$	$2.3^a/5.9^b$ $1.1^a/4.2^b$	38.5 56.4	32.6 30.4	25.7 25.4	27.7 35	3.9 4.9		3.6 4.8	61 80		66 81	4 OA 1 CRPS
Ellanti et al. (2014)	13	35 (18-42)	Dynamic (10) + Static (3)	VDA	12	8* (5-10)	1.5* (1-3)	55.6*	34.9*			2.8*		2.8*	61*		63*	
Sousa et al. (2014)	22	61 (17-98)	Dynamic + Static	VDA	61 (17-98)		2* (0-7)		16* (1-61)				1.9* (1-3)	3.1* (2-4)			57* (43-79)	3 OA 1 NA 1 CRPS
Elgammal and Lukas (2016)	20	43 (24-56)	Dynamic (12) Static (8)	3LT	24 (6-53)	6* (3-10)	3 3.4	37* (11-90)	20* (0-52)	52.1* (32-68)	44 45	4* (2-6)	1.8 3.6	3 3.8	82* (67-105)	59 71	67 90	

* average of the data for outcome measures in both categories (dynamic/static instability or different types of tenodesis techniques); range of the data (if available) is indicated in the parentheses
VDA: Van Den Abbeele et al. (1998) technique, 4BTW: 4-bone tendon weave by Almquist et al. (1991); RASL: reduction and association scapholunate procedure; 3LT: 3-ligament tenodesis by Garcia-Elias et al. (2006)
pre: pre-operative; post: post-operative (at the time of review); early: results measured immediately after the surgery; final: results measured at the final review
VAS: Visual Analogue Score for pain (0 = no pain, 10 = server pain), [a] Rest pain, [b] Strenuous activity pain; DASH score = Disabilities of the Arm, Shoulder and Hand score (Hudak et al., 1996)
OA: osteoarthritis; NA: avascular necrosis; CPRS: complex regional pain syndrome; SL: scapholunate

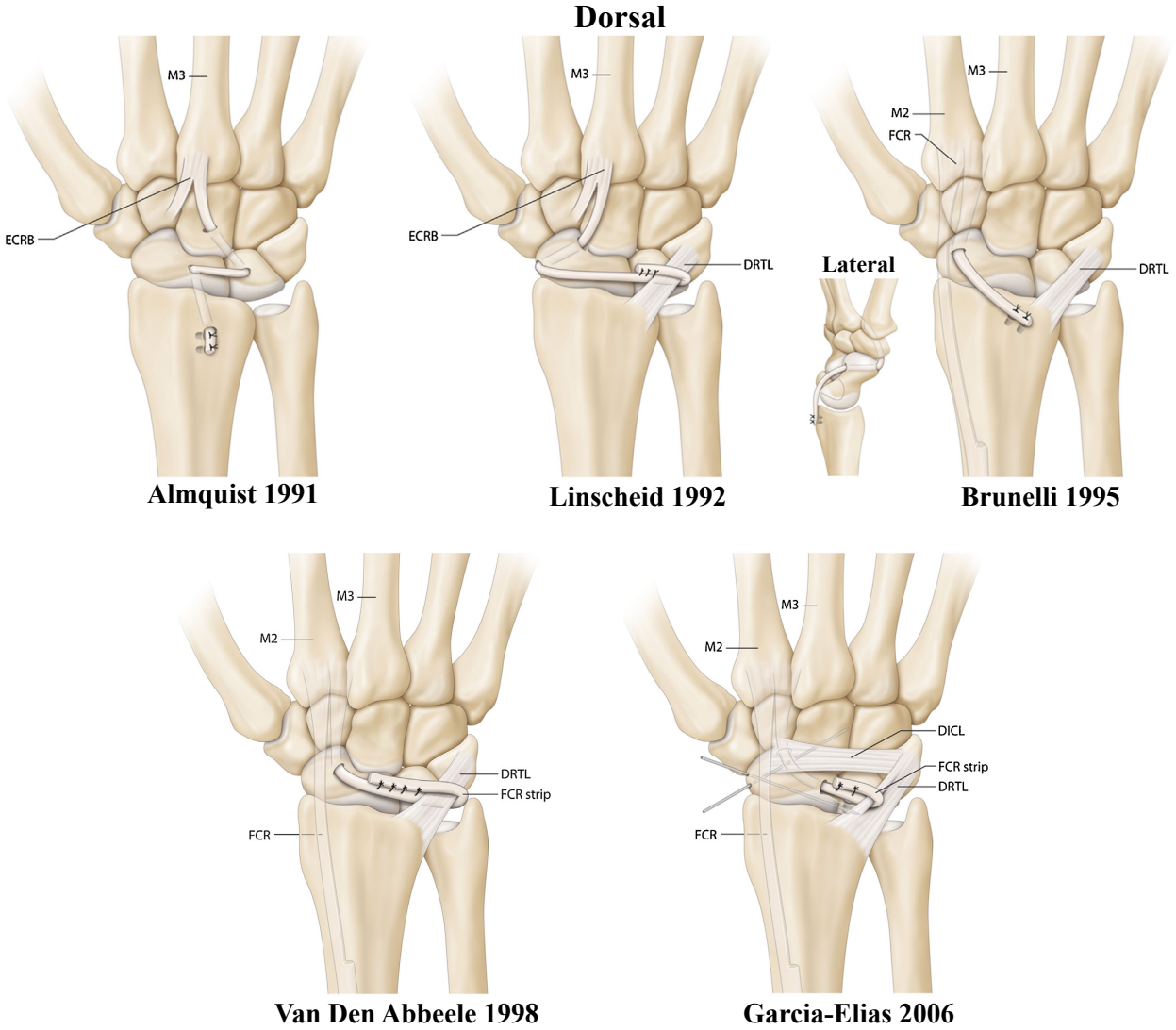

Figure 1.29: Various tenodesis techniques as described in the literature. ECRB: extensor carpi radialis brevis; FCR: flexor carpi radialis; DRTL: dorsal radiotriquetral ligament (now commonly known as the dorsal radiocarpal ligament); DICL: dorsal intercarpal ligament; M2, 3: the second and the third metacarpals. Reproduced from Athlani et al. (2018), with permission from Elsevier.

It is evident that the tenodesis technique generally results in a satisfactory reduction of the scapholunate joint in the short-term; however, the treatment outcome also tends to deteriorate over time. This has been attributed to possible stress relaxation or creeping of the graft (Chabas et al., 2008). Complications such as complex regional pain syndrome (CRPS), neuroma and avascular necrosis have been reported, and cases of continued progression of the instability, and ultimately the development of degenerative osteoarthritis, have also been noted (Garcia-Elias et al., 2006; Pauchard et al., 2013; Sousa et al., 2014).

Surprisingly, it was not until recent years that researchers begun to perform laboratory evaluations of the tenodesis technique. Pollock et al. (2010) compared the radiographic outcomes of the SLIL injury treated with both the modified Brunelli tenodesis (MBT) and the Blatt's capsulodesis (BC) in five cadaver writs. The specimens were fixed to a custom plywood stand and balanced in different static postures with weights attached to their muscle tendons. They found the MBT resulted in statistically better correction of the scapholunate relationship as compared to the BC. In the clinched fist position, the scapholunate gap and angle was 2.6 mm and 58.8°, respectively, after the MBT, and was 4.6 mm and 67.2° after the BC. The authors also manually cycled the specimens with repetitive FEM to allow creeping of the reconstructions as commonly observed in the long-term. Interestingly, considerable deterioration, up to 6°, was found in the radiolunate angle instead of the scapholunate angle for the MBT.

Apart from the ongoing effort to perfect the Brunelli tenodesis, new techniques are continued to be proposed in an attempt to obtain better treatment outcomes. Ross et al. (2013) described a scapholunotriquetral tenodesis (SLTT), in which the SLIL was reconstructed by passing a strip of the FCR tendon longitudinally and centrally through the scaphoid, lunate and triquetrum via transosseous tunnels. The graft was then tensioned using an interference screw in the triquetrum and finally routed back to the scaphoid intra-articularly to provide augmentation to the DIC ligament. With an experimental protocol similar to that described by Pollock et al. (2010), Hsu

et al. (2014) evaluated the efficacy of the SLTT in treating SLIL injuries and compared with that of the 3LT. After cycling the specimens with 100 repetitions of FEM, the authors found the SLTT led to a slightly better reduction in scapholunate diastasis than the 3LT (3.0 mm vs 2.4 mm in the clenched fist position). However, the two techniques were found to provide a comparable amount of corrections in terms of the scapholunate angle (54° vs 53°).

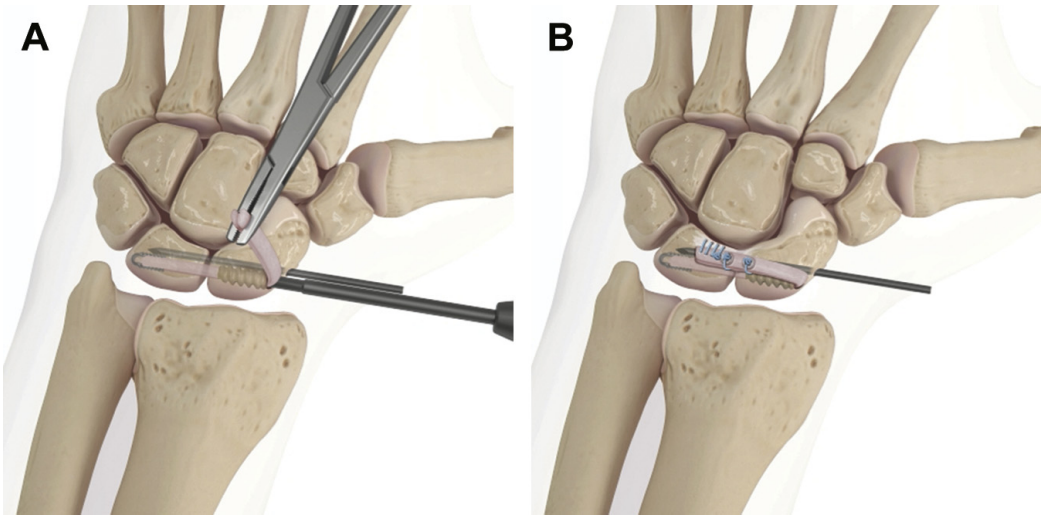

Figure 1.30: Schematics showing the scapholunate axis method described by Lee et al. (2014). **(A)** A tendon autograft is passed through a transosseous tunnel drilled along the central axis of the scapholunate joint to be finally anchored in the lunate. An interference screw is used to tension the graft upon exiting the scaphoid. **(B)** The other end of the tendon graft is brought around dorsally for a d-SLIL reconstruction. Reproduced from Dahl and Huang (2015), with permission from Elsevier.

Lee et al. (2014) proposed the so-called scapholunate axis method (SLAM), in which a two-tailed tendon autograft was secured along the central axis of the scapholunate joint in the coronal plane. Through a transosseous tunnel made across the scapholunate joint, one end of the tendon graft was anchored within the lunate, and was subsequently tensioned upon exiting the scaphoid by means of an interference screw placed alongside (Fig. 1.30A). The reminder of the tendon graft was finally folded ulnarly over the dorsum of the scapholunate joint to facilitate a

d-SLIL reconstruction (Fig. 1.30B). The authors subsequently tested the novel technique in a cadaver model and compared its outcomes with those obtained after the 3LT and the BC. They found both the SLAM and the 3LT resulted in statistically better reductions in the scapholunate gap than those obtained after the BC.

Corella et al. (2013) described a novel arthroscopic ligamentoplasty that claims to reconstruct both the d- and v-SLIL. In essence, a strip of the FCR tendon was routed around the scapholunate joint by means of the bone tunnels made across the scaphoid and the lunate in the sagittal plane (in the dorsal-volar direction). The efficacy of this technique, along with those of the 3LT and the SLAM, were studied by Alonso Rasgado et al. (2017) by means of virtual surgeries using finite element modelling. With the wrist modelled in an ulnarlly deviated clenched fist posture and a total load of 80 N, the authors found the Corella technique was the most effective in restoring the normal scapholunate angle and gap (% difference from that of the intact state for the Corella, SLAM and MBT: 0.0%, 5.0%, 10% for the dorsal SL gap, -5.6%, 16.7%, 33.3% for the volar gap; 0.6%, -6.8%, -5.2% for the SL angle). Interestingly, overcorrections of the scapholunate angle were found for both the SLAM and the MBT.

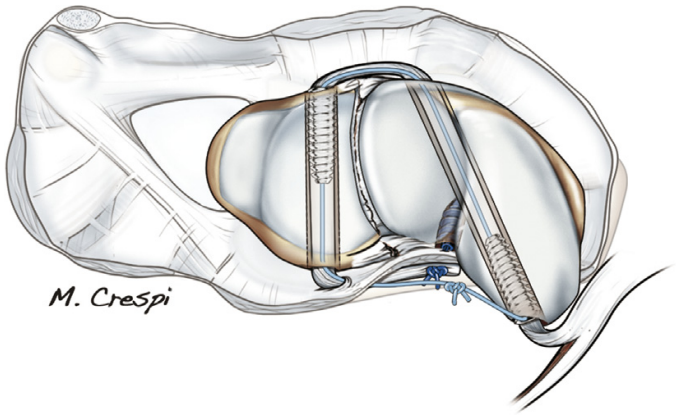

Figure 1.31: Schematics showing the arthroscopic ligamentoplasty described by Corella et al. (2013). Both the v- and d-SLIL are reconstructed using a graft from the FCR tendon, and interference screws are used to fix the tendon graft inside the scaphoid and lunate tunnels. Reproduced from Corella et al. (2017), with permission from Elsevier.

However, these widely-used tenodesis methods have been evaluated solely based on static measurements of the scapholunate relationship in 2D, questions that are fundamental to their valid clinical applications, including whether the reconstruction would impose any obstructions to the complex dynamic carpal motion and its consequence in terms of the force transfer between the carpal bones, or to what extent the surgery restores the normal carpal kinematics and contact mechanics, have yet to be answered.

Furthermore, other unconventional techniques, such as the "dynamic extension assist and volar tenodesis" or the "dynodesis" method (Seradge et al., 2004), after which the scaphoid is thought to be extended and dynamically balanced by transferring two-thirds of the ECR-L tendon to the FCR through a tunnel made in the distal pole of the scaphoid, or the so-called "reduction and association of the scaphoid and lunate" (RASL) procedure (Rosenwas et al., 1997), which intentionally creates a fibrous nonunion at the scapholunate joint by means of a Herbert screw, have all been attempted clinically.

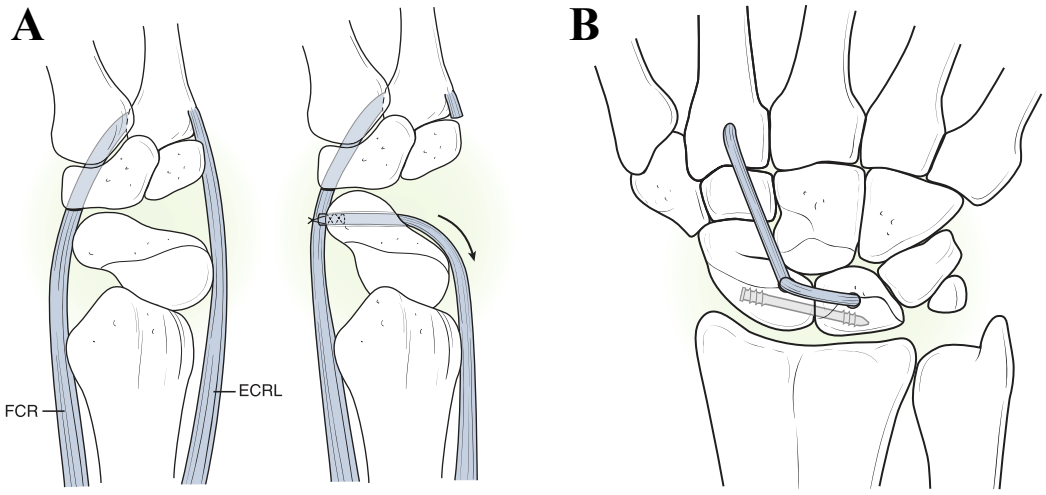

Figure 1.32: Schematics of the **(A)** "dynodesis" and **(B)** RASL technique (performed in conjunction with an ECR-L ligamentoplasty in this particular example). Reproduced from Garcia-Elias and Lluch (2017), with permission from Elsevier.

Chronic Injuries with Irreducible Static Malalignment

Over time, fibrosis may develop around the malrotated carpal bones, along with possible deformation of the subluxated joint surfaces, causing the carpal derangement to become irreducible. Despite this, if the patient has not developed any marked degenerative arthritis, surgical treatment with intercarpal arthrodesis is often considered, aiming to reduce pain, restore carpal alignment, and improve the distribution of force within the articular contact (Garcia-Elias, 2011; Kitay and Wolfe, 2012).

Various types of limited intercarpal arthrodeses have been attempted. Fusing the scaphoid to the lunate (scapholunate arthrodesis) seems to be an intuitive choice, but it has been shown to be the least reliable option with a high rate of nonunion in approximately 50% of the patients (Larsen et al., 1997). Some have attributed this to the small areas of scapholunate contact and the limited bone stocks available for achieving a reliable union, while the presence of the interfacet prominence on the distal radius, along with the high separating tendency of the scapholunate interval induced by downward thrusting of the capitate, are also considered as possible reasons for the failure of the fused unit (Zubairy and Jones, 2003; Watson et al., 2010; Stewart et al., 2014).

Scaphotrapeziotrapezoid (STT) arthrodesis (formerly known as the 'triscaphe' arthrodesis) has also been attempted to hold the collapsed and dorsally subluxated scaphoid in an upright position in the radioscaphoid fossa, thereby restoring the normal joint congruency of the radioscaphoid articulation and reducing the risk of developing osteoarthritis (Watson and Hempton, 1980; Watson et al., 1999). Owing to the restoration of the radioscaphoid contact, the authors believed the STT arthrodesis would also off-load the radiolunate articulation, which would have been under an increased amount of force when the scaphoid had subluxated and become decoupled from the force-bearing column of the wrist. This hypothesis was confirmed later in a computer simulation performed by Ishikawa et al. (1999), as they found the lunocapitate joint and the radiolunate joint

transmitted 42% and 37% less force after STT arthrodesis. And the force transmitted through the radioscaphoid joint and the scaphocapitate joint experienced a mild 16% increase and a significant 147% increase, respectively. Furthermore, the rate of nonunion for this technique has been show to range from 4% to 15%, making it a preferred choice over scapholunate arthrodesis (Larsen et al., 1997; Stewart et al., 2014). However, as the fused scaphoid can no longer rotate into flexion, patients underwent this procedure tend to suffer a substantial loss in the range of wrist motion. In nine patients, Eckenrode et al. (1986) found the postoperative arc of wrist flexion, extension, radial and ulnar deviation became 60%, 65%, 40% and 64% of that of the unoperated side, respectively, along with an average drop of 26% in the grip strength. Furthermore, persistent radial-sided pain has been reported as another major complication of this procedure and has been attributed to the postoperative impingement between the radial styloid and the scaphoid or trapezium (Rogers and Watson, 1989; Kleinman and Carroll IV, 1990). These authors thus advocated that radial styloidectomy to be carried out routinely as part of the STT arthrodesis procedure.

Scaphocapitate (SC) arthrodesis has also been used for the treatment of chronic scapholunate instability (Pisano et al., 1991). This technique is practically similar to STT arthrodesis, as their resultant effects on the carpal kinematics have been shown to be comparable (Garcia-Elias et al., 1989).

With increasing awareness of the importance of the dart-thrower's motion (DTM) in daily activities, radioscapholunate (RSL) arthrodesis has been suggested to spare the midcarpal joint (Garcia-Elias, 2011; Konopka and Chim, 2018), which has been shown to be the key for the DTM (Crisco et al., 2005; Moritomo et al., 2007). In addition to the RSL procedure, excision of the distal scaphoid has also been advocated, such that the ball-and-socket type midcarpal motion can be attained without being obstructed by the STT articulation laterally during wrist flexion and radial deviation (Garcia-Elias et al., 2005).

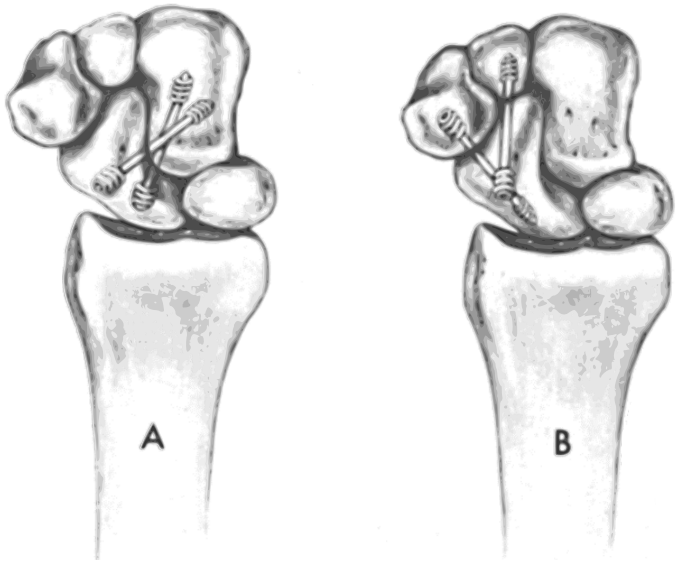

Figure 1.33: Schematics depicting **(A)** SC and **(B)** STT arthrodeses as facilitated by means of Herbert screws. Reproduced from Garcia-Elias et al. (1989), with permission from Elsevier.

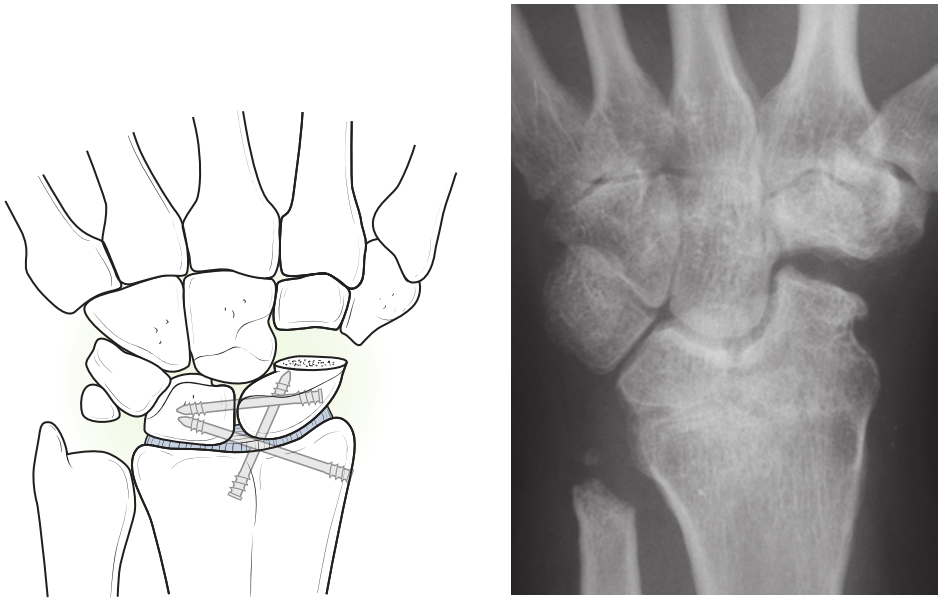

Figure 1.34: An schematic representation (*left*) and a case example (*right*) of the RSL arthrodesis technique. A distal scaphoidectomy is often included to allow a wider range of wrist flexion and radial deviation. Reprinted from Garcia-Elias and Lluch (2017), with permission from Elsevier.

Scapholunate Advanced Collapse

For patients with a SLAC wrist, different salvage procedures are suggested, depending on the location and extent of the arthritic changes.

As the SLAC sequence always starts at the tip of the radial styloid and the radial-distal aspect of the scaphoid (Watson and Ballet, 1984), a radial styloidectomy in the early stage may help alleviate pain and postpone progression of the degenerative arthritis (Garcia-Elias, 2011). However, since excising the radial styloid will disrupt the normal radial inclination of the distal radius, it has been recommended that the syloidectomy should be kept no more than 3 to 4 mm to avoid excessive loss of the radiocarpal contact, preventing further pathological translation of the carpus (Nakamura et al., 2001).

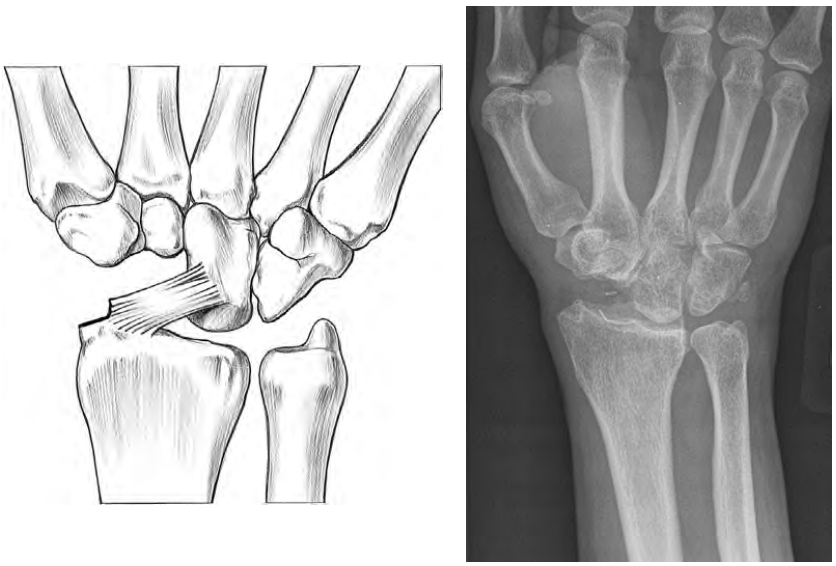

Figure 1.35: Schematic representation (*left*) and case example (*right*) of the proximal row carpectomy technique. The procedure is usually carried out in concert with a radial styloidectomy, in which a portion on the tip of the radial styloid is resected, preserving the RSC ligament. Reprinted from Shah and Abrams (2010), with permission from Wolters Kluwer Health.

For patients with advanced SLAC, proximal row carpectomy (PRC) and "four-corner" fusion (4CF) with scaphoid excision are two of the most com-

monly performed motion-preserving procedures. As the name suggests, PRC involves the excision of the entire proximal row (Fig. 1.35), thereby allowing the capitate in the distal carpal row to articulate with the distal radius through the lunate fossa, resulting in a neo-articulation that roughly allows a ball-and-socket typed movement (Garcia-Elias, 2011). This procedure is thus contraindicated when there are arthritic changes at the lunocapitate interval. 4CF (Fig. 1.36), on the other hand, involves fusion of the capitate, lunate, triquetrum and hamate, and is often performed in combination with a scaphoidectomy (Watson et al., 1999). As the lunate will become the focal point of wrist loading postoperatively, this procedure needs be avoided when there are arthritic changes in the radiolunate articulation. This, however, is rarely the case clinically (Watson and Ballet, 1984).

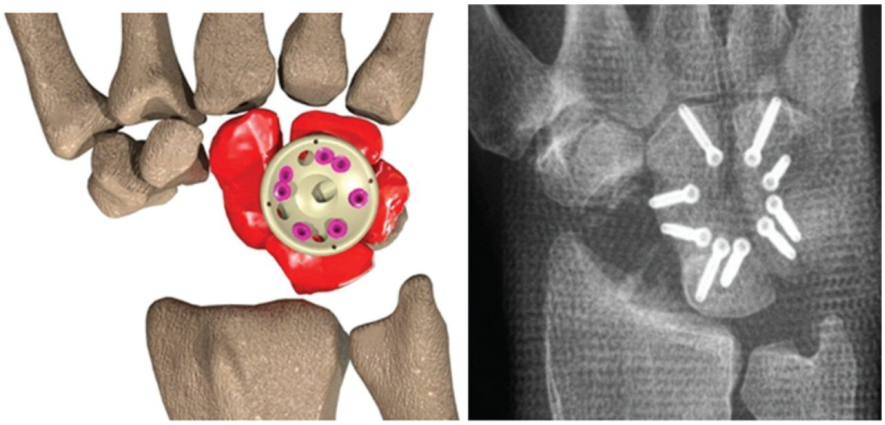

Figure 1.36: Schematic representation (*left*) and case example (*right*) of the four-corner fusion technique. A radio-lucent spider plate was used to facilitate the fusion and the procedure was carried out in concert with a scaphoidectomy (Reprinted from Houvet (2016).)

For the treatment of severe wrist arthritis, hemi- (Boyer and Adams, 2010), and total wrist arthroplasties (Yeoh and Tourret, 2015), as well as motion-sacrificing total wrist arthrodesis (Carlson and Simmons, 1998; Mühldorfer-Fodor et al., 2015), have all been attempted.

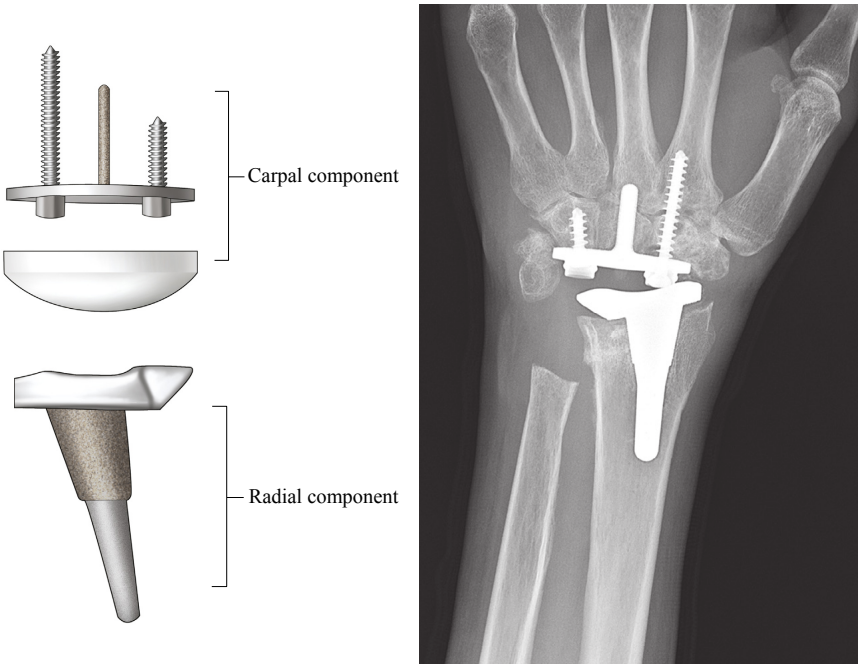

Figure 1.37: An example of total wrist arthroplasty. Adapted from Kelley and Chung (2018), with permission from Elsevier.

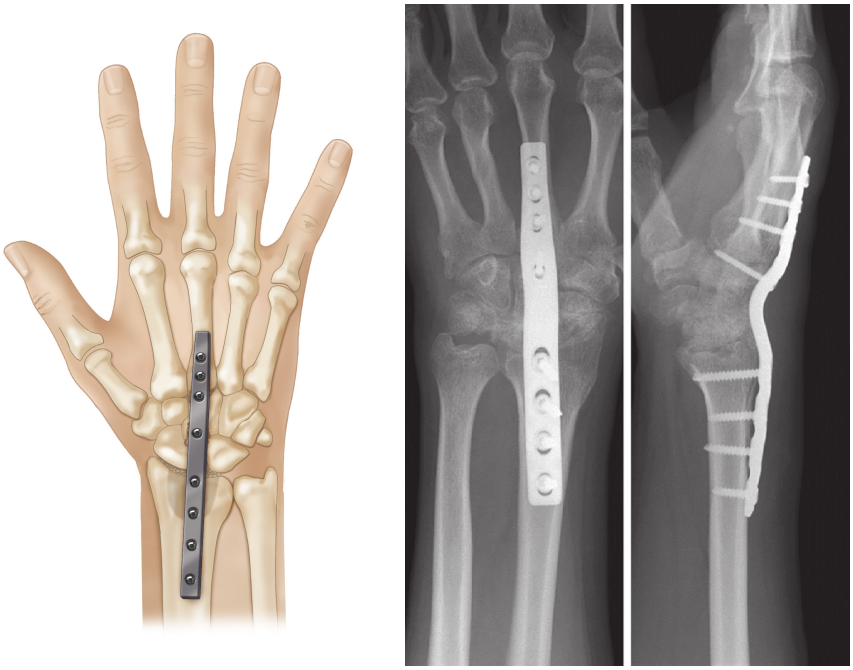

Figure 1.38: An example of total wrist fusion. Adapted from Kamnerdnakta et al. (2018), with permission from Elsevier.

1.5 Experimental Methods Employed For Studying Wrist Biomechanics

In this section, the experimental techniques that have been developed and applied in studying the wrist biomechanics are briefly reviewed. *In-vitro* laboratory testing is a preferred option when the experiment design involves invasive procedures that cannot be performed on live subjects, for instance, pre-clinical evaluations of a newly proposed surgical technique or a novel prosthesis design. However, it is not a trivial task to recreate dynamic carpal motion that is physiologically representative in a cadaver model. A range of testing apparatuses and protocols have been developed in an attempt to archive this goal.

It is also important to make sure the outcome variables are accurately measured after having correctly synthesised the wrist motion in cadaveric specimens. As mentioned previously, since the small and irregularly-shaped carpal bones exhibit complex motion patterns, it is therefore challenging to truthfully capture both their three-dimensional kinematics and contact. To this end, techniques used in the literature to facilitate reliable measurement of these quantities are also reviewed.

1.5.0.1 *In-vitro* Wrist Simulation

Passive Simulation

Passive wrist simulations refer to the experiments in which cadaveric wrist specimens are reanimated by means of external manipulations applied either manually or electromechanically, instead of the muscle contraction that is intrinsic to the joint motion. Perhaps due to the ease of setup and operation, manually actuated passive wrist simulations have been very common (Youm et al., 1978; Berger et al., 1982a; Savelberg et al., 1993; Kobayashi et al., 1997a; Ishikawa et al., 1999; Salvà-Coll et al., 2011; Eschweiler et al., 2016b). In these studies, the cadaveric wrist specimen was manipulated manually

by means of a Steinmann pin drilled into the medullary canal of its third metacarpal. The pin was typically constrained to a protractor-like device such that global wrist motion of the cadaver wrist was prescribed into a preset arc in the plane of interest (Fig. 1.39). The muscle-tendon units of the wrist specimen were often loaded using constant-force springs or dead weights to simulate articular compression related to muscle tones rather than causing actual wrist motion.

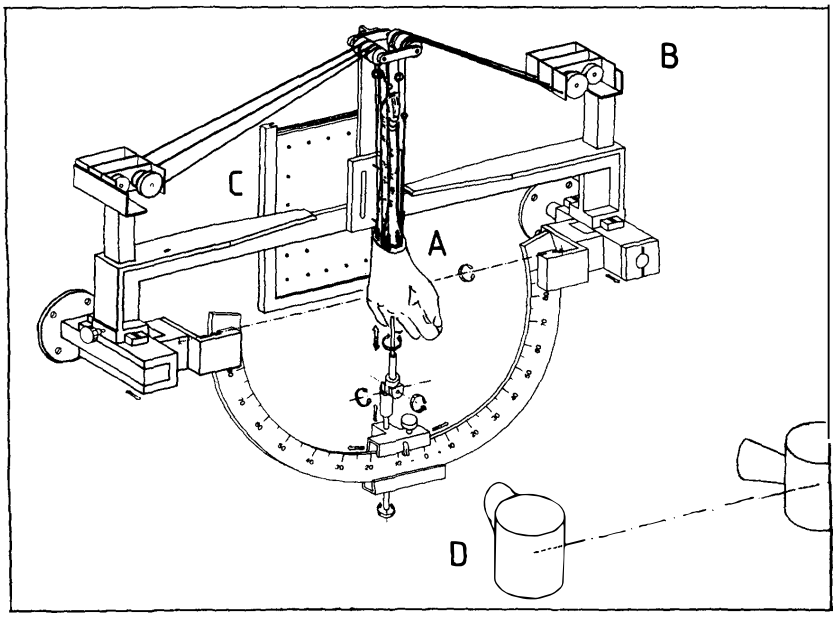

Figure 1.39: An example of the motion constraining apparatus used for passive wrist simulations. The cadaveric wrist specimen **(A)** was secured to the apparatus with its tendon loaded using a number of constant-force springs **(B)**. A Röentgen film cassette **(C)** was placed behind the wrist specimen to allow X-ray projections to be take from different positions **(D)**. Adapted from Savelberg et al. (1993), with permission from Elsevier.

More sophisticated passive wrist simulations involved the use of certain electromechanical devices to manipulate the hand/metacarpals with respect to the forearm. In order to study the biomechanics of the distal radioulnar joint, Haugstvedt et al. (2001) developed a simulation device that was capable to prescribe passive pronation-supination to a cadaveric wrist specimen. With the ulnar held stationary, the forearm rotation was dynamically simulated by means of a stepper motor coupled to the hand of the wrist specimen.

By using a purpose-built rotation device, Eng et al. (2014) simulated passive flexion-extension up to 45° on six cadaver wrists. The hand of the cadaveric specimen was tied eccentrically to the rotor, such that it can be "cranked" continuously relative to the forearm as the motor rotates. Recently, Loisel et al. (2020) described a similar setup through which planar wrist motion, namely FEM and RUD, was passively simulated by strapping the palm of the wrist specimen to a perforated plate coupled to a motor. Fraysse et al. (2014) superimposed planar FEM and RUD, along with a passive hammering motion (reversed DTM) on eight cadaver wrists by means of a six degree-of-freedom Stuart platform (Fig. 1.40). Similarly, the forearm of each cadaveric wrist specimen was held stationary, while its metacarpals were potted and attached to the end-effector of the robotic platform. The cyclic motion was prescribed at 0.1 Hz and an root-mean-square (RMS) accuracy ranging from 1.0° to 2.6° was achieved in controlling the global wrist position.

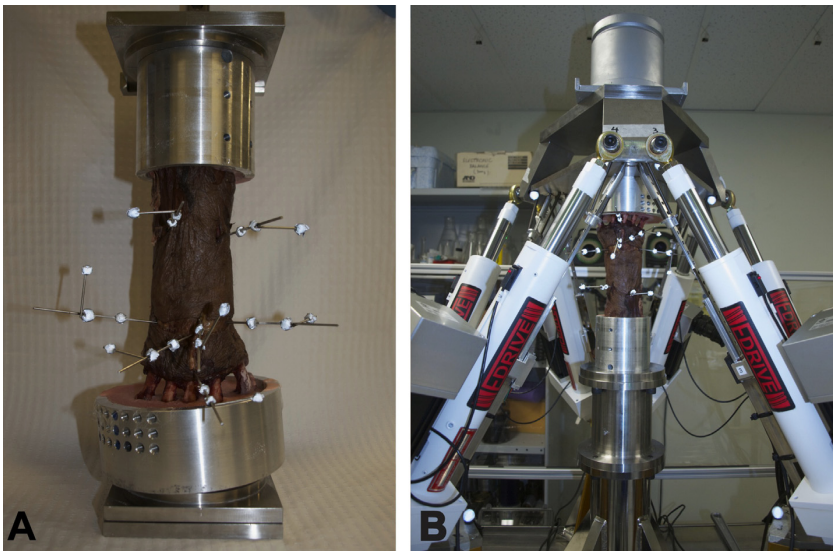

Figure 1.40: The experiment setup developed by Fraysse et al. (2014). **(A)** The cadaveric wrist specimen was potted in a fixture. Retroreflective marker triads were attached to the carpal bones by means of bone pins. **(B)** The whole assembly was mounted in a six degree-of-freedom Stuart platform (referred to as the 'Hexapod robot' in the original text) for passive wrist simulation. Adapted from Fraysse et al. (2014), with permission from Elsevier.

Since the externally imposed manipulation is the sole cause of the joint motion, instead of the coordinated muscle contractions as observed in live subjects, one of the major concerns of these passive simulations has been whether they are physiologically accurate and representative of the *in-vivo* joint motion (Ferreira et al., 2010). Furthermore, it has also been shown that passive testing of cadaveric samples in the absence of joint compression and thereby joint stability provided by muscular loading tends to have lower position repeatability between repeated trials (Johnson et al., 2000; Iglesias, 2015).

Muscle-Driven Simulation

As the name suggests, muscle-driven wrist simulations refer to experiments in which global wrist motion is achieved by actively pulling on the muscle-tendon units of a cadaveric wrist specimen, thus replicating the muscle-activated joint motion as seen *in-vivo*.

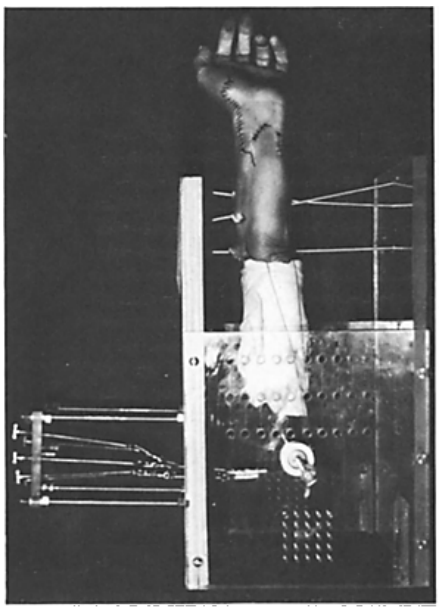

Figure 1.41: The static wrist testing apparatus developed by researchers at Mayo Clinic. Calibrated springs were used to load the muscle tendons of the cadaver wrist. Adapted from Garcia-Elias et al. (1989), with permission from Elsevier.

Primitive attempts of muscle-driven wrist simulations often involved quasi-statically balancing the wrist specimen at certain posture with a set of tuned loads applied to the tendons of the wrist motor muscles (Fig. 1.41) (Ruby et al., 1987; Garcia-Elias et al., 1989; Smith et al., 1989; Horii et al., 1991; Kaufmann et al., 2005). Typically, the initial assignment of load in each muscle tendon was derived based on the muscle's PCSA. Then the applied muscle loadings were often manually adjusted until the cadaver wrist reached static equilibrium at the position of interest.

However, apart from the question as to what extent these muscle forces, as obtained from a seemingly arbitrary tuning process, are physiologically accurate, the approach to study dynamic carpal kinematics and mechanics based on data collected at a collection of static wrist positions itself remains questionable. Patterson et al. (1998) suggested that since the musculoskeletal control required to maintain a static joint position was significantly different from that involved in a continuous action, the attitude of the carpal bones measured at discrete wrist positions might not be indicative of the true three-dimensional carpal motion during dynamic wrist motion.

Muscle-driven dynamic wrist simulations have also been attempted by means of manually pulling on the muscle tendons of the wrist specimen, similar to operating a marionette, by Patterson et al. (2007). Although quality measures such as the accuracy and repeatability of the simulated wrist motion were not reported, it was clear that based on the oscillatory carpal kinematics presented in their publication, the global wrist motion resultant from manual manipulation of the wrist muscles was of poor quality.

During his doctoral studies, Tong (1985) pioneered the research on the development of computer-controlled muscle-driven dynamic wrist simulator. Hydraulic cylinders were employed to pull the muscle tendons, while an electrogoniometer comprising of three rotary potentiometers was fixed to the cadaveric wrist specimen to continuously measure the global wrist positions (Fig. 1.42). In order to have the resultant wrist motion to closely track a preset trajectory, a position control algorithm was developed to automatically adjust the tendon displacements based on the error between the target and

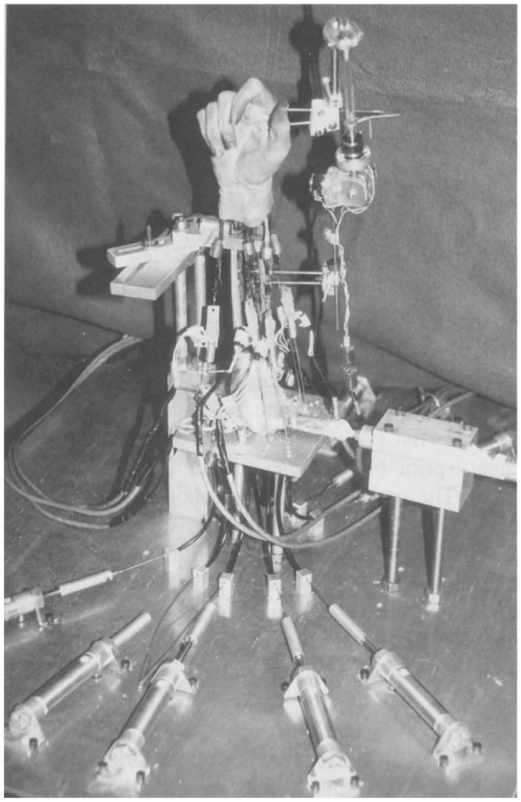

Figure 1.42: The dynamic wrist motion simulator originally developed by Tong (1985) and later improved by Werner et al. (1996). Adapted from Short et al. (1995), with permission from Elsevier.

the currently measured wrist positions. Furthermore, tensions in the muscle tendons were also monitored by means of force transducers attached in-line with the actuators. And a simple force feedback loop was implemented to prevent the tension in any of the muscle tendons from dropping below a preset threshold, thereby approximately replicating the antagonist muscle actions presented *in-vivo* .

This simulator was subsequently improved by Werner et al. (1996), who included the APL muscle into the simulation and replaced the linkage-type electrogoniometer with smaller electromagnetic sensors attached to both the radius and the third metacarpal (Short et al., 2002a). The revised simulator has been shown to be able to perform sinusoidal planar wrist simulations with the undesirable out-of-plane motion measured up to 1°. Furthermore,

it was also capable of simulating more complex wrist motion, such as the oblique dart-thrower's motion and elliptical wrist circumduction.

In contrast, Erhart et al. (2012) believed that "post trauma patients are likely to exert a force controlled motion", and developed a dynamic wrist simulator that was controlled entirely by force. Wrist flexion and extension of approximately 30° were simulated with a mean total force of 167.6 N. For the force applied to each of the wrist muscle tendons to reach its target values, a force control accuracy of 4 N was reported. The major limitation of this apparatus was that it required the muscle forces to be predefined and appropriately tuned for the duration of the prospective wrist motion, as the control loop was only closed on the force level rather than on the resultant global wrist motion. Since the *in-vivo* muscle forces remained an unsolved problem, the authors again resorted to the muscles' PCSAs when formulating the muscle force profiles. Although no position control performance metrics were calculated, the reported trajectory of the simulated global wrist motion deviated significantly from a standard sinusoidal profile.

More recently, Iglesias (2015) developed their version of the dynamic wrist simulator to assist in the study of carpal kinematics (Fig. 1.43). An optical video motion tracking system with a set of active markers were used to track the global wrist position, and servomotors were used to provide muscle tension. Instead of using in-line load cells, force feedback was provided by two T-rosette strain gauges attached to the top and bottom surfaces of the motor mounting bracket. Depending on their actions, wrist muscles were artificially assigned into different 'quadrants'. And a cascaded position-force control structure was implemented for the control of the global wrist motion. A constant load of 8.9 N was maintained in each of the muscles that were deemed as potential antagonists to the current wrist motion. A mean position control accuracy of 0.23° and a force control repeatability of approximately 0.30 N were reported. However, despite the superior performance of this apparatus, doubt still exists with regard to whether the muscle forces that the device applied to the cadaveric wrist specimen were physiological. Not mentioning the unrealistic assumption of a constant antagonistic force, this

simulator did not address the neuromuscular redundancy problem, which arose in the inverse dynamics process of mapping joint kinematics back to the causal muscle forces, in a physiologically meaningful manner.

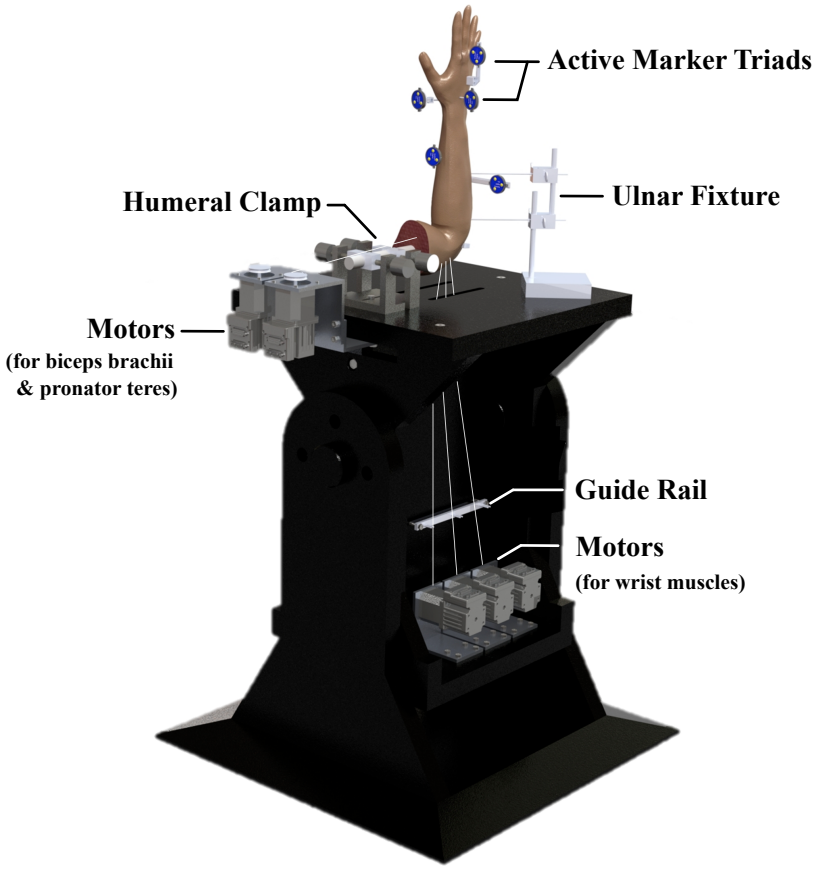

Figure 1.43: The dynamic wrist motion simulator developed by Iglesias (2015). Adapted from Stoesser et al. (2016).

1.5.0.2 Techniques Used to Study Carpal Kinematics

Historical Perspective

Just one year after Röentgen's discovery of X-ray, Bryce (1896) described the relative motion between carpal bones based on planar radiographs of his own wrist. Since then, interest has arisen in measuring and describing the kinematics of individual carpal bones, and a variety of techniques have been used.

Johnston (1907) studied carpal motion through visual inspections of cadaveric specimens dissected at varying wrist positions. Cyriax (1926) estimated the movements of individual carpal bones during passive wrist manipulations. Long needles were driven into each carpal bones to allow their angular displacement to be read from a scale placed transversely to the forearm.

Static postural changes of the carpal bones between different wrist positions were described by von Bonin (1929) and Wright (1935) based on stereoscopic X-ray photos. Cineradiography was later employed to observe the dynamic interactions between carpal bones in live patients (Arkless, 1966). However, limited by the imaging and sensor technologies at the time, the carpal motion reported in these early studies remained descriptive and sometimes speculative.

Sonic Digitisers

Three-dimensional sonic digitisers have been employed to study the motion of both the global wrist (Andrews and Youm, 1979; Erhart et al., 2012), and the individual carpal bones (Berger et al., 1982a,b). The system requires an array of three or more point sound sources, known as spark gaps, to be rigidly attached in a non-collinear pattern on the object whose three-dimensional motion is to be tracked in space (Fig. 1.44). Three liner microphones, tuned to the frequency of the spark gaps, are arranged perpendicular to each other, defining the coordinate axes of the tracking system. The spark gaps are

pulsed rapidly in an alternating pattern, and based on the travel time of the sound from the spark gaps to the microphones, the coordinate of each sound source can be determined. A precision of ±0.5 mm in resolving the three-dimensional location of the spark gap was reported by (Berger et al., 1982b). However, the kinematics of the carpal bones was measured one at a time, given the big form factor of the spark gap. Furthermore, attaching such a device to the tiny carpal bones has also raised concerns over whether it will cause any mechanical impingement or induce undesirable moment that interferes with the physiological carpal motion (Kobayashi et al., 1997a).

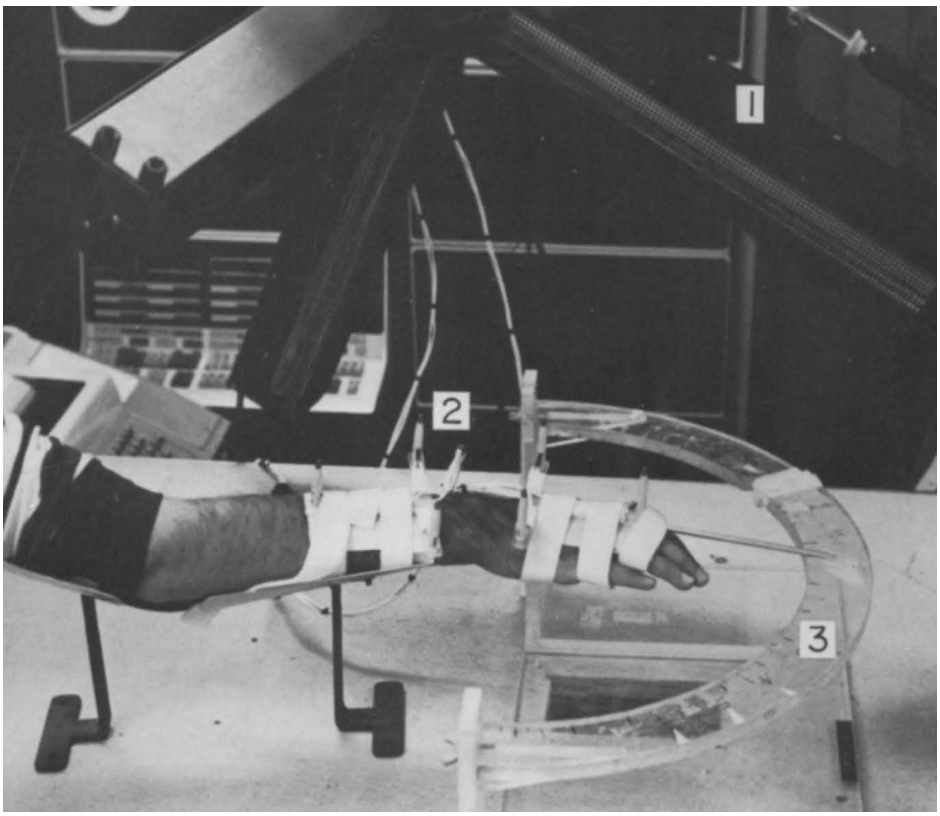

Figure 1.44: An experimental setup where sonic digitisers were employed in concert with a motion constraining device to study wrist kinematics. 1) Three linear microphones arranged orthogonal to each other, 2) spark gaps, 3) protractor-like motion guide Adapted from Andrews and Youm (1979), with permission from Elsevier.

Electromagnetic Motion Trackers

Electromagnetic motion trackers have seen extensive applications in studies involving measurement of the carpal kinematics (Short et al., 2002a; Werner et al., 2004; Salvà-Coll et al., 2011; Eschweiler et al., 2016b; Waters et al., 2016).

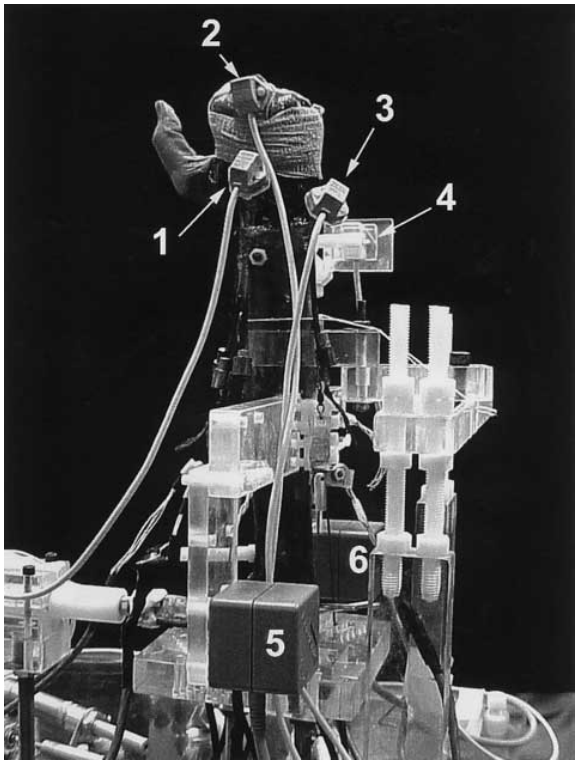

Figure 1.45: An experimental setup in which electromagnetic motion trackers were employed to study carpal kinematics. Sensors were rigidly attached to 1) the scaphoid, 2) third metacarpal, 3) lunate, and 4) radius, by means of non-metallic posts. 5-6) Electromagnetic sources. Adapted from Short et al. (2002b), with permission from Elsevier.

An electromagnetic motion tracking system generally consist of a source or a field generator, which emits an electromagnetic field of known geometry, and a number of sensors that can be attached to the object whose motion is to be tracked in space (Fig. 1.45). In essence, each sensor has three orthogonally oriented magnetic sensing coils, and based on the magnetic field strength as measured by each of the coils, the sensor's three-dimensional position and

orientation with respect to the source can be determined (Welch and Foxlin, 2002). Therefore, any distortions of the reference field may render inaccurate motion tracking. And the presence of ferromagnetic materials, electronic devices and inhomogeneous media that interfere with wave transportations should be kept at a minimum in the vicinity of the electromagnetic motion tracking system. Nonetheless, an accuracy of 0.2° and 0.2 mm in resolving 3D rotations and translations were reported by Short et al. (2002b) when working in conjunction with a dynamic wrist motion simulator. While a value of 0.15° and 0.8 mm were reported by Salvà-Coll et al. (2011) for a similar system. Since a sizeable sensor needs to be directly mounted to the carpal bone whose motion is of interest, electromagnetic tracking also suffers from a similar motion interference problem as the sonic digitisers do. Although smaller variants of the tracking sensors are available (Fig. 1.46), they are usually offered at the expanse of a lowered sampling rate, tracking accuracy and stability (Schicho et al., 2005; Hummel et al., 2006; Franz et al., 2014).

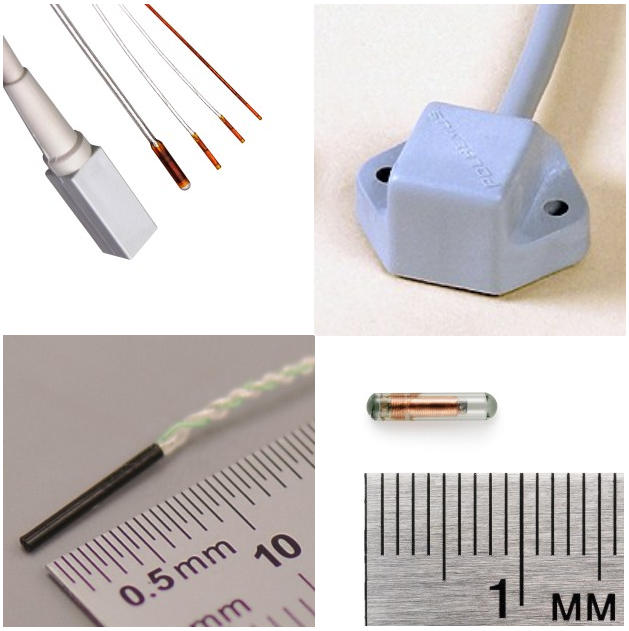

Figure 1.46: Various types of sensors developed for electromagnetic motion tracking. Adapted from Franz et al. (2014), with permission from IEEE.

Video Motion Capture System

Video motion capture systems have been used extensively in the field of biomechanics for studying the kinematics of mainly the larger joints in the human body, such as the knee (Sigward and Powers, 2006; McClelland et al., 2011), the hip (Noehren et al., 2011; Pfister et al., 2014), the shoulder (McCann et al., 1993; Robert-Lachaine et al., 2015), and the spine (Morgenroth et al., 2010; Preuss and Popovic, 2010). Nevertheless, the application of such a system in measuring the complex movements of the small carpal bones has not been uncommon (Patterson et al., 1998; Chanon et al., 2007; Patterson et al., 2007; Bain et al., 2015; Stoesser et al., 2016).

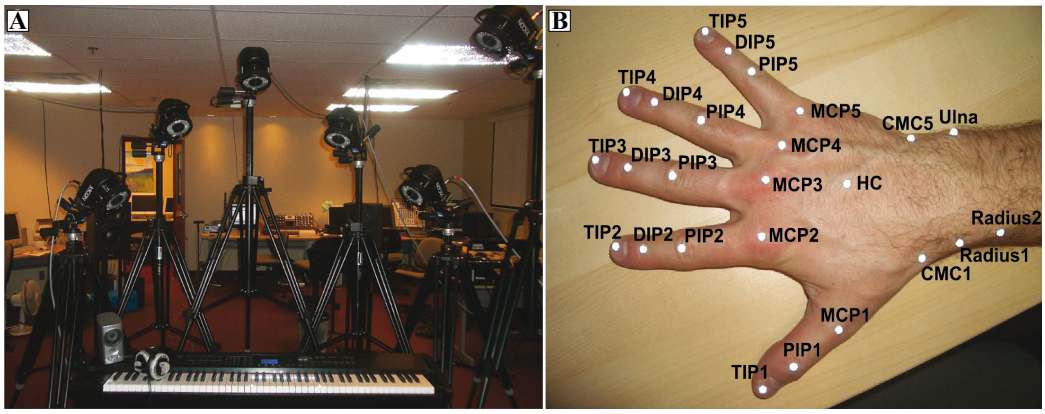

Figure 1.47: An experimental setup in which a video motion capture system was used to track the hand and wrist movement of a pianist during music performance. **(A)** Infrared motion capture cameras were arranged around a digital piano. **(B)** Retro-reflective markers were attached to the fingers, hand and forearm. Adapted from Goebl and Palmer (2013).

A video motion capture system typically consists of an array of markers rigidly attached to the object whose motion is to be tracked, and two or more cameras arranged at different angles towards the object. Similar to other tracking methods, a minimum of three non-collinear markers are required to fully define the rigid body's position and orientation in space. And the markers are categorised as active if they actively illuminates, or as passive if they only reflect the light by virtue of a retroreflective coating. Based on the overlapping projections of the markers taken in a multitude of angles,

their three-dimensional positions can be triangulated in space if the cameras' extrinsic parameters (position, orientation), and intrinsic parameters (focal length, principal point, and lens distortion) are explicitly known. In order to obtain these parameters, a calibration process is often required.

This type of systems has been proven to be applicable for tracking motion of small magnitudes. By using a validation apparatus consisting of three orthogonal motorised linear stages, Windolf et al. (2008) have shown an accuracy as high as 63 ± 5 μm and a precision of 15 μm can be achieved with a four-camera setup in measuring motion confined to a capture volume of $180 \times 180 \times 150$ mm^3. The authors have also found a higher noise level in measuring motion which occurs in a direction that is normal to the cameras' projection plane. And the choice of marker size, as well as the camera arrangement, have been found to have a significant impact on the resultant tracking quality.

Since such systems rely on optical tracking of the markers, a clear line-of-sight must be guaranteed in the duration of the tracking process to obtain an accurate measurement. This demands careful planning when placing both the tracking markers and the cameras. In addition, for most *in-vivo* studies, since the markers are often attached directly to the skin rather than the underlying bones, the accuracy and reliability of the joint kinematics estimated using the movement of skin-mounted markers is known to be negatively impacted by skin movement artefacts (Cerveri et al., 2005; Benoit et al., 2006).

Biplane Radiography

Carpal kinematics has been studied by means of biplane radiography since the late 1980s (Ruby et al., 1987; Garcia-Elias et al., 1989; Smith et al., 1989; Horii et al., 1991; Kobayashi et al., 1997a). In these studies, radio-opaque markers, either of various size or shape, were implanted into a number of carpal bones of the cadaver wrist. Orthogonal biplanar X-ray films were then taken with the wrist placed in static positions (Fig. 1.48). The markers were digitised from every pair of the biplanar radiographs to allow their three-dimensional positions to be triangulated, thereby facilitating tracking

of the carpal bones. An accuracy of 2° in measuring rotations and 0.4 mm in measuring translations have been reported for an earlier version of the biplane setup (Garcia-Elias et al., 1989; Smith et al., 1989).

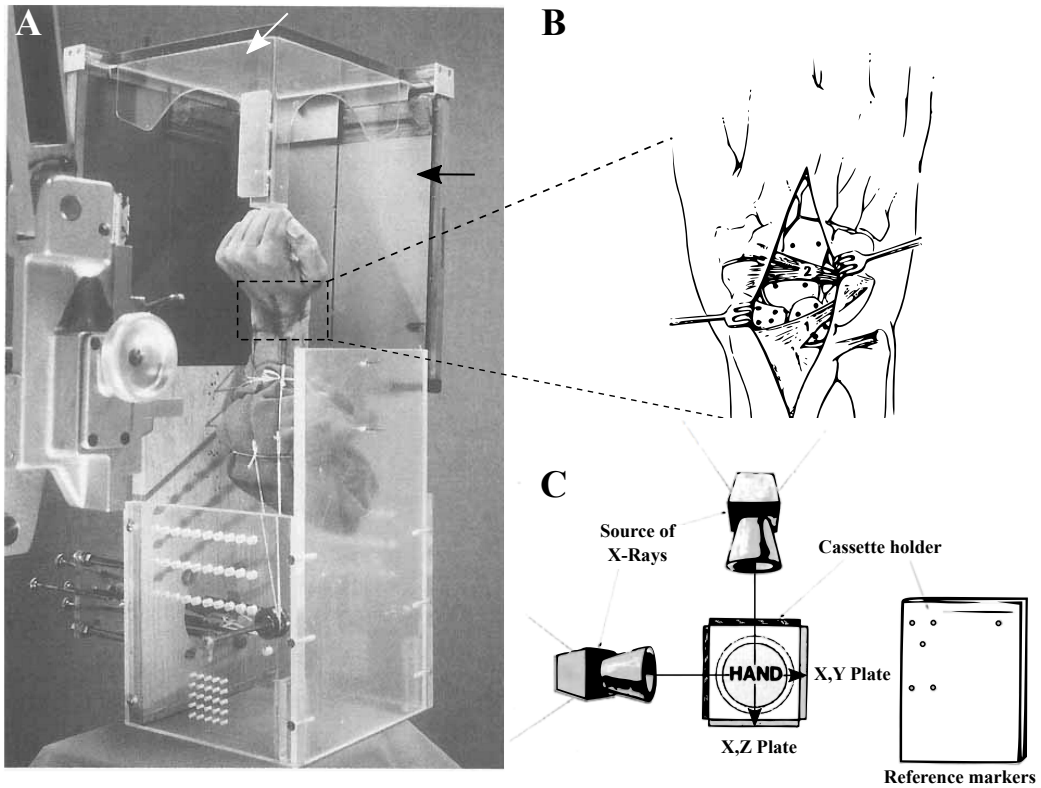

Figure 1.48: **(A)** A photo of the experimental setup used by Smith et al. (1989). Two X-ray sources and their corresponding radiograph cassettes (black arrow) were arranged in an orthogonal relationship. Plates containing reference markers (white arrow) were also incorporated into the cassette holder. **(B)** Radio-opaque markers were implanted dorsally into selected carpal bones. 1) DRC, and 2) DIC ligaments. **(C)** A schematic drawing of the setup. Images reproduced from Smith et al. (1989), with permission from John Wiley and Sons.

With advances in medical imaging, X-ray fluoroscopy has been develop to capture dynamic motion in real-time. Biplane fluoroscopy has been widely used since and has been recognised as one of the most accurate means of measuring joint kinematics both *in-vitro* and *in-vivo* in the field of biomechanics (Tashman and Anderst, 2003; Kaptein et al., 2011; Gray et al., 2017).

A more in-depth discussion can be found later in Section 2.3.1.

Computed Tomography and Magnetic Resonance Imaging

As no invasive bone marking is required, CT- and MRI-based techniques have enabled the study of carpal kinematics to be carried out not only in a cadaver model (Kaufmann et al., 2005, 2006), but also *in-vivo* with living subjects (Feipel and Rooze, 1999; Neu et al., 2001; Moojen et al., 2002; Crisco et al., 2003, 2005; Goto et al., 2005; Moritomo et al., 2006; Xu and Tang, 2009; Garcia-Elias et al., 2014). A collection of volumetric scans are typically obtained with the wrist placed quasi-statically in different positions (Fig. 1.49). And the rotational and translational transformations of the carpal bones between these wrist positions are often estimated by means of markerless registration. This can be achieved by means of surface matching (Snel et al., 2000), or volume matching (Goto et al., 2005), or based on the correspondence between a set of bony landmarks (Feipel and Rooze, 1999). The tracking error of these CT-based techniques is generally less than 2° for measuring rotations and is in the order of 0.5 mm for measuring translations (Neu et al., 2000; Snel et al., 2000; Goto et al., 2005). However, the major concern for this type of methods again revolves around the question of whether the static step-wise acquired carpal kinematics can really be used to approximate those that are happening during dynamic wrist motion. Abrupt changes in the position and orientation of the carpal bones as seen in certain carpal instabilities may go undetected with only static scans of the wrist.

To address this issue, the so-called four-dimensional (4D, with time being the 4th dimension) CT technology has been used to study dynamic motion of carpal bones in more recent years (Carelsen et al., 2005, 2009; Foumani et al., 2009; Leng et al., 2011; Edirisinghe et al., 2014; Zhao et al., 2015; Mat Jais and Tay, 2017a; Brinkhorst et al., 2020). However, the temporal resolution of this emerging technique is still limited, and the wrist motion has to be intentionally held at a slower speed, which might cause the musculoskeletal control facilitating the motion to deviate from that in the normal physiological condition.

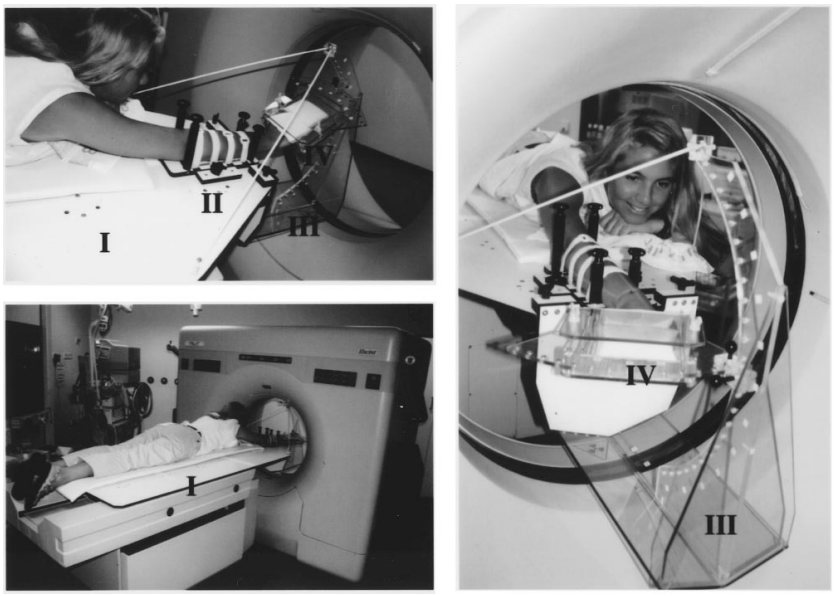

Figure 1.49: An example of the experimental setup that used in CT-based *in-vivo* carpal kinematics studies. The subject typically lies face-down (I) with his/her chin raised, and with the forearm held securely to the table (II). A motion constraining device is often used to guide the subject's wrist motion, such that the flexion-extension (III) and radial-ulnar deviation (IV) can occur according to preset arcs. This allows the subject's wrist to be placed into different desired postures in a reproducible manner. Adapted from Snel et al. (2000), with permission from John Wiley and Sons.

1.5.0.3 Techniques Used to Characterise Articular Contact

Load Cells

Load cells have been used in early studies to measure the force transmitted across the wrist to be subsequently born by the radius and ulna (Palmer and Werner, 1981, 1984; Trumble et al., 1987; Short et al., 1992). In these studies, the cadaveric wrist specimen was often axially loaded in an upright position, with the shafts of its radius and ulna transected and instrumented with S-beam load cells (Fig. 1.50). Since only a point load was measured, this method was typically used to study how the applied axial load apportioned between the radius and ulna, instead of determining any of the contact characteristics of the radioulnocarpal articulations.

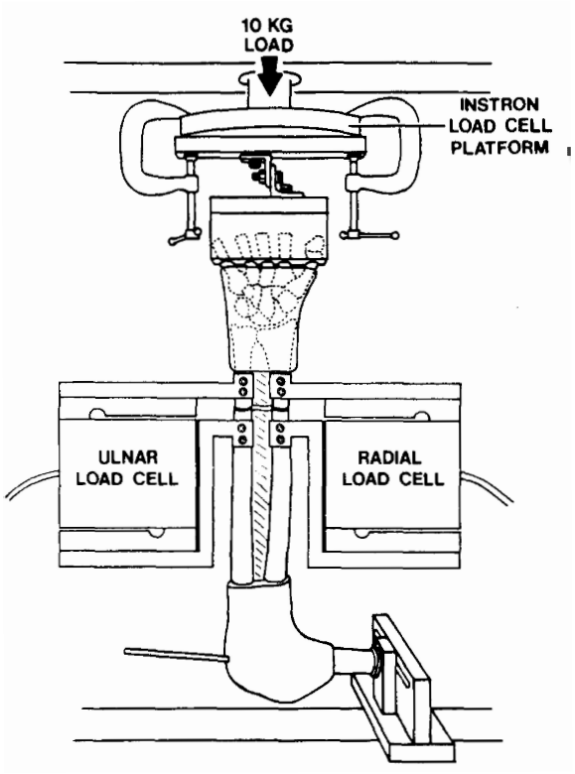

Figure 1.50: An experimental setup that uses load cells to measure the forces transmitted by the radius and ulna. Adapted from Trumble et al. (1987), with permission from Elsevier.

Pressure-Sensitive Films

Since the first introduction by Fukubayashi and Kurosawa (1980) as a means to observe articular contact area and pressure within the knee, Fuji Prescale pressure-sensitive films (Fuji Photo Film, Tokyo, Japan) have been extensively used in orthopaedic research. In regards to the wrist, many attempts have been made based on the use of such pressure-sensitive films to investigate various aspects of the radioulnocarpal contact (Viegas et al., 1987b,a, 1990; Tencer et al., 1988; Blevens et al., 1989; Kazuki et al., 1991; Short et al., 1992; Hogan et al., 2004; Tang et al., 2009; Fischer et al., 2011).

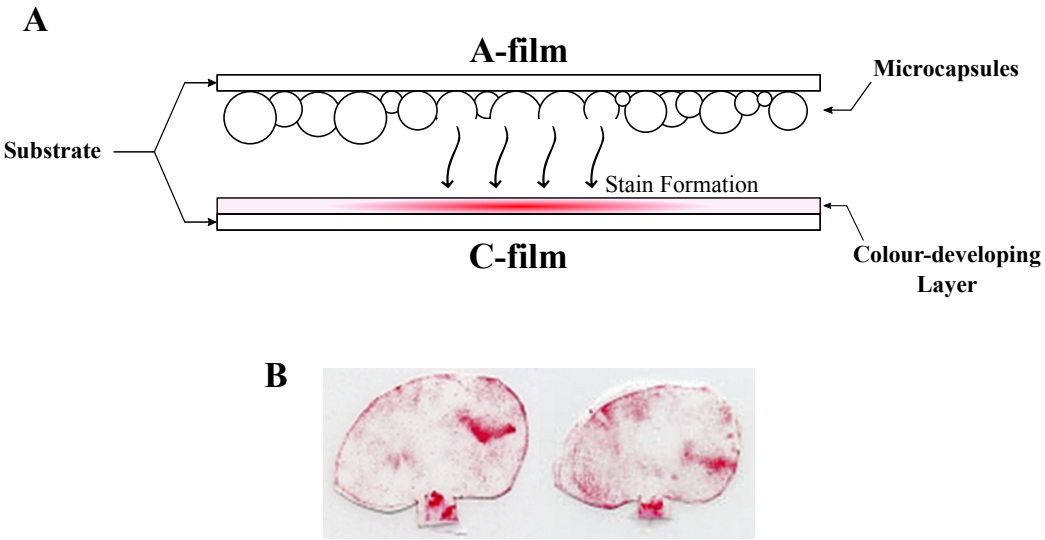

Figure 1.51: **(A)** Schematics showing the working principles of Fuji pressure-sensitive films. **(B)** Examples of the pressure impressions obtained from the radiocarpal joint. Adapted from Fischer et al. (2011), with permission from ASME.

Fuji films are offered in six different pressure ratings, each covering a specific range from 0.05 to 300 MPa. For the wrist, those with a low (2.5-10 MPa) or a super low (0.5-2.5 MPa) pressure rating are among the most frequently used. And Fuji films with a lower pressure rating are often comprised of an A-film and a C-film (Fig. 1.51). The A-film is coated with a layer of densely packed microcapsules filled with a colourless dye, while the opposing surface on the C-film is deposited with a colour-developing layer,

capable of chemically reacting with the dye given by the A-film to develop a characteristic red/magenta stain. Depending on the magnitude of pressure applied to the two-sheet composite, a number of microcapsules coated on the A-film will burst, causing a certain amount of dye to be released and react with the colour-developing medium on the C-film. Hence, based on the optical density of the resulting stain, the pressure acting at any point within the region of contact can be estimated (Liggins et al., 1992).

However, apart from being pressure-dependent, the staining response of Fuji film is also known to be affected by ambient conditions including the temperature and humidity, as well as factors such as the loading rate and the time of pressure retention (Fujifilm Corp., 2017). While a nominal measurement accuracy of $\pm 10\%$ has been published by the manufacturer, caution must be exercised when interpreting the pressure data, as the stain impression might have been corrupted by time-dependent changes, that are not appropriately accounted for in the factory-supplied calibration. Liggins and Finlay (1992) observed gross fluctuations in the mean pixel value of the pressure impression over a period of twenty-four hours, with an overall trend leaning towards gradual darkening of the stain. In a subsequent study, they suggested a 'development period' of fifty hours to be allowed before the stain is digitised for quantitative analysis (Liggins et al., 1995). As for the study of radioulnocarpal contact, the use of Fuji pressure-sensitive films has been shown to produce a measurement variation of $\leq 26\%$ in area, 39% in pressure and 8% in the location of contact centroids (Tencer et al., 1988).

Furthermore, it is often not a trivial task to use Fuji films as they have many practical limitations. Firstly, as the films work based on a staining process, they can be only used for single static measurements. Fresh ones will be needed whenever the contact at a different joint position is to be studied, or a different set of loads is to be applied. However, errors may arise as it is virtually impossible to have the film placed into precisely the same position within the joint space each time, let alone the likelihood of producing pressure artefacts when handling the films during repeated insertion and retrieval. Secondly, since the process of dye transfer between the A-film and

C-film is sensitive to the surrounding humidity, sealing and waterproofing of the film are therefore essential if it is to be placed inside a cadaveric joint. However, the presence of this extra layer may not only increase the thickness of the film but also interfere with the process of stain formation and deposition, adversely affecting the film's pressure response (Liggins, 1997). In addition, as the intra-articular surfaces of most joints have rather complex morphologies, the film may crinkle as it struggles to conform to these non-planar surfaces, resulting in incorrect and misleading pressure impressions. Several methods have been developed to address this issue. Caldwell et al. (1993) developed an algorithm to compensate for crinkle artefact numerically during post-processing of the pressure impressions, while Afoke et al. (1987) and Ateshian et al. (1994) physically cut the film into a shape resembling the planar projection of the joint space to ensure a good conformity.

Flexible Dynamic Pressure Sensors

Advancements in semi-conductor technology have enabled flexible film-type sensors capable of providing real-time contact measurements and pressure mapping to be developed. Based on their working principles, these sensors can be categorised as either resistive or capacitive. And both types of sensors have been applied to facilitate the study of radioulnocarpal contact.

The I-scan pressure measurement system available from Tekscan Inc. (Massachusetts, USA) has been widely used for *in-vitro* contact mapping of the human wrist (Short et al., 1995, 2002b; Teurlings et al., 2000; Fischer et al., 2011; Erhart et al., 2012; Holleran et al., 2013; Daly et al., 2018). The system is typically comprised of a film-typed piezoresistive pressure sensor and a USB handle, which interfaces the sensor with a host PC for control and data acquisition purposes. In essence, the sensor is made of a layer of pressure-sensitive semi-conductive ink sandwiched between two polyester substrates, onto which silver electrical leads have been deposited (Fig. 1.52). The leads are arranged in rows and columns, allowing electrical connections to be formed at their intersections, thereby activating the piezoresistive materials at these locations. Each of those activated locations

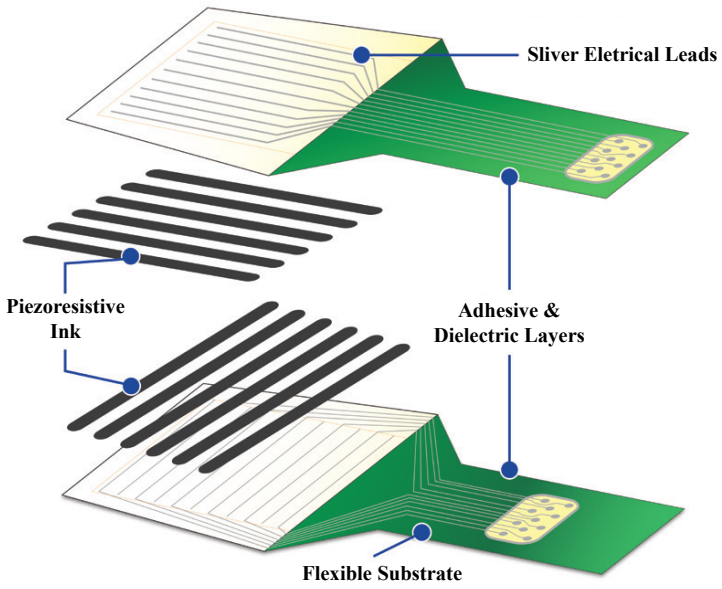

Figure 1.52: Schematics showing the construction of a Tekscan pressure sensor. (Adapted from Tekscan Inc. (2020).)

is referred to as a 'sensel'. And since the electrical resistance of the pressure-sensitive ink changes in inverse proportion to the applied normal force, the pressure distributed over a specific region of interest can therefore be estimated based on the electrical responses given by a grid of sensels covering that region (Tekscan Inc., 2020).

Tekscan offers a wide range of standardised ready-made sensors with a variety of size, shape and measurement capacity. For studies concerning the radioulnocarpal joint, Medical Sensor Model 4201 has been chosen by several researchers (Fischer et al., 2011; Erhart et al., 2012). This particular sensor model is capable of measuring pressure up to 2,000 psi (13.79 MPa), and measures approximately 0.18 mm in thickness and has a 21.1 × 45.7 mm rectangular sensing matrix formed by 264 sensels (27.6 sensels/cm^2) (Tekscan Inc., 2015a). Perhaps due to the low spatial resolution and the large footprint of the Model 4201 sensors, alternative solutions, such as taping multiple branches of a Model 6900 sensor together to form a continuous measuring surface, have also been experimented (Short et al., 1995, 2002b; Daly et al.,

2018). The Model 6900 sensors are offered in two different pressure ratings, either 10,000 psi (68.95 MPa) or 1,100 psi (7.59 MPa), with the latter being obviously more suitable for the contact study of the wrist. The sensor has four separate branches, with each being 0.10 mm in thickness and having a 14.0 $\times$ 14.0 mm square sensing matrix formed by 121 sensels (61.7 sensels/cm^2) (Tekscan Inc., 2015b).

Although these film-typed piezoresistive sensors have allowed dynamic articular contact pressure to be mapped with relative ease, their measurement accuracy and repeatability have been shown to be affected by a wide range of factors. These include variation in sensitivity across individual sensels; loading rate; ambient temperature; curvature of the contact surface; creep of the resistive material, which not only causes the sensor's output to slowly drift under constant force but also render hysteresis in the sensor's dynamic response (Luo et al., 1998; Otto et al., 1999; Morin et al., 2000). In a pilot study conducted by Short et al. (1995), the authors found a 8% increase in the sensor's output after the external load was being held constant for 30 seconds. They also showed a 6°C decrease in temperature led to a 19% decrease in the sensor's output.

Capacitive-based pressure sensors have also been used to study the radioulnocarpal contact (Rikli et al., 2007). The sensor had a rather similar configuration to its piezoresistive counterparts. But instead of relying on the resistance change of a pressure-sensitive ink, the sensor used an elastic dielectric material, whose capacitance changes as a function of its geometric distortions. Compared to those offered by Tekscan, the sensor developed by Rikli et al. (2007) was much thicker (1.60 mm) and had a significantly lower spatial resolution, as each of its sensing units measured approximately 1.5 mm in the sagittal plane and 2.0 mm in the coronal plane.

Joint Proximity Mapping

While placing a pressure sensor into the joint of interest allows for direct evaluation of the joint contact, such an invasive approach is mainly reserved

for laboratory testing involving cadaveric specimens. In addition, specific capsuloligamentous structures overlying the joint are often removed in order to accommodate the pressure measurement device. This may disrupt the normal physiology of the joint, rendering the joint motion and the articular contact simulated on the cadaver model less representative of those in the *in-vivo* condition (Liau et al., 2001; Short et al., 2002b).

To this end, many researchers have attempted to infer joint contact by means of a non-invasive approach called joint proximity mapping, which essentially involves finding the distances between the joint's articulating surfaces (Scherrer et al., 1979; Soslowsky et al., 1992; Ateshian et al., 1994; Lösch et al., 1997; Anderst and Tashman, 2003; Goto et al., 2004; Marai et al., 2004). Joint proximity maps calculated based on three-dimensional geometries of the articular cartilages, usually obtained by means of MRI, are considered as being the most accurate, as the complex topography of the articulating surfaces is automatically accounted for (Cohen et al., 1999; DeFrate et al., 2004). However, for small joint like the radioulnocarpal articulation in the wrist where the cartilage layers become too thin to be realistically captured (Haims et al., 2004; Mutimer et al., 2008), opposing surfaces of the subchondral bones are often used as a surrogate to facilitate the joint proximity calculation, under the assumption that the articular cartilages have uniform thickness and experience negligible deformations (Moritomo et al., 2000a; Foumani et al., 2013; Johnson et al., 2013; Omori et al., 2013; Lalone et al., 2015; Zhao et al., 2015).

In terms of the reliability of this method in estimating joint contact, Lalone et al. (2013) compared the joint proximity map calculated based on inter-bone distances for a cadaveric elbow with the contact pattern obtained experimentally by means of a casting technique. At varying degrees of elbow flexion, the authors found the regions of close proximity consistently tracked the locations of the actual ulnohumeral contact, confirming the valid use of this method in inferring joint contact. In a cadaver model, Wang et al. (2015b) compared the centroid of tibiofemoral contact as calculated based on joint proximities with that derived using the contact stress measured

directly by means of a pressure sensor. The authors, however, found the contact centroids determined by the two methods were correlated mainly in the anteroposterior direction than in the mediolateral direction on both tibial plateaus. This discrepancy was thought to be caused by the negligence of the meniscal-to-cartilage contact, as the joint proximities were calculated solely based on subchondral bony surfaces.

Computational Modelling

Computational methods, such as finite element analysis (FEA) (Ulrich et al., 1999; Oda et al., 2000; Carrigan et al., 2003; Anderson et al., 2005; Gislason et al., 2009; Guo et al., 2009; Bajuri et al., 2012; Varga et al., 2013), and 2D- (Horii et al., 1990; Watanabe et al., 1993; Schuind et al., 1995), or 3D rigid body spring modelling (RBSM) (Iwasaki et al., 1998; Genda and Horii, 2000; Majima et al., 2008; Eschweiler et al., 2016a; Mrquez-Florez et al., 2016), have also been employed as a non-invasive means to study the force transmissions within the wrist. The difference between these two methods mainly lies in the way different parts of the joint are computationally modelled: in RBSM, the bones are often regarded as rigid bodies, while the cartilages are modelled as arrays of compressive springs distributed over the articular surfaces (Fig 1.53); while both of them are modelled as deformable bodies in FEA. And in some studies, the bones were even modelled realistically with inhomogeneous material properties (Gislason et al., 2009; Bajuri et al., 2012; Varga et al., 2013).

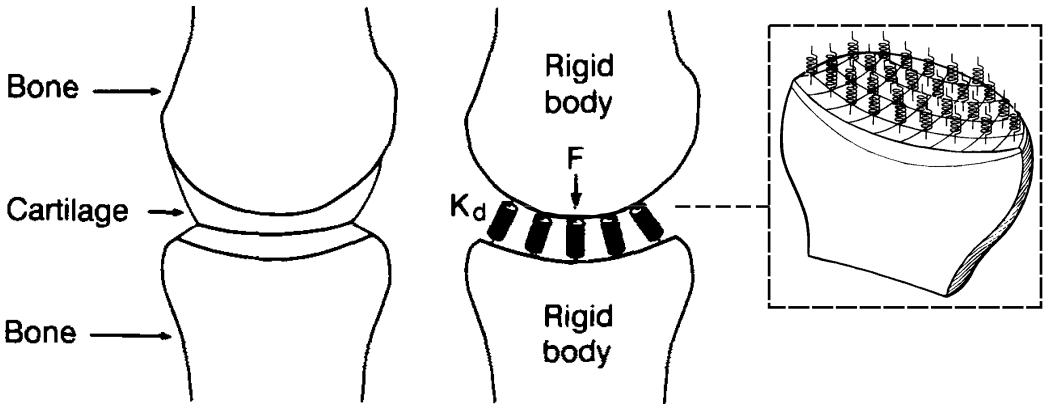

Figure 1.53: The general principle of the RBSM. Adapted from Schuind et al. (1995), with permission from Elsevier.

2

Cadaveric Wrist Testing Platform

Contents

2.1 Introduction 120

2.2 Dynamic Wrist Simulation Apparatus 123

2.2.1 Structural Design 123

2.2.2 Electromechanical Design 131

2.2.3 Motion Control Algorithm 145

2.2.4 Software Implementation 159

2.3 Subsidiary Measurement Systems 163

2.3.1 Biplane X-ray Fluoroscopy System 163

2.3.2 Marker-Based Kinematic Analysis 173

2.3.3 Pressure Measurement System 183

2.4 Summary 186

This chapter outlines the design and development of various subsystems comprising the cadaveric wrist testing platform in detail.

2.1 Introduction

The ability to perform *in-vitro* wrist simulations allows researchers to study the interactions between the bones, ligaments and muscles dynamically in a controlled laboratory setting. It opens up new doors for wrist research, especially for studies involving invasive procedures that are impractical to be experimented in living human subjects. A typical example would be to study the biomechanical consequences of injury to specific carpal ligaments or to evaluate the efficacy of a newly proposed surgical technique or a novel implant design before clinical applications.

Wrist motion can be reproduced on cadaveric specimens, either passively or actively. With the passive simulation being the simplest, where the muscle tendons have been previously loaded with dead weights, which were not intended to induce any movements but merely served as an approximation of the physiological loading conditions (Garcia-Elias et al., 1989; Patterson et al., 2007; Pollock et al., 2010; Eng et al., 2014). Wrist motions were then imposed externally by human operators by means of passive manipulation of the cadaveric specimen. However, investigations that adopted such a method presents concerns about inter-trial repeatability and reliability across specimens, and whether the simulated loading conditions are physiological (Johnson et al., 2000). On the other hand, active simulations typically require the resultant motion to be muscle activated and, to some extent, capable of replicating the *in-vivo* kinetics and kinematics of a native joint. Digital control systems are often implemented to facilitate such simulations, which in turn improves the consistency and repeatability of the resultant motions. Thus, despite being more technically challenging, active simulations are thought to be more physiologically representative in recreating dynamic joint motions (Nishiwaki et al., 2014).

Therefore, in order to facilitate reliable biomechanical investigations of the wrist, a cadaveric wrist testing platform (CWTP), comprised of a novel dynamic wrist simulation apparatus (DWSA) and a set of subsidiary measurement systems, was developed as a self-sufficient "environment", allowing

repeatable wrist motion to be simulated *in-vivo* while accurate measurements of relevant parameters are being made at the same time (Fig. 2.1). The DWSA is a computer-controlled apparatus with the capability of performing repeatable and physiological active kinematic simulations on cadaveric wrists. It was actuated by six stepper-motor-driven actuators and was instrumented with in-line load cells and video motion capture cameras to facilitate a closed-loop control of the cadaveric wrist dynamics. The subsidiary measurement system, including a custom-built biplane X-ray fluoroscopy system and an I-scan pressure measurement system (Tekscan, Massachusetts, USA), was incorporated into the CWTP to allow the 6-DOF carpal kinematics and radiocarpal contact pressure to be measured simultaneously during the motion simulation.

The following sections are dedicated to addressing the design and function of various subsystems comprising the CWTP. The validation experiments performed for the subsystems as well as the CWTP as a whole are described in the subsequent chapter. Specifications of the key components used are provided in Appendix A.

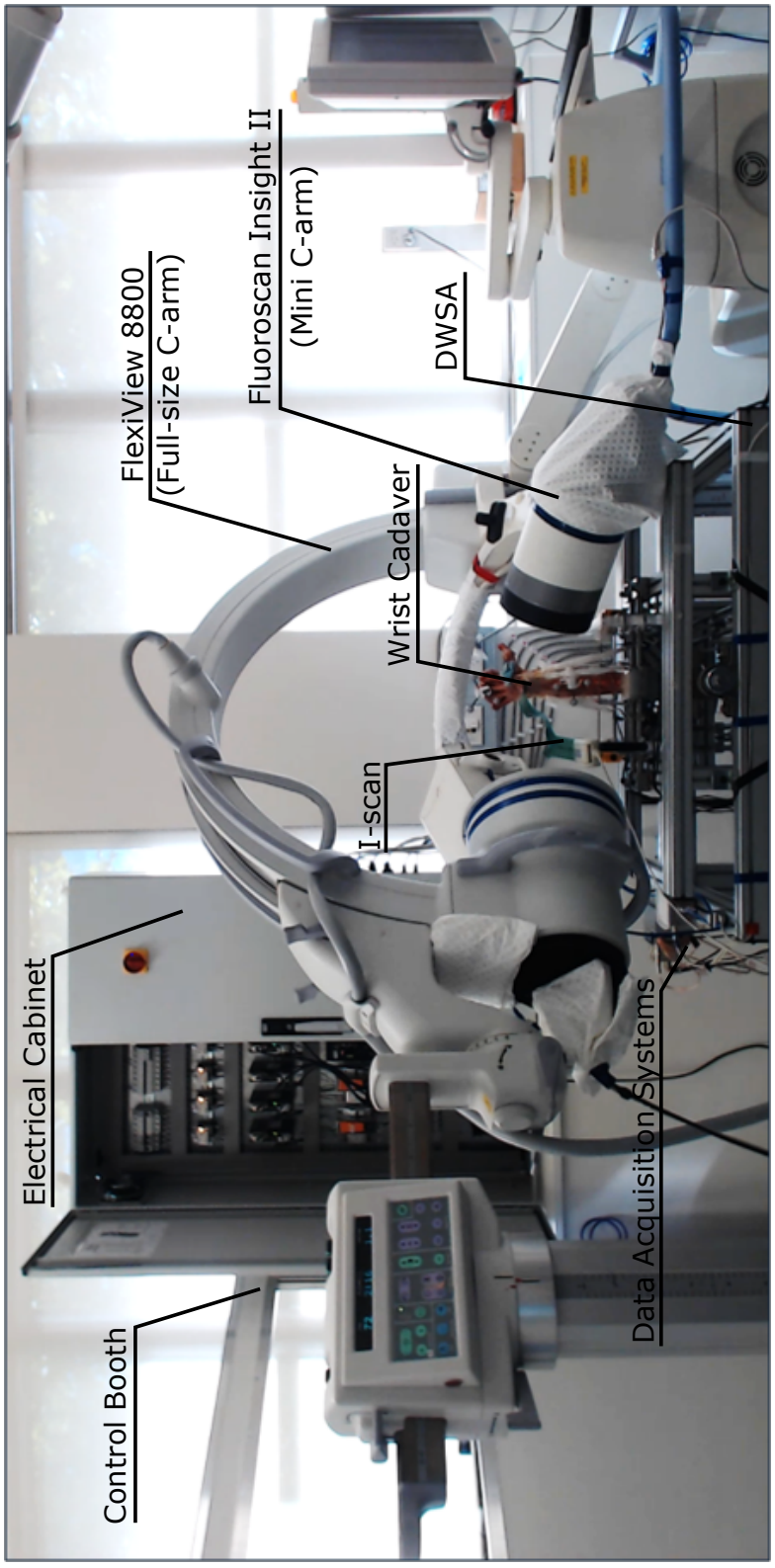

Figure 2.1: Photograph of the CWTP with the biplane X-ray fluoroscopy system (consists of a Mini and Full-size C-arm unit) imaging a wrist specimen undergoing dynamic flexion (the video motion capture system was not shown)

2.2 Dynamic Wrist Simulation Apparatus

The DWSA is a computer-controlled apparatus with the capability of simulating active muscle-activated wrist motion that are both repeatable and physiologically meaningful in cadaveric wrist specimens. This apparatus is actuated by six stepper motors, and is instrumented with uniaxial load cells and a set of video motion capture cameras to provide closed-loop control over the dynamics of the cadaver wrist.

2.2.1 Structural Design

This section provides a thorough description of the mechanical components designed and manufactured for fulfilling the structural requirement of the DWSA. This included the overall framework of the DWSA, mechanisms that provide support and mounting for the cadaveric wrist as well as relevant measurement instruments. In addition, appropriate accessories were also developed to facilitate grasping and routing of the muscle tendons.

2.2.1.1 Apparatus Framework

Structural Skeleton

The structural framework of the DWSA was constructed using aluminium extrusion of various lengths and cross-sections (Fig. 2.2). Off-the-shelf profile (MayTec Australia, New South Wales, Australia) was employed, owing to low-cost, availability, light-weight, low-deflection, good machinability and versatility.

Those slotted aluminium members were interconnected through the use of the Maytec universal and oblique connectors, forming the structural backbone, while T-slot nuts with matching screws were used to mount the mechanical and electro-mechanical components comprising the DWSA to its framework. Both fastening mechanisms could easily be positioned and tight-

ened in place, allowing ease of assembling and reconfiguring of the DWSA.

The design of the structural framework was divided into the specimen cell and the actuator cell based on their relative roles in providing fixations. The specimen cell, consisted of sixteen members of 40×40 and 40×80 mm 4E LP aluminium profile in total, was configured to accommodate all mechanical components necessary to interface the cadaveric wrist to the DWSA. The actuator cell consisted of twenty-nine lengths of aluminium profiles, was devised to provide overall stability for the DWSA as well as the attachment for six stepper-motor-driven actuators with the flexibility to allow their relative positions to be adjusted in all three directions.

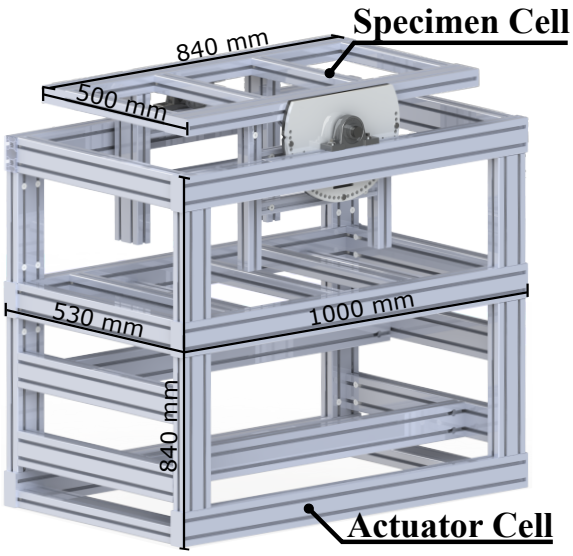

Figure 2.2: CAD model of DWSA's structural framework

Rotation Mechanism

The angular position of the specimen cell was designed to be adjustable through a rotation mechanism (Fig. 2.3). Although not used in the present study, this feature allows dynamic wrist simulations to be performed in different forearm rotations, accommodating the need to study the effect of gravity on wrist biomechanics as future research. In addition, this feature also enhances the versatility of the DWSA, allowing the rig to be readily configured

to accommodate *in-vitro* simulations of other joints in the body such as the shoulder.

The rotation mechanism consisted of two pairs of pillow block bearings (UCP205; AST Bearings, New Jersey, USA) coupled with two stainless steel shafts (25 mm diameter), suspending the specimen cell on top of the actuator cell. A pair of 10 mm thick, 330 mm diameter semi-circular discs with a series of pinholes drilled at 5° intervals were used to lock the two cells in desired angular positions.

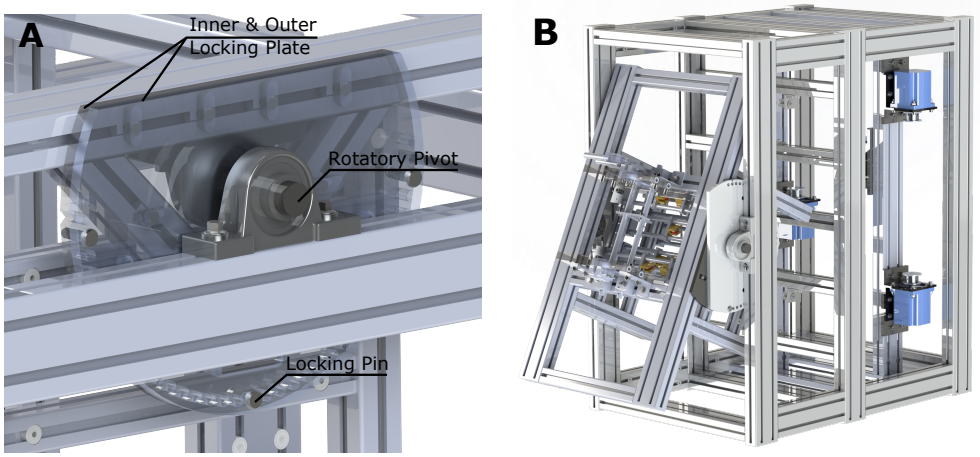

Figure 2.3: **(A)** Angle locking mechanism enlarged, and **(B)** illustration of the DWSA being rotated 90 degrees to accommodate the potential need of performing *in-vitro* simulations of the shoulder joint.

2.2.1.2 Forearm Mounting Fixture

A forearm mounting fixture (Fig. 2.4) was developed to mount cadaveric wrist specimens onto the DWSA. It comprised of an elbow potting block, a Perspex "cage" and a pair of adjustable pin holders. The fixture was designed such that it neither hinders the normal wrist motion nor obstructs the anatomical muscle line of action. The idea of "potting" the specimen proximally at the elbow joint and gripping the Steinmann pins drilled at the mid-forearm level was to allow for an obstruction-free capture volume centred at the wrist joint for various optical measurement systems that require a clear line of sight.

Additionally, apart from being able to provide sufficient structural rigidity, the fixture was also designed to allow easy mounting and dismounting of the cadaver wrist, helping to avoid possible user-contact with the fluoroscopes that might invalidate the calibration of the Röentgen stereo-photogrammetry setup.

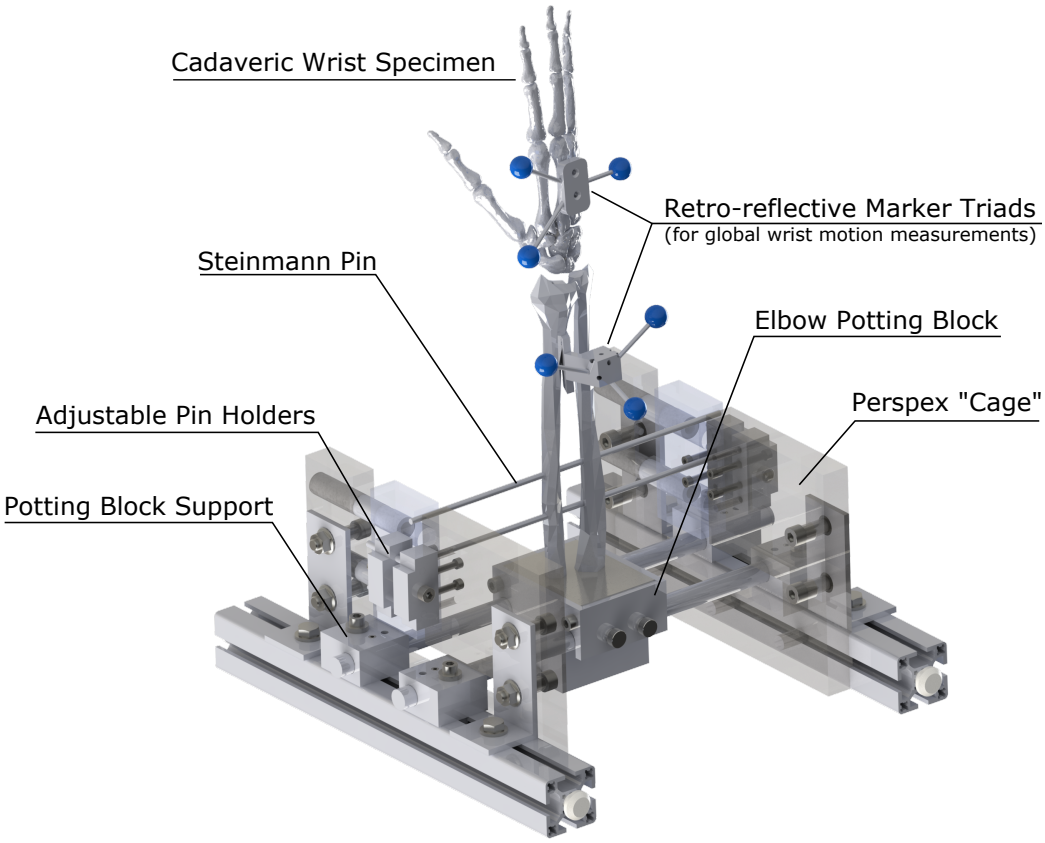

Figure 2.4: CAD model of the forearm mounting fixture

Elbow Potting Block

The elbow potting block was made out of aluminium and approximated a hollow rectangular container with one side being readily detachable. This feature allowed the proximal ends of the disarticulated radius and ulna to be embedded into the potting block using high strength dental plaster (USG Boral, Victoria, Australia). The potting block's grossly cuboid-shaped interior

prevented relative rotations of the plaster casting, while the mostly curved inner surfaces together with the detachable two-piece design of the block facilitated an easy removal of the plaster castings after use. A pair of 14 mm diameter stainless steel rods were used to support the elbow potting block. Semi-circular slots were made on the two longer sides of the elbow potting block allowed the position of the block together with the specimen to be adjusted in the coronal plane. Thumbscrews were used as grub screws allowed the potting block to be locked into the desired position conveniently. The specimen-pot assembly was finally mounted onto frameworks of the specimen cell using four custom-machined adapter blocks and T-slot fasteners, allowing the position of the specimen to be adjusted further in the sagittal plane.

Adjustable Pin Holders

Two Steinmann pins of 4 mm in diameter and 250 mm in length were drilled through shafts of the radius and ulna transversely at a mid-to-distal forearm level to fix the cadaveric wrist specimen in neutral pronation-supination, similar to the method of fixation employed in other investigations concerning the wrist (Garcia-Elias et al., 1989; Berger et al., 1982b; Crowninshield and Brand, 1981; Horii et al., 1991). In addition, the pins also served to enhance the structural integrity of the specimen.

A pair of adjustable pin holders were constructed to clamp the protruding ends of the Steinmann pins, reinforcing the forearm against bending moments generated by the simulated active muscle contractions during dynamic trials. The adjustable pin holder comprised of two 20 mm thick Perspex glass plates and an off-the-shelf machine vice mounted on the lateral side. The inner movable Perspex plate was supported by two guiding rails and attached to the sliding jaw of the vice, with the outer piece was fixed to the static jaw. The adjustable pin holders were installed medially and laterally to the cadaver wrist and were capable of being easily positioned and tightened in place to provide a firm gripping of the pinned specimen. Along with the elbow potting block, this design provided a reliable means of fixing the specimen with a minimal footprint.

2.2.1.3 Tendon-Actuator Connection

Tendon Grip

In order to stimulate muscle contractions through force applications, a reliable means to grasp and attach each muscle tendon of the cadaver wrist to their designated actuators within the DWSA was required.

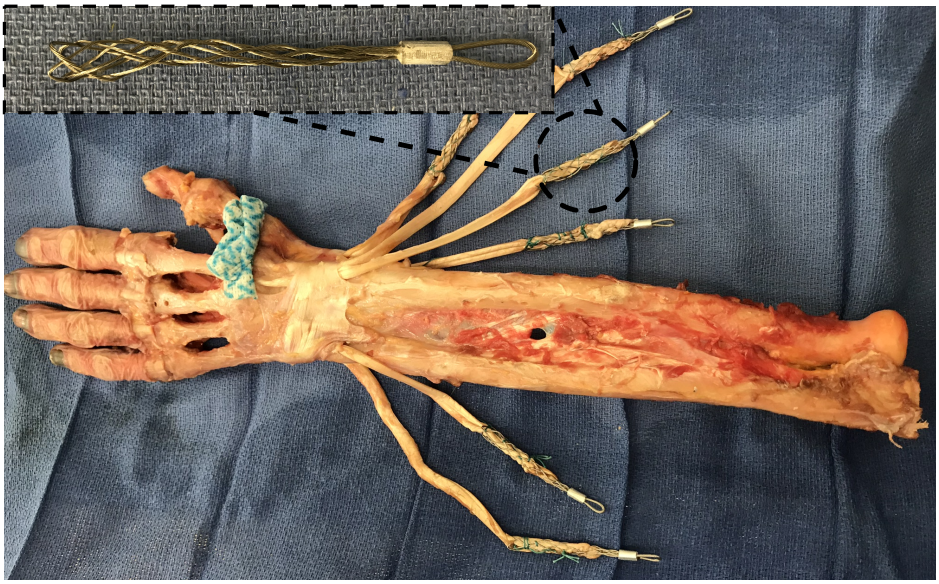

Figure 2.5: Photograph of a dissected cadaveric wrist specimen with its tendons trapped using custom-made wire-woven sleeves.

To achieve this, custom-designed wire-woven sleeves, similar to the finger traps commonly used in orthopaedic traction devices, were manufactured (Fig. 2.5). Non-absorbable sutures (Ethibond Excel, Size 2-0; Ethicon, New Jersey, USA) were added to reinforce the bounding, facilitating a stable and reliable grasp. The eye splice located on the other end of the sleeve provided sites of further attachments. Stainless steel wire rope (1.6 mm thick, 7×7 construction; Keble's Trading, Victoria, Australia), capable of withstanding 1.89 kN, were used to apply loading to the sleeve-trapped tendons via the actuator system.

Tendon Guiding Pulley System

Although the wrist is augmented with the flexor and extensor retinacula, which by nature are pulley-like structures, unphysiological muscle excursions in directions that deviate from the anatomical lines-of-action ought to be avoided to prevent soft-tissue damage such as bowstringing of the tendons as well as to achieve a closer approximation of the *in-vivo* motion of the wrist. A tendon guiding system was therefore constructed to deliver the load and displacement generated by the actuators to the tendons of the wrist specimen without altering each muscle's line-of-action (Fig. 2.6).

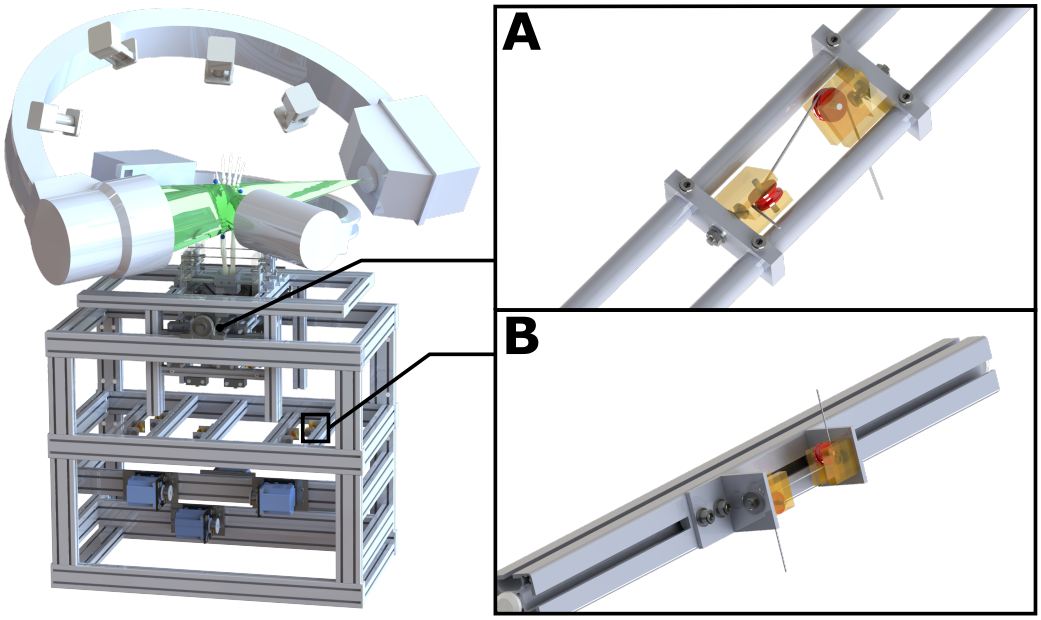

Figure 2.6: CAD Model of the DWSA, showing the enlarged **(A)** primary, **(B)** secondary tendon guiding pulley systems.

Ready-made pulleys (RM302 14 × 6 mm sheave, 200 kg load capacity; Riley Fittings, New South Wales, Australia) were converted into swivelling pulleys, similar to those used in the dynamic shoulder testing apparatus developed by Ackland et al. (2008). These pulleys were then arranged in pairs of two to form the basic building. This double-pulley configuration decoupled the input and output cable directions, providing greater flexibilities in the placement of the downstream elements such as the actuators as well as the

pulley sets themselves. Thus, the tendon guiding system was designed to be span both the specimen cell and the actuator cell, facilitating a gradual two-stage routing of the cables.

The primary pulley system was designed to be installed immediately underneath the wrist specimen at locations closet to their designated muscle tendons, reducing the likelihood of introducing large bending moment to the forearm. Stainless steel shafts and brackets along with grub screws were used to support each pair of the double-pulley sets, allowing their positions to be easily reconfigured in the sagittal plane. The small footprint of this design also permitted a staggered placement of the pulley sets, allowing the anatomical line-of-action of closely situated muscles, such as the extensor carpi radialis longus and brevis (ECR-L and ECR-B) to be preserved. The assembly as a whole was then attached to the framework of the specimen cell through mounting blocks and T-slot nuts to allow the position of the pulley sets to be further adjustable in the coronal plane, making the system to be more versatile in accommodating the anatomical variations across different wrist specimens.

The secondary pulley system was installed with the double-pulley sets tiled across the actuator cell to receive the cables coming from the specimen cell and redistribute them to the close proximities of their corresponding actuators, reducing the friction generated by an otherwise abrupt and awkward cable routing during cell to cell transition. And the secondary pulley system was also made to be readily adjustable to ensure different cable routing configurations would be achievable without needing to rearrange the actuators within the DWSA.

2.2.2 Electromechanical Design

This section provides a detailed description of the hardware, software and algorithms implemented to facilitate digital electromechanical control of the DWSA. Dedicated subsystems and programs were developed for measuring the global joint position as well as the tensions applied to the muscle tendons of the wrist specimen. The control algorithm employed a nested position-force control architecture and addressed challenges such as the neuromuscular redundancy and agonist-antagonist muscle co-contraction in replicating physiological wrist motion.

2.2.2.1 Wrist Position Measurement System

Video Motion Capture System

As mentioned earlier in Section 1.5.0.2, unlike conventional joint position measurement techniques that require motion-obstructive linkages or transducers to be mounted directly onto the subject, video-based motion capture systems provide an indirect means to carry out kinematic analysis via optical imaging. This feature makes them suitable for biomechanical investigations in which the subject's native behaviour is to be respected.

A video motion capture system (Fig. 2.7) was therefore employed in the present study to provide accurate and real-time measurements of the global wrist position. This data was subsequently utilised as the position feedback to achieve closed-loop control of the motion reanimated on the cadaver wrist. The system comprised four optoelectronic motion capturing cameras (Vero v2.2, Vicon Motion System, Oxford, UK) and was capable of tracking precise movements of retro-reflective markers in three-dimensional space (technical specifications can be found in Appendix A.1). In short, this was achieved by triangulating the retro-reflective markers based on their 2D projections, as seen simultaneously by multiple cameras from different angles. In order to facilitate such a triangulation process, calibration of the cameras were performed to establish the mathematical correspondence between the 2D

image-space and the 3D scene-space. And to maintain a valid calibration, the cameras were rigidly mounted to a wall and kept free of disturbances during testing.



Figure 2.7: Photograph showing the arrangement and fixation of the Vicon video motion capture system

Two wall-mounted rails, situated in front of the DWSA's framework at a distance of 2.5 m, were used in concert with clamps to allow a rigid fixation of the cameras. Rubber paddings were added to the sites of clamping to prevent potential slippage or creeping of the fixtures. The cameras were installed in horizontal intervals at varying heights, and oriented to allow their field-of-views to be centred within the capture volume. Such a staggered placement of the camera reduced the likelihood of producing similar projections of the tracking target, which would add little information to the reconstruction calculations and result in unnecessary computational expense. Furthermore, given the substantial footprint of the biplane X-ray fluoroscopy system inside the capture volume (Fig. 2.1), this particular camera arrangement allowed the retro-reflective markers to be visible to at least three cameras at all times, ensuring uninterrupted motion tracking throughout the experiment.

A network switch (GEP-1622; LevelOne, Dortmund, Germany) was used

to provide power as well as means for data exchange with a host PC to the video motion capturing cameras. Vicon Tracker 3.5.1 (Vicon Motion System, Oxford, UK) was used to control the cameras, facilitating motion capture and subsequent analysis. Calibration of the cameras was carried out at the beginning of each dynamic wrist simulation, utilising a calibration wand (Mini-Cal 120; Vicon Motion System, Oxford, UK). The calibration process was repeated until a reprojection error below 0.015 mm was achieved on all cameras. Trajectories of the retro-reflective markers were captured with a very low latency of 3.6 ms at a resolution of 2.2 megapixels and a sampling rate of 300 Hz on the cameras.

DataStream SDK

To facilitate dynamic and closed-loop control of the simulated wrist motion, the DWSA requires real-time measurement of the current wrist position to make effective control adjustments. Unlike most conventional studies, such as the gait analysis, where such a video motion capture system is typically used to record the relevant kinematic data for later offline processing, the time-critical nature of DWSA's control requirement presented a serious challenge, as the marker coordinates collected by the cameras must be made readily accessible to allow for timely "on-line" processing.

To achieve this, Vicon DataStream Software Development Kit (SDK) version 1.7.1 (Vicon Motion System, Oxford, UK) was employed to programmatically access the stream of data exchanged between the motion capture cameras, and Vicon Tracker 3.5.1 installed on the host PC. Custom LabVIEW (National Instruments, Texas, USA) virtual instrument (VI) programs were developed to facilitate function calls through the vendor-supplied .NET assembly. In essence, the 'GetFrame' method was called continuously in a loop to request the latest frame of data stored in the buffer. The 'GetMarkerGlobalTranslation' method was then called upon the returned frame of data to obtain the three-dimensional coordinates of a specific marker in millimetre. Since the software loop was set to execute at a lower frequency, namely 100 Hz, on the host PC asynchronous to the cameras, the time delay of the

obtained measurement was approximately 7 ms, equivalent to one complete sampling cycle of the motion capture system, plus its inherent hardware latency. This delay was considered negligible for DWSA's control system.

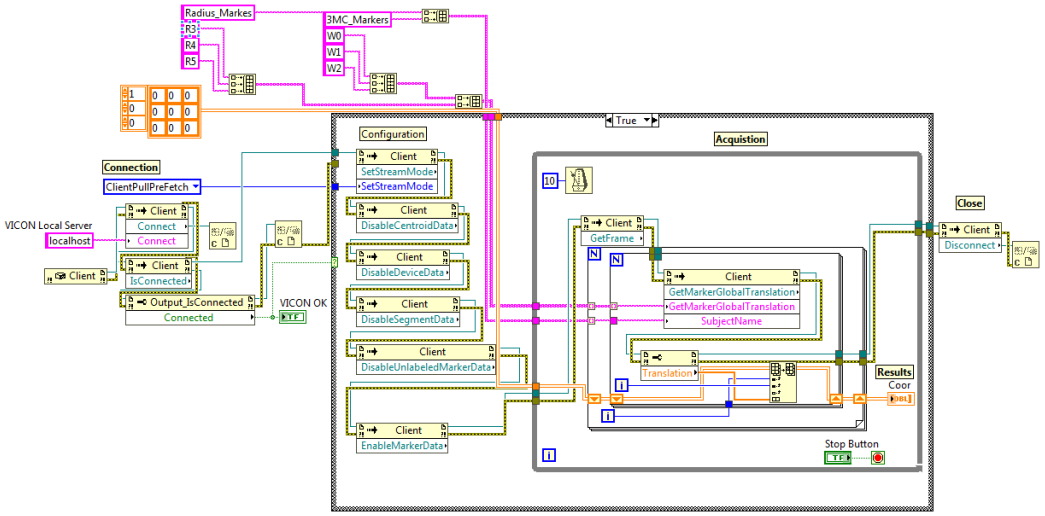

Figure 2.8: An example demonstrating the use of Vicon DataStream SDK in obtaining the real-time coordinates of the retro-reflective markers (designated as W0-2 and R3-5)

Joint Angle Calculation

As discussed in Chapter 1, global wrist motion is typically defined as the motion of the third metacarpal (3MC) relative to the radius, and is considered to be comprised primarily of the flexion-extension motion (FEM) and the radial-ulnar deviation (RUD) of the wrist.

Since knowledge of at least three non-collinear points on a moving segment is necessary for calculating its rigid body motion, triads of retro-reflective markers were rigidly attached to both the radius and the 3MC by means of 3D-printed marker holders to facilitate tracking of the global wrist motion. A volumetric CT scan of the marked wrist specimen was then performed, allowing the body segment coordinate systems to be defined for the radius and the 3MC. Since the retro-reflective coating of the markers are visible on CT scans, the centroid of each marker was estimated by fitting a sphere to the point cloud defined by its coating. This was archived using the sphere fitting functionality available in Geomagic (3D Systems, South Carolina, USA), with an RMS fitting error of around 0.1 mm (Fig. 2.9).

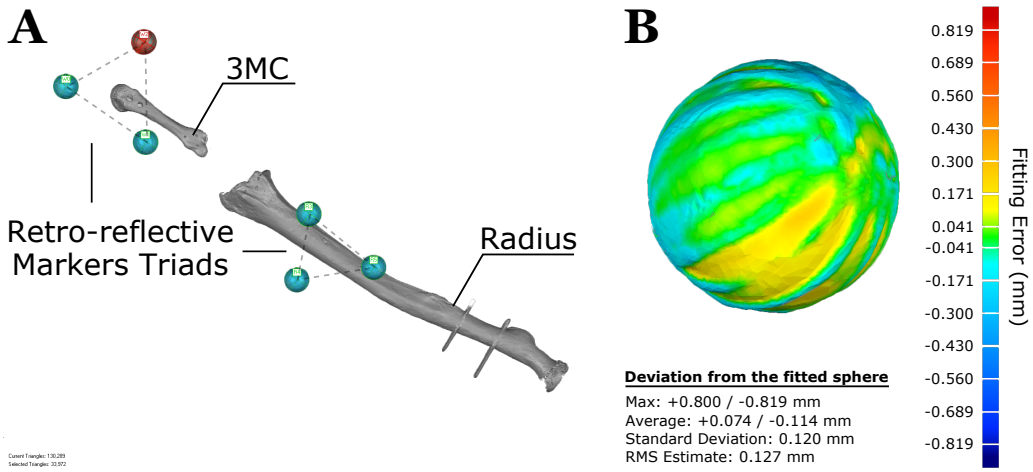

Figure 2.9: **(A)** A screenshot showing spheres being fitted to models of the retro-reflective markers. **(B)** An example showing the typical fitting error: the 3D deviation from the fitted sphere as observed by the point could defined by one of the 3MC markers (shown in red in Figure A) is visualised.

Those marker coordinates were subsequently transformed into the local body segment coordinate system of the radius or the 3MC, namely $\mathcal{R}_{Rad}$ and $\mathcal{R}_{3MC}$, depending on the location and designation of their constituent marker triads. Hence, the positions of the two marker triads expressed locally in their respective body segment coordinate systems could be collectively denoted as two 3-by-3 matrices, $\boldsymbol{P}_{Rad}^{\mathcal{R}_{Rad}}$ and $\boldsymbol{P}_{3MC}^{\mathcal{R}_{3MC}}$, with their constituent marker coordinates stacked as rows. During dynamic wrist simulations, the marker triads fixed to the radius and the 3MC were tracked continuously by the video motion capture system. At a particular instant in time, the 3D positions of the marker triads measured in the coordinate system defined by the motion capture system could be determined, denoted in a similar fashion as $\boldsymbol{P}_{Rad}^{\mathcal{R}_{Mocap}}$ and $\boldsymbol{P}_{3MC}^{\mathcal{R}_{Mocap}}$. Since only the relative orientation of the 3MC was considered, the two local body segment coordinate systems could be shifted to a common origin. Therefore, the rotation transformation that described the angular position of the 3MC relative to the radius at that particular instant could be calculated as follows (Eq. 2.1).

$$\begin{aligned} {}^{\mathcal{R}_{Rad}}\boldsymbol{R}_{\mathcal{R}_{3MC}} &= {}^{\mathcal{R}_{Rad}}\boldsymbol{R}_{\mathcal{R}_{Mocap}} \left({}^{\mathcal{R}_{3MC}}\boldsymbol{R}_{\mathcal{R}_{Mocap}} \right)^{T} \\ &= [\boldsymbol{X}_{3MC}^{\mathcal{R}_{Rad}} \quad \boldsymbol{Y}_{3MC}^{\mathcal{R}_{Rad}} \quad \boldsymbol{Z}_{3MC}^{\mathcal{R}_{Rad}}] = \begin{bmatrix} r_{11} & r_{12} & r_{13} \\ r_{21} & r_{22} & r_{23} \\ r_{31} & r_{32} & r_{33} \end{bmatrix} \end{aligned} \tag{2.1}$$

where rotation matrices ${}^{\mathcal{R}_{Rad}}\boldsymbol{R}_{\mathcal{R}_{Mocap}}$ and ${}^{\mathcal{R}_{3MC}}\boldsymbol{R}_{\mathcal{R}_{Mocap}} \in \mathbb{R}^{3\times3}$, were calculated based on the point-wise correspondence between $\boldsymbol{P}_{Rad}^{\mathcal{R}_{Mocap}}$ and $\boldsymbol{P}_{Rad}^{\mathcal{R}_{Rad}}$, $\boldsymbol{P}_{3MC}^{\mathcal{R}_{Mocap}}$ and $\boldsymbol{P}_{3MC}^{\mathcal{R}_{3MC}}$, respectively, based on the algorithm developed by Söderkvist and Wedin (1993). In essence, the columns of the compound rotation, ${}^{\mathcal{R}_{Rad}}\boldsymbol{R}_{\mathcal{R}_{3MC}}$, were made up by the three basis vectors of $\mathcal{R}_{3MC}$ expressed in $\mathcal{R}_{Rad}$, denoted as $\boldsymbol{X}_{3MC}^{\mathcal{R}_{Rad}}$, $\boldsymbol{Y}_{3MC}^{\mathcal{R}_{Rad}}$, and $\boldsymbol{Z}_{3MC}^{\mathcal{R}_{Rad}}$. Unless otherwise specified, the superscripted, $\mathcal{R}_{Rad}$, was omitted in the following calculation.

According to the ISB recommendations (Wu et al., 2005), the FEM of the wrist is defined as the rotation around the $\boldsymbol{Z}$-axis fixed to the radius. The

corresponding joint angle, α, can be found by calculating the angle included by the $\boldsymbol{Y}$-axis the projection of the $\boldsymbol{Y}_{3MC}$ in the X-Y plane (Fig. 2.10), denoted as $\boldsymbol{y}_{proj}$ (Eq. 2.2).

$$\alpha = \tan^{-1}\left(\frac{-r_{12}}{r_{22}}\right) \tag{2.2}$$

The RUD of the wrist is defined as the rotation around the common axis perpendicular to the $\boldsymbol{Z}$-axis fixed to the radius and the rotated $\boldsymbol{Y}$-axis of the 3MC. This can be easily found by rotating the original system around the $\boldsymbol{Z}$-axis until the direction of its $\boldsymbol{Y}$-axis becomes aligned with $\boldsymbol{y}_{proj}$ (Fig. 2.10). The rotated coordinate system is denoted using axes $\boldsymbol{x}' - \boldsymbol{y}' - \boldsymbol{z}'$. Hence, the rotation occurs around $\boldsymbol{x}'$ is the wrist RUD and the angle included between $\boldsymbol{y}'$ and $\boldsymbol{Y}_{3MC}$ is the corresponding joint angle, denoted as β (Eq. 2.3).

$$\beta = \sin^{-1}(r_{32}) \tag{2.3}$$

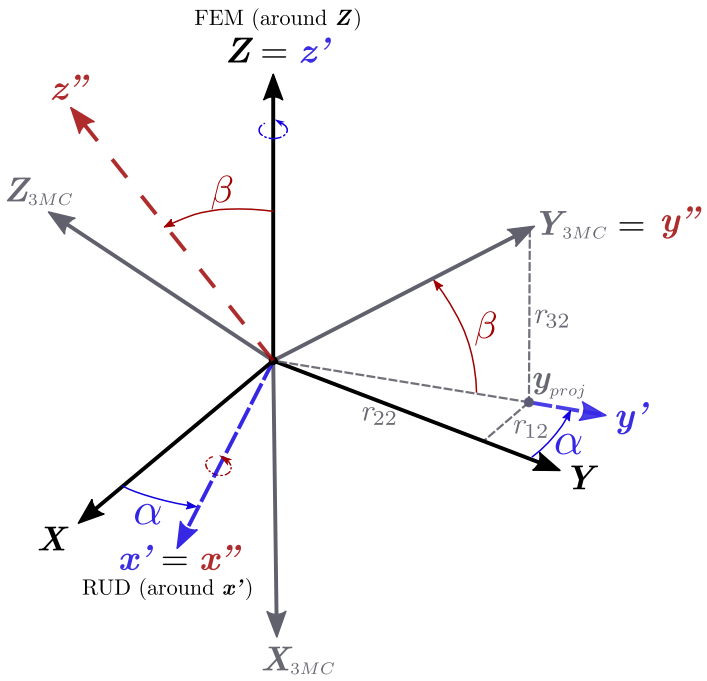

Figure 2.10: Schematic drawing visualising the flexion-extension angle, α, and the radial-ulnar deviation angle, β.

The coordinate system $\boldsymbol{x}' - \boldsymbol{y}' - \boldsymbol{z}'$ after rotation around $\boldsymbol{x}'$ is denoted using $\boldsymbol{x}'' - \boldsymbol{y}'' - \boldsymbol{z}''$ (Fig. 2.11a). For completeness of the calculation, the pronation-supination of the 3MC, denoted as γ, was also calculated. Since the pronation and supination of the wrist is defined as rotation around $\boldsymbol{Y}_{3MC}$, the rotated axis $\boldsymbol{x}''$ and $\boldsymbol{z}''$ must lie in the plane defined by $\boldsymbol{X}_{3MC}$ and $\boldsymbol{Z}_{3MC}$ (Fig. 2.11b). Hence γ can be easily found by calculating the angle included between $\boldsymbol{x}''$ and $\boldsymbol{X}_{3MC}$ (Eq. 2.4).

$$\boldsymbol{x}''^{\mathcal{R}_{XZ_{3MC}}} = \begin{bmatrix} \boldsymbol{X}_{3MC} & \boldsymbol{Z}_{3MC} \end{bmatrix}^T \boldsymbol{x}'' = \begin{bmatrix} r_{11} & r_{21} & r_{31} \\ r_{13} & r_{23} & r_{33} \end{bmatrix} \begin{bmatrix} \cos(\alpha) \\ \sin(\alpha) \\ 0 \end{bmatrix}$$

$$\gamma = \tan^{-1}\left(\frac{r_{13}\cos(\alpha) + r_{23}\sin(\alpha)}{r_{11}\cos(\alpha) + r_{21}\sin(\alpha)}\right) \tag{2.4}$$

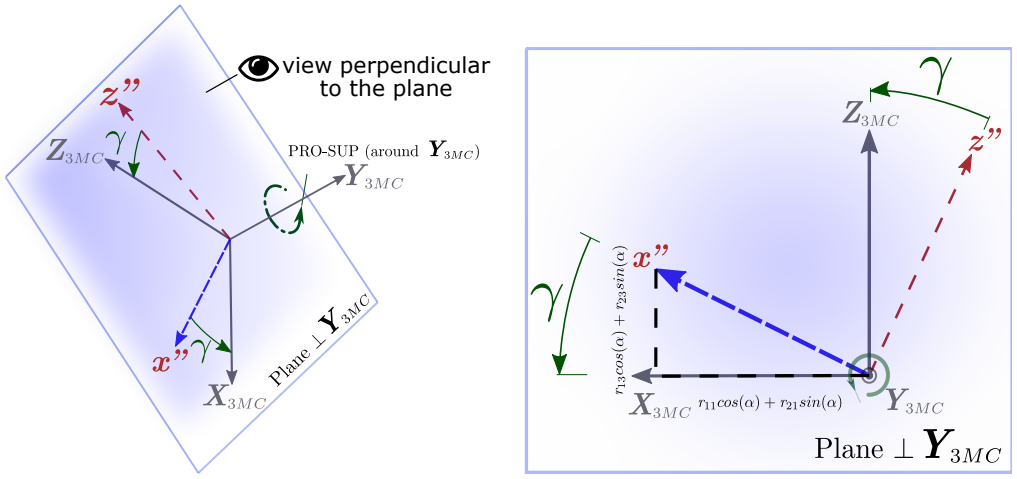

(a) Coordinate System after $\boldsymbol{x}'$ rotation

(b) Plane formed by $\boldsymbol{X}_{3MC}$ and $\boldsymbol{Z}_{3MC}$

Figure 2.11: Schematic drawing visualising the pronation-supination angle, γ.

2.2.2.2 Tendon Force Measurement System

Uniaxial Load Cell

Six light-weight, low-profile uniaxial tension load cells (UMM-K20; Dacell, Chung-Buk, Korea) were connected in series with the sleeve-trapped muscle tendons via custom-designed adapter blocks (Fig. 2.12), to provide real-time force measurements during the dynamic wrist simulations. To ensure the force measurements were not affected by the frictional losses in the pulleys, the load cells were placed closer to the cadaveric specimen and distal to the primary tendon guiding system.

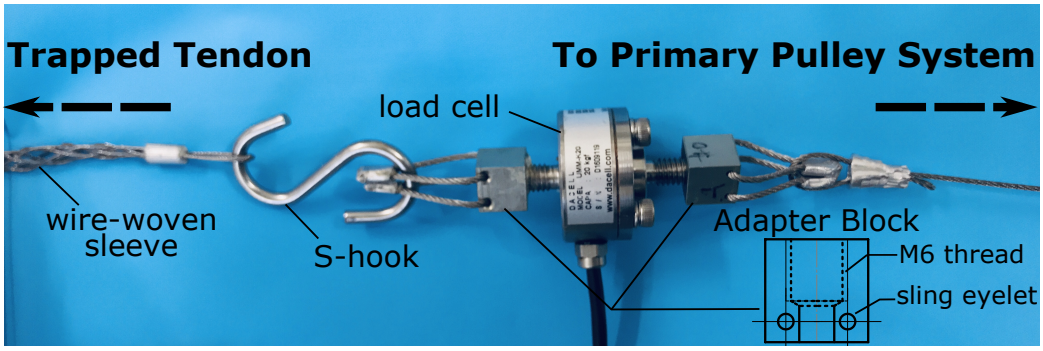

Figure 2.12: Photograph depicting the mechanical connection made between the trapped muscle tendon and the motor attachment, with the uniaxial load cell connected in the middle to facilitate force measurement

The load cell featured a Wheatstone bridge design and was capable of measuring the tension transmitted along its central axis. It had a force rating of 20 kg (196.13 N), which was sufficient when considering the maximum dynamic force in wrist prime movers ($\approx$ 100 N) (Buchanan et al., 1993). The calibration factor necessary for converting the voltage to force measurements was provided by the manufacturer for each load cell in two-point linear form. The typical non-linearity, non-repeatability and hysteresis of the load cell were on the order of 0.1% of its fullscale, ensuring the accuracy and reliability in the force measurements (Appendix A.2).

Analogue Data Acquisition

The load cells in groups of three were attached to two 4-channel bridge input modules (NI-9237; National Instruments, Texas, USA) via D-SUB terminal blocks (Fig. 2.13). These input modules provided excitation and signal conditioning necessary for the operation of the load cells. The four input channels on the module, each featured a 24-bit analogue-to-digital converter (ADC) resolution and a sampling rate up to 50kS/s (kilo samples per second), allowed accurate and high-speed voltage measurements to be taken from the attached load cells simultaneously. The resultant voltages were subsequently converted to force measurements according to the calibration factor of each load cell (Appendix A.3).

A cDAQ-9174 chassis (National Instruments, Texas, USA) was used as the "carrier" for these bridge input modules. It was capable of disciplining the attached modules such that they share the same timing engine with that of the chassis controller, allowing a synchronised force acquisition across the modules. The chassis also provided an interface to the host PC, allowing the measurement data to be transferred via USB. Custom LabVIEW VI programs were developed using the factory-supplied drivers (NI-DAQmx; National Instruments, Texas, USA) to control the acquisition of the analogue data.

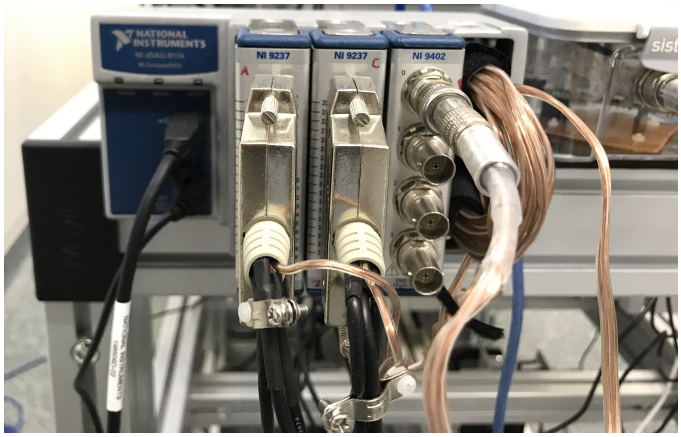

Figure 2.13: Photograph of the two bridge input modules, each connected with a group of three load cells, being hosted by the carrier chassis.

2.2.2.3 Motion Synthesis System

Stepper Motors

Stepper motors were chosen owing to their low-cost, ease of use, high reliability and excellent torque capability when operated at relatively low speeds. Additionally, as the motors were selected such that they could be suitable and reusable for other potential future applications, their power and torque rating might exceed the design requirement for the present study.

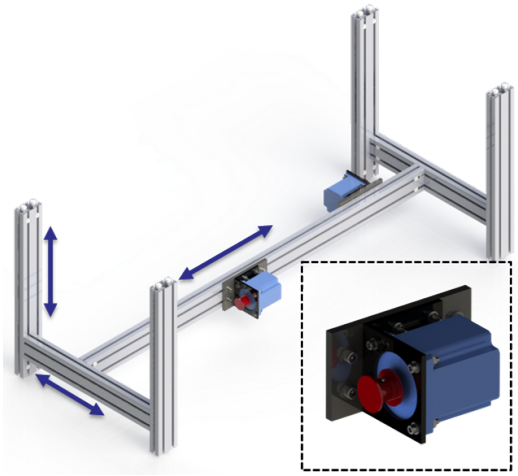

Figure 2.14: CAD model of the stepper motor and its adjustable mounting

Six stepper motor (HV342-01-FL; Parker Hannifin, Ohio, USA) were used to actuate the tendons of six wrist prime movers, simulating the muscle excursion and loading necessary for recreating physiologically meaningful dynamic motion on cadaveric wrist specimens. The stepper motors, in pairs of two, were mounted on opposite sides of the central beams of the actuator cell via adapter plates and T-slot nuts, allowing their position to be fine-tuned to align with the secondary pulley system (Fig. 2.14). The stepper motor required a working voltage of 120 VAC and drew an RMS current of 3.01 Amps. Each motor was capable of generating an approximately 3.2 Nm of continuous torque at a speed of 500 rpm and had a static holding torque up to 5 Nm. Technical details are provided in Appendix A.4.

In order to allow active tendon excursions to be simulated, a simple and cost-effective winder-like solution was employed to convert motor rotation into linear motion of the cables. Custom-machined aluminium spools were attached to the motor shafts by means of grub screws, allowing the cables, which began from the specimen cell and were subsequently regulated by the tendon guide system, to be reeled continuously. The cable was terminated using a small stamped eyelet, and a pan head M3 screw was used to pin the cable to the spool. Both screws were accommodated in the counterbored holes machined eccentrically on the lateral surface of the spool, preserving its geometric roundness and surface integrity, therefore reducing unwanted mechanical disturbances during operation. The spool was 20 mm thick and had an inner barrel diameter of 30 mm, which in turn translated into a cable displacement of 94.2 mm for a complete revolution of the motor shaft. Flanges with an outer diameter of 50 mm were added to the design to prevent the cables from being spun off the spool. In addition, the cable was also trimmed to an appropriate length, such that it could barely make one and a half complete turns around the spool, to reduce the chance of tangling.

Motion Controller and Motor Drives

An 8-axis motion controller (DMC-4183; Galil Motion Control, California, USA) was used to control the motors. The motion controller was connected to a hosting computer via 100BaseT Ethernet to establish high-speed communication. To facilitate real-time and on-line control of the motors, LabVIEW programs were written based on the GalilTools Communication Library (Galil Motion Control, California, USA) to programmatically generate command codes and facilitate data exchange with the motion controller, while the motion controller itself was configured to be listening and continuously responsive to the inbound instructions. However, in order to mitigate mechanical shock, abrupt transitions between diverging motion instructions were kept minimal on the software level through conservative motion planning. The inbuilt acceleration filtering function was also tuned to produce a smooth velocity profile with a negligible delay in response time.

For each motor, an E-AC drive (Parker Hannifin, Ohio, USA) was used to amplify the command pulses encoding step and direction instructions sent from the motion controller to the appropriate power level for driving the motor. The motor drives were configured to achieve a micro-stepping of 50,000 counts per revolution for the stepper motors, which translated into an open-loop position control resolution of approximately 0.0019 mm in linear cable reeling (Appendix A.5).

Power and Electrical System

Two 240 VAC, 50 Hz general power outlets (GPO) were used to meet the power requirement for the present 8-axis motion synthesis system. A single-phase transformer (SD7241; Southern Electronic Service, Victoria, Australia) was used as a step-down unit for each GPO, providing an output voltage of 120 VAC and a current of 14 Amps. E-AC motor drives, in groups of four, were then connected in parallel to each of these transformed power sources. A 24 VDC power supply (PROeco3-120W24V5A; Weidmller Interface, Detmold, Germany) was used to power the motion controller. Since it drew

power from one of the transformed GPOs, an electromagnetic interference (EMI) filter (Corcom 10VV1; TE Connectivity, Schaffhausen, Switzerland) was added to the circuit to suppress the conducted EMI emissions associated with rapid pulse generations in the motor drives. A safety relay system, along with a kill switch was constructed to power off the motor drives in case of emergency.

An electrical cabinet was constructed to provide a centralised housing for the motion controller, motor drives, power supplies and all other relevant electrical accessories, allowing the system to be self-contained and isolated from the test environment (Fig. 2.15). All components and their wirings were neatly arranged for ease of maintenance.

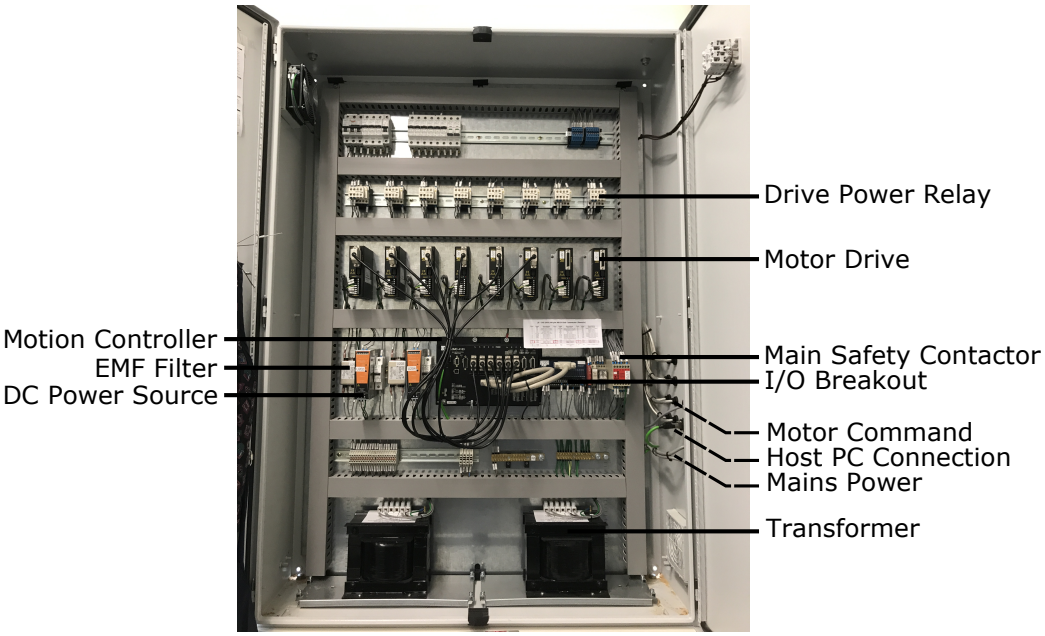

Figure 2.15: Photograph of the electrical cabinet used for powering and controlling the motors of the DWSA.

2.2.3 Motion Control Algorithm

A control algorithm was devised to allow user-prescribed trajectories to be dynamically tracked by the cadaveric plant through coordinated actuation of its tendons that emulates its physiology *in-vivo*. However, a direct mapping between the muscle forces and the joint position is not trivial to achieve, owing to the following reasons.

Unlike other practical control problems, where the plant or the process can be readily approximated utilising some analytical models to achieve optimal a system response, modelling the dynamic behaviour of cadaver wrists is mathematically challenging, let alone the anatomical variability presented in the population and the difficulty in estimating the model parameters. Moreover, unlike in a serial manipulator such as a robot arm where actuators are directly coupled to each of the linkage joints to provide decoupled elementary rotations, skeletal muscles that drive and regulate joint motions, do not exhibit such a deterministic and well-defined actuation capability. Isolated contractions of an individual muscle will typically result in a coupled joint moment, rendering a complex rotational behaviour. In the context of the wrist, a convenient example is the flexor carpi radialis (FCR) muscle, which is capable of generating a joint movement primarily in flexion but combined with a certain degree of radial deviation.

Just like other musculoskeletal structures of the human motor system, the wrist also exhibits the so-called neuro-muscular redundancy, where a voluntary motor task is performed with coordinated recruitment of muscles more than seemingly required. This process involves not only the simultaneous activation of muscle synergists that are assistive to the principle joint movement; but also co-contraction of the agonist-antagonist muscle pairs, which mechanically stiffens the joint to enhance stability and controllability (Baratta et al., 1988; Aagaard et al., 2000). However, from a purely biomechanical viewpoint, having the available musculotendinous actuators that exceed the actual joint DOFs ultimately renders mechanical indeterminacy, where a given joint motion is achievable by a multitude of possible muscle

force combinations.

In essence, these constraints put forward two major design challenges that the DWSA's motion control algorithm had to resolve before active physiological wrist motion could be recreated. Firstly, the algorithm had to work in the absence of a precise model that explains the convoluted dynamics of the biological plant. This also implies that the controller should show adequate tolerance for the anatomical variations among cadaveric specimens and possess robustness in handling plant uncertainties. Secondly, the control algorithm had to incorporate a means to efficiently address the redundancy problem to allow the resultant simulation to be physiologically representative.

To address the aforementioned problems, the overall architecture of the DWSA's control algorithm adopted a two-layer design (Fig. 2.16). Control over the global joint angle of the cadaver wrist was achieved indirectly through the inner force feedback loop, where the muscle loadings were adjusted continuously in accordance with the corrective actions required by the outer position loop. The position-force correspondence involved implicitly during this process was established by pairing two decentralised adaptive controllers (i.e. one for each DOF) with static optimisation, which is a commonly used method in the field of musculoskeletal modelling for estimating muscle forces. The controllers allowed accurate estimation of the joint torques corresponding to the corrective manoeuvre of the wrist specimen had to perform in order to achieve the desired position prescribed by the input trajectory. And thanks to the adaptation laws built into the controllers, the torque estimation was able to be carried out in the absence of a precise model describing the dynamics of the biological plant and solely based on its position feedback. These joint torques were then converted into six muscle forces by means of static optimisation, thus resolving the so-called neuro-muscular redundancy associated with the wrist in a physiologically meaningful manner. Finally, six proportional-integral-derivative (PID) controllers, each augmented with a feedforward module, were employed in the inner force feedback loop to control the muscle forces applied on the wrist specimen, through coordinated, motorised windings of the cables connecting its muscle tendons. Owing to this

nested architecture, the cadaver wrist would only follow a given movement trajectory when the applied muscle forces, which were the causal factors to this apparent motion, closely tracked the force setpoints given by the static optimisation process, thus recreating the dynamic muscle-activated movement of an *in-vivo* wrist.

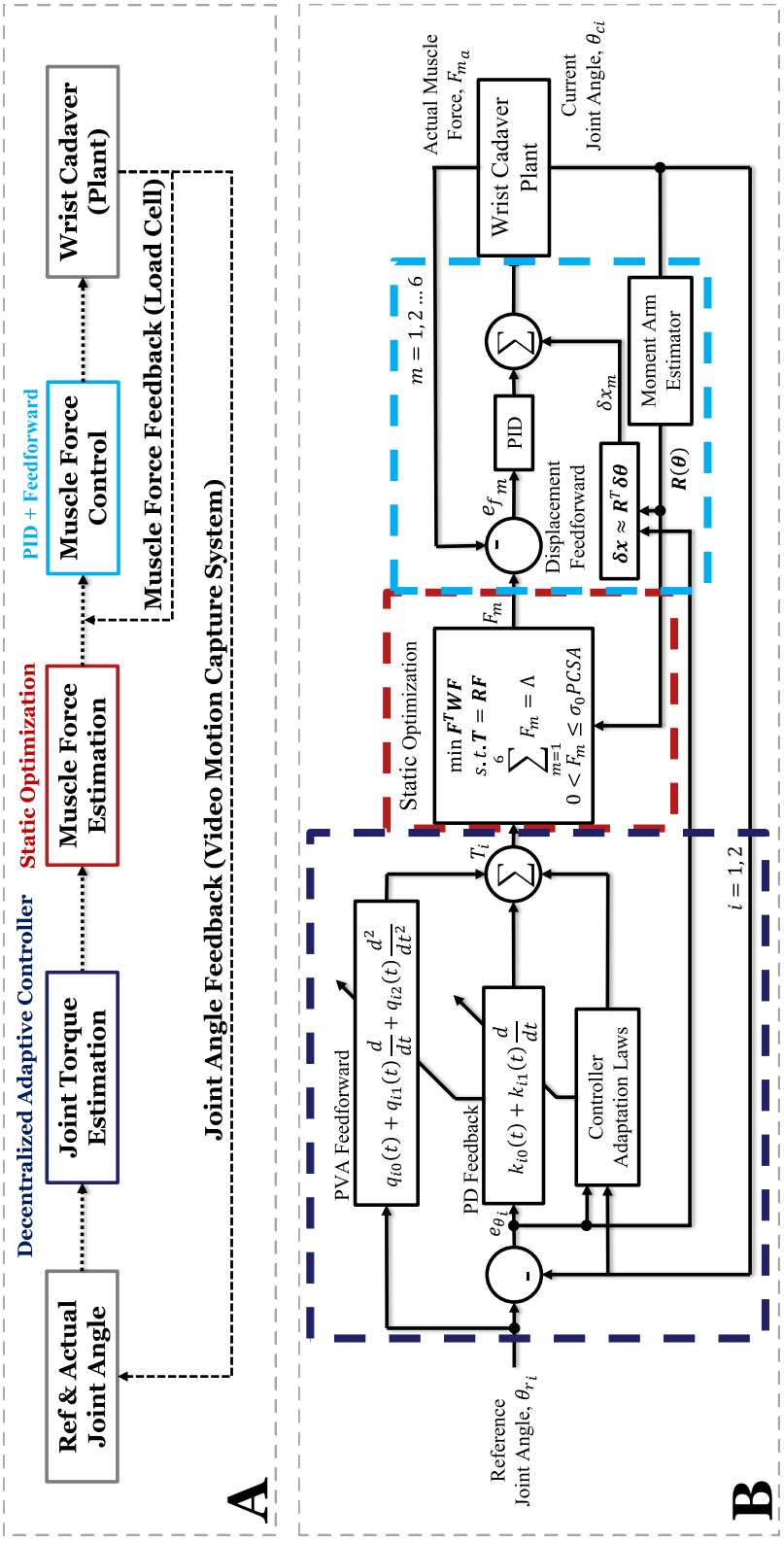

Figure 2.16: Schematic diagram of the control architecture and the function of various parts (**A**), and block diagram of the actual implementation (**B**), including the **decentralised adaptive controller** adopted from Seraji (1989) with modifications, **static optimisation process**, **force control of the muscles**.

Trajectory Planner

A simple piecewise trajectory was used for synthesising angular motion in the cadaveric wrist specimen (Eq. 2.5). Since the wrist can be considered as having two rotational DOFs, two separate trajectories, corresponding to the two joint mobilities, are therefore needed to produce realistic wrist movements in cadaveric specimens. Sinusoidal trajectories, similar to the ones used in previous studies (Tong, 1985; Werner et al., 1996; Erhart et al., 2012; Dimitris et al., 2015), were adopted for the trajectory planner of the DWSA. In the case where pure wrist FEM or RUD is desired, the trajectory that corresponds to the out-of-plane motion is set to zero to allow planar wrist motion of interest to be simulated in isolation. In addition, since the cadaver wrist is likely to assume an arbitrary initial posture, the trajectory planner was therefore designed to facilitate smooth transitional maneuvers to correctly "initialise" the wrist posture prior to the actual dynamic trial.

$$\theta_{ri}(t) = \begin{cases} \frac{\theta_{si}-\theta_{ci}}{2}\sin\left(\frac{2\pi}{\max\limits_{j\in(1,2)}(\theta_{sj}-\theta_{cj})}t-\frac{\pi}{2}\right)+\left(\frac{\theta_{si}+\theta_{ci}}{2}\right) & 0<t\leq t_{\text{trans}} \\ \theta_{si} & t_{\text{trans}}<t\leq t_{i\text{start}} \\ A_i\sin\left(\frac{2\pi}{P_i}(t-t_{i\text{start}})-\frac{\pi}{2}\right)+D_i & t>t_{i\text{start}} \end{cases} \tag{2.5}$$

where the piecewise function $\theta_i(t)$, $i=1,2$ is the reference joint angle trajectory prescribed for the ith DOF of the wrist. θ_{si} and θ_{ci} denotes the desired starting position of the dynamic experiment and the current position measured for the ith DOF of the wrist, respectively. A phase shift of $-\pi/2$ radians or one-quarter of a complete cycle to the right was included such that the motion would always start from the negative movement extremum smoothly with a zero initial velocity. A five-second idling period was included between the transitional period and the actual dynamic trial. The angular trajectories for the two wrist mobilities can be configured independently through A_i, P_i, D_i and $t_{i\text{start}}$, which controls their amplitude, period, vertical shift and their phase difference respectively. An example showing the trajectories used for a cadaver wrist to perform a complete sinusoidal cycle of planar FEM from an

initially flexed and radially deviated posture was illustrated below (Fig. 2.17).

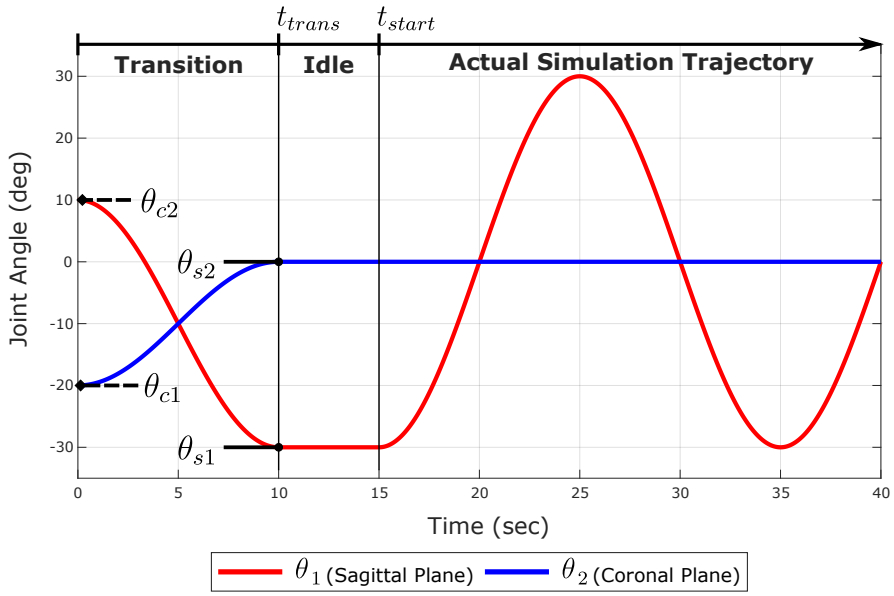

Figure 2.17: An example of the reference trajectories used in simulating wrist DTM in experimental setting

Joint Torque Estimation

Instead of solving for the inverse mapping from the prescribed joint motion trajectories to the necessary muscle forces, it is crucial to realise that the two quantities are related via the joint torque (Eq. 2.6, 2.7)

$$\boldsymbol{T} = \boldsymbol{M}(\boldsymbol{\theta})\ddot{\boldsymbol{\theta}} + \boldsymbol{C}(\boldsymbol{\theta}, \dot{\boldsymbol{\theta}}) + \boldsymbol{V}(\dot{\boldsymbol{\theta}}) + \boldsymbol{G}(\boldsymbol{\theta}) \tag{2.6}$$

$$\boldsymbol{T} = \boldsymbol{R}(\boldsymbol{\theta})\,\boldsymbol{F} \tag{2.7}$$

where $\boldsymbol{T}(t) \in \mathbb{R}^{2\times 1}$ is the vector representing the torques associated with the FEM and RUD of the wrist. $\boldsymbol{\theta}(t) = [\alpha, \beta]^T$ is the vector representing the angular position of the global wrist. In Eq. 2.6, $\boldsymbol{M}(\boldsymbol{\theta}) \in \mathbb{R}^{2\times 2}$ is the symmetric positive-definite inertia matrix of the wrist specimen. $\boldsymbol{C}(\boldsymbol{\theta}, \dot{\boldsymbol{\theta}})$, $\boldsymbol{V}(\dot{\boldsymbol{\theta}})$ and $\boldsymbol{G}(\boldsymbol{\theta})$ are all vectors of the same size, representing the torque

generated by Coriolis and the centrifugal force, friction, and gravity respectively. In Eq. 2.7, $\boldsymbol{R}(\boldsymbol{\theta}) \in \mathbb{R}^{2\times 6}$ is the moment arm matrix, with each of its columns corresponding to a prime mover muscle of the wrist, and the rows representing the muscles' leverage in each of the two DOFs of the joint mobility. $\boldsymbol{F}(t) \in \mathbb{R}^{6\times 1}$ is the collection of muscle forces that are responsible for generating the two joint torques.

The reason that Eq. 2.7 is presented in a "forward dynamics" manner is due to the fact that the inverse mapping of such a transformation cannot be uniquely obtained without additional constraints being provided to the system. Therefore, the difficulties in finding the overall mapping between the global wrist angle and the necessary muscle forces rise only at the stage when this indeterminate problem is encountered, whereas the joint torques still follow a one-to-one correspondence with the joint angles. However, the lack of prior knowledge on the model parameters, $\boldsymbol{M}$, $\boldsymbol{C}$, $\boldsymbol{V}$ and $\boldsymbol{G}$, that govern the cadaveric plant dynamics, prevents direct exploitation of this relation. In addition, the inertia matrix, $\boldsymbol{M}$, is generally non-diagonal, implying a complicated inertial cross-coupling between each DOF of the joint mobility.

These issues suggested the applicability of the decentralised adaptive control scheme (Eq. 2.8) developed in work published by Seraji (1989) and Colbaugh et al. (1990), which concerned the trajectory tracking problem for each individual joint in a robotic manipulator, possessing a coupled dynamics and unknown payload configuration.

$$T_i(t) = \underbrace{\sum_{j=0}^{1} k_{ij}(t) e_i^{(j)}(t)}_{\text{PV Feedback}} + \underbrace{\sum_{j=0}^{2} q_{ij}(t) \theta_{di}^{(j)}(t)}_{\text{PVA Feedforward}} + \underbrace{f_i(t)}_{\substack{\text{Auxiliary} \\ \text{signal}}} \tag{2.8}$$

where the superscript (j) denotes the jth order derivative with respect to time; θ_{di} is the desired joint position, and $e_i = \theta_{di} - \theta_i$ is the tracking error of the present joint DOF; T_i is the estimated torque for the ith DOF of the joint mobility, and is calculated based on the signals generated by a position-velocity (PV) feedback controller which is regulated by the adjustable gain

k_{ij}, and constantly takes the proportional-derivative (PD) action on the position error, a position-velocity-acceleration (PVA) feedforward controller that regulated by the adjustable gain q_{ij} and operates on the reference trajectory, and an adaptive auxiliary controller designed to compensate for disturbances attributed to the dynamic cross-coupling and model uncertainties of the plant. A set of adaption laws (Eq. 2.9, 2.10, and 2.11) were devised using a Lyapunov-stability-based Model Reference Adaptive Control (MRAC) technique to update the controller parameters such that position tracking is achieved asymptotically.

$$k_{ij}(t) = k_{ij}(0) + \alpha_{ij} \int_0^t r_i(t) e_i^{(j)}(t) dt + \beta_{ij} r_i(t) e_i^{(j)}(t) \tag{2.9}$$

$$q_{ij}(t) = q_{ij}(0) + \gamma_{ij} \int_0^t r_i(t) \theta_i^{(j)}(t) dt + \lambda_{ij} r_i(t) \theta_i^{(j)}(t) \tag{2.10}$$

$$f_i(t) = f_i(0) + \delta_{ij} \int_0^t r_i(t) dt + \rho_i r_i(t) \tag{2.11}$$

where $r_i = w_{pi} e_i(t) + w_{vi} \dot{e}_i(t)$ is the combined position and velocity error for the ith DOF of the joint mobility, weighted by w_{pi} and w_{vi} respectively. The $k_{ij}(0)$, $q_{ij}(0)$ and $f_i(0)$ are the initial values for the adjustable gains, while the α_{ij},γ_{ij},δ_{ij} and β_{ij}, λ_{ij}, and ρ_{ij} are the integral and proportional gains controlling the adaptation rates.

In the present control algorithm, two of the decentralised adaptive controller were implemented to independently estimate the joint torques associated with the two DOFs of the wrist in parallel. In order to allow digital implementation, the controllers were discretised: the time derivatives were calculated by analytically differentiating the polynomial fitted to a finite history of data, similar to a Savitsky-Golay filter; whereas the integrations were approximated by accumulating the trapezoidal sum computed between each control iteration.

Muscle Force Estimation

Owing to the redundancy within the system, where the number of unknown muscle forces exceeds the torque equations available, the inverse of Eq. 2.7, which is the mapping from the joint torques back to the relevant muscle forces, therefore, cannot be uniquely derived without having the solution space adequately constrained. Additionally, for the simulated active wrist motion to closely resemble that of the living subjects, these artificially imposed constraints should reflect the actual physiology of the wrist, including muscle synergism and agonist-antagonist co-contraction, as well as the solution process itself should also resemble the human motor control to a certain extent.

To this end, static optimisation, which has been extensively used in the field of musculoskeletal modelling for *in-vivo* muscle force estimations (Crowninshield and Brand, 1981; Anderson and Pandy, 2001; Delp et al., 2007), was incorporated into DWSA's control algorithm to model muscle co-activation. In essence, in addition to the constraint imposed by Eq. 2.7, where the muscle forces should be adequate to produce necessary joint torques, the static optimisation method solves for a neural solution in which the sum of the squared muscle activations is minimised using

$$\min \sum_{m=1}^{6} \left(a_m(t)\right)^2 \tag{2.12}$$

where the muscle activation, a_m, is related to the muscle stress by a proportionality constant, k, the stress of a muscle can be computed by simply dividing muscle force, F_m, by its physiological cross-sectional area (PCSA) given by

$$a_m = k\left(\frac{F_m}{PCSA_m}\right)$$

Owing to the lack of data on the electromyography (EMG) activation pattern of the wrist, co-contraction of agonistic-antagonistic muscle pairs was simulated by imposing a constant-sum constraint on the muscle forces during the overall optimisation process. This simple yet meaningful approach was

inspired by the glenohumeral joint stability constraint commonly imposed in the musculoskeletal modelling of the shoulder, where the requirement for the rotator cuff muscle co-activation was implicitly embedded via the enforcement of a 'concavity compression' boundary condition on the glenohumeral joint force (Favre et al., 2005; Wu et al., 2016). Therefore, instead of manually assigning the relative agonistic-antagonistic potential for each muscle, which can be challenging to identify due to its time-varying and task-specific nature, the level of muscle co-contraction and consequently the joint compression was modulated automatically by the optimisation process based on this constraint. Furthermore, since muscles can be viewed as tensile actuators whose force capacity is bounded by the maximum isometric muscle stress, additional constraint inequalities were considered for each of the prime mover muscles. Hence, the overall optimisation problem can be summarised as follows

$$\min \boldsymbol{F}^T \boldsymbol{W} \boldsymbol{F} \tag{2.13}$$

$$\text{s.t.} \quad \boldsymbol{T} = \boldsymbol{R}\boldsymbol{F} \qquad \sum_{m=1}^{6} F_m = \Lambda \qquad 0 < F_m \leq \sigma_0 PCSA_m$$

where $\boldsymbol{W} \in \mathbb{R}^{6\times6}$ is a diagonal matrix formed by the reciprocal of the squared PCSA of each muscle. The PCSAs used in constructing $\boldsymbol{W}$ was adopted from the anatomical research conducted by Loren and Lieber (1995); Loren et al. (1996); Holzbaur et al. (2007). Λ is the scalar constant-sum constrain of the muscle forces. A value of 150 N was chosen for Λ in an attempt to replicate the loading condition in line with previous *in-vitro* (Ruby et al., 1987), and *in-silico* (Horii et al., 1990; Majima et al., 2008) investigations. σ_0 is the maximum isometric muscle stress, an average value of 33 N/cm^2 for the upper-limb muscles was adopted from Garner and Pandy (2003).

However, in order to enforce the torque constraints, the moment arm matrix, $\boldsymbol{R}(\boldsymbol{\theta}) \in \mathbb{R}^{2\times6}$, which is not only specimen-specific but also dependent on the current position of the wrist, must be estimated with reasonable accuracy in every control iteration. At the onset of every experiment, a CT scan was conducted with the wrist specimen visually placed at a near-neutral position. Based on the volumetric data, the approximate positions

of the distal insertions of the six wrist prime mover muscles could be visually identified. Thanks to the flexor and extensor retinacula of the wrist, the proximal passage sites of the muscle tendons could be located relatively easily and assumed to be fixed with respect to the proximal segment (Fig. 2.18). Thus, for a modest deviation from the neutral position, the moment arms of a specific wrist muscle about the two DOFs of joint mobility could be estimated geometrically (Eq. 2.14).

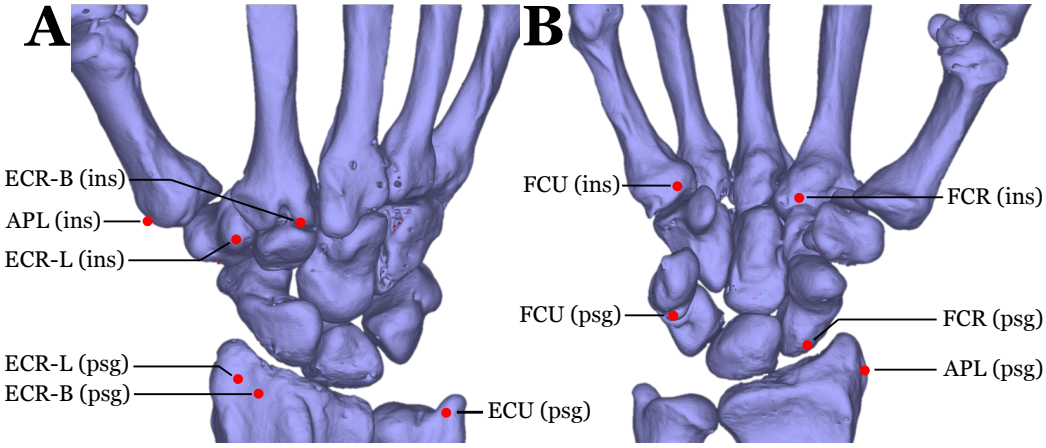

Figure 2.18: **(A)** dorsal view and **(B)** volar view, depicting the distal insertion (ins) and proximal passage (psg) sites identified for each muscle tendon.

$$\boldsymbol{r}_j^{\mathcal{R}_{\text{Capitate}'}} = \boldsymbol{P}_{j\ \text{passage}}^{\mathcal{R}'_{\text{Capitate}}} - [\text{Rot}\,Z(\alpha)\,\text{Rot}\,X(\beta)\,\text{Rot}\,Y(\gamma)]\boldsymbol{P}_{j_{\text{Insertion}}}^{\mathcal{R}_{\text{Capitate}'}}$$

$$R_{ij} = \frac{\left(\widehat{\boldsymbol{e}}_i \times \boldsymbol{r}_j^{\mathcal{R}_{\text{Capitate}'}}\right) \cdot \left(-\boldsymbol{P}_{\text{Cassage}}^{\mathcal{R}'_{\text{Capitate}}}\right)}{\left\|\widehat{\boldsymbol{e}}_i \times \boldsymbol{r}_j^{\mathcal{R}'_{\text{Capitate'}}}\right\|} \tag{2.14}$$

where for the jth muscle, $\boldsymbol{P}_{j\ \text{passage}}^{\mathcal{R}'_{\text{Capitate}}}$ is the location of its distal tendon insertion and is assumed to be moving with the distal segment; whereas $\boldsymbol{P}_{j_{\text{Insertion}}}^{\mathcal{R}_{\text{Capitate}'}}$ represents the exit point of its tendon passage within the retinacula, and is assumed to be fixed to the radius. These quantities are all measured in the coordinate system $\mathcal{R}_{\text{Capitate}'}$, whose axes are defined to be in parallel with

those of the radius ($\mathcal{R}_{Rad}$) in the wrist neutral position and its origin defined at the head of the capitate, which is commonly recognised as the approximate centre of wrist rotation (Youm et al., 1978). $RotZ(\alpha)$, $RotX(\beta)$ and $RotY(\gamma)$ are the elementary rotations around the Z-, X- and Y-axis by the current global wrist angle, α, β, γ respectively. R_{ij} is the element of the matrix $\boldsymbol{R}$, and represents the moment arm of the jth muscle about the ith joint axis. $\widehat{\boldsymbol{e}}_i$ is the unit vector representing the current direction of the ith joint axis, with the FEM occurs about the fixed Z-axis $\widehat{\boldsymbol{e}}_1 = [0, 0, 1]^T$, and a floating $\widehat{\boldsymbol{e}}_2 = RotZ\,(\alpha)\,[1, 0, 0]^T$ axis for wrist RUD.

The aforementioned optimisation for muscle force estimation took the form of a typical quadratic programming problem. Since the problem needed to be solved repeatedly in a time-critical manner to allow for the on-line control implementation, the interior-point optimiser developed by Wächter and Biegler (2006) was used, with custom interfacing LabVIEW VI programs to allow for easy integration into the main control software. In practice, since the muscle forces correspond to a smooth and continuous motion trajectory should not experience abrupt changes, the optimisation results from a successful solution process were used as the initial guess for the subsequent iteration to promote convergence. In case of an unrealistic solution or an optimisation timeout, the constraints were temporarily relaxed, and the muscle forces were extrapolated based on previous values using a second-order polynomial.

Muscle Force Control

Since the DWSA was constructed with a limited budget, stepper motors were used owing to their availability and lowered cost. Stepper motors, as positioning actuators, lack the ability to be operated in "torque mode". In other words, in contrast to a servo motor, the output torque and hence the force generated on the shaft of a stepper motor cannot be easily manipulated, which resulted in additional design complexities in applications where a direct control over forces is preferred.

Nonetheless, based on Hook's law, the elastic behaviour of the plant can be potentially exploited to achieve a similar force control outcome solely with the displacement provided by stepper motors. Consider a simple system consists of an extension spring rigidly fixed at one end and being scratched at the other by means of motorised winding (Fig. 2.19a). A force feedback loop with a proportional-integral-derivative (PID) controller (Eq. 2.15) operated on motor shaft rotations as the manipulated variable will be sufficient to achieve and maintain a specific tensile force setpoint within the system.

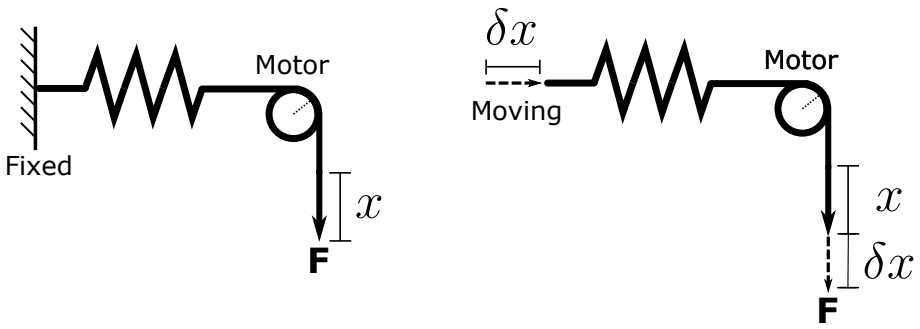

(a) spring with a fixed end (b) spring with one end moving

Figure 2.19: Schematic drawing of the force control problem, illustrating (a) displacement of x required to generate force F, and (b) the same amount of force can be achieved if the additional spring movement δx is compensated.

$$u(t) = K_p e(t) + K_i \int e(t)dt + K_d \frac{d}{dt} e(t) \tag{2.15}$$

Separate to the parameters of the torque estimator, tuning of the PID controller was performed in isolation and *in-situ* for each of the muscle tendons, at the onset of each motion simulation, with the cadaveric wrist specimen securely mounted to the DWSA. Each of the muscle tendons was pre-loaded to a preset value of 7 N, while the wrist being manually held stationary at a near-neutral position. The tunning process followed the commonly-adopted approach developed by Ziegler and Nichols (1993).

However, the simplified system does not accurately reflect the muscle force control problem of DWSA. When the cadaver wrist is in motion, the muscle tendons, modelled as springs, will potentially glide with the hand owing to their distal insertions and therefore can no longer be assumed as stationary (Fig. 2.19b). Movement of the spring itself imposes a strong disturbance to the PID controller and must be adequately accounted for, in order to achieve the desired force setpoint. These displacements can be thought of as the excursions of the muscle-tendon units necessary to meet the kinematic requirement for achieving a particular wrist posture as if the tendons themselves are infinitely stiff.

Therefore, the tendon displacement necessary to achieve a specific force setpoint can be approximated by combining these "movement-permitting" tendon excursions with the unknown elastic "starching" of the tendon itself. A conventional PID controller was used similar to the stationary spring-winding example to handle the latter uncertainty in a closed-loop. Whereas the former was estimated based on the relationship shown in Eq. 2.16 and was used as feedforward instructions to augment the control signals given by the PID controller.

$$\boldsymbol{\delta x} \approx \boldsymbol{R}(\boldsymbol{\theta})^T \boldsymbol{\delta \theta} \tag{2.16}$$

where $\boldsymbol{\delta x} \in \mathbb{R}^{6\times 1}$ denotes the excursions of the six wrist prime mover muscles as if they were rigid. $\boldsymbol{\delta \theta} \in \mathbb{R}^{2\times 1}$ represents a small change in the two angular positions of the cadaver wrist, and $\boldsymbol{R}(\boldsymbol{\theta})^T \in \mathbb{R}^{6\times 2}$ is the transpose of the moment arm matrix.

2.2.4 Software Implementation

Custom LabVIEW VI subroutines were written to interface various electromechanical systems comprising the DWSA. Four self-contained modules, including a measurement module, a motion control module, a graphical user interface (GUI) module and a communication module for the biplane fluoroscopy system, were developed based on these subroutines to fulfil different functional requirements of the DWSA. A top-level VI was constructed to allow integration and coordinated invocation of these modules (Fig. 2.20). With the GUI module handling the data visualisation and operator interactions, the front panel of the top-level VI (Fig. 2.21) served as the main control console for the DWSA, allowing a more intuitive and streamlined workflow in dynamic trials.

The measurement module facilitated real-time measurement of both the global wrist angle and the muscle forces, based on subroutines described previously. These measurements were continuously provided to the motion control module running in parallel. This module was designed to possess two operational states. When the system is in idle state, the motion control module allows the operator to adjust the movement trajectories and the control parameters to be used in the upcoming trials. However, when active wrist simulation is desired, the core of this module, which was devised based on the algorithm described in Section 2.2.3 for converting the desired wrist movements into the appropriate instructions for the motors, is set in motion. Safety measures were also programmed into the motion control module to prevent damage to both the DWSA as well as the wrist specimen currently being tested. The GUI module was developed to facilitate the interaction between the DWSA and the operator: Depending on the user action, the GUI module will invoke relevant subroutines to fulfil the functionality requirement. System status, such as the current wrist position, the applied muscle forces and the control errors, was visualised to allow easy and intuitive operation of the DWSA. The communication module was devised utilising the User Datagram Protocol (UDP) to allow DWSA's data acquisition process to be triggered externally by the biplane fluoroscopy system. In addition,

in order to allow the timestamps of the acquired radiographs to be captured under the DWSA's system clock, a digital input subroutine was also incorporated into the communication module. This process will be explained in detail later.

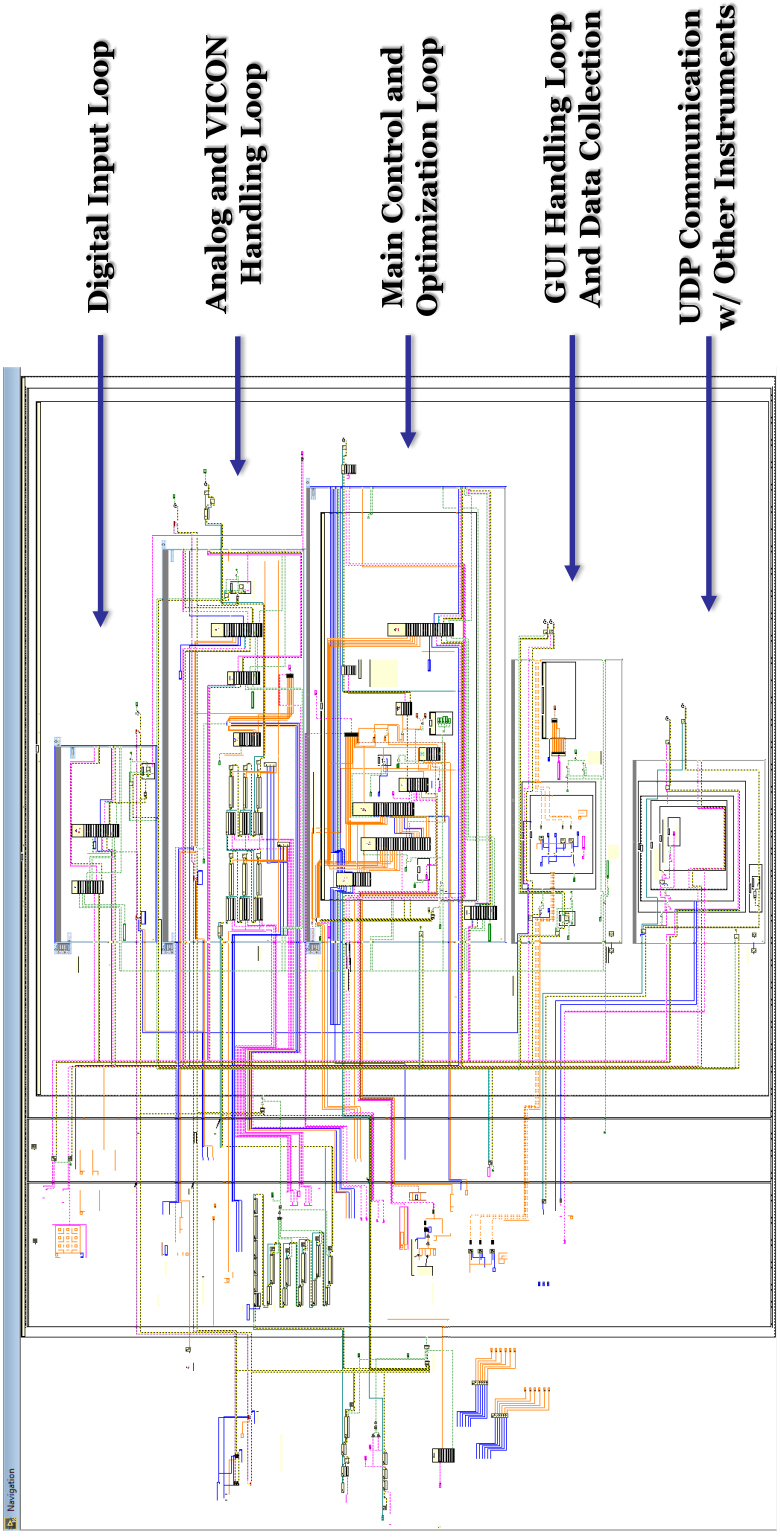

Figure 2.20: LabVIEW block diagram of DWSA's main control VI, showing different modules for fulfilling various functionalities requirements

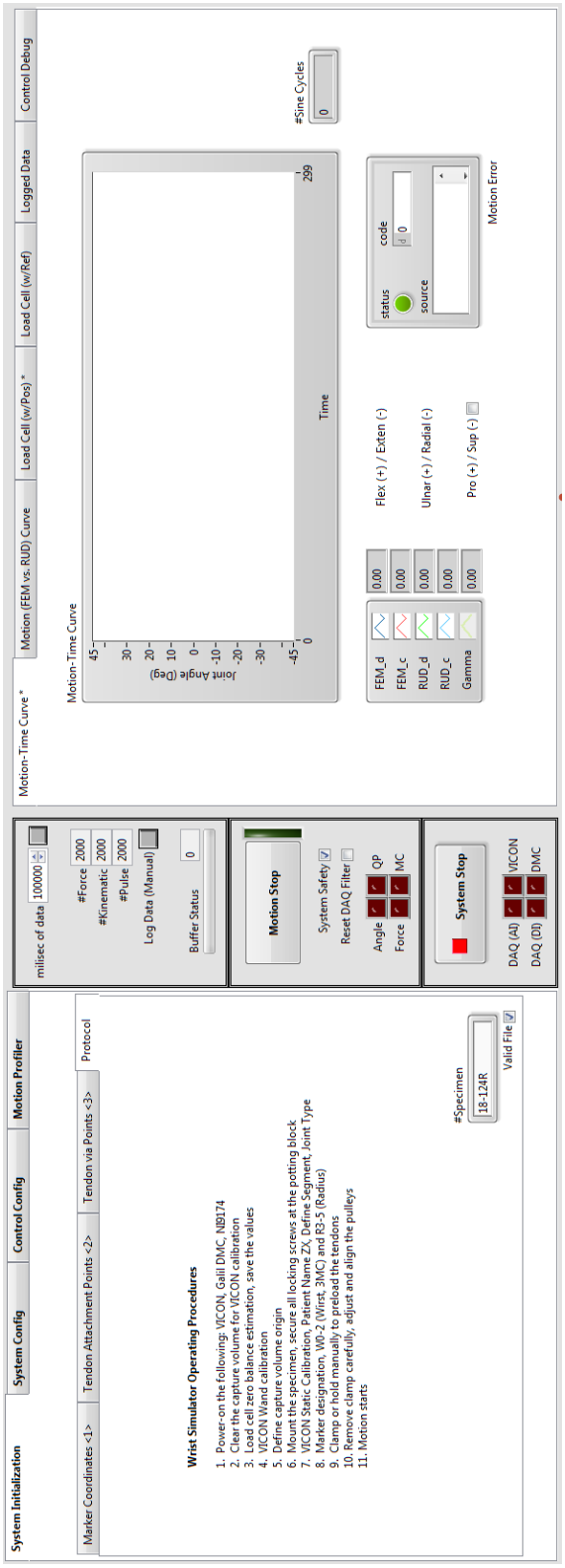

Figure 2.21: Front panel GUI of the DWSA's LabVIEW control console

2.3 Subsidiary Measurement Systems

To facilitate the biomechanical analysis of the simulated wrist motion, a set of subsidiary measurement systems were also integrated into the CWTP. This included a custom-built X-ray fluoroscopy system, intended for the accurate measurement and quantification of the intricate carpal bone movement, as well as an I-scan electronic pressure system for evaluating the radiocarpal intra-articular pressure in real-time.

2.3.1 Biplane X-ray Fluoroscopy System

Conventional methods such as video-based motion capturing or sensor technologies that depend on electromagnetic tracking or sonic pulsation have the inevitable need to use sizeable transducers attached to the rigid body whose motion is to be studied. This is not ideal, especially for the tightly arranged carpal bones, as a stem-like structure that projects out from the carpus will be required to achieve a stable mounting (Berger et al., 1982b; El-Shennawy et al., 2001; Salvà-Coll et al., 2011). However, concerns have been raised by several researchers as these structures are likely to disrupt the physiological carpal motion, not only because of the apparent issue of the mechanical impingement with the surrounding bones, ligaments and tendons but also because of their "moment effect" by acting like small cantilevers (Kobayashi et al., 1997a).

Recently, given its *in-vivo* applicability, the so-called 4D CT (the 4th dimension being the time) has gained increasing popularity in the field of wrist biomechanics studies (Shores et al., 2013; Zhao et al., 2015; Mat Jais and Tay, 2017b). However, due to its limited temporal resolution to date and the strict size constraint of the scanning object, it was considered unsuitable for the present study. On the other hand, biplane X-ray fluoroscopy, along with Röentgen stereo-photogrammetry analysis (RSA), have been proven to be a versatile and reliable means to quantify the kinematics of the knee (Guan et al., 2016, 2017), the ankle (Ito et al., 2015; Wang et al., 2015a),

the wrist (de Lange et al., 1985; Smith et al., 1989; Kobayashi et al., 1997a), and has even seen numerous applications in veterinary research (Tashman and Anderst, 2003; Baier and Gatesy, 2013). To this end, a similar biplane X-ray fluoroscopy system was constructed for accurate quantification of the complex carpal bone motion.

2.3.1.1 Hardware Setup

C-arm Fluoroscopy Units

The biplane fluoroscopy system of the CWTP was developed based on two clinical C-arm X-ray fluoroscopy units. A full-size C-arm unit (OEC Flex-iView 8800; GE Healthcare, Wisconsin, USA) and a mini C-arm unit (Fluoroscan Insight II; Hologic, Massachusetts, USA) was used owing to their availability and lowered cost (see Appendix A.7 for detailed specifications).

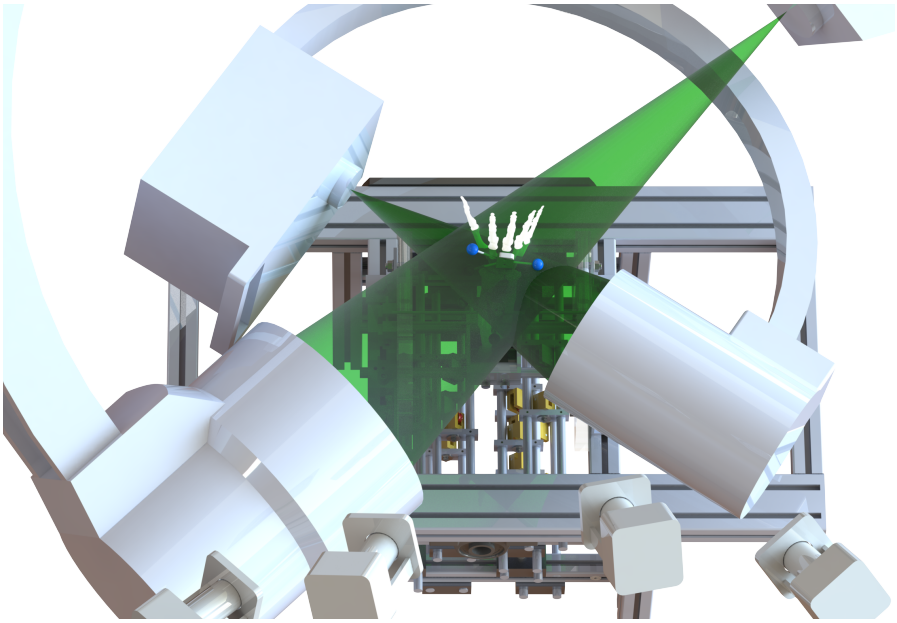

Figure 2.22: Beam configuration of the two C-arm X-ray fluoroscopy units

The two fluoroscopy units were positioned on opposite sides of the DWSA, with their movable C-arms oriented to surround the periphery of the cadaver wrist, forming an inter-beam angle of approximately 72°

(Fig. 2.22). This configuration allowed obstruction-free biplanar radiographs of the wrist specimen to be acquired, while minimised the chance of occluding the retro-reflective markers used for measuring global wrist position by DWSA's video motion capture system. In addition, the approximate beam intersection formed by the two C-arm fluoroscopy units (the capture volume) was carefully configured such that it was centred around the carpus of the cadaveric specimen, encapsulating a region spanning from the distal radius to the base of the metacarpals (Fig. 2.23).

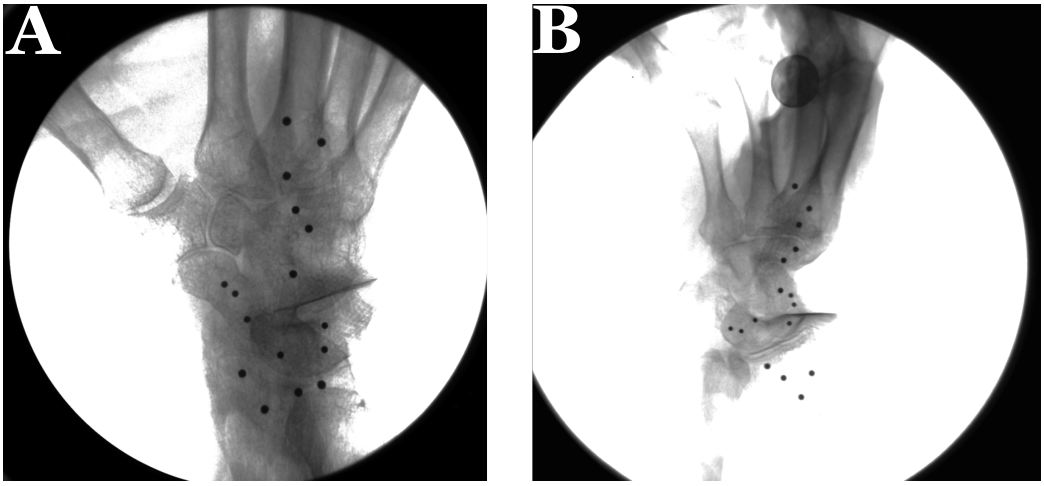

Figure 2.23: An example of the biplanar radiographs taken by **(A)** the mini and **(B)** full-size C-arm units, the radio-opaque markers implanted into the carpal bones can be clearly seen

Camera Addon

In order to facilitate accurate reconstruction of the carpal kinematics via RSA, biplanar radiographs must be acquired from the two C-arm fluoroscopy units in a synchronous fashion. However, this is very difficult to achieve with the native in-built electronics of the two fluoroscopy units intended for clinical use. Nonetheless, the working principle of such a machine relied on fluorescence of the input phosphor of the X-ray image intensifier (XRII), virtually converts the remanent X-ray radiations after penetrating the object being examined into visible light (Wang and Blackburn, 2000).

These projections are then amplified to a suitable intensity and displayed on the output phosphor in real-time. A video camera is often fitted to the image intensifier to facilitate the final analogue-to-digital conversion, thus electronically generating the resultant radiographs. Therefore, the last step in the above-described XRII conversion chain can be exploited to facilitate the simultaneous acquisition of radiographs if the video camera themselves are synchronised (Brainerd et al., 2010; Guan et al., 2016).

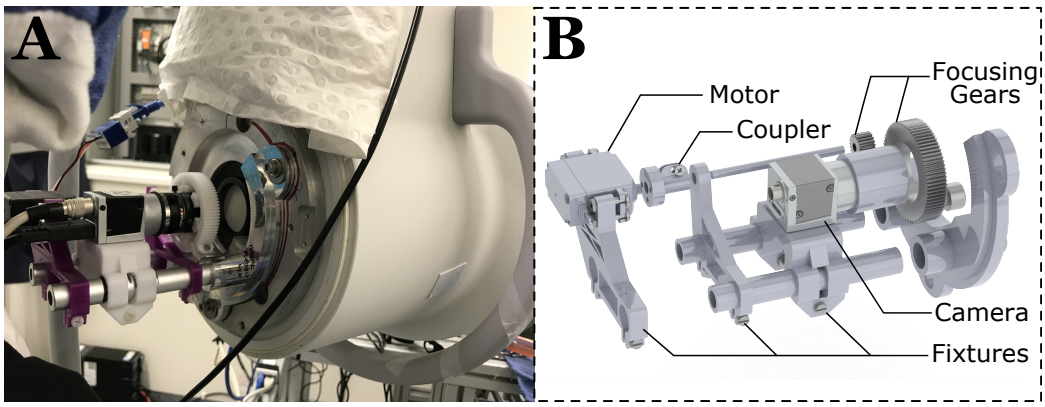

Figure 2.24: **(A)** Photograph of the camera assembly being mounted at the back of the XRII **(B)** Exploded CAD model of the camera assembly

Industrial machine vision cameras outfitted with a global shutter CMOS image sensor were chosen based on their suitability, particularly in capturing moving objects, availability and lowered cost. Two monochrome USB 3.0 machine vision cameras (acA1920-150um, acA1300-200um; Basler, Ahrensburg, Germany) were employed to replace the in-built cameras of the full-size and mini C-arm fluoroscopy units, respectively, acquiring images directly from their XRIIs. The cameras were chosen with differences in their resolutions and sensor geometries to better accommodate the size inconsistency in the XRIIs of the two C-arm units. The output phosphors measured approximately 45 mm and 30 mm in diameter for the XRIIs of the full-size and mini C-arm units respectively. In order to accurately capture the projections visible on these tiny output phosphors in a very limited distance available at the back of the XRIIs, ultra-low distortion close-up lenses (M1224-MPW2 and M2514-MP2; Computar, Tokyo, Japan) were employed and augmented

with spacer rings of carefully chosen dimensions. Miniature servo motors (LD-1501MG; LOBOT, Guangdong, China) were installed to be used in conjunction with the 3D printed lens gearings, allowing the camera focus to be fine-tuned remotely and safely when the fluoroscopy units were in operation. Aluminium adapter plates were then custom-machined to mount the whole assembly onto the back of the XRIIs of the C-arm fluoroscopy units (Fig. 2.24). Detailed technical specifications of the machine vision cameras and the lenses used are provided in Appendix A.8 and A.9, respectively.

2.3.1.2 Software and Control System

Camera Synchronisation

The two Basler cameras possess a 6-pin general-purpose input/output (GPIO) port that allows the exchange of digital signals with other devices. One of the GPIO lines was set to be operated as an input, allowing a common pulse train to be injected as the 'Frame Start Trigger' signal for the two cameras to trigger their frame-wise exposure simultaneously, therefore facilitating the synchronous acquisition of the biplanar radiographs. However, such a process needed to be appropriately timed, as the camera is rendered temporarily irresponsive to this externally supplied 'Frame Start Trigger' signals whenever there is an ongoing event of sensor readout (Fig. 2.25). The internally generated 'Frame Trigger Wait' signal, on the other hand, is indicative of the camera's availability and will be reset to digital high as soon as the camera is ready to be triggered again for the next acquisition cycle. Therefore, in order to avoid potential over triggering of the cameras, the internal 'Frame Trigger Wait' signal was exported and continuously monitored to ensure the proper timing of the externally generated 'Frame Start' trigger signals and consequently the synchronicity of the image acquisition process.

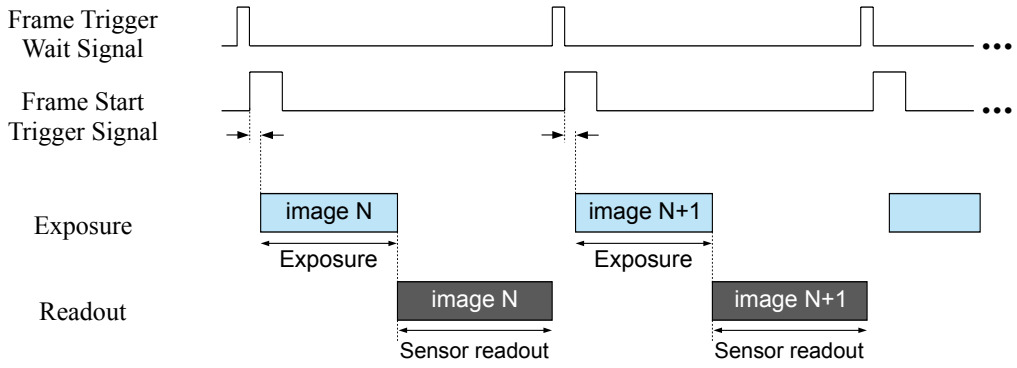

Figure 2.25: Timing chart of the image acquisition process

In the present setup, the frame-wise exposure on both cameras was set to be triggered by a rising edge. A USB development board (Teensy 3.6;

PJRC, Oregon, USA) was used to generate the digital pulses (Fig. 2.26), which effectively acted as a series of 'Frame Start Trigger' signals for the two cameras, through one of its digital input/output (I/O) pins. The 'Frame Trigger Wait' signals of the two cameras were also to fed the board to pace the pulse generation accordingly. A custom LabVIEW VI was developed to communicate with the development board, controlling the pulse generation process. The VI also allowed the characteristics of the pulse train, such as the frequency, pulse width and duration, to be readily adjusted by the operator. To allow the RSA results of the carpal kinematics to be synchronised with

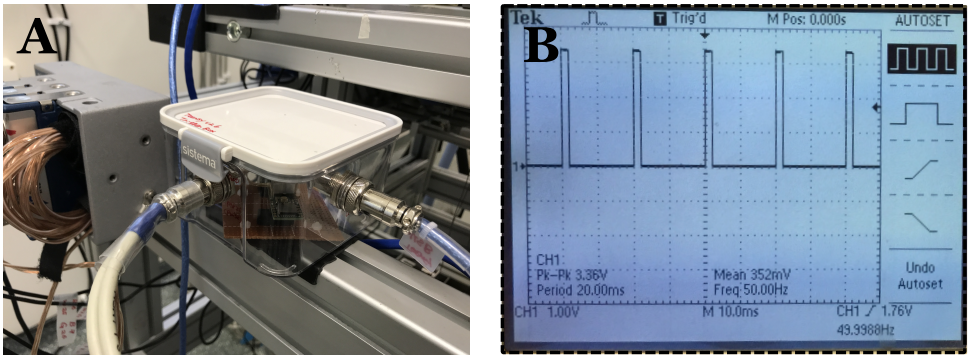

Figure 2.26: **(A)** USB development board used for synchronising the two cameras and **(B)** an example of the pulse signal generated by the board.

the measurements logged by the DWSA, such as the muscle forces and global wrist angles. It was, therefore, necessary to capture the timestamps of the acquired biplanar radiographs under the same system clock that governs the DWSA. As mentioned previously in Section 2.2.4, this was achieved using a digital I/O module (NI-9402; National Instruments, Texas, USA) interfaced with the same chassis carrying the bridge input modules for DWSA's load cells. A stream of the externally generated 'Frame Start Trigger' pulses was fed simultaneously in the digital I/O module to be recorded with a sampling frequency approximately ten times of the designated frame rate. Since a rising edge indicated an event of camera exposure, the timestamp for each frame of the acquired biplanar radiographs was therefore estimated based on the instant corresponds to such a digital transition in the recorded pules train.

X-ray Exposure Control

The two C-arm fluoroscopy units need to be activated in advance of the image acquisition sequence of the retrofitted cameras to allow the desired biplanar radiographs to be taken. In order to avoid compromising the electronic integrity of the C-arm fluoroscopy units, the modifications were limited to their foot-operated exposure switches. Relevant leads were extended to be operated by a 2-channel optically-isolated relay module (SRD05VDCSLC; Songle Relay, Zhejiang, China). Similarly, a USB development board (Arduino Nano; Arduino, Ivrea, Italy) was employed to work in concert with custom LabVIEW VI to facilitate automation in controlling the X-ray exposure. A custom-built control console (Fig. 2.27) was constructed with additional features and safety measures to allow an easy and intuitive operation of the modified biplane fluoroscopy system.

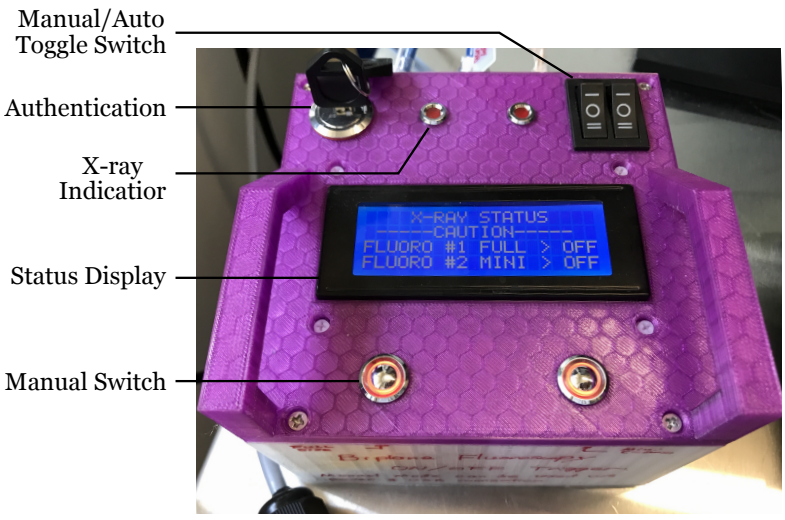

Figure 2.27: Custom X-ray Exposure control console

Image Acquisition

Since the machine vision cameras used in the present study lack non-volatile memory, the acquired image needs to be transferred back to the host PC immediately to prevent potential data losses caused by overrun of the cam-

era's buffer. Therefore, given the time-critical nature of such a processing demand, the sampling rate of the present system must be specified within the hardware limit imposed by the interface bandwidth and the available computational power. Using the theoretical throughput of 400 MB/s for the USB 3.0 interface (Mroczek, 2015), and assuming the biplanar radiographs are acquired in 8-bit monochrome with a resolution of two megapixels, a frame rate up to 100 FPS can be achieved on both cameras. Given the amount of inbound data, an image acquisition LabVIEW VI was developed to be operated on a dedicated PC (Intel i7-4770 quad-core CPU, 16 GB RAM), separated from the one controlling the DWSA, for the process of acquiring and logging of the biplanar radiographs. In essence, this VI was comprised of an image grabber and a data logging subroutine running in parallel. As the host PC is entirely oblivious to the 'Frame Start' trigger signals, the image grabber is set to continually pull the latest available frame of data from the camera buffer and transfer it into a first-in-first-out (FIFO) buffer. In order to prevent data losses, the highest processing priority was given to this process in the software implementation. On the other hand, the data logger regularly monitors the buffer to write any available frames to the hard drive. A solid-state drive (SSD) (Sandisk Ultra 3D; Western Digital, California, USA) with a nominal sequential write speed up to 530 MB/s was used to improve the data logging process.

A top-level VI was developed to consolidate various components of the present biplane X-ray fluoroscopy system through the automated invocation of the corresponding control subroutines. The front panel of the top-level VI (Fig. 2.28) was partitioned for an initiative and streamlined operation. Specifications for the pulse train as well as the file path were gathered with their validity verified before proceeding to the next step. Prior to the actual imaging process, the relay system responsible for activating the X-ray exposure is put on standby, with the image acquisition VI running in the background, waiting for images to be transferred for logging. A keystroke was programmed to initiate the X-ray exposure and the generation of the pulse train, consequently, setting the entire imaging and data acquisition process

in motion. Furthermore, the key that triggers this event was configured to be identical with the keyboard shortcut for initiation of the logging process on the pressure measurement system of the CWTP, achieving a concurrent and approximately synchronised data acquisition between the two different measurement systems.

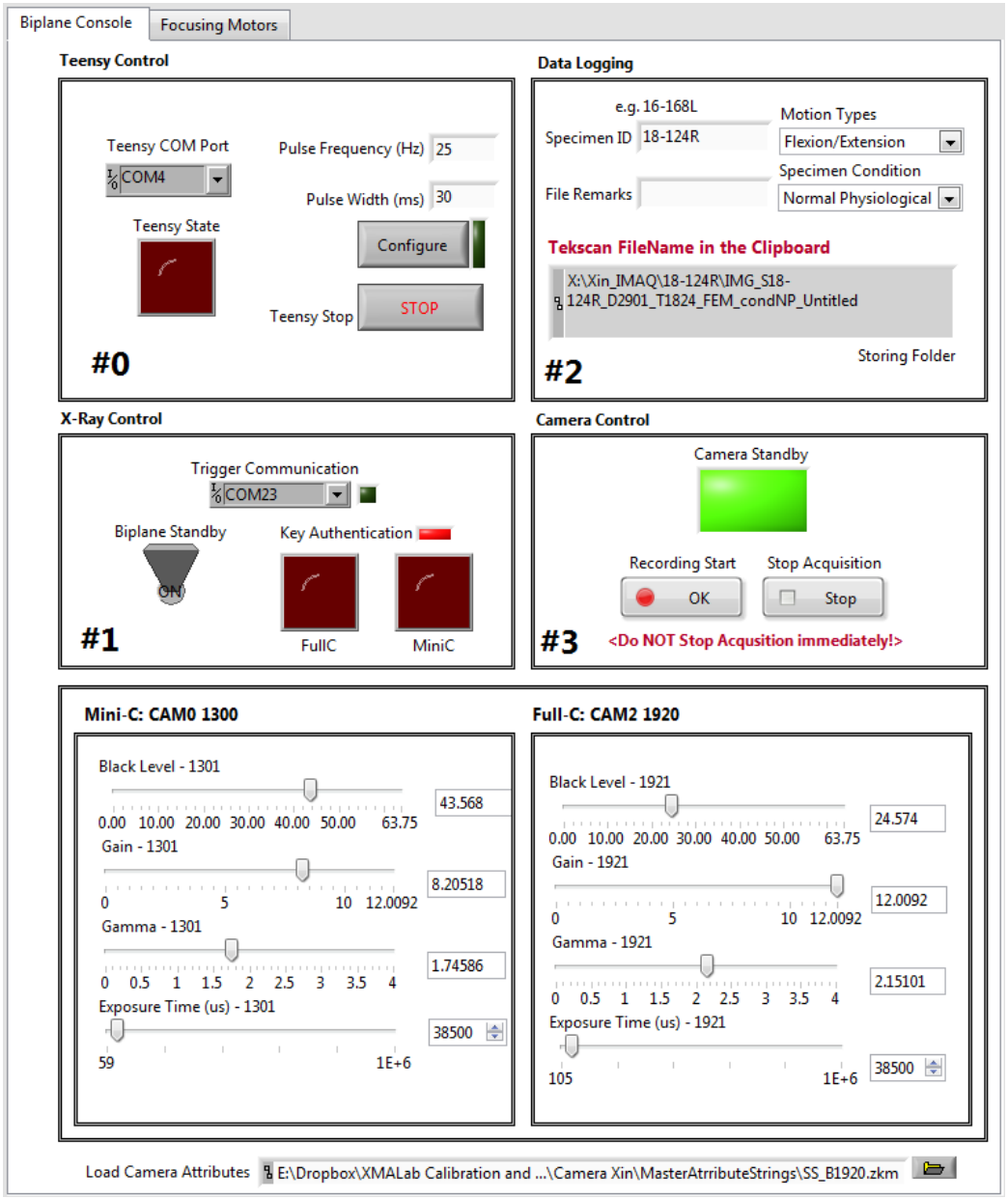

Figure 2.28: Front panel of the top-level LabVIEW VI

2.3.2 Marker-Based Kinematic Analysis

In the present study, marker-based Röentgen stereo-photogrammetry analysis was employed to obtain accurate measurements of the carpal kinematics. In contrast to morphology-based (marker-less) methods, such as scientific rotoscoping, marker-based RSA was chosen owing to its higher throughput and better measurement precision (You et al., 2001; Guan et al., 2016). In addition, the model accuracy, as well as the image quality, can have a more significant impact on the kinematics obtained through morphology-based motion analysis. Since the modification of the present biplane X-ray fluoroscopy system was implemented with inexpensive optical components, the image quality of the recorded radiographs was sometimes less than ideal, thus making the marker-based RSA a more appropriate choice for studying the carpal kinematics.

In essence, radio-opaque markers in clusters of three were surgically implanted into the bones of interest and held in place with droplets of cyanoacrylate adhesive. A CT scan of the specimen was immediately administrated to gain information on the marker placement within each bone. During dynamic motion, biplanar radiographs were recorded to allow three-dimensional coordinates of the bone markers to be reconstructed using RSA. Based on these measurements, the so-called pose estimation was conducted for the bones to derive their 6-DOF kinematics, via appropriate registration techniques.

An open-source software, XMALab (`xromm.org/xmalab`), developed by Knorlein et al. (2016), was employed to facilitate the marker-based RSA of the carpal bone kinematics using the acquired biplanar radiographs. The GUI of this software was structured into three distinct and self-contained layers or 'workspaces', in accordance with the three major stages in the workflow of the marker-based RSA, including the distortion correction of the fluoroscopic images, photogrammetric camera calibration, and marker tracking. Relevant visual feedback is also provided in the workspace for each stage to allow a well-informed and transparent RSA measurement process.

Distortion Correction

Images obtained through fluoroscopic radiography suffer complex distortion patterns introduced primarily by the XRII (Wang and Blackburn, 2000). Such distortion must be effectively corrected for the recorded biplanar radiographs before they can be used in further analysis. In order to aid the computation of the corrective transformations for the biplanar radiographs, two mild-steel sheets each perforated with appropriately sized holes in a hexagonal pattern (Perforated Pattern 218, 208; Arrow Metal, New South Wales, Australia) were used. These perforated sheets were clamped in between two thick pieces of Perspex glasses to prevent deformation such as warping, which could potentially compromise the calculation. Biplanar radiographs were then taken with the sheets mounted immediately next to the XRIIs of the C-arm fluoroscopy machines (Fig. 2.29).

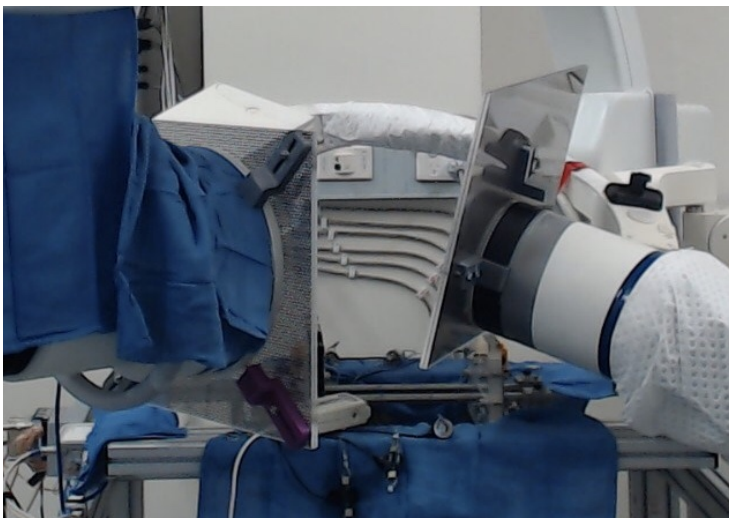

Figure 2.29: Photograph showing distortion correction grids being mounted next to the XRIIs of the full-size and mini C-arm fluoroscopy units

Using the Undistortion workspace in XMALabs, centroids of the perforated holes were determined on each of the resultant radiographs. Based on the correspondence between the present detected locations (distorted) of the centroids and the nominal (undistorted) hexagonal pattern of perforation, the corrective image transformation was computed by XMALab using the

local weighted mean registration (Goshtasby, 1988). The error associated with this step was typically on the order of 0.2 pixels for the present setup, and XMALab automatically undistort all imported radiographs using the obtained transformations from this point onwards.

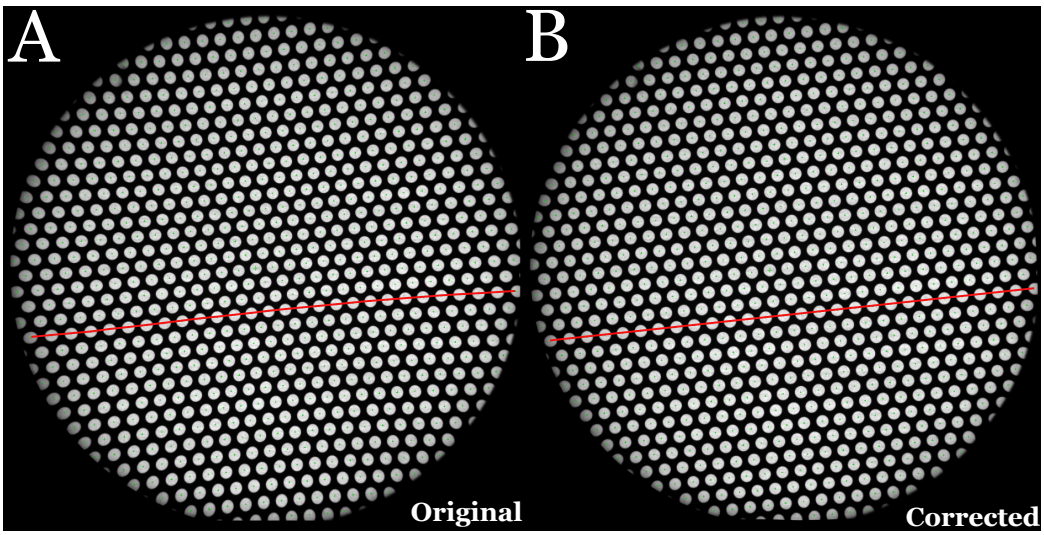

Figure 2.30: **(A)** Original and **(B)** Distortion corrected radiograph of the grid, a line connecting a straight row of the detected centroids was drawn

Camera Calibration

In order to obtain the three-dimensional coordinates of the bone markers from their locations seen on the recorded biplanar radiographs, the projective correspondence between the image space (2D) and scene space (3D) must be established for each camera in the stereophotogrammetric setup. A precise calibration phantom (Fig. 2.31A) was manufactured to facilitate photogrammetric camera calibration for the present biplane X-ray fluoroscopy system. The calibration phantom possessed a cuboid shape (L70×W70×H100) and was ground layer by layer out of a solid Perspex block using a five-axis computer-numerical-control (CNC) machine with a nominal machining accuracy of ±10 μm. The phantom was hollowed out in the middle deliberately to allow easy passage of the X-ray. Blind holes, with appropriately sized diameters and

depths, were drilled in a five-by-four array precisely on each of the lateral surfaces of the calibration phantom. Stainless steel ball bearings with a nominal diameter of 1.2 mm and a geometric tolerance grade of G10 were then carefully press-fitted into those holes until flush with the surface. This configuration minimised the assembly error, allowing the precise three-dimensional locations of the ball bearings to be obtained and used as references for calibrating the cameras. In addition, the three-dimensional "grid" formed by these reference points was sized to provide complete coverage for the volume of interest in the present study, which spans from the distal radius to the base of the third metacarpal, incorporating the entire carpus (Fig. 2.31B).

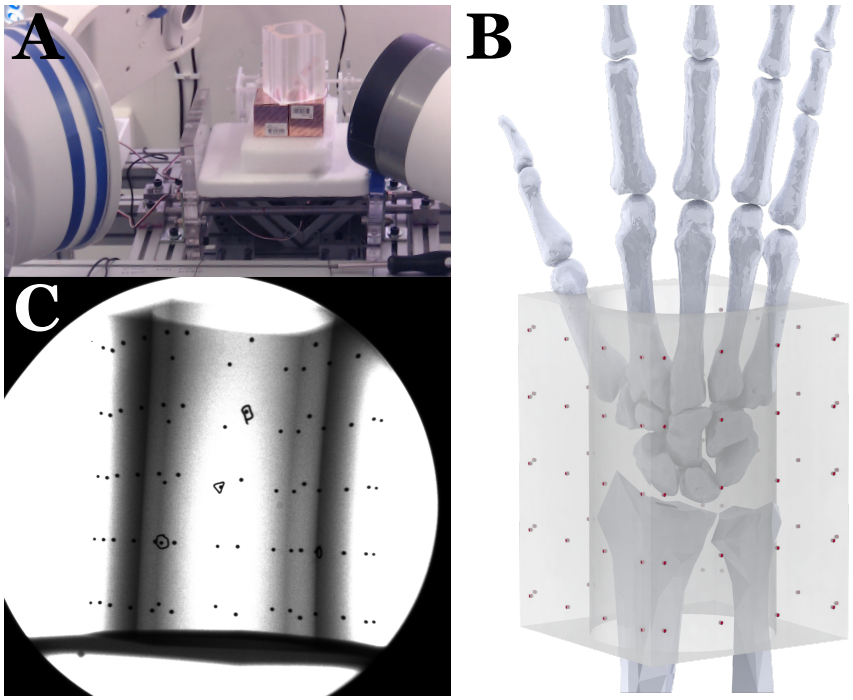

Figure 2.31: **(A)** Photograph showing the calibration phantom being placed in the capture volume **(B)** CAD model of the calibration phantom being superimposed onto that of a cadaveric wrist specimen **(C)** Radiograph of the calibration phantom, radio-opaque shapes are added to aid the registration

To facilitate the photogrammetric calibration in an experimental setting, radiographs of the calibration phantom were taken, allowing the digitisation of the reference points in the image space. Radio-opaque labels in various shapes (circle, triangle, rectangle, hexagon; see Fig. 2.31C) were glued onto the surface of the calibration phantom to assist in registering the detected image space coordinates to their corresponding three-dimensional locations in the scene space. Based on this image-scene correspondence, both the intrinsic and extrinsic parameters for each camera in the stereophotogrammetric setup were calculated by XMALab using the algorithm developed by Zhang (2000). Moreover, the program also allows the camera calibration to be optimised using multiple radiographs that are taken in different angles of the calibration phantom. In the present study, the biplane X-ray fluoroscopy system was calibrated and optimised with the phantom placed in at least eight different poses before the onset of each dynamic trial. The typical reprojection error after the optimisation was found to be consistently less than 1 pixel for the mini and full-size C-arm units.

Marker Digitisation and Tracking

The radio-opaque bone markers must then be digitised from each frame of the recorded biplanar radiographs before their three-dimensional movement trajectories can be reconstructed based on the image-scene correspondence obtained previously. Instead of employing the functionalities offered in XMALab, a custom Matlab (MathWorks, Massachusetts, USA) program, with digital filtering more appropriate for the images acquired by the present setup, was developed for this task. This program (Fig. 2.32) automatically enlarged and upsampled the approximate marker-containing pixel regions and a collection of commonly-used blob detection algorithms including the circular Hough transform ('imfindcircles' implemented in the Matlab Image Processing Toolbox (MathWorks, 2019b)), the maximally stable extremal regions ('detectMSERFeatures' implemented in the Matlab Computer Vision Toolbox (MathWorks, 2019a)) and the Laplacian of Gaussian filter ('feature.blob_log' built into the Python scikit-image library

(Van Der Walt et al., 2014)), were then employed to digitise the marker centroids for each frame. The results given by different detectors were cross-validated to ensure the accuracy and robustness of the digitisation process. However, "tracking" of the bone markers also involved the correct labelling or assignment of the obtained digitisation results to their corresponding marker trajectories. To this end, a Kalman filter ('vision.KalmanFilter' implemented in the Matlab Computer Vision Toolbox (MathWorks, 2019a)) was employed to predict the marker location based on their previous time history. Hence, for a particular bone marker, the digitisation result located in the closet vicinity of the predicted value was chosen to be merged into the overall trajectory, addressing the tracking problem.

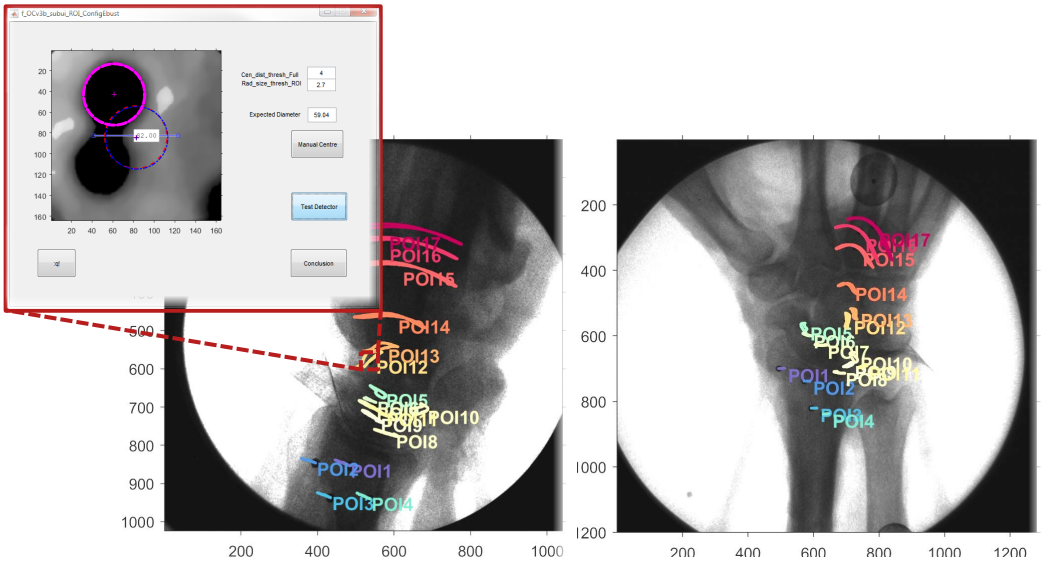

Figure 2.32: Screenshot of the custom-written Matlab program for digitising and tracking the radio-opaque markers. Inset: a subroutine zooms into a marker-containing region, applies image filtering and centroid detection algorithm. Although there are two markers and overlapping each other, the program is still able to determine the correct one to track (magenta).

Finally, the 2D image coordinates of the marker centroids were imported back into XMALab to be corrected for fluoroscopic image distortions before being finally triangulated to reconstruct the three-dimensional movements

of the markers (Hartley and Sturm, 1997). This process is illustrated in (Fig. 2.33).

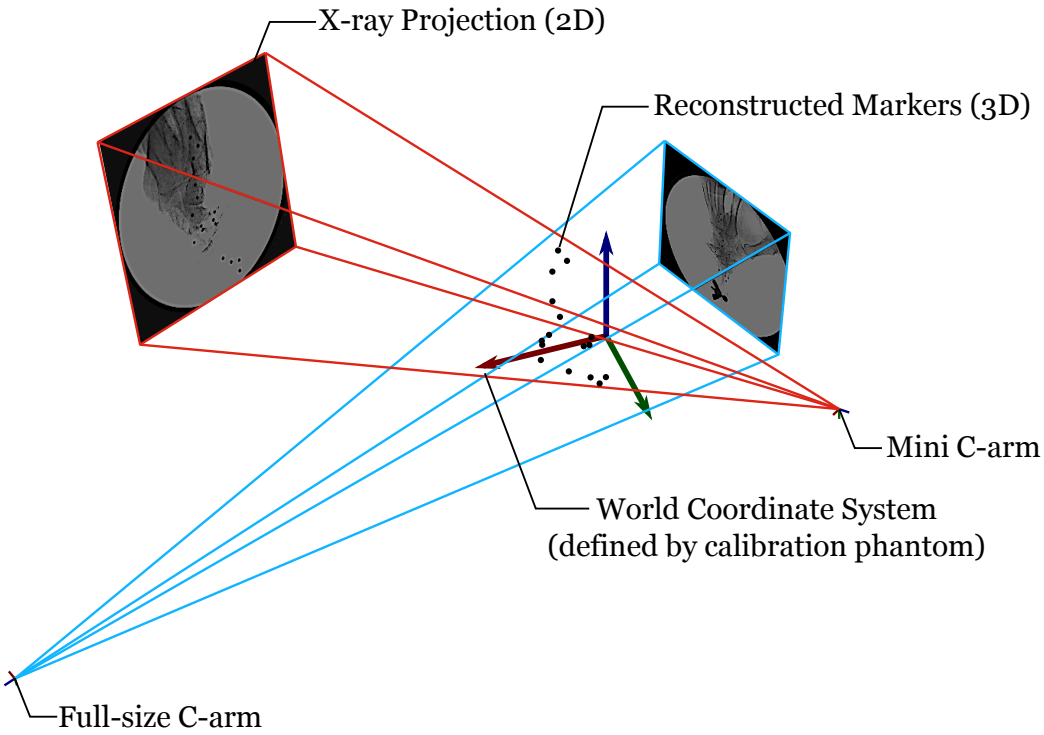

Figure 2.33: A simple illustration of the triangulation process

Definition of Joint Coordinate System

A joint coordinate system (JCS), consists of imaginary local coordinate systems (LCS) fixed to the proximal and distal body segments, was required to facilitate a quantitative and consistent investigation of the joint kinematics. However, the designation of the proximal and distal segments depends entirely on the desired measurement outcome and the joint being studied. In the present context, the radius often is seen as the distal segment and is typically regarded as a common reference for kinematics analysis of the wrist (Wu et al., 2005). As mentioned previously in Section 2.2.2.1, the third metacarpal was seen as the proximal segment and its relative rotation was measured when the global wrist motion was of primary concern. However,

the kinematics of an individual carpal bone is calculated by treating the particular bone of interest as the proximal segment and measuring its relative movement with respect to the radius. In addition, the concept of the proximal and distal segment in the JCS is also extended to describe the relative motion existed in numerous articulations formed by the adjacent carpal bones.

In order to aid the definition of the LCSs, volumetric models were obtained from a previously administrated CT scan of the wrist to aid the LCS definition process. For the radius and the third metacarpal, their LCSs, including the orientation of the coordinate axes and the location of the origin, ought to be determined exclusively based on the anatomical landmarks proposed in the ISB recommendations. However, the same was not applicable to the irregularly shaped carpal bones. Instead, the LCS of the carpal bones were defined rather implicitly by the ISB recommendation: the orientation of their LCS must be aligned with that of the radius when the global wrist was placed in the neutral position, while the origin was defined to be fixed at the volumetric centroids of the carpal bones. This particular LCS definition proved difficult to employ as it will be virtually impossible to perform CT scans with the wrist specimen placed in the exact neutral position. In addition, since the LCS serves as the very foundation for the subsequent kinematic analysis, deviation from the standardised definition will likely to yield erroneous and inconsistent results, when compared with previous studies. Hence, an additional correction step was taken to 'virtually' re-establish the neutral alignment of the carpal bone models obtained from the volumetric CT scan.

To achieve this, the cadaver wrist was first actively manipulated by DWSA to be placed sufficiently close to its true neutral position with a typical residual measured less than 0.02° in both FEM and RUD on the global scale. Static biplanar radiographs of the wrist were then taken to virtually recreate the neutral alignment of the volumetric carpal bone models obtained through the CT scan: for each of the carpal bone models, the bone markers were registered to their corresponding locations reconstructed from the fluoroscopy. A singular value decomposition (SVD) based method

developed by Söderkvist and Wedin (1993) (implemented as the 'soder.m' in Kinemat Toolbox (Reinschmidt and van den Bogert, 1997)) was used to calculate the rigid body transformation necessary for the registration process. With the neutral alignment of the wrist virtually established, the LCS for each of the carpal bones was defined by duplicating the orientation of the radius LCS to the volumetric centroids of the respective carpal bone models.

Pose Estimation

The 6-DOF kinematics of the carpal bones were then calculated through a process called 'pose estimation'. With the LCS appropriately defined for each carpal bone of interest in the previous step, the relative location of its associated bone markers was obtained. By registering these bone markers to the three-dimensional marker movements reconstructed from on the biplanar radiographs recorded during the dynamic wrist simulations, allowing the time history of the carpal bone motion to be reanimated. Additionally, depending on the desired measurement outcome, the reconstructed marker movement was transformed into appropriate coordinate systems before the registration process. The same SVD based approach (Söderkvist and Wedin, 1993; Reinschmidt and van den Bogert, 1997) was employed to calculate the transformation required to register the particular carpal bone from its neutral posture onto the positions shown on various frames of the radiographs. The resultant transformations, each consisted of a rotation matrix and a vector describing the consecutive translation, encapsulating the orientation and position of the carpal bones, respectively. In the present study, Euler angles, owing to their simplicity and ease of interpretation and communication, were used to represent the angular movement of the carpal bones. However, one major shortcoming of this representation is that the rotation sequence must be specified in a way such that the result is clinically meaningful. Furthermore, there was no standardised rotation sequence prescribed explicitly for the wrist by the ISB. Upon careful examination of the Grood and Suntay's convention, which was the foundation in JCS definition of the wrist, the Cardanic sequence corresponding to an intrinsic $Z - X' - Y''$ rotation was found to

be the most appropriate. The choice of this particular rotation sequence was proven to be suitable and was widely applied in previous studies on the carpal bone kinematics (de Lange et al., 1985; Kauer, 1980; Jackson et al., 1994; Kaufmann et al., 2005; Blankenhorn et al., 2007), as well as musculoskeletal modellings involving the wrist (Slavens et al., 2010; Schnorenberg et al., 2014; Iaquinto et al., 2014). The explicit formulae for decomposing the rotation matrices could be derived using an approach similar to the one described in Section 2.2.2.1.

2.3.3 Pressure Measurement System

A pressure measurement system (I-scan; Tekscan, Massachusetts, USA) was incorporated into the CWTP to provide mappings of the radiocarpal contact pressure during dynamic wrist simulations. The I-scan pressure mapping system was chosen over the dye-based pressure measurement films, owing to its real-time and continuous pressure measurement capabilities. A time history of the pressure measurements can be obtained, making the I-scan system ideal for pressure mapping of dynamic systems. Whereas the pressure measurement films use dye-stained impressions left by the contact to indicate pressure distribution. Since the ambient temperature and humidity may affect the optical density of the stain (Liggins et al., 1992), the impressions must be scanned immediately to allow for accurate digitisation, crucial for a precise quantitative measure of the pressure distribution. However, such a laborious procedure and an inherently static measurement capability render the pressure measurement films inapplicable in the present study. In addition, the I-scan system was reported to be superior in terms of the measurement accuracy comparing to the pressure measurement films (DeMarco et al., 2000; Bachus et al., 2006).



Figure 2.34: Photograph of the I-scan pressure measurement system

The Tekscan I-scan system (Fig. 2.34) is comprised of a flexible pressure sensor, a USB data acquisition handle, and operating software. The Tekscan Medical 4000 pressure sensors were used in the present study. The

sensor possesses a dual-branch design with a 27.9 mm by 33 mm rectangular pressure-sensitive matrix included on each side. The working principle of these pressure-sensitive matrices relied on the force-resistance relationship of the piezoresistive material sealed between two flexible polyester substrates. Sliver conducting lines were printed on the two substrates as rows and columns, which intersect to form individual sensing units, called sensels. The Tekscan Medical 4000 was selected for the present study partly due to its high spatial resolution, which measured up to 62.0 sensels/cm^2. The sensor is capable of measuring pressure up to 10,342 kPa. But this maximum capacity may be lowered for a refined measurement resolution by varying the sensor gain using the software. The sensor is approximately 0.1 mm in thickness and extremely flexible, making it suitable to be inserted into the narrow joint space of the radiocarpal articulation, and conforming with the geometry of the articular surface. The resistance of each sensel, and hence the pressure distribution, is measured continuously by the USB data acquisition handle with a sampling frequency up to 100 Hz and in an 8-bit ADC resolution. The I-scan system can be easily operated using the factory-supplied software, facilitating basic functions such as calibration, data logging, visualisation and some rudimentary post-processing. Technical specifications of the I-scan pressure mapping system can be found in Appendix A.10.

2.3.3.1 Synchronisation

For convenience, in the present study, the software for controlling the I-scan system was deployed on the same host PC for the biplane X-ray fluoroscopy system. Since the data logging process on the present I-scan system can only be initiated using the factory-supplied software, the same keyboard shortcut was used for triggering the biplane X-ray fluoroscopy system, allowing the data acquisition to be triggered concurrently on both systems, as described earlier. But again, since the I-scan system was operated on a PC separate to the DWSA, the timestamp for each frame of the acquired pressure mappings must be derived based on the DWSA's system clock to allow for proper synchronisation with the measurement data recorded by the DWSA, similar

to those of the biplanar radiographs. Unlike the cameras retrofitted to the fluoroscopy machines, the data logging process on the present I-scan system cannot be controlled and timed using an externally injected pulse train, let alone exporting any signal indicating the acquisition of each frame. Instead, the pressure mappings were recorded with a constant user-specified sampling rate, and the acquisition of each frame of data was paced presumably according to an internally generated signal. Preliminary studies revealed that the software-timed acquisition was relatively stable and the time variation between the sampling intervals, or the "jitter", was negligible. Hence, the timestamp for each frame of the acquired pressure measurement can be easily derived, if the starting time of the data acquisition process is precisely known. In order to accurately capture the onset of this event, a LabVIEW VI subroutine and the following communication protocol was devised: as soon as the keystroke for initiating the data acquisition process on the I-scan system is detected, the host PC records the present time, t_s, and sends a message to the PC controlling the DWSA via UDP; the DWSA was programmed to acknowledge the successful receipt by responding with another UDP message and simultaneously record the time indicated by its own clock, denoted as t_f; by the time that this repose message made its way back to the original PC, the present time was recorded again and denoted as t_2. Hence, the time delay caused by UDP communication alone can be estimated by halving the duration of this roundtrip, namely $(t_f - t_s)/2$ and the accurate acquisition onset of the I-scan system as measured in the DWSA's system clock can be consequently estimated by compensating t_0 with this delay.

2.4 Summary

A cadaveric wrist testing platform, comprised of a novel dynamic wrist simulation apparatus and subsidiary measurement systems including a custom-built biplane X-ray fluoroscopy system and an I-scan electronic pressure measurement system, was developed as an integrated platform to facilitate biomechanical study of the wrist. The CWTP was capable of performing repeatable motion simulations on a human cadaver wrist and allowed measurements of the complex carpal bone kinematics and intra-articular pressure distribution to be taken at the same time. This chapter provided an in-depth description of the hardware, software and mathematical formulations necessary for the construction and proper functioning of those essential component systems of the CWTP. The signal pathway of the CWTP was illustrated in Fig. 2.35.

The DWSA is a computer-controlled apparatus with the capability of performing tendon-driven active wrist motion simulations on human cadaver wrists in a physiologically meaningful manner. The framework of the DWSA was built predominately using off-the-shelf aluminium extrusions and was functionally divided into the specimen cell and the actuator cell to provide necessary support and attachments for the cadaver wrist and relevant electromechanical instruments, respectively. The proximal heads of the radius and ulna were cemented in a potting fixture with dental plaster, allowing the wrist specimen to be mounted securely onto the DWSA. Steinmann pins were used to fuse the specimen in neutral pronation and supination while having their ends tightly clamped to offer additional structural rigidity. Six stepper motors were employed to generate the muscle loading and excursions necessary to reanimate cadaveric wrist specimens. Stainless steel cables, instrumented with uniaxial tension load cells, were securely attached to tendons of the wrist prime movers. A two-stage tendon guiding system consisting of multiple pairs of swivelling pulley sets were constructed to facilitate gentle routing of the cables, feeding them to the motors without disturbing the anatomical muscles' lines-of-action. A spool-winder mechanism was chosen to convert motor rotation into linear displacement of the cables, thus mimicking

active excursion of the muscles.

Global wrist position of the cadaveric specimen was measured continuously in real-time utilising a video motion capture system, with retro-reflective marker clusters firmly attached to the radius and the 3MC of the wrist. However, a CT scan of the cadaver wrist with the marker clusters attached was required to define the JCS and determine the relative position of the markers. With the means of measuring the muscle forces and joint positions successfully implemented, a control algorithm was developed for the DWSA to generate coordinated muscle contractions that allows the global movement of the cadaver wrist to closely track the user-defined trajectories. However, since the control over the global wrist position must be achieved indirectly through adjusting the forces on the muscle tendons, the control algorithm of the DWSA adopted a two-layer architecture, with a force control loop being nested within a position control loop, which in essence acts on the position error to provide an estimation on the joint torque necessary for the corrective action. However, due to the absence of accurate prior knowledge on the dynamic model of the wrist, the decentralised adaptive control scheme, formerly developed by Seraji (1989), was adopted. The widely-used static optimisation was used to tackle the neuromuscular redundancy, which arises in distributing and converting the joint torques back to the force contribution of each individual muscle. Furthermore, the co-contraction of the agonist-antagonist muscle pairs in the *in-vivo* condition was also approximated via a constant-sum constraint imposed during the optimisation process. Finally, the whole control algorithm was implemented using custom-written LabVIEW VI programs to allow for the integration with other instruments of the CWTP.

The subsidiary measurement system consisted of a custom-built X-ray fluoroscopy system and an I-scan electronic pressure measurement system. The biplane X-ray fluoroscopy system was constructed by retrofitting two clinical C-arm X-ray fluoroscopy units to facilitate marker-based Röentgen stereo-photogrammetry analysis of the carpal bone kinematics. Two industrial machine vision cameras with appropriate lenses were used to replace the

ones originally mounted at the back of the image intensifiers. A USB development board was used to generate the pulse train necessary for achieving synchronous image acquisition on the two cameras, while a control console was constructed to allow an automated activation and deactivation of the X-ray exposure. A series of processing required to enable the marker-based kinematic analysis were described in detail. This included the distortion correction, camera calibration, marker digitisation and tracking, joint coordinate system definition and pose estimation. The off-the-shelf I-scan pressure measurement, on the other hand, was integrated into the CWTP to allow the intra-articular pressure of the wrist to be monitored in real-time during the dynamic motion simulation. Dedicated LabVIEW programs were developed to establish UDP communication between different systems, allowing a simultaneous triggering of the data acquisition process within the CWTP.

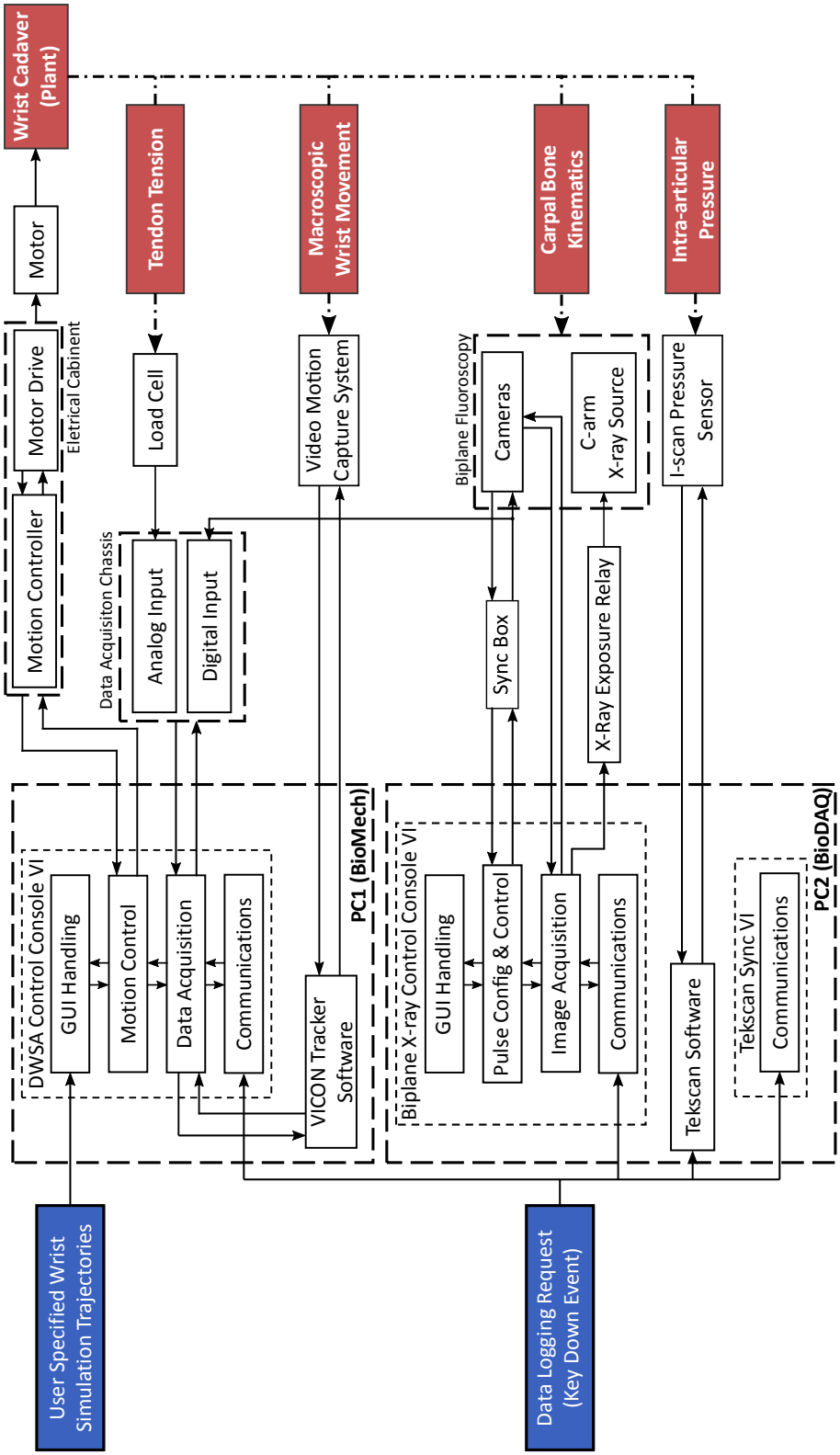

Figure 2.35: Signal pathway of the CWTP, which is operated by two separate host PCs. Dashed arrow denotes a specific property of the cadaver plant is being experimentally measured by an instrument.

3

Validation of the Testing Apparatuses

Contents

3.1 Introduction 192

3.2 Validation of the DWSA 193

3.2.1 Global Wrist Motion 197

3.2.2 Muscle Forces 207

3.3 Validation of the Biplane X-Ray Fluoroscopy System 217

3.3.1 Inter-Marker Distances 219

3.3.2 Rigid Body Kinematics 225

3.4 Joint System Validation of the CWTP 233

3.5 Summary 239

This chapter outlines the various experiments performed to validate the CWTP.

3.1 Introduction

This chapter describes the experiments designed and performed to assess the accuracy and reliability of the CWTP. As described in the previous chapter, the CWTP incorporated a DWSA, capable of simulating active wrist motion on cadaveric specimens in a controlled manner, and a set of subsidiary measurement systems allowing carpal biomechanics to be studied simultaneously. However, given the fact that the CWTP was intended for both synthesising and analysing wrist motions, serving as a self-sufficient "environment" for *in-vitro* investigation of the wrist, a comprehensive series of studies were carried out to assess the accuracy and reliability of these two different aspects of this testing platform. In other words, the quality of wrist motion simulations provided by the DWSA as well as the validity of the measurements, primarily those collected by the custom-built biplane X-ray fluoroscopy system, were assessed. To avoid cross-talk of the measurement errors, the DWSA and the biplane X-ray fluoroscopy system were first validated independently, and then collectively as a whole to test their combined performance and reliability in conducting kinematics studies of the carpus.

3.2 Validation of the DWSA

Since global wrist motion was regarded as a dependent variable in the present study, the quality of the wrist motion simulated on cadaveric specimens would have a direct effect on the validity of the subsequent analysis, contributing substantially towards the measurement error. To this end, a series of studies were carried out based on the joint motion, muscle force, and fluoroscopic image data corresponding to the normal and Stage IV wrist simulations (reported in Section 4.1) to assess the control accuracy and repeatability of the DWSA.

Specimen Preparation

Seven fresh-frozen upper-limbs (age: 82.2 ± 12.5 years) were acquired from five human cadavers registered under the University of Melbourne Body Donor Program, and were screened radiographically at the carpal level for pathological conditions. Among all specimens, there were two contralateral pairs sourced from the same body donor.

The specimens were dissected and prepared using the same protocols as described later in Section 4.1.1.2. In short, the specimens were disarticulated at the elbow and mounted vertically onto the DWSA. Two Steinmann pins were used to fuse the forearm in neutral pronation and supination. Prime mover muscles including the flexor carpi radialis (FCR) and ulnaris (FCU), the extensor carpi radialis brevis (ECR-B) and longus (ECR-L), and the abductor pollicis longus (APL) were detached from their origins and dissected at the musculotendinous junctions. Each muscle tendon was wrapped in saline-soaked fabrics to prevent dehydration. Custom-designed wire-woven sleeves were used to grip the tendons distally, allowing them to be connected in series with their designated actuators within the DWSA via cables instrumented with uniaxial load cells. Skins and other subcutaneous tissues were excised up to the level of the carpus, with care taken to preserve the integrity of the interosseous membrane, joint capsules and retinacula. Retro-reflective

marker triads were rigidly attached to the distal aspects of both the radius and the third metacarpal to facilitate tracking of the global wrist position. The joint capsule of each specimen was then exposed dorsally through a ligament-sparing dorsal capsulotomy suggested by Berger et al. (1995), allowing radio-opaque markers to be embedded into the distal radius, scaphoid, lunate and capitate in clusters of three. The relative placement of the radio-opaque markers was optimised to avoid occlusion, and their implantation was carried out by an experienced hand surgeon under fluoroscopic guidance. Care was taken not to damage the stabilising ligaments.

For each specimen, a CT scan (Siemens Biograph mCT; Munich, Germany) was administrated to obtained the volumetric models of the bones. And based on the CT scan, the relative positions of the markers in the local coordinate systems defined for their designated tracking targets were digitised. This process was performed for both the retro-reflective markers as well as the radio-opaque bone markers to facilitate tracking of the global wrist motion and the microscopic movement of the carpal bones, respectively.

Motion Simulation Protocol

Dynamic simulations of the two planar wrist motions, FEM and RUD, were performed. Sinusoidal trajectories with an amplitude of 30° and 20° were used in simulating the wrist FEM and RUD, respectively. These specific ranges of motion (ROM) were selected in accordance with previous investigations involving dynamic manipulation of cadaver wrists (Tong, 1985; Werner et al., 1996; Erhart et al., 2012; Dimitris et al., 2015). In order to avoid excessive motor accelerations and prolonged solution process of static optimisation, a moderate value of 20 seconds was chosen for the period of the sinusoidal profile. At least three complete cycles of the sinusoidal motions were simulated in each of the dynamic trials. Dynamic wrist simulations were performed with the DWSAs control software running at 100 Hz on the host PC. The global wrist motion and the tension in the muscle tendons were measured simultaneously at the same sampling frequency to provide the necessary control feedbacks. Movement of the carpal bones resulting from the simulated global

wrist motion was imaged simultaneously using the biplane X-ray fluoroscopy system at a rate of 25 Hz.

An oblique wrist motion, commonly known as the "dart thrower's motion" (DTM) which starts from a combined posture of extension and radial deviation to proceed simultaneously towards a coupled flexion and ulnar deviation (Moritomo et al., 2007), was also incorporated into the current test protocol. The importance and clinical relevance of this particular path of wrist motion have been discussed previously. In essence, DTM has been shown to be used commonly in daily activities (Capener, 1956; Palmer et al., 1985; Moritomo et al., 2007; Brigstocke et al., 2014). A few investigators claimed that the scapholunate intercarpal motion was minimised when the wrist was moved in the dart thrower's arc (Saffar and Semaan, 1994; Ishikawa et al., 1999; Werner et al., 2004; Crisco et al., 2005), and a profound functional and clinical implication was thus hypothesised for the oblique plane represented by the DTM. For simplicity, the DTM simulated in the present study was a direct superposition of the two aforementioned planar wrist motion. Namely, each specimen was cycled between a posture of 30° of extension and 20° of radial deviation (radial extension) and a combined 30° of flexion and 20° of ulnar deviation (ulnar flexion).

Simulated Ligament Disruption

In order to study the effect of scapholunate instability on the kinematic behaviours of the carpal bones, ligament disruptions were surgically simulated in the cadaveric wrist specimens. Those lesions were systematically introduced in stages with increasing severity to emulate the progressive nature of the instability (Kitay and Wolfe, 2012). The protocol for ligament severing was drafted based on the speculated etiology and pathomechanics of the instability and will be explained later (Section 4.1.1.5). Since the apparent motion of the global wrist may be seen as a result of the complex interactions between its bony constituents and soft-tissue constraints (An et al., 1991), the attenuation of the ligamentous stabilisers is thus likely to alter the kinematic behaviour of the wrist, introducing unknown disturbances to the

control system of the DWSA. Therefore, to ensure accurate and reproducible wrist simulations were achieved in each stage of ligament severing, validation experiments were repeated with the wrist specimens surgically manipulated to attain the most severe stage of ligament disruptions in the protocol, representing the foreseeable worst-case scenario (described as Stage IV ligament resection in Section 4.1.1.5). The scapholunate interosseous ligament (SLIL), the radioscaphocapitate ligament, the long and short radiolunate ligament, the scaphotrapeziotrapezoid ligament, the dorsal intercarpal ligament, and about 40% of the dorsal radiocarpal ligament were surgically divided.

3.2.1 Global Wrist Motion

Methods

The reliability of the global wrist motion simulated by the DWSA was assessed primarily in terms of accuracy, time delay, and repeatability. Dynamic simulation of the FEM, RUD and DTM were performed before and after the surgical introduction of ligament disruptions in each wrist. To facilitate the analysis, both of the reference trajectory and the control response of the cadaveric plant were recorded at a sampling frequency of 100 Hz.

The global wrist position is characterised by a combination of the joint angles measured in the two major DOFs, namely the flexion/extension in the sagittal plane and the radial/ulnar deviation in the coronal plane. Therefore, to quantify the position control accuracy of the DWSA, the simulated wrist motion was analysed based on the joint angles measured in both planes across all three types of wrist motion. Two different approaches were taken and the position control accuracy was reported based on four measures.

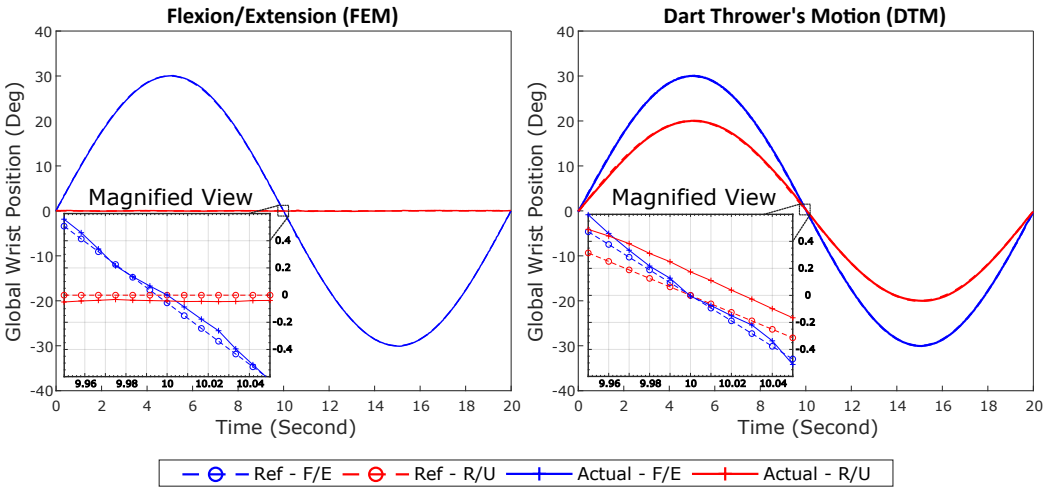

Figure 3.1: Examples of the data recorded during **(A)** FEM, **(B)** DTM. Insect: magnified view, revealing negligible position control error

First, for each DOF of joint mobility, conventional measures including the mean RMS difference and the maximum absolute difference between the

reference and the actual movement trajectory were calculated for specimen across all time instants (Fig. 3.1). For planar motion such as pure FEM or RUD, the position control accuracy was assessed not only using the joint angles measured in the primary direction of wrist motion but also based on the unwanted "residual movement" in the other DOF.

Second, since the global wrist position at a particular instant in time is determined by the unique combination of two joint angles, two performance metrics measuring how close the control target had been archived in both DOFs simultaneously were calculated. The first was based on the Euclidean distance calculated in the imaginary FEM-RUD plane between each point in the reference and the actual trajectories of the wrist motion (Fig. 3.2), namely, $d_{Eul} = \sqrt{(a_{ref} - a_{act})^2 + (\beta_{ref} - \beta_{act})^2}$, where α and β are the joint angles in the sagittal and coronal planes, respectively, at a particular instant in time.

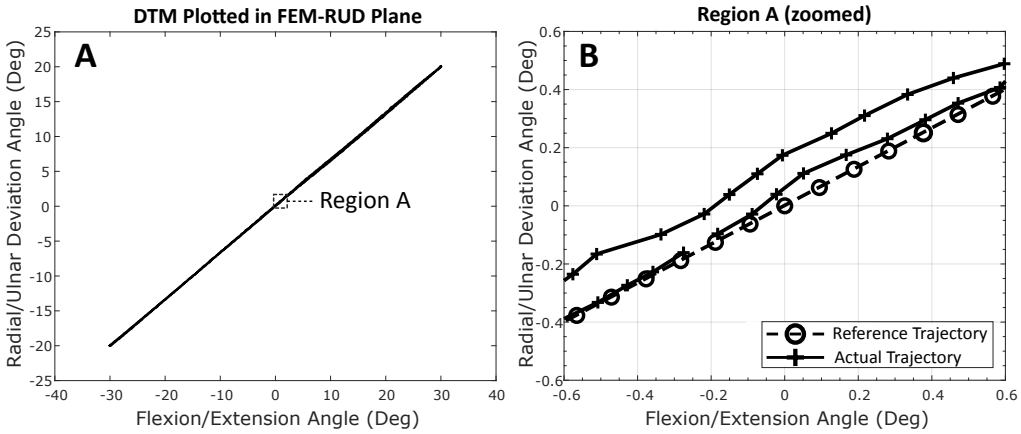

Figure 3.2: An example of the DTM trajectory being plotted in the FEM-RUD plane

The second assessment involved calculating the angles between vectors defining the target and the actual orientations of the third metacarpal in 3D space (Fig. 3.3). This angular discrepancy can be found using $\epsilon = \cos^{-1}\left((RotZ(\alpha_{ref})RotX(\beta_{ref})[0,1,0]^T)\right) \cdot \left((RotZ(\alpha_{act})RotX(\beta_{act})[0,1,0]^T)\right)$, for each point in the reference and the actual movement trajectories. $RotZ$ and $RotX$ are matrices representing the elemental rotations by a given

angle about the Z- and X-axis, respectively.

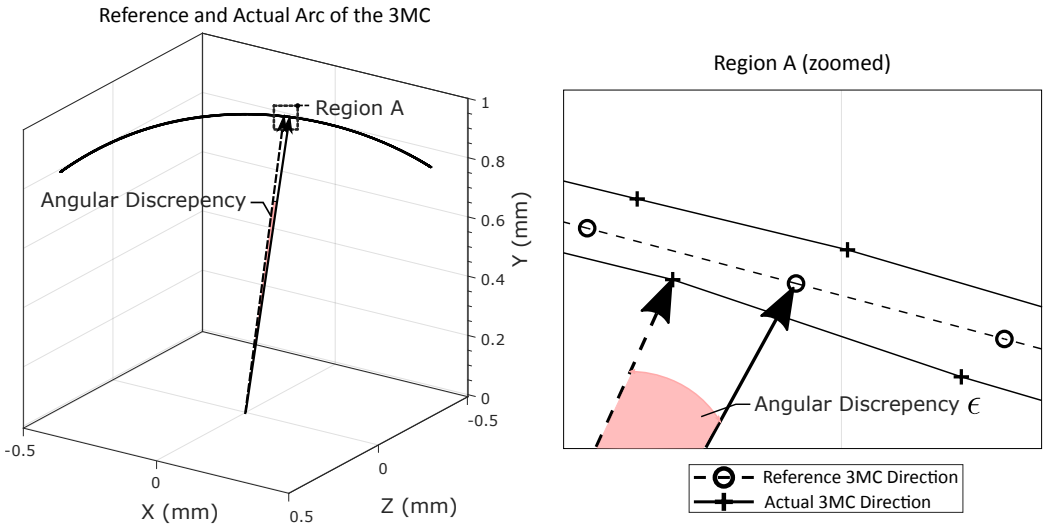

Figure 3.3: An example showing the angular discrepancy, ϵ, between the reference and the actual directions of the 3MC during simulated wrist DTM

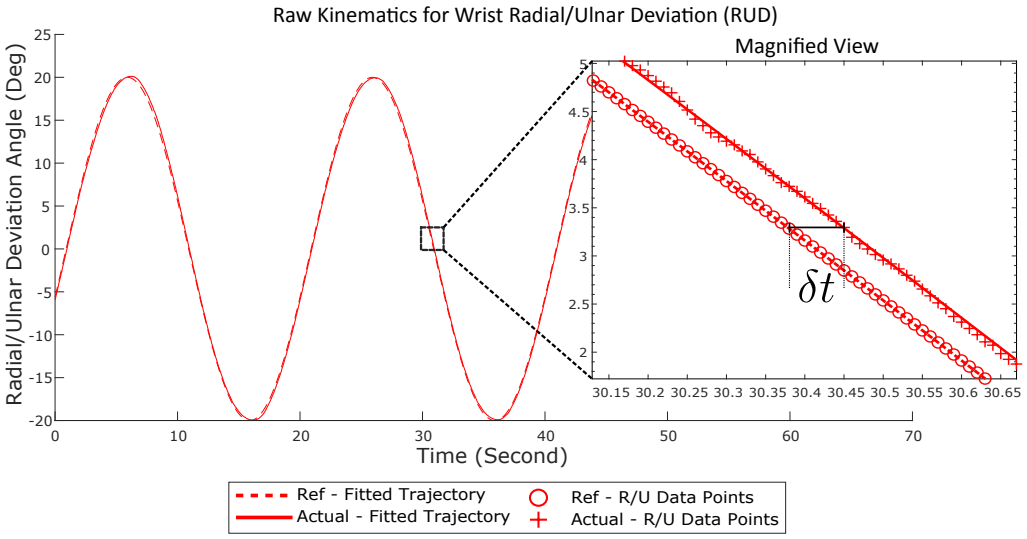

Figure 3.4: An example of the control time delay, δt, exhibited by the DWSA during dynamic wrist simulation.

It was evident that the inaccuracies in the position control of the DWSA were partially caused by the time delay of the simulated wrist movement (Fig. 3.4). This error, in essence, can be characterised by the average phase

difference between the reference trajectory and the actual wrist movement recorded. To take the entire curve into account, a curve-fitting based approach was taken. A sine curve, $f_{ref}(t) = A_0 \sin(B_0 t + C_0)$, was first fitted to the reference trajectory. With explicit knowledge of the model parameters A_0, B_0 and C_0, the same expression was fitted to the trajectory of the actual wrist movement recorded but with an additional variable δt included, namely $f_{act}(t) = A_0 \sin(B_0(t - \delta t) + C_0)$, to encapsulate the phase difference. Because the sole emphasis of the analysis was to find the average time delay, which was effectively captured by the fitting parameter, δt, this approach was considered appropriate. The calculation was similarly performed on movement trajectories recorded for each specimen, before and after the introduction of ligament disruptions.

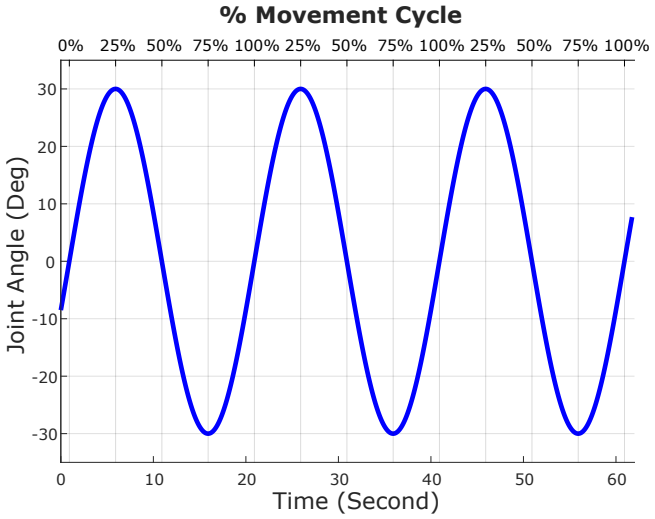

Figure 3.5: An example of normalising time into % movement cycle

Aside from the accuracy of the position control, it is also of critical importance to ensure repeatable wrist movement is obtained between each cycle of the dynamic simulations. In the present context, repeatability may be best interpreted as a measure of the variations in the joint positions assumed by the global wrist at time instants that are periodically equivalent in different cycles of a dynamic motion simulation. To facilitate the analysis, the timestamps of the recorded wrist movement were normalised and temporally "wrapped" into 0 to 100% of a single cycle (Fig. 3.5).

The resultant data points were then linearly interpolated at uniform 0.05% intervals (i.e. 100%/(20 s×100 Hz), to avoid excessive resampling). The standard deviation of the data points correspond to the same percentage of wrist motion (Fig. 3.6) were calculated, and the mean was used to quantify the repeatability for that particular plane of the simulated wrist motion. In addition, similar to the study on the position accuracy, the repeatability was again analysed conjointly for both planes of motion. Specifically, for each group of data that corresponds to the same periodic locations, this involved calculating the standard deviation of their Euclidean distances as defined in the FEM-RUD plane, as well as the standard deviation of their angular divergence from the reference orientation prescribed for the third metacarpal (angular dispersion). An overall measure of repeatability was finally obtained for each set of values by taking the average across all percentages of the movement cycle. The analysis was again conducted for all three types of wrist motion performed by each of the seven specimens and was repeated for measurements obtained after the disruption of the ligament stabilisers.

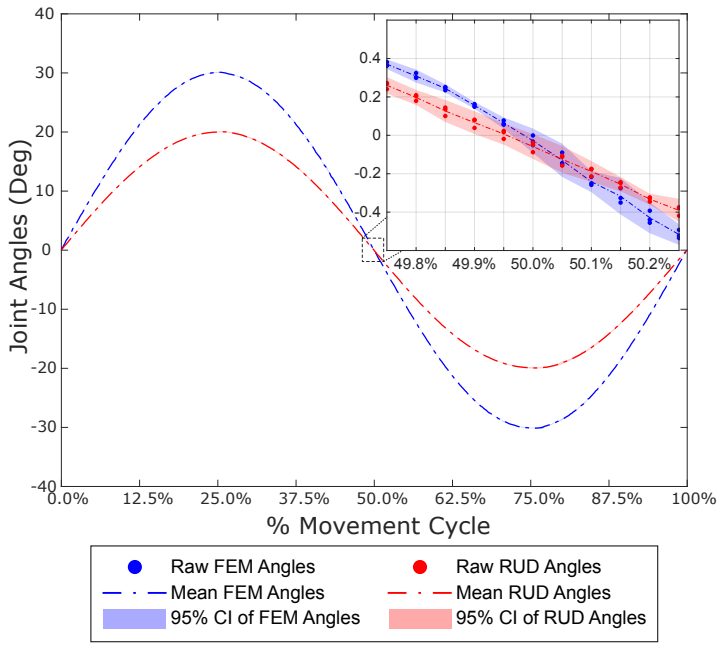

Figure 3.6: An example of the repeatability assessment, the raw data points and the 95% confidence interval were plotted (insect) to show the scattering of the position control performance between different cycles

Results and Discussion

For all three types of wrist movement simulated on cadaveric specimens when they were still in their normal physiological state, the mean RMS difference between the control reference and the actual joint angle measured did not exceed 0.3° in both planes across the full range of motion (Fig. 3.7). Interestingly, fluctuations of the error seemed to correspond with locations where higher accelerations of the cadaveric plant were necessary. However, for the entire range of motion, the average RMS difference did not exceed 0.12° and 0.18°, representing an error of 0.2% and 0.45% of the movement simulated in the sagittal and coronal plane, respectively (Table 3.1). The standard deviation between the RMS errors obtained for each of the seven cadaver wrists was as low as 0.1°, indicating good reproducibility of the position control was achieved between different specimens. In comparison, not mentioning the apparent dominant advantage over those static "jigs" where constrained wrist movement were performed *in-vivo* by living subjects (Neu et al., 2001), or those synthesised on a cadaver model via a trial-and-error based manual adjustments of the tendon force (Patterson et al., 2007), the position control results obtained in the present section was study is an improvement on that reported previously (Tong, 1985). Even though a mean position control accuracy and reproducibility of less than 1° and 1.3° were achieved after modernisation of this earlier wrist simulation apparatus (Short et al., 2002b), these are still several times poorer than the DWSA's performance shown in the present study. In addition, the level of control accuracy and reproducibility demonstrated by the DWSA was also better than those of a most recent development, which was reported to exhibit a mean control accuracy of 0.23° and an average inter-specimen variation of 0.25° (Iglesias, 2015). Notably, for pure planar wrist motions, FEM and RUD, the RMS position error in the out-of-plane movement direction was kept below 0.1° at all times. In comparison, an undesirable out-of-plane error as high as 1° and 4° were reported during FEM and RUD simulations, respectively, for a similar simulator constructed by Iglesias (2015). Furthermore, the present results were an improvement of those obtained in a recent study where cadaveric

wrist specimens were moved passively under the guidance of a 6-DOF Stuart platform (Fraysse et al., 2014). A maximum absolute error that exceeded 0.5°, or 1.25% of the intended motion, was not observed in either plane of joint motion across all wrist simulations performed on the intact specimens. The two combined error measures, designed to reflect the 2-DOF nature of the wrist motion and with their relative emphasis on the magnitude and the directionality of the errors, namely the RMS difference of Euclidian distances measured in the imaginary FEM-RUD plane between the control reference and the actual wrist positions measured, and the RMS of the angle included by vector presenting the target and the actual orientation of the 3MC, that did not exceed 0.15° and 0.2°, respectively. The average control time delay was found to be less than 0.02 s and 0.06 s, or 0.1% and 0.3% of the intended movement period, for motion simulated in the sagittal and coronal plane, respectively (Table 3.2). Repeatability-wise, all relevant metrics were found to be less than 0.1°, indicating a negligible variation in the wrist positions between each cycle of the motion simulation (Table 3.3).

Even after surgically releasing all ligamentous constraints that are known or speculated to provide stability for the scapholunate joint, both of the accuracy and repeatability metrics for all three types of wrist motion simulations observed very limited deteriorations. In particular, the DTM was found to be the most affected, with its mean RMS and maximum position error in increased to approximately 0.18° and 0.7°, respectively. But these were still low and may be considered insignificant relative to the primary outcome measures (wrist angles), despite the fact that they had already represented the worst-case-scenario anticipated for the wrist motion simulations in later study. Therefore, in conclusion, the high sub-degree position control accuracy, repeatability and reproducibility demonstrated by the DWSA in both healthy and ligament-deficient wrists were deemed to be adequate for the purposes of this research project.

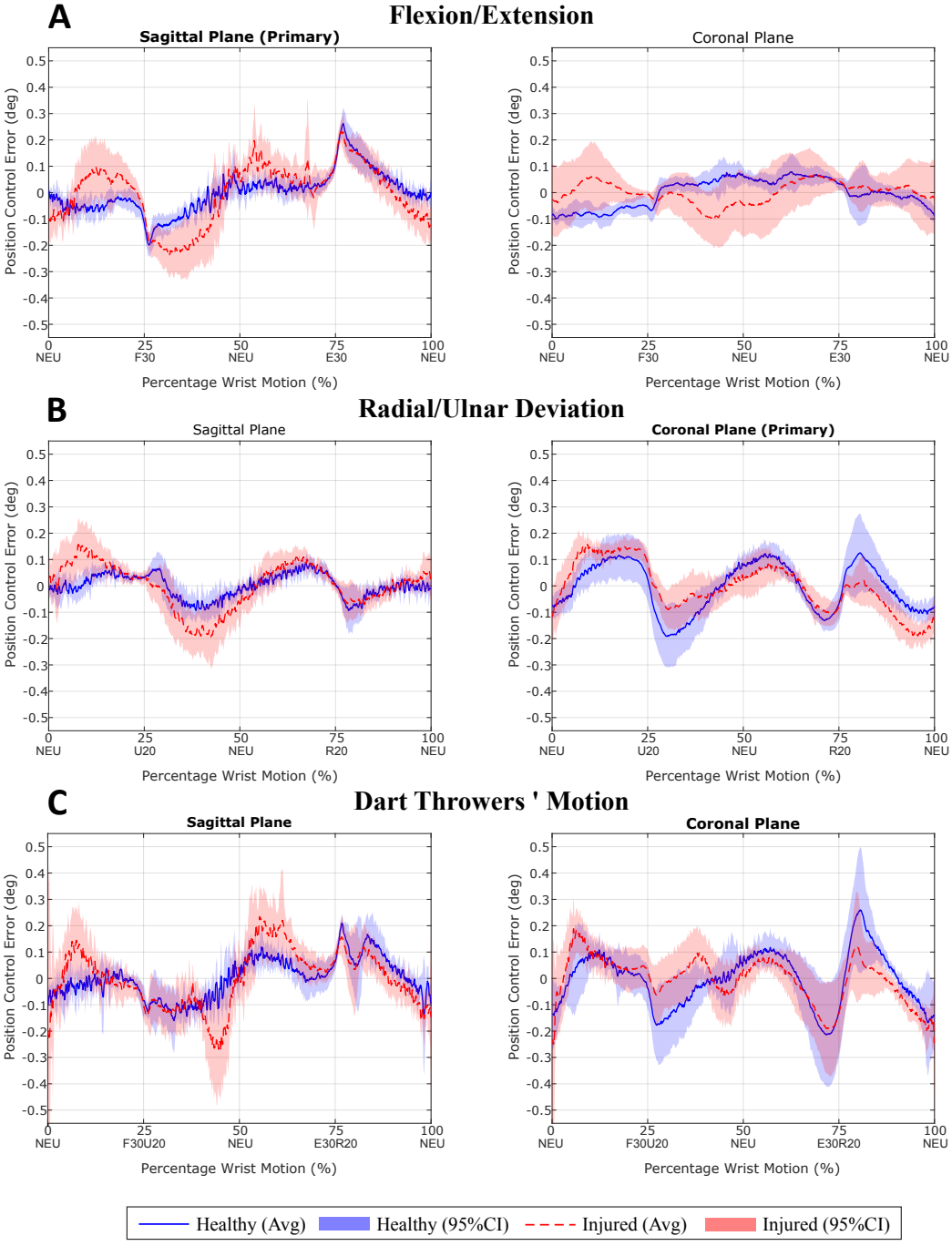

Figure 3.7: The mean RMS error during the course of **(A)** FEM, **(B)** RUD, **(C)** DTM, across 7 wrists in both healthy and ligament deficient conditions. 95% confidence interval of the control error is also shown. NEU: neutral, F: flexion, E: extension, U: ulnar deviation, R: radial deviation.

Table 3.1: Position control accuracy achieved by the DWSA on cadaveric specimens (n = 7), in both healthy and injured state during three different types wrist motion simulations

Condition	Motion	**Accuracy** (deg [SD])					
		RMS Error		**Max Abs. Error**		**RMS Diff. Euclidean**	**RMS 3MC Angular Dev.**
		Sagittal	Coronal	Sagittal	Coronal		
Healthy	FEM	0.098 [0.038]	0.070 [0.017]	0.370 [0.055]	0.208 [0.048]	0.091 [0.021]	0.115 [0.023]
	RUD	0.065 [0.013]	0.152 [0.098]	0.243 [0.054]	0.420 [0.180]	0.121 [0.042]	0.137 [0.041]
	DTM	0.114 [0.050]	0.172 [0.102]	0.440 [0.186]	0.488 [0.249]	0.131 [0.037]	0.168 [0.055]
Injured	FEM	0.147 [0.047]	0.101 [0.033]	0.568 [0.315]	0.296 [0.082]	0.140 [0.042]	0.176 [0.036]
	RUD	0.107 [0.033]	0.159 [0.089]	0.375 [0.074]	0.424 [0.177]	0.125 [0.019]	0.166 [0.022]
	DTM	0.159 [0.059]	0.177 [0.088]	0.706 [0.478]	0.685 [0.313]	0.160 [0.050]	0.200 [0.037]

Table 3.2: Time delay of the DWSA's position control, calculated for all three types of motion simulations performed on seven cadaveric specimens, in both healthy and ligament deficient conditions

Condition	Motion	**Time Delay** (sec [SD])	
		Sagittal	Coronal
Healthy	FEM	0.015 [0.003]	-
	RUD	-	0.058 [0.010]
	DTM	0.017 [0.005]	0.055 [0.010]
Injured	FEM	0.020 [0.006]	-
	RUD	-	0.067 [0.006]
	DTM	0.023 [0.008]	0.063 [0.011]

Table 3.3: Position control repeatability achieved by the DWSA during three different types wrist motion simulations in cadaveric wrist specimens (n = 7) before and after ligament disruptions

		Repeatability (deg [SD])			
Condition	Motion	**Mean std. Wrist Position**		**Mean std. Euclidean Diff.**	**Mean std. 3MC Angular Dev.**
		Sagittal	Coronal		
Healthy	FEM	0.027 [0.002]	0.016 [0.003]	0.027 [0.002]	0.026 [0.003]
	RUD	0.024 [0.005]	0.049 [0.011]	0.049 [0.011]	0.038 [0.008]
	DTM	0.030 [0.004]	0.045 [0.013]	0.033 [0.011]	0.036 [0.013]
Injured	FEM	0.033 [0.010]	0.019 [0.007]	0.033 [0.010]	0.034 [0.010]
	RUD	0.028 [0.005]	0.063 [0.010]	0.063 [0.009]	0.047 [0.009]
	DTM	0.033 [0.005]	0.058 [0.016]	0.037 [0.006]	0.045 [0.014]

3.2.2 Muscle Forces

Methods

As a result of DWSA's nested control architecture (Section 2.2.3), wrist motion simulations with a level of position accuracy and repeatability as high as previously shown, would not be possible if the inner force loop failed in facilitating a timely and effective control of the actuators forces exerted on the muscle tendons. Although the muscle forces are seemingly intermediate to the overall control process in that regard, they are the very factors that generate the simulated wrist motion in the first place. Therefore, a dedicated study to assess the control outcome and reliability of the muscles forces was deemed necessary.

As described earlier, to approximate the neurological co-contraction of the agonist-antagonist muscle pairs, the muscle force setpoints derived from the static optimisation were subjected to an additional constraint, where they must sum up to a user-specified constant, Λ, during the course of the dynamic wrist simulation. Any non-conformity of this constant-sum requirement is indicative of the error in force control. Therefore, for simplicity, the RMS difference between the summation of the tension exerted by the DWSA on each of the muscle tendons and was used to quantify the overall force control accuracy.

On the other hand, to ascertain the kinetic similarity between each cycle of the simulated wrist motion —that is to say, to ensure the forces which caused the apparent, cyclic movement of the wrists are indeed comparable, the force control repeatability of the DWSA was also evaluated. Therefore, like the approach adopted in the previous section, the repeatability of the forces on individual muscle tendons was quantified using the mean of the standard deviations calculated between data points that temporally correspond to the same percentage of the simulated wrist motion. Finally, the assessments were conducted for the muscle forces recoded during dynamic simulations of all three types of wrist motion, performed on the cadaveric

specimens that were initially in their healthy state then surgically modified to simulate ligament disruptions.

Results and Discussion

In terms of the force control accuracy, the average deviation from the constant-sum constraint, Λ, was less than 3.5 N for all three types of wrist motion simulated on both normal physiological and pathological specimens (Table 3.4). This combined error accounted for only 2.33% of the total force setpoint and was considered to be negligible. On average, this suggested that a sub-Newton accuracy was achieved in controlling the force applied to each of the six wrist muscle tendons, surpassing those of the DWSA's predecessors. A force control accuracy of 4 N was reported for the simulator described by Erhart et al. (2012), which relied entirely on a force-control scheme.

Across the seven wrist specimens tested, the mean standard deviation of this combined force error was found to be at most 1 N for all motion simulations performed both before and after injury. This indicated a good force control performance was consistently achieved, despite the presence of the anatomical variations among cadaveric specimens or the disturbances in plant dynamics induced by laceration of the ligaments.

Table 3.4: Combined force control accuracy (average deviation from the constant-sum constraint, Λ) achieved by the DWSA in both healthy and ligament deficient cadaveric wrist specimens (n = 7)

Specimen Condition	Combined Force Error (N [SD])		
	FEM	**RUD**	**DTM**
Healthy	1.265 [0.117]	3.162 [0.852]	2.615 [0.803]
Injured	2.038 [0.490]	3.358 [0.691]	3.298 [0.295]

Across the duration of wrist simulation, the wrist FEM suffered the least deviation from the constant-sum constraint and the combined force error showed minimal variability (Fig. 3.8A). However, for the wrist RUD and

DTM, an elevated control error was observed when the wrist was proceeding back to the neutral position back from the ulnar extreme (Fig. 3.8B, C). This was thought to be associated with the sheer amount of muscle force adjustments happening during that period (Fig. 3.9). One possible reason could be the abrupt reduction in the moment arm of the FCR (Loren et al., 1996). However, in order to maintain a steady torque that continues to radially deviate the wrist, the controller would have to instruct a sharp rise in the force demand in the FCR as well as in other synergistic muscles. This likely led to further control instability as the cadaver wrist must remain dynamically balanced in the sagittal plane without compromising the muscle co-contraction prescribed through the constant-sum constraint, which might be too demanding for the force controller to respond at once.

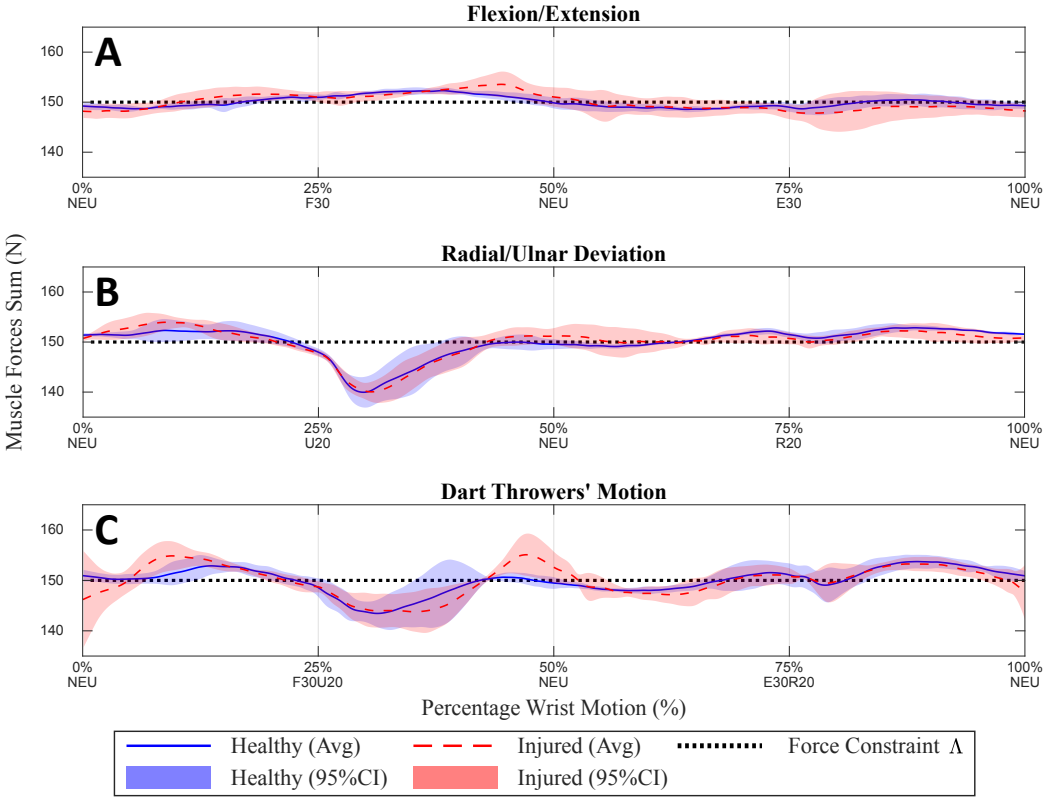

Figure 3.8: Average total muscle forces across the duration of **(A)** FEM, **(B)** RUD, **(C)** DTM, performed on seven wrists before and after ligament disruption. 95% CI of the force sums are shown as shaded regions. NEU: neutral, F: flexion, E: extension, U: ulnar deviation, R: radial deviation.

After the surgical introduction of ligament disruptions, the combined force error for all three types of wrist motion simulation saw a modest increase in both their means and standard deviations, indicating a deterioration in both accuracy and reproducibility. This was expected as these ligamentous structures provided crucial mechanical constraints that keep the intricate intercarpal movement and force balance of the bones within the carpus in check (Mayfield et al., 1976; Kauer, 1980; Ritt et al., 1995; Short et al., 1995). Since the apparent wrist motion is a mere superposition of the carpal bone motion, compromising of these stabilising ligaments would presumably cause the wrists to respond to the moment generated by the muscles in an unstable and unpredictable manner, affecting the nested position-force controller. But in spite of a slight increase in the combined force error, as shown in the previous section, accurate yet stable motion simulations were still achieved on the wrist specimens that sustained ligamentous disruptions representing the most severe case possible in later sections. Interestingly, muscle forces with a slightly different pattern than those adopted in their healthy states were required to perform the same set of wrist motion simulations on ligament-deficient wrists (Fig. 3.9). However, the discussion on why such an activation pattern was observed and what will be the possible implication on muscle's role in stabilising the wrist joint was deemed to go beyond the scope of the current validation study.

Repeatability-wise, owing to the viscoelasticity of the muscle-tendon units (Taylor et al., 1990), and the potential time-related changes in material properties caused by tissue degradation (Van Ee et al., 2000; King et al., 2000), one may surmise higher variability of the forces between different cycles of the simulated wrist movement. However, this was not the case, as the repeatability of the forces applied to any of the six muscle tendons did not experience a variation that exceeded 0.5 N (Table 3.5). This was comparable with the values reported for a recent finger motion simulator that possesses a similar construct (Haddara, 2017). On average, this error accounted for 2% of the forces on each muscle tendons, if the total load of 150 N was to be distributed equally. A smaller than 0.1 N

decline in the control repeatability was observed after the surgical release of the stabilising ligaments, and no substantial variations were observed in the repeatability of the force control outcome between the seven cadaver wrists tested. Therefore, in conclusion, the force control of the DWSA was proven to be valid and effective for both intact and ligament-deficient wrists and was therefore deemed adequate for the present study.

Table 3.5: Repeatability (averaged over all time increments) achieved for controlling the force in each wrist muscles for cadaveric wrist specimens (n = 7) in both healthy and injured states, during all three types of wrist motion simulations

Muscle	Force Repetability (N [SD])					
	FEM		**RUD**		**DTM**	
	Healthy	Injury	Healthy	Injury	Healthy	Injury
APL	0.108 [0.038]	0.201 [0.108]	0.199 [0.027]	0.213 [0.044]	0.152 [0.074]	0.156 [0.075]
ECR-L	0.078 [0.021]	0.094 [0.017]	0.131 [0.044]	0.152 [0.034]	0.203 [0.051]	0.189 [0.053]
ECR-B	0.176 [0.048]	0.250 [0.100]	0.143 [0.035]	0.214 [0.033]	0.272 [0.085]	0.284 [0.090]
ECU	0.156 [0.052]	0.283 [0.151]	0.300 [0.101]	0.379 [0.091]	0.199 [0.075]	0.252 [0.096]
FCR	0.138 [0.044]	0.227 [0.111]	0.187 [0.054]	0.234 [0.047]	0.172 [0.054]	0.199 [0.077]
FCU	0.158 [0.061]	0.238 [0.071]	0.266 [0.059]	0.364 [0.051]	0.418 [0.120]	0.403 [0.145]
AVG	0.135 [0.036]	0.215 [0.065]	0.204 [0.067]	0.259 [0.091]	0.236 [0.098]	0.247 [0.089]

Finally, to determine whether the muscle forces themselves were actually physiologically representative of the *in-vivo* cases, the normalised values of the forces exerted on tendons of the six wrist prime movers (as percentage contributions) were also included (Fig. 3.9). However, due to the shortage of EMG data on the contribution of individual wrist muscles in the current literature and the unavailability of advanced sensor technology that permits muscle forces to be accurately measured *in-vivo*, the muscle forces reported in previous studies remain mostly speculative. Moreover, as reviewed earlier, in some of the studies where a similar cadaveric simulation apparatus was involved, the wrist motion was recreated using either a pure position control strategy with empirically chosen, position-invariant antagonistic forces (Tong, 1985; Werner et al., 1996), or even a replica of the muscle force profiles that resultant from the position control (Erhart et al., 2012), rendering their results and inferences questionable. This was particularly evident in studies performed by Farr et al. (2013) and Dimitris et al. (2015), where the ECR-L was recruited with a force that almost exceeded its maximum tetanic tension (Loren et al., 1996; Gonzalez et al., 1997; Buchanan et al., 1993), and even dictated the entire FEM. In recent advancement of *in-vitro* wrist simulations, Iglesias (2015) came up with a cascaded control architecture where a force loop was coupled directly with a position loop. However, with neither the neuromuscular redundancy presented in the inverse dynamics problem nor the differences in the force-generating potentials of various muscles taken into account, it is not hard to realise that the outcome of such a control structure will still closely resemble that of the pure position control. Besides, frequent exclusions of the APL in cadaveric wrist simulations, a prominent wrist abductor muscle owing to its sizeable moment arm about the axis of RUD (Gonzalez et al., 1997) and was postulated to act as a competent "collateral ligaments" that offers dynamic stability (Kauer, 1980), would potentially lead to a set of muscle forces that are less representative of those *in-vivo*. Therefore, for the reasons stated, an extensive comparison with the existing literature was not considered meaningful.

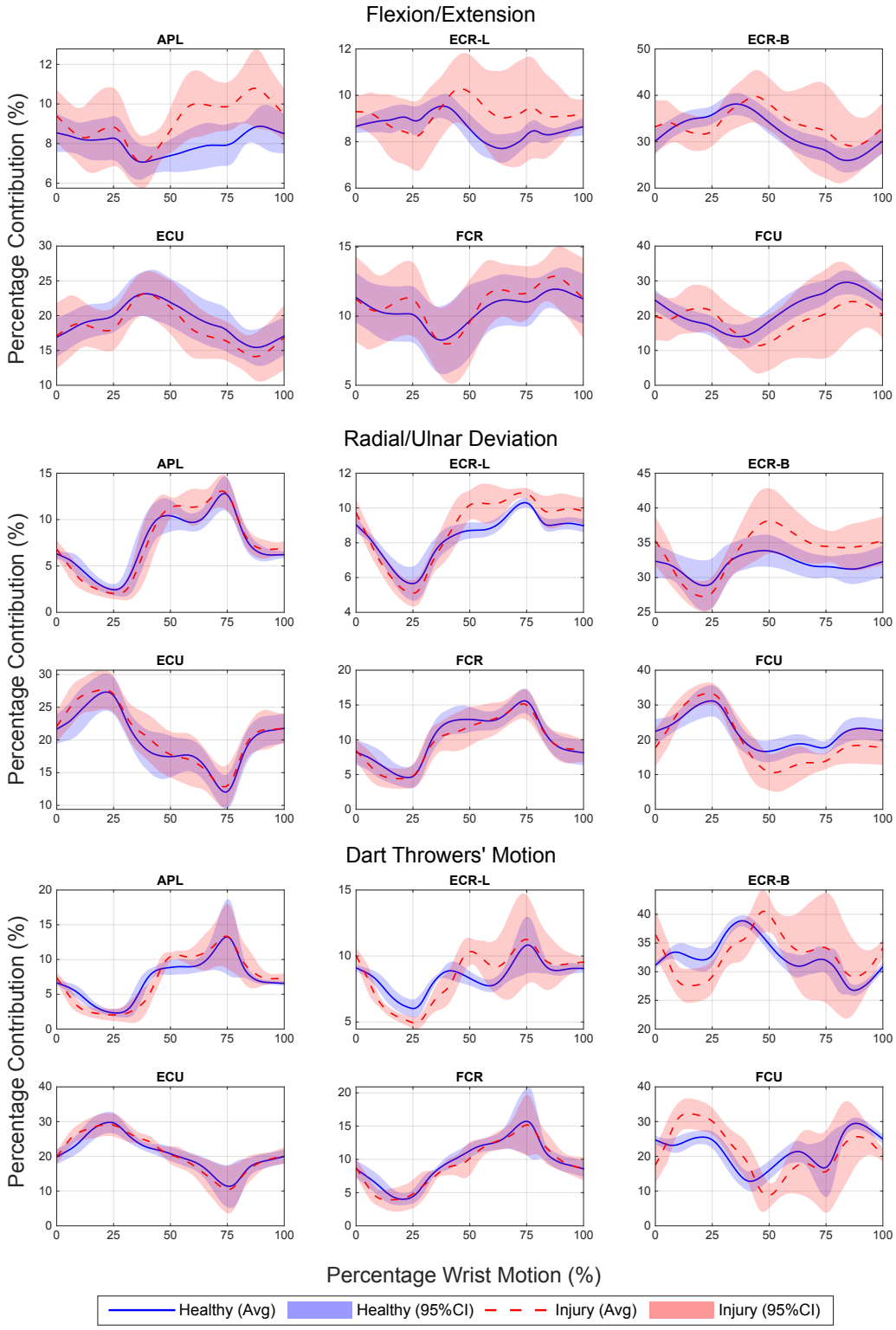

Figure 3.9: Percentage contribution of individual muscles during dynamic wrist motion simulations performed in seven wrists before and after ligament disruptions.

Nonetheless, the results showed a similar trend with those reported by Werner et al. (2010), especially the ones obtained during the dynamic simulation of FEM and DTM. Unfortunately, the force measurements of only two muscles, namely the FCR and FCU, were published in full in their study. Furthermore, despite the differences in the external loading condition and joint movement, the present muscle force measurements, especially the ones correspond to FEM, agree well with the EMG observations reported by Ricci et al. (2015), where the ECR-B and -L bundle, ECU and FCU showed an elevated level of activity during wrist motion. The dominance of the ECRB observed during wrist extension in the present study is in agreement with the consensus (Linscheid et al., 1991), whereas a slightly attenuated contribution of the ECU is thought to attribute to its inferior mechanical advantage in extending the wrist, despite their comparable force-generating capabilities (Horii et al., 1991; Loren et al., 1996; Gonzalez et al., 1997).

Although there may not be sufficient evidence to explicitly verify if muscle forces obtained in the present study were genuinely representative of those *in-vivo*, the method employed in their estimation during the control process, namely the static optimisation, has been studied and cross-validated extensively with measurements acquired by EMG (Heintz and Gutierrez-Farewik, 2007; Modenese et al., 2011; Lenaerts et al., 2008) and instrumented implant (Prilutsky et al., 1997; Heller et al., 2001; Navacchia et al., 2016), in the broader field of biomechanics. However, the implementation of this optimisation method in the present study is not without limitations. Since prior knowledge on the PCSA and moment arm of each muscle being considered is necessary to enable the computation, the final muscle force estimation is, therefore, likely to be influenced by errors and inaccuracies associated with these anatomical parameters. In the present study, a fixed set of muscle PCSAs sourced from the literature were employed for all cadaveric specimens without considering their potential subject-specific variations. In addition, due to absence of a comprehensive and consistent data set on the moment arms of the wrist prime movers, they were estimated in real-time using a simplified geometric approach (Section 2.2.3, Eq. 2.14), where wrist was mod-

elled as a 2-DOF universal joint with its axes of rotation being orthogonal to each other and fixed at the head of the capitate, in the present study. Since data on the anatomical path of the muscles were not readily available, no "wrapping" of the muscles could be accounted for, and their line-of-action had to be determined according to the estimated attachment cites on the proximal and distal segments. This may be considered no different than extrapolating the moment arms solely based on the current joint position and irrespective of the actual anatomy. Hence, like all other extrapolated quantities, the accuracy of the moment arm deteriorates quickly when the wrist moves further away from its neutral position, where the initial moment arm data was taken. And this was more pronounced for the muscle whose moment arm exhibits a non-linear correlation with joint positions. However, despite the fact that this approach is rather crude, it is arguably the only feasible alternative to those experimental approaches such as the centre of rotation or tendon excursion method for determining subject-specific muscles moment arms. Finally, the over-simplification in modelling the human neuromuscular co-contraction by forcibly requiring the muscle forces produced by the static optimisation to possess a constant algebraic sum during the entire course of dynamic simulation may also represent a source of error. Although the use of a single constant, Λ, may not be sufficient for the precise parametrisation of the muscle co-contraction, it enabled variable antagonistic muscle forces to be estimated systematically and dynamically in response to those of the agonists. This rendered the activation pattern in present simulation more physiologically meaningful than those generated with prescribed values (Tong, 1985; Werner et al., 1996; Erhart et al., 2012; Iglesias, 2015), superimposed movements (Fraysse et al., 2014), or position invariant agonistic-antagonistic force ratios (Sharkey and Hamel, 1998; Johnson et al., 2000; Dunning et al., 2003; Ferreira et al., 2010; William Giles et al., 2014).

3.3 Validation of the Biplane X-Ray Fluoroscopy System

The reliability of the CWTP implies not only the capability to synthesise wrist motion on cadaveric specimens that are both accurate and repeatable but also the ability to truthfully capture the simulated movement to enable further analysis. Therefore, as one of the most important measurement instruments integrated into the CWTP, the custom-developed biplane X-ray fluoroscopy system was assessed for its accuracy and precision in characterising 6-DOF kinematics of the carpal bones.

However, in the present study, the rigid body motion of the carpal bones was not measured directly but estimated based on the movement of bone markers, using principles of marker-based RSA described previously (Section 2.3.2). Needless to say that the most immediate results obtained by the biplane X-ray fluoroscopy system were merely the radiographs recorded in two different planes during the course of the simulated dynamic wrist movement. To extract three-dimensional motion trajectories of the bone markers embedded inside the carpal bones, each frame of the radiographs acquired was subjected to a series of processing. As introduced previously, this involved correction for distortions in the acquired radiographs, the digitisation of the marker centroids, and the triangulation of the data obtained from the two imaging planes. But owing to the cascading nature of this process, errors and uncertainties that are inherent to numerical procedures involved in each step are likely to accumulate and propagate throughout the pipeline, affecting the three-dimensional locations reconstructed for each of the bone markers. And since estimating the 6-DOF kinematics of a carpal bone utilises the movement of at least three non-collinear bone markers, the quality of the final result may be affected by the errors associated with each individual constituent markers. Moreover, given the non-linearity of the numerical operations employed during the calculations such as the SVD, different combinations of marker errors may also have an influence on the final outcome, further complicating the assessment process.

To this end, the validation study was split into two parts. Firstly, the accuracy of pinpointing the three-dimensional location of a single marker in space was investigated. But since the marker was triangulated in an arbitrary coordinate system determined by the placement of the calibration phantom, it was challenging to compare its position with some predefined landmarks in another frame of reference. Instead, the assessment was conducted using a commonly adopted approach, where the distances between two markers (hereafter referred to as the 'inter-marker distance') calculated based on their stereo-photogrammetrically triangulated locations in space were compared with a gold standard (You et al., 2001; Anderst and Tashman, 2003; Brainerd et al., 2010; Kaptein et al., 2011; Guan et al., 2016; Knorlein et al., 2016). The rationale of using the inter-marker distance in the assessment is built upon the assumption of rigidity, where the distance between markers fixed on a non-deforming body shall remain constant, and any violation of this condition, as reflected by the disagreement between a reference value and those measured by the biplane fluoroscopy system or the variations of the measurement itself between repeated observations, indicates presence of an error. This error, despite being attributed to the position inaccuracies in both markers, provides an approximation of the upper bound of the discrepancies in locating a single marker. The second part of the study investigated the question of how the error associated with individual markers propagate to affect the kinematic estimation of a rigid body overall. However, it was not a trivial task to synthesise highly accurate rigid body motion that can be used as the gold standard for the comparison, for instance, a precise rotation that occurs around a specific axis in space, an *in-silico* experiment, designed for a close replication of the actual experimental conditions, was performed to facilitate this analysis. Finally, it is worth mentioning that the accuracy and precision obtained for the present system were inclusive of those associated with all necessary intermediate processing.

3.3.1 Inter-Marker Distances

Methods

To quantify the accuracy and precision of the present biplane X-ray fluoroscopy system in measuring the three-dimensional position of a single marker, two different studies were performed to compare the inter-marker distances between the reconstructed marker locations and those of a standard reference.

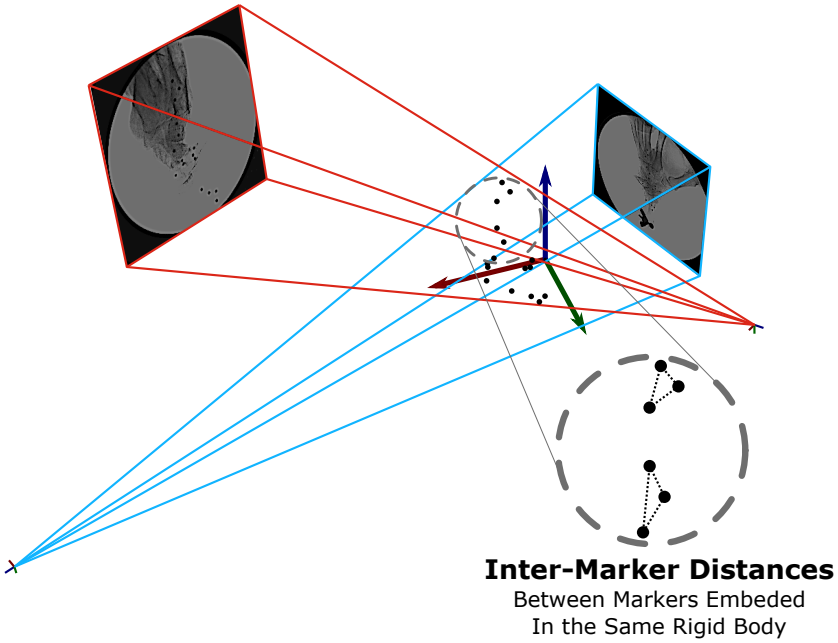

Figure 3.10: Schematics illustrating the marker triangulation process and the concept of inter-marker distance

In the first part of the study, the biplanar radiographs simultaneously recorded during dynamic wrist simulations performed in the validation study of the DWSA were analysed to obtain three-dimensional movement trajectories for each individual radio-opaque markers (hereafter referred to as the *in-situ* study). The inter-marker distances (Fig. 3.10) were then calculated for the marker clusters surgically implanted into the radius, capitate, scaphoid and lunate respectively. Finally, these results were compared with their gold-

standard measurements, which were extracted based on their volumetric CT scans. As mentioned, the CT scan was performed before each dynamic wrist simulation and was conducted in the axial direction using a Siemens Biograph mCT, with an acquisition matrix of 512×512 px, an in-plane pixel size of 0.2852 mm, and a slice thickness and increment of 0.6 mm and 0.1 mm, respectively. Finally, the accuracy was calculated as the pairwise RMS differences between the gold-standard and those calculated based on the marker locations as triangulated from the biplanar radiographs. The precision, on the other hand, was quantified using the standard deviation of the inter-marker distances obtained for each pair of the markers embedded in the same rigid body, similar to the approach adopted by Brainerd et al. (2010) and Guan et al. (2016).

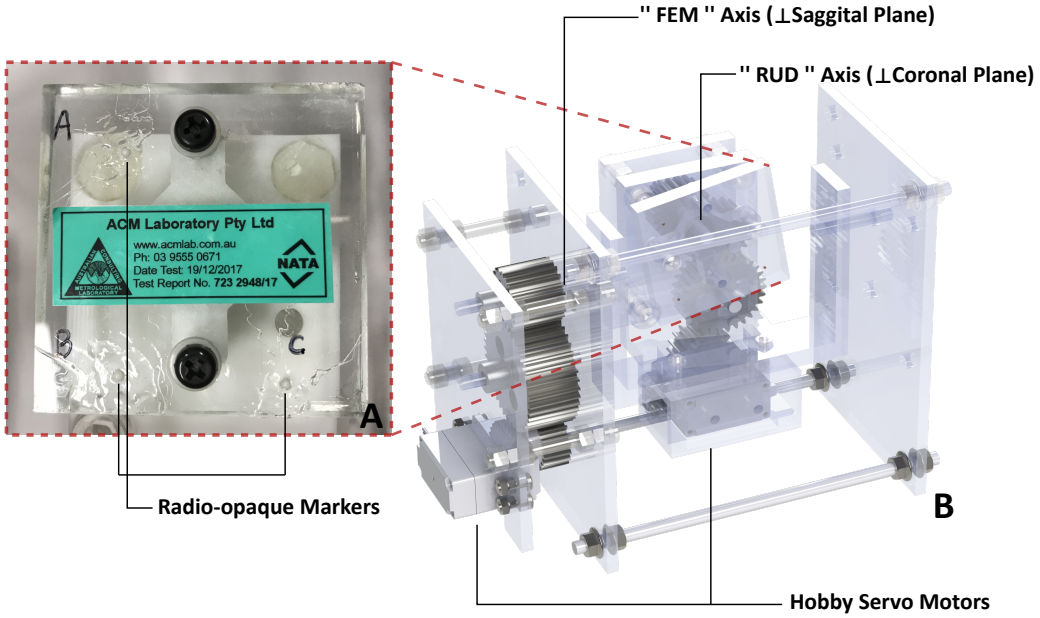

Figure 3.11: **(A)** Photograph of the validation plate and **(B)** CAD model of the custom validation gimbal

Additionally, a second experiment was performed to confirm the results obtained in the *in-situ* validation. A triad of 1 mm radio-opaque marker beads made of zirconium dioxide was glued onto one side of an 8 mm thick glass plate using ultra-clear epoxy resin (Fig. 3.11A, and referred to as the 'validation plate' hereafter). The relative positions of these markers were

measured in-plane by means of an optical coordinate measurement machine (CMM) in an accredited metrology facility (A.C.M. Laboratory, Victoria, Australia) within an accuracy of ± 0.005 mm (detailed report on the measurement results can be found in Appendix A.11). The inter-marker distances calculated based on the coordinate measurements of the validation plate were used as the gold-standard in this part of the study. This validation plate was then rotated in the capture volume by a custom-built 2-DOF validation "gimbal" (Fig. 3.11B). The goal of this device was primarily to simulate wrist rotations that occur in the sagittal and coronal planes, mimicking FEM and RUD. Hence, miniature servo motors, similar to the ones used for remotely adjusting the of the camera focus, were installed in the fixed outer frame and the rotating inner stage of the gimbal, respectively, acknowledging the stationary and the floating axes of rotation as defined in Grood and Suntay's convention (Grood and Suntay, 1983). And in order to capture obstruction-free radiographs of the validation plate, the validation gimbal was constructed primarily using 3D-printed components.

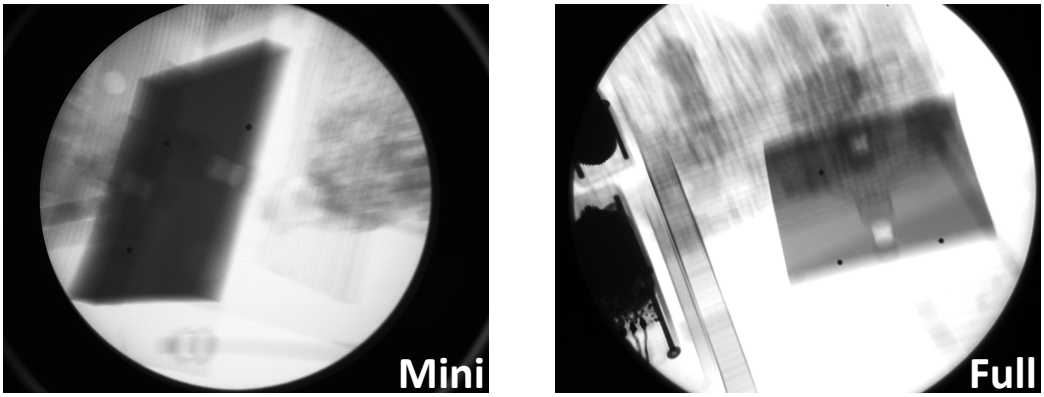

Figure 3.12: Sample radiographs of the validation plate and gimbal assembly

Experiments were carried out both statically and dynamically. In the static experiment, the validation gimbal was rotated randomly in both DOFs to assume 20 different "wrist postures", biplanar radiographs were taken in each of these static positions. For the dynamic experiment, the validation plate was subjected to an uninterrupted sequence of sinusoidal rotations, namely the FEM and RUD was simulated respectively in isolation first, then

followed by their superposition. The sequence was repeated twice, and the sinusoidal motion in each phase of the sequence was executed with a period of 8 seconds. This was chosen partly as an attempt to investigate if motion with elevated speed and acceleration would affect the measurement accuracy of the biplane X-ray fluoroscopy system. The simulated rotation of the validation plate was again recorded with a frame rate of 25 Hz. The accuracy and precision analysis were performed in the same manner as in the first part of this study.

Results and Discussion

For the *in-situ* study, reconstruction of the 66,739 frames of biplanar radiographs obtained from the previous validation experiments resulted in a total of 799,480 pairwise comparisons of the inter-marker distances. This included the biplanar radiographs recorded for all three types of wrist motion as simulated on each of the seven cadaveric specimens. In addition, since the detachment of the scapholunate ligamentous constraints should not alter the relative locations of the bone markers implanted into the same rigid body, the radiographs collected both before and after the simulated injury were utilised.

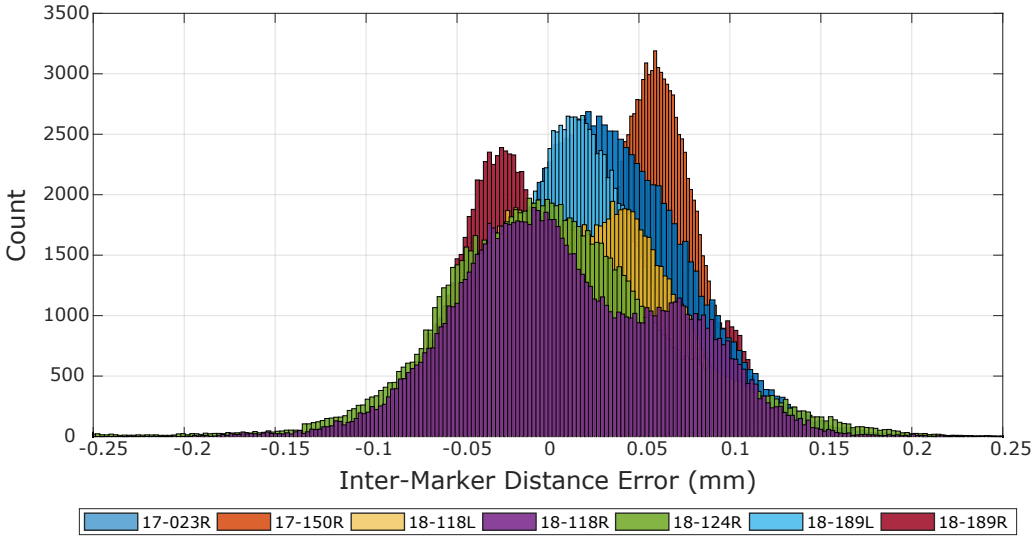

Figure 3.13: Histograms of the inter-marker distance errors recorded for each cadaver

For the marker clusters implanted in each of the cadaver wrists, the discrepancies between their photogrammetrically measured inter-marker distances and the gold-standards provided by the CT scans were plotted (Fig. 3.13). It was evident that the error distributions were almost bell-shaped or normal for most of the specimens, with the majorities fell between an interval of -0.05 to 0.1 mm. However, the likelihood of error was mainly biased towards the positive end, indicating the present biplane X-ray

fluoroscopy system along with the subsequent image processing tended to systematically underestimate the actual location of the bone markers. The resulting accuracy and precision of the present system (Table 3.6) compared well with those previously reported (Tashman and Anderst, 2003; Brainerd et al., 2010; Kaptein et al., 2011; Guan et al., 2016; Mozingo et al., 2018).

Table 3.6: Accuracy and precision of the present biplane fluoroscopy system as characterised by the *in-situ* and stand-alone validation experiments

		Accuracy (RMS diff., mm [SD])	**Precision** (std., mm [SD])
Wrists (*in-situ*)		0.057 [0.009]	0.026 [0.004]
Validation Plate	Static	0.059	0.027
	Dynamic	0.070	0.036

For the standalone experiment performed with the validation plate, the static and dynamic trials resulted in 60 and 3,909 sets of pairwise comparisons of the inter-marker distances, respectively. The system accuracy and precision found in the *in-situ* study was in good agreement with those obtained from the static trial. Despite still being sub-millimetre and considered acceptable, the slightly elevated error level of the dynamic trial was believed primarily due to the inaccuracy in digitising the marker centroid on radiographs that suffered from a more noticeable motion blur, which was caused by the accelerated movement of the validation gimbal. However, since the results in this part of the study was designated as a retrospective verification for those obtained in the previous *in-situ* study, and given the similarity between the two, those results obtained in the *in-situ* study were considered valid and representative of the conditions likely to occur in an actual experimental setting. Therefore, the totality of the error distribution obtained for each wrist in the *in-situ* study was used as the basis or the starting point for simulating their emergence and propagation through the steps of kinematic estimation in the next section.

3.3.2 Rigid Body Kinematics

Methods

In order to assess the accuracy and precision of the present biplane X-ray fluoroscopy system in measuring 6-DOF rigid body kinematics, the position error associated with each individual marker must be "translated" further into the combined effect on the final kinematic estimation of the moving body as a whole. However, a conventional comparative study was proven challenging, as with the available instrumentations, it was a non-trivial task to experimentally synthesise rigid body motion that possesses a sufficiently high degree of accuracy to be qualified as the benchmark or the gold-standard for the comparison. Instead, a Monte Carlo simulation was performed *in-silico* to interrogate how the inaccuracies in the marker positions would interact and propagate through the flow of the whole pose estimation process to affect the final kinematics obtained for the rigid body.

As mentioned previously, the discrepancy in the inter-marker distance measurement provided a useful approximation for the inaccuracy associated with the three-dimensional location of an individual marker in the worst-case-scenario. However, it was evident that instead of having a single fixed value, such a discrepancy demonstrated a whole spectrum of variations in an experimental setting (Section 3.3.1). Therefore, a Gaussian mixture model (GMM) was fitted to the histogram formed by all observations to better approximate their probabilistic distribution (Fig. 3.14). A sample was drawn at random from the resultant distribution and used as the "disturbance" to perturb the "ground-truth" position of a marker, whenever its position was being "measured" virtually by the biplane X-ray fluoroscopy system at that particular iteration of the computer simulation. However, to simulate the measurement noise in the x-, y- and z- location of a single marker, this randomly sampled disturbance, which is a distance in the three-dimensional space by nature, must be decomposed accordingly. By assuming the isotropy of the measurement noise, it is not hard to realise that the perturbed marker location will form a spherical surface that centred at the ground-truth and

characterised by a radius equal to the disturbance. A unit vector in 3D was randomly generated to help in pinpointing the final perturbed location for that specific marker. An asterisk in superscript was used hereafter to indicate values that had been subjected to this artificial process of perturbation or had been derived based on perturbed quantities. For instance, ${\boldsymbol{P}^{*}}_{A}^{\mathcal{R}_{\mathrm{BP}}}$, denotes the perturbed locations of the marker cluster implanted in Bone A as measured in the coordinate system $\mathcal{R}_{BP}$. Or alternatively, ${}^{\mathcal{R}_R}{\boldsymbol{T}^{*}}_{\mathcal{R}_A}$, stands for the transformation from $\mathcal{R}_A$ to $\mathcal{R}_R$, but was calculated using perturbed marker locations. Additionally, unless otherwise specified, a variable that is free of these annotations denotes its unperturbed or ground-truth value.

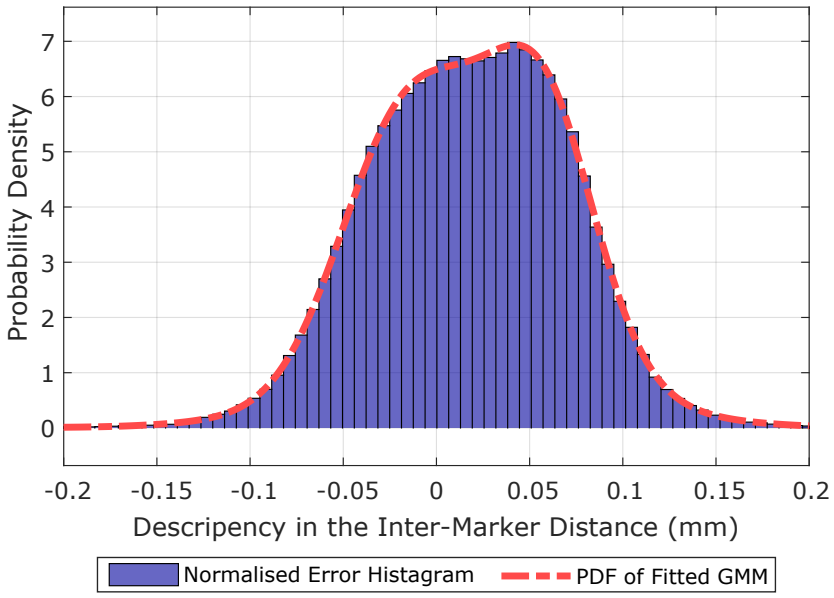

Figure 3.14: A GMM being fitted to the combined error histogram

The computer simulation was conducted with a simplified kinematic model consisted of only two rigid bodies, namely the radius as the proximal segment and the distally situated Bone A, acting as an imaginary mock-up for one of the carpal bones (Fig. 3.15). To realistically emulate the processes involved in the pose estimation, the simulation included two separate parts. As described previously (Section 2.2.2.1), unlike the bones that possess distinguishable and palpable boney landmarks, the LCS of the irregularly shaped carpal bones can only be found by duplicating the orientation of the radial co-

ordinate system at their respective volumetric centres when the wrist assumes its neutral position on a global scale. However, since it was not a trivial

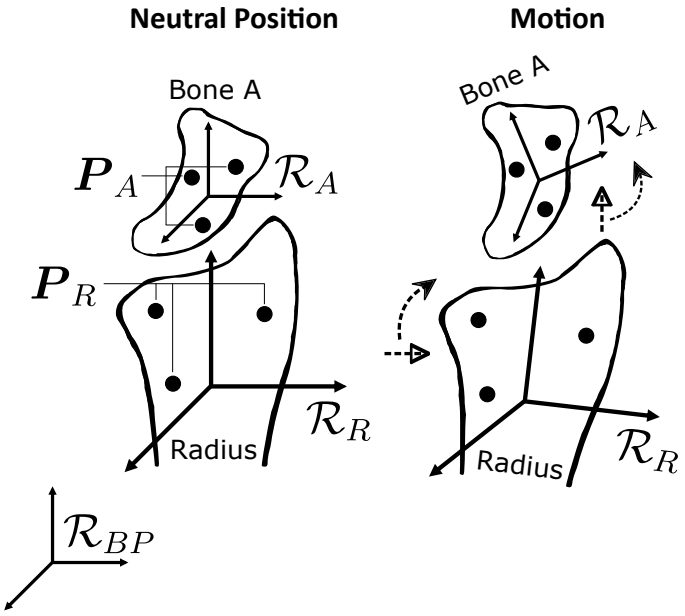

Figure 3.15: Schematics of the mock-up wrist model used in the simulation

task to obtain volumetric scans of the wrist specimen placed precisely in its neutral position, an additional correction step was introduced. In brief, this involved imaging of the wrist specimen using the biplane X-ray fluoroscopy system, after it had been actively moved by the DWSA into the desired neutral position. Hence, according to the three-dimensional positions of the bone markers, which were obtained via stereo-photogrammetric triangulation of the radiographs, the volumetric CT scan was virtually reconfigured to restore the neutral alignment of the wrist, facilitating the LCS definition process for the carpal bones. Given the importance of the LCS definition to the accuracy of the subsequent kinematic calculation and owing to the involvement of the biplane X-ray fluoroscopy system, the error associated with marker positions as introduced in this very initial stage of the analysis must be considered. Therefore, the first part of the simulation study was designed with this particular circumstance in mind. The process flow of the computer simulation was visualised in Fig. 3.16.

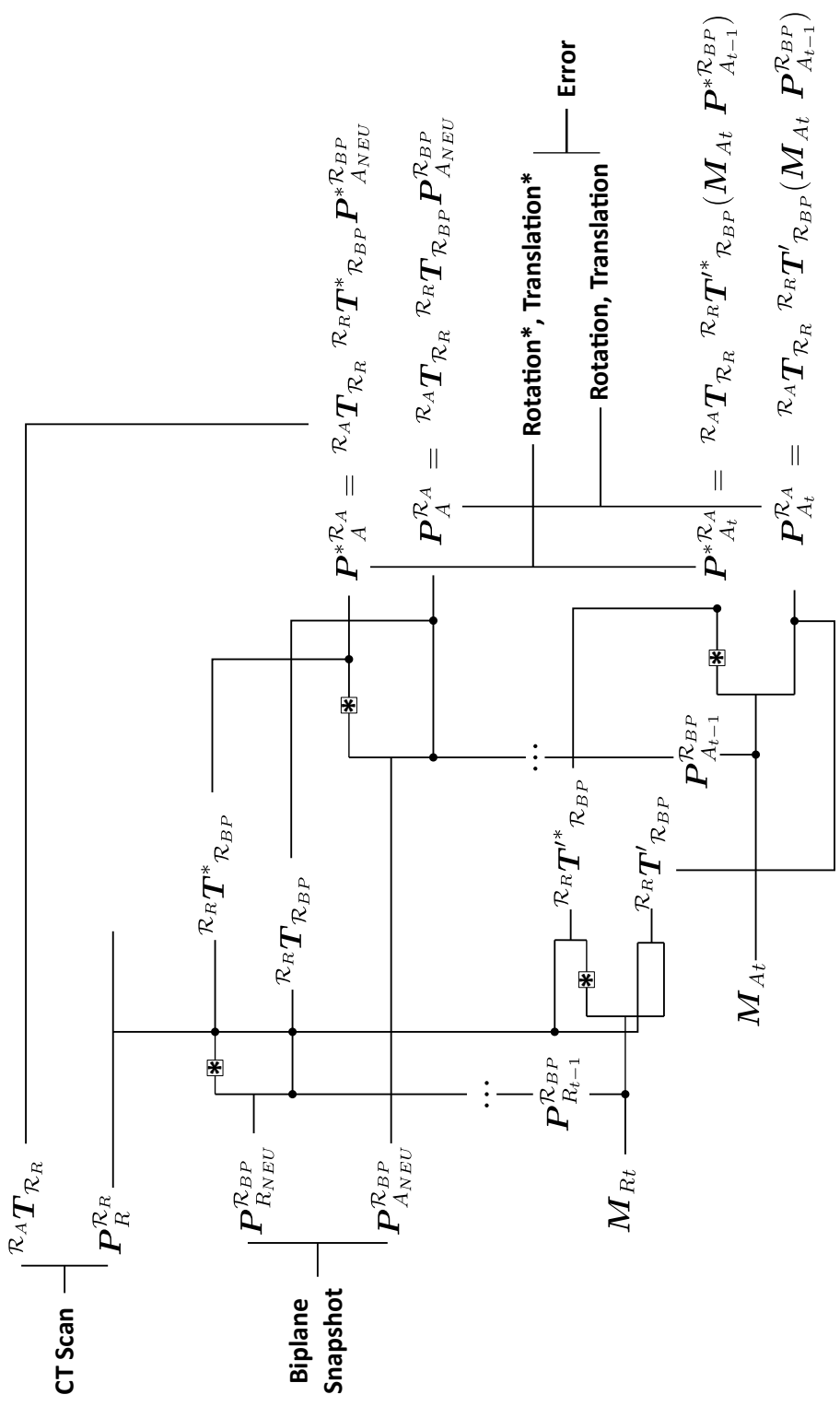

Figure 3.16: Process flow of the computer simulation, $*$ denotes the process of artificially contaminating the variable with noise. The noise was randomly generated according to the distribution of the inter-marker distance errors

For a marker-based kinematic analysis, the purpose of defining the LCS for each of the carpal bones is to allow for the placement of the bone markers to be determined locally in relation to the bones in which they are embedded. This is essentially finding $\boldsymbol{P}_A^{\mathcal{R}_A}$ and $\boldsymbol{P}_R^{\mathcal{R}_R}$, where $\boldsymbol{P}_A$ and $\boldsymbol{P}_R$ denote the collective positions of the marker clusters implanted in Bone A and the radius, respectively. While $\mathcal{R}_A$ and $\mathcal{R}_R$ denote their locally defined coordinate systems. Since the LCS of the radius can be defined solely based on its boney landmarks, which are distinguishable in the volumetric CT scan, $\boldsymbol{P}_R^{\mathcal{R}_R}$ is essentially a known quantity. Furthermore, biplanar radiographic snapshots were taken for the wrist placed in its neutral position to assist the LCS definition process in the aforementioned correction step. This means the three-dimensional positions of the two marker clusters would also become available at that stage, but as they were measured by the biplane X-ray fluoroscopy system, their observed positions would potentially deviate from the groud-truth. Hence, to recreate this process during the simulation, the three-dimensional positions of the two marker sets as measured by the biplane X-ray fluoroscopy system were first generated at random, denoted as $\boldsymbol{P}_{A_{NEU}}^{\mathcal{R}_{BP}}$ and $\boldsymbol{P}_{R_{NEU}}^{\mathcal{R}_{BP}}$, respectively. These error-free marker positions were perturbed to produce $\boldsymbol{P}^{*\mathcal{R}_{BP}}_{A_{NEU}}$ and $\boldsymbol{P}^{*\mathcal{R}_{BP}}_{R_{NEU}}$, using values randomly sampled from the discrepancy distribution obtained from the previous study on inter-marker distances. In order to obtain $\boldsymbol{P}_A^{\mathcal{R}A}$, a chain of coordinate transformations is required. In the error-free case, this chain of transformations can be written as $\boldsymbol{P}_A^{\mathcal{R}_A} = {}^{\mathcal{R}_A}\boldsymbol{T}_{\mathcal{R}_R}\,{}^{\mathcal{R}_R}\boldsymbol{T}_{\mathcal{R}_{BP}}\boldsymbol{P}_{A_{NEU}}^{\mathcal{R}_{BP}}$, where ${}^{\mathcal{R}_R}\boldsymbol{T}_{\mathcal{R}_{BP}} \in \mathbb{R}^{4\times4}$ is the matrix that transforms the coordinate system used by the biplane system, $\mathcal{R}_{BP}$, to the LCS of the radius $\mathcal{R}_R$, and can be calculated based on the correspondence between $\boldsymbol{P}_{R_{NEU}}^{\mathcal{R}_{BP}}$ and $\boldsymbol{P}_R^{\mathcal{R}_R}$; whereas ${}^{\mathcal{R}_A}\boldsymbol{T}_{\mathcal{R}_R} \in \mathbb{R}^{4\times4}$ relates the LCS of Bone A to that of the radius. However, since the LCS of the carpal bone is defined to be a simple offset of that of the radius, this transformation was, therefore, a simple translation by nature and was assumed to be an error-free constant. On the other hand, the chain of transformations can be similarly derived for the perturbed case, namely, $\boldsymbol{P}^{*\mathcal{R}_A}_{A} = {}^{\mathcal{R}_A}\boldsymbol{T}_{\mathcal{R}_R}\,{}^{\mathcal{R}_R}\boldsymbol{T}^*_{\mathcal{R}_{BP}}\boldsymbol{P}^{*\mathcal{R}_{BP}}_{A_{NEU}}$, where ${}^{\mathcal{R}_R}\boldsymbol{T}^*_{\mathcal{R}_{BP}}$ is estimated using the correspondence between $\boldsymbol{P}^{*\mathcal{R}_{BP}}_{A_{NEU}}$ and $\boldsymbol{P}_R^{\mathcal{R}_R}$ in a similar fashion.

After finding $\boldsymbol{P}_{A}^{\mathcal{R}_A}$ and $\boldsymbol{P}^{*\mathcal{R}_A}_{A}$, the three-dimensional locations of the marker clusters, namely $\boldsymbol{P}_{A_{NEU}}^{\mathcal{R}_{BP}}$ and $\boldsymbol{P}_{R_{NEU}}^{\mathcal{R}_{BP}}$, were then subjected to a randomly generated motion series, containing 1,000 frames of combined rotational and translational transformations. However, to ensure the simulation was representative of the actual experiment, these random movements were generated in a way such that they would not cause any markers on the rigid body to traverse a distance that exceeds 10 mm between adjacent frames. To enable the final pose estimation, a similar series of coordinate transformation was applied to the marker locations obtained after the simulated movement. The error-free position of the markers implanted in Bone A is $\boldsymbol{P}_{A_t}^{\mathcal{R}_A} = {}^{\mathcal{R}_A}\boldsymbol{T}_{\mathcal{R}_R}\,{}^{\mathcal{R}_R}\boldsymbol{T'}_{\mathcal{R}_{BP}}(\boldsymbol{M}_{At}\ \boldsymbol{P}_{A_{t-1}}^{\mathcal{R}_{BP}})$, where $\boldsymbol{P}_{A_{t-1}}^{\mathcal{R}_{BP}}$ is the location of the marker cluster embedded in Bone A expressed in $\mathcal{R}_{BP}$, in the previous frame, $t-1$; $\boldsymbol{M}_{At} \in \mathbb{R}^{4\times4}$ is the homogenous transformation corresponding to the current movement simulated for Bone A; ${}^{\mathcal{R}_R}\boldsymbol{T'}_{\mathcal{R}_{BP}}$ is the "updated" transformation, relating $\mathcal{R}_{BP}$ with the $\mathcal{R}_R$ in the current frame. This transformation can be determined using the correspondence between the "moved" radius markers, $\left(\boldsymbol{M}_{Rt}\boldsymbol{P}_{R_{t-1}}^{\mathcal{R}_{BP}}\right)$ and $\boldsymbol{P}_{R}^{\mathcal{R}_R}$. Again, $\boldsymbol{P}_{R_{t-1}}^{\mathcal{R}_{BP}}$ denotes the location of the radius markers as observed in $\mathcal{R}_{BP}$ in the frame $t-1$, and $\boldsymbol{M}_{Rt} \in \mathbb{R}^{4\times4}$ is the transformation corresponding to the random movement applied for the radius in the current frame. On the other hand, the perturbed location of the marker cluster designated for Bone A can be calculated using $\boldsymbol{P}^{*\mathcal{R}_A}_{A_t} = {}^{\mathcal{R}_A}\boldsymbol{T}_{\mathcal{R}_R}\,{}^{\mathcal{R}_R}\boldsymbol{T'}^{*}_{\mathcal{R}_{BP}}(\boldsymbol{M}_{At}\ \boldsymbol{P}^{*\mathcal{R}_{BP}}_{A_{t-1}})$, with the perturbed ${}^{\mathcal{R}_R}\boldsymbol{T'}^{*}_{\mathcal{R}_{BP}}$ determined based on the correspondence between $\left(\boldsymbol{M}_{Rt}\ \boldsymbol{P}^{*\mathcal{R}_{BP}}_{R_{t-1}}\right)$ and $\boldsymbol{P}_{R}^{\mathcal{R}_R}$. Finally, by registering $\boldsymbol{P}_{A}^{\mathcal{R}_A}$ to every $\boldsymbol{P}_{A_t}^{\mathcal{R}_A}$, and $\boldsymbol{P}^{*\mathcal{R}_A}_{A}$ to $\boldsymbol{P}^{*\mathcal{R}_A}_{A_t}$, two sets of transformation matrices were obtained. Based on the method introduced earlier (Eq. 2.2-2.4), these matrices were further decomposed into measures of the rigid body rotations and translations. By comparing the 6-DOF kinematics obtained in the perturbed case with those of the error-free, the effect of the inaccuracy associated with the position of each marker on the final kinematic outcome of the rigid body was thus quantified.

Results and Discussion

Ten million frames were simulated, resulted in a total of thirty million pair-wise comparisons between values obtained through error-free and perturbed pipelines for all three rotational as well as translational components of the 6-DOF kinematics (Fig. 3.17). On average, the RMS error in estimating the rotation and translation of a rigid body, in the presence of measurement inaccuracies associated with the current biplane X-ray fluoroscopy system and all necessary processing steps, was 0.172° and 0.0426 mm, respectively. These errors were considered negligible.

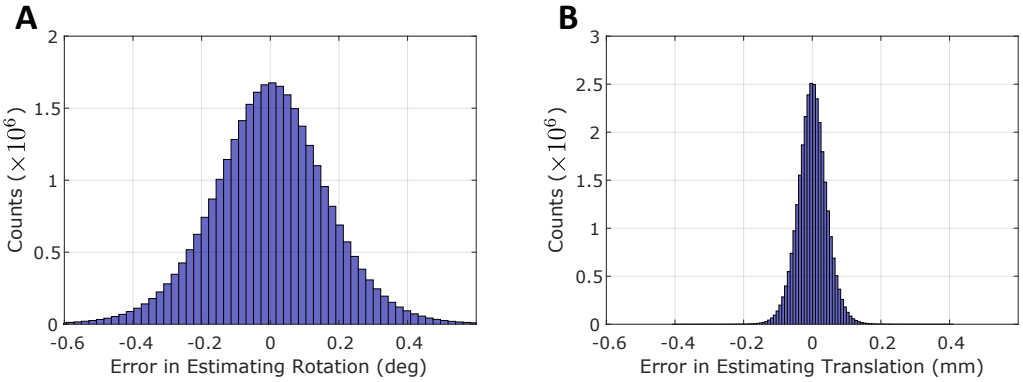

Figure 3.17: Histogram of the errors in estimating the **(A)** rotational and **(B)** translational rigid body kinematics

To date, most studies validated their biplane X-ray fluoroscopy systems solely based on inaccuracies in the inter-marker distances or inscribed angles (angles included between vertices connecting pairs of markers), and only a handful of studies have actually looked at the error in estimating the kinematics of an integral body using the potentially noisy marker locations as measured by such systems. Hurschler et al. (2008) reported a mean accuracy of 0.078° and 0.02 mm in measuring the orientation and three-dimensional location of prosthetic tibial components using marker-based RSA. In the study performed by Miranda et al. (2011), two cylindrical polycarbonate phantoms with a total of twelve tantalum markers embedded were rotated and translated by highly accurate positioning instruments while having their rigid body motion simultaneously tracked by a similar biplane fluoroscopy

system. They found the marker-based technique was capable of tracking rigid body motion to within 0.1° and 0.1 mm under both static and dynamic conditions. Iaquinto et al. (2014) validated their setup with a similar approach, where a custom 'bead wand' was translated and rotated with precisely known increments in the capture volume and found a rotational and translational accuracy of 0.083° and 0.094 mm, respectively.

However, this study was not without limitations. First of all, unlike conventional validation experiments, the present study was conducted purely *in-silico* with virtually simulated rigid body movements. Secondly, the spatial configuration of the markers was known to affect the accuracy of the final kinematic measurements (Söderkvist and Wedin, 1993). However, this was neglected and the bone markers were assumed to be isotropically distributed inside the rigid body during the present simulation experiment. This may not be entirely true under the actual experimental setting, as the markers were implanted manually into the carpal bones by a medical professional under fluoroscopic guidance. Their configuration was designed on-site by the surgeon to best suits the anatomy of the bones while manifesting minimal foreseeable occlusions. Finally, the magnitude and speed of the rigid body motion simulated in the present validation experiment were was exclusively representative of the ones adopted in studies presented in later chapters. Therefore, the validation results reported here may not be applicable in cases where the tracking of more rapid bone motion is to be expected.

3.4 Joint System Validation of the CWTP

Methods

With the DWAS and the biplane X-ray fluoroscopy system separately validated in previous sections, a final validation study was conducted to ascertain the CWTP as a whole is capable of delivering reliable kinematics measurement of the carpal bones. The word 'delivering' was used to reflect the fact that the carpal bone kinematics "produced" by the platform was essentially measured from the global apparent movement simulated in cadaver wrists. Since the wrist simulation was facilitated entirely at the macroscopic scale, no direct control was implemented to regulates the kinematics on the carpal bone level. Therefore, to ensure the validity of the final kinematics outcome, accuracy requirements had to be met within a very tight boundary, in both the synthesis of the global wrist motion and the measurement of this motion at the microscopic level. However, in the present context, it was deemed more appropriate to study the repeatability of the resultant carpal bone kinematics rather than focusing on its consistency or "correctness" as compared to the existing literature.

The validation approach taken was similar to the previous assessment of the control of global wrist motion (Section 3.2.1). Specifically, for each of the dynamic wrist simulations performed, the biplanar radiographs were reconstructed to obtain the 6-DOF kinematics of the scaphoid, lunate, and capitate, as measured with respect to the radius. For each of the selected carpal bones, this included three Euler angles correspond to the consecutive $Z - X' - Y''$ rotations and the translations of its volumetric centroid in 3D. To facilitate the repeatability analysis, the 'Frame Start Trigger' signals of the cameras, recoded alongside the image acquisition (Section 2.3.1.2), were interpreted to allow the temporal values of the carpal bone kinematics to be normalised. The carpal bone kinematics were linearly interpolated at 0.2% intervals (i.e. $100\%/(20\text{ s} \times 25\text{ Hz})$ to avoid excessive resampling) from 0 to 100% of a single movement cycle (Fig. 3.18). For each of the six

kinematic quantities of each selected carpal bones, the standard deviations of the data points that correspond to the same percentages of wrist motion were calculated, and their average was used for qualifying the repeatability corresponding to that particular DOF. Finally, these values were averaged across all rotational and translational DOFs to obtain an "overall" repeatability measure in characterising the two different modes of carpal bone motion, respectively. Finally, similar to other validation studies, the analysis was carried out for all three types of wrist motion, performed both before and after the introduction of the surgically simulated ligament disruptions.

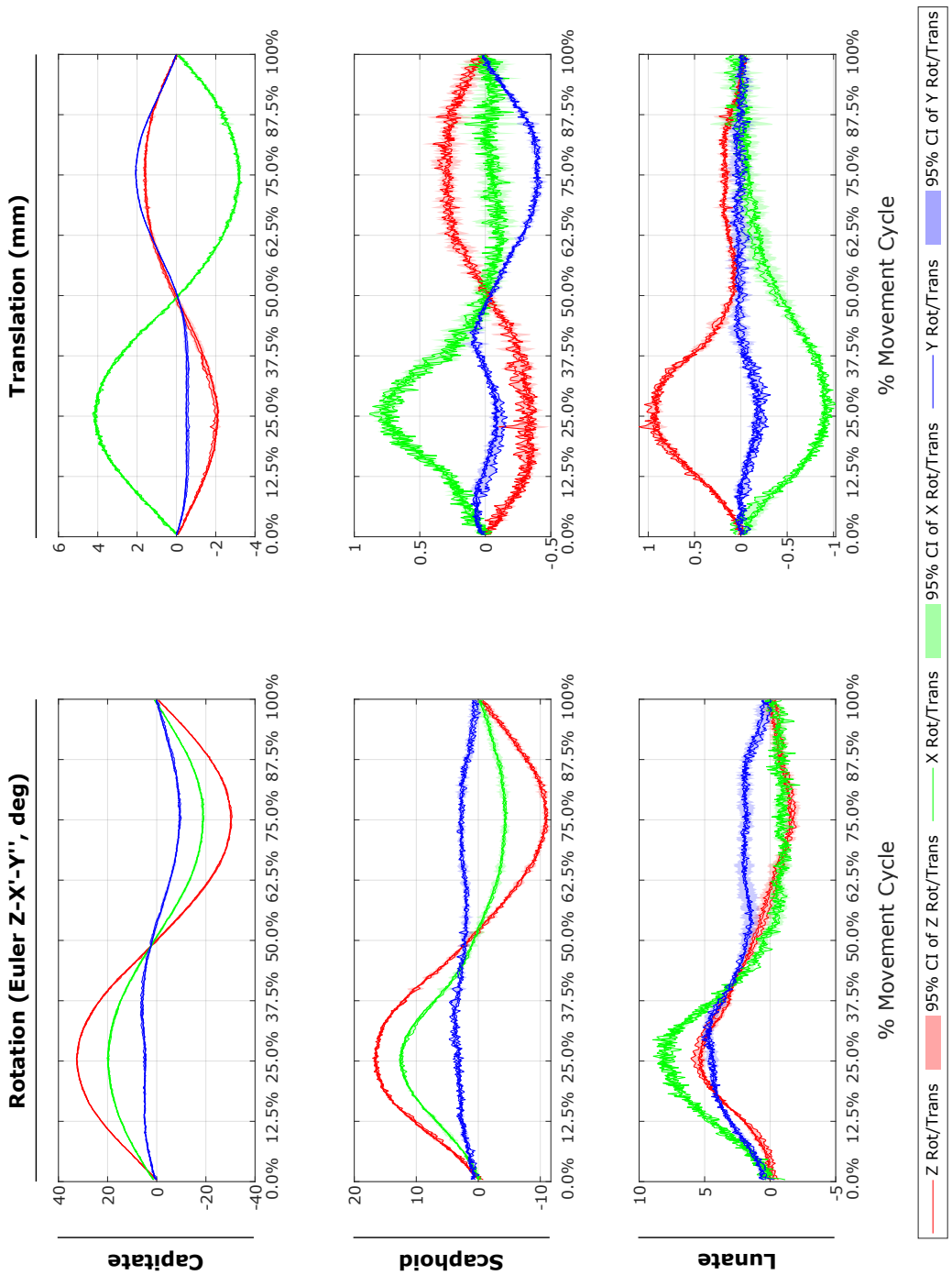

Figure 3.18: An example of the carpal bone motion repeatability. Unfiltered carpal bone kinematics, recorded during three consecutive cycles of DTM of a single specimen, was wrapped and normalised to 0 to 100% of movement cycle and plotted together. The 95% confidence interval were also plotted for each kinematic parameter to show their scattering.

Results and Discussion

The present study investigated the repeatability of carpal kinematics measured from wrist motion simulated at a macroscopic level. On average, the results (Table 3.7) indicated a sub-degree and a less than 0.05 mm repeatability of the CWTP in quantifying the rotational and translational motion of the capitate, scaphoid and lunate during different types of global wrist motion. The kinematic repeatability saw marginal increases after the introduction of ligament disruptions, again confirming the robust performance of the DWSA.

The poorest kinematic repeatability, which was about 0.3°, occurred in quantifying the scaphoid rotation during pure wrist RUD. However, upon a thorough examination of the data processing pipeline and relevant radiographic recordings, this was thought to be primarily caused by deteriorating image quality, particularly in the region around the scaphoid. As the wrist radially deviates, the trapezium and the first metacarpal would start to occlude the scaphoid, requiring X-ray with a higher energy level to penetrate. This was a challenge for the smaller fluoroscopy unit, as it had a lower X-ray rating and was configured to be more aligned with the coronal plane in the current setup. The same phenomenon was not as pronounced during the DTM, thanks to the embedded flexion/extension component which prevented the complete overlapping of the scaphoid and the trapezium.

To date, there are a limited number of studies that have assessed the macroscopic joint movement synthesised using a similar cadaveric simulation apparatus at its "component level", namely the repeatability of the individual bone motion that composes the apparent global joint movement. In a force-controlled elbow simulator developed by Johnson et al. (2000), a repeatability level that did not exceed 0.5° and 1.5° was achieved for controlling the varus/valgus and internal/external rotations between the radius, ulna and the humerus, respectively, in ten intact cadaveric upper limbs. Dunning et al. (2003) further advanced the design of this simulator by bringing in a position feedback loop and compared its repeatability achieved with both intact specimens and the ones suffered instabilities, created as a result of artificially

transecting all supporting capsular and ligamentous structures. Less than 0.2° repeatability was achieved consistently for controlling the varus/valgus angulation and internal/external rotations in both cases. The sub-degree, sub-millimetre repeatability metrics found at the carpal bone level in the present study compared well with those reported previously and were considered acceptable in studying the complex kinematic behaviour of the carpal bones.

Table 3.7: Carpal level kinematic repeatability achieved by the DWSA in cadaver wrists (n = 7), in both healthy and injured conditions

		Rotational Repeatability (deg)			**Translational Repeatability (mm)**		
		Capitate	Scaphoid	Lunate	Capitate	Scaphoid	Lunate
FEM	Healthy	0.169 [0.021]	0.226 [0.062]	0.198 [0.075]	0.033 [0.014]	0.026 [0.010]	0.028 [0.012]
	Injury	0.154 [0.026]	0.273 [0.079]	0.241 [0.104]	0.032 [0.015]	0.027 [0.013]	0.031 [0.015]
RUD	Healthy	0.164 [0.070]	0.279 [0.114]	0.208 [0.067]	0.032 [0.006]	0.029 [0.005]	0.027 [0.007]
	Injury	0.166 [0.062]	0.308 [0.101]	0.224 [0.057]	0.037 [0.017]	0.036 [0.014]	0.031 [0.012]
DTM	Healthy	0.155 [0.054]	0.244 [0.080]	0.195 [0.079]	0.031 [0.012]	0.027 [0.009]	0.027 [0.010]
	Injury	0.166 [0.036]	0.263 [0.094]	0.220 [0.088]	0.036 [0.017]	0.031 [0.015]	0.029 [0.014]

3.5 Summary

A comprehensive series of studies were carried out to assess the accuracy and repeatability of the DWSA and the biplane X-ray fluoroscopy system integrated within the CWTP. Dynamic motion simulations, including pure planar motion such as the FEM and RUD, as well as the composite DTM, were performed on seven fresh-frozen cadaveric wrist specimens. To assess the feasibility of the studies proposed for later chapters, the same set of motion simulations were repeated with each of the wrists subjected to an episode of surgically introduced ligament disruptions. A collection of anatomical structures that were postulated to provide stability for the scapholunate interval by the existing literature were excised, representing the foreseeable worst-case-scenario for the DWSA's control system.

The DWSA, which is responsible for the motion synthesis aspect of the CWTP, was shown to demonstrate a high level of accuracy and repeatability in controlling the global joint position of cadaveric wrist specimens. On average, an RMS position control error of less than 0.18° and a position control repeatability of less than 0.1° were achieved by the DWSA across all three types of wrist motion simulations. The introduction of even the most severe case of ligament injury only resulted in a very slight increase in these position control metrics, suggesting the control system of the DWSA was robust to disturbances and large uncertainties in the plant dynamics. Furthermore, the consistently small inter-specimen standard deviation of the global wrist motion achieved indicated high reproducibility of the position control outcome across different specimens.

Despite the fact that the superior performance in position control had already implied the nesting force control of the DWSA had been achieved within a reasonable margin of error, studies were carried out to evaluate the accuracy and repeatability in controlling the forces applied to each of the wrist tendons. For all three types of wrist motion simulated before and after ligament injury, a combined control error of 3.5 N, accounted for only 2.33% of the total force setpoint, was achieved by the DWSA. Also, the force

applied to each of the six wrist muscle tendons at equivalent time points between motion cycles varied by no more than 0.5 N, suggesting a high level of force control repeatability. Despite the current shortage of EMG data on the contribution of individual wrist muscles in the literature, the force profile reported in the present study demonstrated some similarities with those reported previously.

The biplane X-ray fluoroscopy system, which was used for the measurement and motion analysis aspect of the WTCP, was assessed for its accuracy and precision in characterising 6-DOF kinematics of a rigid body. However, because the knowledge of at least three non-collinear markers was required to allow the three-dimensional pose of a rigid body to be estimated, and error associated with the position measurement of any marker is expected to affect the final kinematic outcomes, a systematic two-step process was adopted for validating the biplane system. First, to characterise the error in measuring the position of a single marker, the commonly-adopted inter-marker distance approach was employed. Two separate experiments, including the use of the *in-situ* data obtained previously in the dynamic wrist simulations and a stand-alone study, served as a confirmation, were conducted in retrospect. In measuring the three-dimensional location of an individual marker, the biplane X-ray fluoroscopy system achieved an average RMS accuracy of 0.057 mm and a precision of 0.026 mm. To interrogate how these would propagate through the flow of the pose estimation process to affect the final kinematics measurement of the rigid body, an *in-silico* Monte Carlo simulation was performed. And the average RMS error for estimating the rotation and translation of a rigid body was shown to be 0.172° and 0.0426 mm, respectively, and considered negligible.

Finally, a joint system validation revealed a sub-degree and a less than 0.05 mm repeatability of the CWTP as a whole in quantifying the complex rotational and translational movement of the carpal bones amidst different types of wrist motion simulations. In conclusion, the CWTP was proven to be a reliable means to carry out biomechanical investigations of the wrist, providing a solid foundation for the studies presented in later chapters.

4

Wrist Biomechanics

Contents

4.1 Carpal Kinematics 242

4.1.1 Materials and Methods 243

4.1.2 Results 267

4.1.3 Discussion 310

4.2 Radiocarpal Contacts 361

4.2.1 Materials and Methods 362

4.2.2 Results and Discussion 372

4.1 Carpal Kinematics

4.1.1 Materials and Methods

4.1.1.1 Specimen Acquisition

Seven upper-limb specimens (age: 82.2 ± 12.5 years) were harvested from five human cadavers registered under the University of Melbourne Body Donor Program (Table 4.1), with consent and as approved by the Human Research Ethics Committee, University of Melbourne (Ethics ID: 1749011.1). Efforts were made to ensure each upper-limb specimen had no prior history of wrist injury or joint disease and the cause of death of each human cadaver did not involve any apparent trauma to the wrist joint.

Table 4.1: Information on the human cadavers used in the present study

Cadaver ID	Gender	Age	Side
17-023	Male	73	R
17-150	Female	63	R
18-124	Female	93	R
18-118	Female	95	L + R
18-189	Male	78	L + R

The upper-limbs were carefully disarticulated at the glenohumeral joint, and plain anteroposterior (AP) and lateral radiographs of the wrists were taken, allowing the wrist to be checked for signs of bone fracturing and degenerative changes. Special attention was paid on the congruencies of the three carpal arcs (Gilula, 1979), and the opening width of the scapholunate interval on the AP view, as well as the radiographic carpal alignment (scapholunate and capitolunate angles) on the lateral view (Fig. 4.1). The radiographic assessment and screening of each wrist was carried out under the supervision of an experienced hand surgeon. In addition, the preliminary radiographic assessment also revealed that there were six incidences of Type I lunate and one Type II lunate (Specimen 18-124R). Each specimen was then manually manipulated to ensure there was no palpable "clunk" or any impingement during dynamic motion.

After acquiring the specimens, they were immediately sealed in bio-

hazard bags to be stored at −20°C awaiting further dissection and testing. Each specimen was exposed to no more than 2 freeze-thaw cycles during testing, which has been shown to have a negligible effect on the material properties of the cadaveric tissues (Van Ee et al., 2000; Changoor et al., 2010; Szarko et al., 2010).

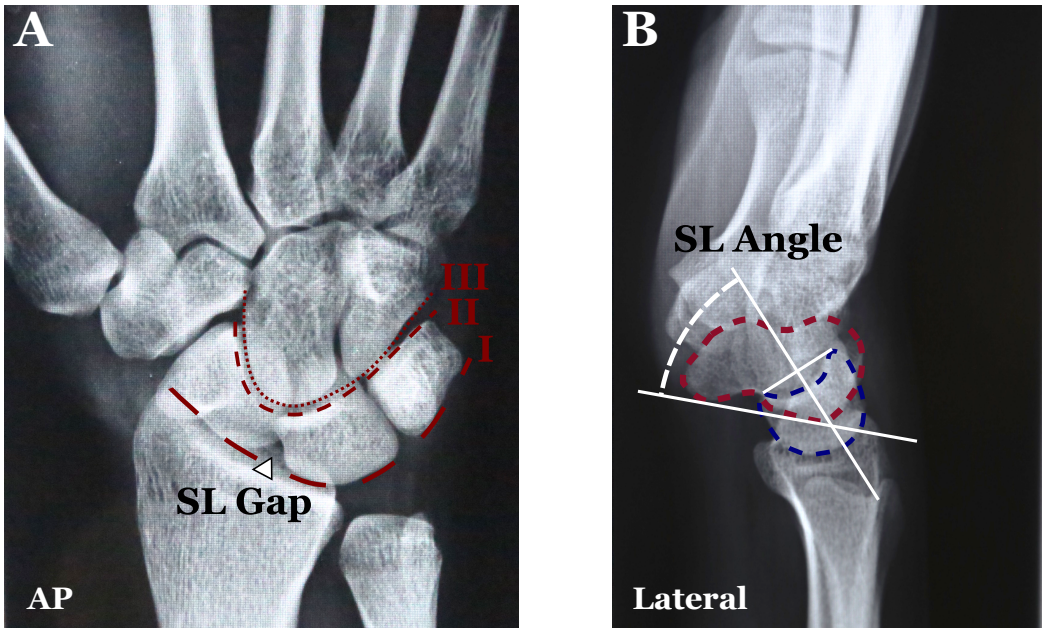

Figure 4.1: An example of the plain radiograph taken for one of the cadaveric wrist specimens, including **(A)** AP view, showing the congruency of I-III carpal arcs as well as the scapholunate (SL) gap width, and **(B)** lateral view. The carpal alignments were examined based on the scapholunate and capitolunate angles (not shown) measured on the radiograph.

4.1.1.2 Specimen Preparation

Dissection

Each upper-limb specimen was thawed overnight in a domestic bar fridge at 2°C for 12 hours and then at room temperature for an additional 2 hours prior to dissection. Specimens were disarticulated at the elbow joint, with care taken to preserve the annular ligament, which held the proximal head of the radius in the radial notch of the ulna. The musculature was exposed

via shallow incisions made along the midline on the volar and dorsal surfaces of the forearm, up to the carpal level. Prime mover muscles of the wrist, including the flexor carpi ulnaris (FCU) and radialis (FCR), extensor carpi radialis brevis (ECR-B) and longus (ECR-L), extensor carpi ulnaris (ECU), and abductor pollicis longus (APL), were detached from their origins to be dissected at the musculotendinous junctions. The muscle bellies of these wrist prime movers were removed, leaving only the tendons intact.

In preparation for the two surgical reconstructions involved in later stages of the present study, the tendons of FCR and ECR-B were further split along the fibres into two strips, with the smaller one measured approximately 8 to 10 cm in length and 3 mm in diameter (Fig. 4.2). The

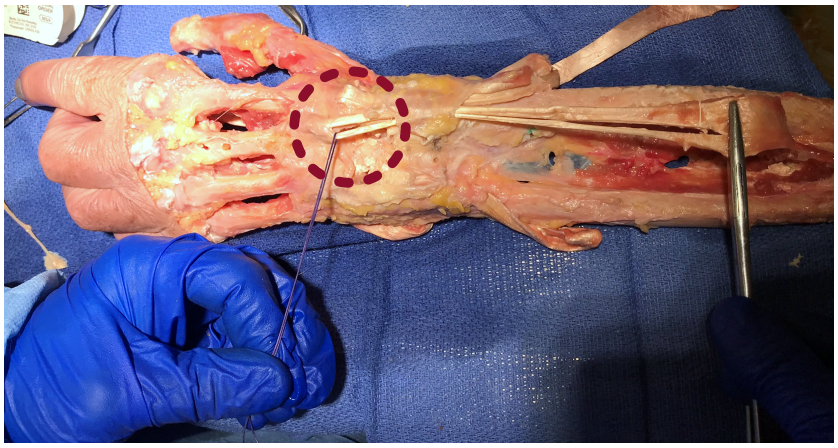

Figure 4.2: Photograph showing the tendon of ECR-B being split along the fibres. The resultant tendon strip was necessary for later SL reconstructions.

prepared tendon strips were preserved in K-Y jelly and carefully wrapped using pieces of saline-moistened cloth. They were then rolled up into small "packets" and sutured to convenient places on the palm and dorsum of the hand to avoid interfering with the tendons.

The remaining tendons were slightly trimmed such that they could be firmly gripped by the custom-designed wire-woven sleeves described earlier. Non-absorbable sutures (Ethibond Excel, Size 2-0; Ethicon, New Jersey, USA) were added to reinforce the bounding. Each of the prepared muscle tendons was kept moistened by applying a generous amount of K-Y jelly,

and was wrapped in saline-soaked gauze to prevent dehydration (Fig. 4.5). Finger muscles, the skin, and all other subcutaneous tissues were then excised. Care was taken to preserve the integrity of the interosseous membrane, the flexor retinaculum and the 1st, 2nd, and 6th compartments of the extensor retinaculum. The cadaveric wrist specimen was then placed in neutral pronation-supination via visual inspection, and was fused by drilling two Steinmann pins of 4 mm in diameter and 250 mm in length transversely at a mid-to-distal forearm level through shafts of the radius and ulna.

Tracking Marker Placement

In order to quantify the kinematics of the carpal bones, the previously described biplane X-ray fluoroscopy system was employed. To further enhance the accuracy of the kinematic analysis, marker-based RSA was chosen, where radio-opaque markers were surgically implanted into the bones of interest to facilitate tracking. To this end, the wrist capsule was surgically approached via a longitudinal incision made over the dorsum and centred on Lister's tubercle. The extensor retinaculum was incised between the III and IV compartment and reflected ulnarly until the dorsal radiocarpal ligament was exposed. The finger extensors were trimmed distally, and the wrist capsule was then opened through a ligament-sparing dorsal capsulotomy (Fig. 4.3).

Similar to Section 3.2, small holes to accommodate radio-opaque markers were predrilled into the dorsal cortices of the scaphoid, lunate and capitate under fluoroscopic guidance. The locations of the holes were carefully designed and optimised by the hand surgeon such that they were situated furtherest away from each other while still being practically accessible and appropriate for the bony anatomy. To this end, the anatomical snuffbox was incised to gain access to the distal aspect of the scaphoid. Extreme caution was exercised not to damage the capsular and interosseous ligaments situated in the vicinity. Spherical radio-opaque markers were then embedded into those pre-drilled holes. To facilitate kinematic analysis of the carpal bones, reference markers were also added to the radius using similar techniques. The sizes of the radio-opaque markers used for different bones varied from 1 to

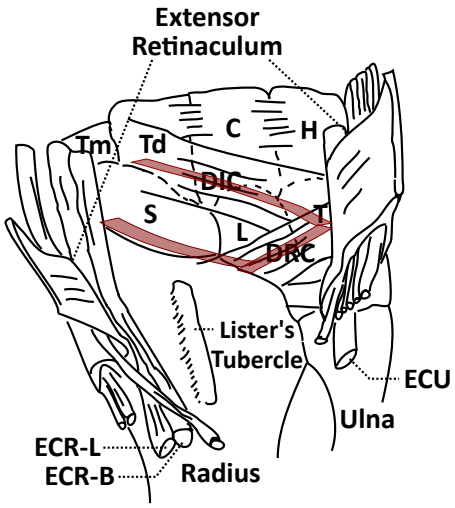

Figure 4.3: Schematics of the ligament-sparing dorsal capsulotomy developed by Berger et al. (1995). The extensor retinaculum was transected and the dorsal intercarpal (DIC) and the dorsal radiocarpal (DRC) ligaments were split along the fibres (transparent red strips)

1.8 mm, allowing them to be visually distinguishable for their marker-bone correspondence under X-ray fluoroscopy. Finally, droplets of cyanoacrylate-based adhesive were added using a syringe to seal the cavities. Care was taken not to glue the joint or leaving any unwanted residuals inside the joint.

To facilitate real-time tracking of the wrist, retro-reflective marker triads were attached to the radius and the third metacarpal by means of 3D-printed "marker holders". The marker holders were custom-designed for optimal spatial placement of the marker triads, allowing them to be visible to the video motion capture system at all times during dynamic wrist simulations. In order to achieve reliable mounting, the bone surfaces of the radius and the third metacarpal were scraped free of remaining soft tissues and degreased using an ethanol-soaked gauze. M3 holes were then drilled on the dorsum of distal one-third of the radius and the distal head of the third metacarpal to allow screw-fastening of the marker holders. A generous amount of Epoxy resin was also added to reinforce the attachment.

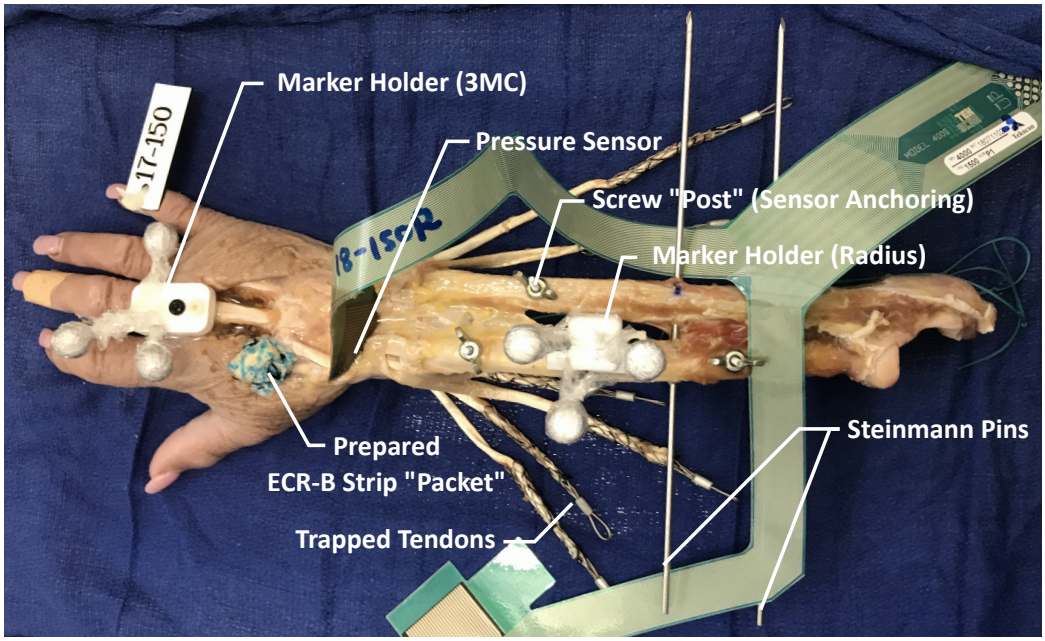

Figure 4.4: Photograph of a dissected and prepared cadaveric wrist specimen before CT scan. The specimen was not yet cemented to the metallic potting block at this stage to avoid significant artifact under CT.

Pressure Sensor Insertion

A Tekscan Medical 4000 pressure sensor which was waterproofed and calibrated beforehand was then inserted into the radiocarpal articulation of the cadaver wrist, through the previously performed dorsal capsulotomy. The sensor was securely held in the articular space via sutures placed through the distal rim of the sensor. The sutures were passed through small piercings made on the volar capsules and anchored to the screws placed volarly into the shaft of the radius and ulna. Preparation and insertion of the pressure sensor will be described in more detail later (Section 4.2.1.1).

Medical Imaging

With the radio-opaque markers implanted into the carpal bones and the retro-reflective markers attached to the radius and 3MC, the wrist specimen was CT scanned. The wrist was placed on a translucent tray and placed

in its approximate neutral position. The scan was then performed along the axial direction of the wrist, using the Siemens Biograph mCT (Munich, Germany) located in the Melbourne Brain Centre Imaging Unit. The imaging protocol was as follows: collimation 64 × 0.6 mm, exposure time 1 s (360°), table feed speed 13.4 mm/s, X-ray tube voltage 140 kV and current 436 mA. A reconstruction matrix of 512 × 512 was used, resulting in an in-plane pixel size of 0.2852 mm, while an increment of 0.1 mm was chosen for the out-of-plane direction. As discussed (Section 2.2.3), since the operation of the DWSA requires knowledge of the approximate locations of the distal insertion and the proximal passage sites of the muscles to be actuated in the dynamic wrist simulations, metallic markers were also added to those locations to assist the later digitisation.

Potting

The proximal radial head and ulna of each cadaveric wrist specimen were cemented to the potting fixture with dental plaster and mounted to the DWSA (Fig. 4.5). The potted specimen was left at room temperature for approximately 20 minutes to allow curing of the plaster. Epoxy resin was applied on top of the plaster to prevent intrusion of the moisture which could potentially weaken the bonding between the specimen and the potting block.

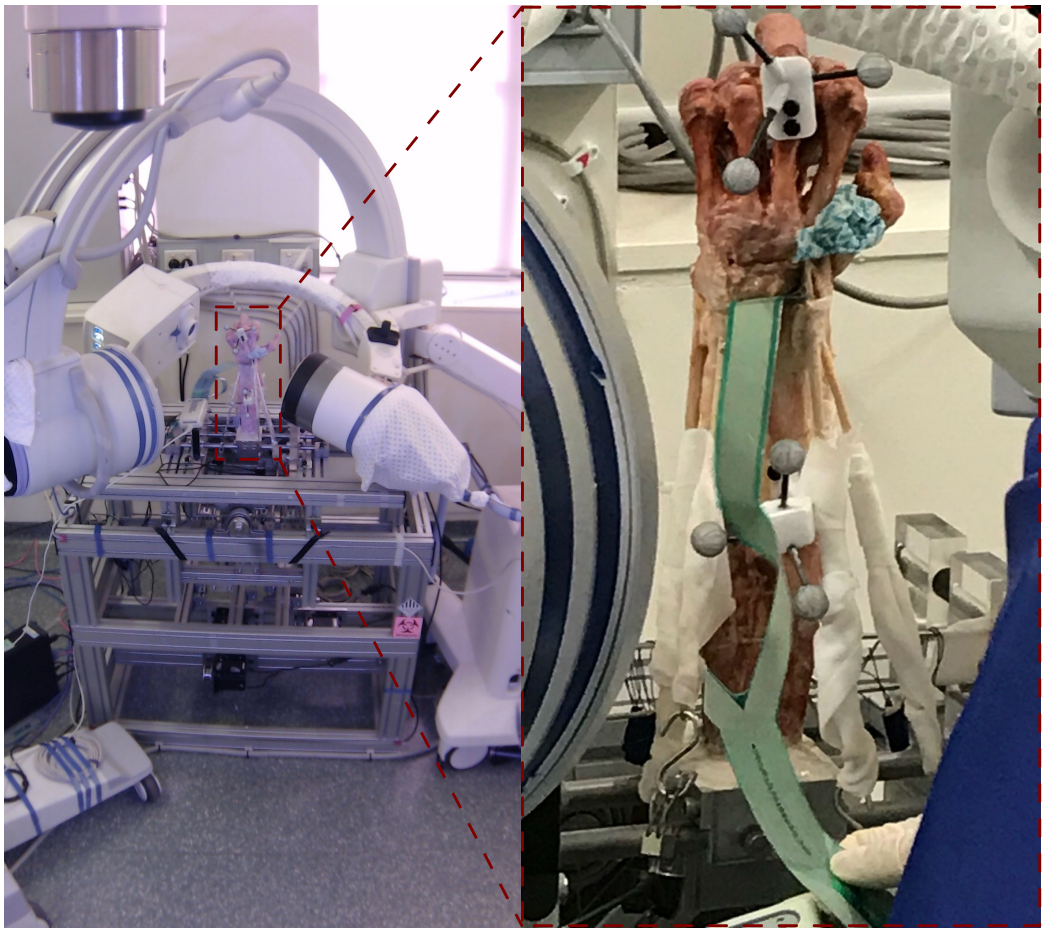

Figure 4.5: Photograph of a cadaveric wrist specimen mounted to the DWSA

4.1.1.3 System Calibration and Preparation

Video Motion Capture System

The video motion capture system was calibrated before the potted wrist specimen was mounted onto the DWSA. A standard "dynamic wand-waving" calibration was performed with the help of Vicon Tracker 3.5.1 (Vicon Motion System, Oxford, UK), using a total of 1,500 frames of data. Due to the limited size of the capture volume included within the CWTP, a scaled-down version of the calibration wand (Mini-Cal 120; Vicon Motion System, Oxford, UK) was used. The calibration process was repeated until a reprojection error below 0.1 pixels, which translated into a world error as low as 0.015 mm, was achieved on all cameras.

Biplane X-ray Fluoroscopy System

The biplane X-ray fluoroscopy system was calibrated using a precisely machined calibration phantom (see Section 2.3.2). With the phantom being placed in different poses, at least eight pairs of biplanar radiographic snapshots were taken, allowing the projective correspondence between the 2D image space and the 3D scene space to be optimally established. From this point onwards, any physical interaction with the video motion capture system and the biplane X-ray fluoroscopy system was prohibited, as this would compromise the calibration of the cameras, leading to inaccurate stereo-photogrammetric reconstructions. To further ensure there had been no such cases, special attention was paid in post-processing of the data to detect any consistent non-compliance of the epiolar constraint across all stereo fluoroscopic image pairs. And since the distortion correction process required grids to be mounted against the XRIIs of the C-arm units, it was performed at the end of each dynamic wrist simulations.

Load Cell

The zero balance of the uniaxial load cells were also re-measured at the onset of every dynamic wrist simulation to ensure force accuracy. This procedure was performed by first collecting 5,000 raw readings from each load cell when placed horizontally and free of any external attachment. The average value of those readings was then used to offset the output given by each load cell. After that, the potted wrist specimen was mounted vertically onto the DWSA. S-shaped hooks were used to connect each of the muscle tendons to its designated load cell and ultimately to the allocated motor. Since the DWSA involved force control, each of the muscle tendons was pre-loaded to a value of 7 N, while the cadaver wrist was being held manually in its neutral position.

Coordinate System Definition and Marker Digitisation

To facilitate the measurement of global wrist angle, which provides position feedback necessary for the DWSA, body-fixed local coordinate systems (LCS) must be defined for the radius and the 3MC. Therefore before the onset of dynamic experiments, the DICOM images resultant from the CT scan were segmented and reconstructed using Mimics (Materialise, Leuven, Belgium). Based on the volumetric model of the wrist specimen, a joint coordinate system (JCS), following the definition advocated by the International Society of Biomechanics (ISB) (Wu et al., 2005), was created for the radius and the 3MC. This permitted the relative location of the retro-reflective markers attached to the radius and the 3MC to be determined in the locally defined reference frames, thus allowing the global wrist position to be measured by the video motion capture system of the DWSA.

Similarly, to allow tracking of carpal bone motion, the LCS of the carpal bones of interest must also be correctly defined. However, as stated earlier (see Section 2.3.2 and 3.3.2), owing to their highly irregular shape, the LCSs could not be defined exclusively based on the boney geometry or palpable landmark, as opposed to the grossly tubular radius and 3MC. Instead, the

LCS of the carpal bones were defined rather implicitly. According to the ISB, their orientation was said to be aligned with that of the radius when the global wrist assumed the neutral position, while the origin was defined to coincide with the volumetric centroid of the carpal bone. Since there was no way to guarantee the wrist specimen was scanned in its exact neutral position, an additional correction step was taken "calibrate" the CT data.

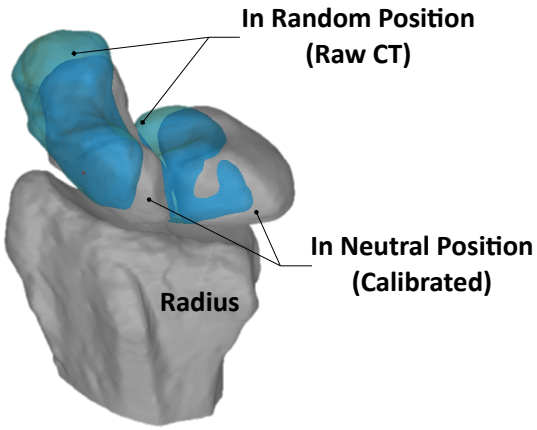

Figure 4.6: Volumetric models of the scaphoid and lunate. The **transparent** ones are their position when the wrist was being CT scanned. The **solid** ones are their position in the neutral wrist position after being calibrated.

In essence, biplanar radiographic snapshots of the cadaver wrist were taken after it had been actively placed into a position that approximated its neutral position. According to the correspondence between the triangulated marker positions and those obtained in CT, the volumetric models of the carpal bones were registered to their corresponding positions on the radiograph, thus virtually re-establishing their neutral alignment (Fig. 4.6). Then, based on the calibrated CT data, the LCS was defined for each of the carpal bones of interest, specifically, the scaphoid, lunate and capitate.

In addition, the anatomical insertion and passage sites of the prime mover muscles were digitised from the volumetric CT data in the near-neutral wrist position. These measurements were subsequently ported into the DWSA's control algorithm to enable the estimation of the moment arms.

4.1.1.4 Testing Protocol and Data Collection

Similar to the validation experiments described previously (Section 3.2), the two planar wrist motions, specifically, FEM and RUD, were dynamically simulated in each cadaveric wrist specimen using the DWSA. Sinusoidal movement trajectories with an amplitude of 30° and 20° were selected for the wrist FEM and RUD, respectively, in accordance with those used in previous studies involving dynamic and muscle-driven simulations of cadaver wrists (Tong, 1985; Werner et al., 1996; Erhart et al., 2012; Dimitris et al., 2015). Since the introduction of ligament divisions and reconstructive surgeries in subsequent phases would render the dynamic response of the cadaveric plant more and more unstable, an extended cycle period of 20 seconds was chosen for the sinusoidal trajectories to ensure stability and repeatability of the simulated wrist motion. A constant level of 150 N was prescribed for the summation of the tendon forces. In addition, simulations of the oblique dart thrower's motion (DTM) were also performed. For simplicity, the movement trajectory was just the direct superposition of those used for simulating the two planar wrist motions. At least three consecutive cycles of the sinusoidal motions were simulated for each type of wrist motion.

During dynamic joint simulations, the global wrist position and the muscle forces were measured and recorded continuously with a sampling frequency of 100 Hz. As a result of the apparent global motion simulated in the cadaver wrist, the microscopic intercarpal motion between the capitate, scaphoid and lunate was captured using the biplane X-ray fluoroscopy system at a frame rate of 25 Hz and an energy level of 75 kVp @ 0.1 mA and 70 kVp @ 1 mA for the mini and full-sized C-arm fluoroscopy units, respectively. The intra-articular pressure distribution within the majority of the radiocarpal joint was also monitored by the I-scan electronic pressure measurement system with a sampling frequency of 100 Hz.

Before the initial commencement of the study, each cadaveric wrist specimen was pre-conditioned by performing 20 consecutive cycles of FEM and RUD simulations. Then, after each stage of the sequential ligament dis-

ruptions and surgical treatments, the biplane X-ray fluoroscopy system was re-calibrated and the above-described dynamic simulations, covering all three types of wrist motions, were repeated. Each specimen was subjected to no more than two frozen-thaw cycles, and the total time taken for each study from the initial dissection to the conclusion of the entire testing regime was no longer than 72 hours. All studies were carried out at 18 °C, and the specimens were irrigated with 0.9% saline solution throughout testing.

4.1.1.5 Sequential Ligament Resection

Anatomic lesions were surgically introduced in increasing severity to the scapholunate (SL) supporting ligaments in an attempt to not only initiate scapholunate instability in each wrist specimen, but also to emulate the progression of this pathology. The SL stabilising ligaments considered and the specific sequence in which these ligaments were severed (Table 4.2) were designed in accordance with the typical injury pattern (Mayfield, 1984), as well as the current consensus on the pathomechanics of the SL instability and pioneering studies concerning the relative contributions of individual SL supporting ligaments via selective sectioning (Mayfield et al., 1976, 1980; Meade et al., 1990; Short et al., 2002b; Elsaidi et al., 2004). This sequence was also illustrated in Fig. 4.7.

Table 4.2: Stages of the incremental resection of the SL supporting ligaments. The predicted outcome for each stage of severing was adopted from Lee et al. (2015), where patterns of ligament lesion were correlated with distinct grades in the arthroscopic classification system developed by Geissler (2013)

Stage	**Ligament Sectioned**	**Predicted Geissler Grade**
I	v- + m-SLIL	$0-2$
II	d-SLIL	$2-3$
III	RSC + LRL	3
IV	DIC + DRC* + STT	4

* Partial sectioning, as the remaining portion was needed in later surgical procedures

According to Mayfield (1984), injury to the carpal ligaments is often associated with a history of forced hyperextension, ulnar deviation, and intercarpal supination of the wrist. With the scaphoid being functionally acting as the mechanical link for the proximal and distal carpal rows (Linscheid et al., 1972), it is brought into extension primarily by the scaphotrapeziotrapezoid (STT) ligament (Drewniany et al., 1985). However, the lunate was tightly checked by a substantial radial connection provided by the long and short radiolunate (L-, SRL) ligaments, preventing it from following the scaphoid into synchronous extension (Berger, 2001). This was believed to

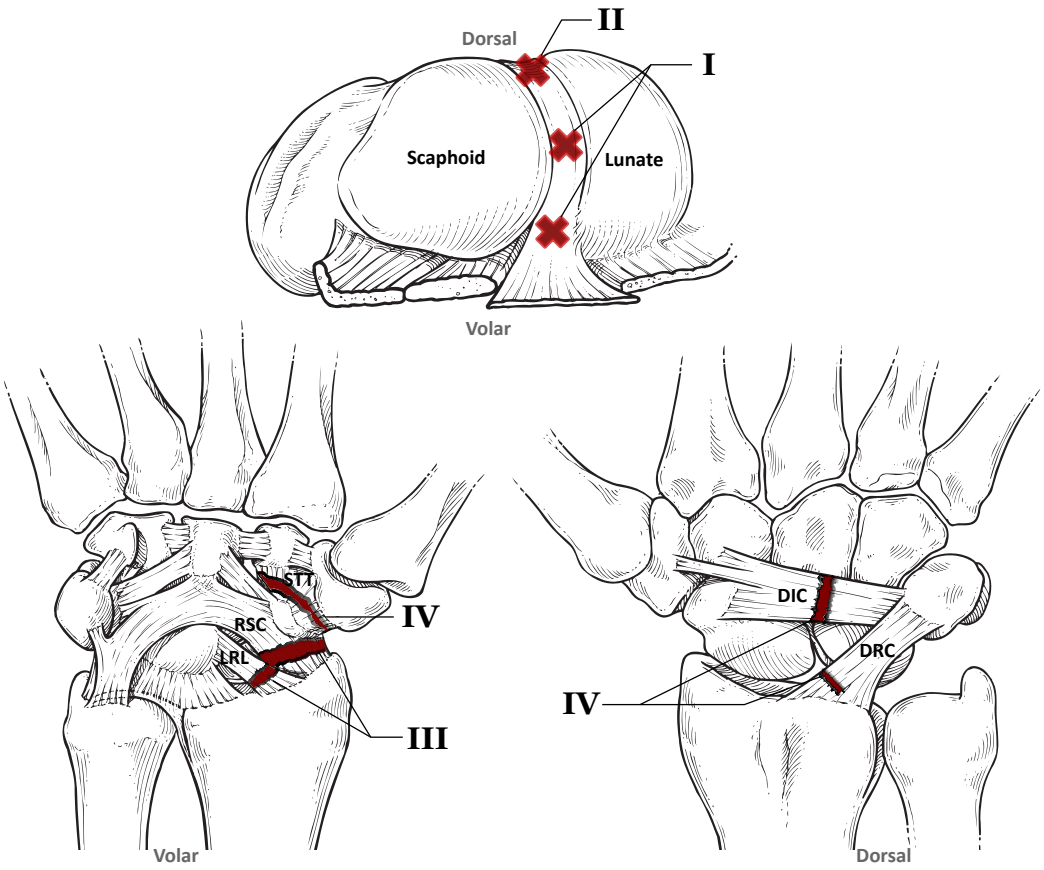

Figure 4.7: Sequence and designated stages of ligament severing

explain the clinical observations where the earliest ligament injury always begin with a partial tear to the volar scapholunate interosseous ligament (v-SLIL) and progressing dorsally (Lee and Elfar, 2015; Mugnai et al., 2016). In addition, the hypermobility of the volar scapholunate articulation (Kauer, 1974), presumably permitted by the relatively weaker ligament constraint provided by the volar and membranous subregions of the SLIL (Berger et al., 1999), were all in support with this finding. To this end, the volar and the fibrocartilaginous membrane (m-) of the scapholunate interosseous ligament were transected in the first stage, prior to their dorsal counterpart (d-SLIL). Precise transection of different subregions of the SLIL was performed by the hand surgeon under loupe magnification using No.15 scalpel blades.

After attenuation or the complete rupture of the SLIL, progressive load-

ing with extension and ulnar deviation of the wrist is speculated to cause disruption of the volarly and radially situated SL supporting ligaments prior to those located dorsally (Johnson, 1980; Mayfield, 1984). This was indeed confirmed clinically by the concurrent rupture of the volar extrinsic ligaments such as the radioscaphocapitate (RSC) or the LRL and SRL in patients who suffered an injury to the SLIL and diagnosed with scapholunate dissociation (Adler et al., 1996). The results from a ligament strain study performed by Xu and Tang (2009) were also in support of this hypothesis. Anatomical studies have also suggested the RSC ligament functionally act as a soft-tissue fulcrum which regulates and checks the scaphoid rotation (Taleisnik, 1976), presumably providing stability to the scaphoid (Berger and Landsmeer, 1990; Ritt et al., 1995; Schmitt et al., 2006) and the scapholunate joint in large (Short et al., 2005; Werner et al., 2011). Linscheid et al. (1972) reported that the RSC must be attenuated in addition to the SLIL before subluxation of the scaphoid or the scapholunate diastasis occurs. Furthermore, the attenuation of those volar extrinsic ligaments was believed to cause widening of the space of Poirier an inherently weak spot located between the RSC and LRL, leading to dorsal dislocation of the capitate with dissociation at the lunocapitate joint to be seen clinically (Gilula and Weeks, 1978). Therefore, owing to the reasons mentioned above, the RSC and LRL ligaments were sectioned in stage III. Since these ligaments are extrinsic to the carpus and situated volarwards, the cadaver wrist was gently distracted in a slightly flexed position to allow access of the scalpel. While having the ligaments released from their attachments on the radius, extreme care was taken to ensure the incision did not pierce through the volar wrist capsule.

The term Dorsal Intercalated Segment Instability (DISI), characterised by abnormal dorsiflexion of the lunate with dorsal and proximal migration of the capitate and the distal carpal row (Linscheid et al., 1972), is sometimes observed clinically in association with the progression of scapholunate instability (Wolfe et al., 1996; Clark and Von Schroeder, 2004; Omori et al., 2013; Ho et al., 2015). However, there is no clear consensus on which ligaments are responsible for producing the DISI deformity. Viegas et al. (1999) performed

an anatomical study of the dorsal ligaments and suggested that the dorsal intercarpal (DIC) and the dorsal radiocarpal (DRC) ligaments might play a key role in delivering radioscaphoid stability, and collectively prevent the development of DISI. Mitsuyasu et al. (2004) reported the DISI deformity was not observed on cadaveric wrist specimens until the dorsal intercarpal (DIC) ligament, in particular, its attachment on the lunate, was disrupted. Fisk (1984) believed the DISI deformity was dependent on the attenuation of the DRC. Therefore, in Stage IV, the entire DIC and approximately 40% of the DRC and ligaments were transected in an attempt to surgically simulate the DISI deformity in the wrist specimens. The reason that the DRC was partially retained was due to its use in the subsequent tenodesis procedures that reconstructed the SLIL and will be explained in the subsequent section. In addition, the STT ligament complex, known to be essential for stabilising the distal pole of the scaphoid with increased flexion (Drewniany et al., 1985; Masquelet et al., 1993), was also divided to produce a static, radiographic "collapse" of the scaphoid, in line with the description of a more advanced stage of scapholunate instability in the clinical grading systems (Messina et al., 2013; Lee et al., 2015). Tendons were retracted, and care was taken not damage the volar capsule.

In each stage, the completeness of the ligament resection was visually evaluated by the hand surgeon, and a complete dissection of the cadaveric specimen was carried out at the conclusion of each experiment to confirm all intended ligamentous lesions had been achieved.

4.1.1.6 Scapholunate Ligament Reconstruction

As reviewed earlier, scapholunate instability presents a spectrum of injuries and depending on the acuteness and severity of the ligament lesion, different treatment procedures are used (Kitay and Wolfe, 2012). However, owing to the frequently delayed diagnosis in the early stage, scapholunate instability is more commonly discovered in the subacute or chronic phases, where the SLIL is irreparable with a static but still reducible carpal malalignment (Garcia-Elias and Lluch, 2017). In the present study, this clinical presentation was simulated through the ligament severing procedures described above, where a multitude of ligamentous constraints was surgically divided in the cadaveric wrist specimen to allow the pathology to develop and progress into a more advanced stage. Despite the fact that a standardised treatment protocol for patients presented with scapholunate instability of this stage is still controversial, a SLIL ligamentoplasty with tendon grafts is often recommended (Palmer et al., 1978; Garcia-Elias et al., 2006; Rohman et al., 2014). To this end, two distinctive reconstructions, including a novel reconstruction of the d-SLIL, and the commonly employed three-ligament tenodesis (3LT), were performed on each of the wrist specimens to be evaluated for their efficacy in restoring the normal kinematics of the scapholunate joint.

Dorsal Transarticular Loop Tenodesis

A novel, unpublished reconstruction of the d-SLIL, originally devised by a senior hand surgeon based on his clinical experience (S. K. Tham, personal communication, Dec 23, 2015) and referred to as the dorsal transarticular loop tenodesis (DTLT), was performed and evaluated for its effectiveness in correcting the scapholunate malalignment. Firstly, the dorsally tilted lunate was corrected and held with a Kirschner wires. The subluxed and dissociated scaphoid was also reduced to its normal alignment. Under fluoroscopy guidance, two connected drill holes, each of 3 mm in width, were created on the dorsum of both the scaphoid and lunate in the region of the d-SLIL insertion (Fig. 4.8A). Care was taken to ensure the two transosseous drill holes started

at roughly the same level and directed in parallel. The previously prepared ECR-B graft was then passed dorsally, initially through the scaphoid and subsequently the lunate in a box-shaped fashion. The remaining graft was finally sutured back to itself, completing a counterclockwise transarticular passage across both the proximal and dorsal scapholunate interval (Fig. 4.8B).

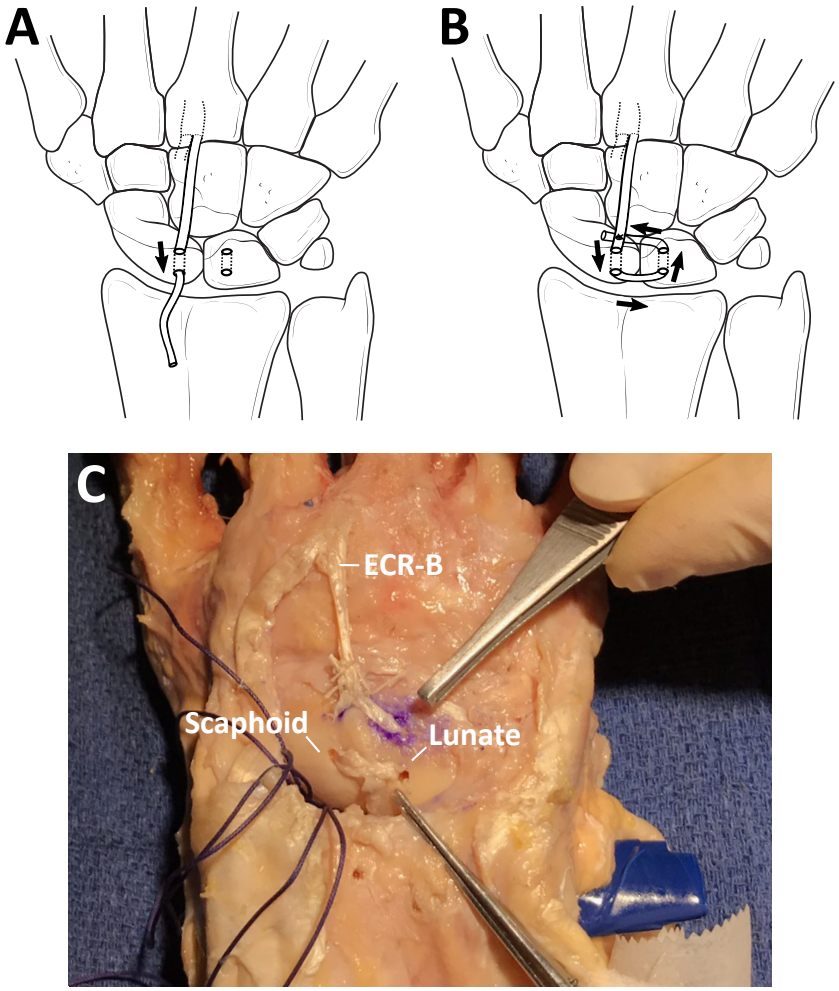

Figure 4.8: Schematics of the novel dorsal transarticular loop tenodesis procedure: **(A)** two connected drill holes were made dorsally on both the scaphoid and lunate, **(B)** the ECR-B graft was passed such that it formed a counterclockwise transarticular loop around the scapholunate interval. **(C)** A photograph showing the outcome of this technique as performed on a cadaver wrist

In practice, a modified DIC capsulodesis (Szabo et al., 2002), which

intends to correct excessive scaphoid flexion, is also performed by the surgeon in conjunction with the reconstruction. However, this additional procedure was omitted for the present study, owing to the previous ligament division step, which had rendered the DIC detached and unworkable.

Three-Ligament Tenodesis

The 3LT was developed by Garcia-Elias et al. (2006), and was derived based on a collection of stabilisation strategies described by Brunelli and Brunelli (1995), Linscheid and Dobyns (1992b) and Van Den Abbeele et al. (1998). This method eliminates the need to tether the tendon graft to the radius, and as the name suggests, it aims not only to reconstruct the d-SLIL, but also to augment the STT and DRC ligaments (Kitay and Wolfe, 2012). In the present study, this method was performed as soon as the ECR-B graft from the previous technique was removed and was carried out in accordance with the procedures originally described. However, in order to accommodate two different reconstruction techniques in the same wrist specimen, minor but necessary modifications were made.

A 3 mm wide, obliquely directed tunnel that entered the scaphoid proximally and dorsally from one of the drill holes created for the DTLT technique and exiting volarly at the scaphoid tubercle was made under fluoroscopic guidance by the hand surgeon. Care was taken upon exiting the scaphoid to ensure the protruding bit did not damage the tendon located in the vicinity. The previously harvested FCR tendon strip was then used as the graft and passed through the tunnel obliquely (Fig. 4.9A). Sutures were attached to the tendon strip to be used as guide wires to facilitate passage of the tendon strip. To avoid fracturing the lunate or disrupting the position of the embedded radio-opaque markers, the tendon graft was passed directly over the dorsum of the lunate without being buried in the cortical bone in a pre-carved trough as described in the original method (Fig. 4.9B). The tendon graft was then passed through a slit made on the distal and ulnar portion of the remaining DRC ligament, allowing it to be folded back onto the lunate (Fig. 4.9C). By using the DRC as a pivot, the tendon graft was tightened until a

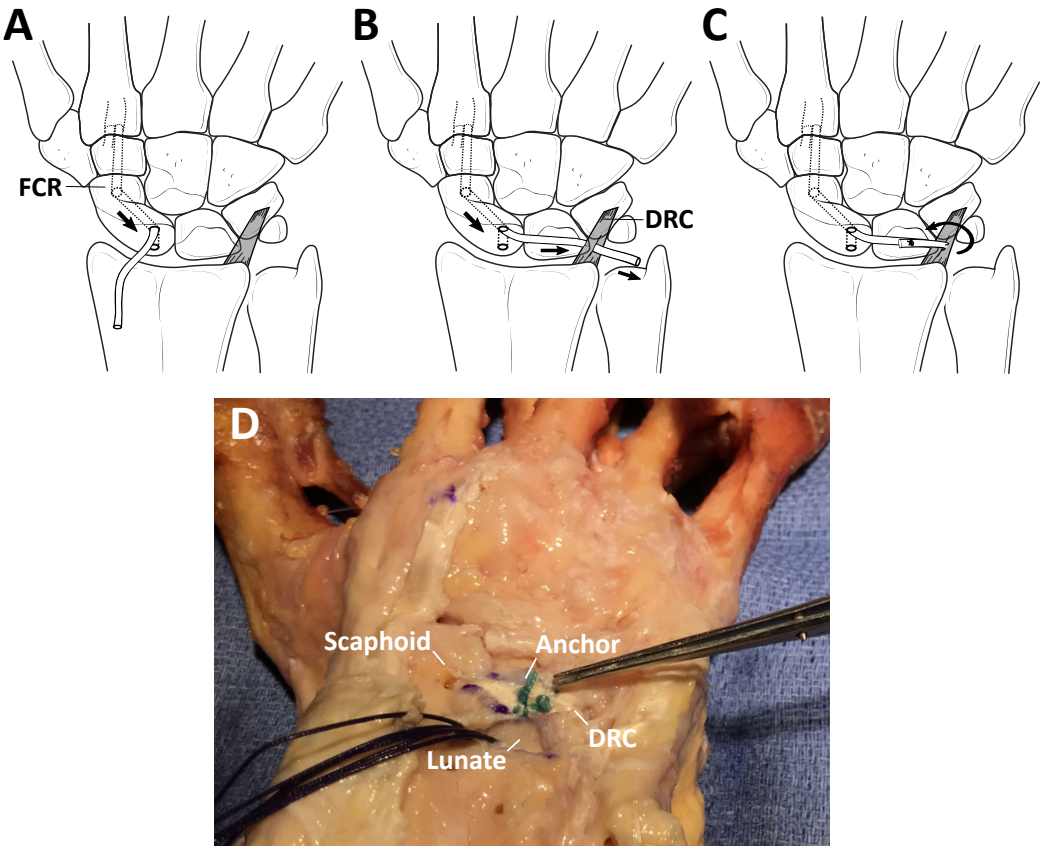

Figure 4.9: Schematics of the 3LT procedure: **(A)** a transosseous tunnel was made obliquely through the scaphoid using one of the drill holes from the previous reconstruction, **(B)** the FCR tendon graft was tunnelled through the scaphoid to be passed over the dorsal lunate, and finally through a slit made on the DRC ligament, **(C)** the tendon graft was tensioned using the DRC as a pulley, and anchored on the dorsum of the lunate. **(D)** A photograph showing the outcome of this technique as performed on a cadaveric wrist specimen.

satisfactory reduction of the scapholunate joint was achieved and Kirschner wires were used to maintain the correct reduction. The cadaver wrist was also manually manipulated with the tendon graft being held with appropriate tautness. This procedure was to ensure there was no perceivable distortion in the desired reduction during the course of dynamic motion. Finally, the FCR graft was secured to the dorsal lunate by means of a radiolucent suture anchor (JuggerKnot Mini 1.0 mm; Zimmer Biomet, Indiana, USA). The wrist joint was rinsed using 0.9% saline for a thorough removal of the debris. Although it was unlikely for the ligament graft sutured distally on the dorsal lunate to impinge on the rim of the distal radius, generous amount of K-Y jelley was applied to promote gliding.

4.1.1.7 Data Analysis

For each specimen in each of the seven experimental stages (intact, four stages of ligament divisions, and two reconstructive surgeries), the 6-DOF kinematics of the scaphoid, lunate, and capitate were calculated for the entire duration of all three modes of wrist motion simulated (FEM, RUD, and DTM). As outlined in Section 3.4, the 6-DOF carpal kinematics include three rotations and three translations as measured with respect to the radius. For each of the selected carpal bones, its rotational motion was described in Euler angles following a $Z - X' - Y''$ sequence, corresponding to intrinsic rotations about the Flexion(+)/Extension(-), Ulnar(+)/Radial(-) deviation, and Pronation(+)/Supination(-) axes, respectively. Its translational motion in the Radial(+)/Ulnar(-), Volar(+)/Dorsal(-), and Proximal(+)/Distal(-) directions were calculated based on the movement of its volumetric centroid along the Z-, X-, and Y-axis, respectively. For each mode of wrist motion, the carpal kinematics was first reconstructed from marker trajectories for all consecutive cycles of the dynamic simulation. A low-pass Butterworth filter with a cut-off frequency of 5 Hz was used to filter the coordinates of the markers. The data were then linearly interpolated at every 0.1% of the motion cycle and were averaged to obtain the carpal kinematics corresponding to one complete cycle of the dynamic wrist simulation.

For all three modes of wrist motion, the carpal kinematics corresponding to each stage of testing were compared with the data recorded in the initial stage with the specimen intact (Stage I) and those measured in the previous stage (for the two reconstructive surgeries, their preceding stage is defined as Stage IV ligament division). The comparison was carried out in quarters of the motion cycle, corresponding to the global wrist motion from the neutral wrist position to the positive extreme set for the current motion profile (0-25%), from the positive extreme back to the neutral position (25-50%), from the neutral position to the negative extreme (50-75%), and finally from the negative extreme back to the neutral position (75-100%). To determine if the carpal kinematics corresponding to a particular segment of the motion cycle were different between stages, the L^2-norm-based one-way functional data

analysis of variance (fdANOVA), proposed by Faraway (1997) and Zhang and Chen (2007) for statistical inference on continuous observations of a random variable, was employed instead of a conventional point-wise comparison. The statistical analysis was performed using the fdANOVA package implemented in R (Górecki and Smaga, 2019), with the level of significance defined as $p<0.05$. But since the package does not provide native support for studies with a repeated-measures design, the fact that the carpal kinematics were measured repeatedly on the same specimen in the present study was implicitly embedded by comparing their specimen-specific difference in carpal kinematics between states to the zero vector across all specimens.

For ease of visualisation, the between-stage difference in carpal kinematics corresponding to each category of comparison was also calculated, and then averaged across each quarter of the motion cycle. The mean and standard deviation of the differences were then calculated for each motion segment across all seven specimens.

Furthermore, to detect if there were any changes in the dynamic behaviour of the carpal bones (or the mean distortion in the shape of the curves) compared with the control (normal physiological wrist), the same comparisons were carried out, but with the data offset to exclude the effect of static postural changes in the carpal bones (represented by a vertical shift in the kinematics-time curve).

Finally, some of the detected changes in the carpal kinematics that were small but significant may ultimately not be clinically relevant. Some researchers regarded a deviation of 2 degrees in rotation (Short et al., 2005), or 2 mm in translation (Werner et al., 2011; Eschweiler et al., 2016b), from the native carpal kinematics measured in the normal physiological condition to be clinically relevant. However, more conservative thresholds of 1 degree and 1 mm were employed in the present study, as research has shown these changes, once started, may continue to develop with repetitive use of the wrist (Short et al., 2002a).

4.1.2 Results

4.1.2.1 Normal Carpal Kinematics (Table 4.3, 4.4 and 4.5)

Neutral Position

First of all, the scaphoid, lunate and the capitate all demonstrated minimal deviation, which were observed to be smaller than 1° in rotation and 0.2 mm in translation, from their "true" zero when the wrist was placed at its wrist position. This again confirmed that their respective bone-fixed LCS was correctly defined as per the ISB recommendations to be aligned with that of the radius, thanks to the corrections steps taken which effectively "calibrated" the volumetric CT scan.

Flexion and Extension

During wrist flexion, scaphoid and lunate flexed synergistically with respect to the radius. However, the scaphoid flexion was almost twice that of the lunate (mean scaphoid-lunate slope for Z-rotation = 0.57, $R^2 = 0.85$) during the entire course of wrist flexion. In addition, the scaphoid flexion was approximately 74% of the global wrist flexion. At 30° of wrist flexion, this measured 22.5° ± 3.5° for the scaphoid and 11.3° ± 4.0° for the lunate. A substantial amount of intercarpal rotation, up to 11.2° ± 1.5° around the Z-axis, was observed between the two bones (the scapholunate motion can be found in Table B.1 in Appendix B). Despite the fact that their conjunct out-of-plane rotation was negligible, both the scaphoid and lunate were consistently observed to have experienced a slight ulnar deviation of comparable magnitude during wrist flexion. In addition, the scaphoid was observed to be marginally more pronated than the lunate. In the distal carpal row, the capitate tracked the global wrist flexion almost linearly (mean 3MC-capitate slope for Z-rotation = 1.04, $R^2 = 0.99$), with minimal conjunct rotation occurring out-of-plane. This indicated an intercarpal Z-rotation, up to 18.7° ± 4.3°, between the capitate and the lunate. Consequently, if the

relative contribution of the radiocarpal and midcarpal joints to the global arc of wrist flexion was to be quantified based on the radiolunate and capitolunate angle in the central column (the capitolunate kinematics was summarised in Table B.2 in Appendix B), a ratio of approximately 38% to 62% was obtained. In terms of the translational movement of the carpal bones, opposite patterns were seen for the scaphoid and lunate. A tendency to translate volarly, ulnarly and proximally with respect to the radius was seen for the scaphoid during wrist flexion. The lunate, on the other hand, was shown primarily to translate in the dorsal direction during wrist flexion. For the capitate, an appreciable amount of volar translation with respect to the radius was also observed. At 30° of wrist flexion, this measured up to 5.25 ± 0.65 mm. As a result, the scaphoid, as well as the capitate, were seen to translate significantly towards the volar aspect of the lunate during the entire course of wrist flexion.

During wrist extension, the scaphoid and lunate also extended, but again with the lunate extending much less than that of the scaphoid (mean scaphoid-lunate slope for Z-rotation = 0.36, $R^2 = 0.65$). At 30° of wrist extension, he scaphoid and lunate extension was measured $-22.1° \pm 4.1°$ and $-6.4° \pm 3.9°$, respectively. It was clear that unlike the scaphoid, whose flexion and extension in response to the flexion and extension of the global wrist was comparable and almost symmetrical (mean 3MC-scaphoid slope = 0.74, $R^2 = 0.92$ during flexion; slope = 0.80, $R^2 = 0.87$ during extension), the extension exhibited by the lunate was, surprisingly, half of that observed during flexion in magnitude. As a result, the scaphoid appeared to be constantly extended in relation to the lunate during wrist extension. At 30° of wrist extension, this intercarpal rotation was measured up to $-15.4° \pm 3.9°$ about the Z-axis. Apart from the primary plane of motion, the scaphoid was shown again to ulnarly deviate but accompanied by an appreciable amount of supination. Meanwhile, the lunate exhibited negligibly small conjunct out-of-plane movements. Hence, the scaphoid consistently appeared to be ulnarly deviated and supinated with respect to the lunate. With again the capitate tracked global wrist extension with

perfect linearity (mean 3MC-capitate slope for Z-rotation = 0.99, $R^2 = 1.00$) and a reduced radiolunate rotation, the wrist extension was determined to be mostly facilitated through the motion midcarpal joint. In terms of carpal translations, the scaphoid was observed to translate towards the radial, dorsal and distal aspect of the radius, opposite to that experienced during wrist flexion. In contrast, minimal lunate translation was observed. For the capitate in the distal row, apart from its substantial dorsal translation that was anticipated given the large volar translation observed during wrist flexion, a significant amount of proximally directed intercarpal translation, up to 2.08 ± 0.61 mm, was also observed in relation to the lunate.

Radial and Ulnar Deviation

A more intriguing kinematic pattern of the carpal bones was seen during coronal plane motion of the global wrist. During ulnar deviation, both of the scaphoid and lunate extended, ulnarly deviated and pronated with respect to the radius. A linear relationship was observed between the extension experience by the two bones (mean scaphoid-lunate slope for Z-rotation = 1.25, $R^2 = 0.90$). At 20° of ulnar deviation, this was approximately $-10.2° \pm 3.5°$ for the scaphoid and $-10.5° \pm 6.2°$ for the lunate. Good synchronicity was also observed in the coronal plane between the two carpal bones (mean scaphoid-lunate slope for X-rotation = 0.85, $R^2 = 0.87$), and an ulnar deviation up to $11.5° \pm 2.2°$ and $9.1° \pm 2.5°$ was observed for the scaphoid and the lunate, respectively. Around the Y-axis, the lunate was shown to exhibit slightly increased conjunct pronation than the scaphoid. On the other hand, with its primary rotation tracked that of the global wrist motion (mean 3MC-capitate slope for X-rotation = 0.96, $R^2 = 0.99$), a substantial amount of pronation, up to $5.1° \pm 2.0°$, larger than that of the scaphoid and lunate, was observed for the capitate. Furthermore, with a lunocapitate ulnar deviation of $10.1° \pm 1.7°$, the radiocarpal and midcarpal joints seemed to have a similar contribution in facilitating the ulnar deviation of the global wrist. In terms of carpal translations, both the scaphoid and lunate showed a tendency to translate

radially, but with that of the lunate being slightly more prominent than that of the scaphoid. In addition, noticeable intercarpal translation towards the distal aspect of the lunate was observed for the scaphoid. Conversely, the capitate showed significant ulnar- and dorsal-wards intercarpal translation with respect to the lunate.

During radial deviation, both the scaphoid and lunate flexed and radially deviated. However, the extent to which the lunate rotated was much less than that of the scaphoid. At 20° of radial deviation of the global wrist, the flexion and radial deviation of the lunate were measured to be $6.6° \pm 3.7°$ and $-2.2° \pm 1.1°$, respectively, (in contrast to those of the scaphoid, measured $10.6° \pm 3.7°$ and $-4.5° \pm 1.9°$). It was also clear that both the primary X-rotation and the conjunct Z-rotation of the lunate were much smaller in magnitude comparing to those experienced during ulnar deviation of the global wrist. For the capitate, apart from the primary rotation again being collinear with the global wrist motion (mean 3MC-capitate slope for X-rotation = 0.98, $R^2 = 1.00$), a noticeable amount of conjunct supination, up to $-6.9° \pm 1.4°$, was observed. And it was evident that the amount of capitate pronation and supination was substantially higher during RUD than FEM. In addition, the midcarpal joint seemed to be the dominant contributor during wrist radial deviation, accounting for up to 86% of the global wrist motion. Radial deviation of the global wrist caused the scaphoid to translate ulnarly and proximally. The lunate seemed to follow the scaphoid to translate ulnar wards but again to a lesser extent. As a consequence, the scaphoid appeared to be mainly proximally and marginally ulnarly situated in relation to the lunate during wrist radial deviation. On the contrary, large radial translation in combination with tangible volar-wards movement was seen for the capitate with respect to the lunate.

Dart Thrower's Motion

In the present study, the trajectory of the simulated DTM was oriented approximately 33.7° to the sagittal plane (with 0° being the pure sagittal motion). At the negative extreme, where the wrist assumed 30° of extension

in combination with 20° of radial deviation, the scaphoid was observed to assume an extended, radially deviated and pronated posture with respect to the radius, measured $-11.0° \pm 5.0°$ (mean 3MC-scaphoid slope for Z-rotation = 0.41, $R^2 = 0.58$), $-7.5° \pm 2.6°$ (mean 3MC-scaphoid slope for X-rotation = 0.42, $R^2 = 0.73$) and $2.1° \pm 2.1°$ around the Z-, X- and Y-axis, respectively. In contrast, the lunate remained surprisingly stationary during the first half of the DTM (radial extension to neutral), with its average rotational shift being less than 2° observable across all three axes. As a result, the scaphoid appeared to be extended and radially deviated posture with respect to that of the lunate throughout the first half of the DTM. Despite the composite nature of the DTM, the capitate continued to be closely tracking that of the global wrist (mean 3MC-capitate slope for Z-rotation = 0.97, $R^2 = 0.99$; slope for X-rotation = 0.99, $R^2 = 1.00$), but an unusual amount of conjunct supination, up to $-11.3° \pm 3.7°$ around the Y-axis, was measured. Furthermore, in the central column, it was evident that the midcarpal joint played a decisive role in this part of the DTM, as the lunocapitate intercarpal rotations in both sagittal and coronal planes were overwhelmingly larger than those observed between the lunate and the radius, and accounted for over 90% of the global wrist extension and radial deviation (3MC-lunocapitate slope for Z-rotation = 0.98, $R^2 = 0.96$; slope for X-rotation = 0.93, $R^2 = 0.97$). In terms of carpal translations, a slight dorsal movement was observed for the scaphoid towards the radial extension phases of the DTM. On the contrary, the lunate appeared to be moving ulnar- and volar-wards away from the scaphoid. On the other hand, an appreciable dorsal, radial and proximal translations were seen for the capitate.

During the second half of the DTM, in which the neutral wrist proceeded towards the symmetric posture in the positive quadrant (ulnar flexion), the scaphoid was seen to flex, ulnarly deviated and marginally pronated, but with noticeably higher magnitudes than those experienced in the other half of the DTM. At the positive extreme characterised by 30° of flexion and 20° of ulnar deviation of the global wrist, these measured $15.5° \pm 4.5°$ (mean 3MC-scaphoid slope for Z-rotation = 0.55, $R^2 = 0.69$), $11.0° \pm 2.1°$ (mean 3MC-scaphoid

slope for X-rotation = 0.57, $R^2 = 0.86$) and $2.1^\circ \pm 2.1^\circ$ for the Z-, X-, and Y-rotation of the scaphoid, respectively. On the other hand, some flexion was observed for the lunate but with high variability between the specimens. However, a tangible degree of ulnar deviation and pronation of the lunate, up to $10.0^\circ \pm 2.1^\circ$ and $4.0^\circ \pm 2.7^\circ$, was seen consistently. As a result, the scaphoid appeared to have assumed a purely flexed posture with respect to the lunate during this part of the DTM. For the capitate, a good correspondence between its Z- and X-rotation with those of the global wrist was again maintained (mean 3MC-capitate slope for Z-rotation = 1.02, $R^2 = 0.99$; slope for X-rotation = 0.92, $R^2 = 0.98$). But unlike during the extension and radial deviation portion of the DTM which induced large conjunct supination, only a slight amount of pronation, approximately $2.9^\circ \pm 1.7^\circ$, was seen. In addition, the midcarpal joint still played an important role in the sagittal plane rotation of the global wrist movement (3MC-lunocapitate slope for Z-rotation = 0.87, $R^2 = 0.78$), but its contribution in the coronal plane was significantly less than that observed during the first half of the DTM. Instead, the ulnar deviation component of the DTM was fulfilled approximately equally via the rotations occurred at the radiocarpal and midcarpal joints. In terms of carpal translations, a substantial amount of volar translation up to 1.22 ± 0.37 mm was seen for the scaphoid. The lunate showed a tendency to translate primarily radially and dorsally, away from the scaphoid. Alternatively, the capitate exhibited a tendency to translate mainly in the volar and ulnar direction with respect to the lunate.

Table 4.3: Mean and standard deviation of the scaphoid kinematics measured relative to the radius

Scaphoid (w.r.t Radius)

Motion	Wrist Position		Rotation [deg]						Translation [mm]					
			Z		**X**		**Y**		**Z**		**X**		**Y**	
	Sagittal	Coronal	FL(+)/EX(-)	sd	UD(+)/RD(-)	sd	PR(+)/SU(-)	sd	RA(+)/UL (-)	sd	VO(+)/DO(-)	sd	PX(+)/DS(-)	sd
NEU			-0.09	0.52	0.64	0.42	-0.27	0.39	-0.03	0.20	0.00	0.10	0.00	0.15
FEM	30FL		22.53	3.53	1.91	2.73	0.66	1.11	-0.66	0.21	0.57	0.37	1.28	0.29
	25		18.57	2.73	1.24	1.75	0.48	1.07	-0.60	0.19	0.50	0.33	1.11	0.24
	20		14.80	1.98	0.82	1.11	0.27	1.03	-0.52	0.17	0.41	0.28	0.93	0.21
	15		11.09	1.30	0.53	0.68	0.09	0.93	-0.40	0.16	0.33	0.21	0.73	0.20
	10		7.32	0.82	0.36	0.43	-0.02	0.73	-0.29	0.16	0.22	0.13	0.51	0.20
	5		3.64	0.56	0.43	0.36	-0.18	0.39	-0.16	0.18	0.11	0.08	0.27	0.18
	5		-2.10	1.19	0.38	0.77	-0.41	0.69	0.10	0.18	-0.15	0.15	-0.17	0.16
	10		-6.02	1.81	0.62	1.00	-0.75	1.02	0.23	0.20	-0.32	0.25	-0.42	0.23
	15		-10.11	2.36	0.94	1.16	-1.06	1.21	0.35	0.24	-0.53	0.35	-0.67	0.30
	20		-14.00	3.02	1.33	1.02	-1.50	1.70	0.48	0.29	-0.74	0.44	-0.90	0.35
	25		-18.03	3.67	1.76	0.93	-1.66	1.75	0.61	0.35	-0.96	0.51	-1.14	0.42
	30EX		-22.07	4.07	2.35	0.74	-1.71	1.89	0.76	0.43	-1.19	0.57	-1.39	0.49
RUD		20UD	-10.15	3.54	11.50	2.15	2.97	1.83	0.43	0.50	0.02	0.41	-2.19	0.55
		15	-8.05	3.50	8.04	1.65	1.01	1.60	0.23	0.33	-0.08	0.34	-1.36	0.33
		10	-5.08	2.64	5.01	1.34	-0.08	1.30	0.09	0.20	-0.09	0.28	-0.73	0.18
		5	-1.85	1.33	2.41	1.14	-0.58	1.09	-0.03	0.18	-0.07	0.21	-0.23	0.10
		5	2.80	0.72	-1.05	0.63	0.10	0.67	-0.24	0.22	0.06	0.12	0.43	0.18
		10	5.75	1.33	-2.28	0.92	0.00	0.80	-0.38	0.19	0.06	0.16	0.74	0.23
		15	8.33	2.64	-3.34	1.31	0.10	1.18	-0.48	0.17	0.08	0.23	1.00	0.29
		20RD	10.62	3.67	-4.49	1.92	0.49	2.24	-0.56	0.16	0.09	0.32	1.25	0.38
DTM	30FL	20UD	15.54	4.46	11.01	2.10	2.11	2.13	-0.13	0.49	1.22	0.37	-0.28	0.53
	24	16	11.73	4.25	7.81	1.48	1.33	1.66	-0.22	0.36	0.80	0.28	-0.06	0.44
	18	12	8.02	3.86	5.11	1.04	0.64	1.10	-0.29	0.23	0.50	0.18	0.12	0.31
	12	8	4.76	2.97	3.12	1.07	0.12	0.70	-0.30	0.15	0.30	0.13	0.19	0.19
	6	4	1.95	1.83	1.47	1.15	-0.14	0.57	-0.26	0.14	0.13	0.14	0.21	0.12
	6	4	-1.10	0.93	-0.62	0.80	0.32	0.90	-0.03	0.17	-0.05	0.14	0.12	0.12
	12	8	-3.32	0.98	-2.02	0.78	-0.08	1.05	0.02	0.20	-0.19	0.21	0.14	0.18
	18	12	-5.87	2.47	-3.76	1.10	-0.38	1.28	0.07	0.26	-0.34	0.28	0.18	0.26
	24	16	-8.22	4.26	-5.44	1.79	-0.68	1.83	0.11	0.37	-0.43	0.37	0.24	0.35
	30EX	20RD	-11.04	4.97	-7.53	2.58	-1.61	3.30	0.16	0.46	-0.55	0.40	0.36	0.47

Rotation: FL = flexion (+); EX = extension (-); UD = ulnar deviation (+); RD = radial deviation(+); PR = pronation (+); SU = supination (-).
Translation: RA = radial translation (+); UL = ulnar translation (-); VO = volar translation (+); DO = dorsal deviation (+); PX = proximal translation (+); DS = distal translation (-).

Table 4.4: Mean and standard deviation of the lunate kinematics measured relative to the radius

Lunate (w.r.t Radius)

Motion	Wrist Position		Rotation [deg]						Translation [mm]					
	Sagittal	Coronal	**Z** FL(+)/EX(-)	sd	**X** UD(+)/RD(-)	sd	**Y** PR(+)/SU(-)	sd	**Z** RA(+)/UL (-)	sd	**X** VO(+)/DO(-)	sd	**Y** PX(+)/DS(-)	sd
NEU			-0.06	1.07	0.01	0.76	-0.08	0.33	-0.13	0.11	-0.01	0.14	0.09	0.18
FEM	30FL		11.31	3.99	1.97	1.49	0.14	1.43	0.06	0.18	-0.79	0.44	-0.11	0.14
	25		8.97	3.45	1.37	1.29	0.19	1.46	-0.03	0.16	-0.58	0.35	-0.06	0.14
	20		6.77	2.75	0.80	1.20	0.15	1.33	-0.09	0.13	-0.41	0.29	-0.02	0.15
	15		4.80	2.01	0.39	1.10	0.01	1.05	-0.11	0.09	-0.27	0.24	0.03	0.16
	10		3.00	1.46	0.18	0.97	-0.03	0.72	-0.12	0.06	-0.16	0.20	0.05	0.17
	5		1.39	1.22	0.11	0.78	-0.01	0.41	-0.13	0.07	-0.08	0.17	0.07	0.17
	5		0.72	1.79	-0.43	1.10	0.08	0.55	-0.13	0.14	-0.15	0.18	0.10	0.17
	10		-0.52	1.78	-0.48	1.21	-0.04	0.71	-0.11	0.18	-0.07	0.18	0.11	0.17
	15		-1.75	1.81	-0.45	1.33	-0.09	0.87	-0.09	0.22	-0.01	0.18	0.11	0.18
	20		-3.08	2.14	-0.29	1.48	-0.01	0.96	-0.05	0.27	0.06	0.20	0.12	0.19
	25		-4.62	2.87	-0.04	1.60	0.22	0.98	0.02	0.32	0.15	0.25	0.11	0.20
	30EX		-6.41	3.86	0.41	1.71	0.57	1.07	0.13	0.37	0.26	0.32	0.11	0.22
RUD		20UD	-10.49	6.16	9.07	2.50	3.66	1.96	1.64	0.65	0.21	0.32	-0.11	0.26
		15	-7.61	5.20	5.51	1.93	1.82	1.46	0.84	0.43	0.16	0.28	0.06	0.22
		10	-3.92	4.10	2.88	1.58	0.82	1.21	0.27	0.27	0.04	0.23	0.13	0.20
		5	-0.86	2.41	0.98	1.31	0.09	0.90	-0.06	0.17	-0.06	0.19	0.15	0.18
		5	0.70	1.75	-0.53	0.81	-0.21	1.02	-0.17	0.10	0.00	0.30	0.07	0.17
		10	2.73	1.95	-1.28	0.93	-0.41	0.74	-0.26	0.09	-0.07	0.30	0.03	0.17
		15	4.61	2.86	-1.73	1.10	-0.69	0.75	-0.32	0.07	-0.12	0.35	0.01	0.17
		20RD	6.57	3.66	-2.16	1.11	-1.12	0.91	-0.36	0.09	-0.16	0.41	-0.04	0.16
DTM	30FL	20UD	5.03	5.25	10.03	2.06	3.97	2.74	1.42	0.73	-0.64	0.42	-0.12	0.29
	24	16	3.17	4.62	7.11	1.53	3.03	2.16	0.83	0.52	-0.47	0.34	0.04	0.23
	18	12	1.58	3.70	4.45	1.09	1.89	1.50	0.34	0.34	-0.27	0.27	0.14	0.18
	12	8	0.50	2.77	2.56	1.10	0.81	1.04	0.02	0.24	-0.10	0.22	0.18	0.16
	6	4	-0.07	2.16	1.27	1.14	-0.03	0.85	-0.17	0.20	0.00	0.18	0.19	0.14
	6	4	0.17	2.32	0.00	0.95	0.31	0.78	-0.18	0.16	-0.05	0.27	0.16	0.15
	12	8	0.15	1.73	-0.55	1.15	-0.06	0.93	-0.24	0.18	0.02	0.27	0.15	0.15
	18	12	0.04	0.98	-0.87	1.40	-0.22	1.12	-0.27	0.21	0.08	0.28	0.13	0.16
	24	16	-0.29	1.62	-1.16	1.38	-0.31	1.46	-0.29	0.25	0.18	0.37	0.10	0.17
	30EX	20RD	-1.48	3.58	-1.66	0.97	-1.00	2.26	-0.34	0.29	0.45	0.68	-0.02	0.22

Rotation: FL = flexion (+); EX = extension (-); UD = ulnar deviation (+); RD = radial deviation(+); PR = pronation (+); SU = supination (-).
Translation: RA = radial translation (+); UL = ulnar translation (-); VO = volar translation (+); DO = dorsal deviation (+); PX = proximal translation (+); DS = distal translation (-).

Table 4.5: Mean and standard deviation of the capitate kinematics measured relative to the radius

Capitate (w.r.t Radius)

Motion	Wrist Position		Rotation [deg]						Translation [mm]					
			Z		**X**		**Y**		**Z**		**X**		**Y**	
	Sagittal	Coronal	FL(+)/EX(-)	sd	UD(+)/RD(-)	sd	PR(+)/SU(-)	sd	RA(+)/UL (-)	sd	VO(+)/DO(-)	sd	PX(+)/DS(-)	sd
NEU			0.16	0.52	0.63	0.39	-0.66	0.53	-0.17	0.23	-0.08	0.04	0.09	0.23
FEM	30FL		31.35	1.23	0.15	0.78	-0.29	2.86	-0.41	0.44	5.25	0.65	-0.32	0.68
	25		25.89	1.05	0.32	0.74	-0.30	2.36	-0.39	0.38	4.35	0.52	-0.40	0.62
	20		20.64	0.84	0.41	0.57	-0.34	1.80	-0.38	0.31	3.44	0.38	-0.42	0.56
	15		15.42	0.51	0.40	0.38	-0.34	1.20	-0.34	0.24	2.55	0.25	-0.37	0.49
	10		10.25	0.33	0.42	0.34	-0.52	0.70	-0.29	0.21	1.64	0.13	-0.27	0.41
	5		5.21	0.48	0.50	0.35	-0.64	0.51	-0.24	0.20	0.77	0.08	-0.12	0.32
	5		-5.10	0.32	0.26	0.39	0.54	0.60	0.07	0.28	-0.69	0.18	0.26	0.22
	10		-10.09	0.37	0.32	0.42	0.00	0.81	0.13	0.30	-1.43	0.21	0.55	0.16
	15		-15.17	0.30	0.32	0.46	-0.61	1.16	0.19	0.35	-2.17	0.22	0.89	0.13
	20		-20.28	0.32	0.29	0.60	-1.10	1.59	0.27	0.41	-2.86	0.26	1.27	0.14
	25		-25.33	0.35	0.28	0.60	-1.51	1.99	0.36	0.49	-3.52	0.30	1.69	0.17
	30EX		-30.41	0.40	0.36	0.63	-1.75	2.48	0.46	0.58	-4.14	0.35	2.15	0.21
RUD		20UD	0.19	0.52	20.00	1.02	5.13	2.00	-1.48	0.73	-1.22	0.93	-0.21	0.29
		15	0.14	0.58	14.99	0.87	3.75	1.75	-1.24	0.59	-0.91	0.79	-0.02	0.25
		10	0.21	0.58	10.21	0.64	2.51	1.38	-0.96	0.44	-0.52	0.56	0.05	0.22
		5	0.25	0.61	5.47	0.44	1.17	1.01	-0.61	0.34	-0.18	0.25	0.09	0.22
		5	0.29	0.54	-4.77	0.39	-0.89	0.75	0.28	0.17	0.06	0.05	0.13	0.25
		10	0.38	0.61	-9.74	0.24	-2.65	0.77	0.69	0.13	0.32	0.31	0.16	0.31
		15	0.36	0.65	-14.65	0.23	-4.67	0.96	1.10	0.17	0.56	0.51	0.20	0.36
		20RD	0.35	0.81	-19.50	0.36	-6.92	1.42	1.51	0.22	0.86	0.67	0.22	0.42
DTM	30FL	20UD	31.14	1.54	19.21	1.05	2.87	1.70	-2.04	0.53	4.49	0.55	-0.60	0.65
	24	16	25.07	1.16	15.44	1.04	2.80	1.81	-1.72	0.45	3.54	0.52	-0.50	0.54
	18	12	18.80	0.52	11.79	0.86	2.30	1.58	-1.43	0.37	2.58	0.49	-0.37	0.44
	12	8	12.51	0.48	8.14	0.56	1.21	1.45	-1.11	0.28	1.64	0.40	-0.23	0.31
	6	4	6.40	0.63	4.46	0.44	-0.03	1.20	-0.75	0.22	0.75	0.28	-0.05	0.21
	6	4	-6.06	0.31	-3.42	0.28	-0.49	0.82	0.34	0.18	-0.86	0.12	0.43	0.15
	12	8	-12.11	0.40	-7.37	0.29	-2.49	1.09	0.73	0.18	-1.56	0.17	0.81	0.15
	18	12	-18.17	0.43	-11.35	0.27	-5.04	1.42	1.10	0.18	-2.17	0.31	1.25	0.17
	24	16	-24.08	0.58	-15.37	0.47	-8.16	1.94	1.46	0.19	-2.69	0.48	1.74	0.19
	30EX	20RD	-29.00	1.58	-19.48	1.05	-11.32	3.67	1.81	0.24	-3.09	0.54	2.16	0.16

Rotation: FL = flexion (+); EX = extension (-); UD = ulnar deviation (+); RD = radial deviation(+); PR = pronation (+); SU = supination (-).
Translation: RA = radial translation (+); UL = ulnar translation (-); VO = volar translation (+); DO = dorsal deviation (+); PX = proximal translation (+); DS = distal translation (-).

4.1.2.2 Carpal Pathokinematics Following Ligament Resection (Fig. 4.11-4.19 and Appendix B.1-B.6)

In contrast to previous studies, where pathological changes in the carpal kinematics were evaluated based on either radiographic examinations in 2D or incomplete measurements that only captured carpal motion in selected planes, the following section presents a comprehensive collection of the carpal kinematics measured in all six degrees of freedom following each of the four stages of ligament resection.

Data Visualisation

The mean trajectory corresponding to the carpal kinematics in each of the six degrees of freedom (three rotational and three translational components) was plotted for the scaphoid, lunate, and capitate during different modes of wrist simulations (Fig. 4.10i).

Two different types of analyses were performed with their emphasis on detecting both the absolute difference in the data between two different stages as well as the difference in their patterns or the shapes of the curves. These analyses were performed on the data corresponding to every quarter of the motion cycle, and their outcomes were also visualised for ease of interpretation.

The two bar plots summarised the results given by the former analysis, where, for each stage of testing, the mean difference in carpal rotations and translations were examined over each quarter of the motion cycle and compared with those of the normal physiological control (Fig. 4.10ii), as well as those in the previous stage (Fig. 4.10iii). And to evaluate if the two reconstructive surgeries were effective in treating severe ligament injuries, the second comparison was carried out using the results obtained in Stage IV ligament division. The mean and the standard deviation of the values corresponding to all seven specimens were visualised, with the asterisks indicating the statistical outcomes obtained using the L^2-norm-based one-way

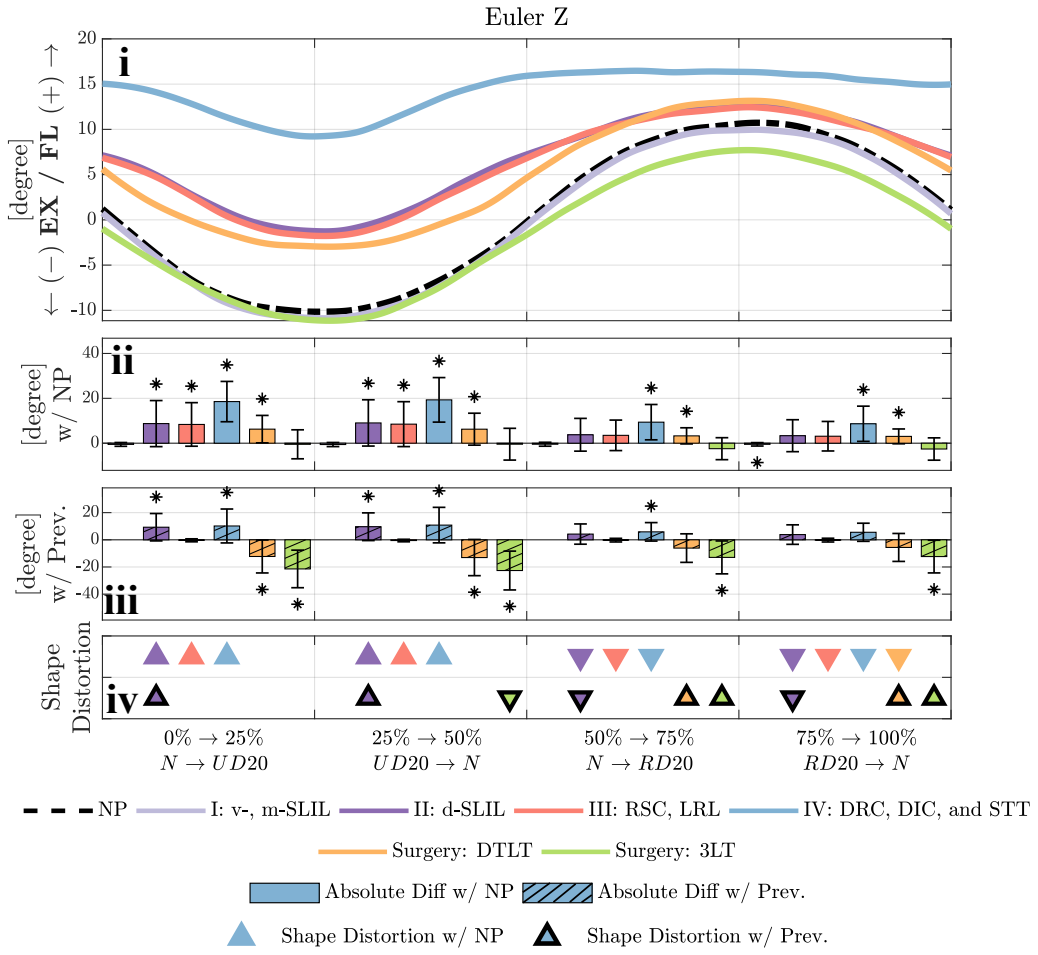

Figure 4.10: An example showing how carpal kinematics and the outcomes of three different types of analyses were visualised across different stages of ligament resection in Fig. 4.11-4.19 and Appendix B.1-B.6. Analyses were performed for the data corresponding to each quarter of the motion cycle. **(i)** The mean absolute trajectories corresponding to one of the six kinematic parameters measured for each stage of ligament division or surgical reconstruction (standard deviation is omitted for clarity). **(ii)** The mean absolute difference between the data measured in the current stage (colour-coded) and in the normal physiological (NP) stage. **(iii)** The mean absolute difference between the data measured in the current stage and the previous stage. Note: for the two surgeries, this is defined as Stage IV. Error bar: standard deviation; *: the difference is statistically significant ($p < 0.05$). **(iv)** Statistically significant mean shape distortions were detected for the current stage when compared to the data in the NP (upper row, solid triangles) and when compared to the data in the previous stage (bottom row, triangles with black edges). The orientation of the triangle represents the direction in which the shape change is occurring (towards the positive or the negative side of the curve).

fdANOVA mentioned previously (Section 4.1.1.7).

The latter analysis, whose main focus was on the mean shape difference between two curves, was deemed necessary as this reflected the change in carpal bones' dynamic behaviours in response to alterations in the wrist anatomy. However, this difference could be subtle and hard to uncover in light of large carpal malalignment. To this end, the trajectories corresponding to the carpal kinematics in each stage were first offset to exclude the difference in their starting positions. Above-described stage-wise comparisons were then carried out in a similar fashion on the resultant trajectories. Triangular indicators were used to report if there was a statistically significant change in the shape or general trend of the data corresponding to each quarter of the movement cycle (Fig. 4.10iv). The indicators were arranged in two rows, with those in the top row representing the comparisons with the trajectory corresponding to the NP, while those in the bottom row represented the comparisons with that corresponding to the previous stage. An upright triangle indicates the trajectory experienced an upward distortion towards the positive side, whereas an inverted triangle indicates a distortion towards the negative side.

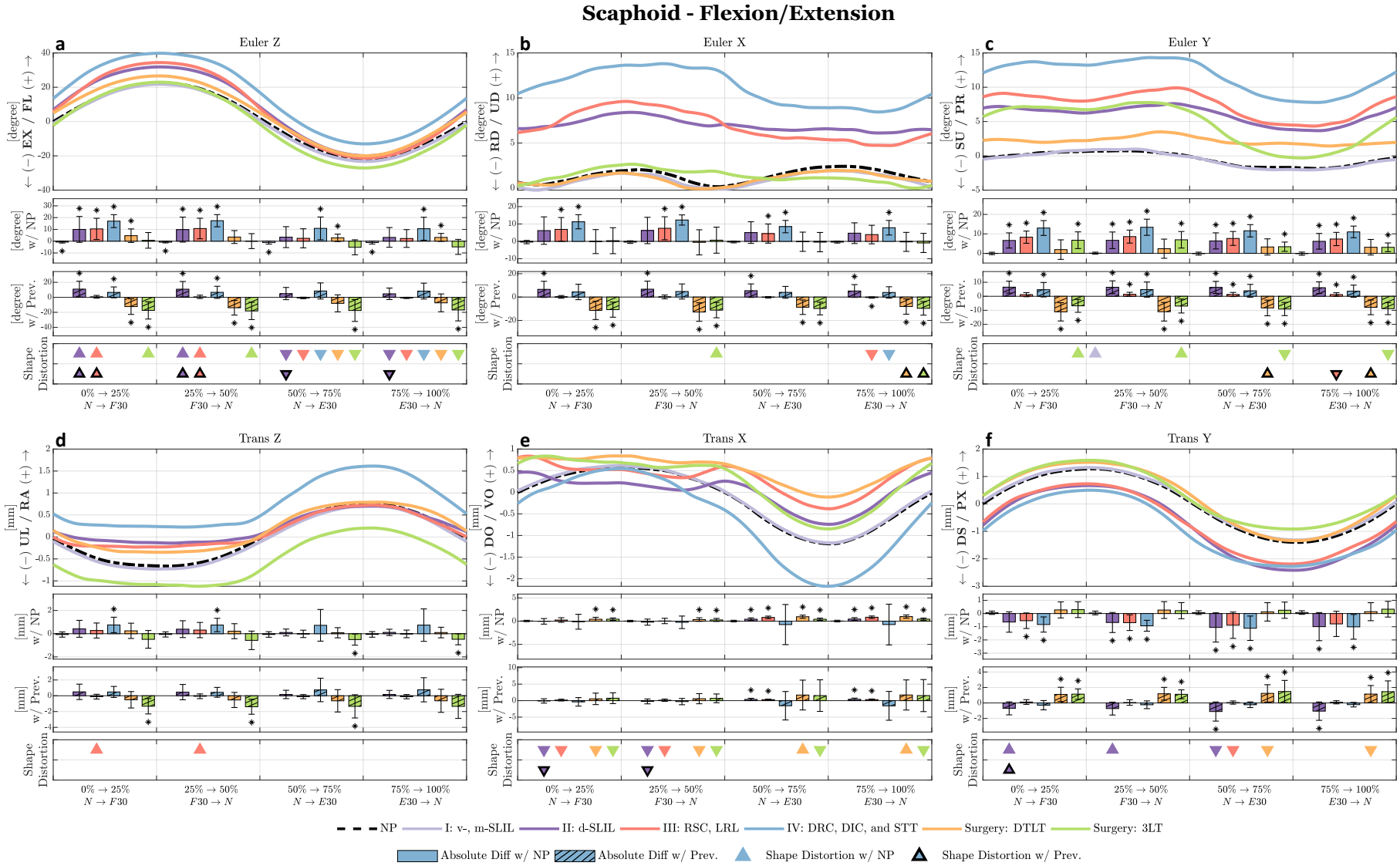

Figure 4.11: Scaphoid kinematics (w.r.t the radius) measured during FEM following incremental ligament resection and two different SLIL reconstructions. * denotes a statistically significant difference. FL = flexion, EX = extension; UD = ulnar deviation, RD = radial deviation; PR = pronation, SU = supination.

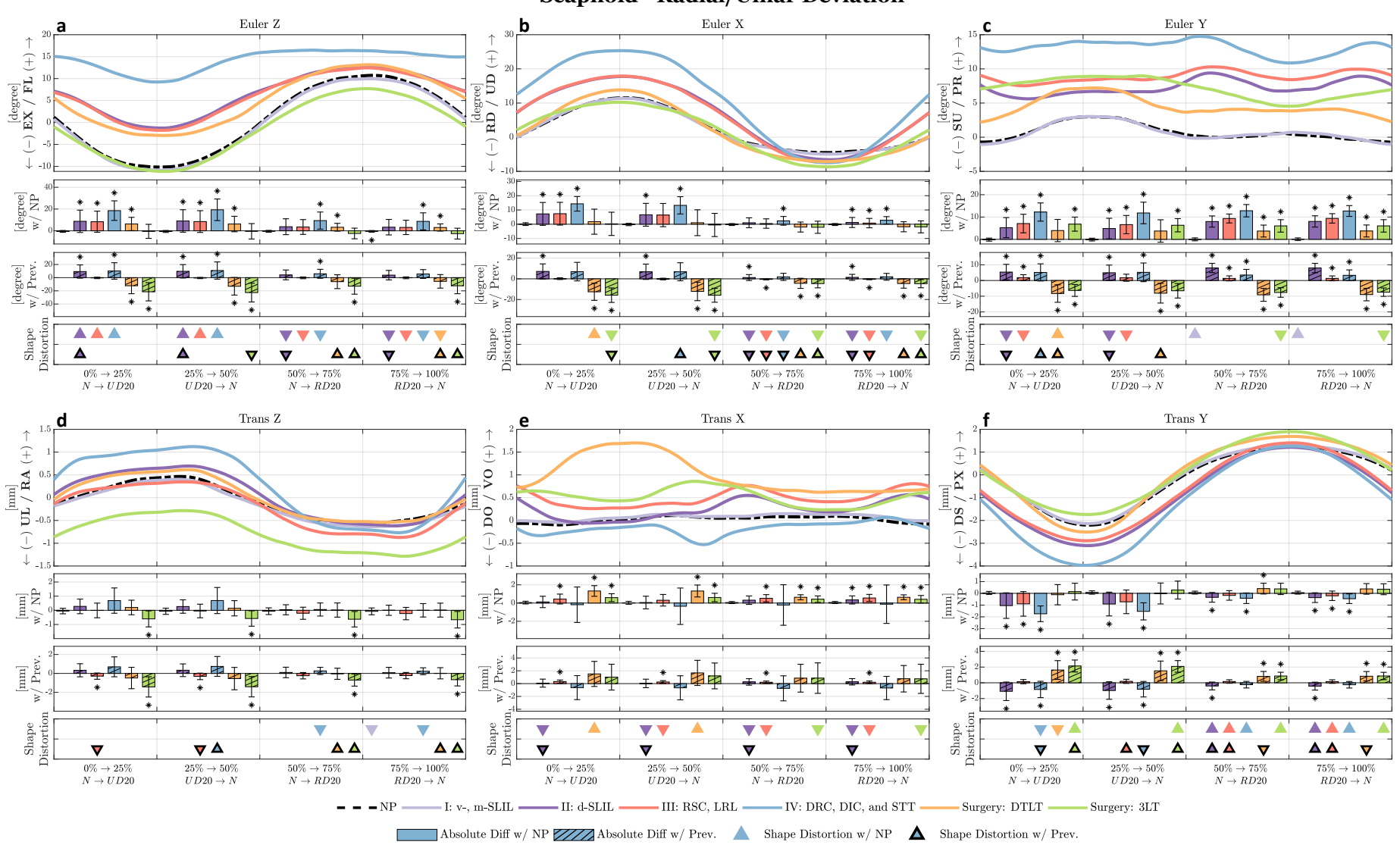

Figure 4.12: Scaphoid kinematics (w.r.t the radius) measured during RUD following incremental ligament resection and two different SLIL reconstructions. * denotes a statistically significant difference. FL = flexion, EX = extension; UD = ulnar deviation, RD = radial deviation; PR = pronation, SU = supination.

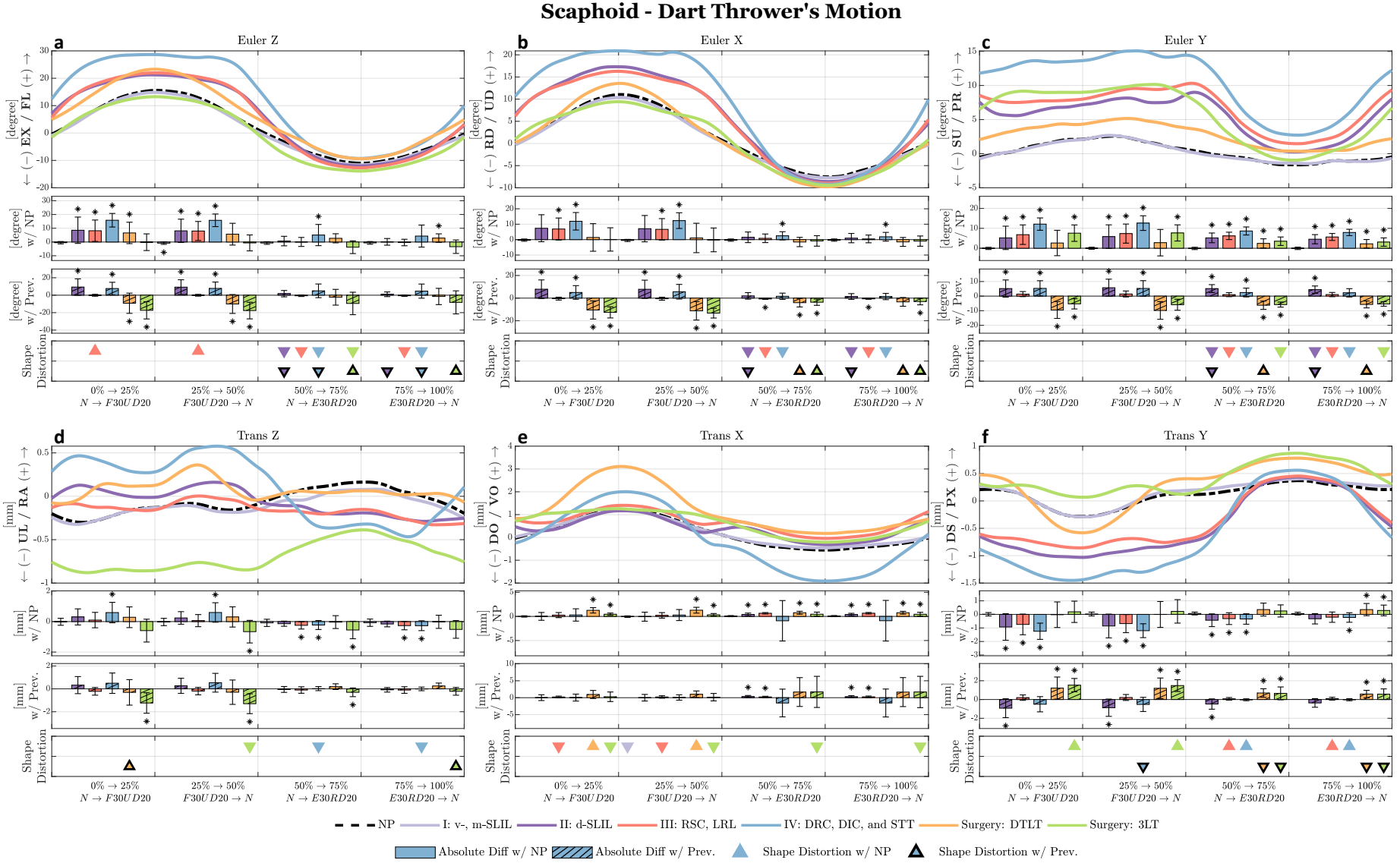

Figure 4.13: Scaphoid kinematics (w.r.t the radius) measured during DTM incremental ligament resection and two different SLIL reconstructions. * denotes a statistically significant difference. FL = flexion, EX = extension; UD = ulnar deviation, RD = radial deviation; PR = pronation, SU = supination.

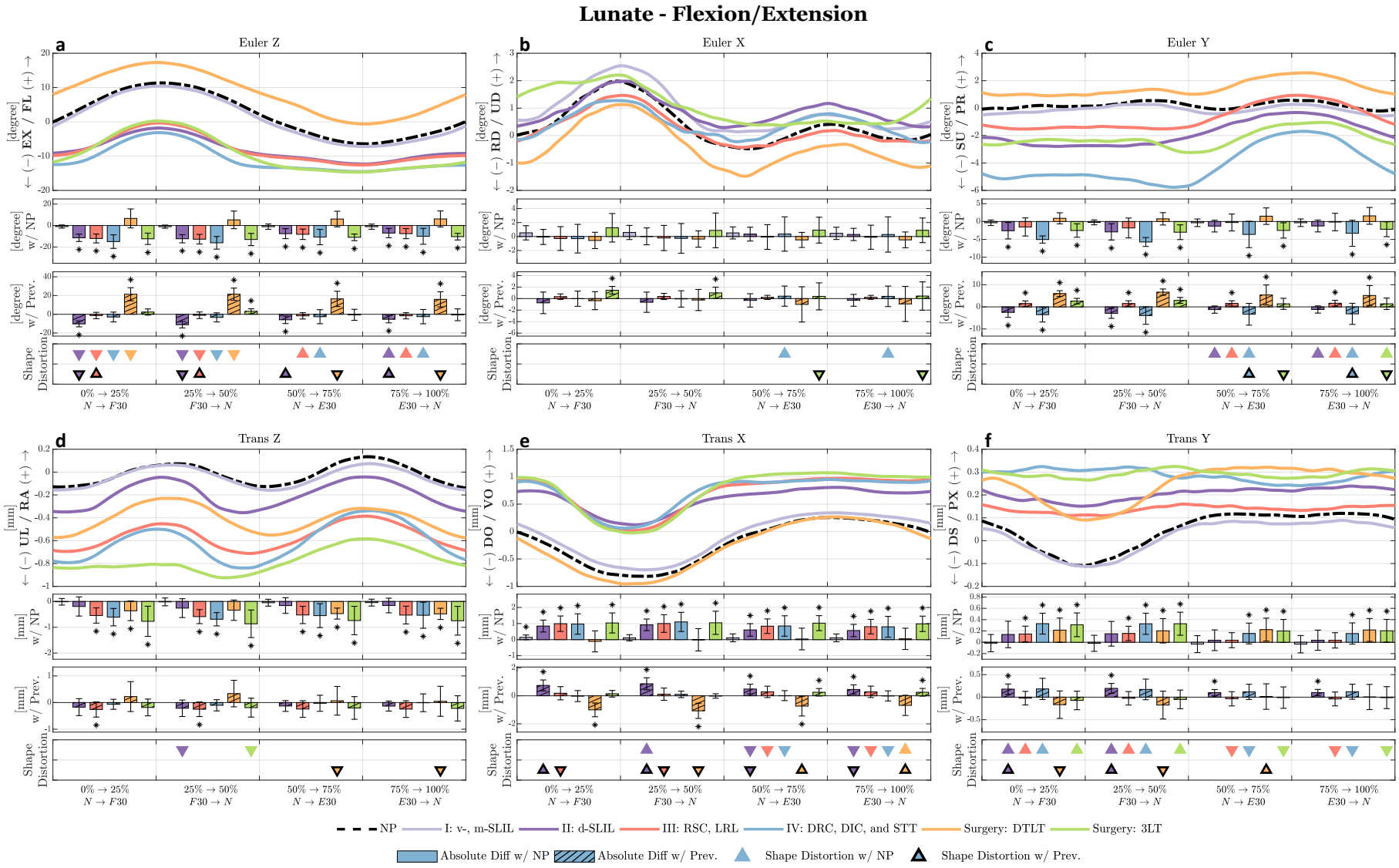

Figure 4.14: Lunate kinematics (w.r.t the radius) measured during FEM following incremental ligament resection and two different SLIL reconstructions. * denotes a statistically significant difference. FL = flexion, EX = extension; UD = ulnar deviation, RD = radial deviation; PR = pronation, SU = supination.

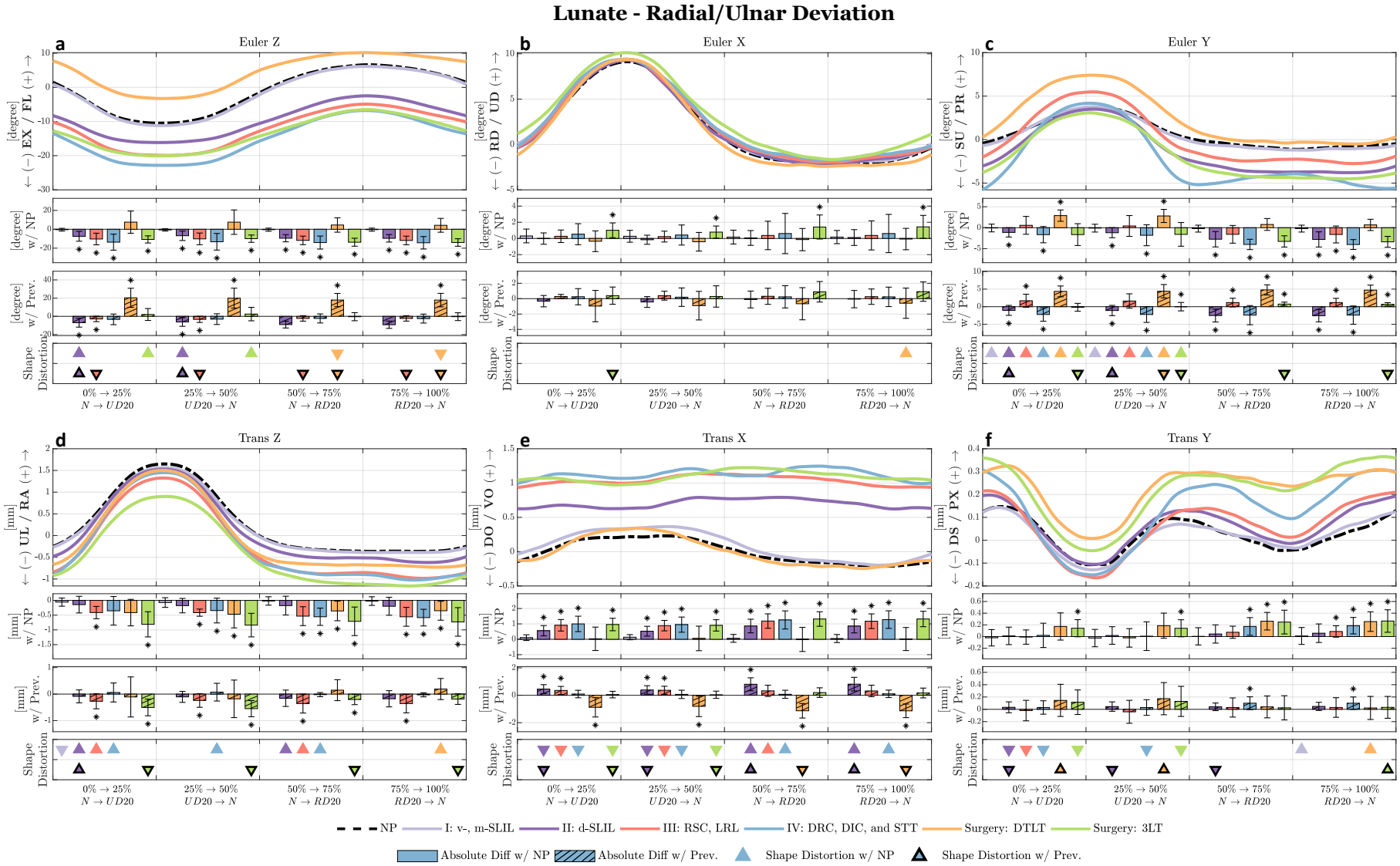

Figure 4.15: Lunate kinematics (w.r.t the radius) measured during RUD following incremental ligament resection and two different SLIL reconstructions. * denotes a statistically significant difference. FL = flexion, EX = extension; UD = ulnar deviation, RD = radial deviation; PR = pronation, SU = supination.

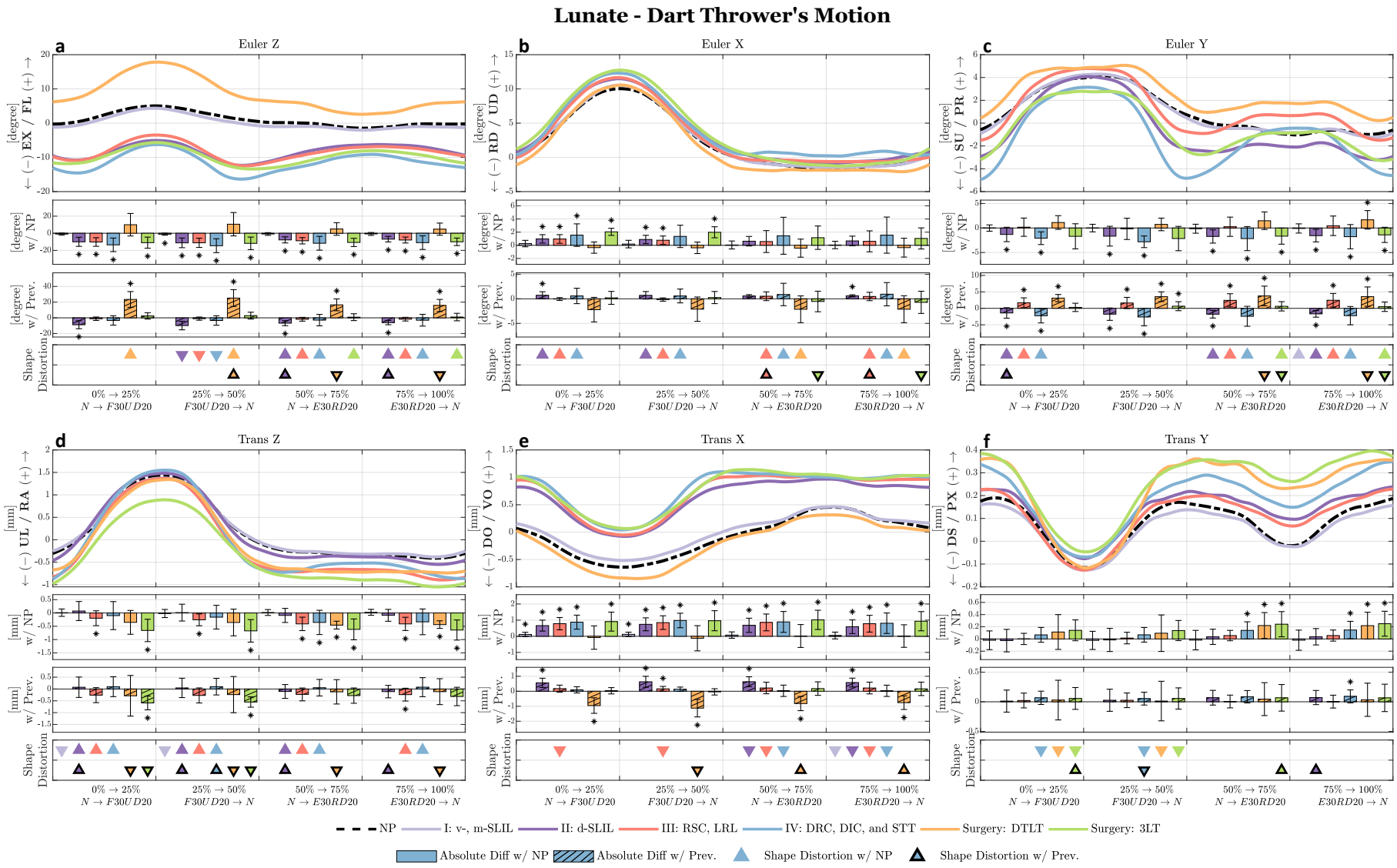

Figure 4.16: Lunate kinematics (w.r.t the radius) measured during DTM following incremental ligament resection and two different SLIL reconstructions. * denotes a statistically significant difference. FL = flexion, EX = extension; UD = ulnar deviation, RD = radial deviation; PR = pronation, SU = supination.

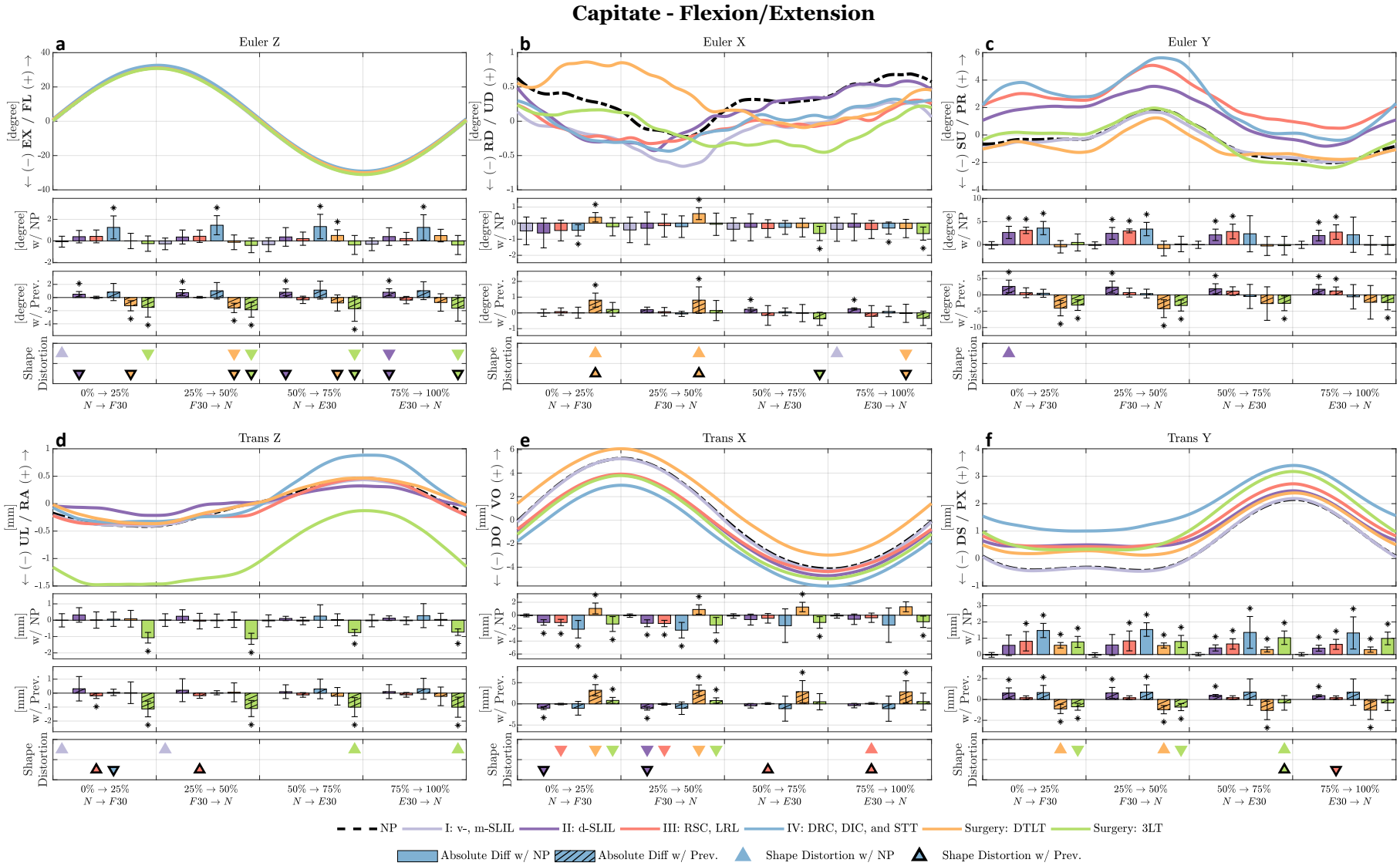

Figure 4.17: Capitate kinematics (w.r.t the radius) measured during FEM following incremental ligament resection and two different SLIL reconstructions. * denotes a statistically significant difference. FL = flexion, EX = extension; UD = ulnar deviation, RD = radial deviation; PR = pronation, SU = supination.

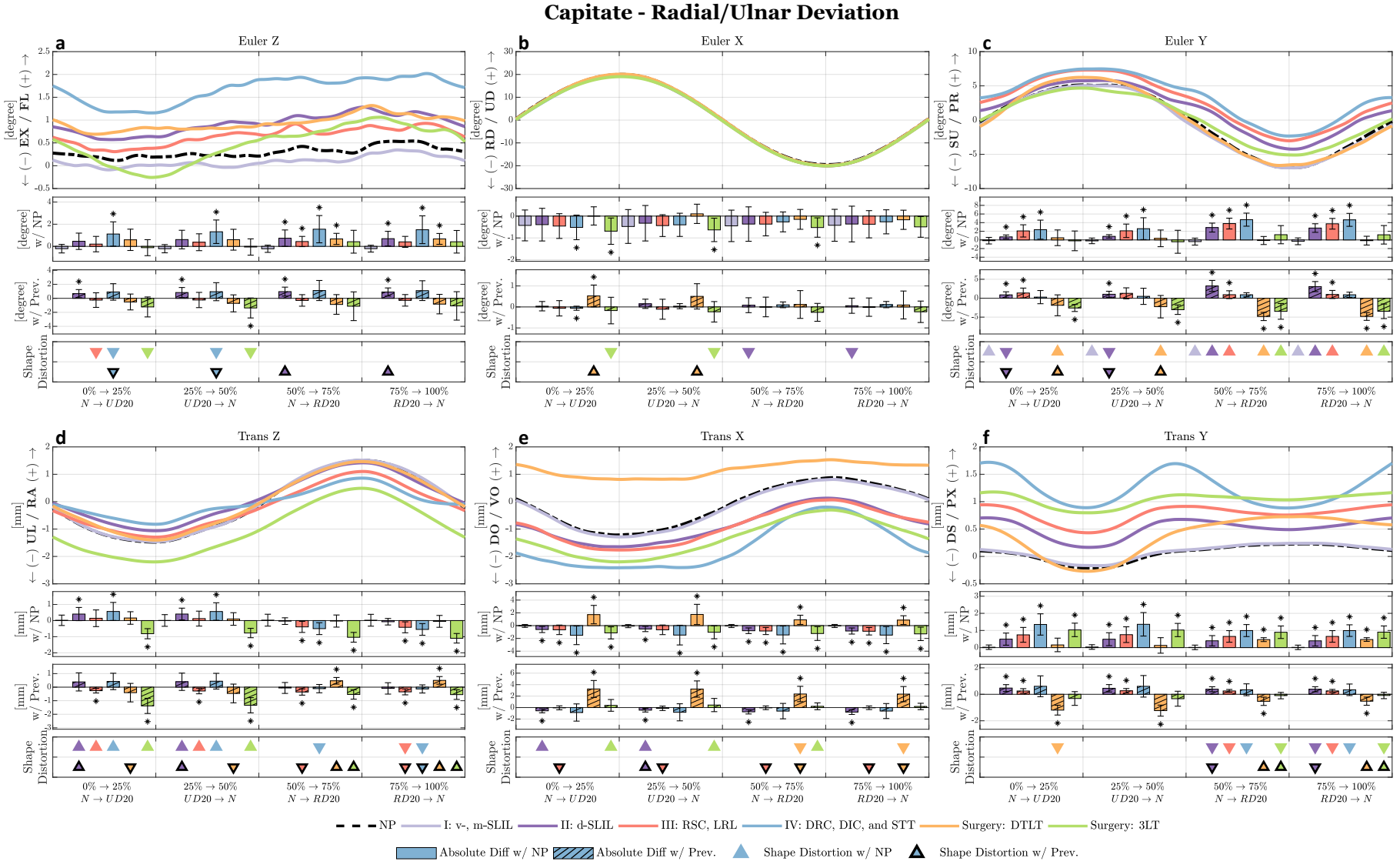

Figure 4.18: Capitate kinematics (w.r.t the radius) measured during RUD following incremental ligament resection and two different SLIL reconstructions. * denotes a statistically significant difference. FL = flexion, EX = extension; UD = ulnar deviation, RD = radial deviation; PR = pronation, SU = supination.

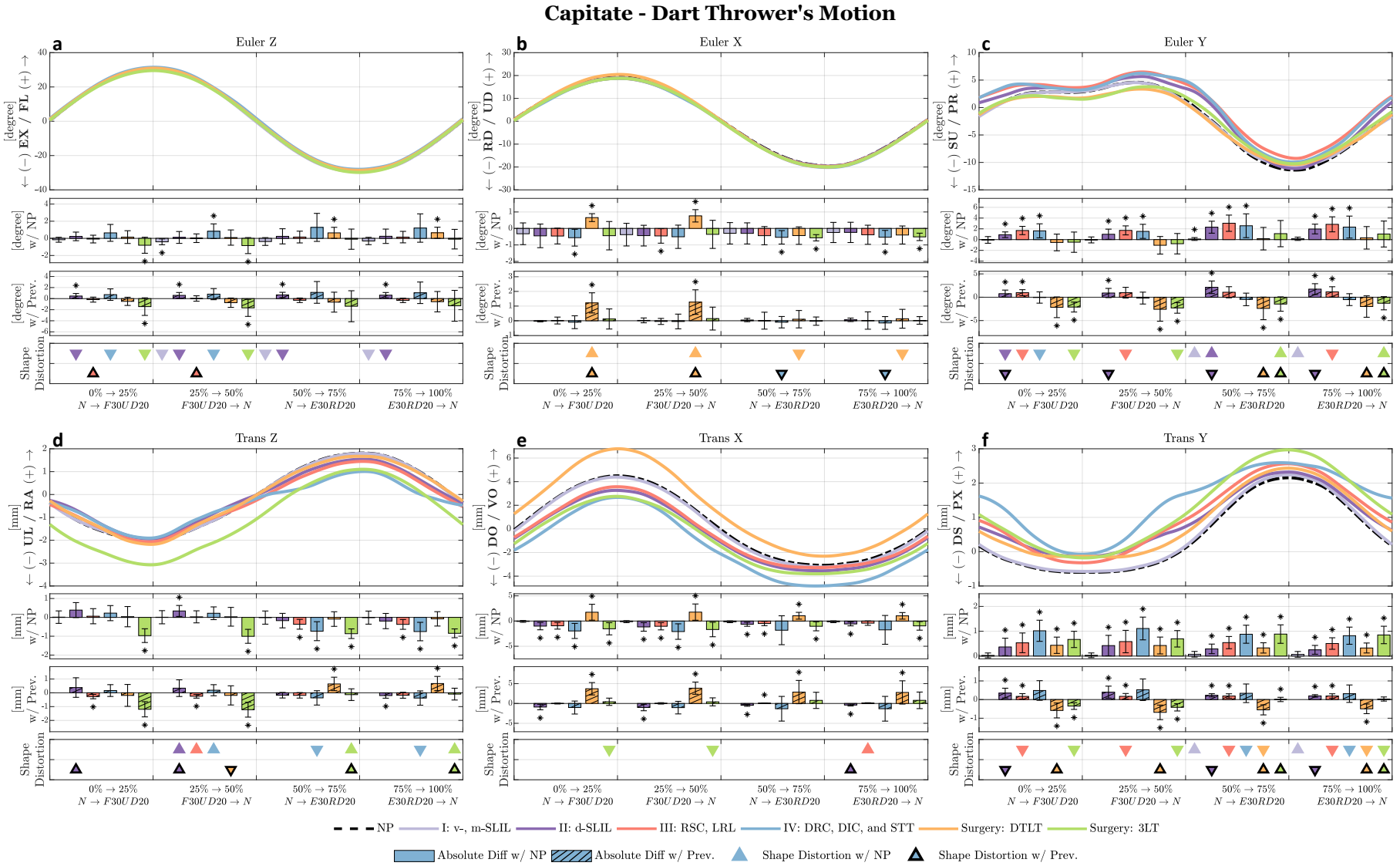

Figure 4.19: Capitate kinematics (w.r.t the radius) measured during DTM following incremental ligament resection and two different SLIL reconstructions. * denotes a statistically significant difference. FL = flexion, EX = extension; UD = ulnar deviation, RD = radial deviation; PR = pronation, SU = supination.

Stage I: resection of the v- and m-SLIL

With a few minor exceptions, dividing both the volar (v-) and proximal membranous (m-) subregions of the SLIL generally caused negligible alterations to the normal carpal kinematics and the scapholunate relation.

A slight but statistically significant extension was observed for the scaphoid with respect to the radius and was seen to be especially pronounced during extension of the global wrist (Fig. 4.11a). On average, this difference measured -1.2° ($p=0.025$) for the Z-component of the radioscaphoid rotation, comparing to the values recorded in the normal physiological stage. The lunate, on the other hand, showed slightly more volar translation with respect to the radius during global wrist flexion and ulnar flexion after sectioning the v- and m-SLIL (Fig. 4.14e and Fig. 4.16e). These changes, however, were both less than 0.20 mm in magnitude. A small amount of ulnar deviation, about 0.4° in magnitude, was also observed for the lunate in both FEM and RUD after releasing the v- and m-SLIL (Fig. 4.14b and Fig. 4.15b). Although this was shown to be statistically insignificant when viewed solely from the radius, the change was more noticeable if it was examined in relation to the scaphoid. It was clear that over the whole of the FEM simulation, the X-component (coronal plane) of the scapholunate angle was statistically different to that in the normal physiological state (Fig. B.1b). On average, this difference measured -0.8° ($p=0.002$) and -0.8° ($p=0.009$) during flexion and extension, respectively. On the other hand, the division of both the v- and m-SLIL caused the Y-component (transverse plane) of the capitolunate angle to be slightly more into pronation (Fig. B.4c and Fig. B.6b). Despite being statistically significant, especially during FEM or DTM, this change was only about 0.4° in magnitude.

Stage II: resection of the d-SLIL

Further releasing of the dorsal (d-) subregion of the SLIL not only altered the static posture of the scaphoid and lunate but also produced a range of

statistically significant changes in their kinematic behaviours during all three types of dynamic wrist motion.

Static Alignment in Neutral Position

It was evident that the complete loss of the SLIL caused a significant amount of change to the normal alignment of the carpal bones, which should be otherwise in parallel with the radius when the wrist is in the neutral position. Instead, the scaphoid was shown to assume a posture that was substantially more flexed, ulnarly deviated, pronated and distally translated with respect to the radius, as compared to that in Stage I or Stage NP (the starting point of a-c and f in Fig. 4.11-4.13). On average, these increments measured 7.0°, 6.8° and 7.4° around the Z-, X-, Y-axis, respectively and −0.73 mm along the Y-axis. These pathological malalignments were considered as static or permanent in nature, as the trajectories correspond to the absolute values of these kinematic parameters appeared as if they were "shifted" from the ones of the previous stages in almost the entire duration of all wrist motion.

The lunate posture, on the other hand, became appreciably more extended and supinated in relation to the radius as compared to that in the normal physiological stage, and measured −9.0° and −2.7° on average around the Z- and Y-axis, respectively (the starting point of a and c in Fig. 4.14-4.16). Interestingly, despite small in magnitude, the lunate posture was observed to be less ulnarly deviated compared to the one seen after Stage I ligament resection. In addition, an appreciable amount of volar translation, measured up to 0.73 mm, accompanied by a perceivable but less significant amount of ulnar and proximal movement, were also observed for the changes in the lunate posture when viewed relative to the radius (the starting point of d-f in Fig. 4.14-4.16).

In terms of the scapholunate alignment, the further release of the d-SLIL caused a mean increase of 16.0°, 7.3° and 10.3° in the scapholunate angles in the sagittal, coronal and transverse plane, respectively (the starting point of a-c in Fig. B.1-B.3). The centroid of the scaphoid appeared to be slightly radially and dorsally translated and appreciably distal to that of the lunate after the ligament division (the starting point of d-f in Fig. B.1-B.3). And

the average change in the distance between their centroids was approximately 1.09 mm (vector sum of the change along the Z-, X-, and Y-axis).

Furthermore, the capitate was noticeably pronated, dorsally and proximally translated in relation to the radius (the starting point of c, e and f in Fig. 4.17-4.19), measured 1.1° around the Y-axis, −0.84 mm and 0.69 mm along the X- and Y-axis, respectively, after the release of the d-SLIL. Consequently, the capitolunate alignment in the central column was observed to be more flexed in the sagittal plane and twisted into pronation in the transverse plane, owing to a more extended and supinate radiolunate posture after the division of the d-SLIL (the starting point of a, c in Fig. B.4-B.6). The centroid of the capitate appeared significantly dorsally with respect to the lunate. And the proximal translation of the capitate centroid might be indicative of the distal enlargement of the scapholunate interval, which allowed the capitate to be "wedged" into the space between the scaphoid and lunate under axial load.

Flexion and Extension

During global wrist flexion, the absolute scaphoid flexion, ulnar deviation, and pronation measured with respect to the radius were observed to be significantly increased by a mean of 10.9° ($p=0.020$), 6.6° ($p=0.033$), and 6.5° ($p<0.001$), respectively, compared to those in Stage I ligament resection (Fig. 4.11a-c). However, as in order to investigate to what extent the pattern of the scaphoid kinematics was altered as a result of further releasing the d-SLIL, the influence of the static malalignment of the scaphoid was then excluded. The pattern analysis indicated that during global wrist flexion, complete division of the SLIL significantly increased the net radioscaphoid flexion by a mean of 3.2° ($p<0.001$) comparing to that in the normal stage, and by a mean of 2.8° ($p<0.001$) comparing to that in Stage I (Fig. 4.11a). The other rotational parameters, however, saw negligible distortions in their patterns. In terms of the radioscaphoid translations, although no statistical changes were observable for their absolute values following the ligament resection, their dynamic patterns were shown to be statistically altered. It was clear that the conjunct volar translation of the scaphoid as seen during flexion of the

native wrists was now lost and replaced by some irregular dorsal movements (mean shape difference: -0.49 mm, p=0.020; Fig. 4.11e). And the curve corresponding to the radioscaphoid translation along the Y-axis was found to be distorting slightly towards the proximal end, suggesting the scaphoid now exhibit an increased amount of net proximal translation in relation to the radius after (mean shape difference: 0.21 mm, p=0.036; Fig. 4.11f). In contrast, the lunate saw a mean increase of 10.3° (p<0.001) and 2.5° (p=0.014) in its absolute extension and supination, respectively with respect to the radius, compared to the ones measured following Stage I ligament resection during wrist flexion (Fig. 4.14a and Fig. 4.14c). Within these changes, however, only the Z-component of the radiolunate rotation saw alterations in terms of its pattern. And unlike the scaphoid which demonstrated an extended range of dynamic flexion after the release of the d-SLIL, the net flexion exhibited by the lunate was found to be attenuated as compared to that in Stage I (mean shape difference: $-3.3°$, p<0.001; Fig. 4.14a). In addition, it was also clear that there was some "retardation" in lunate flexion when responding to the flexion of the global wrist. On the other hand, the absolute radiolunate translations saw only a marginal shift towards the radial direction but exhibited a statistically significant increase of 0.74 mm (p<0.001) and 0.18 mm (p<0.001) in the volar and proximal direction, respectively, compared to the values measured in Stage I (Fig. 4.14e and f). With a clearly less responsive trajectory, the net dynamic translation exhibited by the lunate in both the dorsal and distal directions was also statistically lowered following the release of the d-SLIL. In terms of the scapholunate rotation, the most noticeable change occurs in its sagittal plane component (measured around the Z-axis), which saw a significant increase of 21.1° (p<0.001) and 5.9° (p<0.001) in its absolute value and dynamic pattern as observed during global wrist flexion, respectively (Fig. B.1a). Furthermore, after the release of the d-SLIL, the scapholunate angle measured in the sagittal plane seemed to have first experienced a steep rise but followed by an interesting flattening during late wrist flexion. This essentially means the scaphoid and lunate was actually flexing in good synchronicity during that period even without the most immediate ligamentous association. And surprisingly, the vector

sum of the scaphoid translation relative to the lunate also decreased to a minimum of 0.53 mm (versus 2.07 mm in normal writs) during this period. In addition, the scapholunate angle in the other two planes, however, stayed almost unchanged throughout the global wrist flexion. Furthermore, apart from the significant increase in the absolute value of the capitolunate angle measured in the sagittal plane, the complete division of the SLIL also caused its dynamic pattern to be significantly distorted towards flexion (mean shape difference: 3.3°, $p<0.001$; Fig. B.4a). This suggests that the contribution of the midcarpal joint in facilitating the flexion of the global wrist was increased to compensate for the attenuating in the radiolunate movement.

During global wrist extension, the absolute radioscaphoid rotation was again observed to possess more ulnar deviation and pronation compared to that recorded in Stage I ligament resection and was considered primarily due to the static change in the scaphoid posture. However, during this part of wrist motion, the increase in the absolute scaphoid flexion caused by dividing the d-SLIL (mean absolute difference: 5.0°, $p=0.16$) was not as significant as the one observed during global wrist flexion (Fig. 4.11a). This attenuation in the overall increase of the scaphoid flexion implies that the scaphoid must have exhibited an extended amount of extension. This finding was in agreement with the outcome of the pattern analysis, where a mean shape distortion of $-3.2°$ ($p=0.002$) was found for the trajectory of the scaphoid extension after releasing the d-SLIL. On the other hand, the ligament division caused the scaphoid to possess statistically more translations in both the volar (0.38 mm, $p=0.017$) and distal directions (1.11 mm, $p=0.045$) with respect to the radius, as compared to those recorded during global wrist extension in Stage I ligament resection. Again, these were considered to be mostly a result of the static malalignment of the scaphoid (initial shifts in trajectories), as no major shape distortions were flagged in the subsequent pattern analysis. Interestingly, the division of the d-SLIL seemed to have produced no noticeable alterations to the physiological radial translation of the scaphoid during global wrist extension.

In terms of the lunate, excluding the influence of its static malalignment,

its net pronation during global wrist extension was statistically larger compared to that in the normal physiological stage (mean shape difference: 0.8°, p=0.006; Fig. 4.14c). In addition, similar to the findings in wrist flexion, the lunate became less responsive and remained relatively stationary in its pathological posture after the ligament resection, when there should have been more conjunct volar movements during wrist extension (mean shape difference: -0.11 mm, p<0.001; Fig. 4.14e). In terms of the intercarpal motion, even with the global wrist in extension, the scapholunate angle in the sagittal plane was still statistically more flexed, by an amount of 11.1° (p<0.001), than that in the previous stage (Fig. B.1a). In terms of its dynamic pattern, however, the ligament division caused a statistical increase in the net extension exhibited by the scaphoid relative to the lunate (mean shape difference: −4.1°, p<0.001). This again suggests the increased mobility of the scaphoid after dividing the d-SLIL, but such increase seems to be more pronounced during flexion than in extension. In addition, the flattening in the sagittal plane scapholunate angle, as seen during mid to late wrist flexion, was now absent. In terms of the scapholunate translations, the vector sum of the scaphoid movement relative to the lunate increased monotonically to reach a peak of 3.14 mm (versus 2.18 mm in normal wrists) at 30° of wrist extension. Again, apart from the significant increase in the absolute value of the capitolunate angle measured in the sagittal plane, the complete division of the SLIL also caused a statistical distortion in its dynamic pattern (mean shape difference: −0.8°, p=0.018; Fig. B.4a). This change, however, was far less than that observed during flexion, suggesting the contribution of the midcarpal joint in facilitating the global wrist extension was virtually unchanged by the loss of the SLIL.

Radial and Ulnar Deviation

In light of the static malalignment of the scaphoid and lunate, their absolute rotations measured during ulnar deviation of the global wrist were observed to be substantially different from those recorded in the normal wrists and the wrists that sustained Stage I ligament resection. For the scaphoid, the average difference was 9.3° (p=0.024), 7.2° (p=0.016) and 5.3°

(p=0.005) for its absolute rotational parameter around the Z-, X- and Y-axis, respectively, as compared to that before the release of the d-SLIL in Stage I. For the lunate, only the rotational components for the Z- and Y-axis saw statistically change after the release of the d-SLIL, measured $-7.0°$ ($p<0.001$) and $-1.1°$ (p=0.031), respectively, with respect to those in the previous stage. This information, however, is deemed of little value in deciphering how the kinematic behaviour of the individual carpal bone has to change in order to accommodate for the disruption of certain ligamentous constraints while still functioning to achieve more or less the same global wrist motion. Therefore, apart from the difference that is in apparent association with the static malalignment of the carpal bones, the modifications to their dynamic patterns after the release of the d-SLIL were again analysed in a similar fashion and described in detailed. For the scaphoid, the net adaptive extension in response to the global wrist ulnar deviation was statistically attenuated as compared to that recorded in Stage I ligament resection (mean shape difference: 2.9°, $p<0.001$; Fig. 4.12a). The physiological conjunct pronation of the scaphoid during ulnar deviation, however, was seen to be lost and replaced by an abnormal dynamic rotation into supination (mean shape difference: $-3.4°$, $p<0.001$; Fig. 4.12c). Interestingly, no statistically significant pattern change was detected for the ulnar deviation of the dynamic radioscaphoid rotation. In terms of radiocarpal translations, the scaphoid was observed to experience statistically more net dorsal movement after the release of the d-SLIL compared to that in the previous stage (mean shape difference: -0.43mm, p=0.0017; Fig. 4.12e). Similar to that in the scaphoid, the division of the d-SLIL also a significantly attenuated the net adaptive extension of the lunate (mean shape difference: 2.2°, p=0.036; Fig. 4.12a) as compared to that observed in Stage I, clearly indicating the loss of association with the scaphoid. On the other hand, the lunate exhibited statistically more dynamic rotation in pronation (mean shape difference: 1.3°, p=0.003; Fig. 4.12c) following the resection of the d-SLIL. On the contrary, the X-axis component of the radiolunate rotation saw minimal alterations in both its absolute value and dynamic pattern. In addition, the radiolunate translations were observed to have experienced statistically significant pattern changes in

all three components after the division of the d-SLIL. However, apart from the now less responsive volar/dorsal translations whose pattern sustained the most substantial distortion (mean shape difference: −0.21 mm, p=0.005; Fig. 4.15e), the pattern changes seen by the other two components were both less than 0.1 mm in magnitude.

In terms of the intercarpal rotation, apart from the initial static malalignment, the scapholunate angle remained almost constant in the sagittal plane and saw only marginal variations in the coronal plane throughout the wrist ulnar deviation (Fig. B.2a and b). In the transverse plane, however, the scapholunate angle was shown to be statistically different from that in the normal wrist and in Stage I ligament release in terms of both their absolute value and pattern (Fig. B.2c). This was somehow anticipated, given the abnormal dynamic supination shown by the scaphoid and the increase in the dynamic pronation experienced by the lunate after the division of the d-SLIL. In terms of the intercarpal translations, the scaphoid was seen to be displaced significantly distal relative to the lunate, and the vector sum of the scapholunate displacement increased monotonically to reach a peak of 3.19 mm (versus 2.42 mm in normal wrists) at 20° of wrist ulnar deviation after the ligament division. Furthermore, the complete division of the SLIL did not cause any significant alteration to the in-plane radiocarpal and midcarpal contribution to the global wrist ulnar deviation, as the capitolunate alignment on the coronal plane remained basically unchanged (Fig. B.5b).

During radial deviation of the global wrist, the complete division of the SLIL caused the absolute radioscaphoid rotation around the X- and Y-axis to become statistically different from those in Stage I (Fig. 4.12b and c). On average, these differences measured 1.2° (p=0.031) and 8.0° (p<0.001), respectively, for the radial deviation and pronation of the scaphoid with respect to the radius. No statistical difference was observed for the radioscaphoid flexion occurred conjunctly during wrist radial deviation after releasing the d-SLIL (Fig. 4.12a). It was also clear that the difference in the absolute radioscaphoid flexion and radial deviation were appreciably lower than those

observed during ulnar deviation. However, under the presence of the large initial malalignment, these seemingly "improved" radioscaphoid angulations actually suggested the net radioscaphoid movement in those DOFs must have been changed dramatically. The net radioscaphoid flexion during wrist radial deviation was statistically less (mean shape difference: $-2.2°$, p=0.006) than that measured before the division of the d-SLIL, whereas the net radial deviation of the scaphoid with respect to the radius drastically increased (mean shape difference: $-6.0°$, p<0.001). On the other hand, although no statistical difference was found for the absolute radioscaphoid translation along the X-axis, the net dorsal movement of the scaphoid saw a statistically increase (mean shape difference: -0.24 mm, p=0.001; Fig. 4.12e) after the ligament release, which was also observed during wrist ulnar deviation. In addition, the net scaphoid translation along the Y-axis in the proximal direction saw a significant increase (mean shape difference: 0.65 mm, p=0.002) compared to that in Stage I, despite the small difference between their absolute values (mean difference: -0.40 mm, p=0.027). In terms of the radiolunate motion, its absolute rotational component around the Z- and Y-axis were again statistically different from those in Stage I and those differences, measured $-9.1°$ (p<0.001) and $-2.5°$ (p=0.001), respectively. Unlike the ones seen for the scaphoid, these differences in the radiolunate rotation were larger in magnitude comparing to saw those during wrist ulnar deviation. However, these differences were mainly attributed to the static deformity of the lunate as no further distortion in its dynamic pattern of rotation was found. In terms of radiolunate translations, the absolute volar movement of the lunate during radial deviation was statistically different from that measured in Stage I (0.80 mm, p<0.001; Fig. 4.15e), and was also higher than that observed during ulnar deviation. And if the influence from the initial radiolunate malalignment is again excluded, it is evident that instead of translating dorsally, the lunate exhibited small net movement towards the volar radius (mean shape difference: 0.14 mm, p=0.002) after dividing the d-SLIL. With a decreasing scapholunate rotation around the X-axis, it was clear the scaphoid became gradually in parallel with the lunate in the coronal plane during wrist extension. The dynamic pattern of the

scapholunate radial deviation, however, saw a substantial change, where the scaphoid showed significantly more net radial deviation with respect to the lunate (mean shape difference: -6.3°, p=0.001) after the ligament division (Fig. B.2b). In terms of intercarpal translations, apart from the fact that the scaphoid was still distally translated relative to the lunate, the absolute value of the scapholunate translation was much closer to that in the normal case during radial deviation (mean difference: -0.44 mm, p=0.015; Fig. B.2f) than ulnar deviation. However, this was mainly due to the increased net proximal movement of the scaphoid (mean shape difference: 0.68 mm, p=0.002) with respect to the lunate after the complete division of the SLIL. The vector sum of the scaphoid movement relative to the lunate again increased monotonically to reach a peak of 1.34 mm at 20° of wrist radial deviation and seemed to be unaffected by the complete loss of the SLIL. In terms of the capitolunate relation, similar to that observed in ulnar deviation, the in-plane radiocarpal and midcarpal contribution to the primary global wrist motion seems to be unchanged before and after dividing the d-SLIL (Fig. B.5b). However, after the ligament release, the absolute capitolunate angulation in the transverse plane became more pronated (mean difference: 5.2°, p<0.001) than that observed in Stage I and during ulnar deviation. However, the net supination exhibited by the capitate with respect to the lunate actually decreased (mean shape difference: 1.3°, p=0.001) after the ligament division.

Dart Thrower's Motion

During ulnar flexion of the global wrist, the absolute radioscaphoid flexion, ulnar deviation and pronation were statistically different from the ones observed before the division of the d-SLIL. On average, these difference measured 9.3° (p=0.029), 7.9° (p=0.032) and 5.2° (p=0.049) for the absolute rotations around the Z-, X- and Y-axis, respectively (Fig. 4.13a, b, and c). The rotational behaviour of the scaphoid, however, was considered to be unaffected by the division of the d-SLIL, as no statistical distortions were detected in their patterns. In terms of translations, the division of the d-SLIL caused statistical change only in the absolute values of the radioscaphoid movement along the X-axis (-0.93 mm, p=0.041; Fig. 4.13f), and did not induce any

appreciable distortions in the translational behaviour of the scaphoid. On the other hand, the absolute radiolunate flexion, ulnar deviation and pronation were also statistically different from the ones recorded before the division of the d-SLIL. The average difference measured -8.8° ($p<0.001$), 0.7° ($p=0.011$) and -1.4° ($p=0.036$) for the radiolunate rotation around the Z-, X- and Y-axis, respectively (Fig. 4.16a, b, and c). Surprisingly, in contrast to that seen in pure wrist flexion, the complete division of the SLIL did not seem to induce any statistical alterations in the pattern of the net radiolunate flexion experienced during ulnar flexion of the global wrist. A slight increase in the net lunate pronation (mean shape difference: 0.8°, $p=0.001$) was again detected, similar to that observed in the pure wrist ulnar deviation. In addition, despite being statistically significant, the alteration saw by the X-component of the radiolunate rotation in both its absolute value and pattern were small. On the other hand, the alterations in the absolute radiolunate translations were smaller compared to those measured in pure wrist flexion but not in ulnar deviations.

In terms of the scapholunate relations, the absolute scapholunate rotation in the sagittal and transverse plane was found to be statistically different from those in Stage I, with a mean increase of 17.6° ($p=0.002$) and 8.9° ($p=0.009$), respectively (Fig. B.3a and c). In contrast, the change in the absolute scapholunate rotation in the coronal plane was found to be statistically insignificant after the ligament division. This, however, was presumably owing to an increased inter-specimen variation in this quantity which caused the inability to reject the null hypothesis. Nonetheless, the effect of completely dividing the SLIL had on the three rotational components of the absolute scapholunate motion during wrist ulnar flexion was less pronounced than that seen during pure wrist flexion. In addition, unlike those in pure wrist flexion, the scapholunate translation during wrist ulnar flexion experienced very little change in the absolute values of both its X- and Z-component after the complete division of the SLIL (Fig. B.3d and f). On the other hand, the vector sum of the scaphoid movement relative to the lunate again increased monotonically to reach a peak of 2.16 mm (versus 2.44 mm in normal writs)

at 30° of wrist flexion coupled with 20° of ulnar deviation. This was smaller than that in pure wrist ulnar deviation but substantially larger than that observed in pure flexion after the ligament division.

During radial extension of the global wrist, the alterations induced by the complete division of the SLIL in the absolute radioscaphoid rotation around both the Z- and X-axis were exceptionally small and statistically insignificant (Fig. 4.13a and b). The absolute radioscaphoid rotation around the Y-axis, on the other hand, was again shown to be statistically different from that recorded in Stage I (Fig. 4.13c). However, these differences were noticeably smaller, in contrast to the ones observed during ulnar flexion. In terms of the dynamic patterns, further release of the d-SLIL permitted greater mobility for the scaphoid, as the net extension (mean shape difference: $-6.6°$, p=0.033) and radial deviation (mean shape difference: $-4.9°$, p=0.023) and supination (mean shape difference: $-2.8°$, p=0.003) demonstrated by the radioscaphoid articulation all saw statistical increase comparing to the values measured prior to the ligament division. On the other hand, no major statistical alterations were found for the absolute radioscaphoid translations following the ligament release during radial extension of the wrist. In terms of the absolute radiolunate motion, the Euler rotation around the Z- and Y-axis was statistically different from that measured prior to the division of the d-SLIL. On average, these measured $-6.8°$ ($p<0.001$) and -1.78 (p=0.001), respectively. Noticeably, these changes were smaller than the ones seen in pure wrist radial deviation but larger than those in pure extension. By excluding the difference caused by the initial malalignment and only focus on pattern changes, the lunate was observed to be dynamically flexing (mean shape difference: 2.6°, p=0.018) during wrist radial extension after the complete SLIL disruption, instead of marginally extending as seen in the normal physiological stage.

In terms of the scapholunate relations, it was clear the impact of dividing the SLIL had on the absolute scapholunate angulation was statistically less in wrist radial extension and especially in its later stage, than in ulnar flexion. However, dynamically, the scaphoid exhibited significantly greater rotational movement in relation to the lunate in all three planes. In addition,

the capitate exhibited statistically less supination with respect to the radius during wrist radial extension after the complete disruption of the SLIL. On the other hand, the vector sum of the scaphoid movement relative to the lunate reached a peak of 1.34 mm (versus 1.19 mm in normal writs) at 30° of wrist extension combined with 20° of radial deviation. And this value was similar to that observed in pure wrist radial deviation.

Stage III: resection of the RSC and LRL

Further release of both the RSC and LRL in addition to the SLIL, produced less distinctive changes in carpal kinematics compared to those observed in Stage II.

The pathological malalignment of the scaphoid, lunate and capitate in the transverse plane saw an appreciable amount of deterioration, as their Euler rotation around the Y-axis exhibited a permanent shift towards pronation. This was seen to be more pronounced during both wrist ulnar deviation (Fig. 4.12c, Fig. 4.15c, and Fig. 4.18c) and wrist extension (Fig. 4.11c, Fig. 4.14c, and Fig. 4.17c). In addition, dividing both the RSC and LRL caused the lunate to become statistically more extend during ulnar deviation (Fig. 4.15a).

In terms of carpal translations, further transecting the RSC and LRL caused the scaphoid to permanently shifted towards the volar and ulnar aspects of the wrist. The former was seen to be the most pronounced during extension, as the absolute radioscaphoid translation was significantly less dorsal (mean difference: 0.30 mm, $p<0.001$; Fig. 4.11e). The latter was evident during ulnar deviation, as the absolute radioscaphoid translation in the radial direction was statistically less as compared to that in Stage II (mean difference: -0.29 mm, $p=0.013$; Fig. 4.12d). The lunate also exhibited a static shift in the volar and ulnar direction with respect to the radius. In addition, the radiolunate translation in the ulnar direction during wrist radial deviation was seen to be statistically more than that in Stage II (mean difference: -0.36 mm, $p=0.014$; Fig. 4.15d), and the radiolunate translation

in the volar direction was more pronounced in wrist ulnar deviation where the lunate was undergoing simultaneous extension (mean difference: 0.35 mm, p=0.003; Fig. 4.15e). The capitate was seen to be further translated ulnarly and proximally with respect to the radius, comparing to that seen in Stage II. Similarly, the abnormal ulnar translation of the capitate became more noticeable during wrist radial deviation (mean difference: -0.36 mm, p<0.001; Fig. 4.18d).

In terms of the alteration in the dynamic carpal motion, dividing the selected volar extrinsic ligaments induced a statistically significant increase in the net flexion exhibited by the scaphoid during global wrist flexion compared to that in Stage II (mean shape difference: 1.2°, p<0.001; Fig. 4.11a). On the other hand, the pattern change for the lunate was far more intriguing. During global wrist flexion, the lunate was similarly seen to exhibited more dynamic flexion (mean shape difference: 0.6°, p=0.001; Fig. 4.14a). The lunate was also seen to exhibit an increased amount of dynamic extension during wrist ulnar deviation, (mean shape difference: −1.0°, p=0.047; Fig. 4.15a), but demonstrate a less amount of dynamic flexion during wrist radial deviation (mean shape difference: −0.4°, p=0.002). In addition, the lunate was also seen to exhibit an increased dynamic dorsal translation during wrist flexion as compared to that in Stage II (mean shape difference: -0.11 mm, p<0.001; Fig. 4.14e), whereas the same was seen for the capitate during wrist extension (mean shape difference: -0.10 mm, p=0.044; Fig. 4.18e).

In terms of scapholunate relations, the division of both the RSC and LRL did not cause noticeable alterations in the relative rotation between the scaphoid and lunate. In contrast, the scaphoid was found to be statistically more radially translated in relation to the lunate throughout the entire FEM and DTM. However, the changes were less than 0.2 mm and considered marginal. In terms of the capitolunate relations, transecting those volar ligaments caused the capitate to lean statistically towards the radial aspect of the lunate in both pure ulnar deviation (Fig. B.5b) and ulnar flexion (Fig. B.6b) of the global wrist. These changes, however, were around approximately 1°.

Stage IV: resection of the DIC, DRC and STT

The subsequent division of the DIC, a portion of the DRC, and the STT produced a series of noticeable static and dynamic changes that further deteriorated the carpal kinematics which was already in a pathological state.

In the neutral position of the wrist, the static posture of the scaphoid became appreciably more flexed, ulnarly deviated and pronated with respect to the radius. On average, this measured 13.6°, 11.2° and 12.3° around the Z-, X- and Y-axis, respectively (the starting point of a, b and c in Fig. 4.11-4.13). Under this influence, the trajectories corresponding to these rotational parameters measured in all three types of dynamic wrist motion were again seen to be permanently shifted. The absolute radioscaphoid rotation around the Z-axis was observed to be the most affected after Stage IV ligament division in pure wrist ulnar deviation (mean difference: 10.2°, p=0.047; Fig. 4.12a), whereas its X-component (mean difference: 5.0°, p=0.046; Fig. 4.13b) and Y-component (mean difference: 5.3°, p=0.013; Fig. 4.13c) were the most affected in ulnar flexion. In terms of the alteration in patterns of the scaphoid rotation, the division of the DIC, a portion of the DRC, and the STT caused the scaphoid to exhibit statistically more dynamic extension (mean shape difference: −1.8°, p=0.036; Fig. 4.13a) during radial extension of the wrist, more dynamic radial deviation (mean shape difference: −3.4°, p=0.047; Fig. 4.12b) during pure wrist radial deviation. In terms of the radioscaphoid translations, the scaphoid was observed to be more radially shifted with respect to the radius during both pure wrist flexion (mean difference: 0.76 mm, p=0.006; Fig. 4.11e) and during the combined ulnar flexion (mean difference: 0.59 mm, p=0.029; Fig. 4.13e) as compared to those seen in the normal writs. All these findings suggest that the ligamentous restraint on the radial, dorsal and distal aspect of the scaphoid became attenuated, causing the radioscaphoid motion to become more dependent on the boney geometry.

The static posture of the lunate in the neutral wrist position became marginally more extended and substantially more supinated with respect to the radius following Stage IV ligament division. On average, the static

radiolunate angulation measured −13.0° and −5.2° about the Z- and Y-axis, respectively. The increase in the absolute radiolunate supination was most noticeable dynamically during global wrist flexion (mean difference: −3.5°, p=0.010; Fig. 4.15a) after the ligament division. The radiolunate translations, in contrast, saw negligible changes after the ligament division.

The capitate rotation, on the other hand, did not see any appreciable changes after Stage IV ligament resection. However, the capitate was observed to be more proximally migrated during wrist flexion (mean difference: 0.66 mm, p=0.036; Fig. 4.17f) as compared to the value seen in Stage III. In addition, the capitate seemed to demonstrate an increased tendency to translate dorsally. However, this was found to be statistically insignificant due to increased data variability. All these findings clearly suggest that the capitate was less constrained for its coronal plane movement and its tendency to migrate into the scapholunate interval.

After the ligament division, the most noticeable change in the relative scapholunate rotation was observed to have occurred during ulnar flexion. Comparing to those in Stage III, the increase in the absolute values of the scapholunate flexion, ulnar deviation and pronation measured 10.5° (p=0.032), 6.2° (p=0.023), and 9.0° (p=0.014), respectively (Fig. B.3a,b and c). And the most noticeable change in the relative scapholunate translation was seen to have occurred during ulnar deviation, where the absolute values of the scapholunate radial deviation and distal translation were increased by an amount of 0.64 mm (p=0.048) and 0.88 mm (p=0.04). The capitolunate relation, on the other hand, was also the most impacted during ulnar deviation, where an increase of 3.5° (p<0.001) and 0.33mm (p=0.032) was seen for the absolute values of the capitolunate pronation and radial translation, respectively.

4.1.2.3 Carpal Kinematics Following Reconstructive Surgery (Fig. 4.11-4.19, and Appendix B.1-B.6)

Dorsal Transarticular Loop Tenodesis

The novel dorsal transarticular loop tenodesis (DTLT) seemed inadequate to fully rectify the static flexion deformity of the scaphoid, as the curves corresponding to the radioscaphoid rotation around the Z-axis in the sagittal plane for all three wrist motion still appeared to be shifted from those recorded in the native state. The residual scaphoid flexion was observed to be more prominent during wrist flexion (Fig. 4.11a), ulnar deviation (Fig. 4.12a) and combined ulnar flexion (Fig. 4.13a). On average, these measured 4.7° (p=0.050), 6.3° (p=0.012), and 6.6° (p=0.041), respectively, as compared to those in Stage NP. In terms of dynamic patterns, the DTLT helped in reducing the abnormal increase in the net radioscaphoid extension exhibited during wrist extension after the complete division of the SLIL. Compared to that in the native state, the pattern distortion was lowered from −3.8° (p=0.004), as seen in Stage III ligament resection, to an average of −1.5° (p=0.030) after the DTLT procedure. In addition, the attenuated net adaptive flexion of the scaphoid during wrist radial deviation was partly restored by the DTLT procedure. Comparing to that in the native state, this was corrected from a severe pattern distortion of −5.9° (p<0.001) in Stage IV to a mild value of −1.6° (p=0.017).

In the transverse plane, the static pronation deformity of the scaphoid seemed to be improved but not fully rectified after the DTLT procedure. And the scaphoid was still statistically more pronated than that in the native state with respect to the radius, especially during radial deviation (Fig. 4.12c), and combined radial extension (Fig. 4.13c). On average, these measured 3.71° (p=0.002) and 2.4° (p=0.031), respectively. However, the DTLT seemed to help in restoring the dynamic pattern of the radioscaphoid rotation around the Y-axis, as the unusual dynamic supination exhibited by the scaphoid during wrist extension (Fig. 4.11c), ulnar deviation (Fig. 4.12c) and combined radial extension (Fig. 4.13c) after the incremental ligament divisions were

effectively suppressed. And the mean reduction measured 1.5° (p=0.035), 2.6° (p=0.022) and 3.5° (p=0.005), respectively, as compared to that in Stage IV. On the other hand, the pathological ulnar deviation of the scaphoid, observable after the complete division of the SLIL, was effectively corrected after the DTLT procedure. And the dynamic pattern of the radioscaphoid rotation in the coronal plane seemed to be also restored back to a near-normal level for all three wrist motion. In terms of correcting the positional malalignment of the scaphoid, the DTLT performed well in correcting the substantial amount of radial, dorsal and distal shift of the scaphoid, as seen following Stage IV ligament resection. However, the DTLT produced an "overcorrection" that caused the scaphoid to become substantially volarly translated with respect to the radius. This was particularly noticeable during ulnar deviation (Fig. 4.12e) and combined ulnar flexion (Fig. 4.13e) of the global wrist. And these abnormal increases as compared to the radioscaphoid volar translation in the native state measured 1.32 mm (p<0.001) and 1.26 mm (p<0.001), respectively.

In general, unlike the insufficient reduction of the scaphoid, the DTLT effectively reinstated normal lunate kinematics but at the expense of introducing unwanted overcorrections. In the sagittal plane, the significant radiolunate extension, as seen in Stage IV, was successfully rectified. And the average magnitude of this rectification was observed to be as high as 23.4° (p<0.001) before and after the DTLT procedure for wrist ulnar flexion (Fig. 4.16a). This seemed to indicate an overcorrection in which the lunate was in excessive flexion with respect to the radius. However, due to the variability in the data, no statistical inference could be drawn in regards to whether the absolute radiolunate rotation in the sagittal plane had deviated from its native state after the DTLT. In terms of dynamic patterns, the DTLT seemed to have also helped in restoring the dynamic radiolunate extension, which had been attenuated considerably after dorsal collapsing of the lunate. This was most noticeable in both wrist extension (Fig. 4.14a) and radial extension (Fig. 4.16a), and the increase in the dynamic radiolunate extension after the DTLT reconstruction measured 3.4° (p<0.001) and 2.5° (p=0.015), re-

spectively. On the other hand, the radiolunate rotation in the coronal plane, which remained almost unchanged throughout different stages of incremental ligament resection, was also not altered by the DTLT procedure.

In the transverse plane, the static deformity of radiolunate supination was successfully treated after the DTLT, but again with a slight overcorrection towards excessive pronation. In addition, the net pronation exhibited dynamically by the lunate during wrist ulnar deviation (Fig. 4.15c) also saw an appreciable increase, measured 2.1° ($p<0.001$) compared to that in the native state, after the DTLT procedure. The DTLT was also seen to lead to a generally good outcome in treating the radiolunate malalignment that is locational or translational in nature. Most noticeably, the substantial volar shift of the lunate, as seen after Stage III ligament division, was successfully corrected. The radiolunate malalignment in the radial/ulnar direction along the Z-axis and in the proximal/distal directions along the Y-axis was improved but not fully rectified. Nonetheless, the dynamic pattern of the normal radiolunate translations in these directions seemed to be restored after the DTLT. This could be clearly seen from the returning of the dynamic distal translation exhibited by the lunate during wrist flexion (Fig. 4.14f).

Although the radioscaphoid and radiolunate rotation were not returned to levels that could precisely resemble their native state, the normal physiological intercarpal rotation between the scaphoid and lunate was almost completely restored in all three anatomical planes after the DTLT procedure. Nonetheless, a number of minor motion aberrations were still noted. The scaphoid appeared to be statistically more radially deviated in relation to the lunate by an amount of $-2.4°$ ($p<0.001$) and $-3.2°$ ($p<0.001$), respectively, in both flexion (Fig. B.1b) and radial deviation (Fig. B.2b) as compared to those in the normal case. In addition, it was also statistically more pronated with respect to the lunate by an amount of 2.2° ($p<0.001$) during radial deviation (Fig. B.2c) comparing to that in the normal case. In terms of the intercarpal translation between the scaphoid and lunate, although the residual misalignment in the radial/ulnar and the volar/dorsal directions were generally less than 0.50 mm, the outcome of the DTLT was met with

significant deterioration. This was evident in wrist ulnar deviation, during which the scapholunate alignment in the volar/dorsal direction became significantly disrupted (Fig. B.2e), owing to the large radioscaphoid volar translation.

The DTLT seemed to have a little effect in the capitate rotation, apart from correcting its abnormal pronation as seen after the complete loss of the SLIL. Nonetheless, the capitate was seen to have become more volarly shifted, presumably as a result of the excessive lunate flexion caused by the DTLT. In addition, the pathological proximal migration of the capitate was also reduced. This was clearly seen in wrist extension (Fig. B.4f) and radial extension (Fig. B.6f) and was thought to be indicative of the successful restoration of the congruency of the distal scapholunate joint, which effectively acts as a "seat" for the capitate in intact wrists.

Three-Ligament Tenodesis

The Three-Ligament Tenodesis (3LT) seemed to outperform the DTLT in re-stabilising the scaphoid in the sagittal plane. It was clear that the static radioscaphoid flexion was completely rectified, and the dynamic pattern of the radioscaphoid rotation in the sagittal plane was also restored to a near-normal level in various global wrist motion. In contrast to the DTLT, the 3LT performed particularly well in reinstating the adaptive flexion and extension of the scaphoid, which was exhibited in normal wrists during wrist RUD (Fig. 4.12a). In the coronal plane, the static deformity of the radioscaphoid ulnar deviation was also adequately rectified. However, the dynamic pattern of the radioscaphoid rotation around the X-axis seemed to be distorted towards radial deviation during wrist RUD after the 3LT procedure (Fig. 4.12b). As compared to those in the native state, the scaphoid saw a decrease of 1.6° ($p=0.002$) in its net ulnar deviation and experienced an increase of 3.4° ($p<0.001$) in its net radial deviation. In the transverse plane, the outcome of the 3LT was deemed inferior to that of the DTLT, as the scaphoid was still seen to be statically shifted in significant pronation in all three modes of wrist motion. And compared to that of the intact state, the mean difference in

the radioscaphoid pronation was observed to be as high as 7.6° ($p<0.001$) in wrist ulnar flexion after the 3LT (Fig. 4.13c). In addition, the reconstruction also seemed to offer a limited amount of remedy for the dynamic pattern of the radioscaphoid rotation in the transverse plane, which had been altered substantially since Stage II. In terms of the radioscaphoid translations, the 3LT seemed to lead to an excessive ulnar shift of the scaphoid, measured up to 0.70 mm. This was thought to be related to the looping and the pre-tensioning of the FCR graft via the ulnarly situated DRC ligament. In the dorsal/volar direction, despite both the DTLT and the 3LT were unable to precisely return the radioscaphoid translation back to its native state, the 3LT was considered inferior in constraining the dorsal translation of the scaphoid, especially during wrist extension (Fig. 4.11e). However, it did not introduce any unwanted volar movement of the scaphoid as the DTLT did during wrist ulnar deviation or ulnar flexion.

In the present study, the 3LT, however, failed to correct the abnormal radiolunate motion, as the lunate still remained to be collapsed into extension and supination and volarly shifted, comparable to that seen after the division of the SLIL. Furthermore, the dynamic pattern of the radiolunate rotation in the sagittal plane during various wrist motion also did not see any major improvements as compared to their pre-operative state. Instead, the lunate seemed to become more ulnarly deviated, and ulnarly shifted after the 3LT. Given the significant drawback in correcting the static radiolunate deformity, the 3LT achieved a less ideal restoration of the normal scapholunate relation than the DTLT. In the entire duration of all three modes of wrist motion, the scapholunate angle in both the sagittal plane and the transverse plane were significantly different from those seen in the intact state. The difference in the scapholunate angle in the sagittal plane was seen to be more pronounced in wrist motion that involved flexion of the scaphoid and lunate, namely during wrist flexion, radial deviation and ulnar flexion, but was observed to be less significant in wrist motion where the two bones were extending. For example, the scapholunate angle in the sagittal plane was observed to differ from its native level by an amount as high as 11.9° ($p<0.001$) during

wrist flexion but the difference decreased to a value of 5.0° (p=0.002) in wrist extension. In the transverse plane, the substantial amount of residual scapholunate pronation indicated the dorsal diastasis of the scapholunate interval might still be present after the reconstruction. The 3LT also seemed to be insufficient in effectively preventing the volar opening of the scapholunate interval, given the abnormal scaphoid supination relative to the lunate as observed during wrist extension (Fig. B.1c) and radial extension (Fig. B.3c) after the complete division of the SLIL was still present. Nonetheless, a satisfactory outcome in the restoration of the normal intercarpal translation between the scaphoid and lunate was obtained after the 3LT procedure.

In the distal row, the abnormal pronation of the capitate was effectively rectified after the 3LT. However, similar to the lunate, the capitate was also appeared to be significantly ulnarly translated with respect to the radius. In addition, since a normal radiolunate relation was not restored, a significant amount of dorsal shift of the capitate was still observable. Furthermore, since an adequate reduction of the scapholunate diastasis was not achieved, the capitate was still observed to be migrated proximally, especially in extreme wrist extension (Fig. B.4f) and combined radial extension (Fig. B.6f).

4.1.3 Discussion

4.1.3.1 Normal Carpal Kinematics

A thorough understanding of the complex carpal kinematics of the normal physiological wrist is useful for orthopaedic surgeons who are confronted by the challenge of both effectively diagnosing and treating ligamentous injuries of the wrist, which could often be very subtle in their initial stage. Since the first published account on normal carpal kinematics by Bryce (1896), who took a series of radiographs of his own hand using the Rontgen X-ray, which was just discovered in the year before, many have endeavoured to understand the movement of individual carpal bones and their delicate interactions that made the global wrist motion possible. However, with each of those irregularly shaped carpal bones rotating while translating in space, it was not until the past three decades when the advancements in sensor and imaging technologies permitted the quantitative analysis of this sophisticated and subtle movement in 3D.

The primary goal of this part of the study has been to establish a solid baseline for the comparisons in later stages, where, by comparing the 6-DOF carpal kinematics of the normal wrist with those obtained after each stage of ligament injuries or different surgical treatments, their effect can thus be rigorously evaluated in biomechanical terms. Therefore, in order to ensure the validity of those comparative analyses, the normal carpal kinematics were cross-checked with those reported in the literature.

Control of the Global Wrist Position

In most studies that concern carpal kinematics, the control over global wrist position has been achieved by first manually and visually aligning the dorsum of the hand or the 3MC with that of the forearm to define the neutral position of the wrist, then actively or passively manipulate the 3MC with some motion constraining jigs in which a protractor was often instrumented to measure the angle between the current and the initially defined neutral position (de Lange

et al., 1985; Kobayashi et al., 1997a; Ritt et al., 1998; Neu et al., 2001; Stoesser et al., 2016; Eschweiler et al., 2016b). However, Wolfe et al. (2000) noticed that the actual position of the wrist (as quantified by the capitate) varied from the targeted position in their *in-vivo* study, suggesting external references might be poor and inadequate in indicating the true wrist position. Indeed, the wrist position measured in those studies might have deviated from the ground-truth if visual examination and a protractor was the only means in defining the neutral wrist position and determining the angulation between the coordinate axes of the 3MC with those of the radius in space. Since the carpal kinematics are reported as absolute three-dimensional attitudes of the carpal bones and are often described in relation to some predefined positions of the global wrist, ineffective control over this independent variable will lead to inaccurate measurements to be obtained. Furthermore, concerns have long been raised in regards to whether wrist simulations with passive and externally imposed movements could effectively represent the true physiology and dynamics of the *in-vivo* wrist motion (Smith et al., 1989).

In the present study, the control over the global wrist position was not accomplished by constraining motion of the cadaver wrist in any form. Instead, this was achieved in a contactless approach with a video-based motion analysis system. The radius and 3MC were instrumented with retro-reflective markers, and a CT scan was performed to determine the three-dimensional position of the markers in relation to the bones on which they were attached. Based on this information, the precise spatial configuration of the 3MC in relation to the radius was then calculated by DWSA in real-time, allowing the global wrist position to be controlled continuously with a mean RMS accuracy less than 0.3° (as shown in Section 3.2.1).

Flexion and Extension

In general, the overall movement patterns demonstrated in this thesis concur with those commonly accepted, as discovered unanimously in early studies. During the sagittal plane motion of the wrist, the principle carpal motion has been observed to be occurring around the Z-axis, following that of the global

wrist. The arc of the excursion of the bones in the proximal row has been seen to not surpassing than that of the global wrist, owing to the contribution made by the synergistic movement of the midcarpal joint (Sarrafian et al., 1977; Volz et al., 1980). Among the proximal row, the scaphoid rotation has been reported to be the greatest while that of the lunate being the least and significantly lagged behind the global wrist motion, indicating a significant amount of intercarpal rotations (Kauer, 1980; Berger et al., 1982b; de Lange et al., 1985; Ruby et al., 1987; Garcia-Elias et al., 1989). The results of this thesis correlated with those findings very well. Early morphological studies also postulated that the relative rotation between the scaphoid and lunate might originate from the difference between the curvatures of their proximal facets (Kauer, 1986), and the significant amount scaphoid rotation was also thought to be indicative of its special role in coordinating synchronous movement between the two carpal rows (Garcia-Elias et al., 1989). In addition, some have speculated the high degree of radioscaphoid motion to be the primary reason for the postoperative loss of motion and the high failure rate of radioscapholunate fusion seen clinically (Nagy and Büchler, 1997; Wolfe et al., 2000).

On the other hand, despite being relatively smaller in magnitude, the out-of-plane rotations around the X- (radial/ulnar deviation) and Y-axis (pronation/supination), have been reported for the scaphoid and lunate during wrist flexion and extension by several groups of researchers. However, the literature is rife with controversies when it comes to the exact direction of those conjunct rotations. Nonetheless, the scaphoid and the lunate have been consistently reported to possess an appreciable amount of ulnar deviation during wrist flexion (de Lange et al., 1985; Smith et al., 1989; Garcia-Elias et al., 1989). The same was also noticed in later studies performed *in-vitro* by Kobayashi et al. (1997a), Kaufmann et al. (2006) and Short et al. (2007), and *in-vivo* by Wolfe et al. (2000) and Foumani et al. (2009). The present results are in good agreement with this observation. In addition, Kobayashi et al. (1997a) further reported that the scaphoid and lunate seemed to rotate in opposite directions around the Y-axis during

both wrist flexion and extension. This pattern was observed only partially in the present study, where the scaphoid supinated and also ulnarly deviated while the lunate pronated during wrist extension. This dorsal engagement of the scaphoid and lunate, however, might well explain the opening of the volar gap of the scapholunate articulation during wrist extension, as initially observed by Kauer (1974, 1980).

Another point worth mentioning was the debated "screw-vice" theory proposed originally by Macconaill (1941), who depicted the lunate to be pressed against the scaphoid during wrist extension by the triquetrum, and the consolidated proximal carpal row, in turn, captures the capitate. Although a small amount of coupled radial translation was detected for the scaphoid and lunate during wrist extension in the present study, similar to those observed by Crisco et al. (2005), with the absence of the triquetrum kinematics, it is still too early to draw any definitive conclusion in regards to this theory. For the dorsal-volar translations in the sagittal plane, the present results correlate perfectly with those reported by Werner et al. (2011), who noticed the scaphoid and lunate demonstrate tendencies to translated in an opposite direction during the sagittal plane motion of the global wrist. Namely, they found the lunate tends to translate dorsally while the scaphoid tends to translate volarly in wrist flexion and vice versa. Furthermore, they noticed that, despite the difference in direction, the scaphoid translated the most while the lunate translated the least during wrist extension. This specific observation was also reflected in the present results.

Based on the carpal bone morphology, Kauer (1980) hypothesised that the scaphoid would rotate faster in the volar and dorsal direction comparing to the lunate, owing to a more curved articular surface. And as a result, he postulated the scaphoid must shift downward in flexion and upward in extension with respect to the lunate. This postulation is in very good agreement with the present observation, where the scaphoid was observed to translate proximally and distally with respect to the lunate during flexion and extension.

For the distal row, it has been demonstrated that the relative rotation

between the capitate and the third metacarpal is so small that the radio-capitate angulation has long been used as an indicator of the gross position of the global wrist (Andrews and Youm, 1979; Patterson et al., 1998). But apart from that, the out-of-plane rotation of the capitate, as well as its translation has been shown to be much more complex during wrist motion. Using a CT-based approach, Neu et al. (2001) showed the capitate undergoes small amount of pronation, ulnar deviation and ulnar translation during wrist flexion, while it supinates, ulnar deviate and translated radially during wrist extension. The present results are in perfect agreement with those observations, except for the small capitate pronation during wrist flexion. Besides, owing to the difference between the methods used in representing the kinematic data, the substantial amount of volar distal and dorsal proximal translations of the capitate as seen in the present results, which reflected the flexion and extension of the global wrist, were absent in their study.

To validate the actual numerical values of the present results, a more rigorous comparison was carried out. However, although a sizeable body of knowledge exists for the normal carpal kinematics, the present results were compared only with a selection of studies in a quantitative sense, owing to the following reasons. First, many studies were performed without an effective means to control the global wrist position at which the three-dimensional attitude of the carpal bones was measured (Berger et al., 1982b; Garcia-Elias et al., 1989; Horii et al., 1991; Kaufmann et al., 2006; Blankenhorn et al., 2007). Instead, the wrist was held in maximum flexion or extension, or in arbitrary postures determined visually, with no apparent measures in restricting the unwanted out-of-plane movement of the wrist. The carpal kinematics measured in those positions would be inherently different from those that occurred during pure sagittal wrist motion, and therefore, considered less representative and excluded in the comparison. Second, with the primary focus being measuring the carpal kinematics in the primary plane of wrist motion, the conjunct out-of-plane rotations of the carpal bones were often neglected (Wolfe et al., 2000; Goto et al., 2005; Stoesser et al., 2016), leaving the full 3D picture of the carpal bone rotation incomplete. Furthermore,

the concurrent translations of the carpal bones were also frequently overlooked in kinematic investigations (Ritt et al., 1998; Kaufmann et al., 2006; Stoesser et al., 2016), probably due to the technological limitations in effectively detecting those subtle translocations. Nonetheless, the *in-vitro* dataset contributed by Kobayashi et al. (1997a) and the *in-vivo* dataset contributed by Moojen et al. (2002), were both very comprehensive and in line with the present selection criteria. In addition, the former is arguably the most accurate and iconic in the field even to this date, owing to the large sample size and small standard deviation of measurement. Furthermore, since the screw-axis (or the finite helical axis) representation was adopted for reporting the rotations and translations, the present kinematic measurements were subjected to appropriate conversions to facilitate a meaningful comparison (Woltring, 1994).

Except for the consistently lower lunate extension observed in the present study, it is evident that the present results concur with those measured both *in-vivo* and *in-vitro* (Table 4.6). The abnormal lunate extension was likely caused by the intra-articular presence of the pressure sensor. Since the sensor was inserted dorsally into the radiocarpal joint in the preservation of its volar capsule, the sensor was allowed to be driven dorsally on the articular surface of the distal radius when the proximal row flexed. And when the proximal row extended, the pressure sensor was likely to be driven volarly, but because of the still intact volar capsule, this relative motion was not permitted, causing the sensor to be slightly crimped on the volar aspect inside the joint. This anomaly presumably made the dynamic extension difficult for the proximal carpal row, and especially for the lunate, which serves as the cornerstone of the force-bearing central column of the wrist Weber (1980); Patterson and Viegas (1995). Similar findings were reported by Short et al. (2002b), who recorded significantly less lunate extension in cadaver wrists that underwent a dorsal capsulotomy and had a custom-made pressure sensor inserted into the joint. They also reported the scaphoid and lunate exhibited abnormal radial deviation and supination during wrist flexion. These changes, however, were not seen in the present study.

Table 4.6: Carpal kinematics measured during global wrist flexion and extension compared with the values reported previously by a selection of studies

Study	Bone	Rotation (screw-axis angle decomposed in the anatomical system, deg)					
		Flexion 30°			Extension 30°		
		Z FL(+)/EX(-)	X UD(+)/RD(-)	Y PR(+)/SU(-)	Z FL(+)/EX(-)	X UD(+)/RD(-)	Y PR(+)/SU(-)
Ritt et al. (1998)* N = 9	Scaphoid	20.4	0.5	1.4	-25.7	2.2	-1.8
	Lunate	12.6	2.1	0.6	-14.5	1.6	0.1
	Capitate	31.7	0.1	2.5	-30.1	0.2	-1.0
Kobayashi et al. (1997a) N = 22	Scaphoid	20.6 [2.8]	2.1 [2.2]	1.6 [2.2]	-26 [3.2]	0.8 [2.1]	-0.7 [2.6]
	Lunate	11.5 [3.9]	3.3 [1.9]	0.3 [1.7]	-15.4 [3.9]	0.9 [1.5]	0.5 [1.8]
	Capitate	31.5 [1.2]	0.6 [1.6]	1.3 [2.5]	-30.2 [1.1]	0 [1.4]	-1 [1.8]
Moojen et al. (2002)† N = 10	Scaphoid	19.2 [3.7]	2.8 [1.0]	-0.1 [2.8]	-27.5 [1.9]	-2.4 [2.5]	-1.0 [1.2]
	Lunate	9.0 [5.0]	3.0 [1.3]	1.6 [1.5]	-20.9 [4.8]	-2.1 [1.8]	-1.8 [1.3]
	Capitate	30.0 [0.0]	3.9 [3.3]	1.7 [2.7]	-30.0 [0.0]	-4.4 [2.2]	0.2 [2.4]
Present Study N = 7	Scaphoid	22.5 [3.5]	1.7 [2.8]	1.0 [1.0]	-22.1 [4.1]	2.0 [0.9]	-2.2 [1.8]
	Lunate	11.3 [4.0]	2.0 [1.4]	0.3 [1.5]	-6.4 [3.8]	0.4 [1.7]	0.5 [1.0]
	Capitate	31.3 [1.2]	0.2 [1.4]	-0.3 [2.6]	-30.4 [0.4]	-0.1 [0.6]	-1.8 [2.5]
Study	Bone	Translation (screw-axis translation decomposed in the anatomical system, mm)					
		Flexion 30°			Extension 30°		
		Z RA(+)/UL(-)	X VO(+)/DO(-)	Y PX(+)/DS(-)	Z RA(+)/UL(-)	X VO(+)/DO(-)	Y PX(+)/DS(-)
Kobayashi et al. (1997a) N = 22	Scaphoid	-0.2 [0.3]	0.0 [0.1]	0.0 [0.1]	0.6 [0.3]	0.0 [0.1]	0.0 [0.1]
	Lunate	0.2 [0.3]	0.0 [0.1]	0.0 [0.0]	0.3 [0.3]	0.0 [0.0]	0.0 [0.1]
	Capitate	-0.2 [0.4]	0.0 [0.0]	0.0 [0.0]	0.3 [0.3]	0.0 [0.0]	0.0 [0.0]
Moojen et al. (2002)† N = 10	Scaphoid	-0.2 [0.2]	-0.2 [0.6]	1.2 [0.6]	0.4 [0.3]	-2.1 [0.8]	-1.6 [0.2]
	Lunate	0.3 [0.2]	-0.4 [0.5]	-0.4 [0.3]	0.1 [0.5]	0.4 [0.3]	0.2 [0.1]
	Capitate	-0.7 [0.4]	4.8 [0.7]	2.0 [0.4]	1.2 [0.3]	-7.5 [0.9]	-0.3 [0.7]
Present Study N = 7	Scaphoid	-0.6 [0.2]	-0.1 [0.1]	0.0 [0.0]	0.7 [0.4]	-0.1 [0.0]	0.1 [0.1]
	Lunate	-0.1 [0.1]	0.0 [0.0]	0.0 [0.0]	0.1 [0.3]	0.0 [0.1]	0.0 [0.1]
	Capitate	-0.4 [0.4]	0.0 [0.0]	0.0 [0.0]	0.6 [0.4]	0.0 [0.0]	0.0 [0.0]

* only reported the average carpal rotations
† *in-vivo* study

Reduced lunate extension implies an increased contribution must have been made by the midcarpal joint in order to achieve a designated amount of global wrist extension. Therefore in order to gain a deeper insight into this alteration, the relative in-plane proportion of the radioscaphoid, radiolunate and the capitolunate angulation to the total arc of wrist motion was calculated and compared with those derived from the existing studies (Table 4.7). It is evident that while the values are in range with those reported for wrist flexion, the radiolunate contribution to the total arc of wrist extension recorded in the present study is considerably smaller. Although this poses a major drawback as it limits the present normal carpal

kinematics data, especially the lunate kinematics during wrist extension, to be extrapolated into clinical applications, this kinematic was considered to be well controlled and have a limited impact to the validity of the study, as the main emphasis was to measure the change after various extents of ligament injuries and subsequent surgeries relative to those in the initial state, rather than reporting the absolute values measured in each state. In addition, the normal alignment of the scaphoid and lunate (as represented by the scapholunate angle), which was of arguably critical importance for researches concerning the scapholunate joint, was appeared to be unaffected.

Table 4.7: Results of the present thesis compared with those previously reported in the literature values for radiocarpal and scapholunate angles, and percentage contribution of the radioscaphoid, radiolunate and capitolunate articulation in the sagittal plane during global wrist flexion and extension

Study	Repr.	Flexion 30						Extension 30					
		Radioscaphoid		Radiolunate		Scapholunate	Capitolunate	Radioscaphoid		Radiolunate		Scapholunate	Capitolunate
		[deg]	[% Contr.]	[deg]	[% Contr.]	[deg]	[% Contr.]	[deg]	[% Contr.]	[deg]	[% Contr.]	[deg]	[% Contr.]
de Lange et al. (1985)*	Euler	19.2	63.8	11.7	39.0	7.5	61.0	-25.3	84.2	-11.5	38.2	-11.5	61.8
Kobayashi et al. (1997a)	Screw	20.6	68.7	11.5	38.3	9.1	66.7	-26.0	86.7	-15.4	51.3	-15.4	49.3
Werner et al. (1997b)	NM	26.4	88.0	15.3	51.0	11.1	54.0	-28.5	95.0	-11.4	38.0	-11.4	53.0
Ritt et al. (1998)	Screw	20.4	68.0	12.6	42.0	7.8	63.7	-25.7	85.7	-14.5	48.3	-14.5	52.0
Wolfe et al. (2000)†	Screw	23.3	77.7	13.9	46.2	9.4	53.8	-29.1	96.9	-20.7	69.0	-20.7	31.0
Moojen et al. (2002)†	Screw	19.2	64.0	9.0	30.0	10.2	70.0	-27.5	91.7	-20.9	69.7	-20.9	30.3
Goto et al. (2005)†	Euler	20.2	67.3	9.4	31.3	10.8	70.3	-25.6	85.3	-14.4	48.0	-14.4	51.0
Short et al. (2007)‡	NM	25.1	83.7	15.4	51.3	9.7	48.7	-25.1	83.7	-12.7	42.3	-12.7	57.7
Stoesser et al. (2016)	NM	28.1	93.7	19.5	65.0	8.6	35.0	-26.4	88.0	-13.3	44.3	-13.3	56.0
de Roo et al. (2019)†	Screw	NM	-	NM	-	8.7	-	NM	-	NM	-	-8.7	-
Present Study	Euler	22.5	75.1	11.3	37.7	11.2	62.4	-22.1	-73.6	-6.4	21.4	-15.4	81.6
		% Contributions Reported For Other Postions in Flexion						% Contributions Reported For Other Postions in Extension					
Berger et al. (1982b)			75.0		55.0		45.0		78.0		59.0		41.0
Garcia-Elias et al. (1989)			NM		49.7		50.3		NM		62.1		37.9
Smith et al. (1989)			73.0		43.0		57.0		80.0		54.0		46.0
Ishikawa et al. (1999)			NM		53.3		46.7		NM		49.6		53.1
Kaufmann et al. (2006)			75.0		50.0		50.0		92.0		52.0		48.0
Blankenhorn et al. (2007)			NM		50.0		32.3		NM		52.0		30.0

Repr.: the formalism in which the carpal rotation was represented
% Contr.: the percentage contribution to the arc of global wrist motion
NM: not mentioned
* average of the values reported for separately two specimens
† *in-vivo* study
‡ linear extrapolation was involved as their global wrist extension terminated at approximately 28°

Radial and Ulnar Deviation

The movement patterns of the carpal bones during the coronal plane motion of the wrist, despite their intricacy, were also correlated very well with those reported in studies performed both *in-vitro* (de Lange et al., 1985; Ruby et al., 1987; Garcia-Elias et al., 1989; Kobayashi et al., 1997a; Kaufmann et al., 2005; Blankenhorn et al., 2007), and *in-vivo* (Moojen et al., 2002; Foumani et al., 2009). In the present results, the scaphoid and lunate in the proximal row have been shown to simultaneously extend, ulnarly deviate and pronate during wrist ulnar deviation; and both flex and radially deviate during wrist radial deviation, with a small amount of supination observable only for the lunate. It has also been shown that the amount of conjunct Z-rotation (flexion/extension) almost always exceeds that occurs in the primary plane of motion, which is similar to the observations reported elsewhere (Horii et al., 1991; Savelberg et al., 1991; Ritt et al., 1998; Moojen et al., 2002). Studies have suggested this "rocking chair"-like conjunct rotation of the proximal row is essentially an adaptation in maintaining a constant spatial and articular congruency between the radius and the distal row (Linscheid, 1986; Garcia-Elias et al., 1989; Moritomo et al., 2007). Indeed, in the present results, the capitate has been shown to exhibit only supination and pronation out-of-plane during wrist radial and ulnar deviation, without apparent flexion/extension or proximal/distal translations that could indicate possible alterations in the height of the distal row.

In terms of intercarpal motion, the relative rotation between the scaphoid and lunate during the coronal plane motion of the wrist was found to be small in the present study, especially during ulnar deviation. On the other hand, it was evident that the midcarpal joint, as represented by the lunocapitate angulation, exhibited rotations that closely resemble the DTM. Namely, the capitate was seen to exhibit radial extension during radial deviation of the wrist and ulnar flexion during ulnar deviation. An appreciable amount of coupled pronation and supination was also seen. These findings are in good agreement with those reported *in-vivo* by Moritomo et al. (2004). Furthermore, an increased lunocapitate

angulation was seen during wrist radial deviation, suggesting the relative importance of the midcarpal joint in facilitating this specific mode of wrist motion. These findings correlate well with those reported previously (Horii et al., 1991; Savelberg et al., 1991; Kobayashi et al., 1997a; Ritt et al., 1998; Moojen et al., 2002).

In terms of carpal translations, the bones in the proximal row were found to be shifting in the direction opposite to that of the primary rotation en bloc (*e.g.* they are seen to translating ulnarly while the global wrist is radially deviating). Interestingly, a substantial amount of proximal-distal translations of the scaphoid were also observed, similar to those reported *in-vivo* (Moojen et al., 2002). This was thought to be primarily due to the radial inclination of the scaphoid fossa. For the distal carpal row, the present results are in good agreement with those reported *in-vivo* by Moojen et al. (2002), who found the capitate to exhibit a translation directed primarily ulnarly and dorsally during ulnar deviation, and radially and volarly during wrist radial deviation. Interestingly, this observation seems to support the kinematic theory proposed by Weber (1984), in which the extension of the proximal row during wrist ulnar deviation was thought to be primarily caused by the dorsal translation of the distal row. He believed this action effectively tightens the volarly situated radioscaphocapitate and scaphotrapezial ligaments, hoisting the scaphoid into an extended posture, and owing to the underlying interosseous ligament, the rest of the proximal row followed the scaphoid into extension. Despite the consistency with the present results, this theory could not be proved without clear indication showing recruitment of the relevant ligaments.

Similarly, to assess the numerical values of the present results, a more rigorous comparison was carried out (Table 4.8). Again, it appeared that the rotational shift of the scaphoid and lunate around the Z-axis during ulnar deviation was smaller than those previously reported, possibly owing to the involvement of conjunct extension. This reduction was presumably replaced by an increased amount of scaphoid ulnar deviation, signalling the loss of adaptation of the proximal row and the transition from column-like kinemat-

Table 4.8: Carpal kinematics measured during global wrist radial and ulnar deviation compared with the values reported previously by a selection of studies

Study	Bone	Rotation (screw-axis angle decomposed in the anatomical system, deg)					
		Ulnar Dev. 15°			Radial Dev. 15°		
		Z FL(+)/EX(-)	X UD(+)/RD(-)	Y PR(+)/SU(-)	Z FL(+)/EX(-)	X UD(+)/RD(-)	Y PR(+)/SU(-)
Ritt et al. (1998)* (N = 9)	Scaphoid	-12.0	5.3	1.6	9.7	-5.4	0.1
	Lunate	-12.6	5.7	1.1	9.1	-2.6	-1.0
	Capitate	2.4	15.3	6.4	1.7	-15.9	-3.7
Kobayashi et al. (1997a) (N = 22)	Scaphoid	-12.5 [3.2]	4.3 [2.6]	2.2 [2.4]	8.5 [3.0]	-4.2 [2.4]	0.8 [1.8]
	Lunate	-13.9 [4.3]	5.7 [2.8]	1.4 [2.0]	7.0 [3.1]	-1.7 [1.7]	-1.2 [1.6]
	Capitate	2.7 [1.1]	15.9 [1.4]	6.8 [2.6]	1.3 [1.5]	-14.6 [2.1]	-3.9 [2.6]
Moojen et al. (2002)† (N = 10)	Scaphoid	-16.1 [8.3]	7.6 [3.4]	1.5 [4.1]	11.8 [7.1]	-4.1 [2.7]	0.8 [3.2]
	Lunate	-17.8 [9.3]	8.8 [2.3]	0.0 [4.3]	11.2 [8.4]	-4.0 [2.9]	-0.1 [3.0]
	Capitate	-2.5 [4.3]	15 [0.0]	6.0 [2.5]	1.0 [4.7]	-15.0 [0.0]	-5.5 [3.8]
Present Study (N = 7)	Scaphoid	-8.0 [3.5]	8.1 [1.6]	0.5 [1.5]	8.3 [2.6]	-3.3 [1.3]	-0.1 [1.2]
	Lunate	-7.5 [5.2]	5.6 [2.0]	1.4 [1.5]	4.6 [2.9]	-1.7 [1.1]	-0.8 [0.7]
	Capitate	0.6 [0.4]	15.0 [0.9]	3.8 [1.7]	1.0 [0.7]	-14.6 [0.2]	-4.7 [1.0]
Study	Bone	Translation (screw-axis translation decomposed in the anatomical system, mm)					
		Ulnar Dev. 15°			Radial Dev. 15°		
		Z RA(+)/UL(-)	X VO(+)/DO(-)	Y PX(+)/DS(-)	Z RA(+)/UL(-)	X VO(+)/DO(-)	Y PX(+)/DS(-)
Kobayashi et al. (1997a) (N = 22)	Scaphoid	0.4 [0.3]	-0.1 [0.1]	-0.1 [0.1]	-0.4 [0.2]	0.2 [0.1]	0.0 [0.1]
	Lunate	0.5 [0.3]	-0.2 [0.2]	-0.1 [0.1]	-0.2 [0.2]	0.1 [0.1]	0.0 [0.1]
	Capitate	-0.2 [0.2]	-1.2 [0.6]	-0.5 [0.3]	-0.1 [0.1]	0.6 [0.4]	0.2 [0.2]
Moojen et al. (2002)† (N = 10)	Scaphoid	0.7 [0.5]	-0.9 [0.8]	-2.5 [0.8]	-0.4 [0.3]	0.1 [0.6]	1.4 [0.8]
	Lunate	1.9 [0.7]	0.8 [0.3]	-0.1 [0.5]	-0.7 [0.9]	-0.8 [0.4]	-0.3 [0.4]
	Capitate	-1.3 [0.6]	-3.1 [1.7]	-0.8 [0.6]	1.7 [0.6]	1.2 [1.4]	0.4 [0.6]
Present Study (N = 7)	Scaphoid	0.1 [0.1]	-0.2 [0.1]	0.0 [0.0]	-0.4 [0.2]	0.2 [0.1]	0.0 [0.1]
	Lunate	0.4 [0.3]	-0.3 [0.3]	-0.1 [0.1]	-0.2 [0.1]	0.1 [0.1]	0.1 [0.1]
	Capitate	0.0 [0.0]	-0.9 [0.7]	-0.3 [0.2]	0.0 [0.0]	0.5 [0.5]	0.2 [0.1]

* only reported the average carpal rotations
† *in-vivo* study

ics towards a more row-like movement. However, the appreciable amount of residual Z-rotation of the capitate reported in those studies during the pure coronal wrist motion raises doubts over the reliability of those measurements. Namely, whether the increased scaphoid and lunate extension were reflective of the reality or merely an artifact that stem from an inaccurate control of the global wrist position. In order to gain a more complete picture, the in-plane contribution of the scaphoid, lunate and the midcarpal joint (represented by the capitolunate angulation) to the arc of primary wrist motion was again calculated and compared with those gathered from the literature.

It was clear that the contribution of the radioscaphoid, radiolunate and the midcarpal joint to the global wrist motion in the coronal plane, calculated based on the previously reported carpal kinematics measurements, possessed a higher degree of variability (Table 4.9). This reflected the issue of variability of carpal kinematics among individuals, which has been noticed by many researchers (Feipel and Rooze, 1999; Moojen et al., 2002). Despite the fact that there were large variations in the previously reported radioscaphoid and radiolunate angles, the scapholunate angle remained relatively consistent between studies and was consistently smaller than the value measured during wrist ulnar deviation in the present study. Although it was still unclear whether the insertion of a pressure sensor made the scaphoid to adapt a more column-like kinematic pattern, it was evident that the difference was small and was thus considered negligible. Therefore, in summary, the present results are in good agreement with the majority of previously reported findings, laying a solid foundation for the comparative analyses to come.

Table 4.9: Results of the present thesis compared with those previously reported in the literature for radiocarpal and scapholunate angles, and percentage contribution of the radioscaphoid, radiolunate and capitolunate articulation in the sagittal plane during global wrist radial and ulnar deviation

Study	Representations	Ulnar Deviation 15						Radial Deviation 15					
		Radioscaphoid		Radiolunate		Scapholunate	Capitolunate	Radioscaphoid		Radiolunate		Scapholunate	Capitolunate
		[deg]	[% Contr.]	[deg]	[% Contr.]	[deg]	[% Contr.]	[deg]	[% Contr.]	[deg]	[% Contr.]	[deg]	[% Contr.]
de Lange et al. (1985)	Euler	7.9	52.7	5.6	37.3	2.3	62.7	-7.8	52.0	-3.4	22.7	-4.4	77.3
Kobayashi et al. (1997a)	Screw	4.3	28.7	5.7	38.0	-1.4	68.0	-4.2	28.0	-1.7	11.3	-2.5	86.0
Ritt et al. (1998)	Screw	5.3	35.3	5.7	38.0	-0.4	64.0	-5.4	36.0	-2.6	17.3	-2.8	88.7
Moojen et al. (2002)	Screw	7.6	50.7	8.8	58.7	-1.2	41.3	-4.1	27.3	-4.0	26.7	-0.1	73.3
Goto et al. (2005)	Euler	3.8	25.3	2.9	19.3	0.9	69.3	-2.5	16.7	-2.5	16.7	0.0	48.4
Short et al. (2007)	NM	6.2	41.3	6.0	40.0	0.2	60.0	NM	-	NM	-	-	-
de Roo et al. (2019)	Screw	NM	-	NM	-	-0.1	-	NM	-	NM	-	0.1	-
Present Study	Euler	8.0	53.3	5.5	36.7	2.4	60.9	-3.3	22.2	-1.7	11.5	-1.7	83.6
		% Contributions Reported For Other Postions in Ulnar Deviation						% Contributions Reported For Other Postions in Radial Deviation					
Garcia-Elias et al. (1989)			45.5		58.6		41.4		39.9		23.3		76.7
Smith et al. (1989)			57.0		50.7		49.3		55.2		33.5		66.5
Ishikawa et al. (1999)			NM		48.9		51.1		NM		28.3		71.7
Kaufmann et al. (2005)			33.3		36.4		63.6		18.2		13.6		86.4
Blankenhorn et al. (2007)			NM		36.4		60.6		NM		13.6		86.4

Dart Thrower's Motion

Although it has been historically established that the human wrist is predisposed to an oblique motion (Fick, 1901; Capener, 1956) in which the wrist starts from an extended and radially deviated position to proceed into a combined flexion and ulnar deviation, now frequently referred to as the DTM (Moritomo et al., 2007), the clinical implication of this motion was not realised until the late 1990s. After having reviewed the outcomes of radioscapholunate arthrodesis for fifteen patients, Sturzenegger and Büchler (1991) found the residual wrist motion, which was achieved primarily through the midcarpal joint after the surgery, was restricted to a path that closely resembles the DTM. From both a morphological and kinesiological viewpoint, Saffar and Semaan (1994) described a multitude of factors that might explain the natural preference of the DTM. They suggested the DTM grants the wrist more mobility and agility, as this oblique motion allows the midcarpal joint to be utilised to a greater extent. Indeed, as seen in the results discussed earlier, the scaphoid and lunate have a tendency to extend during wrist ulnar deviation, while they are inclined to flex during wrist flexion. Therefore, by extrapolating these findings, an extended range of wrist motion is achievable presumably with a small rotational shift of both the scaphoid and lunate, if the global wrist follows such a path that is obliquely oriented between the sagittal and the coronal plane.

The presumption that minimal scapholunate dissociation occurring with the DTM has subsequently inspired rehabilitation protocols and orthosis designs specifically for patients underwent surgical repair or reconstructions of the scapholunate interosseous ligament since early controlled DTM is thought to provide an alternative to prolonged immobilisation while keeping the stress in the scapholunate joint at a lower level (Bergner et al., 2019). However, despite the increased awareness and perceived importance of the DTM, the 6-DOF carpal kinematics which facilitates such an oblique motion of the wrist has rarely been rigorously reported, making it very difficult to validate the present results quantitatively. In fact, the very definition of this functional plane, as to how it is obliquely oriented relative to the other anatomical

planes, is still obscure.

Werner et al. (1997a) were among the first few who pioneered the biomechanical investigation of the DTM. With their version of the wrist simulator, a dynamic DTM that extends from 10° of extension and 10° of radial deviation to 15° of flexion and 10° of ulnar deviation was simulated in six cadaver wrists. Although no numerical values were reported for the carpal kinematics collected during the DTM, they concluded that the bones in the proximal row did not function as a single unit and did not traverse in the same plane as the global wrist. In addition, they found the excursion of the bones in the proximal carp row exhibited significantly less excursion compared to that in planar wrist motion.

Ishikawa et al. (1999) studied the relative contribution of the radiocarpal and midcarpal joints during a passive DTM set at an angle of 23° to the sagittal plane using ten cadaver wrists. Notably, a total of 10 kg force, apportioned to the PCSA of each muscle-tendon units, were applied in an attempt to recreate the physiological loading condition. They found the midcarpal joint contributions, as represented by the radiolunate angulation, were appreciably larger in DTM than those in wrist motion solely confined to the sagittal plane (57.7% in radial extension versus 53.1% in pure extension, and 61.0% in ulnar flexion versus 46.7% in pure flexion). They also observed that the relative rotation between the scaphoid and lunate was attenuated during DTM compared with that observed during sagittal motion (11.7° in radial extension versus 13.1° in pure extension, 4.9° in ulnar flexion versus 8.1° in pure flexion).

Goto et al. (2005) studied the midcarpal kinematics on twelve healthy subjects using incremental MRI-based technique. For their *in-vivo* DTM, a higher lunate contribution at the midcarpal joint was reported (80.2% in radial extension, 77.3% in ulnar flexion), whereas an approximately equal contribution was found for the scaphoid at both the radiocarpal and midcarpal joint (49.3% in radial extension, 50.6% in ulnar flexion). The DTM plane they initially reported was a complicated one but was later clarified to be oriented at 31° from the sagittal plane, coinciding with the plane in

which the isolated STT motion takes place during sagittal motion of the wrist (Moritomo et al., 2007).

These values were in basic correlation with the present results, presumably owing to the similarity in the obliquity of the DTM studied. With the DTM oriented at 33.7° to the sagittal plane in the present study, the midcarpal joint accounted for 94.9% and 90.2% of the sagittal plane rotation in radial extension and ulnar flexion, respectively, and was larger than the 81.6% and 62.4% calculated in the pure extension and flexion case. On the other hand, the scaphoid contribution to the global wrist motion found to be 36.8% in radial extension and 51.8% in ulnar flexion on average. It was evident that the lunate showed a significantly less sagittal plane rotation in DTM than in other types of wrist motion. This phenomenon has also been noticed by several researchers. In a follow-up study, Werner et al. (2004) studied the scaphoid and lunate motion in a series of *in-vitro* wrist simulations, in which DTM with nine variations of obliquities were performed. They found when the DTM was aligned 36.8° from the sagittal plane, the lunate motion was minimal, with its vector excursion (a vector sum of its flexion/extension and radial ulnar deviation) measured as low as 22% that of the 3MC. And the minimal motion of the scaphoid was attained for DTM performed at an angle of 45° to the sagittal plane. These findings were later confirmed *in-vivo* by Crisco et al. (2005), who analysed a large range of incremental CT scans and predicted the minimal lunate motion to be attainable in DTM angled approximately 30° from the sagittal plane. Built on this study, Upal et al. (2006) further examined the elongation of the SLIL during DTM, and based on a linear regression model, they predicted the fibers in the palmar subregion of the SLIL would sustain minimal elongation if DTM was performed in the plane associated with the minial lunate motion. Although ligament strains were not measured in the present study, the reduced scapholunate angle observed correlated with their claims to some extent.

4.1.3.2 Carpal Pathokinematics

Stage I: resection of the v- and m-SLIL

Over the years, many researchers have endeavoured to study the role of the SLIL in stabilising the scaphoid and lunate. Anatomically, the SLIL has been shown to be divisible into three histologically distinct subregions, namely, the dorsal (d-), the volar (v-) and the membranous (m-) (Berger, 1996b). Material property studies have demonstrated the d-SLIL to be mechanically the strongest and are believed to be more important in restraining the scaphoid and lunate motion (Kauer, 1980; Berger, 1997; Sokolow and Saffar, 2001). With this perception, the majority of acute repairs or surgical reconstructions of the SLIL are directed with their emphasis placed exclusively on the restoration of the d-SLIL (Lavernia et al., 1992; Weiss, 1998; Wyrick et al., 1998; Harvey et al., 2007; Ross et al., 2013). However, follow-up studies have shown that a sizable portion of these techniques have been met with the loss of scapholunate reduction and radiographic deterioration in the long term (Moran et al., 2005; Gajendran et al., 2007; Soong et al., 2013; Nienstedt, 2013). New variants of the existing procedures are continued to be proposed in order to rectify this issue, and the idea of including the v-SLIL in the repair or the reconstruction as an attempt to restore the normal ligamentous anatomy of the scapholunate joint has its gained popularities among surgeons (Dunn and Johnson, 2001; Henry, 2013; Corella et al., 2013; Eng et al., 2014; Ho et al., 2015). However, a very limited number of studies have specifically looked at the relative importance of the v-SLIL on maintaining the normal kinematics of the scaphoid and lunate, giving little biomechanical justification to the inclusion of the v-SLIL in the reconstructive procedure. In addition, there are also no postoperative follow-up studies that could give clinical evidence to support such a strategy. Therefore, in the present study, the v-SLIL was divided together with the much weaker fibrocartilaginous m-SLIL, to allow their potentially subtle contribution to the scapholunate stability to be quantified in isolation.

In general, the findings in the present study showed the division of both

the v- and m-SLIL induced insignificant changes in the scaphoid and lunate kinematics, and these subregions of the SLIL were therefore considered to be of little importance in stabilising the scapholunate joint. This largely correlates with the observation in previous histological studies and material testings of the SLIL. Berger (1996b) showed the v-SLIL is much thinner than the stout d-SLIL, which is composed of transversely oriented collagen fibres and takes an average thickness of 3 mm. He also made a remark about the atypical fibrocartilaginous m-SLIL, which felt more pliable when bluntly probed, in contrast to the taut consistency of the d-SLIL. In a subsequent study, Berger et al. (1999) assessed the yield strength of all three subregions of the SLIL. By using a material testing machine fitted with an additional rotatory actuator, the authors approximate both the translational and torsional loading scenarios that the SLIL might encounter within the scapholunate joint during wrist motion. They showed the ultimate strength of the d-SLIL (260.3 ± 118.1 N) to be more than twice that of the v-SLIL (117.9 ± 21.3 N) and over four times that of the m-SLIL (62.7 ± 32.2 N). In addition, by further measuring the incremental scapholunate rotation permitted after dividing various subregions of the SLIL, the same group of researchers found releasing both the v- and m-SLIL, or v- and d-SLIL produced comparable changes in the scapholunate angle ($5.1° \pm 1.5°$ and $6.48° \pm 1.5°$, respectively). Based on this result, they concluded the v- and m- might also contribution to the rotational constraint of the scapholunate joint and further inferred the necessity of reconstructing those structures in surgery. However, this was not seen in the present study. A possible explanation could be the difference in the condition underwhich the scapholunate joint was loaded. In their study, the scapholunate bone-ligament-bone complex was taken out from the radiocarpal joint of the cadaveric wrist specimens and was directly subjected to the translational and torsional loadings that were created artificially. This, however, is certainly not the case in the present study, where the wrist motion was achieved via physiological tendon loading and the radiocarpal anatomy was preserved in its native state.

In an early kinematic study performed by Ruby et al. (1987), the authors

found that the rotational shifts in the scaphoid and lunate were comparable in wrists that only had their d-SLIL sectioned and in the ones that saw a complete SLIL division along with disruptions in a multitude of other ligaments. Apart from the most immediate conclusion that one might draw on the importance of the d-SLIL, this finding might also suggest that the contribution of the v- and m-SLIL in maintaining the normal scapholunate motion is almost negligible. Meade et al. (1990) performed a radiographic evaluation of the change in the scapholunate angle after sequentially sectioning a collection of the scapholunate stabilising ligaments in six cadaver wrists. With the radioscapholunate (RSL) already sectioned in the first stage, they found the further release of the v-SLIL caused a mean increase of 3.7° in the scapholunate angle measured on planar radiographs. However, this could not be substantiated in the present study as the increase in the scapholunate angle in the sagittal plane measured approximately 0.48° after releasing both the v- and the m-SLIL. This difference was thought to be attributed to the difference in the angle measurement method, and the accuracy of using planar radiographs to quantify a potentially subtle angular change in 3D is questionable, let alone the order in which the ligaments were sectioned in the two studies was different.

By using screws as radio-opaque markers, Mitsuyasu et al. (2004) radiographically measured the change in the radioscaphoid and radiolunate angles following sequential sectioning of various scapholunate supporting ligaments. He found when the v-SLIL was release in addition to a partial dorsal capsulectomy, the radioscaphoid angle measured 1.6° in flexion and 0.22° in extension in loaded and unloaded cadaver wrists, respectively. And the radiolunate angle measured 0.97° in extension and 0.23° in flexion in loaded and unloaded wrists, respectively. The present results correlate only with their radiolunate angle measured in the loaded wrists. Based on the dynamic wrist motion simulator developed by Tong (1985) and Werner et al. (1996), Waters et al. (2016) studied the relative contribution of both the d- and the v-SLIL in stabilising the scapholunate joint in a cadaver model. The authors found a marginal increase in the scaphoid flexion and ulnar

deviation and a minor increase in the lunate extension after dividing the v-SLIL in-isolation. Compared with the changes seen after the division of the d-SILI, these results were much smaller and considered insignificant, leading to the authors to conclude that the v-SLIL is of less importance in providing scapholunate stability. Although this is in broad agreement with the present result, the current observation, especially of the change in the scaphoid, contrasts their findings. In the present study, after the v- and m-SLIL were release, the scaphoid became marginally extended, radially deviated, and supinated, while the lunate also extended but ulnarly deviated. Although these changes were all less than 0.5° in magnitude, these were all clear indications of the loss of the scapholunate restraint in the volar and proximal aspect. During wrist extension, the scaphoid extension also slightly increased, which again suggests the scapholunate motion became dorsally hinged after the release of the v- and m-SLIL. Another interesting point is that the lunate became less ulnarly deviated but more supinated upon the incremental release of the d-SLIL. This finding was once again in line with the dorsally hinged scapholunate relation.

In conclusion, given the negligible changes in carpal kinematics observed after dividing the v- and m-SLIL, their significance in providing overall stability to the scapholunate joint might be limited. One may therefore surmise that including these structures in surgical reconstructions of the SLIL might not lead to additional benefits biomechanically or clinically. However, since other ligamentous structures surrounding the scapholunate joint were still intact, they might have provided secondary stabilisation in the absence of the v-SLIL. Hence, it is difficult to draw a definitive conclusion at this stage. But it is certain that an isolated disruption to the v-SLIL will not lead to a major carpal dysfunction.

Stage II: resection of the d-SLIL

The complete sectioning of the SLIL induced significant changes in scaphoid and lunate kinematics in most planes of wrist motion. Generally speaking, the scaphoid became significantly more flexed, ulnarly deviated and pronated with respect to the radius, whereas the lunate became more extended, supinated and volarly translated. The lunate, on the other hand, was observed to exhibit abnormal extension, supination and translated volarly and slightly ulnarly with respect to the radius. Interestingly, the complete division of the SLIL seems to have minimal impact on the radiolunate rotation around the X-axis in the coronal plane. In addition, the change in the scaphoid and lunate kinematics during DTM was found to be somewhere in between those observed during the two planar wrist motion. The capitate, on the other hand, exhibited increased pronation, dorsal and proximal translation after incrementally sectioning the d-SLIL. These changes were again seen to be the most pronounced during global wrist flexion.

These observations are in reasonable agreement with those predicted in early anatomical studies. As mentioned earlier, the stability of the proximal carpal row, which is a true intercalated segment free of any tendinous insertions, is achieved through a delicate interplay between the mechanical forces exerted by the surrounding structure, its boney architecture, and a complex networks of ligamentous supports (Linscheid, 1986; Gould et al., 2015). Given the obliquity of the scaphoid and the geometry of the radioscaphoid fossa, it has long been established that the scaphoid tends to rotate into flexion and pronation when axially loaded (Garcia-Elias, 1997; Salvà-Coll et al., 2011; Garcia-Elias and Lluch, 2017). This is believed to be counterbalanced by the lunate, which exhibit an inherent tendency to rotate into extension. However, there is still debate around the mechanism behind this phenomenon. Kauer (1980) believed it is the volarly wedge-shaped morphology (the height of the bone is larger at the volar aspect) of the lunate that causes it to predispose to extension under the axial load transmitted through the capitate. However, Weber (1984) hypothesised this to be due the triquetrum, which tends to rotate into extension by virtue of the helicoid shaped triquetrum-

hamate articulation, that tows the dissociated lunate into extension through the lunotriquetral interosseous ligament if the SLIL is torn. In addition, presumably through the STT and the scaphocapitate ligaments, the trapezium will be pulled towards the volar aspect by the already flexed and pronated scaphoid, and with the lunate and triquetrum rotated into extension, the rigidly bounded distal row will be forcefully twisted into pronation (Garcia-Elias, 2013b).

The present results also correlate well with the observations reported by many who have also studied the stabilising role of the SLIL via selective ligament sectioning. Ruby et al. (1987) are probably among the first few who quantitatively measured the shifts in the scaphoid and lunate attitude in 3D after the complete division of the SLIL. Four cadaver wrists were used and loaded in combined flexion and ulnar deviation, at which they believed the scapholunate joint was stressed to a greater extent. They observed the scaphoid was primarily collapsed into flexion and pronation, forming an angle of 21.6° with the lunate in the sagittal plane following the complete division of the SLIL. Meade et al. (1990) measured the change in the scapholunate angle on lateral radiographs and found a significant increase of 27° after the SLIL was sectioned. Mitsuyasu et al. (2004) loaded five cadaver wrists and recorded a radioscaphoid angle of 7.24° in flexion and a radiolunate angle of 2.49° in extension after sequentially dividing the v-SLIL, the DIC attachments on the scaphoid and trapezium, and the d-SLIL.

The pathokinematics of the scaphoid and lunate after the division of the SLIL have also been measured dynamically by many researchers. In a series of studies, with an improved version of the wrist simulator developed by Tong (1985) and Werner et al. (1996), researchers from the same group evaluated the effect of sectioning a variety of scapholunate-supporting ligaments in different combinations and permutations during dynamic planar wrist motion (Short et al., 1995, 2002b, 2005, 2007; Waters et al., 2016). Eschweiler et al. (2016b) simulated FEM and RUD passively on eight cadavers and evaluated the effect of completely dividing the SLIL on the scaphoid and lunate motion. Based on the apparatus developed by Iglesias (2015), Stoesser et al. (2016)

also studied the stabilising roles of several scapholunate stabilisers during dynamically simulated planar wrist motion on a cadaver model. Since these studies have all included the division of the SLIL, a quantitative comparison was carried out with the results of the present thesis. However, the comparison could not be performed in full for all 6 DOFs of the scaphoid and lunate kinematics, as the majority of studies focused only on the change in the rotational behaviour of the bones following the ligament division. In addition, since almost all studies looked at planar wrist motion only, and owing to the difference in their range of dynamic wrist simulations, the comparison was conducted for the rotational attitude of the scaphoid and the lunate measured at a limited number of wrist positions, namely, the neutral, 30° of flexion, 20° of extension (Table 4.10), 15° of ulnar deviation and 5° of radial deviation (Table 4.11). It is clear that there are large variations in the values reported by various studies (even between repeats performed by the same group of researchers). And with the significant lack of data, especially the rotational component around the X- and Y-axis, it is highly challenging for one to fully appreciate the scaphoid and lunate rotation after the division of the SLIL.

Nonetheless, the increase in the radioscaphoid flexion and ulnar deviation appear to be consistently the most pronounced during global wrist flexion but became less significant during wrist extension (Table 4.10). The abnormal increase in the radiolunate extension seems to also peak during global wrist flexion. And the increase in the radioscaphoid ulnar deviation seems to be amplified during ulnar deviation of the global wrist and again became attenuated during radial deviation (Table 4.11). These trends are all reflected in the present results. In terms of the magnitude of the changes, the present results are in good agreement with those reported by Short et al. (2005) and Waters et al. (2016) but contrast with those reported by the others. This was thought to mainly stem from the difference in the muscle loading applied to the cadaveric wrist specimens and the way in which the dynamic wrist motion was simulated between studies. Eschweiler et al. (2016b) loaded the tendon of each wrist muscle with a force of 5 N, and the wrist motion was manually initiated, then "actuated" entirely by gravity acting

on the hand. They observed less distinct alterations in the scaphoid and lunate kinematics after sectioning the SLIL. The tendon load applied in the experiment performed by Stoesser et al. (2016) was also found to be smaller than the one used in the present study. On average, a total of 65 N and 87 N was distributed across five wrist muscles during FEM and RUD, respectively (data digitised from the force values reported by Iglesias (2015)). In contrast, the summation of the forces applied to the wrist muscles was kept constant at a level of 150 N throughout the dynamic simulation in the present study.

In terms of the static malalignment induced by dividing the SLIL, despite the large variations in the values reported by different researchers, the present results support the observation that the division of the SLIL does not necessarily lead to immediate formation of a DISI deformity (Kitay and Wolfe, 2012), given the radiolunate, the capitolunate and the scapholunate angle did not exceed the diagnostic threshold of 15°, 30° and 24° (radiographically 70°, but measures 46° in normal writs) in the sagittal plane (Watson et al., 1993; Gilula et al., 2002).

Another point of confusion is around the fact that the abnormal scaphoid pronation was only reported in biomechanical studies performed by Ruby et al. (1987) and Short et al. (1995), but was then described as insignificant and omitted in the subsequent studies carried out by the same group of researchers (Short et al., 2002b, 2005, 2007). The only noticeable difference, however, was that the wrist specimens in studies where the abnormal radioscaphoid pronation was observed following the division of the SLIL sustained a dorsal capsulotomy similar to the one performed in the present study, and the dorsal capsule of the wrist was kept open throughout the experiment (Short et al., 1995). However, it is still unclear whether a dorsal capsulotomy through the DIC and DRC ligaments really causes the scaphoid to exhibit pathological pronation after the SLIL is disrupted,

Table 4.10: Angular attitude of the scaphoid and lunate at neutral wrist position, flexion of 30°, and extension of 20°, reported in the present study and compared with data in the literature

Study		NEU			Flexion 30°			Extension 20°		
		Z FL(+)/EX(-)	X UD(+)/RD(-)	Y PR(+)/SU(-)	Z FL(+)/EX(-)	X UD(+)/RD(-)	Y PR(+)/SU(-)	Z FL(+)/EX(-)	X UD(+)/RD(-)	Y PR(+)/SU(-)
Short et al. (1995)										
	Scaphoid	+1.40		+3.10	+3.50		+5.50	+0.90		+1.50
	Lunate	-2.40			-4.60			-0.20		
Short et al. (2002b)										
	Scaphoid	0.00	+3.30		+2.90	+3.30		-0.80	-1.40	
	Lunate	-5.50	-0.40		-7.60	-1.10		-1.20	-0.40	
Short et al. (2005)										
	Scaphoid	+6.20	+4.60		+7.00	+5.80		+4.20	+3.20	
	Lunate	-9.90	-0.50		-16.40	-2.90		-3.00	-0.40	
Waters et al. (2016)										
	Scaphoid	+13.80								
	Lunate	-9.15			-10.15			-4.15		
Stoesser et al. (2016)										
	Scaphoid	+2.78			+5.29			0.00		
	Lunate	-3.72			-3.92			-3.37		
Present Study										
	Scaphoid	+7.12	+6.13	+7.67	+9.30	+6.45	+5.59	+3.47	+5.20	+6.86
	Lunate	-8.93	+0.25	-2.62	-13.15	0.00	-2.88	-7.68	+0.88	-1.02

Table 4.11: Angular attitude of the scaphoid and lunate at ulnar deviation of 15° and radial deviation of 5°, reported in the present study and compared with data in the literature

Study		Ulnar Dev. 15°			Radial Dev. 5°		
		Z FL(+)/EX(-)	X UD(+)/RD(-)	Y PR(+)/SU(-)	Z FL(+)/EX(-)	X UD(+)/RD(-)	Y PR(+)/SU(-)
Short et al. (1995)							
	Scaphoid						+4.00
	Lunate				-4.40		
Short et al. (2002b)							
	Scaphoid	+2.80	+2.20		-0.40	+1.00	
	Lunate	-2.40	0.00		-3.90	-0.40	
Short et al. (2005)							
	Scaphoid	+9.90	+6.30		+5.50	+3.80	
	Lunate	-5.30	-4.20		-11.70	+1.50	
Waters et al. (2016)							
	Scaphoid	+10.40			+14.00		
	Lunate						
Stoesser et al. (2016)							
	Scaphoid	+1.62			+2.03		
	Lunate	-3.18			-4.00		
Present Study							
	Scaphoid	+9.48	+7.23	+4.63	+5.58	+4.57	+9.18
	Lunate	-7.07	+0.14	-0.63	-9.75	+0.29	-2.60

as Short et al. (2007) again reported that dividing both the DIC and DRC induced negligible changes in the scaphoid and lunate kinematics, advocating the legitimacy in performing a dorsal capsulotomy that incises through these structures. Nonetheless, the abnormal scaphoid pronation and lunate supination were observed *in-vivo* by Omori et al. (2013). By studying the CT scan of three scapholunate dissociated wrists, they found the scaphoid possessed an average static malalignment of 22° in flexion, 2° in ulnar deviation and 8° in pronation, while the lunate assumed a posture of 18° in extension, 8° in ulnar deviation, and 10° in supination. These grossly correlate with the observation in the present study.

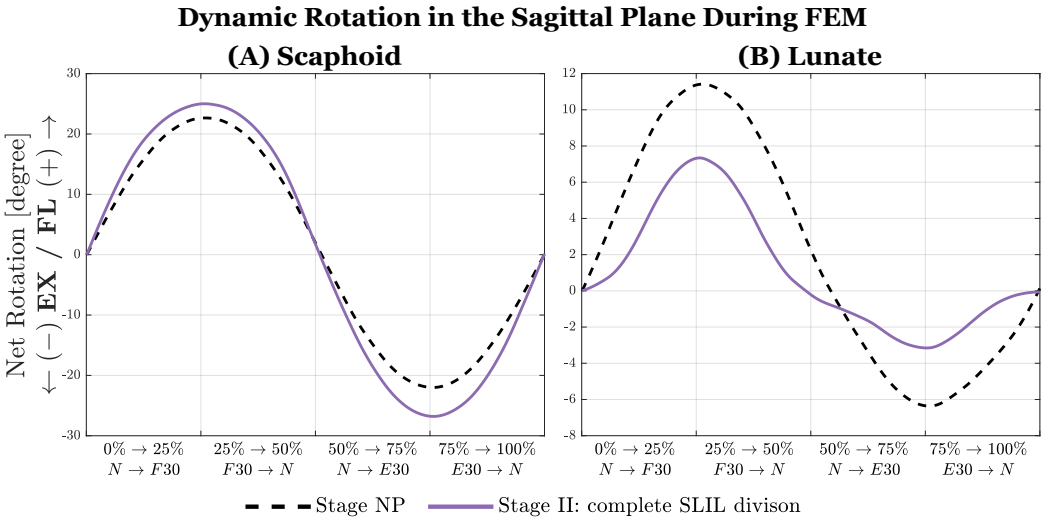

Figure 4.20: Dynamic rotation exhibited by **(A)** Scaphoid and **(B)** Lunate, in the sagittal plane during global wrist FEM. The curves are isolated from Fig. 4.11a and Fig. 4.14a, and are the average of all seven wrist specimens.

The present study is perhaps the first to include an analysis on how and to what extent the ligament division would alter the dynamic pattern of a specific carpal bone. This was considered essential as these subtle pattern distortions would be otherwise difficult to detect, especially under significant ligament injury where static malalignment of the carpal bones is presented. After the complete division of the SLIL, the analysis indicated that the net flexion and extension exhibited by the scaphoid was significantly increased during global wrist FEM (Fig. 4.20A), whereas the lunate showed a statisti-

cal decrease in its rotation in the sagittal plane (Fig. 4.20B). This suggests that the scaphoid became more flexible while the lunate motion became less responsive and presumably less influenced by that of the scaphoid. This finding correlates well with clinical observations (Werner et al., 2005), as well as the kinematic results reported by Short et al. (2005), where the trajectory corresponds to the scaphoid following the division of the SLIL spans longer, while that of the lunate is shortened. In addition, when the SLIL was sectioned, the net adaptive flexion and extension exhibited by the scaphoid during global wrist RUD reduced significantly (Fig. 4.21). Noticeably, this was accompanied by the loss of the dynamic pronation exhibited by the scaphoid in wrist ulnar deviation and a significant increase in the net scaphoid radial deviation during wrist radial deviation. These findings suggest that

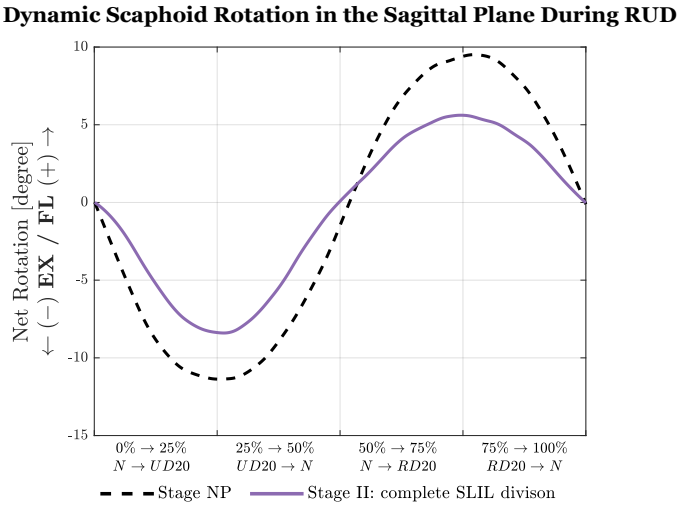

Figure 4.21: Dynamic rotation exhibited by the scaphoid in the sagittal plane during global wrist RUD. The curves are isolated from Fig. 4.12a and are the average of all seven wrist specimens.

instead of showing an adaptive column-like behaviour, the scaphoid rotation became more rigid and row-like. This also correlates with the clinical finding that once dissociated from the lunate, the scaphoid seems to 'no longer behave as a proximal row bone but follow the capitate as if it was a distal row element' (Garcia-Elias, 2011). Furthermore, the division of the SLIL caused the net capitolunate rotation in the sagittal plane to statistically

increase during both flexion and extension (Fig. B.4a). This implies that in scapholunate dissociated wrists, the midcarpal joint motion serves as the primary contributor that enables global wrist FEM. This finding correlates with the *in-vivo* lunate kinematics reported by Wolfe et al. (1994).

In conclusion, given the large change in the scaphoid and lunate kinematics observed after the complete division of the SLIL, the present results support the notion that the SLIL serves as the primary stabiliser of the scapholunate joint (Kitay and Wolfe, 2012).

Stage III: resection of the RSC and LRL

Transecting the RSC and LRL in conjunction with the SLIL caused mild alterations in carpal kinematics compared to those seen following Stage II ligament division. This finding is in agreement with the broad notion that these volar extrinsic ligaments serve to provide important secondary stability to the scapholunate joint (Short et al., 2005; Werner et al., 2011; Lee et al., 2015; Stoesser et al., 2016; Werner and Short, 2018). The specific motion restraint that these ligaments provide, as to in what way and in which part of the wrist motion they are recruited, however, is still debated. Therefore the purpose of this part of the present study was to shed some light on their functional roles in modulating the carpal kinematics.

In the absence of the SLIL, RSC and LRL, the scaphoid and capitate were observed to rotate into further pronation. And this change was seen to be more pronounced during wrist ulnar deviation and extension. More noticeably, during extension, the absolute radioscaphoid translation was statistically more volar, and the capitate demonstrated appreciably more dynamic dorsal translation. All these findings unanimously imply the movability of the scaphoid and capitate was increased in the volar and radial direction. This correlates well with the pathoanatomy in this stage, where the RSC, which arises volarly from the radial styloid and coursed distally and ulnarly beneath the waist of the scaphoid to insert on the proximal scaphoid tuberosity and the capitate (Berger and Landsmeer, 1990), was disrupted (Fig. **??**). And the

present observations indeed correlate well with the lengthening of the RSC observed *in-vivo* during ulnar deviation (Xu and Tang, 2009), and extension (Tang et al., 2011).

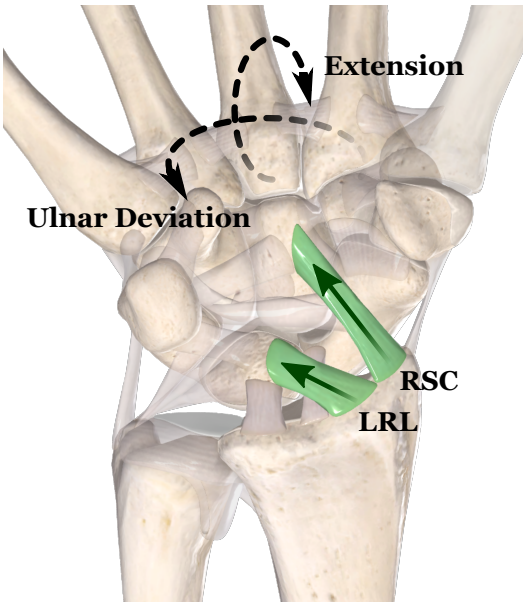

Figure 4.22: The anatomy of the radioscaphocapitate (RSC) ligament and the long radiolunate (LRL) ligament. These ligament are believed to be under tension during ulnar deviation and extension.

Given the specific anatomy of the RSC, it has long been postulated to act as a soft-tissue fulcrum or a sling that volarly supports the scaphoid rotation, regulating its flexion (Taleisnik, 1976). In the present thesis, only a small amount of volar collapsing of the scaphoid was seen after the division of the RSC and was statistically insignificant. One possible explanation could be that the RSC alone could not effectively prevent the substantial scaphoid flexion caused by the complete attenuation of the SLIL and might be already elongated given its disadvantageous position at relative to the scaphoid. Short et al. (2005) sectioned the RSC in isolation and also observed minimal change in the scaphoid flexion. In the present study, the scaphoid was observed to mostly pronate following Stage III ligament resection. This observation is in agreement with that reported by Ritt et al. (1995), who measured the restraining torques of fourteen cadaver wrists that sustained

incremental division of nine capsuloligamentous structures and concluded the RSC was primary pronation constraint. In a cadaver model, Werner and Short (2018) also observed the scaphoid to pronate significantly after the RSC was released in conjunction with the SLIL and the STT ligament. Furthermore, in terms of radioscaphoid translations, the abnormal increase in the volar movement after the RSC was disrupted was in good agreement with that observed by Viegas et al. (1995). The authors found after the RSC was released, the pressure centroid of the radioscaphoid articulation moved significantly in the volar direction. Many believe the RSC has a role in transmitting the dorsal translation of the distal row to the scaphoid, thus hoisting the scaphoid into simultaneous extension during global wrist extension (Kitay and Wolfe, 2012). This effectively explains why dividing the RSC in Stage III induced statistically more dynamic dorsal movement of the capitate during wrist extension.

In Stage III of ligament division, the lunate was seen to be less supinated (more pronated) and translated more volarly and ulnarly with respect to the radius as compared to the previous stage. The pronation of the lunate was seen to be most evident during ulnar deviation. This finding is in agreement with that reported by Ritt et al. (1995), who suggested the palmar LRL also provides constraint against pronation. Furthermore, this is also in agreement with the *in-vivo* ligament elongation measurements reported by (Xu and Tang, 2009). In addition, the lunate was also statistically more extended during ulnar deviation. Following the ligament division, the abnormal ulnar shift in the radiolunate translation was observed to be more pronounced during wrist radial deviation. And the abnormal volar shift was pronounced during the adaptive radiolunate extension exhibited during ulnar deviation. In addition, the dynamic dorsal translation exhibited by the lunate during wrist flexion saw a statistically significant increase, while the dynamic extension exhibited by the lunate during ulnar deviation also showed an appreciable increase. Collectively, these findings implied that the lunate motion affords less constraints imposed from the volar and radial aspect of the radius. This again correlated well with the pathoanatomy, where the

LRL that links the distal radius with the radial aspect of the palmar horn of the lunate (Berger and Landsmeer, 1990), was disrupted (Fig. **??**). And given the volar and ulnar inclination of the distal radius, it is anticipated that an unchecked lunate will translocate in these directions. The present results correlate well with that reported by Rayhack et al. (1987), who observed the carpus to be ulnarly subluxed when the palmar radiocarpal ligaments were disrupted. This, however, was only agreed partially by Viegas et al. (1995), who found the pressure centroid of the radiolunate contact showed a significant volar movement but exhibited only a marginal amount of ulnar movement after dividing the RSC and LRL. In a more recent study, Werner et al. (2011) examined the pathological carpal translations following ligamentous injuries on a cadaver model. They also found the lunate centroid to translate primarily ulnarly and volarly after dividing the SLIL in conjunction with a multitude of the radiocarpal ligaments situated on the volar side.

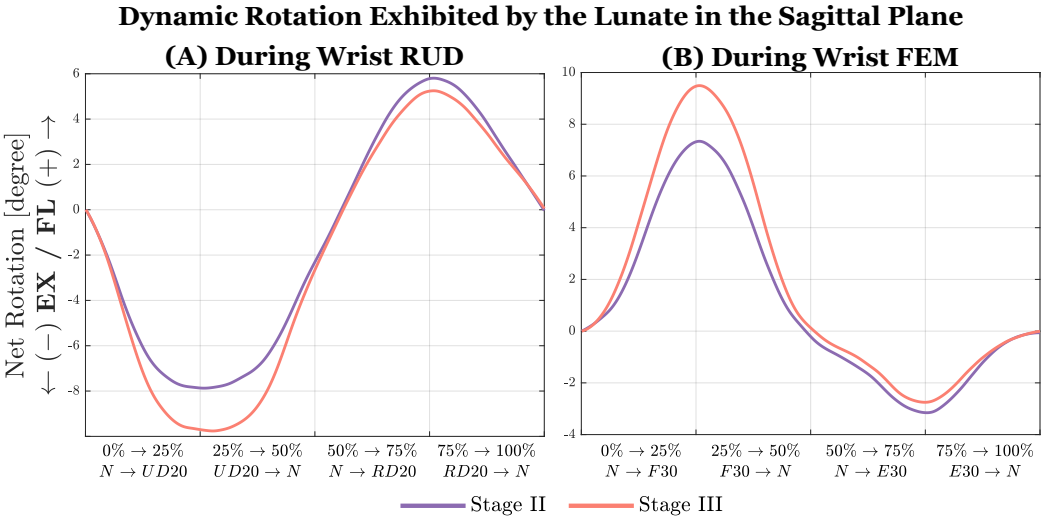

Figure 4.23: Dynamic rotation exhibited by the lunate in the sagittal plane during **(A)** RUD and **(B)** FEM of the global wrist. The curves are isolated from Fig. 4.14a and Fig. 4.15a, and are the average of all seven wrist specimens.

Apart from the findings that are similar to the ones reported previously by various researchers, in the present study, a rather peculiar change was observed for the dynamic pattern of the lunate motion. After the ligament

division in Stage III, the lunate was seen to exhibit more dynamic adaptive extension during ulnar deviation but less dynamic adaptive flexion during radial deviation (Fig. 4.23A). As discussed earlier, the former observation is well in line with the pathoanatomy, where the loss of the volar constraint permitted more extension of the lunate towards the dorsal radius. The latter, on the other hand, was thought to be due to the further attenuation of the association or "compactness" of the scapholunate joint, since the adaptive flexion exhibited by the lunate during wrist radial deviation was believed to be primarily induced by the scaphoid under the influence of the STT joint. Based on these observations, one might expect the same changes to be seen during FEM. However, the lunate was observed to exhibit more dynamic flexion during planar wrist flexion, and exhibit a minimal amount of change in its dynamic extension during wrist extension (Fig. 4.23B). This may seem counterintuitive, but it is important to realise that the mechanism that drives the lunate into flexion and extension in FEM is not the same with that in RUD. During wrist flexion, the lunate is driven primarily by the capitate, and since the lunate had already collapsed into extension at the onset of Stage III, it was therefore anticipated the net flexion would increase after the ligament division. During wrist extension, since the midcarpal joint dominated in facilitating the global wrist movement following the complete loss of the SLIL, it was also comprehensible that minimal changes occurred at the radiolunate level.

Stage IV: resection of the DIC, DRC and STT

The subsequent sectioning of the DIC, a portion of the DRC, and the STT caused the scaphoid to collapse further into flexion, ulnar deviation and pronation. These observations are in agreement with those reported previously by Short et al. (2007), and Werner and Short (2018). In the present study, these pathological changes were observed to be much larger than those seen in the previous stage and were comparable to the ones seen after the division of the SLIL. This suggests that either the dorsal ligaments or the STT might be important in providing secondary stability

to the scaphoid. By arthroscopically examining of the wrist that sustained sequential ligament lesions, Lee et al. (2015) found attenuations of the dorsal ligaments were the key to the progression from a Geissler grade 3 injury into a grade 4 injury. This was supported by the present study, as the pathological changes in the radioscaphoid rotation were found to be more pronounced during wrist motion in which the DIC and the DRC were recruited (Fig. **??**). This included the ulnar deviation, flexion, as well as the combined ulnar flexion of the global wrist (Savelberg et al., 1993; Xu and Tang, 2009; Tang et al., 2011). In addition, in the present study, the scaphoid was found to be more radially shifted with respect to the radius during flexion and ulnar flexion as compared to that seen in Stage III.

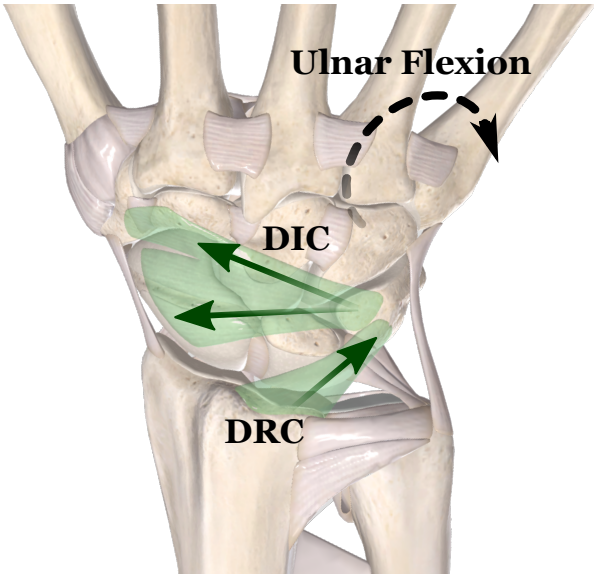

Figure 4.24: The anatomy of the dorsal radiocarpal (DRC) ligament and the dorsal intercarpal (DIC) ligament. These ligament are believed to be under tension during ulnar flexion of the global wrist.

Viegas et al. (1999) believed that through a lateral "V" configuration, the DIC and the DRC ligament work in tandem to deliver indirect dorsal stability to the proximal pole of the scaphoid, while still permitting flexible radioscaphoid motion through "scissoring" of the two ligaments. This might provide an explanation for the amplification of the abnormal radioscaphoid

motion during flexion and ulnar flexion. In the present study, the pattern analysis showed the scaphoid started to exhibit statistically more dynamic rotation in the coronal plane (Fig. 4.25A) throughout the wrist RUD with appreciably attenuated adaptive flexion and extension in the sagittal plane (Fig. 4.25B). This correlates with the disruption of the STT ligament, as this ligament is thought to be responsible for pulling the scaphoid into extension during wrist ulnar deviation (Garcia-Elias, 2013b). Noticeably, the magnitude of the dynamic radial deviation of the scaphoid was now comparable to that of the global wrist. This implies the congruent adaptative flexion of the scaphoid was completely lost and presumably replaced by column-like rotations that solely dictated by the bony geometry (Werner et al., 2007).

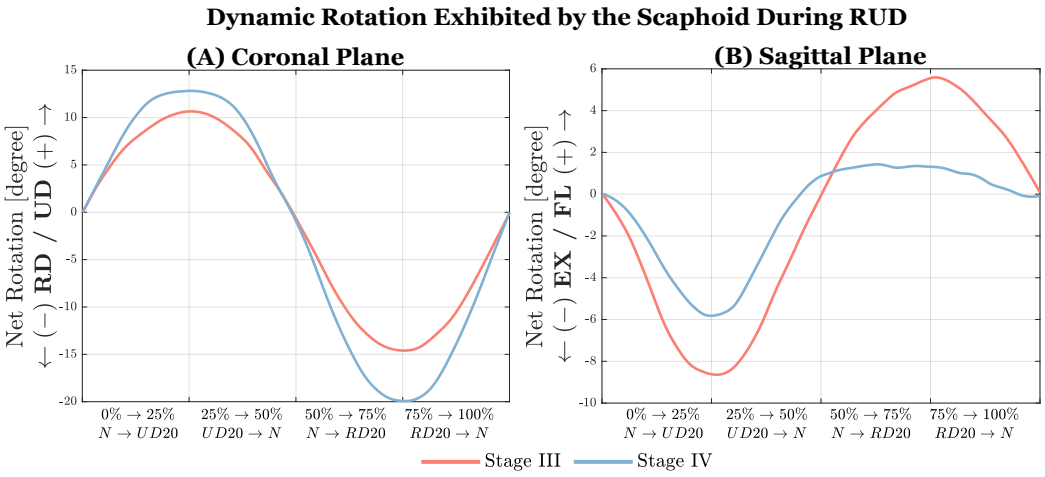

Figure 4.25: Dynamic rotation exhibited by the scaphoid **(A)** in the coronal plane and **(B)** in the sagittal plane during RUD of the global wrist. The curves are isolated from Fig. 4.12b and Fig. 4.12a, and are the average of all seven wrist specimens.

The lunate kinematics was found to be relatively unaffected by the present stage of ligament division, except for being statistically more supinated as compared to that in the previous stage. In addition, the capitate was seen to be more proximally migrated with its radial and ulnar translation significantly attenuated. Dorsal translation of the capitate was observed in some specimens but was statically insignificant due to the increased data variability. These findings concur with the pathoanatomy, as

the DIC is believed to act as a labrum that binds the dorsal aspect of the scaphocapitolunate articulation (Berger, 1997).

However, in this stage of ligament resection, there was considerably more variability between the carpal kinematics measured in different wrist specimens, given the significant increase in the standard deviation of the data. To some extent, this correlates with the experimental observation that the carpal movement had become dynamically unstable and disordered after the ligamentous injuries simulated in the present stage. But the large variability in the data might have prevented certain changes in the resultant carpal kinematics from being revealed with sufficient statistical power. Hence the results reported for this stage of ligament division in the present study might be incomprehensive compared to the reality.

4.1.3.3 Carpal Kinematics Following Reconstructive Surgery

As mentioned previously, scapholunate dissociation is the most frequently diagnosed pattern of carpal instability (Jones, 1988). And it has been associated with scapholunate advanced collapse (SLAC) pattern if left untreated (Watson and Ballet, 1984), which in turn leads to progressive arthritis in the radioscaphoid and capitolunate joints (Watson and Ryu, 1986). However, owing to the frequent negligence as well as the difficulties in early diagnosis, scapholunate instability is often treated in a subacute or a chronic setting (Garcia-Elias, 2011), where the remnants of the torn SLIL have shown diminished healing potential or signs of degeneration, precluding direct repair of the ligament (Rohman et al., 2014). For patients having an irreparable SLIL but with the absence of an irreducible carpal derangement or arthritic changes in the cartilage, some form of reconstructive surgery that aims to re-establish the normal scapholunate relation is often recommended to relieve pain, restore wrist function and mitigate the risk of progressing into SLAC. These include soft-tissue techniques such as capsulodesis, ligament reconstruction that uses tendon graft or bone-ligament-bone autografts, and rigid fixations such as pseudoarthrosis at the scapholunate joint with Herbert screws or limited intercarpal fusion (Kitay and Wolfe, 2012).

However, as discussed in the review of literature, there is no current consensus on which of these techniques being the optimal choice in managing chronic scapholunate instability and ligament injuries. Intercarpal arthrodesis has been performed in the early days but is not currently in use owing to a high rate of nonunion (Larsen et al., 1997), loss of wrist motion (Kleinman et al., 1982; Watson and Ryu, 1986), and alteration of the normal joint kinematics and contact (Garcia-Elias et al., 1989; Holleran et al., 2013). In contrast, soft-tissue techniques are believed in having the theoretical advantage of preserving more intercarpal motion and are therefore preferred by hand surgeons (Szabo et al., 2002). However, a varying degree of success rate and a mixed result has been reported these soft-tissue techniques, raising concerns in terms of their reliability and efficacy (Zarkadas et al., 2004). More alarmingly, the techniques that see extensive application nowadays have not

been subjected to any prior biomechanical validation (Short et al., 2009). Instead, their ability in restoring the normal scapholunate relation and carpal function are often evaluated empirically based on postoperative radiographic measurement of the scapholunate angle and gap width, grip strength, or patient-reported measures that quantitate one's subjective perceptions after the surgery. However, let alone the measurements made on planar radiographs are prone to projection errors (Loisel et al., 2020), tracking changes in these quantities might not fully evaluate the surgery-induced alterations of the carpal kinematics in 3D. In addition, these static radiographic measurements are also unlikely to be able to indicate any surgery-induced changes in the dynamic behaviour of the carpal bones during active wrist movements.

To date, there is only one study that has carried out such a rigorous evaluation based on the three-dimensional scapholunate kinematics measured before and after surgery (Short et al., 2009). However, the authors have only studied the dorsal intercarpal ligament capsulodesis originally developed by Szabo et al. (2002) and concluded that applying this technique alone is inadequate to re-stabilise the scaphoid and lunate. This is in agreement with the clinical observations that the capsulodesis tends to address the abnormal scaphoid alignment in the sagittal plane only and is generally unable to reliably suppress the scapholunate gapping in the coronal plane (Moran et al., 2005; Gajendran et al., 2007). In addition, the method of using electromagnetic sensors mounted on the dorsum of the scaphoid and the lunate to allow tracking of the carpal kinematics in the study performed by Short et al. (2009) has also aroused some doubts and criticism (Loisel et al., 2020).

On the other hand, tenodesis procedures in which tendon grafts are weaved in a manner that aims to provide multiplanar control of the scaphoid kinematics are generally believed to outperform the conventional capsulodesis techniques (Kang et al., 2018). Therefore, the main goal of this part of the present study was to evaluate the outcome of two tenodesis techniques, including the newly invented DTLT and the famous and commonly used 3LT, in a biomechanical model based on the carpal kinematics measured obstruct-free using biplane X-ray fluoroscopy.

Dorsal Transarticular Loop Tenodesis

The present study shows the DTLT is capable of restoring the kinematics of the scaphoid, lunate and capitate back to a near-normal state, even under the extreme circumstance where the primary and secondary scapholunate stabilisers have been severely disrupted, which consequently resulted in a substantial amount of static carpal deformity. Given the similarity between the scapholunate motion measured postoperatively and that of the native state, this technique is also proven to be adequate in re-associating the scaphoid and lunate.

However, a full restoration was not achieved by the DTLT as it was shown to perform less well in certain planes or during certain wrist motions, revealing potential flaws in the design of this technique. Most noticeably, the DTLT failed to achieve a sufficient reduction of the volarly collapsed scaphoid, resulting in a mean residual radioscaphoid angle of approximately 6° and a mean misalignment of 0.7 mm. These might be related to the dorsal and proximal placement of the tendon graft, which let alone will provide little mechanical advantage against flexion of the scaphoid, it will even cause the scaphoid to be dorsally hoisted into flexion if the tendon graft is under excessive tension. This is indeed the case, as the abnormal scaphoid flexion was observed to be more pronounced when the wrist was moving towards flexion or ulnar flexion, during which the radially and dorsally originated ECR-B graft was gradually under tension. These findings indicate that the DTLT might be insufficient in restoring scaphoid stability, as it does not seem to provide adequate control over the distal pole of the scaphoid. This problem has also been realised clinically by the original developer of the DTLT procedure, who advocates an additional dorsal capsulodesis that transfers the trapezium and trapezoid insertion of the DIC onto the dorsum of the distal scaphoid to be performed to augment the reconstruction (S. K. Tham, personal communication, December 23, 2015). This step, however, was omitted as the DIC was completely transected in the previous stage. Therefore, in the present thesis, there was uncertainty about whether the augmented version of the DTLT would achieve an improved outcome in reducing and stabilising

the scaphoid. Furthermore, owing to the way in which the tendon graft was weaved, the DTLT demonstrated a limited capability in re-establishing the link between the scaphoid and the distal carpal row at the STT articulation. This was particularly evident during wrist RUD, as the DTLT led to an inferior outcome in restoring the rocking-chair-like, adaptive radioscaphoid rotation in the sagittal plane, comparing to that after the 3LT procedure (Fig. 4.26).

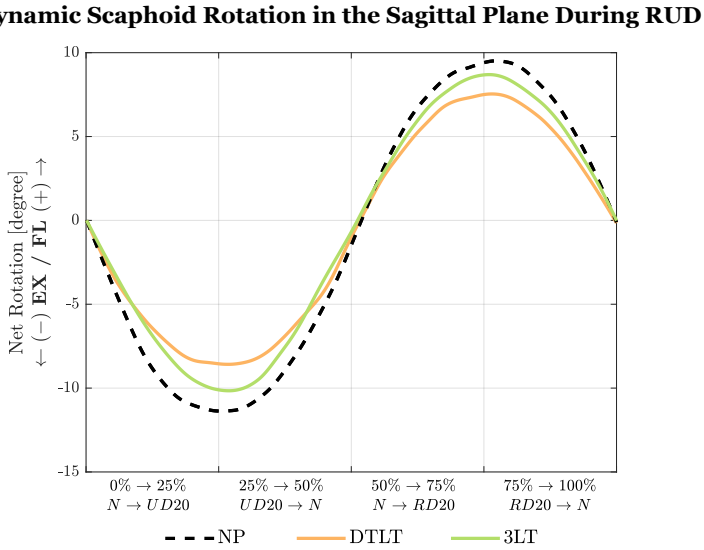

Figure 4.26: Dynamic rotation exhibited by the scaphoid in the sagittal plane during wrist RUD following the DTLT and 3LT procedures. The curves are isolated from Fig. 4.12a, and are the average of all seven wrist specimens.

This is not surprising as a dedicated reconstruction of the STT ligament is included in the 3LT procedure by tunnelling the FCR graft obliquely and through the scaphoid along its longitudinal axis, whereas no attention is paid by the DTLT in this regard. This is not desirable as an undercorrected posture of the distal scaphoid could lead to an altered contact with the trapezium and the trapezoid. Therefore, apart from performing a separate dorsal capsulodesis that complements the reconstruction, the DTLT procedure could be potentially improved if the tendon weave is constructed such that extension of the distal scaphoid is encouraged. One possible modification of the DTLT could be to anchor the remaining tendon graft to the dorsum

of the distal scaphoid instead of directly suturing it back to the ECR-B at the proximal scaphoid. Alternatively, the idea of tunnelling the tendon graft obliquely through the scaphoid in the 3LT technique may be a viable alternative augmentation.

Another noticeable issue is that the pattern of the scaphoid translation along the X-axis seems to be changed after the DTLT procedure, as an unusual amount of volar translation was observed for the scaphoid when the wrist was ulnarly deviating. The lunate, on the other hand, was observed to pronate statistically more. This finding suggests that the scaphoid was actually precessing around the lunate in the direction of pronation. Since the ECR-B graft is radially situated, it will be tightened during wrist ulnar deviation, twisting both the scaphoid and the lunate as a unit towards the volar radius. But unlike the lunate, the scaphoid is more radially situated and will be displaced out of contact with the radius during ulnar deviation, this volarly directed twist will, therefore, not only pronate but also volar shift the scaphoid.

Another major concern of the DTLT was that it does not explicitly reconstruct the v-SLIL, as the transarticular tendon weave was only set to cross proximally over the dorsum of the scapholunate joint. This construct was initially thought to be inadequate against the volar opening of the scapholunate interval, as the v-SLIL has been found to sustain increased tension when the wrist is loaded under extension (Lee et al., 2010). In the present study, this risk was indeed present, as the scaphoid was observed to abnormally supinate in relation to the lunate during extension and radial extension after the complete loss of the SLIL. However, the DTLT seems to have performed reasonably well in suppressing this pathological supination of the scaphoid, ensuring the scapholunate interval does not open asymmetrically from the volar side. The DTLT was also seen to be effective in preventing the capitate from wedging proximally into the scapholunate interval, lending further evidence that this reconstruction is competent in closing the scapholunate interval.

The DTLT procedure was observed to have effectively rectified the ab-

normally extended posture of the lunate (DISI). In a number of specimens, however, the reconstruction was seen to have even overcorrected the lunate into flexion. This was due to the inconsistency in reducing the lunate, as the carpal bones were manually aligned by the orthopaedic surgeon with their resultant alignment visually examined. Although this appeared to be empirical and there was a lack of rigorous and quantitative control over the reconstruction outcomes across different cadaveric wrist specimens, it reflected the way in which the surgery is performed in reality, and might therefore represent a valid methodology in the present study. Despite being a complication, a slightly flexed lunate might be helpful in returning the normal range of its dynamic extension, which has been observed to be significantly attenuated when a DISI deformity is present. Furthermore, as opposed to DISI, excessive flexion of the lunate seems to be rarely associated with any form of degenerative osteoarthropathy (Tischler et al., 2014).

Ultimately, the DTLT may be challenging to perform, given the need to drill two parallel tunnels on the dorsum of the scaphoid and lunate. Given the limited space available and the catastrophic consequences of tunnel fractures, appropriate planning on the placement of the guidewires is therefore critical. It is advisable that the procedures are planned and practised virtually first using the CT scan of the patient. Another concern is the poor vascularisation in the vicinity of the scapholunate joint (Garcia-Elias et al., 2006), which might prevent adequate incorporation of the tendon graft into the healing bone. Therefore, some form of direct graft-to-bone fixation, such as the use of interference screws, might also be beneficial in maintaining the long-term outcome of the DTLT reconstruction.

Three-Ligament Tenodesis

The 3LT has long been used in treating chronic scapholunate dissociation, as it is believed to reconstruct the d-SLIL while augmenting secondary stabilisers, namely the STT and DRC ligaments (Garcia-Elias et al., 2006), and obviates the need to tether the tendon weave to the distal radius as described in the original procedure (Brunelli and Brunelli, 1995). Despite its popularity in clinical use, however, the effect of 3LT on the carpal kinematics has not been rigorously evaluated to date. In other words, this technique has been employed on patients without knowing if it would perform as originally intended biomechanically, and to what extent it would change carpal kinematics or inducing any unwanted complications. Instead, the surgical outcome is often assessed retrospectively based on static radiographic measurements of the scapholunate angle and gap width. And conflicting results have been reported regarding the efficacy of the 3LT in restoring as well as maintaining the normal carpal function.

After reviewing the radiographs of fifteen patients who received a similar tenodesis procedure at a follow-up of thirty-six months, Moran et al. (2006) found statistically significant postoperative improvements in the scapholunate angle, but the radiolunate angle and the scapholunate diastasis remained almost unchanged. The authors also noted that the tenodesis led to an inferior outcome consistently in patients with static scapholunate instability, and the radiographic improvements in carpal alignments after the surgery seemed to deteriorate over time. Two patients in their study were found to have developed radiocarpal arthritis. On the contrary, in a retrospective analysis of nineteen patients, Chabas et al. (2008) found that the radiographic scapholunate widening was significantly improved after the surgery and was maintained at an average follow-up of thirty-seven months. The authors, however, also noted deteriorations of the scapholunate and the radiolunate angle over time. Recurrence of the DISI deformity was observed in five patients at the time of follow-up, and one case of SLAC was reported. Furthermore, Pauchard et al. (2013); De Smet et al. (2013) and Ellanti et al. (2014) reported that the tenodesis resulted in mediocre or inappreciable ra-

diographic improvements, making the authors question the reliable uses of this technique in treating scapholunate instabilities.

In the present study, the 3LT was shown to demonstrate a superior biomechanical efficacy in stabilising the scaphoid in the sagittal plane in contrast to the DTLT. After the reconstruction, the static flexion deformity of the scaphoid was fully rectified, and the dynamic radioscaphoid rotation was returned to a near-normal level in the sagittal plane. This included the restoration of the adaptive radioscaphoid flexion and extension exhibited during wrist RUD and was thought to be attributed to the reconstruction of the STT ligament incorporated in the 3LT procedure. In the transverse plane, however, the 3LT is proven to be inadequate in correcting the severe radioscaphoid malrotation, as the amount of radioscaphoid pronation was merely reduced to a level comparable to that in Stage II. Furthermore, the 3LT seems to be ineffective in restraining the significant amount of dynamic supination exhibited by the scaphoid during extension and radial extension, observable after the complete division of the SLIL. This observation was thought to be attributed to the passive starching of the FCR graft during wrist extension. Since the tendon graft was tunnelled obliquely through the scaphoid and pre-tensioned using the DRC ligament, the ulnar and dorsal directed pull was unable to counteract the scaphoid supination, leading to the widening of the volar scapholunate interval. Therefore, it is advisable that some forms of complementary v-SLIL reconstruction to be performed in conjunction to the 3LT, similar to the procedures described by Corella et al. (2013). Alternatively, a transarticular tendon weave through the central axis of the scapholunate interval, similar to the one developed by Hsu et al. (2014), could be considered to reduce the supinating potential and promote better apposition of the scaphoid and the lunate. Furthermore, the tendons of the radially located extensor muscles, namely the ECR-L and -B, could also be considered as grafting material as they tighten during flexion but not in extension. This could result in a more effective reduction of the scaphoid as it is in-line with the need for different dynamic wrist motion.

The 3LT resulted in a poor reduction of the lunate, as the lunate re-

mained statically collapsed in DISI with its dynamic extension still being significantly attenuated. This was somehow anticipated, as the tendon graft was not securely fixed to the bone upon leaving the scaphoid, and by anchoring it solely to the dorsal lunate would be presumably insufficient to obtain a reliable reconstruction of the d-SLIL. This could be observed from the lack of association between the lunate motion and that of the scaphoid, as well as the persistent proximal migration of the capitate. Thus reconstructing the DIC ligament alone in a SLIL-deficient wrist might not be able to provide sufficient radiolunate stability to keep the lunate properly reduced. Therefore, it might be beneficial to add an interference screw at the proximal exit of the scaphoid tunnel to provide a better graft-to-bone fixation.

The poor lunate reduction has also been noted clinically for the 3LT procedure or other similar modifications of the Brunelli technique, such as the one described by Van Den Abbeele et al. (1998). Moran et al. (2006) performed a retrospective analysis in fifteen patients and reported that the radiolunate angle was increased from a preoperative value of 9° to 14° at the final follow-up evaluation in patients who had dynamic carpal instability. This was changed from an average of 16° before surgery to a final value 14° in patients with static carpal instability. Chabas et al. (2008) reported that the reconstruction only led to a minor immediate correction of the radiolunate angle. At final follow-up, recurrence of the DISI deformity was observed in five patients out of a cohort of nineteen. Pauchard et al. (2013) also found that the radiolunate angle was worsened postoperatively in patients diagnosed with dynamic carpal instability, and observed no appreciable improvement on the angular anomaly of the lunate for those who developed static DISI deformity. Pollock et al. (2010) evaluated the efficacy of both the modified Brunelli technique and Blatt capsulodesis on five cadaver wrists. Although their radiolunate angles, which were measured radiographically, do not exactly correlate with the values reported in the present study, it is still clear that the tenodesis technique provided a limited remedy to the abnormal lunate posture, especially in wrist flexion and ulnar deviation. Similar trends were also seen in the data reported by Wayne and Tremols (2019), who

studied the outcome of the tenodesis reconstruction both experimentally in one cadaver wrist, and computationally via rigid body simulations.

The inferior bone reduction in specific wrist motion is believed to be related to the loosening of the reconstruction, as a graft from the FCR tendon will presumably become slack during wrist flexion. Furthermore, since the graft is tightened ulnarly, ulnar deviation of the global wrist will also reduce the tension in the reconstruction. Additionally, the fact that the reconstruction is tightened ulnarly through the DRC is believed to be responsible for other complications. In the present study, it was evident that the 3LT not only exacerbated the pathological ulnar translation of the lunate, it also caused the scaphoid to unphysiologically shift towards the ulnar side of the wrist. Furthermore, excessive ulnar tightening of the tendon graft might also supinate the lunate, compromising its proper reduction in the transverse plane. However, this is a dilemma as the scaphoid ought to be pulled in supination in order to have its malrotation in pronation corrected. Therefore, it is advisable to avoid tethering and tightening the reconstruction using the DRC ligament or at anywhere located ulnarly beyond the midpoint of the dorsal lunate, and an interference screw could be used to facilitate the fixation.

4.1.3.4 Limitation

There are a number of limitations that ought to be taken into account when interpreting the results. First of all, this research employed a cadaver model where carpal kinematics was measured from dynamic wrist motions that were "actively" simulated using a custom-developed testing apparatus. However, owing to the static indeterminacy of the musculoskeletal system, there is virtually an infinite number of muscle force combinations which will produce the same motion on the global wrist. Given lack of comprehensive EMG data, the muscle forces that drove the dynamic wrist simulation in the present study were entirely estimated based on the commonly used static optimisation technique. Co-contractions of agonist-antagonist muscle pairs were approximated using a constant-sum constraint imposed during the optimisation process. It is unclear as to what extent the present study would replicate the *in-vivo* physiology of the wrist, and whether a different set of muscle forces would result in any substantial alterations in the carpal kinematics even if the motion of the global wrist is exactly the same. Furthermore, with the discovery of mechanoreceptors and nerve fibres within the substances of various wrist ligaments (Petrie et al., 1997; Hagert et al., 2007; Tomita et al., 2007), it has been suggested that the carpal stability is achieved not only mechanically through the dense network of soft-tissues but also neurologically through the intricate interplay in the sensorimotor system. Studies on the *in-vivo* wrist proprioception have shown that the wrist muscles demonstrate distinct patterns of reflex activation that might be protective for the carpus following disturbance of the SLIL (Vekris et al., 2011; Hagert et al., 2009, 2015). And many studies have suggested that wrist muscles might have a role in stabilising the carpus dynamically and could be potentially re-educated to better adapt to impaired carpal motion caused by deficiency of certain carpal ligaments (Salvà-Coll et al., 2011; Esplugas et al., 2016). These sophisticated neuromuscular controls, however, were not modelled explicitly in the present study, and the carpal ligaments were considered as mere passive units that provide structural restraints only for the carpal bones. The muscle forces were estimated by the controller and adjusted in closed-loop based on the

corrective actions necessary to achieve the desired joint position. Although there was a noticeable difference between the controller-estimated muscle forces in achieving the same stable global wrist motion before and after ligament division, it was unknown whether this difference could be representative of the dynamic stability as provided by the wrist muscles *in-vivo*. Moreover, owing to the use of cadaveric specimens, this study was merely a "time-zero" evaluation of the reconstruction procedures that did not take any effect of soft-tissue healing and scar formation into account. Therefore, care must be taken when extrapolating the present results to clinical applications.

Secondly, owing to the strict selection criteria that ruled out a multitude of joint diseases and abnormalities, the present study was limited by the number of available cadaveric specimens. Nonetheless, a total of seven wrists were tested, which compared well with the sample size used in a variety of other previous studies concerning the changes in carpal kinematics following ligament disruptions (Short et al., 2002b; Mitsuyasu et al., 2004; Kaufmann et al., 2006; Eschweiler et al., 2016b; Padmore et al., 2019), or surgical treatments (Garcia-Elias et al., 1989; Short et al., 2009; Eng et al., 2014; Loisel et al., 2020). And despite the low sample size, the present study was still able to observe many significant differences. Furthermore, owing to the availability of the specimens, other possible permutations of the order in which the ligaments were divided in the present study were not attempted. However, it is deemed of little clinical importance as the sequence used in the present study is considered to better reflect the current concept on the pathogenesis of scapholunate instability (Mayfield et al., 1980; Taleisnik, 1988), and has also been shown to be associated with the progression of Geissler grade (Lee et al., 2015).

In addition, given the relatively small sample size, the present study also did not consider the effect of lunate morphology. It has been shown previously that wrist with a type II lunate exhibit different carpal kinematics (Nakamura et al., 2000; Galley et al., 2007), and might respond differently in cases of scapholunate ligament disruption (Rhee et al., 2009; Kim et al., 2016; Pang et al., 2018). However, a retrospective analysis of the CT scans of

the wrist specimens showed there was only one case of type II lunate being incorporated in the present study, which was therefore considered having limited influences on the overall results.

Thirdly, the normal anatomy of the wrist might have been compromised during the process of specimen preparation. Most noticeably, a dorsal capsulotomy was performed to allow radio-opaque markers to be embedded into the carpal bones, and the dorsal capsule was kept open during the dynamic simulation to accommodate for the pressure sensor inserted dorsally into the radiocarpal joint. Small holes were also made on the volar capsule to allow passage of the cables used to secure the pressure sensor within the articular space. These alterations made to the wrist anatomy are necessary trade-offs if the joint pressure during the dynamic wrist simulations is to be simultaneously measured, and they do pose a genuine concern regarding the reliability of the absolute values reported for the carpal kinematics. However, since the goal of the present study was mainly to examine within-specimen changes in the carpal kinematics following various degrees of ligament division and surgical treatments, the experiments were designed such that each specimen acted as its own control.

Fourthly, although the reconstructive surgeries were performed by the same surgeon, there were no explicit measures to control their consistencies across different cadaveric wrist specimens. The outcome of the surgery was only visually examined and was judged entirely based on the surgeon's experience. Inevitably, this resulted in increased data variability. As mentioned previously, although this seems to lack rigorous standardisation, it is reflective of the clinical reality and therefore considered acceptable. In addition, owing to the length of time required for specimen preparation and testing, the material properties of the tissues might have been changed and become less representative of those seen in living patients.

Fifthly, to ensure the resultant joint motions were repeatable and consistently stable across all specimens in different stages of ligament division, wrist simulations were performed within a narrow range of $\pm 30^\circ$ FEM and $\pm 20^\circ$ RUD, using a sinusoidal trajectory of 0.05 Hz. In addition, a value of 150

N was also chosen to constrain the summation of the tendon forces during the solution process. These limitations presented a substantial deviation from the functional wrist motion as seen in day-to-day activities, and the results of the present study may therefore be less representative of the carpal motion occurring at a fast rate or during labour-intensive tasks that require an elevated amount of muscle forces. However, apart from the limiting factors attributed to the hardware, the test protocol adopted in the present study was tailored in favour of the control stability and accuracy of the cadaveric specimens. In fact, the DWSA was found to be capable of performing wrist simulations up to 0.2 Hz, namely producing up to 24°/s of joint motion, in a phantom study. The benefit of faster simulations, however, was deemed to not justify the resulting degradation in control performance, especially when severe ligament disruptions had been introduced to the specimens in later stages. Since the carpal bones exhibit intricate multiplanar motion, it would have been difficult to accurately measure the subtle alterations in carpal kinematics induced solely as a result of ligament division or reconstructive surgeries, if the wrist simulations had not been performed consistently with the high level of control accuracy and repeatability archived in the present study. The reason that only 150 N was prescribed to the control system was partly attributed to the involvement of the pressure sensors. Since higher muscle forces translate directly into increased joint contact and friction, the pressure sensor, which was composed of two flexible polyester sheets, may therefore have a higher chance of being delaminated, leading to measurement errors and sensor failures, if a higher force sum had been used in the present study. In addition, the presence of a large shear force would also make the task of holding the pressure sensor stationary inside the articular space far more challenging. But apart from these technical difficulties, the reported changes in carpal kinematics would have had an increased magnitude if a higher force sum had been used in the present study.

Sixthly, the present study did not explicitly quantify the muscles' contribution to stabilising the wrist after ligament division. As reviewed previously, certain wrist muscles have been shown to have a role in the dynamic stabil-

isation of the carpus and the potential to be re-educated to activate in a manner that compensates for the carpal instability caused by ligament deficiency. In the present study, to ensure the stability of the wrist simulations, the DWSA's control system automatically adjusted the distribution of the muscle forces in response to the increased uncertainties in the cadaveric plant dynamics caused by the introduction of the ligament divisions and subsequent reconstructions. It is unclear whether these adjustments in muscle forces are physiological and truly reflective of the adaptive changes in muscle recruitment occurring post-trauma in living subjects, since muscle forces generally cannot be measured in human subjects *in-vivo*. It is also unclear how a control system made to favour the stability of the global wrist motion might have affected the carpal kinematics in the present study, preventing abrupt changes such as clunking of the scaphoid, which has been commonly seen clinically, from being truthfully reproduced and detected in a cadaver model.

Seventhly, due to the complexity of the test regime appointed in the present study, wrist simulations were only repeated for a limited number of cycles in each stage of ligament division and reconstructive surgeries to prevent putrefaction of the specimens. Despite the fact that each cadaveric specimen had been pre-conditioned in its normal physiological state by 20 cycles of FEM and RUD, moving the specimen only three times in different modes of motion might not be truly reflective of the repetitive and continued use of a ligament-deficient wrist observed after injury or surgical reconstruction in the clinical setting. Therefore in future studies, one may consider cycling the wrist specimen through more repetitions of simulated motion, ideally in the order of a few hundred to a few thousand cycles (Ritt et al., 1998; Short et al., 2002a; Eng et al., 2014; Hsu et al., 2014; Lee et al., 2014), before collecting any kinematic data.

Finally, the effect of the sequence in which the two reconstructive surgeries were performed was not investigated in the present study. However, it is not expected to cause a major difference in the present results, as the reconstruction left by the DTLT procedure had been completely removed prior to the commencement of 3LT.

4.2 Radiocarpal Contacts

A Preliminary Study

4.2.1 Materials and Methods

In this thesis, the contact biomechanics of both the radioscaphoid and the radiolunate articulations was investigated. A preliminary study was performed to qualitatively examine the change in the radiocarpal contacts after the wrist had sustained an episode of simulated ligamentous injuries and subsequent reconstructive surgeries. Two distinct approaches were taken to facilitate the analysis. As mentioned, an electronic pressure sensor was employed to measure the simultaneous pressure distribution within the radiocarpal articulation during the dynamic wrist simulation. In addition, based on the carpal kinematics obtained in the previous section, the proximity map for the radioscaphoid and the radiolunate fossa was also calculated to supplement the sensor measurement. The detailed procedures for both approaches will be discussed in the following sections.

4.2.1.1 Pressure Sensor Measurement

Sensor Preparation and Calibration

A Tekscan Medical 4000 pressure sensor (Fig. 4.27) was prepared and calibrated before being inserted into the radiocarpal articulation. First of all, except for the distal aspect of the sensor (the volarly situated edge when inserted into the joint space), the excessive plastic substrate was trimmed off from the perimeter of the sensor. Care was taken not to cut into the sensing elements (sensels) and cables. Low friction Teflon (PTFE) tapes of 0.05 mm in thickness (YLH-7005MA; JIAET, Jiangsu, China) were then used to completely seal the sensor, offering protection against water incursion as well as the shear forces acting on the sensor.

The prepared pressure sensor was pre-condition and calibrated one day prior to the dynamic experiment using a material testing machine (Model 5848 MicroTester; Instron, Massachusetts, USA) fitted with a 2 kN load cell (Fig. 4.28A). The machine was configured to be accurately controlled by force feedback with its PID controller properly tuned. The pressure sensor

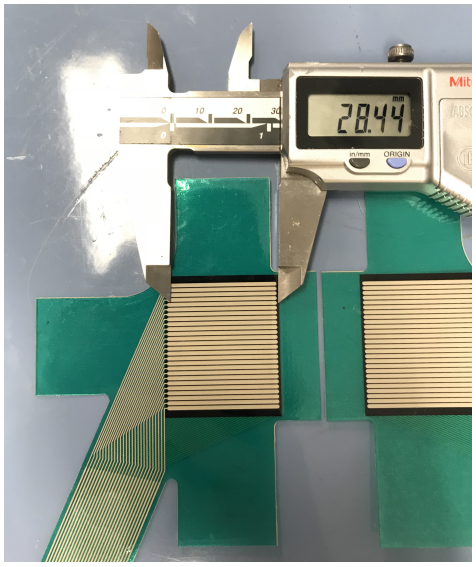

Figure 4.27: Photograph of an unprepared Tekscan Medical 4000 pressure sensor (both branches are shown)

was then sandwiched between two pieces of rubber to even out the load distribution, as well as to approximate the loading condition inside the radiocarpal joint (Fig. 4.28B). Medium-hard rubber was chosen owing to its similar material properties to those of the articular cartilage (Lindley, 1966; Sokoloff, 1966). However, to ensure the load was transferred solely through the effective sensing region of the pressure sensor, the top rubber piece was precisely tailored such that its deformed shape matches the exact dimension of the sensing matrix under load.

Before the actual calibration, the sensor was pre-conditioned for 10 minutes using a sinusoidal force profile which had a period of 30 s and an amplitude of 300 N. Then the sensor was subjected to 11 different static load levels ranging from 100 N to 600 N in a randomised order. Load levels which went beyond the expected maximum force value of 150 N were used to provide adequate coverage for unanticipated, local peak pressures. The force was gradually ramped from zero to the desired value in about 30 seconds and was held constant for 5 seconds before the raw sensor readings were recorded. Between each loading cycle, an interval of 120 seconds was given as recommended by the manufacturer. Instead of using the default calibration

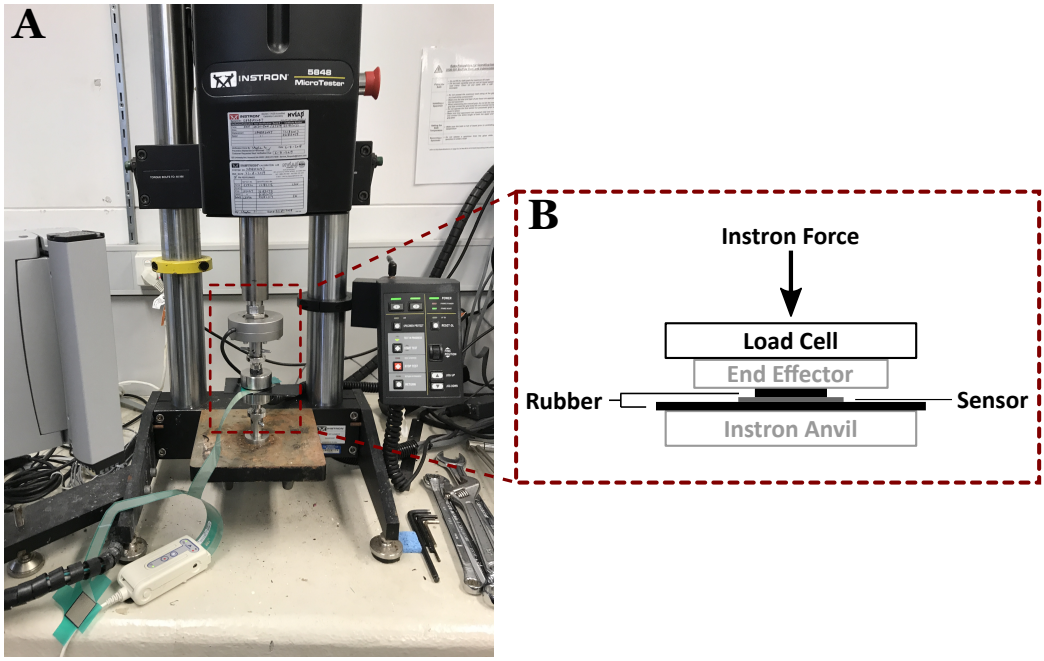

Figure 4.28: **(A)** Photograph of the pressure sensor being calibrated using an Instron 5848 MicroTester, **(B)** Schematics showing the loading configuration

method built into the software, an improved algorithm, initially developed by Brimacombe et al. (2009), was adopted in the present study.

In essence, the algorithm assumes the force-resistance response of each sensel follows a cubic relationship (Eq. 4.1), and by minimising the difference between the experimentally applied force and the force calculated based on the sensor's pressure reading (Eq. 4.2) for all 11 pairs of force levels through a least-square optimisation (Eq. 4.3), the appropriate polynomial coefficients that calibrate the pressure sensor can thus be determined.

$$p_i = ax_i^3 + bx_i^2 + cx_i + d \tag{4.1}$$

$$f = s\sum_{i=1}^{M} p_i \tag{4.2}$$

$$\min \sum_{n=1}^{N} (f_n - F_n)^2 \tag{4.3}$$

where a, b, c and d are the cubic calibrating coefficients to be determined. f is the force calculated based on the current pressure reading of the sensor. s is the area of each sensel, and p_i represents the pressure of the ith sensel. M is the number of sensels comprising the pressure sensor. f_n and F_n denotes the nth calculated force and the experimentally applied force, respectively. N is the total number of force levels used for calibrating the sensor, and was 11 for the present study.

In the present study, a typical calibration error less than 2 N was obtained (Fig. 4.29B). Based on the calibration curve obtained, the raw sensal values in each frame of the sensor measurements were converted into the pressure in different grid locations, and the resultant map was interpolated in 2D (bilinear, 5×5) for visualisation purposes.

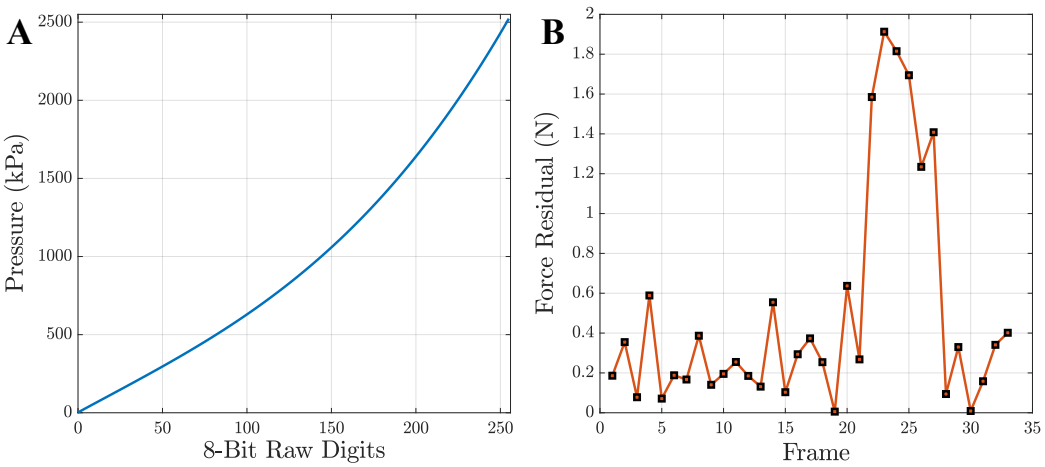

Figure 4.29: An example of the **(A)** calibration curve and **(B)** calibration error (discrepancy between the experimentally applied forces and the forces calculated based on the current calibration)

Sensor Placement and Fixation

The sensor was securely held in the articular space via sutures placed through the distal rim of the sensor. In order to allow secured placement of the sutures on the pressure sensor, the plastic substrate distal to the sensing matrix was carefully folded into a thin strip to gain extra strength (Fig. 4.30). This 3 mm wide strip was further reinforced with Teflon impregnated fibreglass-based tapes (AGF-100FR; Chukoh Chemical Industries, Tokyo, Japan).

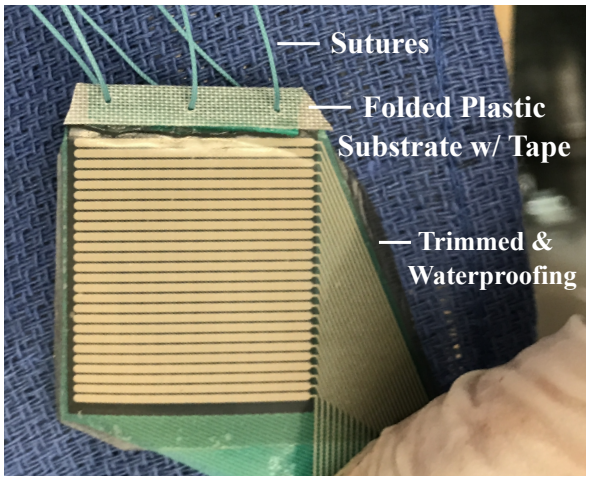

Figure 4.30: Photograph of a prepared pressure sensor

The sutures were then passed through small piercings made on the volar capsules to be finally anchored to three screws drilled volarly into the shaft of both the radius and ulna (Fig. 4.31). Furthermore, the sutures were also marked at the appropriate length to ensure the sensor could be re-placed into the same position inside the joint space in a reproducible manner if the sensor had been withdrawn for various reasons.

In order to precisely locate the pressure sensor with respect to the articular surface, each cadaveric wrist specimen was CT scanned with the pressure sensor inserted and appropriately positioned. A thin layer of copper foil was applied temporarily to mark the effective sensing region of the pressure sensor in CT scan (Fig. 4.32).

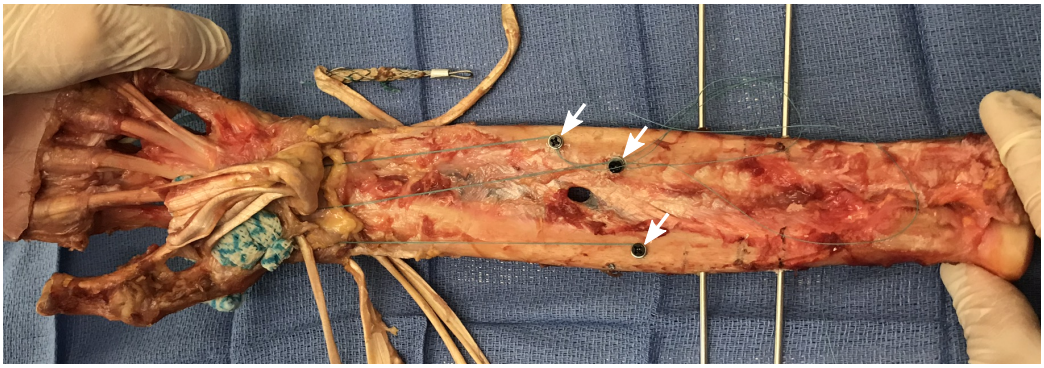

Figure 4.31: Photograph showing the pressure sensor being anchored to three screws (white arrows) drilled volarly into the radius and ulna

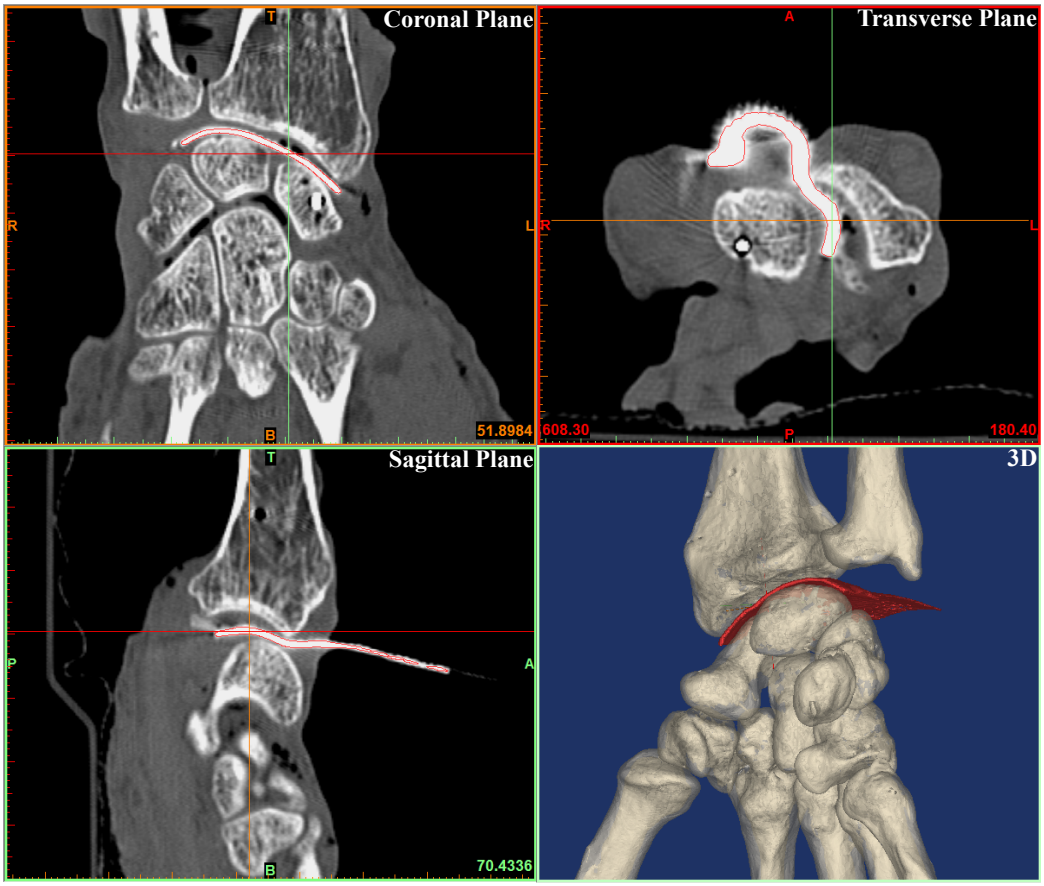

Figure 4.32: CT scan of a wrist specimen. The pressure sensor was inserted into the radiocarpal articulation with its sensing matrix (red) marked using copper foil.

4.2.1.2 Joint Proximity Measurement

Proximity Mapping

Joint proximity mapping is the visual representation of the distance between the subchondral surfaces of two opposing bones. In order to facilitate the proximity calculation of the radiocarpal joint, the surface geometries of the distal radius, scaphoid and lunate were first segmented and reconstructed from the CT scan using Mimics. The resultant models were then smoothed and re-meshed using in-built functions in Geomagic such that every constituting triangular facets was about 0.02 mm^2 in size (Fig. 4.33).

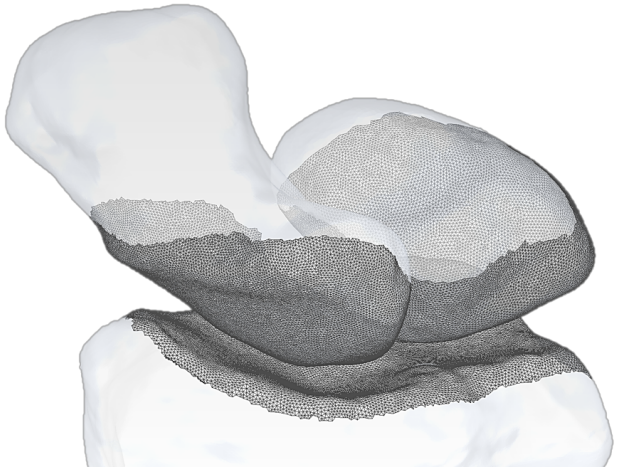

Figure 4.33: Bone surface models used for joint proximity calculation

For each frame of the carpal kinematics acquired previously, these surface models were registered according to the three-dimensional position of their radio-opaque markers, and their mesh vertices and facet centroids were used as discrete bony landmarks to calculate the joint proximity at that particular instant. Since the inferred joint contact on the distal radius was desired, the inter-bone distances were calculated such that they were perpendicular to the surface model of the distal radius, and a custom MATLAB program was written to facilitate this process. Briefly, for the centroid of every triangular facet on the surface model of the distal radius, the point on the opposing bone model that would make the connecting vector colinear with the normal vector

of the current facet was sought within a preset search radius. However, since the mesh vertices are discrete, there might not be any point on the opposing bone that is in perfect alignment with the facet normal (the dot product of their directions equals 1). For all vectors connecting the facet centroid and the points on the opposing bone within the search radius, the vector whose direction has the highest dot product with the facet normal was subsequently chosen as a potential candidate (Fig. 4.34), given the dot product is just the cosine of the angle included between that vector and the facet normal.

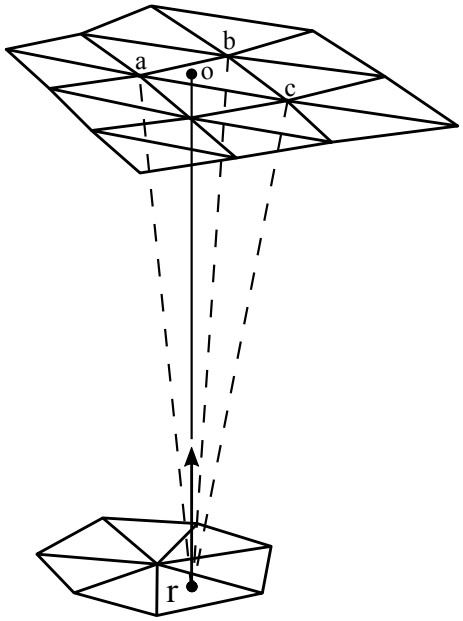

Figure 4.34: Schematics showing the proximity calculation process for one facet located on the distal radius (lower surface). For its facet centroid, r, the true proximity vector ***ro***, which is collinear with the facet normal, is approximated by the vector that has the smallest included angle with the facet normal, namely the vector ***ra***.

And if the surface model has sufficiently high spatial resolution and is without abrupt changes in profile, the projection of this candidate vector onto the facet normal can be, therefore, used as a good estimation of the joint proximity at the current triangular facet on the distal radius. In the present study, a lower bound of 0.98, which stands for an included angle of at most 11.5° between the vector and the facet normal, was set for the collinearity

criterion in selecting the candidate vector. Moreover, for regions with a higher local curvature, instead of testing collinearity against the normal vector of individual facets, the average value of their facet normal was used for the facets comprising the region collectively.

For each wrist, the resultant proximity maps obtained for both the radioscaphoid and radiolunate articulations were normalised to account for anatomical variations in the joint geometry between specimens. Ideally, the joint proximities measured at the true wrist neutral position prior to the introduction of any load or ligamentous disruptions ought to be used. These data, however, were not available in the present study. Instead, the mean distance between the radius and the scaphoid and between the radius and lunate, as measured using the CT scans, were used to normalise the maps for the radioscaphoid and the radiolunate proximities, respectively. The use of subchondral bone models instead of the actual geometries of the cartilage may reduce the accuracy of the resultant proximity maps. However, incorporating this normalisation step might, to an extent, address the issue of omitting cartilage thickness during the proximity calculation.

Weighted Centroid of Proximity

The weighted centroids of proximity (WCoP) were calculated for both the radioscaphoid and radiolunate articulations in their respective local coordinate systems. The computation was performed in accordance with a previously validated technique (Eq. 4.4), widely used for the contact analysis of the knee joint (Anderst and Tashman, 2003; Beveridge et al., 2014; Marouane et al., 2016). However, instead of adopting the original weighting scheme, that were designed based on a somewhat arbitrary choice of distance thresholds, a percentile-based proximity weighting was employed in the present study.

$$\mathbf{WCoP} = \frac{\sum_{i=1}^{n} w_i \cdot \boldsymbol{X}_i}{\sum_{i=1}^{n} \boldsymbol{X}_i} \tag{4.4}$$

where $\boldsymbol{X}_i$ denotes the coordinates at which the ith joint proximity is

calculated. w_i is the weighting factor assigned for the ith joint proximity according to its percentile ($<5^{\text{th}}$: 32, 5-10th: 8, 10-25th: 2, 25-50th: 0.5, 50-75th: 0.1, and $>75^{\text{th}}$: 0.025).

4.2.2 Results and Discussion

Ligament Resection

Unfortunately, due to the high failure rate of the pressure sensors, a comprehensive set of pressure measurements, including the data corresponding to all three modes of wrist motion across all seven specimen conditions, could only be reliably obtained in three out of the seven wrists tested.

Throughout the incremental resections of the scapholunate supporting ligaments, one of the most noticeable changes was the dorsal and radial migration of the radioscaphoid contact. This condition was most pronounced in Stage IV ligament release for all three specimens (Fig. 4.36a-c), as the sensor measured radioscaphoid contact appeared to "ride" on top of the dorsal rim of the distal radius, even when the wrist was placed in its neutral position. This dramatic change was also evident in the joint proximity calculations presented alongside, where the proximity map of the radioscaphoid articulation became separated from that of the radiolunate articulation and appeared to be concentrated along the dorsal radius with an incongruent and mostly elliptical contour. These observations replicate the classic scapholunate instability patterns, such as scapholunate diastasis and rotatory subluxation of the proximal scaphoid pole. As shown earlier, the destabilised scaphoid was observed to gradually collapse into a posture of flexion, ulnar deviation and pronation. Watson and Ballet (1984) found this type of scaphoid malrotation was associated with a specific pattern of degenerative arthritis, which starts as localised arthrosis of the scaphoid fossa and begins at the radial styloid and then progresses to involve the entire radioscaphoid articulation. Since the scaphoid fossa accommodates the boat-shaped scaphoid with an elliptical articular configuration, the authors used the analogy of a pair of nesting teaspoons to depict the normal congruent radioscaphoid contact. However, if the top spoon, which represents the scaphoid, is pathologically rotated relative to the lower one representing the scaphoid fossa of the distal radius, it will inevitably rise up to sit on the edge of the lower spoon. Based on this concept, the authors suggest the incongruous scaphoid will impact on both

the volar and dorsal periphery of the distal radius, causing rapid cartilage breakdown at this region. In the present study, the dorsally and the radially migrated radioscaphoid contact is indeed consistent with the location of arthritis developed in the early stages of SLAC (Watson and Ryu, 1986; Tischler et al., 2014). The volar impaction of the collapsed scaphoid as predicted by Watson's nesting teaspoon model, however, is only visible in one specimen during radial deviation (Fig. 4.43j). Although this could be attributed to the unique boney anatomy of the patient, volar contact of a collapsed scaphoid has never been reported both *in-vivo* (Johnson et al., 2013; Omori et al., 2013) and *in-vitro* (Burgess, 1987; Blevens et al., 1989). Given the insufficient sensor coverage over the volar aspect of the scaphoid fossa, a definitive conclusion, therefore, can not be drawn based on the results of the present study, and more research is required to verify whether the teaspoon model could accurately elucidate the change in the radioscaphoid contact.

Based on the joint proximity maps and sensor measurements, it is not difficult to see that for different cadaveric wrist specimens, there was a variation in the stage of ligament division at which noticeable scapholunate instability had developed. In specimens with advanced age like 18-118R (Table 4.1), significant scapholunate diastasis with traces of rotatory subluxation of the scaphoid readily observable as soon as the whole SLIL was divided (Fig. 4.35h). Presumably, this was due to ligamentous laxity and joint hypermobility, mainly as a result of the age-related degradation in the material properties of soft-tissues (Lee et al., 1999; Carmeli et al., 2003; Wang et al., 2006). In relatively younger specimens, however, signs of significant scaphoid instability were absent until the majority of the supporting ligaments was disrupted in Stage IV. This explains the large variability seen in the carpal kinematics data for that stage and is actually reflective of the clinical observation that an isolated SLIL injury does not immediately result in perceptible scapholunate malalignment in some patients (O'Meeghan et al., 2003).

In relation to the lunate, it has been demonstrated to become dorsally tilted and translated more volarly and ulnarly with the advancement of the simulated ligament injury. In the joint proximity maps calculated for the

neutral wrist, this change in the lunate posture is clearly seen. Comparing to that of the intact wrist, the region of higher radiolunate proximity seems to have expanded and propagated towards the volar and ulnar aspects of the distal radius in Stage IV (Fig. 4.38a-c). This trend is in good agreement with those previously reported by Viegas et al. (1987a). The pattern of the radiolunate contact observed in the present study, however, suffered a higher degree of variability between different wrist specimens. Blevens et al. (1989) described the radiolunate contact remained approximately circular with its centroid located near the centre of the lunate fossa. This closely resembles the radiolunate proximity map of specimen 18-118R. However, for 17-150R and 18-189L, the higher proximity zones seem to be more asymmetrical and skewed towards the dorsal and the ulnar aspect of the distal radius, bearing a close resemblance to the radiolunate contact illustrated by Johnson et al. (2013), Omori et al. (2013) and Lalone et al. (2015). In addition, despite the similarity in the final manifestation of radiolunate deformity, noticeable variation was again observed for the onset of this abnormality across different specimens. In specimens suffered from ligamentous laxity like 18-118R, the lunate became appreciably extended as early as in Stage II ligament division. However, this was not the case until Stage III in 18-189L and Stage IV in 17-150R.

Another noticeable finding was that the scaphoid seemed to be gradually dissociated from the force transmission column while it was progressively destabilised by the sequential ligament division (Fig. 4.35a to Fig. 4.36a, and Fig. 4.35b-h). This was particularly noticeable when the wrist was placed in flexion (Fig. 4.37b-h, and Fig. 4.37c to Fig. 4.38c). Subsequently, the radiolunate contact was observed to take up an increased amount of pressure. These trends concur with the results reported by Blevens et al. (1989). After sequentially sectioning the SLIL, the STT and various other volar ligaments, these authors found both the contact force and area of the radioscaphoid articulation slowly decreased with the progression of scaphoid instability, whereas those of the radiolunate articulation saw consistent increases.

The present contact analysis also suggests that instability of the scaphoid

is accentuated when the wrist is placed in flexion, ulnar deviation or combined ulnar flexion (a-c in Fig. 4.38, 4.42 and 4.46). However, with one exception where the scaphoid was "squeezed" out of the joint to become completely dislocated in 17-150R (a in Fig. 4.40, 4.44 and 4.48), extension, radial deviation and radial extension of the wrist seem to help as the subluxed scaphoid were observed to be forcibly reduced back into the radioscaphoid fossa during these motion (b-c in Fig. 4.40, 4.44 and 4.48). These findings are consistent with the results reported in the previous section. Comparing to those in wrist flexion, ulnar deviation and ulnar flexion, during which the radioscaphoid joint was gradually separated, the scaphoid kinematics in extension, radial deviation and their combination, was observed to have been affected by the incremental ligament division to a lesser extent. And similar observations have also been noted in many other studies (Blevens et al., 1989; Sikora et al., 2019). Therefore, it might be advantageous to splint the wrist in radial extension, for better stability postoperatively. Additionally, Werner et al. (2007) reported that the bony geometry of the radioscaphoid fossa might have a role in determining the level of severity of scapholunate instability. In a cadaver model, the authors demonstrated that even in light of significant ligament disruptions, the wrists that possessed a higher degree of palmar inclination and a deeper radioscaphoid fossa tended to be more stable, and a greater amount of force was required to completely dislocate the scaphoid. In relation to the present study, this is indeed the case, as the wrist specimen in which severe dislocation of the scaphoid had occurred was found to have the smallest and the shallowest radioscaphoid fossa with the least amount of palmar inclination. Therefore for patients with similar osseous anatomy, caution must be exercised, and any wrist motion that might stress the radioscaphoid articulation must not be attempted before the scaphoid malrotation is appropriately rectified. And given the potential stabilising role of the bony geometry, a better consistency in the manifestation of simulated ligamentous injuries could be obtained if the specimens included in future studies are screened such that they all have a comparable osseous anatomy.

Reconstructive Surgery

In regards to the outcomes of the reconstructive surgeries, it was evident that the DTLT outperformed the 3LT technique in rectifying the abnormal radiolunate contact, despite the large inter-specimen variability. The radiolunate proximities calculated postoperatively at the neutral wrist position after the 3LT still looked as if they were skewed towards the volar and ulnar aspects of the distal radius, suggesting an inadequate reduction of the DISI deformity (Fig. 4.36d-f); whereas the radiolunate proximities recorded after the DTLT procedure appeared to have improved towards those seen in the native state (Fig. 4.36g-i).

However, the DTLT reconstruction is not without shortcomings. As mentioned previously in the kinematics section, this technique was shown to be insufficient in correcting the pathological scaphoid flexion. This deficiency was also seen to be reflected in the radioscaphoid articular contact. In the two relatively younger specimens, the postoperative region of higher joint proximity was observed to become more volar and radial (Fig. 4.36d, f), as compared to those in the native state. Regrettably, owing to the limited sensor coverage over the radioscaphoid fossa, this was only seen in specimen 17-150R in both flexion (Fig. 4.38d) and radial deviation (Fig. 4.44d). Furthermore, the DTLT seems to be unable to re-associate the scaphoid back to the force bearing column of the wrist, as the average radioscaphoid contact pressure in all three wrists appeared to have dropped significantly, to a level even below those seen in the normal physiological stage. However, with the scaphoid still partially collapsed in abnormal flexion and no attention paid to reconstruct the structures that stabilise the distal part of the scaphoid, this observation is not surprising.

The 3LT procedure, on the other hand, seems to outperform the DTLT in terms of the capability to restore the normal force transmission through the radioscaphoid articulation. The pattern of the radioscaphoid contact, however, was observed to become consistently more ulnar and dorsal on the distal radius (Fig. 4.36g-i). This is in agreement with the previous finding that

the 3LT seems to be less effective in correcting the abnormal radioscaphoid pronation. And owing to the way the tendon graft was routed and tightened, this technique was also shown to exacerbate the ulnar translation of the carpus.

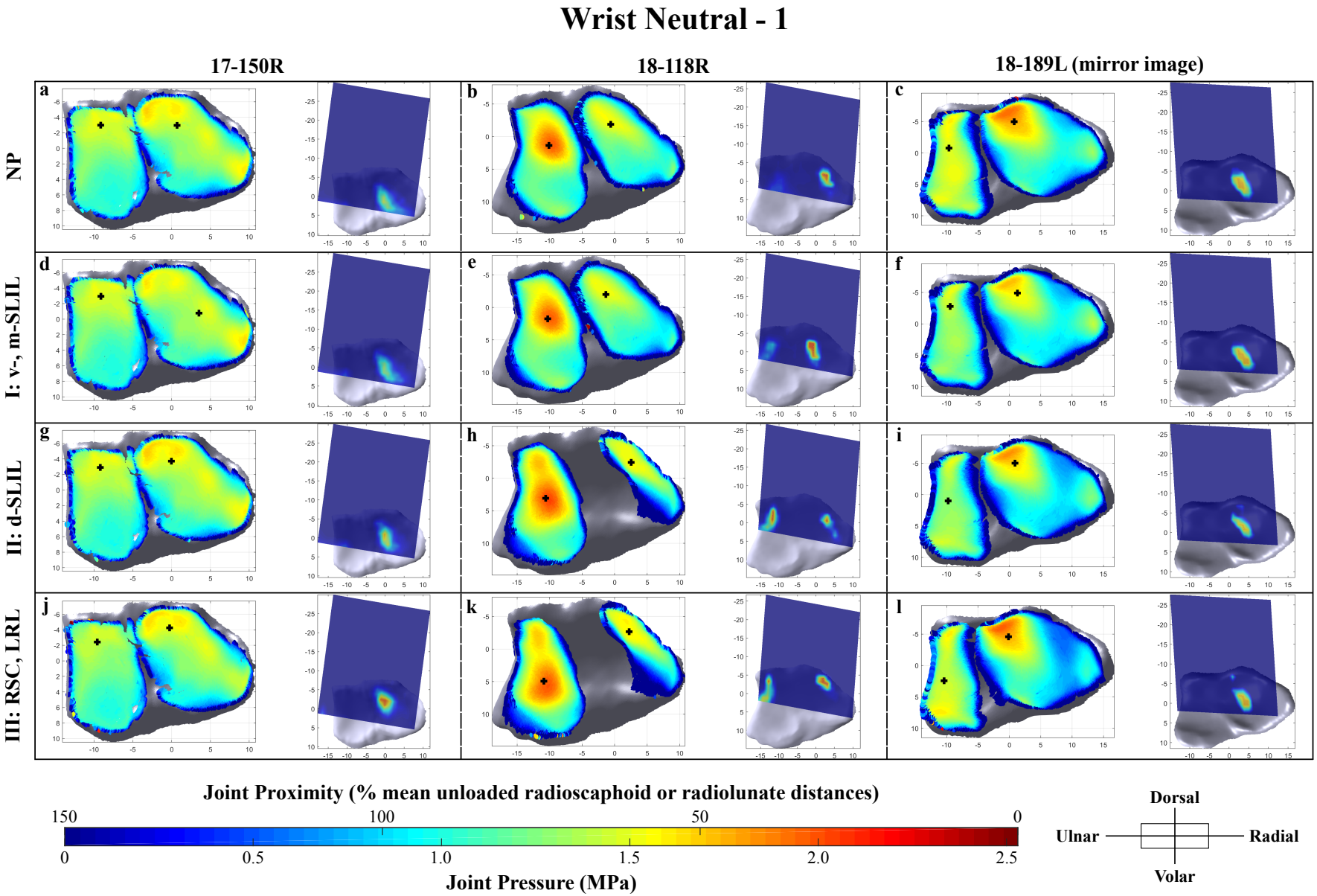

Figure 4.35: Maps showing joint proximities (*left* in each sub-figures) and interpolated joint pressure measurements (*right*) at wrist neutral position. The pressure maps were obtained through bilinear interpolation (5×5) of the raw sensal measurements given by the Tekscan sensors.

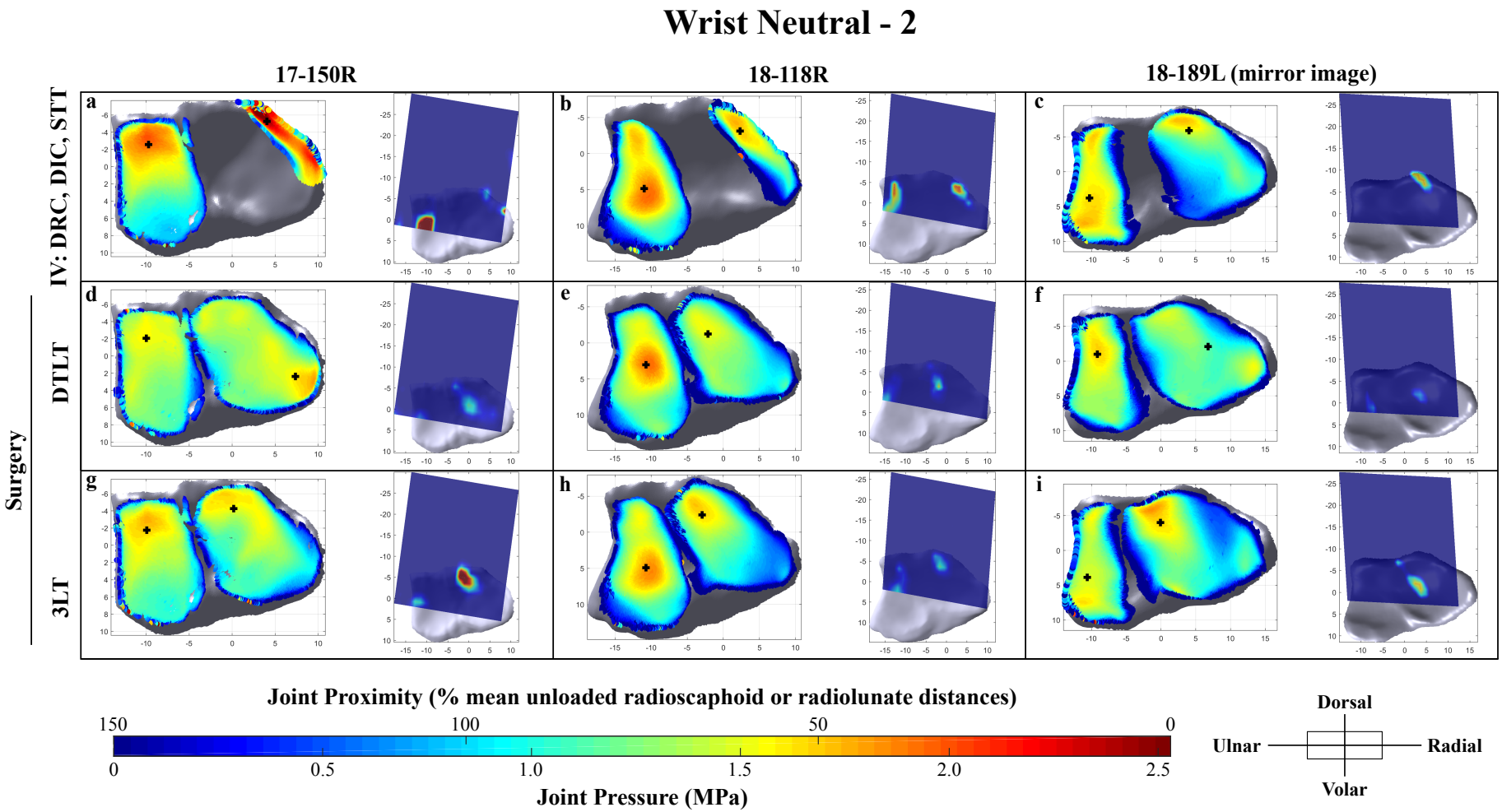

Figure 4.36: Maps showing joint proximities (*left* in each sub-figures) and interpolated joint pressure measurements (*right*) at wrist neutral position (continued). The maps are shown in a way that the radiocarpal joint is viewed distally, with the top side of the figure being dorsal and the right hand side being radial. Columns represent from which specimen the data were recorded, while rows representing different conditions of the specimen. The colour bar is shared by the two types of measurements. The joint proximity calculated for each point on the articular surface is shown in percentages of the mean unloaded radioscaphoid or radiolunate distances, while the joint pressure as measured using Tekscan sensors is shown in MPa. The centroid of joint proximities (marked as '+') was calculated for both radioscaphoid and radiolunate contact.

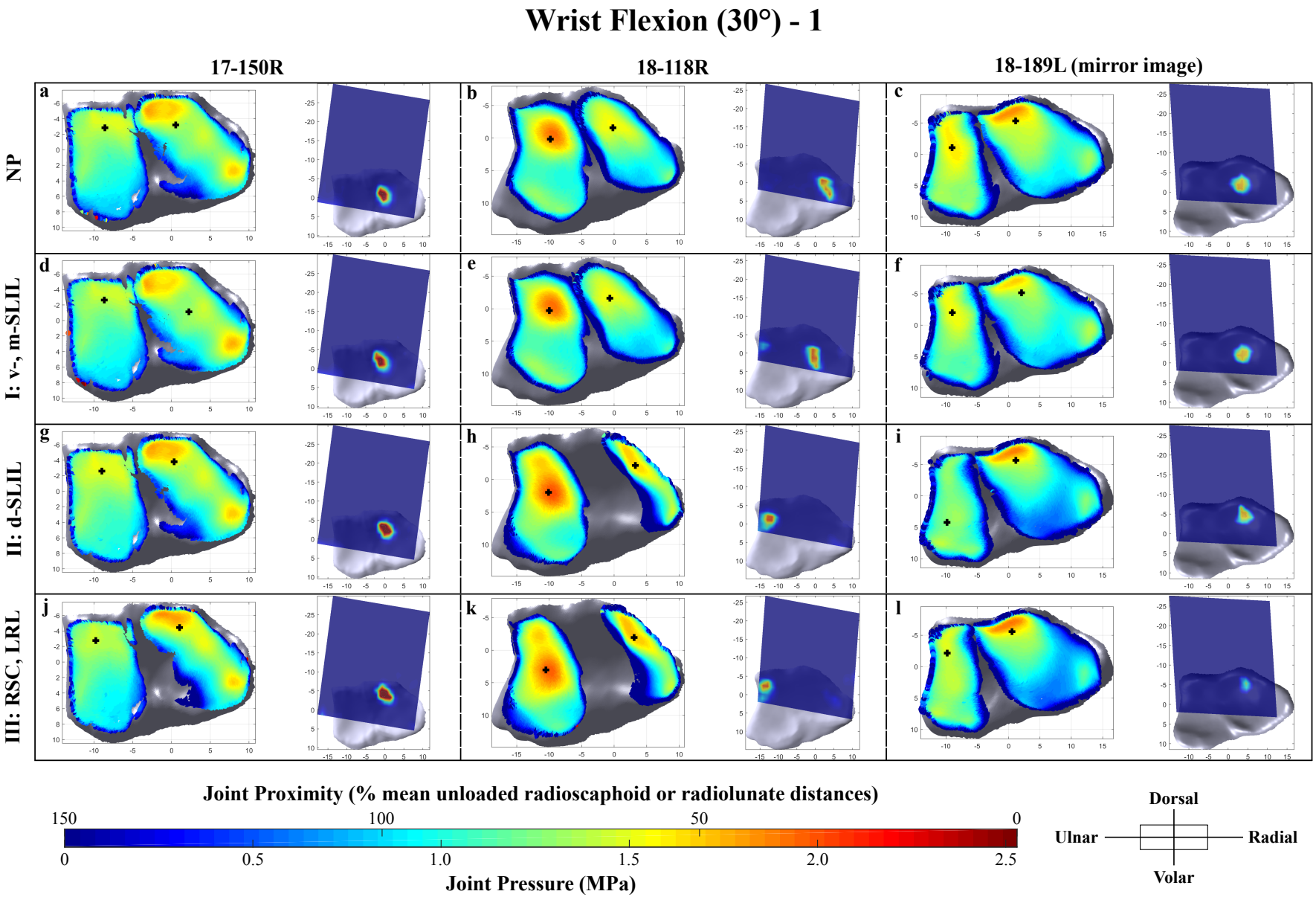

Figure 4.37: Maps showing joint proximities (*left* in each sub-figures) and interpolated joint pressure measurements (*right*) at 30 degrees of global wrist flexion. The pressure maps were obtained through bilinear interpolation (5×5) of the raw sensal measurements given by the Tekscan sensors.

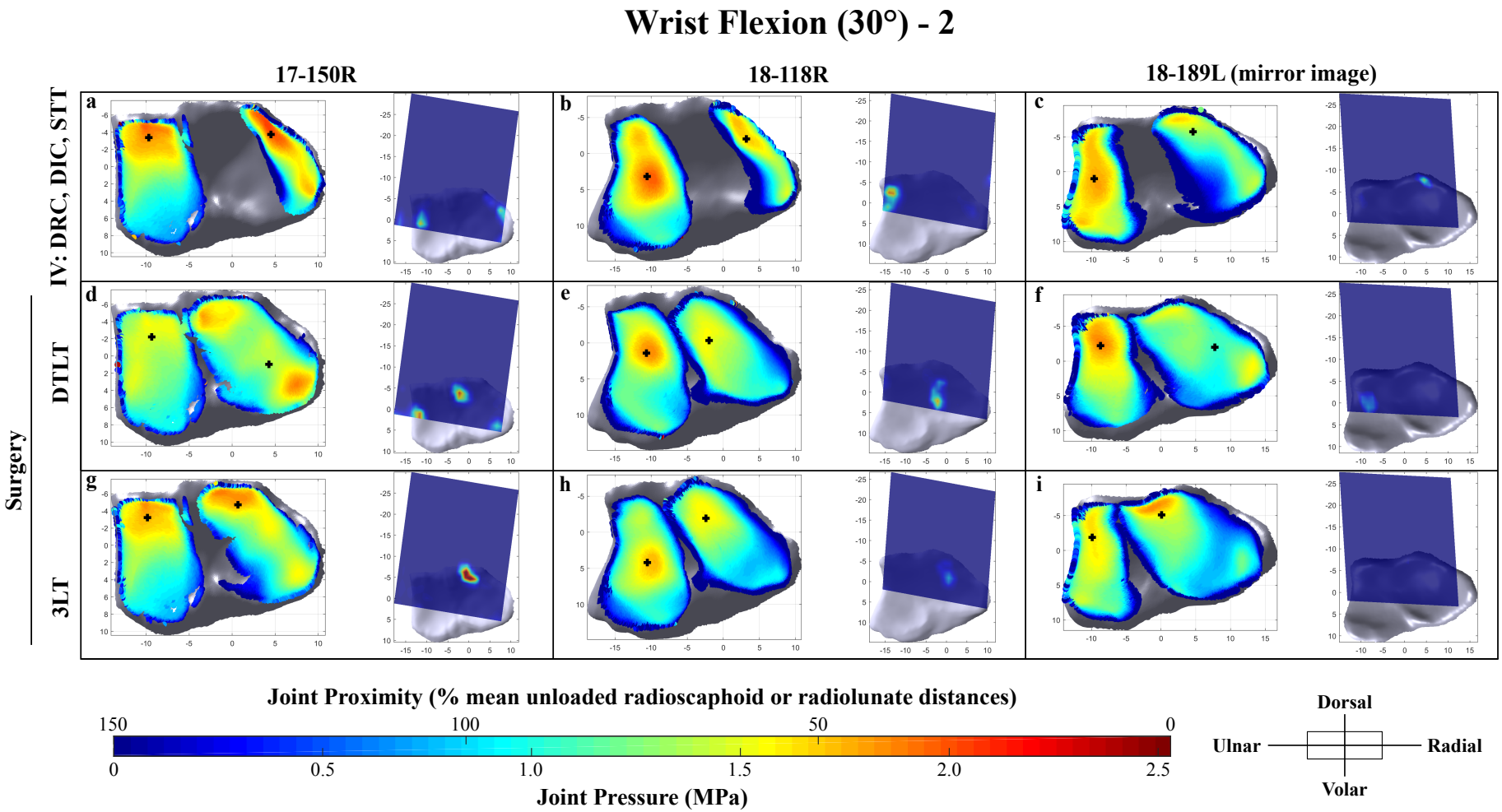

Figure 4.38: Maps showing joint proximities (*left* in each sub-figures) and interpolated joint pressure measurements (*right*) at 30 degrees of global wrist flexion (continued). The maps are shown in a way that the radiocarpal joint is viewed distally, with the top side of the figure being dorsal and the right hand side being radial. Columns represent from which specimen the data were recorded, while rows representing different conditions of the specimen. The colour bar is shared by the two types of measurements. The joint proximity calculated for each point on the articular surface is shown in percentages of the mean unloaded radioscaphoid or radiolunate distances, while the joint pressure as measured using Tekscan sensors is shown in MPa. The centroid of joint proximities (marked as '+') was calculated for both radioscaphoid and radiolunate contact.

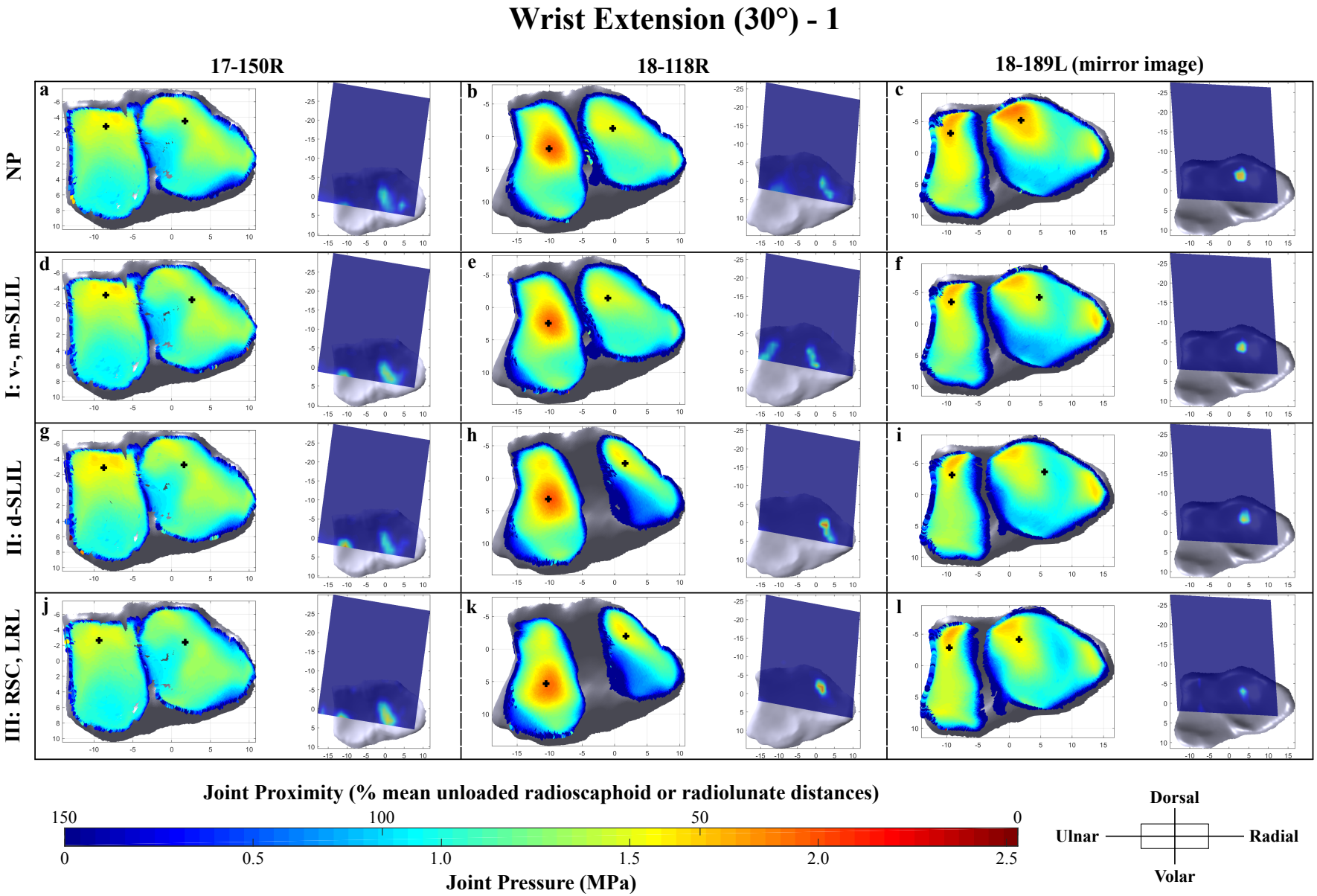

Figure 4.39: Maps showing joint proximities (*left* in each sub-figures) and interpolated joint pressure measurements (*right*) at 30 degrees of global wrist extension. The pressure maps were obtained through bilinear interpolation (5×5) of the raw sensal measurements given by the Tekscan sensors.

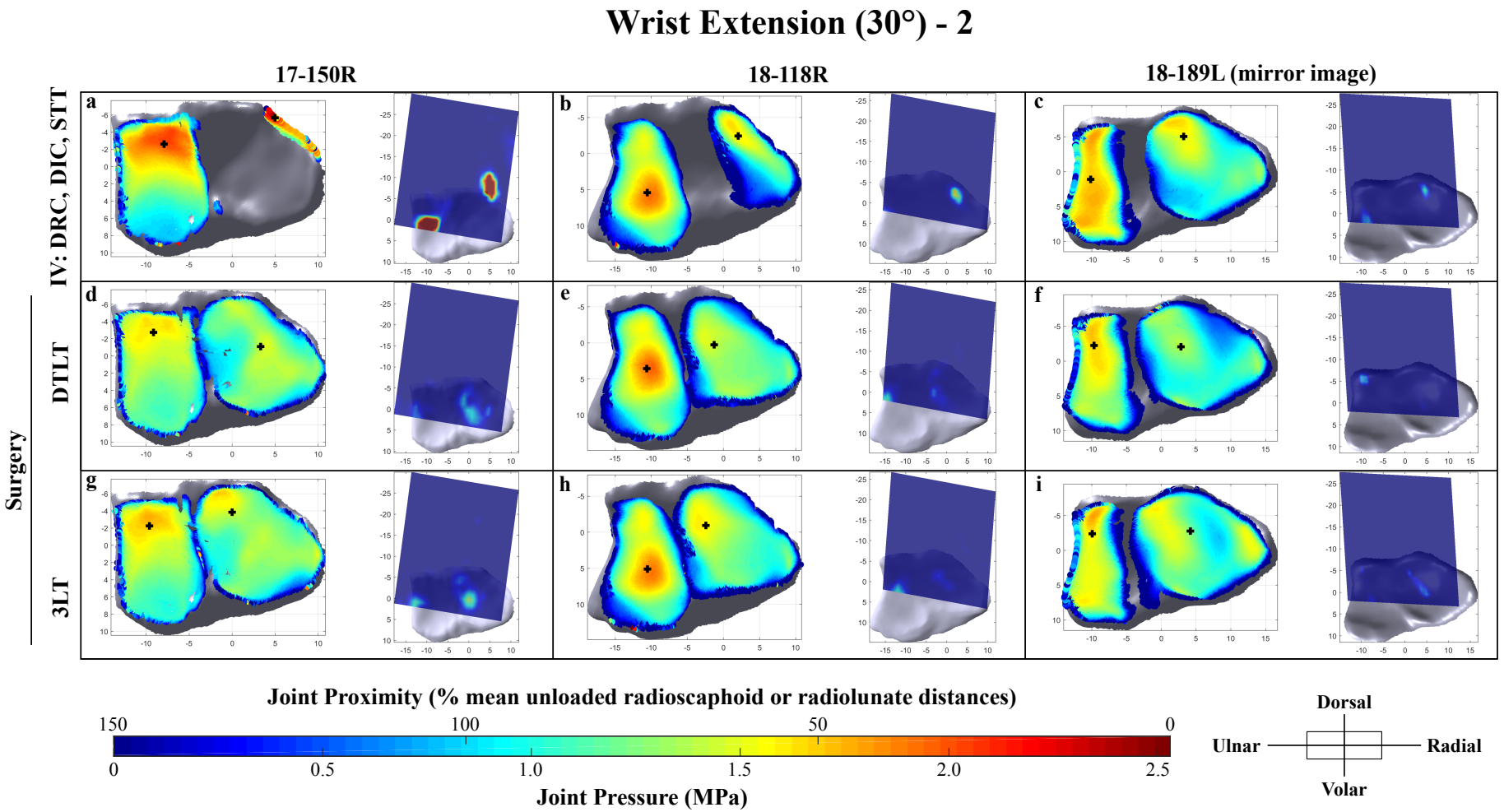

Figure 4.40: Maps showing joint proximities (*left* in each sub-figures) and interpolated joint pressure measurements (*right*) at 30 degrees of global wrist extension (continued). The maps are shown in a way that the radiocarpal joint is viewed distally, with the top side of the figure being dorsal and the right hand side being radial. Columns represent from which specimen the data were recorded, while rows representing different conditions of the specimen. The colour bar is shared by the two types of measurements. The joint proximity calculated for each point on the articular surface is shown in percentages of the mean unloaded radioscaphoid or radiolunate distances, while the joint pressure as measured using Tekscan sensors is shown in MPa. The centroid of joint proximities (marked as '+') was calculated for both radioscaphoid and radiolunate contact.

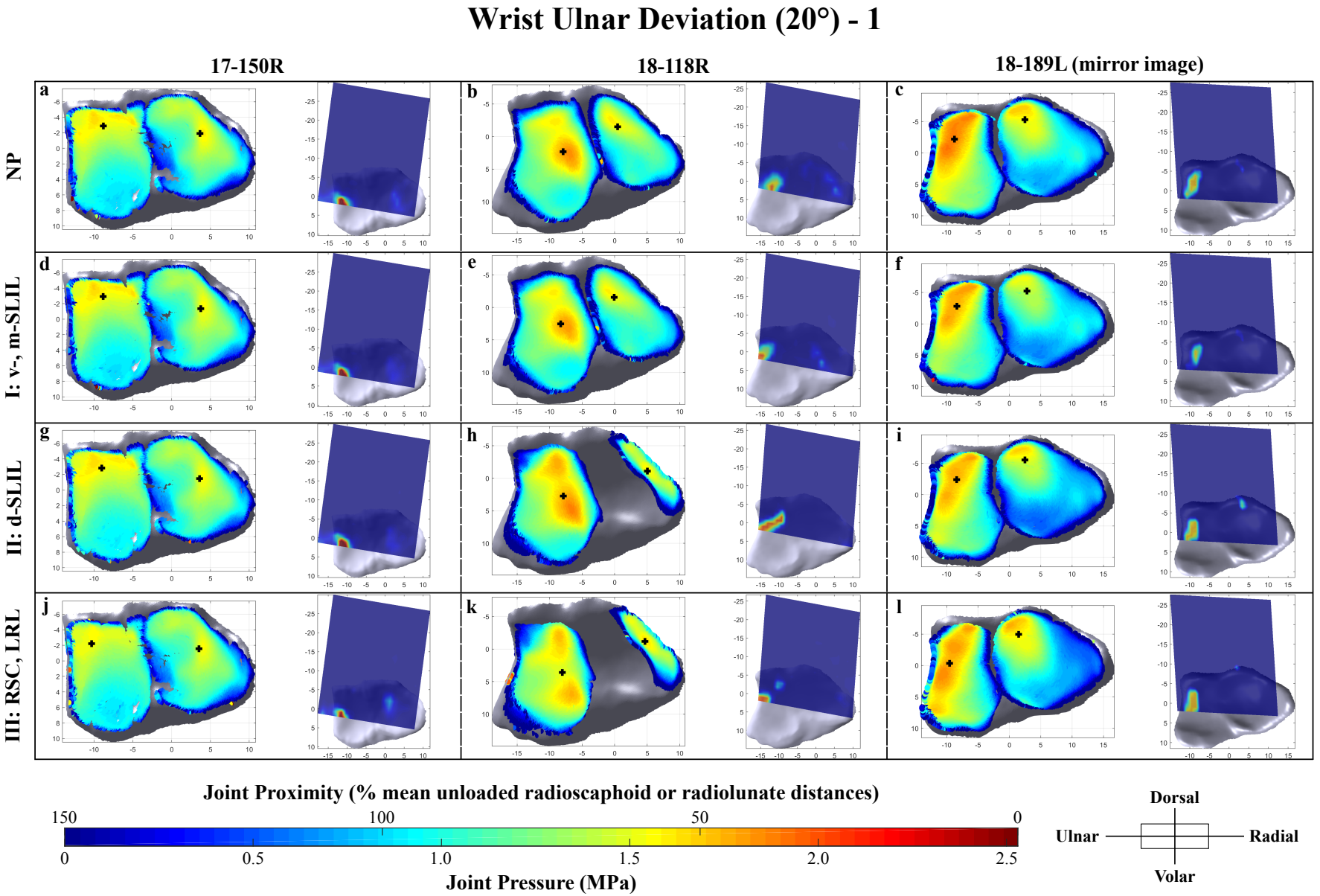

Figure 4.41: Maps showing joint proximities (*left* in each sub-figures) and interpolated joint pressure measurements (*right*) at 20 degrees of global wrist ulnar deviation. The pressure maps were obtained through bilinear interpolation (5×5) of the raw sensal measurements given by the Tekscan sensors.

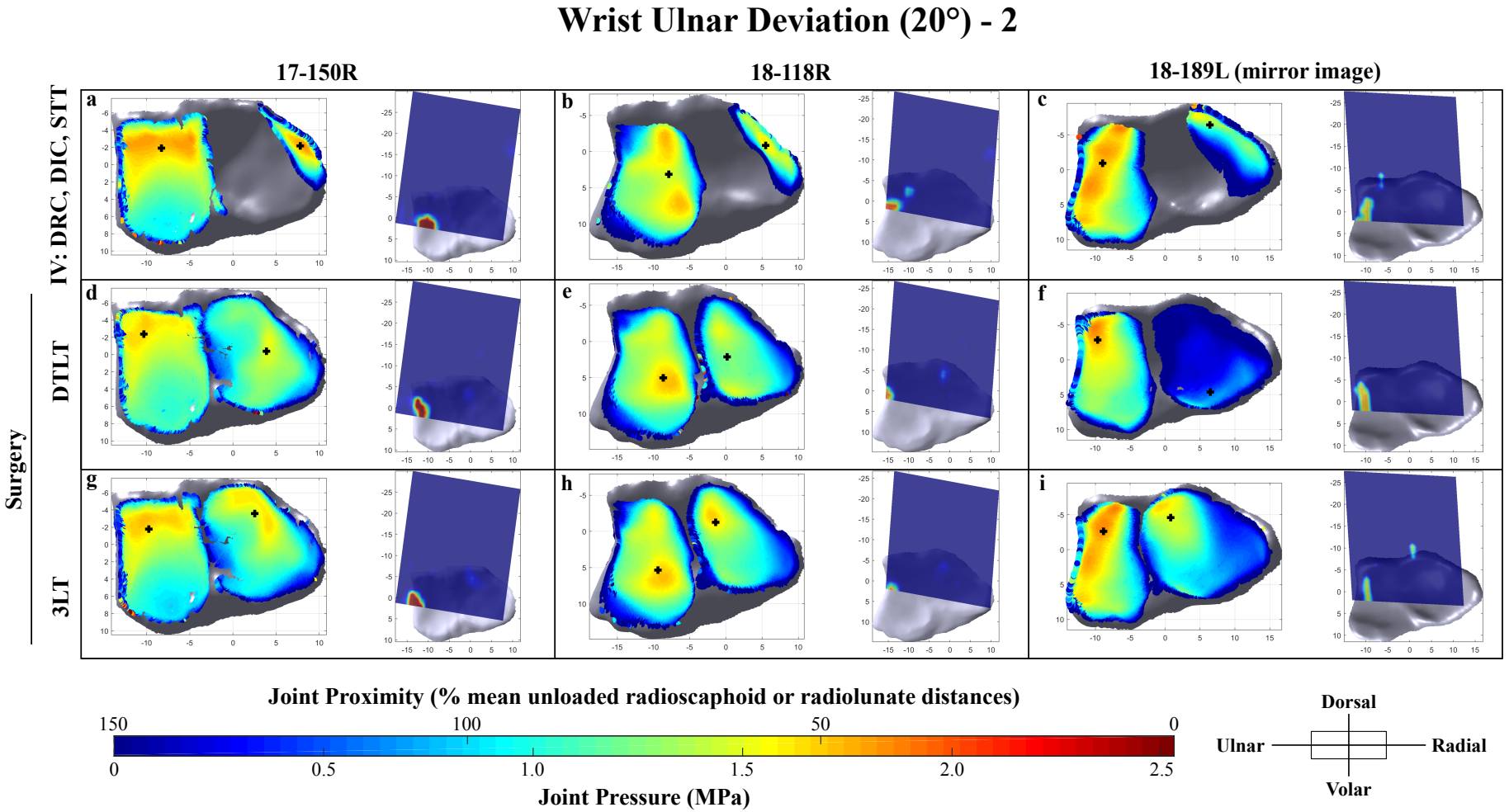

Figure 4.42: Maps showing joint proximities (*left* in each sub-figures) and interpolated joint pressure measurements (*right*) at 20 degrees of global wrist ulnar deviation (continued). The maps are shown in a way that the radiocarpal joint is viewed distally, with the top side of the figure being dorsal and the right hand side being radial. Columns represent from which specimen the data were recorded, while rows representing different conditions of the specimen. The colour bar is shared by the two types of measurements. The joint proximity calculated for each point on the articular surface is shown in percentages of the mean unloaded radioscaphoid or radiolunate distances, while the joint pressure as measured using Tekscan sensors is shown in MPa. The centroid of joint proximities (marked as '+') was calculated for both radioscaphoid and radiolunate contact.

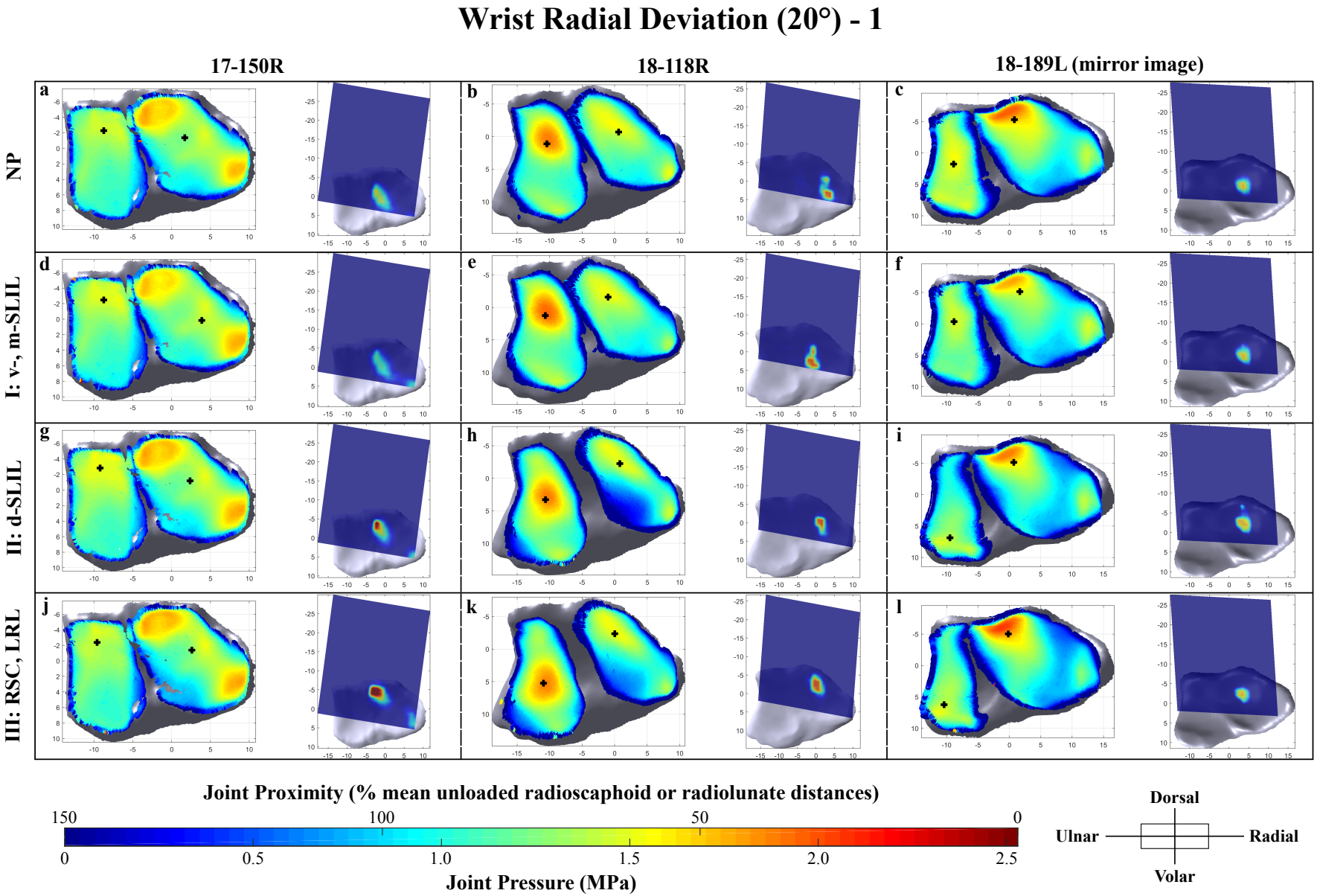

Figure 4.43: Maps showing joint proximities (*left* in each sub-figures) and interpolated joint pressure measurements (*right*) at 20 degrees of global wrist radial deviation. The pressure maps were obtained through bilinear interpolation (5×5) of the raw sensal measurements given by the Tekscan sensors.

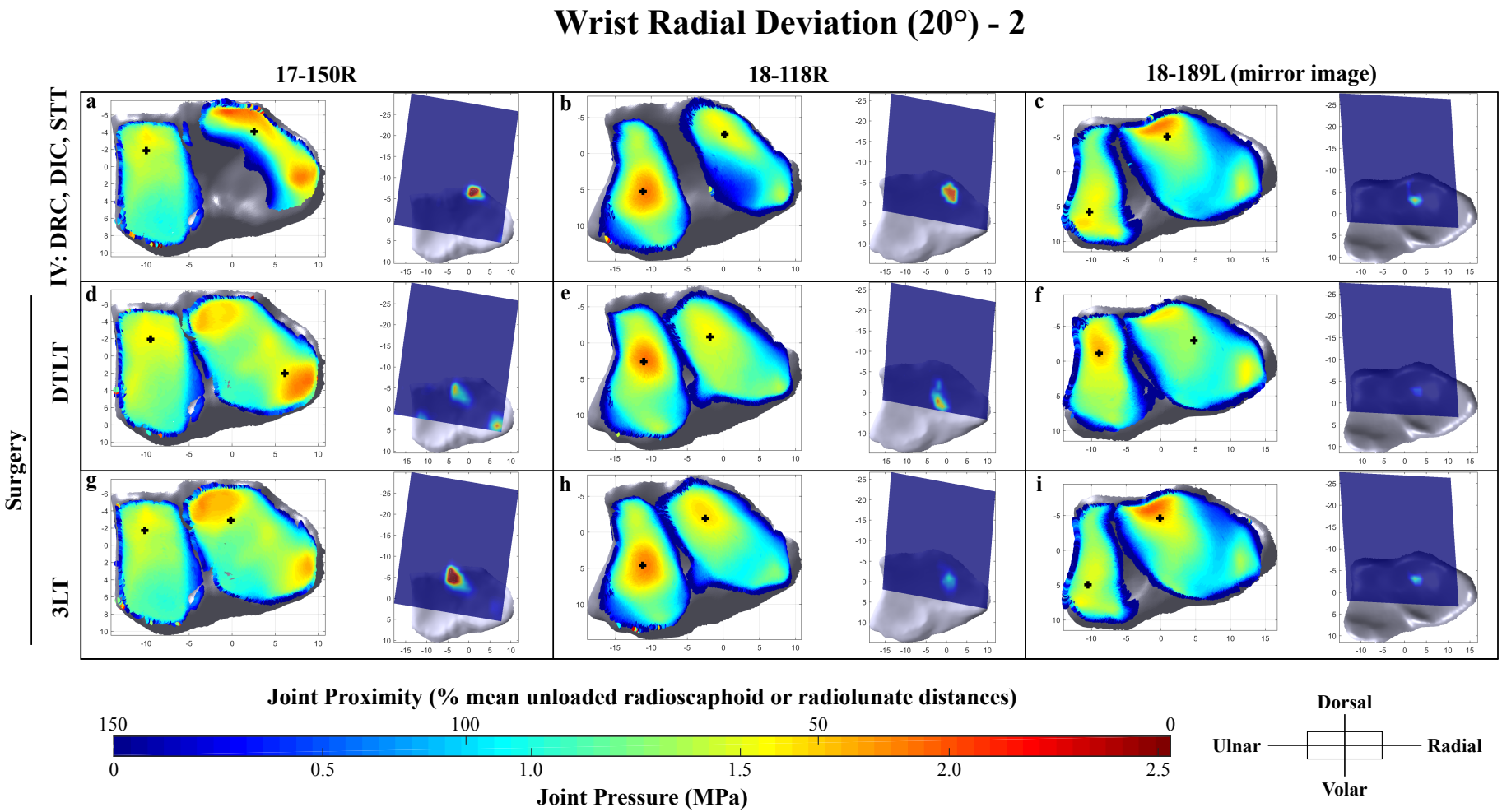

Figure 4.44: Maps showing joint proximities (*left* in each sub-figures) and interpolated joint pressure measurements (*right*) at 20 degrees of global wrist radial deviation (continued). The maps are shown in a way that the radiocarpal joint is viewed distally, with the top side of the figure being dorsal and the right hand side being radial. Columns represent from which specimen the data were recorded, while rows representing different conditions of the specimen. The colour bar is shared by the two types of measurements. The joint proximity calculated for each point on the articular surface is shown in percentages of the mean unloaded radioscaphoid or radiolunate distances, while the joint pressure as measured using Tekscan sensors is shown in MPa. The centroid of joint proximities (marked as '+') was calculated for both radioscaphoid and radiolunate contact.

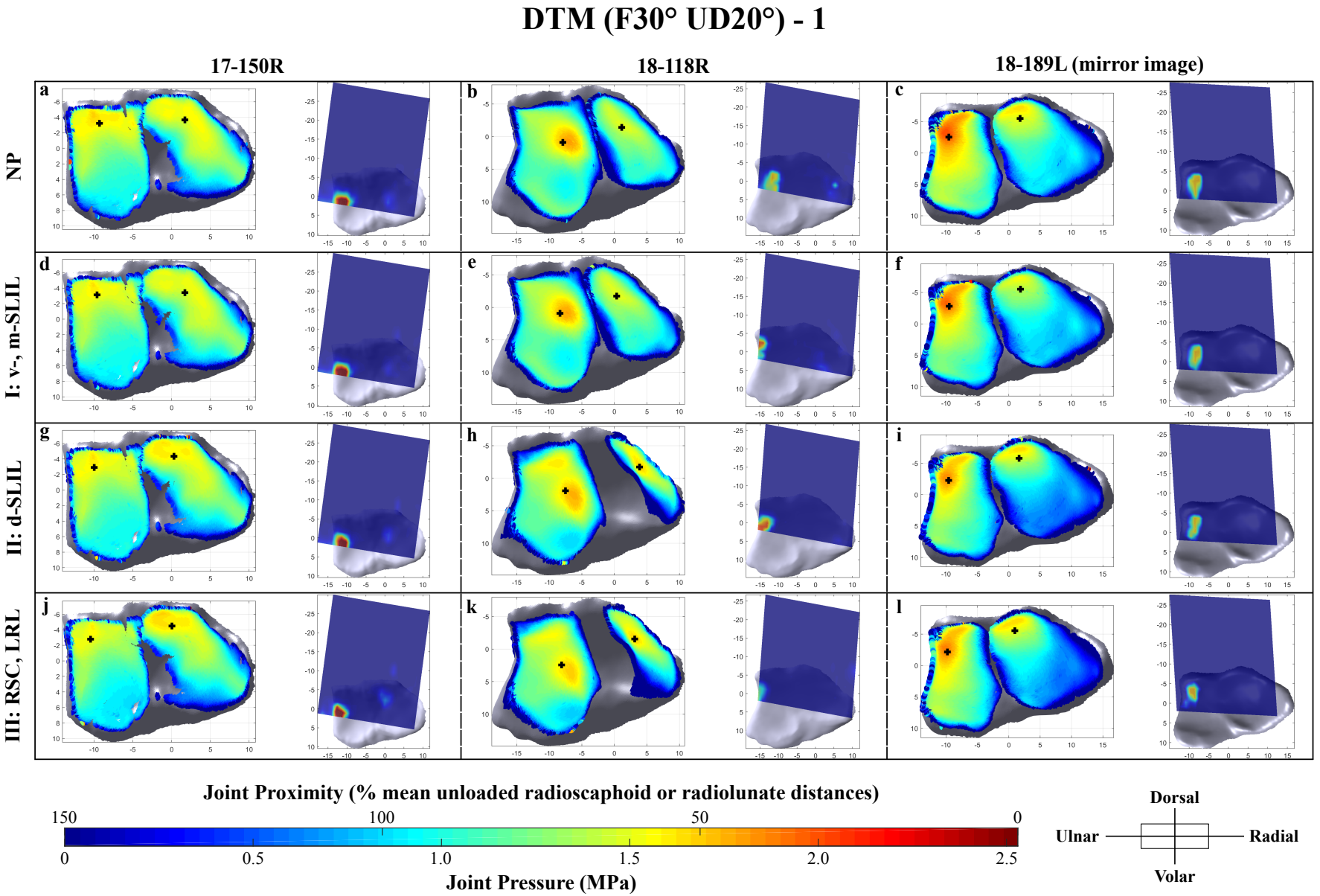

Figure 4.45: Maps showing joint proximities (*left* in each sub-figures) and interpolated joint pressure measurements (*right*) at 30 degrees of global wrist flexion combined with 20 degrees of wrist ulnar deviation. The pressure maps were obtained through bilinear interpolation (5×5) of the raw sensal measurements given by the Tekscan sensors.

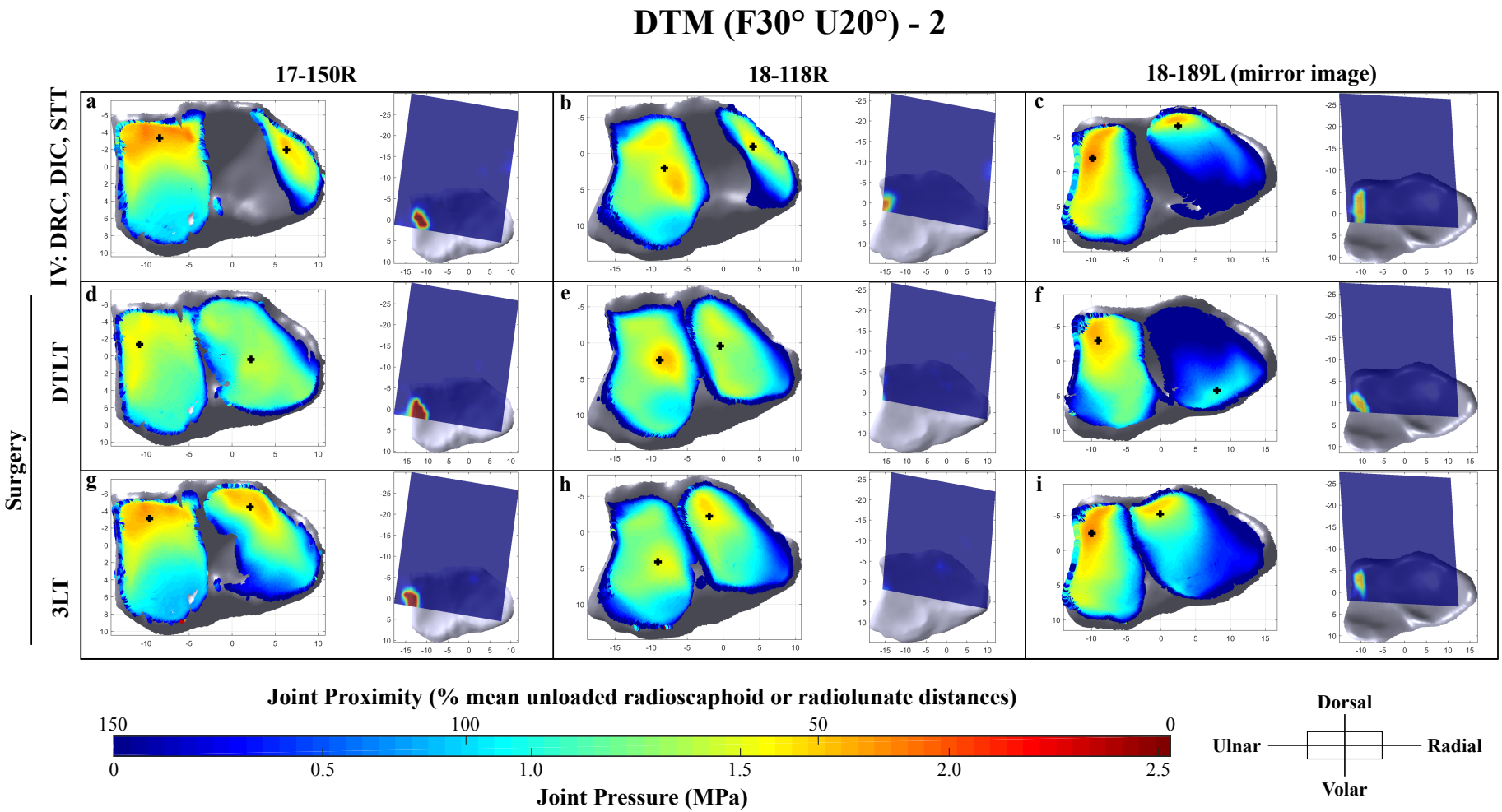

Figure 4.46: Maps showing joint proximities (*left* in each sub-figures) and interpolated joint pressure measurements (*right*) at 30 degrees of global wrist flexion combined with 20 degrees of wrist ulnar deviation (continued). The maps are shown in a way that the radiocarpal joint is viewed distally, with the top side of the figure being dorsal and the right hand side being radial. Columns represent from which specimen the data were recorded, while rows representing different conditions of the specimen. The colour bar is shared by the two types of measurements. The joint proximity calculated for each point on the articular surface is shown in percentages of the mean unloaded radioscaphoid or radiolunate distances, while the joint pressure as measured using Tekscan sensors is shown in MPa. The centroid of joint proximities (marked as '+') was calculated for both radioscaphoid and radiolunate contact.

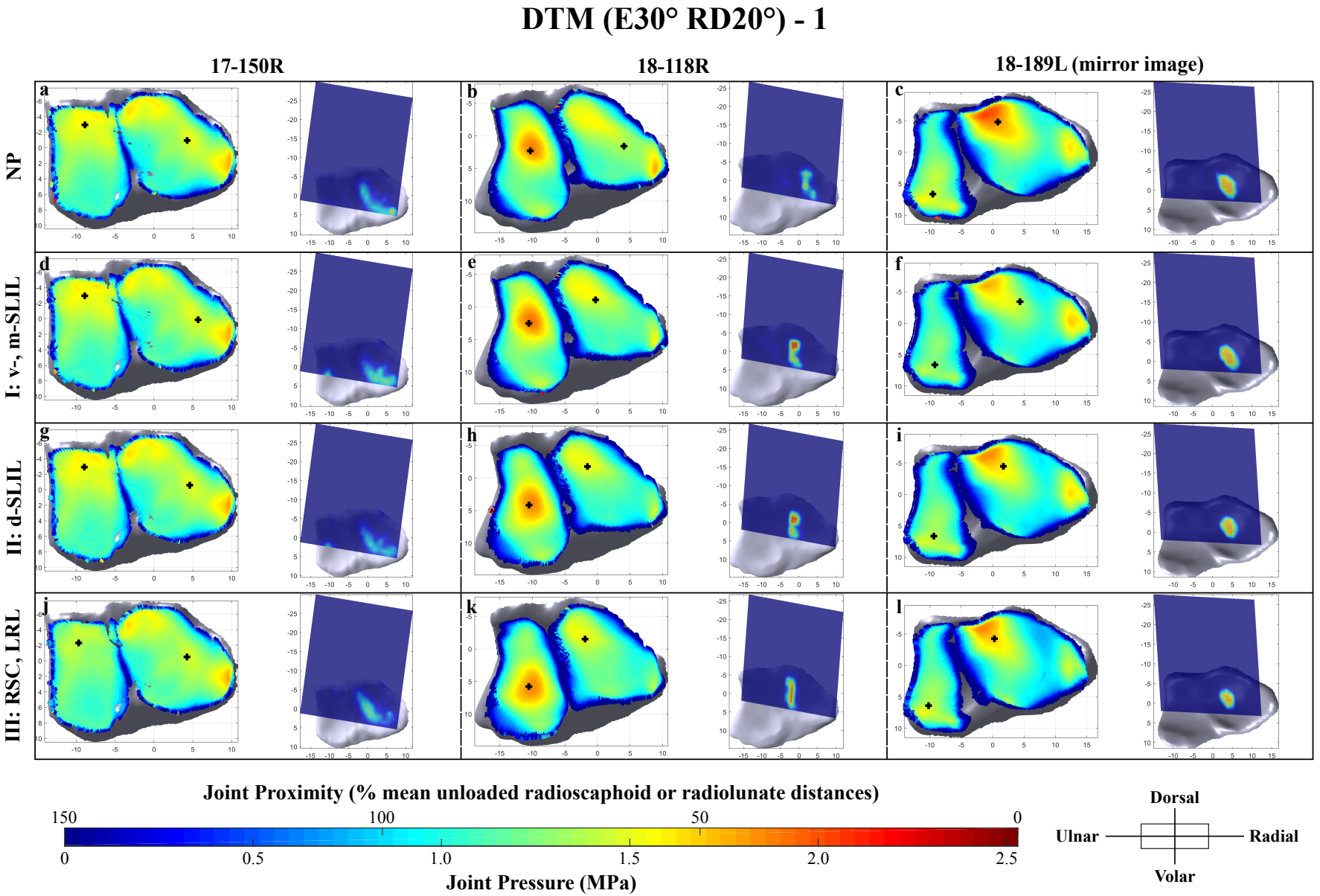

Figure 4.47: Maps showing joint proximities (*left* in each sub-figures) and interpolated joint pressure measurements (*right*) at 30 degrees of global wrist extension combined with 20 degrees of wrist radial deviation. The pressure maps were obtained through bilinear interpolation (5×5) of the raw sensal measurements given by the Tekscan sensors.

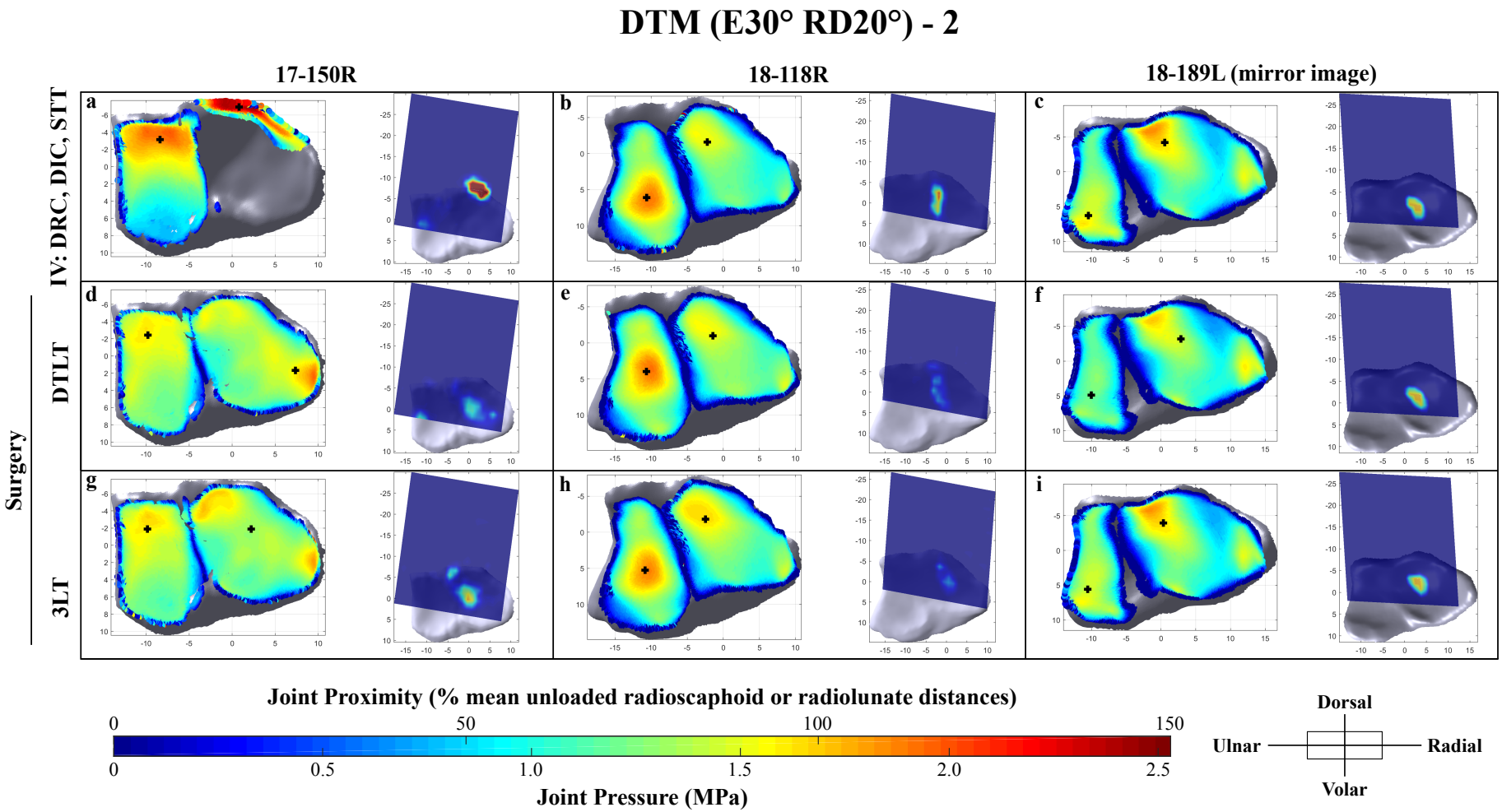

Figure 4.48: Maps showing joint proximities (*left* in each sub-figures) and interpolated joint pressure measurements (*right*) at 30 degrees of global wrist extension combined with 20 degrees of wrist radial deviation (continued). The maps are shown in a way that the radiocarpal joint is viewed distally, with the top side of the figure being dorsal and the right hand side being radial. Columns represent from which specimen the data were recorded, while rows representing different conditions of the specimen. The colour bar is shared by the two types of measurements. The joint proximity calculated for each point on the articular surface is shown in percentages of the mean unloaded radioscaphoid or radiolunate distances, while the joint pressure as measured using Tekscan sensors is shown in MPa. The centroid of joint proximities (marked as '+') was calculated for both radioscaphoid and radiolunate contact.

Limitation and Strength

Undeniably, this part of the study suffered from a number of limitations, with the most significant of which being the small sample size. Across all seven specimen conditions and three modes of global wrist motion, a complete and reliable series of radiocarpal pressure measurements was obtained in only three out of the seven wrists in the present study. Given the limited amount of useable data, statistical inferences was impossible. And due to the high inter-specimen variability, the analysis of the changes in radiocarpal contact was limited to a qualitative and observational nature in the present study. The low success rate of pressure measurement was attributed to the Tekscan sensors failing frequently and prematurely inside the articulation. A number of factors that might have contributed to sensor failures were identified as follows:

Firstly, although each pressure sensor had been coated with Teflon tapes and a generous amount of K-Y jelly when secured inside the joint articulation, it still sustained considerable wear damage and was subsequently short-circuited due to water incursion. As the summation of muscle forces was held at a constant level of 150 N by the DWSA throughout the dynamic wrist simulation, this choice of the force level might ultimately have been too high for the substrate material of the pressure sensor. Furthermore, the creation of sharp edges on the carpal bones when making the holes for the radio-opaque markers might have also exacerbated the attrition of the pressure sensor.

Secondly, pull-out of the sutures securing the sensor inside the articular space accounted for another major failure mode of the pressure sensor. Constrained by the width of the dorsal capsular opening and the limited space available in the radiocarpal articulation, the sutures were only placed volarly at the distal non-sensing regions of the pressure sensor. As described previously, to increase the strength of those piercing sites and to further reduce the footprint of the sensor, the distal non-sensing substrate was slighted folded and reinforced using fibreglass tapes. But apparently, such a fixation

strategy is proven to be unreliable in preventing the relative motion of the pressure sensor against the significant amount of friction experienced by the wrists in the present study. Furthermore, the volar aspect of the distal radius could not be effectively covered due to the presence of this extra band of the folded substrate, resulting in the significant dorsal overhang of the sensor in the present study and consequently incomplete pressure maps.

Thirdly, crimping of the pressure sensor was not uncommon, as it struggled to conform or wrap smoothly over the radiocarpal articular surface, which has a complex biconcave configuration. The narrow dorsal opening created through the capsulotomy also caused considerable wrinkling of the pressure sensor laterally, leading to false pressure spikes that had to be excluded. All these problems amount to the fact that the Tekscan Medical 4000 pressure sensor is not specifically designed to be fitted inside the wrist joint. In fact, this type of sensors see frequent use in bigger joints such as the knee (Mootanah et al., 2014; Gu, 2016), and there are really not many commercially available articular pressure measurement solutions that suit the requirement of the present study in terms of their physical size and spatial resolution. Rikli et al. (2007) used a capacitive sensor with a custom-designed banana-shaped profile to measure the articular pressure across the radioulnocarpal joint from the tip of the radial styloid to the TFCC. However, it suffered from a low spatial resolution, as the sensor was unable to distinguish any pressure changes over an area that is less than 1.5 mm in the sagittal plane and 2.0 mm in the coronal plane. Apart from a "made-to-measure" solution, Short et al. (1995) and Daly et al. (2018) taped several "fingers" of the Tekscan Model 6900 pressure sensor together to form a sensing matrix that is large enough for the radiocarpal and radioulnocarpal articular surface. This approach was attempted in a pilot study (Fig. 4.49), but abandoned eventually as the overlapping regions seemed to be interfering with the pressure measurement given by the two lower sensors. As the amount of sensor overlapping was unknown and hard to control between different trials, it was deemed difficult to virtually join the pressure maps given by different sensors. Besides, there was minimal non-sensing substrate to be used for

securing the pressure sensor within the articular space. In future studies, it is therefore recommended to have the pressure sensor custom-designed with a carefully planned fixation strategy to achieve a better sensor coverage over the radiocarpal articular surface and a more reliable pressure measurement.

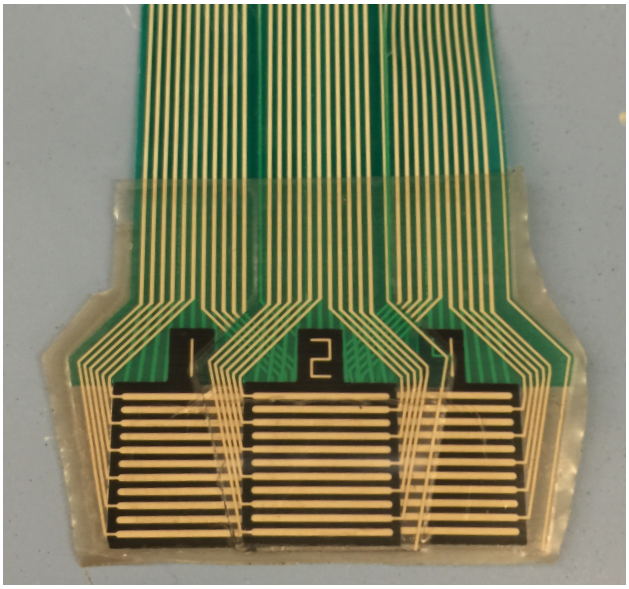

Figure 4.49: Photograph of a Tekscan Model 6900 pressure sensor with three of its measuring figures being taped together.

Fourthly, the cadaveric wrist specimens used in the present study were not screened to ensure they all had similar joint anatomy. As described earlier, it has been shown that the bony anatomy of the radiocarpal articulation might have a role in moderating the severity of carpal instability. In addition, it has also been demonstrated that the ulnar variance, which measures the difference between the levels of radiocarpal and ulnocarpal articular surfaces, might affect the force transmission in the carpus, especially that of the radiolunate articulation (Horii et al., 1990; Kazuki et al., 1991; Schuind et al., 1992; Ledoux et al., 2008). Therefore, it might be beneficial to control those morphological variations in the specimens in future studies. In addition, since the elbow joint of the specimen was potted in paster with the forearm fused in neutral pronation and supination using Steinmann pins, assessment

of the radiocarpal contact characteristics was not performed at other forearm rotations. However, it has been shown that the amount of ulnar variance can vary as a function of elbow position and forearm rotation (Palmer et al., 1982; Jung et al., 2001). Furthermore, the present study also did not model hand grip, as specimens were loaded solely through the tendons of the wrist motor muscles. However, *in-vivo* results have suggested that with maximal hand grip, there is relative proximal motion of the radius with respect to the ulna, which leads to an increase in ulnar variance by approximately 2 mm (Friedman et al., 1993).

Fifthly, the present study analysed the changes in carpal kinematics and radiocarpal articular contact by comparing the data corresponding to the same global wrist motion simulated in specimens before and after the introduction of the ligament divisions and subsequent surgeries. This approach, however, implicitly assumed the neuromuscular control of the wrist is in favour of achieving the desired global motion (position-controlled) after ligamentous injuries than maintaining the muscle forces at a similar level when the wrist was intact (force-controlled). Although most studies concerning the biomechanical effect of carpal instabilities or other pathological conditions were performed with a controlled global wrist motion, there is still no direct evidence that can fully support this approach. Erhart et al. (2012) believed "post trauma patients are likely to exert a force controlled motion accepting limited displacement" and measured the radiocarpal contact pressure during wrist simulations that were achieved with a controlled set of muscle forces. Although the muscle forces were constrained to sum to a constant level in the present study, the recruitment of individual muscles were adjusted by the DWSA's control system automatically in response to the alterations in the cadaveric plant's native anatomy to ensure the stability of the wrist simulations across different specimens and specimen conditions.

Finally, as mentioned before, the use of subchondral bone models instead of the true cartilage geometries in the joint proximity analyses might have led to inaccuracies in the results.

Apart from the limitations listed above, the present study also had a

few strengths. Despite its qualitative nature and the large inter-specimen variability, this study is perhaps the first to report the change in radiocarpal contact following a series of ligament division and two subsequent surgical reconstructions. Furthermore, it is also advantageous to report both the joint proximities and the actual sensor measurements, as it helps in avoiding pitfalls in relying solely on any one of them. As described earlier, owing to the difficulties in measuring the pressure within a tight articular space directly, many researchers have resorted to the non-invasive joint proximity mapping approach to infer the articular contact. This approach might be valid for healthy joints but can also be quite unpredictable and bring out misleading results if the normal anatomy of the joint is compromised. In the present study, this could be better appreciated using the results for wrist ulnar deviation in Stage IV ligament division (Fig U2 a-c). If the joint proximity maps had been examined without any additional support from the actual sensor measurements, the elevated and more incongruent radioscaphoid proximity would have deceptively led to the false inference that the abnormally high radioscaphoid contact pressure persisted during wrist ulnar deviation. Clearly, this was not the case, and the higher radioscaphoid proximity was simply due to the fact that the scaphoid had been dissociated from the carpus and its proximal pole remained subluxed on the dorsal rim of the distal radius. However, this does not imply that the joint proximity maps do not add any value to the analysis. Instead, they complemented the actual pressure measurements, which suffered substantially from the senor coverage issue in the present study. Moreover, unlike in other studies where the relative position of the pressure measurement device with respect the joint articular surface was often determined visually by the investigator Viegas et al. (1990); Kazuki et al. (1991); Fischer et al. (2011); Daly et al. (2018), CT scan was employed in the present study to find the precise location of the pressure sensor, enabling the measurement results to be visualised in a more realistic and anatomically accurate manner. Furthermore, despite the fact that the results were only reported for a limited selection of wrist positions, the contact pressure within the radiocarpal articulation was actually measured simultaneously during dynamic wrist simulations in the present

study. Despite being practically challenging, this approach is considered more physiologically accurate, in contrast to the static loading schemes adopted in most other similar studies (Blevens et al., 1989; Hara et al., 1992; Hogan et al., 2004; Tang et al., 2009; Daly et al., 2018).

5

Conclusions

Normal wrist function is ensured by a delicate interplay between bony architecture and soft-tissue constraints. Disruptions of this balance may alter carpal kinematics and joint contact, impairing the normal physiology and biomechanics of the wrist. The scapholunate interosseous ligament (SLIL), whose integrity is of pivotal importance to the normal scapholunate motion and arguably to that of the wrist as a whole, has been recognised as the most commonly injured carpal ligament. If injury to this ligament is missed in early diagnosis, mild forms of scapholunate instability are likely to ensue. If left untreated, prolonged exposure to the altered joint kinematics and mechanics lead to progression of the pathology, ultimately resulting in degenerative arthritis.

The review of literature presented in Chapter 1 revealed that although the SLIL has been shown to be the primary stabiliser of the scapholunate joint, consensus on the relative contribution of the secondary ligamentous stabilisers in the complex supportive network surrounding the joint has yet been established. Moreover, as carpal motion was often studied in selected planes or with a sole focus on the rotational behaviours of the carpal bones in earlier attempts, accurate data on three-dimensional carpal pathokinematics and mechanics during dynamic wrist motion remains lacking. The primary focus of this dissertation was, therefore, to advance understanding of the alterations in the carpal biomechanics that take place in different stages of scapholunate instability. Furthermore, the review of literature also exposed an alarming reality that many surgical techniques advocated for the treatment of scapholunate instability have seen clinical applications without solid biomechanical proof of efficacy. To this end, two existing surgical reconstructive techniques, including a novel method known as the DTLT and the widely used 3LT, were evaluated in terms of the extent to which they restore the normal carpal biomechanics.

Cadaveric Wrist Testing Platform

To answer the aforementioned research questions, a novel cadaveric wrist testing platform, comprised of a dynamic wrist simulation apparatus (DWSA) with integrated measurement systems, was developed to facilitate reliable *in-vitro* investigations of the wrist. Dynamic wrist simulations were facilitated by the DWSA through coordinated muscle force applications. Electromechanical actuators instrumented with load cells were attached to the wrist prime movers to simulate muscle activations, and the global wrist positions were continuously tracked using a video-based motion capture system. A two-layer control architecture, with a force control loop being nested within a position control loop, was adopted for the control algorithm of the DWSA. A decentralised adaptive controller was employed to operate on the position feedback so that the joint torques required for the corrective action to achieve the target position can be estimated at that particular instant, in the absence of a precise dynamic model describing the cadaveric plant. The widely-used static optimisation method was adopted to tackle the neuromuscular redundancy problem, which arose in the inverse process of mapping joint torques back into the forces exerted by individual muscles about the joint. The optimisation was carried out in each control cycle with the muscle stress, a quantity that is proportional to the muscle activation, being continuously minimised. A constant-sum constraint was imposed during the muscle force computations to allow the phenomenon of agonist-antagonist muscle co-activation to be implicitly simulated on a cadaver model. A X-ray biplane fluoroscopy system was custom-built and integrated into the testing platform to allow the complex three-dimensional carpal motion to be accurately measured by means of Röentgen stereo-photogrammetry analysis. And an electronic piezoresistive pressure measurement system was employed to monitor the articular contact within the radiocarpal joint simultaneously during dynamic wrist simulations.

System Validations

A comprehensive set of validation experiments were carried out to assess the performance of each individual component comprising the CWTP. In order to evaluate the control capability of the DWSA, which was responsible for the motion synthesis aspect of the testing platform, dynamic wrist simulation experiments were conducted using a total of seven cadaveric specimens. Different modes of wrist motion, including planar motions such as FEM and RUD, and their superposition, representing DTM in an oblique plane, were simulated. It was shown that the dynamic wrist motion achieved by the DWSA on wrist cadavers tracked the desired trajectory with an excellent level of accuracy and repeatability. In particular, the RMS error in controlling the global wrist position within each cycle of motion was found to be less than 0.18°, and the mean variation in the global wrist positions achieved at periodically equivalent time points between each cycle was found to be less than 0.10°. The superior control performance was maintained even after the most severe case of ligamentous injuries were introduced to the cadaveric plants, suggesting the robustness and applicability of the DWSA.

The custom-built biplane X-ray fluoroscopy system was also evaluated for its performance but in two separate steps. In the first experiment, the system's capability in locating the three-dimensional position of a single radio-opaque marker was assessed. An RMS accuracy of 0.057 mm and a precision of 0.026 mm were obtained. Based on these metrics, an *in-silico* experiment was conducted to interrogate how these errors propagated through the pose estimation process to affect the final kinematic outcome of the rigid body. The results indicated that with the current biplane X-ray fluoroscopy system, the rotational and translational motion of a rigid body could be resolved to an accuracy of 0.172° and 0.0426 mm, respectively.

Finally, with individual components of the testing platform being successfully validated for their performance, a joint system validation was conducted. The results showed highly repeatable carpal kinematics data were obtainable using the testing platform as a whole, thus proving its validity for

the subsequent experiments.

Effect of Ligament Divisions on Carpal Kinematics

Stage I: v- and m-SLIL

The scaphoid was slightly more extended, about 1.22° in wrist extension. The lunate was observed to be ulnarly deviated by about 0.4° and volar translated by < 0.2 mm, in wrist flexion and ulnar flexion. These changes were deemed small, and therefore the present finding did not support the notion that these structures should be included in the reconstruction.

Stage II: d-SLIL

The incremental division of the d-SLIL caused the most significant changes in the scaphoid and lunate kinematics. In general, the scaphoid became significantly flexed, ulnarly deviated and pronated with respect to the radius, while the lunate became abnormally extended, supinated and translated volarly and slightly ulnarly. Interestingly, the lunate rotation in the coronal plane was not affected by the complete division of the SLIL. These results were in general agreement with those previously published, except for a higher lunate extension, which might relate to the advanced age of the specimens, higher muscle forces applied and introduction of a pressure sensor in the radiocarpal joint in the present study.

In addition, the changes in the scapholunate kinematics recorded during the radial extension phase of the DTM, however, were found to be minimal. This might be attributed to the stability provided by means of the bony articulation, and might be a potentially preferable position for splinting after reconstructive surgeries.

This study is perhaps the first to look at alterations in the dynamic patterns of the carpal motion. The analysis showed that the net flexion and extension exhibited by the scaphoid during wrist motion in the sagittal plane

were increased, while those of the lunate became significantly attenuated. The former implied greater scaphoid mobility in the sagittal plane after the division of the SLIL; the retardation of the lunate motion implied the loss of scapholunate association, which correlated well with the pathoanatomy. In addition, the adaptive rocking-chair-like flexion and extension exhibited by the scaphoid during wrist radial and ulnar deviation were also significantly attenuated, suggesting a transition towards a more row-like scaphoid rotation.

Stage III: RSC and LRL

Incrementally dividing the RSC and LRL ligaments induced relatively mild alterations, as the scaphoid and capitate were observed to rotate into further pronation, while the lunate became slightly less supinated.

Small but statistically significant ulnar translations of the lunate and capitate were observed, and the scaphoid translated slightly more towards the volar aspect of the wrist. These changes were typically on the order of 0.30 mm, and were especially pronounced during wrist extension and ulnar deviation. Changes in the dynamic patterns of the scaphoid and lunate kinematics also correlated well with the pathoanatomy, suggesting greater mobility towards the ulnar and dorsal aspect of the wrist after the ligament division.

Stage IV: DIC, DRC and STT

For the scaphoid, this stage of ligament division induced the second highest change in its static malalignment, as it collapsed further into flexion, ulnar deviation and pronation. The scaphoid flexion was most affected in wrist ulnar deviation, with a mean of 10.2° of increase. And the increase in scaphoid ulnar deviation and pronation were the highest in wrist ulnar flexion, both on the order of magnitude of 5°.

The dynamic extension exhibited by the scaphoid during radial extension

was found to be increased slightly by 1.8°, while 3.4° more dynamic radial deviation was observed during wrist radial deviation. These were in line with the pathoanatomy. And the concurrent loss of the adaptive flexion and extension exhibited by the scaphoid during wrist radial and ulnar deviation suggested that the scaphoid motion was more row-like than column-like, and dictated presumably by the bony geometry.

Although not statistically significant, cases of large radial and dorsal translation of the scaphoid were observed in several specimens after the ligament release.

The lunate was relatively unaffected by this stage of ligament division, except for being statistically more supinated. This change was most pronounced during flexion, measured 3.5°. For the capitate, significant dorsal translation was observed in some specimens. These were thought to be due to the loss of the dorsal carpal ligaments, which effectively act as a labrum protecting the dorsum of the carpus. In addition, the capitate was also more proximally migrated, with significant attenuation of its dynamic translation in the radial and ulnar directions. This implied that the capitate had firmly wedged into the scapholunate interval.

Effect of Reconstructive Surgeries on Carpal Kinematics

Dorsal Transarticular Loop Tenodesis

The dorsal transarticular loop tenodesis (DTLT) reconstruction led to successful restoration of the normal scaphoid rotation in the coronal plane. However, the reduction in both the sagittal and transverse planes was insufficient, as the scaphoid still appeared to be flexed about 6° and pronated about 3° as compared to its native state. This might be related to the sole dorsal and proximal placement of the graft, leaving the distal pole of the scaphoid unchecked. The reconstructions ability to re-establish the link between the scaphoid and the distal carpal row was also shown to be inferior to that achieved by the 3LT, as the adaptive flexion and extension exhibited by the scaphoid during wrist radial and ulnar deviation were only partially restored. A complementary dorsal capsulodesis might be therefore necessary to correct the residual scaphoid flexion.

After the surgery, the scaphoid exhibited an unusually high amount of volar translation, while the lunate pronated statistically more during wrist ulnar deviation. This was thought to be attributed to the passive stretching of the radially situated ECR-B tendon, which presumably twisted the scaphoid and lunate as a unit towards the volar aspect of the radius.

The unusual dynamic supination of the scaphoid, observable since Stage II in wrist extension, ulnar deviation and radial extension, were suppressed. This implied the asymmetric volar opening of the scapholunate interval was corrected, even though an explicit reconstruction of the v-SLIL was not included in the DTLT technique.

The DTLT also led to successful reduction of the dorsally collapsed lunate, which in turn restored its dynamic extension. The abnormal lunate supination was also corrected. However, cases of overcorrections were observed in these two planes.

The pronated and proximally migrated capitate was effectively reduced as the scapholunate alignment being restored to a near-normal state. However, the excessive lunate flexion, as a result of overcorrections induced by the technique, caused the capitate to become significantly volarly translated up to 2 mm in some cases.

Three-Ligament Tenodesis

The 3LT reconstruction achieved an excellent restoration of the scaphoid flexion deformity in the sagittal plane, outperforming the DTLT. The adaptive scaphoid flexion and extension exhibited during wrist radial and ulnar deviation were also reinstated after the procedure, presumably due to the reconstruction of the STT ligament. However, poor results in correcting the abnormal scaphoid pronation were obtained, as the residual rotational malalignment was observed to be as high as 7.6°. The dynamic pattern of the scaphoid rotation in the transverse plane was also not restored after the procedure, with a substantial amount of supination being observed during wrist extension, signalling a possible volar opening of the scapholunate interval. This was somehow expected as the ulnar and dorsal directed pull of the tendon graft might be unable to counteract this tendency. Therefore, it may be beneficial to have the v-SLIL reconstructed in conjunction to the 3LT.

Disappointing results were also obtained in the lunate reduction, as the lunate remained collapsed in significant extension and supination. This correlated with the marginal postoperative improvements in the radiolunate angle reported clinically. A transosseous passage of the tendon graft may be considered, instead of burying it in a trough carved on the lunate.

The 3LT not only did not correct the ulnar translation of the carpus, and the ulnar tensioning of the tendon graft prescribed by the technique might have even exacerbated this pathology.

Effect on Radiocarpal Contact

A preliminary study was carried out to analyse the changes in the radiocarpal contact pattern following each stage of ligament divisions or reconstructive surgeries. Two different approaches, both experimental, by means of an electronic pressure sensor placed inside the articulation, and computational, by inferring joint contact based on the inter-bone proximities calculated using kinematics data, were used to facilitate the analysis. Unfortunately, owing to the high failure rate of the pressure sensors, the experimental measurements were only obtained for three out of seven cadaveric wrist specimens. Given the small sample size, only qualitative comparisons were performed.

With incremental sectioning of the scapholunate-supporting ligaments, the radioscaphoid contact was observed to gradually separate from the radiolunate contact to become radially and dorsally translated. The most dramatic change in the radioscaphoid contact happened with rotatory subluxation of the scaphoid, in which the scaphoid appeared as if it rode on the dorsal rim of the distal radius. This occurred prematurely in Stage II ligament division in a specimen with advanced age, and in Stage IV in specimens that were less advanced in age. The articular pressure measurements indicated that when the scaphoid was subluxated, it tended to become decoupled from the force bearing column of the wrist, thus overloading the lunate. The radiolunate contact, on the other hand, was found to shift towards the volar and ulnar aspect of the distal radius, which was in good agreement with the pathological extension, supination and ulnar translation of the lunate as seen previously in the kinematics analysis.

In regards to the two reconstructive surgeries, the postoperative patterns of the radiocarpal contact were again observed to reflect the findings of the kinematics analysis. Specifically, despite the inter-specimen variability, it was shown that the DTLT outperformed the 3LT procedure in restoring the normal radiolunate contact. The radioscaphoid contact, however, was only slightly improved after the DTLT, as the scaphoid remained in abnormal flexion and decoupled from the force bearing column. The 3LT was supe-

rior in this regard but owing to the way the tendon graft was routed and tensioned, the undesirable ulnar translation and residual scaphoid pronation still hindered a complete restoration of the normal radioscaphoid contact.

Future Directions

Although the cadaveric wrist testing platform developed in the present study has been shown to be able to facilitate highly accurate biomechanical assessments of the wrist, there is still room for further improvement. A number of future research directions are thus suggested. Firstly, instead of the hypothetical sinusoidal profile used in the present study, dynamic wrist simulations could be performed with a more realistic motion trajectory tracked from living subjects. Secondly, since the muscle forces were predicted using static optimisation and apportioned based on their respective PCSA rather than actual activation, a separate *in-vivo* experiment could be performed to measure muscle EMG signals during realistic wrist motion. This information could then be incorporated into the DWSA's control algorithm, such that the wrist cadaver could be reanimated in a more physiologically accurate manner, truthfully replicating the *in-vivo* wrist motion. Thirdly, marker-less tracking could be implemented to eliminate the need to implant radio-opaque markers into the small carpal bones, which typically involves some degrees of disruption of the native anatomy. Fourthly, as described earlier, the pressure sensor used in the present study is not purposely-built for the wrist and had unfortunately caused several issues such as inadequate coverage of the articular surface and a large sensor overhang at the dorsal side of the wrist. In addition, the off-the-shelf solution does not provide any means for securing the sensor inside the articular space. Improvised fixations that make use of the non-sensing substrate of the sensor for suture placement were proven to be not very reliable. Therefore, it will be beneficial to have the pressure sensor custom-designed with appropriate dimensions and reinforced locations for suture passage. Alternatively, computer simulations could be performed, and the results reported in the present study could be potentially useful for model validation. Finally, with the CWTP, the effect of injuries to other parts of the wrist, or different types of surgical procedures or prosthesis designs could also be studied in future research (Fig. 5.1).

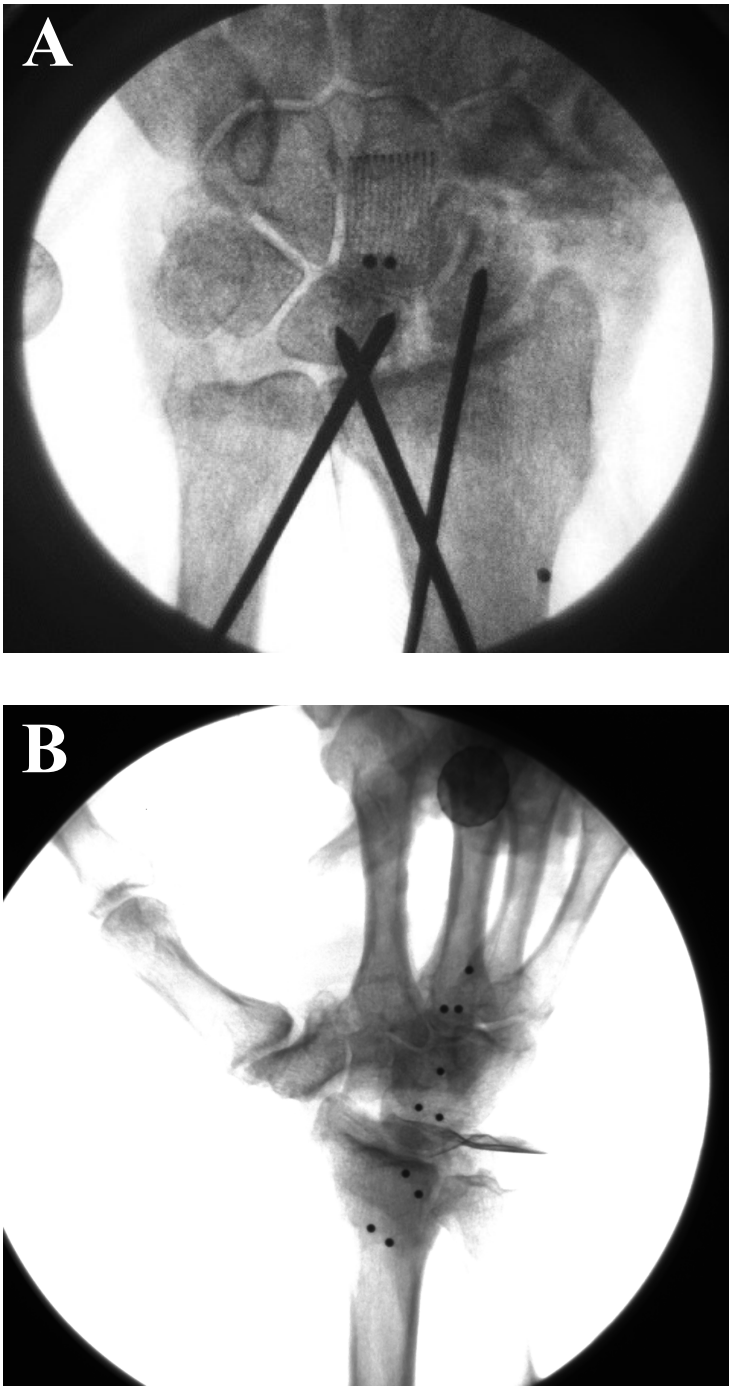

Figure 5.1: Pilot studies concerning other types of surgical methods were also conducted using the CWTP developed in the present study. These included **(A)** radioscapholunate (RSL) arthrodesis (simulated by means of K-wires), and **(B)** proximal row carpectomy (PRC).

References

Aagaard, P., Simonsen, E. B., Andersen, J. L., Magnusson, S. P., Bojsen-Møller, F., and Dyhre-Poulsen, P. (2000). Antagonist muscle coactivation during isokinetic knee extension. *Scandinavian Journal of Medicine and Science in Sports*, 10(2):58–67.

AAOS (1965). *Joint motion : method of measuring and recording.* Churchill Livingstone, Chicago.

Ackland, D. C., Pak, P., Richardson, M., and Pandy, M. G. (2008). Moment arms of the muscles crossing the anatomical shoulder. *Journal of Anatomy*, 213(4):383–390.

Adler, B. D., Mark Logan, P., Janzen, D. L., Favero, K. J., Gropper, P. T., Boyle, J. C., Lawson, I. B., and Connell, D. G. (1996). Extrinsic radiocarpal ligaments: Magnetic resonance imaging of normal wrists and scapholunate dissociation. *Canadian Association of Radiologists Journal*, 47(6):417–422.

Afoke, N., Byers, P., and Hutton, W. (1987). Contact pressures in the human hip joint. *The Journal of Bone and Joint Surgery. British volume*, 69-B(4):536–541.

Almquist, E. E., Bach, A. W., Sack, J. T., Fuhs, S. E., and Newman, D. M. (1991). Four-bone ligament reconstruction for treatment of chronic complete scapholunate separation. *The Journal of Hand Surgery*, 16(2):322 – 327.

Alonso Rasgado, T., Zhang, Q., Jimenez Cruz, D., Bailey, C., Pinder, E., Mandaleson, A., and Talwalkar, S. (2017). Analysis of tenodesis techniques for treatment of scapholunate instability using the finite element method. *International Journal for Numerical Methods in Biomedical Engineering*, 33(12):1–12.

An, K.-N., Berger, R. A., and Cooney, W. P. (1991). *Biomechanics of the wrist joint.* Springer-Verlag.

Anderson, D. D., Deshpande, B. R., Daniel, T. E., and Baratz, M. E. (2005). A three-dimensional finite element model of the radiocarpal joint: distal radius fracture step-off and stress transfer. *The Iowa orthopaedic journal*, 25:108–117.

Anderson, F. C. and Pandy, M. G. (2001). Static and dynamic optimization solutions for gait are practically equivalent. *Journal of Biomechanics*, 34(2):153–161.

Andersson, J. K. (2017). Treatment of scapholunate ligament injury: Current concepts. *EFORT Open Reviews*, 2(9):382–393.

Andersson, J. K. and Garcia-Elias, M. (2013). Dorsal scapholunate ligament injury: a classification of clinical forms. *Journal of Hand Surgery: European Volume*, 38(2):165–169.

Anderst, W. J. and Tashman, S. (2003). A method to estimate in vivo dynamic articular surface interaction. *Journal of Biomechanics*, 36(9):1291–1299.

Andrews, J. G. and Youm, Y. (1979). A biomechanical investigation of wrist kinematics. *Journal of Biomechanics*, 12(1):83–93.

Apergis, E. P. (2013). *Wrist Anatomy*, chapter 2, pages 7–37. Springer-Verlag, Milan, 1st edition.

Arkless, R. (1966). Cineradiography in normal and abnormal wrists. *The American journal of roentgenology, radium therapy, and nuclear medicine*, 96(4):837–844.

Ateshian, G. A., Kwak, S. D., Soslowsky, L. J., and Mow, V. C. (1994). A stereophotogrammetric method for determining in situ contact areas in diarthrodial joints, and a comparison with other methods. *Journal of Biomechanics*, 27(1):111–124.

Athlani, L., Pauchard, N., Detammaecker, R., Huguet, S., Lombard, J., Dap, F., and Dautel, G. (2018). Treatment of chronic scapholunate dissociation with tenodesis: A systematic review. *Hand Surgery and Rehabilitation*, 37(2):65–76.

Austin, N. M. (2005). The Wrist and Hand Complex. In Levangie, P. K. and Norkin, C. C., editors, *Joint Structure and Function: A comprehensive analysis*, chapter 9, pages 305–311. F.A. Davis Company, Philadelphia, fourth edition.

Bachus, K. N., DeMarco, A. L., Judd, K. T., Horwitz, D. S., and Brodke, D. S. (2006). Measuring contact area, force, and pressure for bioengineering applications: Using Fuji Film and TekScan systems. *Medical Engineering and Physics*, 28(5):483–488.

Baier, D. B. and Gatesy, S. M. (2013). Three-dimensional skeletal kinematics of the shoulder girdle and forelimb in walking Alligator. *Journal of Anatomy*, 223(5):462–473.

Bain, G. I., Clitherow, H. D., Millar, S., Fraysse, F., Costi, J. J., Eng, K., McGuire, D. T., and Thewlis, D. (2015). The effect of lunate morphology on the 3-dimensional kinematics of the carpus. *Journal of Hand Surgery*, 40(1):81–89.e1.

Bajuri, M. N., Kadir, M. R. A., Raman, M. M., and Kamarul, T. (2012). Mechanical and functional assessment of the wrist affected by rheumatoid arthritis: A finite element analysis. *Medical Engineering and Physics*, 34(9):1294–1302.

Baratta, R., Solomonow, M., Zhou, B. H., Letson, D., Chuinard, R., and D'Ambrosia, R. (1988). Muscular coactivation. The role of the antagonist musculature in maintaining knee stability. *The American journal of sports medicine*, 16(2):113–122.

Battistella, F. (2009). Arthroscopic thermal shrinkage for scapholunate ligament injuries. In Slutsky, D. J. and Osterman, A. L., editors, *Fractures and Injuries of the Distal Radius and Carpus: the cutting edge.*, chapter W7, pages 67 – 73. W.B. Saunders, Philadelphia, 1st edition.

Belhaouane, R., Lebeau, N., Maes-Clavier, C., Hustin, C., Krief, E., Bonnaire, B., Warin, M., Rotari, V., and David, E. (2016). Reproducibility of X-rays and CT arthrography in SLAC, SNAC, SCAC wrists. *Hand Surgery and Rehabilitation*, 35(6):393–400.

Benoit, D. L., Ramsey, D. K., Lamontagne, M., Xu, L., Wretenberg, P., and Renström, P. (2006). Effect of skin movement artifact on knee kinematics during gait and cutting motions measured in vivo. *Gait & Posture*, 24(2):152–164.

Berdia, S., Short, W. H., Werner, F. W., Green, J. K., and Panjabi, M. (2006). The hysteresis effect in carpal kinematics. *The Journal of Hand Surgery*, 31(4):594.e1 – 594.e8.

Beredjiklian, P. K., Dugas, J., and Gerwin, M. (1998). Primary Repair of the Scapholunate Ligament. *Techniques in Hand & Upper Extremity Surgery*, 2(4):269–273.

Berger, R. A. (1996a). The anatomy and basic biomechanics of the wrist joint. *Journal of Hand Therapy*, 9(2):84–93.

Berger, R. A. (1996b). The gross and histologic anatomy of the scapholunate interosseous ligament. *The Journal of Hand Surgery*, 21(2):170–178.

Berger, R. A. (1997). The ligaments of the wrist. A current overview of anatomy with considerations of their potential functions. *Hand clinics*, 44(1):63–82.

Berger, R. A. (2001). The Anatomy of the Ligaments of the Wrist and Distal Radioulnar Joints. *Clinical Orthopaedics and Related Research*, 383:32–40.

Berger, R. A. (2010). Wrist Anatomy. In Cooney, W. P., editor, *The Wrist: diagnosis and operative treatment*, chapter 3, pages 25–76. Lippincott Williams & Wilkins, Rochester, 2nd edition.

Berger, R. A., Bishop, A. T., and Bettinger, P. C. (1995). New dorsal capsulotomy for the surgical exposure of the wrist. *Annals of Plastic Surgery*, 35(1):54–59.

Berger, R. A. and Blair, W. F. (1984). The radioscapholunate ligament: A gross and histologic description. *The Anatomical Record*, 210(2):393–405.

Berger, R. A., Blair, W. F., Crowninshield, R. D., and Flatt, A. E. (1982a). The scapholunate ligament. *Journal of Hand Surgery*, 7(1):87–91.

Berger, R. A., Crowninshield, R. D., and Flatt, A. E. (1982b). The three-dimensional rotational behaviors of the carpal bones. *Clinical Orthopaedics and Related Research*, 167(167):303–310.

Berger, R. A. and Garcia-Elias, M. (1991). General Anatomy of the Wrist. In An, K.-N., Berger, R. A., and Cooney, W. P., editors, *Biomechanics of the Wrist Joint*, chapter 1, pages 1–22. Springer-Verlag New York, Rochester, 1st edition.

Berger, R. A., Imeada, T., Berglund, L., and An, K. N. (1999). Constraint and material properties of the subregions of the scapholunate interosseous ligament. *Journal of Hand Surgery*, 24(5):953–962.

Berger, R. A. and Landsmeer, J. M. (1990). The palmar radiocarpal ligaments: A study of adult and fetal human wrist joints. *Journal of Hand Surgery*, 15(6):847–854.

Bergner, J. L., Farrar, J. Q., and Coronado, R. A. (2019). Dart thrower's motion and the injured scapholunate interosseous ligament: A scoping review of studies examining motion, orthoses, and rehabilitation. *Journal of Hand Therapy*.

Beveridge, J. E., Shrive, N. G., and Frank, C. B. (2014). Repeatability and precision of a weighted centroid method for estimating dynamic in vivo tibiofemoral surface interactions in sheep. *Computer Methods in Biomechanics and Biomedical Engineering*, 17(16):1853–1863.

Bickert, B., Sauerbier, M., and Germann, G. (2000). Scapholunate ligament repair using the mitektmbone anchor: Technique and preliminary results. *The Journal of Hand Surgery: British & European Volume*, 25(2):188–192.

Bishop, A., Gabel, G., and Carmichael, S. (1994). Flexor carpi radialis tendinitis. part i: Operative anatomy. *The Journal of bone and joint surgery. American volume*, 76(7):10091014.

Blankenhorn, B. D., Pfaeffle, H. J., Tang, P., Robertson, D., Imbriglia, J., and Goitz, R. J. (2007). Carpal Kinematics After Proximal Row Carpectomy. *Journal of Hand Surgery*, 32(1):37–46.

Blatt, G. (1987). Capsulodesis in reconstructive hand surgery. dorsal capsulodesis for the unstable scaphoid and volar capsulodesis following excision of the distal ulna. *Hand clinics*, 3(1):81102.

Blevens, A. D., Light, T. R., Jablonsky, W. S., Smith, D. G., Patwardhan, A. G., Guay, M. E., and Woo, T. S. (1989). Radiocarpal articular contact characteristics with scaphoid instability. *Journal of Hand Surgery*, 14(5):781–790.

Boabighi, A., Kuhlmann, J. N., and Kenesi, C. (1993). The distal ligamentous complex of the scaphoid and the scapho-lunate ligament. an anatomic, histological and biomechanical study. *The Journal of Hand Surgery: British & European Volume*, 18(1):65–69.

Boone, D. C. and Azen, S. P. (1979). Normal range of motion of joints in male subjects. *The Journal of bone and joint surgery. American volume*, 61(5):756 – 759.

Boyer, J. S. and Adams, B. (2010). Distal radius hemiarthroplasty combined with proximal row carpectomy: case report. *The Iowa orthopaedic journal*, 30:168–173.

Brainerd, E. L., Baier, D. B., Gatesy, S. M., Hedrick, T. L., Metzger, K. A., Gilbert, S. L., and Crisco, J. J. (2010). X-Ray reconstruction of moving morphology (XROMM): Precision, accuracy and applications in comparative biomechanics research. *Journal of Experimental Zoology Part A: Ecological Genetics and Physiology*, 313 A(5):262–279.

Brand, P. W. (1985). *Mechanics of Individual Muscles at Individual Joints*, chapter 8, pages 139–156. C.V. Mosby, St. Louis, 1st edition.

Brigstocke, G. H., Hearnden, A., Holt, C., and Whatling, G. (2014). In-vivo confirmation of the use of the dart thrower's motion during activities of daily living. *Journal of Hand Surgery: European Volume*, 39(4):373–378.

Brimacombe, J. M., Wilson, D. R., Hodgson, A. J., Ho, K. C., and Anglin, C. (2009). Effect of calibration method on Tekscan sensor accuracy. *Journal of Biomechanical Engineering*, 131(3):1–4.

Brinkhorst, M., Streekstra, G., van Rosmalen, J., Strackee, S., and Hovius, S. (2020). Effects of axial load on invivo scaphoid and lunate kinematics using four-dimensional computed tomography. *Journal of Hand Surgery (European Volume)*, 45(9):974–980.

Brown, R. R., Fliszar, E., Cotten, A., Trudell, D., and Resnick, D. (1998). Extrinsic and Intrinsic Ligaments of the Wrist: Normal and Pathologic Anatomy at MR Arthrography with Three-Compartment Enhancement. *Radiographics*, 18(3):667–674.

Brumfield, R. H. and Champoux, J. A. (1984). A biomechanical study of normal functional wrist motion.

Brumfield, R. H., Nickel, V. L., and Nickel, E. (1966). Joint motion in wrist flexion and extension. *Southern Medical Journal*, 59(8):909–910.

Brunelli, G. A. and Brunelli, G. R. (1995). A new technique to correct carpal instability with scaphoid rotary subluxation: A preliminary report. *The Journal of Hand Surgery*, 20(3, Part 2):S82–S85.

Bryce, T. H. (1896). On Certain Points in the Anatomy and Mechanism of the Wrist-Joint Reviewed in the Light of a Series of Röntgen Ray Photographs of the Living Hand. *Journal of anatomy and physiology*, 31(Pt 1):59–79.

Buchanan, T. S., Moniz, M. J., Dewald, J. P., and Rymer, W. Z. (1993). Estimation of muscle forces about the wrist joint during isometric tasks using an EMG coefficient method. *Journal of Biomechanics*, 26(4-5):547–560.

Buijze, G. A., Lozano-Calderon, S. A., Strackee, S. D., Blankevoort, L., and Jupiter, J. B. (2011). Osseous and ligamentous scaphoid anatomy: Part i. a systematic literature review highlighting controversies. *The Journal of Hand Surgery*, 36(12):1926 – 1935.

Burgess, R. C. (1987). The effect of rotatory subluxation of the scaphoid on radio-scaphoid contact. *Journal of Hand Surgery*, 12(5):771–774.

Caldwell, N. J., Hale, J. E., Rudert, M. J., and Brown, T. D. (1993). An algorithm for approximate crinkle artifact compensation in pressure-sensitive film recordings. *Journal of Biomechanics*, 26(8):1001–1009.

Campbell, D., Campbell, R., O'Connor, P., and Hawkes, R. (2013). Sports-related extensor carpi ulnaris pathology: a review of functional anatomy, sports injury and management. *British Journal of Sports Medicine*, 47(17):1105–1111.

Camus, E. (2013). Carpal biomechanics: Application to ligamentous injuries. In Camus, E. and Van Overstraeten, L., editors, *Carpal Ligament Surgery: Before Arthritis*, pages 19–37. Springer, Paris.

Capener, N. (1956). The hand in surgery. *The Journal of bone and joint surgery. British volume*, 38 B(1):128–151.

Carelsen, B., Bakker, N. H., Strackee, S. D., Boon, S. N., Maas, M., Sabczynski, J., Grimbergen, C. A., and Streekstra, G. J. (2005). 4d rotational x-ray imaging of wrist joint dynamic motion. *Medical Physics*, 32(9):2771–2776.

Carelsen, B., Jonges, R., Strackee, S. D., Maas, M., van Kemenade, P., Grimbergen, C. A., van Herk, M., and Streekstra, G. J. (2009). Detection of In Vivo Dynamic 3-D Motion Patterns in the Wrist Joint. *Biomedical Engineering, IEEE Transactions on*, 56(4):1236–1244.

Carlson, J. R. and Simmons, B. P. (1998). Wrist arthrodesis after failed wrist implant arthroplasty. *The Journal of Hand Surgery*, 23(5):893 – 898.

Carmeli, E., Patish, H., and Coleman, R. (2003). The aging hand. *Journals of Gerontology - Series A Biological Sciences and Medical Sciences*, 58(2):146–152.

Carrigan, S. D., Whiteside, R. a., Pichora, D. R., and Small, C. F. (2003). Development of a three-dimensional finite element model for carpal load transmission in a static neutral posture. *Annals of Biomedical Engineering*, 31(6):718–725.

Cautilli, G. P. and Wehb, M. A. (1991). Scapho-lunate distance and cortical ring sign. *The Journal of Hand Surgery*, 16(3):501 – 503.

Cerveri, P., Pedotti, A., and Ferrigno, G. (2005). Kinematical models to reduce the effect of skin artifacts on marker-based human motion estimation. *Journal of Biomechanics*, 38(11):2228–2236.

Chabas, J. F., Gay, A., Valenti, D., Guinard, D., and Legre, R. (2008). Results of the Modified Brunelli Tenodesis for Treatment of Scapholunate Instability: A Retrospective Study of 19 Patients. *Journal of Hand Surgery*, 33(9):1469–1477.

Changoor, A., Fereydoonzad, L., Yaroshinsky, A., and Buschmann, M. D. (2010). Effects of refrigeration and freezing on the electromechanical and biomechanical properties of articular cartilage. *Journal of Biomechanical Engineering*, 132(6):1–6.

Chanon, J., Aumonier, P., Van Sint Jan, S., Dugailly, P., Sobczak, S., Rooze, M., Salvia, P., and Feipel, V. (2007). Coordinate System Validation for Kinematics Analysis of the Carpal Bones. *Journal of Biomechanics*, 40(Supplement 2):S191.

Chennagiri, R. J. R. and Lindau, T. R. (2013). Assessment of scapholunate instability and review of evidence for management in the absence of arthritis. *Journal of Hand Surgery: European Volume*, 38(7):727–738.

Clark, D. L. and Von Schroeder, H. P. (2004). Scapholunate ligament injury: The natural history. *Canadian Journal of Surgery*, 47(4):298–299.

Cobb, T. K., Dalley, B. K., Posteraro, R. H., and Lewis, R. C. (1993). Anatomy of the flexor retinaculum. *The Journal of Hand Surgery*, 18(1):91 – 99.

Cohen, M. S. and Taleisnik, J. (1998). Direct Ligamentous Repair of Scapholunate Dissociation with Capsulodesis Augmentation. *Techniques in Hand & Upper Extremity Surgery*, 2(1):18–24.

Cohen, Z. A., McCarthy, D. M., Kwak, S. D., Legrand, P., Fogarasi, F., Ciaccio, E. J., and Ateshian, G. A. (1999). Knee cartilage topography, thickness, and contact areas from mri: in-vitro calibration and in-vivo measurements. *Osteoarthritis and Cartilage*, 7(1):95 – 109.

Colbaugh, R., Seraji, H., and Glass, K. (1990). Adaptive impedance control of redundant manipulators. In *Proceedings of the IEEE Conference on Decision and Control*, volume 5, pages 2661–2666.

Corella, F., Del Cerro, M., Ocampos, M., and Larrainzar-Garijo, R. (2013). Arthroscopic Ligamentoplasty of the Dorsal and Volar Portions of the Scapholunate Ligament. *The Journal of Hand Surgery*, 38(12):2466–2477.

Corella, F., Del Cerro, M., Ocampos, M., Simon de Blas, C., and Larrainzar-Garijo, R. (2017). Arthroscopic Scapholunate Ligament Reconstruction, Volar and Dorsal Reconstruction. *Hand Clinics*, 33(4):687–707.

Craigen, M. A. C. and Stanley, J. K. (1995). Wrist kinematics: Row, column or both? *Journal of Hand Surgery*, 20(2):165–170.

Crisco, J. J., Coburn, J. C., Moore, D. C., Akelman, E., Weiss, A. P. C., and Wolfe, S. W. (2005). In vivo radiocarpal kinematics and the dart thrower's motion. *Journal of Bone and Joint Surgery - Series A*, 87(12 I):2729–2740.

Crisco, J. J., Pike, S., Hulsizer-Galvin, D. L., Akelman, E., Weiss, A. P. C., and Wolfe, S. W. (2003). Carpal Bone Postures and Motions Are Abnormal in Both Wrists of Patients with Unilateral Scapholunate Interosseous Ligament Tears. *Journal of Hand Surgery*, 28(6):926–937.

Crowninshield, R. D. and Brand, R. A. (1981). A physiologically based criterion of muscle force prediction in locomotion. *Journal of Biomechanics*, 14(11):793–801.

Cyriax, E. F. (1926). On the Rotary Movements of the Wrist. *Journal of Anatomy*, 60(Pt 2):199–201.

Dahl, J. W. and Huang, J. I. (2015). Chronic Scapholunate Ligament Injuries. Treatment with Supplemental Fixation. *Hand Clinics*, 31(3):457–465.

Daly, B. T., Werner, F. W., Cavallaro, S. M., Tucci, E. R., and Harley, B. J. (2018). Effect of Push-Up Position on Wrist Joint Pressures in the Intact Wrist and Following Scapholunate Interosseous Ligament Sectioning. *Journal of Hand Surgery*, 43(4):339–345.

Darlis, N. A., Weiser, R. W., and Sotereanos, D. G. (2005). Partial scapholunate ligament injuries treated with arthroscopic debridement and thermal shrinkage. *Journal of Hand Surgery*, 30(5):908–914.

de Lange, A., Kauer, J. M., and Huiskes, R. (1985). Kinematic behavior of the human wrist joint: A roentgenstereophotogrammetric analysis. *Journal of Orthopaedic Research*, 3(1):56–64.

de Roo, M. G., Muurling, M., Dobbe, J. G., Brinkhorst, M. E., Streekstra, G. J., and Strackee, S. D. (2019). A four-dimensional-CT study of in vivo scapholunate rotation axes: possible implications for scapholunate ligament reconstruction. *Journal of Hand Surgery: European Volume*, 44(5):479–487.

De Smet, L., Goeminne, S., and Degreef, I. (2013). Does the "three-ligament tenodesis" procedure restore carpal architecture in static chronic scapholunate dissociation. *Acta Orthopaedica Belgica*, 79(3):271–274.

DeFrate, L. E., Sun, H., Gill, T. J., Rubash, H. E., and Li, G. (2004). In vivo tibiofemoral contact analysis using 3d mri-based knee models. *Journal of Biomechanics*, 37(10):1499 – 1504.

Delp, S. L., Anderson, F. C., Arnold, A. S., Loan, P., Habib, A., John, C. T., Guendelman, E., and Thelen, D. G. (2007). OpenSim: Open-source software to create and analyze dynamic simulations of movement. *IEEE Transactions on Biomedical Engineering*, 54(11):1940–1950.

DeMarco, A. L., Rust, D. A., and Bachus, K. N. (2000). Measuring Contact Pressure and Contact Area in Orthopedic Applications: Fuji Film Vs. Tekscan. *Orthopaedic Research Society*, page 0518.

Deshmukh, S. C., Givissis, P., Belloso, D., Stanley, J. K., and Trail, I. A. (1999). Blatt's capsulodesis for chronic scapholunate dissociation. *The Journal of Hand Surgery: British & European Volume*, 24(2):215–220.

Destot, É. (1926). *The classic. Injuries of the wrist. A radiological study. Translated by Atkinson, F.R.B.*, pages 24–34. Paul E. Hoeber, New York.

Dimitris, C., Werner, F. W., Joyce, D. A., and Harley, B. J. (2015). Force in the Scapholunate Interosseous Ligament During Active Wrist Motion. *Journal of Hand Surgery*, 40(8):1525–1533.

Drewniany, J. J., Palmer, A. K., and Flatt, A. E. (1985). The scaphotrapezial ligament complex: An anatomic and biomechanical study. *Journal of Hand Surgery*, 10(4):492–498.

Dunn, M. J. and Johnson, C. (2001). Static scapholunate dissociation: A new reconstruction technique using a volar and dorsal approach in a cadaver model. *Journal of Hand Surgery*, 26(4):749–754.

Dunning, C. E., Gordon, K. D., King, G. J., and Johnson, J. A. (2003). Development of a motion-controlled in vitro elbow testing system. *Journal of Orthopaedic Research*, 21(3):405–411.

Easterling, K. J. and Wolfe, S. W. (1994). Scaphoid shift in the uninjured wrist. *The Journal of Hand Surgery*, 19(4):604 – 606.

Eckenrode, J. F., Louis, D. S., and Greene, T. L. (1986). Scaphoid-trapezium-trapezoid fusion in the treatment of chronic scapholunate instability. *The Journal of Hand Surgery*, 11(4):497–502.

Edirisinghe, Y., Troupis, J. M., Patel, M., Smith, J., and Crossett, M. (2014). Dynamic motion analysis of dart throwers motion visualized through computerized tomography and calculation of the axis of rotation. *Journal of Hand Surgery (European Volume)*, 39(4):364–372.

El-Shennawy, M., Nakamura, K., Patterson, R. M., and Viegas, S. F. (2001). Three-dimensional kinematic analysis of the second through fifth carpometacarpal joints. *Journal of Hand Surgery*, 26(6):1030–1035.

Elgammal, A. and Lukas, B. (2016). Mid-term results of ligament tenodesis in treatment of scapholunate dissociation: A retrospective study of 20 patients. *Journal of Hand Surgery: European Volume*, 41(1):56–63.

Ellanti, P., Sisodia, G., Al-Ajami, A., Ellanti, P., and Harrington, P. (2014). The modified Brunelli procedure for scapholunate instability: a single centre study. *Hand surgery : an international journal devoted to hand and upper limb surgery and related research : journal of the Asia-Pacific Federation of Societies for Surgery of the Hand*, 19(1):39–42.

Elsaidi, G. A., Ruch, D. S., Kuzma, G. R., and Smith, B. P. (2004). Dorsal wrist ligament insertions stabilize the scapholunate interval: Cadaver study. *Clinical Orthopaedics and Related Research*, 425(425):152–157.

Eng, K., Wagels, M., and Tham, S. K. (2014). Cadaveric scapholunate reconstruction using the ligament augmentation and reconstruction system. *Journal of wrist surgery*, 3(3):192–7.

Erhart, S., Lutz, M., Arora, R., and Schmoelz, W. (2012). Measurement of intraarticular wrist joint biomechanics with a force controlled system. *Medical Engineering and Physics*, 34(7):900–905.

Eschweiler, J., Stromps, J. P., Fischer, M., Schick, F., Rath, B., Pallua, N., and Radermacher, K. (2016a). A biomechanical model of the wrist joint for patient-specific model guided surgical therapy: Part 2. *Proceedings of the Institution of Mechanical Engineers, Part H: Journal of Engineering in Medicine*, 230(4):326–334.

Eschweiler, J., Stromps, J. P., Rath, B., Pallua, N., and Radermacher, K. (2016b). Analysis of wrist bone motion before and after SL-ligament resection. *Biomedizinische Technik*, 61(3):345–357.

Esplugas, M., Garcia-Elias, M., Lluch, A., and Llusá Pérez, M. (2016). Role of muscles in the stabilization of ligament-deficient wrists. *Journal of Hand Therapy*, 29(2):166–174.

Faraway, J. J. (1997). Regression Analysis for a Functional Response. *Technometrics*, 39(3):254–261.

Farr, L. D., Werner, F. W., McGrattan, M. L., Zwerling, S. R., and Harley, B. J. (2013). Wrist tendon forces with respect to forearm rotation. *Journal of Hand Surgery*, 38(1):35–39.

Favre, P., Sheikh, R., Fucentese, S. F., and Jacob, H. A. (2005). An algorithm for estimation of shoulder muscle forces for clinical use. *Clinical Biomechanics*, 20(8):822–833.

Feipel, V. and Rooze, M. (1999). Three-dimensional motion patterns of the carpal bones: An in vivo study using three-dimensional computed tomography and clinical applications. *Surgical and Radiologic Anatomy*, 21(2):125–131.

Ferreira, L. M., Johnson, J. A., and King, G. J. (2010). Development of an active elbow flexion simulator to evaluate joint kinematics with the humerus in the horizontal position. *Journal of Biomechanics*, 43(11):2114–2119.

Fick, R. (1901). Ergebnisse einer Untersuchung der Handbewegungen mit X-strahlen. *Verhandlungen der Anatomischen Gesellschaft*, 15:175–184.

Fischer, K. J., Johnson, J. E., Waller, A. J., McIff, T. E., Bruce Toby, E., and Bilgen, M. (2011). MRI-based modeling for radiocarpal joint mechanics: Validation criteria and results for four specimen-specific models. *Journal of Biomechanical Engineering*, 133(10):101004.

Fisk, G. R. (1970). Carpal instability and the fractured scaphoid. *Annals of the Royal College of Surgeons of England*, 46(2):63–76.

Fisk, G. R. (1984). The wrist. *The Journal of Bone and Joint Surgery. British volume*, 66-B(3):396–407.

Foumani, M., Strackee, S. D., Jonges, R., Blankevoort, L., Zwinderman, A. H., Carelsen, B., and Streekstra, G. J. (2009). In-vivo three-dimensional carpal bone kinematics during flexionextension and radioulnar deviation of the wrist: Dynamic motion versus step-wise static wrist positions. *Journal of biomechanics*, 42(16):2664–2671.

Foumani, M., Strackee, S. D., Van De Giessen, M., Jonges, R., Blankevoort, L., and Streekstra, G. J. (2013). In-vivo dynamic and static three-dimensional joint space distance maps for assessment of cartilage thickness in the radiocarpal joint. *Clinical Biomechanics*, 28(2):151–156.

Frankel, V. H. (1977). The Terry-Thomas Sign. *Clinical Orthopaedics and Related Research*, Nov-Dec(129):321–322.

Franz, A. M., Haidegger, T., Birkfellner, W., Cleary, K., Peters, T. M., and Maier-Hein, L. (2014). Electromagnetic tracking in medicine -A review of technology, validation, and applications. *IEEE Transactions on Medical Imaging*, 33(8):1702–1725.

Fraysse, F., Costi, J. J., Stanley, R. M., Ding, B., McGuire, D., Eng, K., Bain, G. I., and Thewlis, D. (2014). A novel method to replicate the kinematics of the carpus using a six degree-of-freedom robot. *Journal of Biomechanics*, 47(5):1091–1098.

Friedman, S. L., Palmer, A. K., Short, W. H., Mark Levinsohn, E., and Halperin, L. S. (1993). The change in ulnar variance with grip. *Journal of Hand Surgery*, 18(4):713–716.

Fujifilm Corp. (2017). *Prescale Pressure Measurement Film: Instruction Manual*. Midtown West, 7-3, Akasaka 9-chome, Minato-ku, Tokyo, Japan.

Fukubayashi, T. and Kurosawa, H. (1980). The contact area and pressure distribution pattern of the knee: A study of normal and osteoarthrotic knee joints. *Acta Orthopaedica*, 51(1-6):871–879.

Gajendran, V. K., Peterson, B., Slater Jr., R. R., and Szabo, R. M. (2007). Long-Term Outcomes of Dorsal Intercarpal Ligament Capsulodesis for Chronic Scapholunate Dissociation. *Journal of Hand Surgery*, 32(9):1323–1333.

Galley, I., Bain, G. I., and McLean, J. M. (2007). Influence of Lunate Type on Scaphoid Kinematics. *Journal of Hand Surgery*, 32(6):842–847.

Garcia-Elias, M. (1997). Kinetic analysis of carpal stability during grip. *Hand clinics*, 13(1):151–158.

Garcia-Elias, M. (1999). Definition of carpal instability: The Anatomy and Biomechanics Committee of the International Federation of Societies for Surgery of the Hand. *Journal of Hand Surgery*, 24(4):866–867.

Garcia-Elias, M. (2011). Carpal Instability. In Wolfe, S. W., editor, *Green's operative hand surgery.*, volume 1, chapter 15, pages 465–522. Churchill Livingstone, Philadelphia, sixth edition.

Garcia-Elias, M. (2013a). Understanding Wrist Mechanics: A Long and Winding Road. *Journal of Wrist Surgery*, 02(01):005–012.

Garcia-Elias, M. (2013b). Wrist Biomechanics. In Apergis, E. P., editor, *Fracture-Dislocations of the Wrist*, chapter 3, pages 43–58. Springer Science & Business Media, first edition.

Garcia-Elias, M., Alomar Serrallach, X., and Monill Serra, J. (2014). Dart-throwing motion in patients with scapholunate instability: A dynamic four-dimensional computed tomography study. *Journal of Hand Surgery: European Volume*, 39(4):346–352.

Garcia-Elias, M., Cooney, W. P., An, K. N., Linscheid, R. L., and Chao, E. Y. (1989). Wrist kinematics after limited intercarpal arthrodesis. *Journal of Hand Surgery*, 14(5):791–799.

Garcia-Elias, M., Lluch, A., Ferreres, A., Papini-Zorli, I., and Rahimtoola, Z. O. (2005). Treatment of radiocarpal degenerative osteoarthritis by radioscapholunate arthrodesis and distal scaphoidectomy. *Journal of Hand Surgery*, 30(1):8–15.

Garcia-Elias, M. and Lluch, A. L. (2017). Wrist instabilities, misalignments, and dislocations. In Wolfe, S. W., Hotchkiss, R. N., Kozin, S. H., Pederson, W. C., and Cohen, M. S., editors, *Green's Operative Hand Surgery*, chapter 13, pages 418–478. Elsevier, Philadelphia, PA, USA, seventh edition.

Garcia-Elias, M., Lluch, A. L., and Stanley, J. K. (2006). Three-ligament tenodesis for the treatment of scapholunate dissociation: Indications and surgical technique. *Journal of Hand Surgery*, 31(1):125–134.

Garcia-Elias, M., Ribe, M., Rodriguez, J., Cots, M., and Casas, J. (1995). Influence of joint laxity on scaphoid kinematics. *Journal of Hand Surgery*, 20(3):379–382.

Garcia-Elias, M., Smith, D. K., Ruby, L. K., Horii, E., An, K.-N., Linscheid, R. L., Chao, E. Y. S., and Cooney, W. P. (1994). Normal and abnormal carpal kinematics. In Schuind, F., An, K. N., Cooney, W. P., and Garcia-Elias, M., editors, *Advances in the Biomechanics of the Hand and Wrist*, pages 247–253. Springer US, Boston, MA.

Garg, R., Kraszewski, A. P., Stoecklein, H. H., Syrkin, G., Hillstrom, H. J., Backus, S., Lenhoff, M. L., Wolff, A. L., Crisco, J. J., and Wolfe, S. W. (2014). Wrist kinematic coupling and performance during functional tasks: Effects of constrained motion. *The Journal of Hand Surgery*, 39(4):634 – 642.e1.

Garner, B. A. and Pandy, M. G. (2003). Estimation of musculotendon properties in the human upper limb. *Annals of Biomedical Engineering*, 31(2):207–220.

Geissler, W. B. (2013). Arthroscopic management of scapholunate instability. *Journal of wrist surgery*, 2(2):129–135.

Geissler, W. B. (2015). *Wrist and Elbow Arthroscopy*.

Geissler, W. B., Freeland, A. E., Savoie, F. H., Mcintyre, L. W., and Whipple, T. L. (1996). Intracarpal soft-tissue lesions associated with an intra-articular fracture of the distal end of the radius. *Journal of Bone and Joint Surgery - Series A*, 78(3):357–365.

Gellman, H., Kauffman, D., Lenihan, M., Botte, M. J., and Sarmiento, A. (1988). An in vitro analysis of wrist motion: The effect of limited intercarpal arthrodesis and the contributions of the radiocarpal and midcarpal joints. *Journal of Hand Surgery*, 13(3):378–383.

Genda, E. and Horii, E. (2000). Theoretical stress analysis in wrist joint neutral position and functional position. *Journal of Hand Surgery*, 25 B(3):292–295.

Gilford, W., Bolton, R., and Lambrinudi, C. (1943). The mechanism of the wrist joint with special reference to fractures of the scaphoid. *Guys Hosp Rep*, 92:52–59.

Gilula, L. A. (1979). Carpal injuries: Analytic approach and case exercises. *American Journal of Roentgenology*, 133(3):503–517.

Gilula, L. a., Mann, F. a., Dobyns, J. H., and Yin, Y. (2002). Wrist Terminology as Defined by the International Wrist Investigators' Workshop (IWIW). *The Journal of Bone & Joint Surgery*, 84(suppl 1):S1–S66.

Gilula, L. A. and Weeks, P. M. (1978). Post-traumatic ligamentous instabilities of the wrist. *Radiology*, 129(3):641–651.

Gislason, M. K., Nash, D. H., Nicol, A., Kanellopoulos, A., Bransby-Zachary, M., Hems, T., Condon, B., and Stansfield, B. (2009). A Three-dimensional finite element model of maximal grip loading in the human wrist. *Proceedings of the Institution of Mechanical Engineers, Part H: Journal of Engineering in Medicine*, 223(7):849–861.

Goebl, W. and Palmer, C. (2013). Temporal control and hand movement efficiency in skilled music performance. *PLOS ONE*, 8(1):1–10.

Goldfarb, C. A. and Gelberman, R. H. (2010). The Blatt Capsulodesis. In Gelberman, R. H., editor, *Master Techniques in Orthopaedic Surgery: The Wrist*, Master techniques in orthopaedic surgery, chapter 20, pages 223–233. Lippincott Williams & Wilkins, Philadelphia, third edition.

Gonzalez, R. V., Buchanan, T. S., and Delp, S. L. (1997). How muscle architecture and moment arms affect wrist flexion-extension moments. *Journal of Biomechanics*, 30(7):705–712.

Górecki, T. and Smaga, U. (2019). Fdanova: An r software package for analysis of variance for univariate and multivariate functional data. *Comput. Stat.*, 34(2):571597.

Goshtasby, A. (1988). Image registration by local approximation methods. *Image and Vision Computing*, 6(4):255–261.

Goto, A., Moritomo, H., Murase, T., Oka, K., Sugamoto, K., Arimura, T., Masumoto, J., Tamura, S., Yoshikawa, H., and Ochi, T. (2005). In vivo three-dimensional wrist motion analysis using magnetic resonance imaging and volume-based registration. *Journal of Orthopaedic Research*, 23(4):750–756.

Goto, A., Moritomo, H., Murase, T., Oka, K., Sugamoto, K., Arimura, T., Nakajima, Y., Yamazaki, T., Sato, Y., Tamura, S., Yoshikawa, H., and Ochi, T. (2004). In vivo elbow biomechanical analysis during flexion: three-dimensional motion analysis using magnetic resonance imaging. *Journal of Shoulder and Elbow Surgery*, 13(4):441 – 447.

Gould, H. P., Berger, R. A., and Wolfe, S. W. (2015). The origin and meaning of intercalated segment. *Journal of Hand Surgery*, 40(12):2471–2472.

Gray, H. A., Guan, S., and Pandy, M. G. (2017). Accuracy of mobile biplane X-ray imaging in measuring 6-degree-of-freedom patellofemoral kinematics during overground gait. *Journal of Biomechanics*, 57:152–156.

Grood, E. S. and Suntay, W. J. (1983). A joint coordinate system for the clinical description of three-dimensional motions: Application to the knee. *Journal of Biomechanical Engineering*, 105(2):136–144.

Gu, W. (2016). *In vitro measurement and computational modelling of knee-joint contact mechanics during simulated load-bearing activity*. PhD thesis, The University of Melbourne.

Guan, S., Gray, H. A., Keynejad, F., and Pandy, M. G. (2016). Mobile biplane X-Ray imaging system for measuring 3D dynamic joint motion during overground gait. *IEEE Transactions on Medical Imaging*, 35(1):326–336.

Guan, S., Gray, H. A., Schache, A. G., Feller, J., de Steiger, R., and Pandy, M. G. (2017). In vivo six-degree-of-freedom knee-joint kinematics in overground and treadmill walking following total knee arthroplasty. *Journal of Orthopaedic Research*, 35(8):1634–1643.

Güenther, G. B. (1850). *Das Handgelenk in mechanischer, anatomischer und chirurgischer Beziehung*. JA Meissner.

Guo, X., Fan, Y., and Li, Z. M. (2009). Effects of dividing the transverse carpal ligament on the mechanical behavior of the carpal bones under axial compressive load: A finite element study. *Medical Engineering and Physics*, 31(2):188–194.

Gupta, N., Bhatt, N., Bansal, I., Li, S., and Kumar, Y. (2018). Tennis Players and Water Polo Athletes Now Have Something in Common to Talk About: MRI Findings of Extensor Carpi Ulnaris Chronic Subsheath Injury. *Cureus*, 10(4):e2489–e2489.

Haddara, M. (2017). Development of an Active Finger Motion Simulator: With In-Vitro Assessments of Tendon Loads and Joint Kinematics. Master's thesis, The University of Western Ontario.

Hagert, C. (1992). The distal radioulnar joint in relation to the whole forearm. *Clinical orthopaedics and related research*, 275:5664.

Hagert, E., Garcia-Elias, M., Forsgren, S., and Ljung, B. O. (2007). Immunohistochemical Analysis of Wrist Ligament Innervation in Relation to Their Structural Composition. *Journal of Hand Surgery*, 32(1):30–36.

Hagert, E., Lluch, A., and Rein, S. (2015). The role of proprioception and neuromuscular stability in carpal instabilities. *Journal of Hand Surgery: European Volume*, 41(1):94–101.

Hagert, E., Persson, J. K., Werner, M., and Ljung, B. O. (2009). Evidence of Wrist Proprioceptive Reflexes Elicited After Stimulation of the Scapholunate Interosseous Ligament. *Journal of Hand Surgery*, 34(4):642–651.

Haims, A. H., Moore, A. E., Schweitzer, M. E., Morrison, W. B., Deely, D., Culp, R. W., and Forman, H. P. (2004). MRI in the Diagnosis of Cartilage Injury in the Wrist. *American Journal of Roentgenology*, 182(5):1267–1270.

Hara, T., Horii, E., An, K.-N., Cooney, W. P., Linscheid, R. L., and Chao, E. Y. S. (1992). Force distribution across wrist joint: Application of pressure-sensitive conductive rubber. *The Journal of Hand Surgery*, 17(2):339–347.

Hartley, R. I. and Sturm, P. (1997). Triangulation. *Computer Vision and Image Understanding*, 68(2):146–157.

Harvey, E. J., Berger, R. A., Osterman, a. L., Fernandez, D. L., and Weiss, A. P. (2007). Bone-Tissue-Bone Repairs for Scapholunate Dissociation. *Journal of Hand Surgery*, 32(2):256–264.

Haugstvedt, J. R., Berglund, L. J., Neale, P. G., and Berger, R. A. (2001). A dynamic simulator to evaluate distal radio-ulnar joint kinematics. *Journal of Biomechanics*, 34(3):335–339.

Heintz, S. and Gutierrez-Farewik, E. M. (2007). Static optimization of muscle forces during gait in comparison to EMG-to-force processing approach. *Gait and Posture*, 26(2):279–288.

Heller, M. O., Bergmann, G., Deuretzbacher, G., Dürselen, L., Pohl, M., Claes, L., Haas, N. P., and Duda, G. N. (2001). Musculo-skeletal loading conditions at the hip during walking and stair climbing. *Journal of Biomechanics*, 34(7):883–893.

Henke, W. (1859). Die bewegungen der handwurzel. *Zeitschrift fr rationelle Medicin.*, 7:27–41.

Henry, M. (2013). Reconstruction of both volar and dorsal limbs of the scapholunate interosseous ligament. *Journal of Hand Surgery*, 38(8):1625–1634.

Herregodts, S., De Baets, P., Victor, J., and Verstraete, M. (2015). Use of Tekscan pressure sensors for measuring contact pressures in the human knee joint. *International Journal Sustainable Construction & Design*, 6(2):7.

Ho, P.-c., Wong, C., and Tse, W.-l. (2015). Arthroscopic-Assisted Combined Dorsal and Volar Scapholunate Ligament Reconstruction with Tendon Graft for Chronic SL Instability. *Journal of Wrist Surgery*, 04(04):252–263.

Hogan, C. J., McKay, P. L., and Degnan, G. G. (2004). Changes in radiocarpal loading characteristics after proximal row carpectomy. *Journal of Hand Surgery*, 29(6):1109–1113.

Holleran, A. M., Quigley, R. J., Rafijah, G. H., and Lee, T. Q. (2013). Radioscapholunate arthrodesis with excision of the distal scaphoid: Comparison of contact characteristics to the intact wrist. *Journal of Hand Surgery*, 38(4):706–711.

Holzbaur, K. R. S., Murray, W. M., Gold, G. E., and Delp, S. L. (2007). Upper limb muscle volumes in adult subjects. *Journal of Biomechanics*, 40(4):742–749.

Horii, E., An, K. N., and Linscheid, R. L. (1993). Excursion of prime wrist tendons. *The Journal of Hand Surgery*, 18(1):83 – 90.

Horii, E., Garcia-Elias, M., An, K. N., Bishop, A. T., Cooney, W. P., Linscheid, R. L., and Chao, E. Y. (1990). Effect on force transmission across the carpus in procedures used to treat Kienböck's disease. *Journal of Hand Surgery*, 15(3):393–400.

Horii, E., Garcia-Elias, M., An, K. N., Bishop, A. T., Cooney, W. P., Linscheid, R. L., and Chao, E. Y. S. (1991). A kinematic study of luno-triquetral dissociations. *The Journal of Hand Surgery*, 16(2):355–362.

Houvet, P. (2016). Intercarpal fusions: indications, treatment options and techniques. *EFORT Open Reviews*, 1(2):45–51.

Hsu, J. W., Kollitz, K. M., Jegapragasan, M., and Huang, J. I. (2014). Radiographic evaluation of the modified brunelli technique versus a scapholunotriquetral transosseous tenodesis technique for scapholunate dissociation. *Journal of Hand Surgery*, 39(6):1041–1049.

Hudak, P. L., Amadio, P. C., Bombardier, C., Beaton, D., Cole, D., Davis, A., Hawker, G., Katz, J. N., Makela, M., Marx, R. G., Punnett, L., and Wright, J. (1996). Development of an upper extremity outcome measure: The dash (disabilities of the arm, shoulder, and head). *American Journal of Industrial Medicine*, 29(6):602–608.

Hummel, J., Figl, M., Birkfellner, W., Bax, M. R., Shahidi, R., Maurer, C. R., and Bergmann, H. (2006). Evaluation of a new electromagnetic tracking system using a standardized assessment protocol. *Physics in Medicine and Biology*, 51(10).

Humphry, G. M. (1858). *A Treatise on the Human Skeleton (including the Joints)*. Macmillan, Jena.

Hurschler, C., Seehaus, F., Emmerich, J., Kaptein, B. L., and Windhagen, H. (2008). Accuracy of model-based RSA contour reduction in a typical clinical application. *Clinical Orthopaedics and Related Research*, 466(8):1978–1986.

Iaquinto, J. M., Tsai, R., Haynor, D. R., Fassbind, M. J., Sangeorzan, B. J., and Ledoux, W. R. (2014). Marker-based validation of a biplane fluoroscopy system for quantifying foot kinematics. *Medical Engineering and Physics*, 36(3):391–396.

Iglesias, D. J. (2015). Development of an in-vitro passive and active motion Simulator for the investigation of wrist function and Kinematics. Master's thesis, The University of Western Ontario.

Imbriglia, J. E. (2004). Proximal Row Carpectomy. In Berger, R. A. and Weiss, A.-P. C., editors, *Hand surgery*, pages 1331–1337. Lippincott Williams & Wilkins, Philadelphia.

Ishikawa, J. I., Cooney, W. P., Niebur, G., An, K. N., Minami, A., and Kaneda, K. (1999). The effects of wrist distraction on carpal kinematics. *Journal of Hand Surgery*, 24(1):113–120.

Ito, K., Hosoda, K., Shimizu, M., Ikemoto, S., Kume, S., Nagura, T., Imanishi, N., Aiso, S., Jinzaki, M., and Ogihara, N. (2015). Direct assessment of 3D foot bone kinematics using biplanar X-ray fluoroscopy and an automatic model registration method. *Journal of Foot and Ankle Research*, 8(1):1–10.

Iwasaki, N., Genda, E., Barrance, P. J., Minami, A., Kaneda, K., and Chao, E. Y. (1998). Biomechanical analysis of limited intercarpal fusion for the treatment of Kienbock's disease: A three-dimensional theoretical study. *Journal of Orthopaedic Research*, 16(2):256–263.

Izadpanah, A. and Kakar, S. (2016). Acute Scapholunate Ligament Injuries: Current Concepts. *Operative Techniques in Sports Medicine*, 24(2):108–116.

Jackson, W. T., Hefzy, M. S., and Guo, H. (1994). Determination of wrist kinematics using a magnetic tracking device. *Medical Engineering and Physics*, 16(2):123–133.

Jantea, C. L., An, K.-N., Linscheid, R. L., and Cooney, W. P. (1994). *The Role of the Scapho — Trapezial — Trapezoidal Ligament Complex on Scaphoid Kinematics*, pages 345–361. Springer US, Boston, MA.

Johnson, J. A., Rath, D. A., Dunning, C. E., Roth, S. E., and King, G. J. W. (2000). Simulation of elbow and forearm motion in vitro using a load controlled testing apparatus. *Journal of biomechanics*, 33(5):635–639.

Johnson, J. E., Lee, P., McIff, T. E., Toby, E. B., and Fischer, K. J. (2013). Scapholunate ligament injury adversely alters in vivo wrist joint mechanics: An MRI-based modeling study. *Journal of Orthopaedic Research*, 31(9):1455–1460.

Johnson, R. P. (1980). The acutely injured wrist and its residuals. *Clinical Orthopaedics and Related Research*, NO 149:33–44.

Johnston, H. M. (1907). Varying Positions of the Carpal Bones in the Different Movements at the Wrist: Part I. *Journal of anatomy and physiology*, 41(Pt 4):280–28092.

Jones, W. A. (1988). Beware the sprained wrist. The incidence and diagnosis of scapholunate instability. *Bone & Joint Journal*, 70-B(2):293–297.

Jung, J. M., Baek, G. H., Kim, J. H., Lee, Y. H., and Chung, M. S. (2001). Changes in ulnar variance in relation to forearm rotation and grip. *The Journal of Bone and Joint Surgery. British volume*, 83-B(7):1029–1033.

Kamal, R. N., Starr, A., and Akelman, E. (2016). Carpal Kinematics and Kinetics. *Journal of Hand Surgery*, 41(10):1011–1018.

Kamnerdnakta, S., Kelley, B. P., and Chung, K. C. (2018). Procedure 48 - total wrist arthroplasty. In Chung, K. C., editor, *Operative Techniques: Hand and Wrist Surgery*, pages 450 – 462. Elsevier, third edition edition.

Kang, L., Dy, C., Wei, M., Hearns, K., and Carlson, M. (2018). Cadaveric Testing of a Novel Scapholunate Ligament Reconstruction. *Journal of Wrist Surgery*, 07(02):141–147.

Kaptein, B. L., Shelburne, K. B., Torry, M. R., and Erik Giphart, J. (2011). A comparison of calibration methods for stereo fluoroscopic imaging systems. *Journal of Biomechanics*, 44(13):2511–2515.

Kauer, J. M. (1974). The interdependence of carpal articulation chains. *Acta Anatomica*, 88(4):481–501.

Kauer, J. M. (1980). Functional anatomy of the wrist. *Clinical Orthopaedics and Related Research*, NO 149(149):9–20.

Kauer, J. M. (1986). The Mechanism of the Carpal Joint. *Clinical Orthopaedics and Related Research*, 202:16–26.

Kaufmann, R., Pfaeffle, J., Blankenhorn, B., Stabile, K., Robertson, D., and Goitz, R. (2005). Kinematics of the midcarpal and radiocarpal joints in radioulnar deviation: An in vitro study. *Journal of Hand Surgery*, 30(5):937–942.

Kaufmann, R. A., Pfaeffle, H. J., Blankenhorn, B. D., Stabile, K., Robertson, D., and Goitz, R. (2006). Kinematics of the Midcarpal and Radiocarpal Joint in Flexion and Extension: An In Vitro Study. *Journal of Hand Surgery*, 31(7):1142–1148.

Kazuki, K., Kusunoki, M., and Shimazu, A. (1991). Pressure distribution in the radiocarpal joint measured with a densitometer designed for pressure-sensitive film. *The Journal of Hand Surgery*, 16(3):401–408.

Kelley, B. P. and Chung, K. C. (2018). Procedure 49 - total wrist fusion. In Chung, K. C., editor, *Operative Techniques: Hand and Wrist Surgery*, pages 463 – 470. Elsevier, third edition edition.

Kijima, Y. and Viegas, S. F. (2009). Wrist Anatomy and Biomechanics. *Journal of Hand Surgery*, 34(8):1555–1563.

Kim, B. J., Kovacevic, D., Lee, Y. M., Seol, J. H., and Kim, M. S. (2016). The role of lunate morphology on scapholunate instability and fracture location in patients treated for scaphoid nonunion. *Clinics in Orthopedic Surgery*, 8(2):175–180.

King, G. J., Pillon, C. L., and Johnson, J. A. (2000). Effect of in vitro testing over extended periods on the low-load mechanical behaviour of dense connective tissues. *Journal of Orthopaedic Research*, 18(4):678–681.

Kitay, A. and Wolfe, S. W. (2012). Scapholunate instability: Current concepts in diagnosis and management. *Journal of Hand Surgery*, 37(10):2175–2196.

Kleinman, W. B. and Carroll IV, C. (1990). Scapho-trapezio-trapezoid arthrodesis for treatment of chronic static and dynamic scapho-lunate instability: A 10-year perspective on pitfalls and complications. *Journal of Hand Surgery*, 15(3):408–414.

Kleinman, W. B., Steichen, J. B., and Strickland, J. W. (1982). Management of chronic rotary subluxation of the scaphoid by scapho-trapezio-trapezoid arthrodesis. *Journal of Hand Surgery*, 7(2):125–136.

Knorlein, B. J., Baier, D. B., Gatesy, S. M., Laurence-Chasen, J. D., and Brainerd, E. L. (2016). Validation of XMALab software for Marker-based XROMM. *Journal of Experimental Biology*, 219(23):3701–3711.

Kobayashi, M., Berger, R. A., Nagy, L., Linscheid, R. L., Uchiyama, S., Ritt, M., and An, K.-N. N. (1997a). Normal kinematics of carpal bones: A three-dimensional analysis of carpal bone motion relative to the radius. *Journal of Biomechanics*, 30(8):787–793.

Kobayashi, M., Garcia-Elias, M., Nagy, L., Ritt, M. J., An, K.-N., Cooney, W. P., and Linscheid, R. L. (1997b). Axial loading induces rotation of the proximal carpal row bones around unique screw-displacement axes. *Journal of Biomechanics*, 30(11):1165 – 1167.

Konopka, G. and Chim, H. (2018). Optimal management of scapholunate ligament injuries. *Orthopedic Research and Reviews*, 10:41–54.

Lalone, E. A., Grewal, R., King, G. W., and MacDermid, J. C. (2015). Evaluation of an Image-Based Tool to Examine the Effect of Fracture Alignment and Joint Congruency on Outcomes after Wrist Fracture. *The Open Orthopaedics Journal*, 9(1):168–178.

Lalone, E. A., McDonald, C. P., Ferreira, L. M., Peters, T. M., King, G. W., and Johnson, J. A. (2013). Development of an image-based technique to examine joint congruency at the elbow. *Computer Methods in Biomechanics and Biomedical Engineering*, 16(3):280–290.

Landsmeer, J. M. F. (1961). Studies in the anatomy of articulation. i. the equilibrium of the "intercalated" bone. *Acta morphologica Neerlando-Scandinavica*, 3:287303.

Larsen, C. F., Jacoby, R. A., and McCabe, S. J. (1997). Nonunion rates of limited carpal arthrodesis: A meta-analysis of the literature. *Journal of Hand Surgery*, 22(1):66–73.

Lavernia, C. J., Cohen, M. S., and Taleisnik, J. (1992). Treatment of scapholunate dissociation by ligamentous repair and capsulodesis. *The Journal of Hand Surgery*, 17(2):354–359.

Lawand, A. and Foulkes, G. D. (2003). The "clenched pencil" view: A modified clenched fist scapholunate stress view. *Journal of Hand Surgery*, 28(3):414–418.

Ledoux, P., Lamblin, D., Wuilbaut, A., and Schuind, F. (2008). A finite-element analysis of kienböck's disease. *Journal of Hand Surgery: European Volume*, 33(3):286–291.

Lee, D. J. and Elfar, J. C. (2015). Carpal Ligament Injuries, Pathomechanics, and Classification. *Hand Clinics*, 31(3):389–398.

Lee, S. K., Model, Z., Desai, H., Hsu, P., Paksima, N., and Dhaliwal, G. (2015). Association of lesions of the scapholunate interval with arthroscopic grading of scapholunate instability via the Geissler classification. *Journal of Hand Surgery*, 40(6):1083–1087.

Lee, S. K., Park, J., Baskies, M., Forman, R., Yildirim, G., and Walker, P. (2010). Differential Strain of the Axially Loaded Scapholunate Interosseus Ligament. *Journal of Hand Surgery*, 35(2):245–251.

Lee, S. K., Zlotolow, D. A., Sapienza, A., Karia, R., and Yao, J. (2014). Biomechanical comparison of 3 methods of scapholunate ligament reconstruction. *Journal of Hand Surgery*, 39(4):643–650.

Lee, T. Q., Dettling, J., Sandusky, M. D., and McMahon, P. J. (1999). Age related biomechanical properties of the glenoid-anterior band of the inferior glenohumeral ligament-humerus complex. *Clinical Biomechanics*, 14(7):471–476.

Lenaerts, G., De Groote, F., Demeulenaere, B., Mulier, M., Van der Perre, G., Spaepen, A., and Jonkers, I. (2008). Subject-specific hip geometry affects predicted hip joint contact forces during gait. *Journal of Biomechanics*, 41(6):1243–1252.

Leng, S., Zhao, K., Qu, M., An, K.-N., Berger, R., and McCollough, C. H. (2011). Dynamic ct technique for assessment of wrist joint instabilities. *Medical Physics*, 38(S1):S50–S56.

Liau, J. J., Hu, C. C., Cheng, C. K., Huang, C. H., and Lo, W. H. (2001). The influence of inserting a Fuji pressure sensitive film between the tibiofemoral joint of knee prosthesis on actual contact characteristics. *Clinical Biomechanics*, 16(2):160–166.

Lichtman, D. M., Schneider, J. R., Swafford, A. R., and Mack, G. R. (1981). Ulnar midcarpal instabilityClinical and laboratory analysis. *Journal of Hand Surgery*, 6(5):515–523.

Liggins, A. B. (1997). *The practical application of Fuji Prescale pressure-sensitive film*, pages 173–189. Springer US, Boston, MA.

Liggins, A. B. and Finlay, J. B. (1992). Recording contact areas and pressures in joint interfaces. In Little, E. G., editor, *Experimental mechanics: technology transfer between high tech engineering and biomechanics : proceedings of the International Conference on Experimental Mechanics*, pages 71–88. Amsterdam.

Liggins, A. B., Hardie, W. R., and Finlay, J. B. (1995). The spatial and pressure resolution of fuji pressure-sensitive film. *Experimental Mechanics*, 35(2):166–173.

Liggins, A. B., Stranart, J. C. E., Finlay, J. B., and Rorabeck, C. H. (1992). Calibration and Manipulation of Data from Fuji Pressure-sensitive Film. In Little, E. G., editor, *Experimental mechanics : technology transfer between high tech engineering and biomechanics : proceedings of the International*

Conference on Experimental Mechanics, pages 61–70. Elsevier Science Publishers, Amsterdam.

Lindley, P. B. (1966). Load-compression relationships of rubber units. *Journal of Strain Analysis*, 1(3):190–195.

Links, A. C., Chin, S. H., Waitayawinyu, T., and Trumble, T. E. (2008). Scapholunate Interosseous Ligament Reconstruction: Results With a Modified Brunelli Technique Versus Four-Bone Weave. *Journal of Hand Surgery*, 33(6):850–856.

Linscheid, R. and Dobyns, J. (1992a). Treatment of scapholunate dissociation. rotatory subluxation of the scaphoid. *Hand clinics*, 8(4):645652.

Linscheid, R. L. (1986). Kinematic considerations of the wrist. *Clinical Orthopaedics and Related Research*, NO. 202(202):27–39.

Linscheid, R. L., An, K. N., and Gross, R. M. (1991). Quantitative analysis of the intrinsic muscles of the hand. *Clinical Anatomy*, 4(4):265–284.

Linscheid, R. L. and Dobyns, J. H. (1992b). Treatment of scapholunate dissociation: Rotatory subluxation of the scaphoid. *Hand Clinics*, 8(4):645–652.

Linscheid, R. L. and Dobyns, J. H. (2002). Dynamic carpal stability. *The Keio Journal of Medicine*, 51(3):140–147.

Linscheid, R. L., Dobyns, J. H., Beabout, J. W., and Bryan, R. S. (1972). Traumatic instability of the wrist. *The Journal of Bone and Joint Surgery American Volume*, 54(8):1612–1632.

Linscheid, R. L., Dobyns, J. H., Beckenbaugh, R. D., Cooney, W. P., and Wood, M. B. (1983). Instability patterns of the wrist. *The Journal of Hand Surgery*, 8(5, Part 2):682 – 686.

Loisel, F., Durand, S., Persohn, S., Aubry, S., Lepage, D., Bonnet, X., and Skalli, W. (2020). Scapholunate kinematics after flexible anchor repair. *Medical Engineering and Physics*, 75:59–64.

Loren, G. J. and Lieber, R. L. (1995). Tendon biomechanical properties enhance human wrist muscle specialization. *Journal of Biomechanics*, 28(7):791–799.

Loren, G. J., Shoemaker, S. D., Burkholder, T. J., Jacobson, M. D., Fridén, J., and Lieber, R. L. (1996). Human wrist motors: Biomechanical design and application to tendon transfers. *Journal of Biomechanics*, 29(3):331–342.

Lösch, A., Eckstein, F., Haubner, M., and Englmeier, K.-H. (1997). A non-invasive technique for 3-dimensional assessment of articular cartilage thickness based on mri part 1: Development of a computational method. *Magnetic Resonance Imaging*, 15(7):795 – 804.

Luo, Z. P., Berglund, L. J., and An, K. N. (1998). Validation of F-scan pressure sensor system: A technical note. *Journal of Rehabilitation Research and Development*, 35(2):186–191.

Macconaill, M. A. (1941). The mechanical anatomy of the carpus and its bearings on some surgical problems. *Journal of anatomy*, 75(Pt 2):166–175.

Majima, M., Horii, E., Matsuki, H., Hirata, H., and Genda, E. (2008). Load Transmission Through the Wrist in the Extended Position. *Journal of Hand Surgery*, 33(2):182–188.

Marai, G. E., Laidlaw, D. H., Demiralp, C., Andrews, S., Grimm, C. M., and Crisco, J. J. (2004). Estimating joint contact areas and ligament lengths from bone kinematics and surfaces. *IEEE Transactions on Biomedical Engineering*, 51(5):790–799.

Marouane, H., Shirazi-Adl, A., and Adouni, M. (2016). Alterations in knee contact forces and centers in stance phase of gait: A detailed lower extremity musculoskeletal model. *Journal of Biomechanics*, 49(2):185–192.

Masquelet, A. C., Strube, F., and Nordin, J. Y. (1993). The Isolated Scapho-Trapezio-Trapezoid Ligament Injury: Diagnosis and surgical treatment in four cases. *Journal of Hand Surgery*, 18(6):730–735.

Mat Jais, I. S. and Tay, S. C. (2017a). Kinematic analysis of the scaphoid using gated four-dimensional CT. *Clinical Radiology*, 72(9):794.e1–794.e9.

Mat Jais, I. S. and Tay, S. C. (2017b). Kinematic analysis of the scaphoid using gated four-dimensional CT. *Clinical Radiology*, 72(9):794.e1–794.e9.

MathWorks, I. (2019a). *Computer Vision Toolbox*. Natick, Massachusetts, United States.

MathWorks, I. (2019b). *Image Processing Toolbox*. Natick, Massachusetts, United States.

Matsuki, H., Horii, E., Majima, M., Genda, E., Koh, S., and Hirata, H. (2009). Scaphoid nonunion and distal fragment resection: Analysis with three-dimensional rigid body spring model. *Journal of Orthopaedic Science*, 14(2):144–149.

Mayfield, J. K. (1984). Patterns of injury to carpal ligaments. A spectrum. *Clinical Orthopaedics and Related Research*, NO. 187(187):36–42.

Mayfield, J. K., Johnson, R. P., and Kilcoyne, R. F. (1976). The ligaments of the human wrist and their functional significance. *The Anatomical Record*, 186(3):417–428.

Mayfield, J. K., Johnson, R. P., and Kilcoyne, R. K. (1980). Carpal dislocations: Pathomechanics and progressive perilunar instability. *Journal of Hand Surgery*, 5(3):226–241.

McCann, P., Wootten, M., Kadaba, M., and Bigliani, L. (1993). A kinematic and electromyographic study of shoulder rehabilitation exercises. *Clinical orthopaedics and related research*, (288):179188.

McClelland, J. A., Webster, K. E., Feller, J. A., and Menz, H. B. (2011). Knee kinematics during walking at different speeds in people who have undergone total knee replacement. *The Knee*, 18(3):151 – 155.

McLean, J. M., Bain, G. I., Watts, A. C., Mooney, L. T., Turner, P. C., and Moss, M. (2009). Imaging recognition of morphological variants at the midcarpal joint. *The Journal of Hand Surgery*, 34(6):1044 – 1055.

Meade, T. D., Schneider, L. H., and Cherry, K. (1990). Radiographic analysis of selective ligament sectioning at the carpal scaphoid: A cadaver study. *Journal of Hand Surgery*, 15(6):855–862.

Messina, J., Van Overstraeten, L., Luchetti, R., Fairplay, T., and Mathoulin, C. (2013). The EWAS Classification of Scapholunate Tears: An Anatomical Arthroscopic Study. *Journal of Wrist Surgery*, 02(02):105–109.

Michelotti, B. and Chung, K. C. (2018). Procedure 21 - scapholunate ligament repair. In Chung, K. C., editor, *Operative Techniques: Hand and Wrist Surgery*, pages 180 – 191. Elsevier, third edition edition.

Minami, A., Kato, H., and Iwasaki, N. (2003). Treatment of scapholunate dissociation: Ligamentous repair associated with modified dorsal capsulodesis. *Hand Surgery*, 08(01):1–6.

Miranda, D. L., Schwartz, J. B., Loomis, A. C., Brainerd, E. L., Fleming, B. C., and Crisco, J. J. (2011). Static and Dynamic Error of a Biplanar Videoradiography System Using Marker-Based and Markerless Tracking Techniques. *Journal of Biomechanical Engineering*, 133(12):1–8.

Mitsuyasu, H., Patterson, R. M., Shah, M. A., Buford, W. L., Iwamoto, Y., and Viegas, S. F. (2004). The role of the dorsal intercarpal ligament in dynamic and static scapholunate instability. *The Journal of Hand Surgery*, 29(2):279–288.

Mizuseki, T. and Ikuta, Y. (1989). The dorsal carpal ligaments: Their anatomy and function. *Journal of Hand Surgery*, 14(1):91–98.

Modenese, L., Phillips, A. T., and Bull, A. M. (2011). An open source lower limb model: Hip joint validation. *Journal of Biomechanics*, 44(12):2185–2193.

Moojen, T. M., Snel, J. G., Ritt, M. J., Kauer, J. M., Venema, H. W., Bos, K. E., and Den Heeten, G. J. (2002). Three-dimensional carpal kinematics in vivo. *Clinical Biomechanics*, 17(7):506–514.

Mootanah, R., Imhauser, C. W., Reisse, F., Carpanen, D., Walker, R. W., Koff, M. F., Lenhoff, M. W., Rozbruch, S. R., Fragomen, A. T., Dewan, Z., Kirane, Y. M., Cheah, K., Dowell, J. K., and Hillstrom, H. J. (2014). Development and validation of a computational model of the knee joint for the evaluation of surgical treatments for osteoarthritis. *Computer Methods in Biomechanics and Biomedical Engineering*, 17(13):1502–1517.

Moran, S. L., Cooney, W. P., Berger, R. A., and Strickland, J. (2005). Capsulodesis for the treatment of chronic scapholunate instability. *Journal of Hand Surgery*, 30(1):16–23.

Moran, S. L., Ford, K. S., Wulf, C. A., and Cooney, W. P. (2006). Outcomes of Dorsal Capsulodesis and Tenodesis for Treatment of Scapholunate Instability. *Journal of Hand Surgery*, 31(9):1438–1446.

Morgenroth, D. C., Orendurff, M. S., Shakir, A., Segal, A., Shofer, J., and Czerniecki, J. M. (2010). The relationship between lumbar spine kinematics during gait and low-back pain in transfemoral amputees. *American Journal of Physical Medicine and Rehabilitation*, 89(8):635–643.

Morin, E. L., Bryant, J. T., Reid, S. A., and Whiteside, R. A. (2000). Calibration issues of tekscan systems for human pressure assessment. *NATO-RTO Meeting Proceedings: MP-056*, 24:1–7.

Moritomo, H., Apergis, E. P., Herzberg, G., Werner, F. W., Wolfe, S. W., and Garcia-Elias, M. (2007). 2007 IFSSH Committee Report of Wrist Biomechanics Committee: Biomechanics of the So-Called Dart-Throwing Motion of the Wrist. *Journal of Hand Surgery*, 32(9):1447–1453.

Moritomo, H., Goto, A., Sato, Y., Sugamoto, K., Murase, T., and Yoshikawa, H. (2003). The triquetrum-hamate joint: An anatomic and in vivo three-dimensional kinematic study. *Journal of Hand Surgery*, 28(5):797–805.

Moritomo, H., Murase, T., Goto, A., Oka, K., Sugamoto, K., and Yoshikawa, H. (2004). Capitate-based kinematics of the midcarpal joint during wrist radioulnar deviation: An in vivo three-dimensional motion analysis. *Journal of Hand Surgery*, 29(4):668–675.

Moritomo, H., Murase, T., Goto, A., Oka, K., Sugamoto, K., and Yoshikawa, H. (2006). In vivo three-dimensional kinematics of the midcarpal joint of the wrist. *Journal of Bone and Joint Surgery - Series A*, 88(3):611–621.

Moritomo, H., Viegas, S. F., Elder, K. W., Nakamura, K., DaSilva, M. F., Boyd, N. L., and Patterson, R. M. (2000a). Scaphoid nonunions: A 3-dimensional analysis of patterns of deformity. *Journal of Hand Surgery*, 25(3):520–528.

Moritomo, H., Viegas, S. F., Nakamura, K., DaSilva, M. F., and Patterson, R. M. (2000b). The scaphotrapezio-trapezoidal joint. Part 1: An anatomic and radiographic study. *Journal of Hand Surgery*, 25(5):899–910.

Mozingo, J. D., Akbari Shandiz, M., Marquez, F. M., Schueler, B. A., Holmes, D. R., McCollough, C. H., and Zhao, K. D. (2018). Validation of imaging-based quantification of glenohumeral joint kinematics using an unmodified clinical biplane fluoroscopy system. *Journal of Biomechanics*, 71:306–312.

Mroczek, K. (2015). USB FIFO interface for FPGA based DAQ applications. *Proceedings of the 2015 IEEE 8th International Conference on Intelligent Data Acquisition and Advanced Computing Systems: Technology and Applications, IDAACS 2015*, 2(September):666–671.

Mrquez-Florez, K., Vergara-Amador, E., Gaviln-Alfonso, M., and Garzn-Alvarado, D. (2016). Load distribution on the radio-carpal joint for carpal

arthrodesis. *Computer Methods and Programs in Biomedicine*, 127:204 – 215.

Mugnai, R., Della Rosa, N., and Tarallo, L. (2016). Scapholunate interosseous ligament injury in professional volleyball players. *Hand Surgery and Rehabilitation*, 35(5):341–347.

Mühldorfer-Fodor, M., Reger, A., Schoonhoven, J. V., Mittlmeier, T., and Prommersberger, K. J. (2015). The effect of midcarpal versus total wrist fusion on the hand's load distribution during gripping. *Journal of Hand Surgery*, 40(11):2183–2190.

Muscolino, J. E. (2011). *Kinesiology: the skeletal system and muscle function*. Mosby, St. Louis, second edition.

Mutimer, J., Green, J., and Field, J. (2008). Comparison of mri and wrist arthroscopy for assessment of wrist cartilage. *Journal of Hand Surgery (European Volume)*, 33(3):380–382.

Nagao, S., Patterson, R. M., Buford, W. L., Andersen, C. R., Shah, M. A., and Viegas, S. F. (2005). Three-dimensional description of ligamentous attachments around the lunate. *Journal of Hand Surgery*, 30(4):685–692.

Nagy, L. and Büchler, U. (1997). Long-term results of radioscapholunate fusion following fractures of the distal radius. *Journal of Hand Surgery: European Volume*, 22(6):705–710.

Nakamura, K., Beppu, M., Patterson, R. M., Hanson, C. A., Hume, P. J., and Viegas, S. F. (2000). Motion analysis in two dimensions of radial-ulnar deviation of type I versus type II lunates. *Journal of Hand Surgery*, 25(5):877–888.

Nakamura, T., Cooney, W. P., Lui, W. H., Haugstvedt, J. R., Zhao, K. D., Berglund, L., and An, K. N. (2001). Radial styloidectomy: A biomechanical study on stability of the wrist joint. *Journal of Hand Surgery*, 26(1):85–93.

Nathan, R. and Blatt, G. (2000). Rotary subluxation of the scaphoid: Revisited. *Hand Clinics*, 16(3):417–431.

Navacchia, A., Rullkoetter, P. J., Schütz, P., List, R. B., Fitzpatrick, C. K., and Shelburne, K. B. (2016). Subject-specific modeling of muscle force and knee contact in total knee arthroplasty. *Journal of Orthopaedic Research*, 34(9):1576–1587.

Navarro, A. (1921). Luxaciones del carpo. In *Anales de la Facultad de Medicina*, volume 6, pages 113–141.

Nelson, D. L., Mitchell, M. A., Groszewski, P. G., Pennick, S. L., and Manske, P. R. (1994). *Wrist Range of Motion in Activities of Daily Living*, pages 329–334. Springer US, Boston, MA.

Netter, F. H. (2014). *Atlas of human anatomy*. Saunders, Philadelphia, sixth edition.

Neu, C. P., Crisco, J. J., and Wolfe, S. W. (2001). In vivo kinematic behavior of the radio-capitate joint during wrist flexion-extension and radio-ulnar deviation. *Journal of Biomechanics*, 34(11):1429–1438.

Neu, C. P., McGovern, R. D., and Crisco, J. J. (2000). Kinematic accuracy of three surface registration methods in a three-dimensional wrist bone study. *Journal of Biomechanical Engineering*, 122(5):528–533.

Neumann, D. A. (2010). *Kinesiology of the Musculoskeletal System: Foundation for Rehabilitation*. Mosby, St. Louis, second edition.

Nienstedt, F. (2013). Treatment of static scapholunate instability with modified Brunelli tenodesis: Results over 10 years. *Journal of Hand Surgery*, 38(5):887–892.

Nishiwaki, M., Welsh, M., Gammon, B., Ferreira, L. M., Johnson, J. A., and King, G. J. (2014). Distal radioulnar joint kinematics in simulated dorsally angulated distal radius fractures. *Journal of Hand Surgery*, 39(4):656–663.

Noehren, B., Scholz, J., and Davis, I. (2011). The effect of real-time gait retraining on hip kinematics, pain and function in subjects with patellofemoral pain syndrome. *British Journal of Sports Medicine*, 45(9):691–696.

Nowak, M. D. (1991). Material Properties of Ligaments. In An, K.-N., Berger, R. A., and Cooney, W. P., editors, *Biomechanics of the Wrist Joint*, chapter 8, pages 139–156. Springer-Verlag New York, Rochester, 1st edition.

Oda, M., Hashizume, H., Miyake, T., Inoue, H., and Nagayama, N. (2000). A stress distribution analysis of a ceramic lunate replacement for kienbck's disease. *The Journal of Hand Surgery: British & European Volume*, 25(5):492 – 498.

Ogawa, T., Tanaka, T., Yanai, T., Kumagai, H., and Ochiai, N. (2013). Analysis of soft tissue injuries associated with distal radius fractures. *BMC Sports Science, Medicine and Rehabilitation*, 5(1):1–4.

O'Meeghan, C. J., Stuart, W., Mamo, V., Stanley, J. K., and Trail, I. A. (2003). The natural history of an untreated isolated scapholunate interosseus ligament injury. *Journal of Hand Surgery*, 28(4):307–310.

Omori, S., Moritomo, H., Omokawa, S., Murase, T., Sugamoto, K., and Yoshikawa, H. (2013). In vivo 3-dimensional analysis of dorsal intercalated segment instability deformity secondary to scapholunate dissociation: A preliminary report. *Journal of Hand Surgery*, 38(7):1346–1355.

Otto, J. K., Brown, T. D., and Callaghan, J. J. (1999). Static and dynamic response of a multiplexed-array piezoresistive contact sensor. *Experimental Mechanics*, 39(4):317–323.

Padmore, C., Stoesser, H., Langohr, G. D., Johnson, J., and Suh, N. (2019). Carpal Kinematics following Sequential Scapholunate Ligament Sectioning. *Journal of Wrist Surgery*, 08(02):124–131.

Palmer, A. K., Dobyns, J. H., and Linscheid, R. L. (1978). Management of post-traumatic instability of the wrist secondary to ligament rupture. *Journal of Hand Surgery*, 3(6):507–532.

Palmer, A. K., Glisson, R. R., and Werner, F. W. (1982). Ulnar variance determination. *Journal of Hand Surgery*, 7(4):376–379.

Palmer, A. K. and Werner, F. W. (1981). The triangular fibrocartilage complex of the wrist–anatomy and function. *The Journal of Hand Surgery*, 6(2):153–162.

Palmer, A. K. and Werner, F. W. (1984). Biomechanics of the distal radioulnar joint. *Clinical Orthopaedics and Related Research*, NO. 187(187):26–35.

Palmer, A. K., Werner, F. W., Murphy, D., and Glisson, R. (1985). Functional wrist motion: A biomechanical study. *Journal of Hand Surgery*, 10(1):39–46.

Panchal-Kildare, S. and Malone, K. (2013). Skeletal anatomy of the hand. *Hand Clinics*, 29(4):459–471.

Pang, E. Q., Douglass, N., and Kamal, R. N. (2018). Association of Lunate Morphology With Carpal Instability in Scapholunate Ligament Injury. *Hand*, 13(4):418–422.

Pappou, I. P., Basel, J., and Deal, D. N. (2013). Scapholunate ligament injuries: A review of current concepts. *Hand*, 8(2):146–156.

Patterson, R. and Viegas, S. F. (1995). Biomechanics of the Wrist. *Journal of Hand Therapy*, 8(2):97–105.

Patterson, R. M., Nicodemus, C. L., Viegas, S. F., Elder, K. W., and Rosenblatt, J. (1998). High-speed, three-dimensional kinematic analysis of the normal wrist. *Journal of Hand Surgery*, 23(3):446–453.

Patterson, R. M., Williams, L., Andersen, C. R., Koh, S., and Viegas, S. F. (2007). Carpal Kinematics During Simulated Active and Passive Motion of the Wrist. *Journal of Hand Surgery*, 32(7):1013–1019.

Pauchard, N., Dederichs, A., Segret, J., Barbary, S., Dap, F., and Dautel, G. (2013). The role of three-ligament tenodesis in the treatment of chronic scapholunate instability. *Journal of Hand Surgery: European Volume*, 38(7):758–766.

Pérez, A. J., Jethanandani, R. G., Vutescu, E. S., Meyers, K. N., Lee, S. K., and Wolfe, S. W. (2019). Role of Ligament Stabilizers of the Proximal Carpal Row in Preventing Dorsal Intercalated Segment Instability: A Cadaveric Study. *Journal of Bone and Joint Surgery - American Volume*, 101(15):1388–1396.

Petrie, S., Collins, J., Solomonow, M., Wink, C., and Chuinard, R. (1997). Mechanoreceptors in the palmar wrist ligaments. *Journal of Bone and Joint Surgery - Series B*, 79(3):494–496.

Pevny, T., Rayan, G. M., and Egle, D. (1995). Ligamentous and tendinous support of the pisiform, anatomic and biomechanical study. *The Journal of Hand Surgery*, 20(2):299 – 304.

Pfister, A., West, A. M., Bronner, S., and Noah, J. A. (2014). Comparative abilities of microsoft kinect and vicon 3d motion capture for gait analysis. *Journal of Medical Engineering & Technology*, 38(5):274–280.

Pisano, S. M., Peimer, C. A., Wheeler, D. R., and Sherwin, F. (1991). Scaphocapitate intercarpal arthrodesis. *Journal of Hand Surgery*, 16(2):328–333.

Pollock, P. J., Sieg, R. N., Baechler, M. F., Scher, D., Zimmerman, N. B., and Dubin, N. H. (2010). Radiographic Evaluation of the Modified Brunelli Technique Versus the Blatt Capsulodesis for Scapholunate Dissociation in a Cadaver Model. *The Journal of Hand Surgery*, 35(10):1589–1598.

Porter, M. and Stockley, I. (1984). Functional index: a numerical expression of post-traumatic wrist function. *Injury*, 16(3):188 – 192.

Preuss, R. A. and Popovic, M. R. (2010). Three-dimensional spine kinematics during multidirectional, target-directed trunk movement in sitting. *Journal of Electromyography and Kinesiology*, 20(5):823 – 832.

Prilutsky, B. I., Herzog, W., and Allinger, T. L. (1997). Forces of individual cat ankle extensor muscles during locomotion predicted using static optimization. *Journal of Biomechanics*, 30(10):1025–1033.

Pulos, N. and Bozentka, D. J. (2015). Carpal Ligament Anatomy and Biomechanics. *Hand Clinics*, 31(3):381–387.

Rainbow, M. J., Wolff, A. L., Crisco, J. J., and Wolfe, S. W. (2016). Functional kinematics of the wrist. *Journal of Hand Surgery: European Volume*, 41(1):7–21.

Rayhack, J. M., Linscheid, R. L., Dobyns, J. H., and Smith, J. H. (1987). Posttraumatic ulnar translation of the carpus. *The Journal of Hand Surgery*, 12(2):180–189.

Redjal, H. R. and Rafijah, G. H. (2009). Perilunate Injuries of the Wrist. In Slutsky, D. J. and Osterman, A. L., editors, *Fractures and Injuries of the Distal Radius and Carpus: the cutting edge.*, chapter 43, pages 425–435. W.B. Saunders, Philadelphia, 1st edition.

Reinschmidt, C. and van den Bogert, T. (1997). KineMat: a MATLAB toolbox for three-dimensional kinematic analyses. *Calgary, Canada: Human Performance Laboratory, The University of Calgary.*

Rhee, P. C., Moran, S. L., and Shin, A. Y. (2009). Association Between Lunate Morphology and Carpal Collapse in Cases of Scapholunate Dissociation. *Journal of Hand Surgery*, 34(9):1633–1639.

Ricci, F. P. F., Santiago, P. R. P., Zampar, A. C., Pinola, L. N., and Fonseca, M. d. C. R. (2015). Upper extremity coordination strategies depending on task demand during a basic daily activity. *Gait and Posture*, 42(4):472–478.

Rikli, D. A., Honigmann, P., Babst, R., Cristalli, A., Morlock, M. M., and Mittlmeier, T. (2007). Intra-Articular Pressure Measurement in the Radioulnocarpal Joint Using a Novel Sensor: In Vitro and In Vivo Results. *Journal of Hand Surgery*, 32(1):67–75.

Rimington, T. R., Edwards, S. G., Lynch, T. S., and Pehlivanova, M. B. (2010). Intercarpal ligamentous laxity in cadaveric wrists. *The Journal of Bone and Joint Surgery. British volume*, 92-B(11):1600–1605.

Ritt, M. J., Linscheid, R. L., Cooney, W. P., Berger, R. A., and An, K. N. (1998). The lunotriquetral joint: Kinematic effects of sequential ligament sectioning, ligament repair, and arthrodesis. *Journal of Hand Surgery*, 23(3):432–445.

Ritt, M. J., Stuart, P. R., Berglund, L. J., Linscheid, R. L., Conney, W. P., and An, K. N. (1995). Rotational stability of the carpus relative to the forearm. *Journal of Hand Surgery*, 20(2):305–311.

Robert-Lachaine, X., Allard, P., Godbout, V., and Begon, M. (2015). 3d shoulder kinematics for static vs dynamic and passive vs active testing conditions. *Journal of Biomechanics*, 48(12):2976 – 2983.

Rogers, W. D. and Watson, H. K. (1989). Radial styloid impingement after triscaphe arthrodesis. *Journal of Hand Surgery*, 14(2 PART 1):297–301.

Rohman, E. M., Agel, J., Putnam, M. D., and Adams, J. E. (2014). Scapholunate interosseous ligament injuries: A retrospective review of treatment and outcomes in 82 wrists. *Journal of Hand Surgery*, 39(10):2020–2026.

Rosati, M., Parchi, P., Cacianti, M., Poggetti, A., and Lisanti, M. (2010). Treatment of acute scapholunate ligament injuries with bone anchor. *Musculoskeletal Surgery*, 94(1):25–32.

Rosenwas, M. P., Miyasaka, K. C., and Strauch, R. J. (1997). The RASL Procedure: Reduction and Association of the Scaphoid and Lunate Using the Herbert Screw. *Techniques in Hand & Upper Extremity Surgery*, 1(4):263–272.

Ross, M., Loveridge, J., Cutbush, K., and Couzens, G. (2013). Scapholunate ligament reconstruction. *Journal of wrist surgery*, 2(2):110–115.

Ruby, L. K., An, K. N., Linscheid, R. L., Cooney, W. P., and Chao, E. Y. (1987). The effect of scapholunate ligament section on scapholunate motion. *Journal of Hand Surgery*, 12(5):767–771.

Ruby, L. K., Conney, W. P., An, K. N., Linscheid, R. L., and Chao, E. Y. (1988). Relative motion of selected carpal bones: A kinematic analysis of the normal wrist. *Journal of Hand Surgery*, 13(1):1–10.

Ryu, J., Cooney, W. P., Askew, L. J., An, K. N., and Chao, E. Y. (1991). Functional ranges of motion of the wrist joint. *Journal of Hand Surgery*, 16(3):409–419.

Saffar, P. and Semaan, I. (1994). The Study of the Biomechanics of Wrist Movements in an Oblique Plane A Preliminary Report. In Schuind, F., An, K. N., Cooney, W. P., and Garcia-Elias, M., editors, *Advances in the Biomechanics of the Hand and Wrist*, pages 305–311. Springer US, Boston, MA.

Salvà-Coll, G., Garcia-Elias, M., Llusá-Pérez, M., and Rodríguez-Baeza, A. (2011). The role of the flexor carpi radialis muscle in scapholunate instability. *Journal of Hand Surgery*, 36(1):31–36.

Salvà-Coll, G., Garcia-Elias, M., Llusá-Pérez, M., and Rodríguez-Baeza, A. (2012). Role of the extensor carpi ulnaris and its sheath on dynamic carpal stability. *Journal of Hand Surgery: European Volume*, 37(6):544–548.

Sandow, M. J., Fisher, T. J., Howard, C. Q., and Papas, S. (2014). Unifying model of carpal mechanics based on computationally derived isometric constraints and rules-based motion - The stable central column theory. *Journal of Hand Surgery: European Volume*, 39(4):353–363.

Sarrafian, S. K., Melamed, J. L., and Goshgarian, G. M. (1977). Study of Wrist Motion in Flexion and Extension. *Clinical Orthopaedics and Related Research*, 126:153–159.

Savelberg, H. H., Kooloos, J. G., De Lange, A., Huiskes, R., and Kauer, J. M. (1991). Human carpal ligament recruitment and threedimensional carpal motion. *Journal of Orthopaedic Research*, 9(5):693–704.

Savelberg, H. H. C. M., Otten, J. D. M., Kooloos, J. G. M., Huiskes, R., and Kauer, J. M. G. (1993). Carpal bone kinematics and ligament lengthening studied for the full range of joint movement. *Journal of biomechanics*, 26(12):1389–1402.

Scherrer, P. K., Hillberry, B. M., and Van Sickle, D. C. (1979). Determining the In-Vivo Areas of Contact in the Canine Shoulder. *Journal of Biomechanical Engineering*, 101(4):271–278.

Schicho, K., Figl, M., Donat, M., Birkfellner, W., Seemann, R., Wagner, A., Bergmann, H., and Ewers, R. (2005). Stability of miniature electromagnetic tracking systems. *Physics in Medicine and Biology*, 50(9):2089–2098.

Schmitt, R., Froehner, S., Coblenz, G., and Christopoulos, G. (2006). Carpal instability. *European Radiology*, 16(10):2161–2178.

Schnorenberg, A. J., Slavens, B. A., Wang, M., Vogel, L. C., Smith, P. A., and Harris, G. F. (2014). Biomechanical model for evaluation of pediatric upper extremity joint dynamics during wheelchair mobility. *Journal of Biomechanics*, 47(1):269–276.

Schuind, F., Cooney, W. P., Linscheid, R. L., An, K. N., and Chao, E. Y. (1995). Force and pressure transmission through the normal wrist. A theoretical two-dimensional study in the posteroanterior plane. *Journal of Biomechanics*, 28(5):587–601.

Schuind, F. A., Linscheid, R. L., An, K. N., and Chao, E. Y. (1992). A normal data base of posteroanterior roentgenographic measurements of the wrist. *Journal of Bone and Joint Surgery - Series A*, 74(9):1418–1429.

Schünke, M., Schulte, E., and Schumacher, U. (2006). *Thieme Atlas of anatomy: general anatomy and musculoskeletal system.* Thieme Medical Publishers, St. Louis, second edition.

Seradge, H., Baer, C., Dalsimer, D., Seradge, A., Shafi, R., and Parker, W. (2004). Treatment of dynamic scaphoid instability. *Journal of Trauma - Injury, Infection and Critical Care*, 56(6):1253–1260.

Seraji, H. (1989). Decentralized Adaptive Control of Manipulators: Theory, Simulation, and Experimentation. *IEEE Transactions on Robotics and Automation*, 5(2):183–201.

Shah, A. M. and Abrams, R. (2010). Radial Styloidectomy. In Gelberman, R. H., editor, *Master Techniques in Orthopaedic Surgery: The Wrist*, Master techniques in orthopaedic surgery, chapter 17, pages 197–202. Lippincott Williams & Wilkins, Philadelphia, third edition.

Sharkey, N. A. and Hamel, A. J. (1998). A dynamic cadaver model of the stance phase of gait: Performance characteristics and kinetic validation. *Clinical Biomechanics*, 13(6):420–433.

Shores, J. T., Demehri, S., and Chhabra, A. (2013). Kinematic "4 Dimensional" CT Imaging in the Assessment of Wrist Biomechanics Before and After Surgical Repair. *Eplasty*, 13:e9.

Short, W. H., Werner, F. W., Fortino, M. D., and Palmer, A. K. (1992). Distribution of pressures and forces on the wrist after simulated intercarpal fusion and Kienböck's disease. *Journal of Hand Surgery*, 17(3):443–449.

Short, W. H., Werner, F. W., Fortino, M. D., Palmer, A. K., and Mann, K. A. (1995). A dynamic biomechanical study of scapholunate ligament sectioning. *Journal of Hand Surgery*, 20(6):986–999.

Short, W. H., Werner, F. W., Green, J. K., and Masaoka, S. (2002a). Biomechanical evaluation of ligamentous stabilizers of the scaphoid and lunate. *Journal of Hand Surgery*, 27(6):991–1002.

Short, W. H., Werner, F. W., Green, J. K., and Masaoka, S. (2005). Biomechanical evaluation of the ligamentous stabilizers of the scaphoid and lunate: Part II. *Journal of Hand Surgery*, 30(1):24–34.

Short, W. H., Werner, F. W., Green, J. K., Sutton, L. G., and Brutus, J. P. (2007). Biomechanical Evaluation of the Ligamentous Stabilizers of the Scaphoid and Lunate: Part III. *Journal of Hand Surgery*, 32(3):297.e1–297.e18.

Short, W. H., Werner, F. W., Green, J. K., Weiner, M. M., and Masaoka, S. (2002b). The effect of sectioning the dorsal radiocarpal ligament and insertion of a pressure sensor into the radiocarpal joint on scaphoid and lunate kinematics. *Journal of Hand Surgery*, 27(1):68–76.

Short, W. H., Werner, F. W., and Sutton, L. G. (2009). Dynamic Biomechanical Evaluation of the Dorsal Intercarpal Ligament Repair for Scapholunate Instability. *Journal of Hand Surgery*, 34(4):652–659.

Sigward, S. M. and Powers, C. M. (2006). The influence of gender on knee kinematics, kinetics and muscle activation patterns during side-step cutting. *Clinical Biomechanics*, 21(1):41 – 48.

Sikora, S., Tham, S., Harvey, J., Garcia-Elias, M., Goldring, T., Rotstein, A., and Ek, E. (2019). The Twist X-Ray: A Novel Test for Dynamic Scapholunate Instability. *Journal of Wrist Surgery*, 08(01):061–065.

Slater, R. R., Szabo, R. M., Bay, B. K., and Laubach, J. (1999). Dorsal intercarpal ligament capsulodesis for scapholunate dissociation:

Biomechanical analysis in a cadaver model. *Journal of Hand Surgery*, 24(2):232–239.

Slavens, B. A., Sturm, P. F., and Harris, G. F. (2010). Upper extremity inverse dynamics model for crutch-assisted gait assessment. *Journal of Biomechanics*, 43(10):2026–2031.

Smith, D. K., An, K. N., Cooney, W. P., Linscheid, R. L., and Chao, E. Y. (1989). Effects of a scaphoid waist osteotomy on carpal kinematics. *Journal of Orthopaedic Research*, 7(4):590–598.

Snel, J. G., Venema, H. W., Moojen, T. M., Ritt, M. J., Grimbergen, C. A., and Den Heeten, G. J. (2000). Quantitative in vivo analysis of the kinematics of carpal bones from three-dimensional CT images using a deformable surface model and a three-dimensional matching technique. *Medical Physics*, 27(9):2037–2047.

Söderkvist, I. and Wedin, P. Å. (1993). Determining the movements of the skeleton using well-configured markers. *Journal of Biomechanics*, 26(12):1473–1477.

Sokoloff, L. (1966). Elasticity of aging cartilage. *Federation proceedings*, 25(3):1089–1095.

Sokolow, C. and Saffar, P. (2001). Anatomy and histology of the scapholunate ligament. *Hand clinics*, 17(1):77–81.

Soong, M., Merrell, G. A., Ortmann IV, F., and Weiss, A. P. C. (2013). Long-term results of bone-retinaculum-bone autograft for scapholunate instability. *Journal of Hand Surgery*, 38(3):504–508.

Soslowsky, L. J., Flatow, E. L., Bigliani, L. U., Pawluk, R. J., Ateshian, G. A., and Mow, V. C. (1992). Quantitation of in situ contact areas at the glenohumeral joint: A biomechanical study. *Journal of Orthopaedic Research*, 10(4):524–534.

Sousa, M., Aido, R., Freitas, D., Trigueiros, M., Lemos, R., and Silva, C. (2014). Scapholunate ligament reconstruction using a flexor carpi radialis tendon graft. *Journal of Hand Surgery*, 39(8):1512–1516.

Souza, E. F. (2001). The Wrist: Functional Anatomy and Kinesiology. In Frank G. Shellock, C. M. P., editor, *Kinematic MRI of the joints : functional anatomy, kinesiology, and clinical applications*, chapter 15, page 300. CRC Press, Boca Raton.

Standring, S. and Gray, H. (2008). *Gray's anatomy: the anatomical basis of clinical practice*. Churchill Livingstone, Edinburgh, 40th edition.

Stewart, D. T., Froelich, J. M., and Shin, A. Y. (2014). Intercarpal arthrodeses. *Journal of Hand Surgery*, 39(2):373–377.

Stoesser, H., Padmore, C., Nishiwaki, M., Gammon, B., Langohr, G., and Johnson, J. (2016). Biomechanical Evaluation of Carpal Kinematics during Simulated Wrist Motion. *Journal of Wrist Surgery*, 06(02):113–119.

Sturzenegger, M. and Büchler, U. (1991). Radio-scapho-lunate partial wrist arthrodesis following comminuted fractures of the distal radius. *Annales de Chirurgie de la Main*, 10(3):207–216.

Svoboda, S. J., Eglseder, W. A., and Belkoff, S. M. (1995). Autografts from the foot for reconstruction of the scapholunate interosseous ligament. *The Journal of Hand Surgery*, 20(6):980 – 985.

Szabo, R. M. (2008). Scapholunate Ligament Repair With Capsulodesis Reinforcement. *Journal of Hand Surgery*, 33(9):1645–1654.

Szabo, R. M., Slater, R. R., Palumbo, C. F., and Gerlach, T. (2002). Dorsal intercarpal ligament capsulodesis for chronic, static scapholunate dissociation: Clinical results. *Journal of Hand Surgery*, 27(6):978–984.

Szarko, M., Muldrew, K., and Bertram, J. E. (2010). Freeze-thaw treatment effects on the dynamic mechanical properties of articular cartilage. *BMC Musculoskeletal Disorders*, 11.

Taleisnik, J. (1976). The ligaments of the wrist. *Journal of Hand Surgery*, 1(2):110–118.

Taleisnik, J. (1988). Current concepts review. Carpal instability. *The Journal of bone and joint surgery. American volume*, 70(8):1262–1268.

Taleisnik, J., Gelberman, R. H., Miller, B. W., and Szabo, R. M. (1984). The extensor retinaculum of the wrist. *Journal of Hand Surgery*, 9(4):495–501.

Talwalkar, S. C., Edwards, A. T., Hayton, M. J., Stilwell, J. H., Trail, I. A., and Stanley, J. K. (2006). Results of tri-ligament tenodesis: A modified brunelli procedure in the management of scapholunate instability. *The Journal of Hand Surgery: British & European Volume*, 31(1):110–117.

Tang, J. B., Gu, X. K., Xu, J., and Gu, J. H. (2011). In vivo length changes of carpal ligaments of the wrist during dart-throwing motion. *Journal of Hand Surgery*, 36(2):284–290.

Tang, P., Gauvin, J., Muriuki, M., Pfaeffle, J. H., Imbriglia, J. E., and Goitz, R. J. (2009). Comparison of the "Contact Biomechanics" of the Intact and Proximal Row Carpectomy Wrist. *Journal of Hand Surgery*, 34(4):660–670.

Tashman, S. and Anderst, W. (2003). In-vivo measurement of dynamic joint motion using high speed biplane radiography and CT: Application to canine ACL deficiency. *Journal of Biomechanical Engineering*, 125(2):238–245.

Taylor, D. C., Dalton, J. D., Seaber, A. V., and Garrett, W. E. (1990). Viscoelastic properties of muscle-tendon units: The biomechanical effects of stretching. *The American Journal of Sports Medicine*, 18(3):300–309.

Tekscan Inc. (2015a). *Sensor Datasheet: Medical Sensor 4201 (Rev. A)*. 307 West First Street, South Boston, MA, USA.

Tekscan Inc. (2015b). *Sensor Datasheet: Medical Sensor 6900 (Rev. A)*. 307 West First Street, South Boston, MA, USA.

Tekscan Inc. (2020). *I-Scan: Product Selection Guide (Rev. H)*. 307 West First Street, South Boston, MA, USA.

Tencer, A. F., Viegas, S. F., Cantrell, J., Chang, M., Clegg, P., Hicks, C., O'Meara, C., and Williamson, J. B. (1988). Pressure distribution in the wrist joint. *Journal of Orthopaedic Research*, 6(4):509–517.

Teurlings, L., Miller, G. J., and Wright, T. W. (2000). Pressure mapping of the radioulnar carpal joint: Effects of ulnar lengthening and wrist position. *Journal of Hand Surgery*, 25 B(4):346–349.

Tischler, B. T., Diaz, L. E., Murakami, A. M., Roemer, F. W., Goud, A. R., Arndt, W. F., and Guermazi, A. (2014). Scapholunate advanced collapse: a pictorial review. *Insights into Imaging*, 5(4):407–417.

Tomita, K., Berger, E. J., Berger, R. A., Kraisarin, J., and An, K. N. (2007). Distribution of Nerve Endings in the Human Dorsal Radiocarpal Ligament. *Journal of Hand Surgery*, 32(4):466–473.

Tong, J. J.-C. (1985). *Wrist Motion Simulator*. PhD thesis, Syracuse University, Ann Arbor.

Trumble, T., Glisson, R. R., Seaber, A. V., and Urbaniak, J. R. (1987). Forearm force transmission after surgical treatment of distal radioulnar joint disorders. *Journal of Hand Surgery*, 12(2):196–202.

Ulrich, D., van Rietbergen, B., Laib, A., and Rüegsegger, P. (1999). Load transfer analysis of the distal radius from in-vivo high-resolution ct-imaging. *Journal of Biomechanics*, 32(8):821 – 828.

Upal, M. A., Crisco, J. J., Moore, D. C., Sonenblum, S. E., and Wolfe, S. W. (2006). In Vivo Elongation of the Palmar and Dorsal Scapholunate Interosseous Ligament. *Journal of Hand Surgery*, 31(8):1326–1332.

Valdes, K. and LaStayo, P. (2013). The value of provocative tests for the wrist and elbow: A literature review. *Journal of Hand Therapy*, 26(1):32 – 43.

Van Den Abbeele, K. L., Loh, Y. C., Stanley, J. K., and Trail, I. A. (1998). Early results of a modified brunelli procedure for scapholunate instability. *Journal of Hand Surgery: European Volume*, 23(2):258–261.

Van Der Walt, S., Schönberger, J. L., Nunez-Iglesias, J., Boulogne, F., Warner, J. D., Yager, N., Gouillart, E., and Yu, T. (2014). Scikit-image: Image processing in python. *PeerJ*, 2014(1):e453.

Van Ee, C. A., Chasse, A. L., and Myers, B. S. (2000). Quantifying skeletal muscle properties in cadaveric test specimens: Effects of mechanical loading, postmortem time, and freezer storage. *Journal of Biomechanical Engineering*, 122(1):9–14.

Varga, P., Schefzig, P., Unger, E., Mayr, W., Zysset, P. K., and Erhart, J. (2013). Finite element based estimation of contact areas and pressures of the human scaphoid in various functional positions of the hand. *Journal of Biomechanics*, 46(5):984 – 990.

Vekris, M. D., Mataliotakis, G. I., and Beris, A. E. (2011). The scapholunate interosseous ligament afferent proprioceptive pathway: A human in vivo experimental study. *Journal of Hand Surgery*, 36(1):37–46.

Viegas, S. F. (2010). Ligamentous Repair for Acute Scapholunate Dissociation. In Gelberman, R. H., editor, *Master Techniques in Orthopaedic Surgery: The Wrist*, Master techniques in orthopaedic surgery, chapter 19, pages 211–222. Lippincott Williams & Wilkins, Philadelphia, third edition.

Viegas, S. F., Patterson, R. M., Peterson, P. D., Pogue, D. J., Jenkins, D. K., Sweo, T. D., and Hokanson, J. A. (1990). Evaluation of the biomechanical efficacy of limited intercarpal fusions for the treatment of scapho-lunate dissociation. *Journal of Hand Surgery*, 15(1):120–128.

Viegas, S. F., Patterson, R. M., Todd, P. D., and McCarty, P. (1993). Load mechanics of the midcarpal joint. *The Journal of Hand Surgery*, 18(1):14 – 18.

Viegas, S. F., Patterson, R. M., and Ward, K. (1995). Extrinsic wrist ligaments in the pathomechanics of ulnar translation instability. *Journal of Hand Surgery*, 20(2):312–318.

Viegas, S. F., Tencer, A. F., Cantrell, J., Chang, M., Clegg, P., Hicks, C., O'Meara, C., and Williamson, J. B. (1987a). Load transfer characteristics of the wrist. Part I. The normal joint. *Journal of Hand Surgery*, 12(6):971–978.

Viegas, S. F., Tencer, A. F., Cantrell, J., Chang, M., Clegg, P., Hicks, C., O'Meara, C., and Williamson, J. B. (1987b). Load transfer characteristics of the wrist. Part II. Perilunate instability. *Journal of Hand Surgery*, 12(6):978–985.

Viegas, S. F., Yamaguchi, S., Boyd, N. L., and Patterson, R. M. (1999). The dorsal ligaments of the wrist: Anatomy, mechanical properties, and function. *Journal of Hand Surgery*, 24(3):456–468.

Volz, R. G., Lieb, M., and Benjamin, J. (1980). Biomechanics of the wrist. *Clinical Orthopaedics and Related Research*, 149:112–117.

von Bonin, G. (1929). A Note on the Kinematics of the Wrist-Joint. *Journal of Anatomy*, 63(Pt 2):259–262.

Wächter, A. and Biegler, L. T. (2006). On the implementation of an interior-point filter line-search algorithm for large-scale nonlinear programming. *Mathematical Programming*, 106(1):25–57.

Walsh, J. J., Berger, R. A., and Cooney, W. P. (2002). Current status of scapholunate interosseous ligament injuries. *The Journal of the American Academy of Orthopaedic Surgeons*, 10(1):32–42.

Wang, B., Roach, K. E., Kapron, A. L., Fiorentino, N. M., Saltzman, C. L., Singer, M., and Anderson, A. E. (2015a). Accuracy and feasibility of high-speed dual fluoroscopy and model-based tracking to measure in vivo ankle arthrokinematics. *Gait and Posture*, 41(4):888–893.

Wang, H., Chen, T., Koff, M. F., Hutchinson, I. D., Gilbert, S., Choi, D., Warren, R. F., Rodeo, S. A., and Maher, S. A. (2015b). Measured Knee Contact Location During Simulated Gait. 47(10):2483–2489.

Wang, I. N. E., Mitroo, S., Chen, F. H., Lu, H. H., and Doty, S. B. (2006). Age-dependent changes in matrix composition and organization at the ligament-to-bone insertion. *Journal of Orthopaedic Research*, 24(8):1745–1755.

Wang, J. and Blackburn, T. J. (2000). The AAPM/RSNA physics tutorial for residents: X-ray image intensifiers for fluoroscopy. *Radiographics*, 20(5):1471–1477.

Watanabe, K., Nakamura, R., Horii, E., and Miura, T. (1993). Biomechanical analysis of radial wedge osteotomy for the treatment of Kienböck's disease. *Journal of Hand Surgery*, 18(4):686–690.

Waters, M. S., Werner, F. W., Haddad, S. F., McGrattan, M. L., and Short, W. H. (2016). Biomechanical Evaluation of Scaphoid and Lunate Kinematics Following Selective Sectioning of Portions of the Scapholunate Interosseous Ligament. *Journal of Hand Surgery*, 41(2):208–213.

Watson, H., Ottoni, L., Pitts, E. C., and Handal, A. G. (1993). Rotary subluxation of the scaphoid: a spectrum of instability. *The Journal of Hand Surgery: British & European Volume*, 18(1):62–64.

Watson, H., Weinzweig, J., and Zeppieri, J. (1997). The natural progression of scaphoid instability. *Hand clinics*, 13(1):3949.

Watson, H. K. and Ballet, F. L. (1984). The SLAC wrist: Scapholunate advanced collapse pattern of degenerative arthritis. *Journal of Hand Surgery*, 9(3):358–365.

Watson, H. K. and Hempton, R. F. (1980). Limited wrist arthrodeses. I. The triscaphoid joint. *Journal of Hand Surgery*, 5(4):320–327.

Watson, H. K. and Ryu, J. (1986). Evolution of arthritis of the wrist. *Clinical Orthopaedics and Related Research*, NO. 202(202):57–67.

Watson, H. K., Sorelle, J. R., Wollstein, R., and Haass, E. A. L. (2010). STT Arthrodesis. In Gelberman, R. H., editor, *Master Techniques in Orthopaedic Surgery: The Wrist*, chapter 23, pages 263–270. Lippincott Williams & Wilkins, Philadelphia, third edition.

Watson, H. K., Weinzweig, J., Guidera, P. M., Zeppieri, J., and Ashmead, D. (1999). One thousand intercarpal arthrodeses. *Journal of Hand Surgery*, 24 B(3):307–315.

Watts, A. C., McLean, J. M., Fogg, Q., and Bain, G. I. (2011). Scaphoid anatomy. In Slutsky, D. and Slade, J., editors, *The Scaphoid*, chapter 1, pages 3–10. Thieme, New York, 3rd edition.

Wayne, J. S. and Tremols, E. J. (2019). Computational wrist analysis of functional restoration after scapholunate dissociation repair. *Medical and Biological Engineering and Computing*, 57(7):1465–1479.

Weber, E. R. (1980). Biomechanical implications of scaphoid waist fractures. *Clinical Orthopaedics and Related Research*, NO 149:83–89.

Weber, E. R. (1984). Concepts governing the rotational shift of the intercalated segment of the carpus. *The Orthopedic Clinics Of North America*, 15(2):193–207.

Weiss, A. P. (1998). Scapholunate ligament reconstruction using a bone-retinaculum-bone autograft. *Journal of Hand Surgery*, 23(2):205–215.

Weiss, A.-P. C., Sachar, K., and Glowacki, K. A. (1997). Arthroscopic debridement alone for intercarpal ligament tears. *Journal of Hand Surgery*, 22(2):344–349.

Weiss, K. E. and Rodner, C. M. (2007). Osteoarthritis of the wrist. *The Journal of Hand Surgery*, 32(5):725 – 746.

Welch, G. and Foxlin, E. (2002). Motion tracking: no silver bullet, but a respectable arsenal. *IEEE Computer Graphics and Applications*, 22(6):24–38.

Werner, F. and Short, W. (2018). Carpal Pronation and Supination Changes in the Unstable Wrist. *Journal of Wrist Surgery*, 07(04):298–302.

Werner, F. W. (2010). Wrist Biomechanics. In Cooney, W. P., editor, *The Wrist: diagnosis and operative treatment*, chapter 4, pages 77–118. Lippincott Williams & Wilkins, Rochester, second edition.

Werner, F. W., Green, J. K., Short, W. H., and Masaoka, S. (2004). Scaphoid and lunate motion during a wrist dart throw motion. *Journal of Hand Surgery*, 29(3):418–422.

Werner, F. W., Palmer, A. K., Fortino, M. D., and Short, W. H. (1992). Force transmission through the distal ulna: Effect of ulnar variance, lunate fossa angulation, and radial and palmar tilt of the distal radius. *Journal of Hand Surgery*, 17(3):423–428.

Werner, F. W., Palmer, A. K., Somerset, J. H., Tong, J. J., Gillison, D. B., Fortino, M. D., and Short, W. H. (1996). Wrist joint motion simulator. *Journal of Orthopaedic Research*, 14(4):8.

Werner, F. W., Short, W. H., Fortino, M. D., and Palmer, A. K. (1997a). The relative contribution of selected carpal bones to global wrist motion during simulated planar and out-of-plane wrist motion. *Journal of Hand Surgery*, 22(4):708–713.

Werner, F. W., Short, W. H., Fortino, M. D., and Palmer, A. K. (1997b). The relative contribution of selected carpal bones to global wrist motion during simulated planar and out-of-plane wrist motion. *Journal of Hand Surgery*, 22(4):708–713.

Werner, F. W., Short, W. H., and Green, J. K. (2005). Changes in patterns of scaphoid and lunate motion during functional arcs of wrist motion induced by ligament division. *Journal of Hand Surgery*, 30(6):1156–1160.

Werner, F. W., Short, W. H., Green, J. K., Evans, P. J., and Walker, J. A. (2007). Severity of Scapholunate Instability Is Related to Joint Anatomy and Congruency. *The Journal of Hand Surgery*, 32(1):55–60.

Werner, F. W., Short, W. H., Palmer, A. K., and Sutton, L. G. (2010). Wrist Tendon Forces During Various Dynamic Wrist Motions. *Journal of Hand Surgery*, 35(4):628–632.

Werner, F. W., Sutton, L. G., Allison, M. A., Gilula, L. A., Short, W. H., and Wollstein, R. (2011). Scaphoid and lunate translation in the intact wrist and following ligament resection: A cadaver study. *Journal of Hand Surgery*, 36(2):291–298.

White, T. D., Black, M. T., and Folkens, P. A. (2012). *Hand: Carpals, Metacarpals, and Phalanges*, volume 1, chapter 10, pages 199–208. Academic Press, San Diego, third edition.

Whitty, L. A. and Moran, S. L. (2009). Modified brunelli tenodesis for the treatment of scapholunate instability. In Slutsky, D. J. and Osterman, A. L., editors, *Fractures and Injuries of the Distal Radius and Carpus*, chapter 49, pages 481 – 488. W.B. Saunders, Philadelphia.

William Giles, J., Miguel Ferreira, L., Singh Athwal, G., and Andrew Johnson, J. (2014). Development and Performance Evaluation of a Multi-PID Muscle Loading Driven in Vitro Active-Motion Shoulder Simulator and Application to Assessing Reverse Total Shoulder Arthroplasty. *Journal of Biomechanical Engineering*, 136(12):1–10.

Windolf, M., Götzen, N., and Morlock, M. (2008). Systematic accuracy and precision analysis of video motion capturing systems-exemplified on the Vicon-460 system. *Journal of Biomechanics*, 41(12):2776–2780.

Wintman, B. I., Gelberman, R. H., and Katz, J. N. (1995). Dynamic scapholunate instability: Results of operative treatment with dorsal capsulodesis. *Journal of Hand Surgery*, 20(6):971–979.

Wolfe, S. W. (2001). Scapholunate instability. *Journal of the American Society for Surgery of the Hand*, 1(1):45–60.

Wolfe, S. W., Crisco, J. J., and Katz, L. D. (1994). The Use of Cine-Computed Tomography to Investigate Carpal Kinematics. In Schuind, F., An, K. N., Cooney, W. P., and Garcia-Elias, M., editors, *Advances in the Biomechanics of the Hand and Wrist*, pages 465–473. Springer US, Boston, MA.

Wolfe, S. W., Katz, L. D., and Crisco, J. J. (1996). Radiographic progression to dorsal intercalated segment instability. *Orthopedics*, 19(8):691–695.

Wolfe, S. W., Neu, C., and Crisco, J. J. (2000). In vivo scaphoid, lunate, and capitate kinematics in flexion and in extension. *Journal of Hand Surgery*, 25(5):860–869.

Woltring, H. J. (1994). 3-D attitude representation of human joints: A standardization proposal. *Journal of Biomechanics*, 27(12):1399–1414.

Wright, R. D. (1935). A Detailed Study of Movement of the Wrist Joint. *Journal of anatomy*, 70(Pt 1):137–142.1.

Wu, G., Van Der Helm, F. C., Veeger, H. E., Makhsous, M., Van Roy, P., Anglin, C., Nagels, J., Karduna, A. R., McQuade, K., Wang, X., Werner, F. W., and Buchholz, B. (2005). ISB recommendation on definitions of joint coordinate systems of various joints for the reporting of human joint motion - Part II: Shoulder, elbow, wrist and hand. *Journal of Biomechanics*, 38(5):981–992.

Wu, W., Lee, P. V., Bryant, A. L., Galea, M., and Ackland, D. C. (2016). Subject-specific musculoskeletal modeling in the evaluation of shoulder muscle and joint function. *Journal of Biomechanics*, 49(15):3626–3634.

Wyrick, J. D., Youse, B. D., and Kiefhaber, T. R. (1998). Scapholunate ligament repair and capsulodesis for the treatment of static scapholunate dissociation. *Journal of Hand Surgery: European Volume*, 23(6):776–780.

Xu, J. and Tang, J. B. (2009). In Vivo Length Changes of Selected Carpal Ligaments During Wrist Radioulnar Deviation. *Journal of Hand Surgery*, 34(3):401–408.

Yeoh, D. and Tourret, L. (2015). Total wrist arthroplasty: A systematic review of the evidence from the last 5 years. *Journal of Hand Surgery: European Volume*, 40(5):458–468.

Yin, Y. and Gilula, L. A. (2001). Imaging of the symptomatic wrist. In Watson, H. K. and Weinzweig, J., editors, *The Wrist*, pages 61–82. Lippincott-Raven, Philadelphia.

You, B.-m. M., Siy, P., Anderst, W., and Tashman, S. (2001). In vivo measurement of 3-D skeletal kinematics from sequences of biplane radiographs: Application to knee kinematics. *IEEE Transactions on Medical Imaging*, 20(6):514–525.

Youm, Y. and Flatt, A. E. (1984). Design of a total wrist prosthesis. *Annals of Biomedical Engineering*, 12(3):247–262.

Youm, Y., McMurtry, R. Y., Flatt, A. E., and Gillespie, T. E. (1978). Kinematics of the wrist. I. An experimental study of radial-ulnar deviation and flexion-extension. *Journal of Bone and Joint Surgery - Series A*, 60(4):423–431.

Zanetti, M., Hodler, J., and Gilula, L. A. (1998). Assessment of dorsal or ventral intercalated segmental instability configurations of the wrist: Reliability of sagittal MR images. *Radiology*, 206(2):339–345.

Zarkadas, P. C., Gropper, P. T., White, N. J., and Perey, B. H. (2004). A survey of the surgical management of acute and chronic scapholunate instability. *Journal of Hand Surgery*, 29(5):848–857.

Zhang, J. T. and Chen, J. (2007). Statistical inferences for functional data. *Annals of Statistics*, 35(3):1052–1079.

Zhang, Z. (2000). A flexible new technique for camera calibration. *IEEE Transactions on Pattern Analysis and Machine Intelligence*, 22(11):1330–1334.

Zhao, K., Breighner, R., Holmes, D. r., Leng, S., McCollough, C., and An, K.-N. (2015). A technique for quantifying wrist motion using four-dimensional computed tomography: approach and validation. *Journal of biomechanical engineering*, 137(7):1–5.

Ziegler, J. G. and Nichols, N. B. (1993). Optimum settings for automatic controllers. *Journal of Dynamic Systems, Measurement and Control, Transactions of the ASME*, 115(2B):220–222.

Zubairy, A. I. and Jones, W. A. (2003). Scapholunate fusion in chronic symptomatic scapholunate instability. *The Journal of Hand Surgery: British & European Volume*, 28 B(4):311–314.

Appendices

A

Specifications of Key Components Comprising the CWTP

This appendix contains the specifications of key components used on the cadaveric wrist testing platform (CWTP). The metrology certificate for the bead location on the plate used in the validation of the biplane X-ray fluoroscopy system is also attached.

A.1 Vicon Motion Capture Camera



Technical Specifications	Vero v13	Vero v2.2	Vero X
Resolution	1.3MP 1280 * 1024	2.2MP 2048 * 1088	1.3MP 1280 * 1024
Frame Rate (Full Frame) FPS	250	330	250
Pixel Shutter Type	Global	Global	Global
Lens	Vicon 6-12mm varifocal	Vicon 6-12mm varifocal	4mm fixed focal length
Minimum FOV (H x V) degrees: Wide - Tele -	W: 55.2 x 43.9 T: 27.2 x 21.8	W: 98.1 x 50.1 T: 44.1 x 23.6	W: 79.0 x 67.6
Strobe	850nm 'IR	850nm 'IR	850nm 'IR'
Power Consumption	12W	12W	12W
Connectivity	RJ45/Cat5e	RJ45/Cat5e	RJ45/Cat5e
Weight	575g	575g	560g
Camera external dimensions	HxWxD: 83 x 80 x 135 mm	HxWxD: 83 x 80 x 135 mm	HxWxD: 83 x 80 x 112 mm

A.2 Uniaxial Load Cell

>Model UMM, UMMA, UMMC

Compression or Tension load cell.
These load cells are extremely small and lightweight.
Protection Class IP66

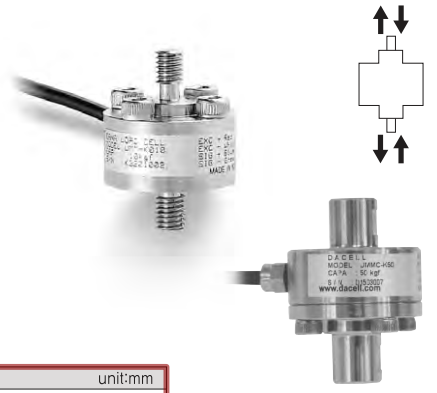

UMMC

UMMA unit:mm

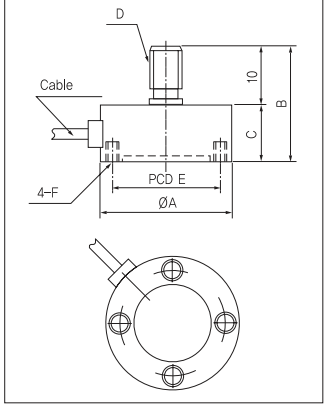

UMM unit:mm

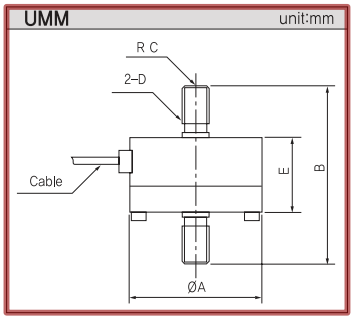

WIRING INFORMATION

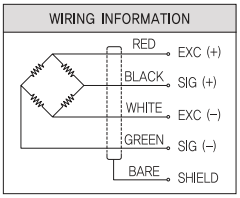

>SPECIFICATIONS

Specifications	Accuracy
Rated capacity(R.C.)	1kgf, 2kgf, 5kgf, 10kgf, 20kgf, 50kgf, 100kgf, 200kgf
Rated output(R.O.)	0.7~1.2mV/V
Nonlinearity	0.1% of R.O.
Hysteresis	0.1% of R.O.
Repeatability	0.1% of R.O.
Zero balance	±2% of R.O.
Temperature effect, on rated output	0.1% of LOAD / 10℃
Temperature effect, on zero balance	0.05% of R.O. / 10℃
Temperature range, compensated	-10~60℃
Temperature range, safe	-10~80℃
Terminal resistance input	350±30Ω
Terminal resistance output	350±2Ω
Insulation resistance bridge/case	2000MΩ
Excitation recommended	5V
Safe overload	120% R.C.
Cable length	Ø3.4core shield cable, 3m

UMMC unit:mm

Capacity : 10kgf~200kgf

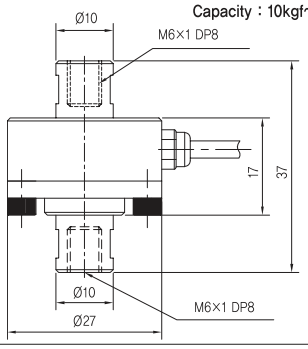

>DIMENSIONS TABLE(UMMA/UMM)

unit:mm

Capacity	UMMA						UMM				
	A	B	C	D	E	F	A	B	C	D	E
1kgf (9.807N)	23	20	10	M3×0.5	18	M3DP5	23	34	20	M3×0.5	14
2kgf (19.61N)	23	20	10	M3×0.5	18	M3DP5	23	34	20	M3×0.5	14
5kgf (49.03N)	23	20	10	M3×0.5	18	M3DP5	23	34	20	M3×0.5	14
10kgf (98.07N)	27	21	11	M6×1	22	M3DP5	27	37	30	M6×1	17
20kgf (196.1N)	27	21	11	M6×1	22	M3DP5	27	37	30	M6×1	17
50kgf (490.3N)	27	21	11	M6×1	22	M3DP5	27	37	30	M6×1	17
100kgf (980.7N)	27	21	11	M6×1	22	M3DP5	27	37	30	M6×1	17
200kgf (1.961kN)	27	21	11	M6×1	22	M3DP5	27	37	30	M6×1	17

★Specifications are subject to change without notice.

A.3 Analogue Data Acquisition Device

SPECIFICATIONS

NI cDAQ™-9174

NI CompactDAQ Four-Slot USB Chassis

These specifications are for the National Instruments CompactDAQ 9174 chassis only. These specifications are typical at 25 °C unless otherwise noted. For the C Series I/O module specifications, refer to the documentation for the C Series I/O module you are using.

Analog Input

Input FIFO size.....127 samples per slot

Maximum sample rate[1].....Determined by the C Series I/O module or modules

Timing accuracy[2].....50 ppm of sample rate

Timing resolution[3].....12.5 ns

Number of channels supported.....Determined by the C Series I/O module or modules

Analog Output

Number of channels supported

Hardware-timed task

Onboard regeneration.....16

Non-regeneration.....Determined by the C Series I/O module or modules

[1] Performance dependent on type of installed C Series I/O module and number of channels in the task.

[2] Does not include group delay. For more information, refer to the documentation for each C Series I/O module.

[3] Does not include group delay. For more information, refer to the documentation for each C Series I/O module.

NATIONAL INSTRUMENTS

Non-hardware-timed task.....Determined by the C Series I/O module or modules

Maximum update rate

Onboard regeneration.....1.6 MS/s (multi-channel, aggregate)

Non-regeneration.....Determined by the C Series I/O module or modules

Timing accuracy.....50 ppm of sample rate

Timing resolution.....12.5 ns

Output FIFO size

Onboard regeneration.....8,191 samples shared among channels used

Non-regeneration.....127 samples per slot

AO waveform modes.....Non-periodic waveform, periodic waveform regeneration mode from onboard memory, periodic waveform regeneration from host buffer including dynamic update

Digital Waveform Characteristics

Waveform acquisition (DI) FIFO.....127 samples per slot

Waveform generation (DO) FIFO.....2,047 samples

Digital input sample clock frequency

Streaming to application memory.....System-dependent

Finite.....0 to 10 MHz

Digital output sample clock frequency

Streaming from application memory.....System-dependent

Regeneration from FIFO.....0 to 10 MHz

Finite.....0 to 10 MHz

Timing accuracy.....50 ppm

Physical Characteristics

Weight (unloaded).....Approx. 574 g (20.2 oz)

Dimensions (unloaded).....159.5 mm × 88.1 mm × 58.9 mm (6.28 in. × 3.47 in. × 2.3 in.) Refer to the following figure.

If you need to clean the chassis, wipe it with a dry towel.

Figure 1. NI cDAQ-9174 Dimensions

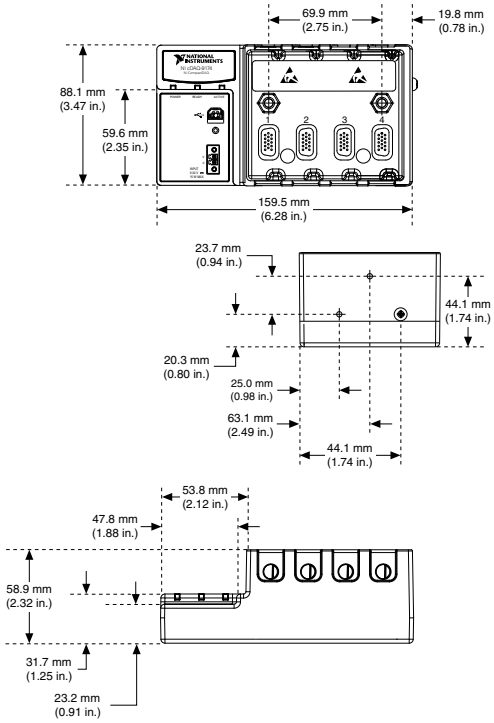

DATASHEET

NI 9237

4 AI, ±25 mV/V, 24 Bit, 50 kS/s/ch Simultaneous, Bridge Completion



- 4 channels, 50 kS/s per channel simultaneous AI
- ±25 mV/V input range, 24-bit resolution
- Programmable half- and full-bridge completion with up to 10 V internal excitation
- 60 VDC, Category I bank isolation
- RJ50 or D-SUB connectivity options
- -40 °C to 70 °C operating range, 5 g vibration, 50 g shock

The NI 9237 simultaneous bridge module for use with CompactDAQ and CompactRIO contains all the signal conditioning required to power and measure up to four bridge-based sensors simultaneously. The four RJ50 jacks provide direct connectivity to most torque or load cells and offer custom cable solutions with minimal tools. The high sampling rate and bandwidth of the NI 9237 offer a high-quality, high-speed strain or load measurement system with zero interchannel phase delay. With 60 VDC isolation and 1,000 Vrms transient isolation, the NI 9237 has high-common-mode noise rejection and increased safety for both the operator and test system.

The NI 9237 can perform offset/null as well as shunt calibration and remote sense, making the module the best choice for strain and bridge measurements.

The NI 9944 and NI 9945 are accessories for use with quarter-bridge sensors. These accessories have a female RJ50 connector on one end and screw terminals on the other end.

NATIONAL INSTRUMENTS

Data Rates

The frequency of a master timebase (f_M) controls the data rate (f_s) of the NI 9237. The NI 9237 includes an internal master timebase with a frequency of 12.8 MHz, but the module also can accept an external master timebase or export its own master timebase. To synchronize the data rate of an NI 9237 with other modules that use master timebases to control sampling, all of the modules must share a single master timebase source.

The following equation provides the available data rates of the NI 9237:

$$f_s = \frac{f_M \div 256}{n}$$

where n is any integer from 1 to 31.

However, the data rate must remain within the appropriate data rate range. When using the internal master timebase of 12.8 MHz, the result is data rates of 50 kS/s, 25 kS/s, 16.667 kS/s, and so on down to 1.613 kS/s depending on the value of n. When using an external timebase with a frequency other than 12.8 MHz, the NI 9237 has a different set of data rates.

Note The NI 9151 R Series Expansion chassis does not support sharing timebases between modules.

NI 9237 Specifications

The following specifications are typical for the range -40 °C to 70 °C unless otherwise noted.

Caution Do not operate the NI 9237 in a manner not specified in this document. Product misuse can result in a hazard. You can compromise the safety protection built into the product if the product is damaged in any way. If the product is damaged, return it to NI for repair.

Input Characteristics

Number of channels	4 analog input channels
Bridge completion	
Half and Full	Internal
Quarter	External
ADC resolution	24 bits
Type of ADC	Delta-Sigma (with analog prefiltering)
Sampling mode	Simultaneous

Internal master timebase (f_M)	
Frequency	12.8 MHz
Accuracy	±100 ppm maximum
Data rate range (f_s) using internal master timebase	
Minimum	1.613 kS/s
Maximum	50 kS/s
Data rate range (f_s) using external master timebase	
Minimum	391 S/s
Maximum	51.36 kS/s
Data rates (f_s)	($f_M \div 256$) $\div n$, where n = 1, 2, …, 31
Typical input range	±25 mV/V
Scaling coefficient	2.9802 nV/V per LSB
Overvoltage protection between any two pins	±30 V

Table 1. Accuracy

Measurement Conditions[1]		Percent of Reading (Gain Error[2])	Percent of Range[3] (Offset Error)
Calibrated	Typical (25 °C, ±5 °C)	0.05%	0.05%
	Maximum (– 40 to 70 °C)	0.20%	0.25%
Uncalibrated[4]	Typical (25 °C, ±5 °C)	0.20%	0.10%
	Maximum (– 40 to 70 °C)	0.55%	0.35%

Gain drift	10 ppm/°C maximum
Offset drift	
2.5 V excitation	0.6 µV/V per °C
3.3 V excitation	0.5 µV/V per °C
5 V excitation	0.3 µV/V per °C
10 V excitation	0.2 µV/V per °C

1 Before offset null or shunt calibration.
2 Applies at a data rate of 50 kS/s. Lower data rates can have up to 0.20% of reading additional gain error.
3 Range equals 25 mV/V.
4 Uncalibrated accuracy refers to the accuracy achieved when acquiring data in raw or unscaled modes and in which calibration constants that are stored in the module are not applied to the data.

DATASHEET

NI 9402

4 DIO, LVTTL, Bidirectional, 55 ns



- BNC connectivity
- CompactDAQ counter compatibility
- Individually configurable channel directions

The NI 9402 is a digital input/output module for any CompactDAQ or CompactRIO system. You can configure the direction of the channels for input or output on a per-channel basis. Each channel features 1,000 Vrms transient isolation between the channel and the backplane.

With CompactRIO, you can use the LabVIEW FPGA Module to program the NI 9402 for implementing custom, high-speed counter/timers; digital communication protocols; pulse generation; and much more.

Kit Contents	• NI 9402 • NI 9402 Getting Started Guide
Accessories	• BNC-to-BNC Male Cables (779697-02)

NATIONAL INSTRUMENTS

Input/Output Characteristics

Number of channels	4 DIO channels
Default power-on line direction	Input
Input/output type	LVTTL, single-ended
Digital logic levels	
Maximum input voltage	5.25 V
Input high, V_{IH}	2 V minimum
Input low, V_{IL}	0.8 V maximum
Output high, V_{OH} (3.4 V maximum)	
Sourcing 100 µA	3.0 V minimum
Sourcing 2 mA	2.8 V minimum
Output low, VOL	
Sinking 100 µA	0.1 V maximum
Sinking 2 mA	0.3 V maximum
Maximum I/O switching frequency	
4 channels	16 MHz
2 channels	20 MHz
I/O propagation delay[1],[2]	55 ns maximum, 18 ns typical
I/O pulse width distortion[2]	25 ns maximum
Input low current, I_{IL} (V_{IN} = 0 V)	-55 µA maximum
Input high current, I_{IH} (V_{IN} = 4.5 V)	150 µA maximum
Input impedance	
Input capacitance	50 pF maximum
Input resistance	49 kΩ minimum
Input rise/fall rate	10 ns/V maximum
Input protection	±30 V maximum on one channel at a time
MTBF	1,482,777 hours at 25 °C; Bellcore Issue 2, Method 1, Case 3, Limited Part Stress Method

[1] Propagation delay is the maximum amount of time it takes for an input or output signal to propagate between the backplane and the I/O connector, and does not include any additional delay introduced by the cable.

[2] Measured at the I/O connector of a load with requirements similar to the NI 9402 and driven through a 2 m coaxial cable.

A.4 Stepper Motor

LV & HV Series — Stepper Motors

HV Technical Specifications

Parameter	Units	HV171	HV172	HV173	HV231	HV232	HV233	HV341	HV342	HV343
Static Torque	oz-in	56	77	93	97	166	298	550	1091	1285
	Nm	0.40	0.54	0.66	0.68	1.17	2.10	3.88	7.70	9.07
Rotor Inertia	oz-in^2	0.18	0.28	0.37	0.7	1.5	2.6	7.66	14.8	21.9
	kg-cm^2	0.033	0.051	0.068	0.128	0.275	0.476	1.402	2.708	4.008
Drive Current										
Series	A (pk)	1.14	1.20	1.20	1.76	1.38	1.76	3.87	4.26	5.03
	A (rms)	0.81	0.85	0.85	1.24	0.98	1.24	2.74	3.01	3.56
Parallel	A (pk)	2.28	2.50	2.50	3.52	2.76	3.52	7.74	8.52	10.06
	A (rms)	1.61	1.77	1.77	2.49	1.95	2.49	5.47	6.02	7.11
Phase Inductance										
Series	mH	14.29	12.42	10.76	5.49	12.28	15.35	15.44	25.00	12.19
Parallel	mH	3.57	3.11	2.69	1.37	3.07	3.84	3.86	6.25	3.05
Resistance										
Series	Ohms	11.09	5.80	5.43	3.35	3.41	5.07	2.01	2.83	1.27
Parallel	Ohms	2.77	1.45	1.36	0.84	0.85	1.27	0.50	0.71	0.32
Detent Torque	oz-in	1.34	2.35	2.14	2.8	5.1	7.9	14.6	22.4	34.0
	Nm	0.009	0.017	0.015	0.020	0.036	0.056	0.103	0.158	0.240
Thrust Load	lb	6.00	6.00	6.00	13	13	13	25.0	25.0	25.0
	kg	2.73	2.73	2.73	5.91	5.91	5.91	11.36	11.36	11.36
Radial Load	lb	6.00	6.00	6.00	15.0	15.0	15.0	39.0	39.0	39.0
(0.79" from face)	kg	2.73	2.73	2.73	6.82	6.82	6.82	17.73	17.73	17.73
Motor Weight	lb	0.40	0.60	0.70	1.05	1.50	2.20	3.85	5.94	8.44
	kg	0.18	0.27	0.32	0.48	0.68	1.00	1.75	2.70	3.84
Certifications	CE - LVD	No	No	No	No	No	No	No	No	No
	CE - EMC	No	No	No	No	No	No	No	No	No
	UL	No	No	No	No	No	No	No	No	No

LV & HV Wiring - E-DC, E-AC, ZETA & Gemini

Series Wiring Model	Frame	A+	A-	B+	B-	Notes
LV	11, 14	Red	Black	White	Green	Internally wired in series
LV & HV	17, 23, 34	Red	Black	White	Green	Link Yellow and Blue, Link Orange and Brown
Parallel Wiring Model						
LV	11, 14	NA	NA	NA	NA	Internally wired in series, parallel wiring not available
LV & HV	17, 23, 34	Red/ Blue	Black/ Yellow	White/ Brown	Orange/ Green	None

LV Wiring - ViX Drive

Series Wiring Model	Frame	A+	A-	B+	B-	Notes
LV	11, 14	Red	Black	Green	White	Internally wired in series
LV	17, 23, 34	Red	Black	Green	White	Link Yellow and Blue, Link Orange and Brown
Parallel Wiring Model						
LV	11, 14	NA	NA	NA	NA	Internally wired in series, parallel wiring not available
LV	17, 23, 34	Red/ Blue	Black/ Yellow	Orange/ Green	White/ Brown	None

LV & HV Series Stepper Motors

Dimensions

LV/HV 17

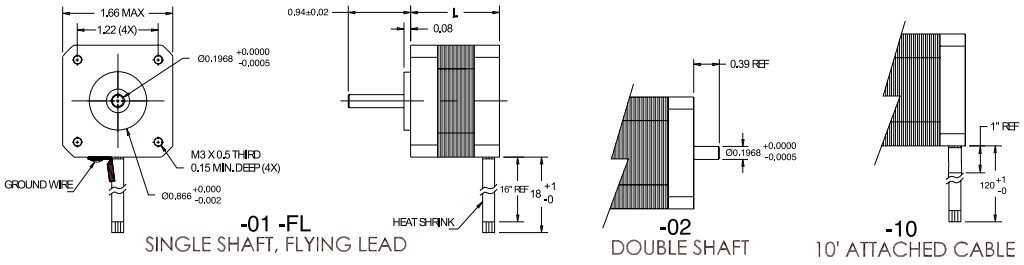

LV/HV 23

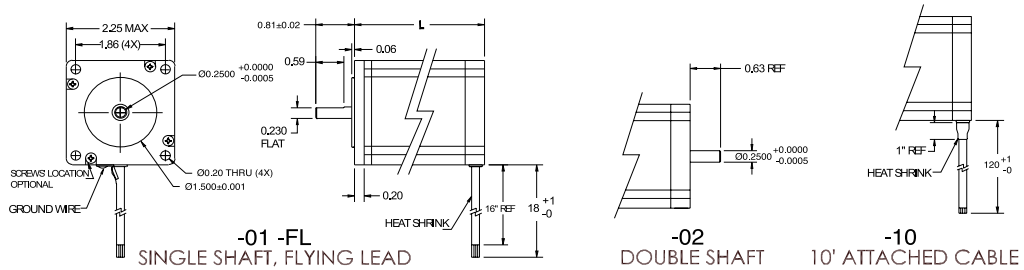

LV/HV 34

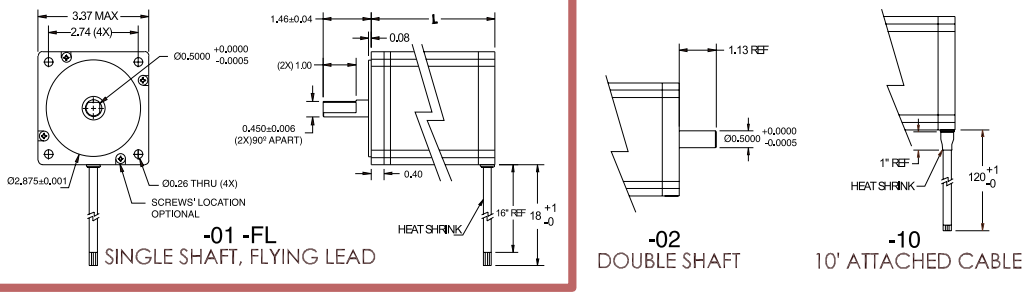

LV/HV Motor Lengths in IN (mm)

LV/HV171	LV/HV172	LV/HV173	LV/HV231	LV/HV232	LV/HV233	LV/HV341	LV/HV342	LV/HV343
1.34 (34.04)	1.57 (39.88)	1.89 (48.01)	1.73 (43.94)	2.17 (55.12)	3.10 (78.74)	2.60 (66.04)	3.78 (96.01)	5.00 (127.0)

A.5 Motor Drive

E Series Connections

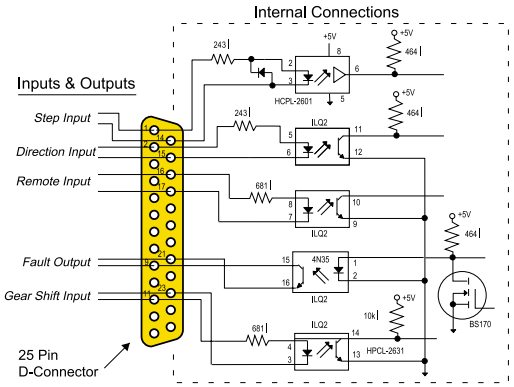

E Series Screw-Terminal	
Pin No	Signal
1 (Top)	LINE
2	NEUTRAL
3	GND
4	MOTOR GND
5	A+
6	A-
7	B+
8 (Bottom)	B-

E-AC Dimensions

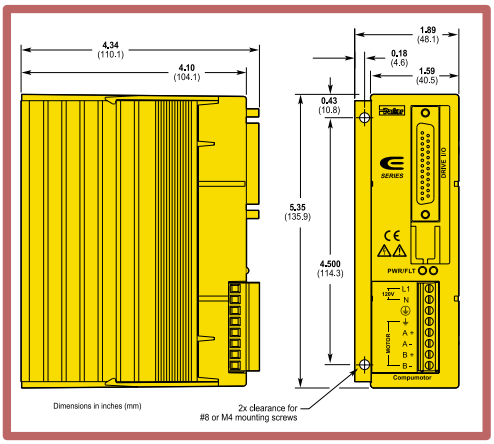

E-DC Drive Dimensions

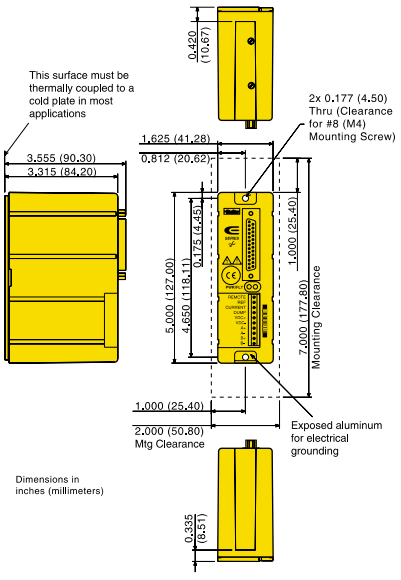

Catalog 8000-4/USA

E-AC E SERIES

E-AC Specifications

	Parameter	Value
Power Input		
Performance	AC	95 - 132 VAC @single phase 50/60 Hz
	Accuracy	±5 arc min (0.0833°) typical. Unloaded-bidirectional with Compumotor supplied motors. Other motors may exhibit different absolute accuracy. ±1 arc min (0.0167°) typical/per each frictional load equal to 1% rated torque. Loaded-in addition to unloaded accuracy.
	Repeatability	±5 arc sec (0.0014°) typical. Unloaded-one revolution returning to start point from same direction.
	Hysteresis	Less than 2 arc min (0.0334°) unloaded-bidirectional.
	Resolution	16 selectable choices: 200, 400, 1000, 2000, 5000, 10000, 12800, 18000, 20000, 21600, 25000, 25400, 25600, 36000, 50000, 50800
	Waveform	Selectable. Allows waveform shaping for optimum smoothness or relative accuracy. Pure sine; -4%, -6%, -8%, 3rd harmonic.
Amplifier		
	Type	20 kHz fixed frequency, variable duty cycle pulse width modulated (PWM) Current Controlled, bipolar chopper
	Number of Phases	2
	Output Current	0.02–3.5 Amps peaks of Sine
	Standby Current Reduction	50% of selected motor current
	Nominal Chopping Frequency	20 kHz
	Max Stepping Rate	2 MHz max pulse rate; 50 rps max speed
	Step Input	High-going pulse, 200 nsec min width; max pulse rate is 2 MHz; User-supplied driver for the step and direction inputs should be capable of providing a minimum of 6.5 mA to maximum of 15 mA
	Direction Input	Logic High = positive (CW) rotation—3.5–5.0V Logic Low = negative (CCW) rotation—0–0.4V User-supplied driver for the step and direction inputs should be capable of providing a minimum of 6.5 mA to a maximum of 15 mA. The direction input must be stable for at least 200 nsec before the drive receives the first pulse
	Fault Output	Open-Collector/Emitter, Vce = 70 VDC, Vce sat = 0.3 VDC, Ic = 40 mA (max) Maximum dissipation = 40 mW Conducting = normal operation Non conduction = drive fault
Protective Circuts	Short Circuit*	Phase-to-phase, phase-to-ground If AC supply drops below 85VAC
	Overtemperature*	The drive will fault if heat plate exceeds 55°C
Environmental	Drive Temp	Max allowable ambient temperature is 122°F (50°C). Fan cooling may be required if airflow is restricted.
	Humidity	0 to 95%, Non-condensing
Physical	Drive Dimensions	5.35 x 4.34 x 1.9in (133 x 109 x 48 mm)
	Weight	1.2 lbs
Motor	Type	Two-phase hybrid permanent magnet, 1.8°
	Number of Leads	4, 6, or 8
	Inductance Range	0.5 minimum; 5 to 50 mH recommended range; 100 mH max

* Drive shuts down in conditions listed. Power must be cycled or drive reset to resume operations.

See Servo Drive section for the full line of Gemini servo drives and drive/controllers.

A.6 Motion Controller

DMC-4183-BOX8

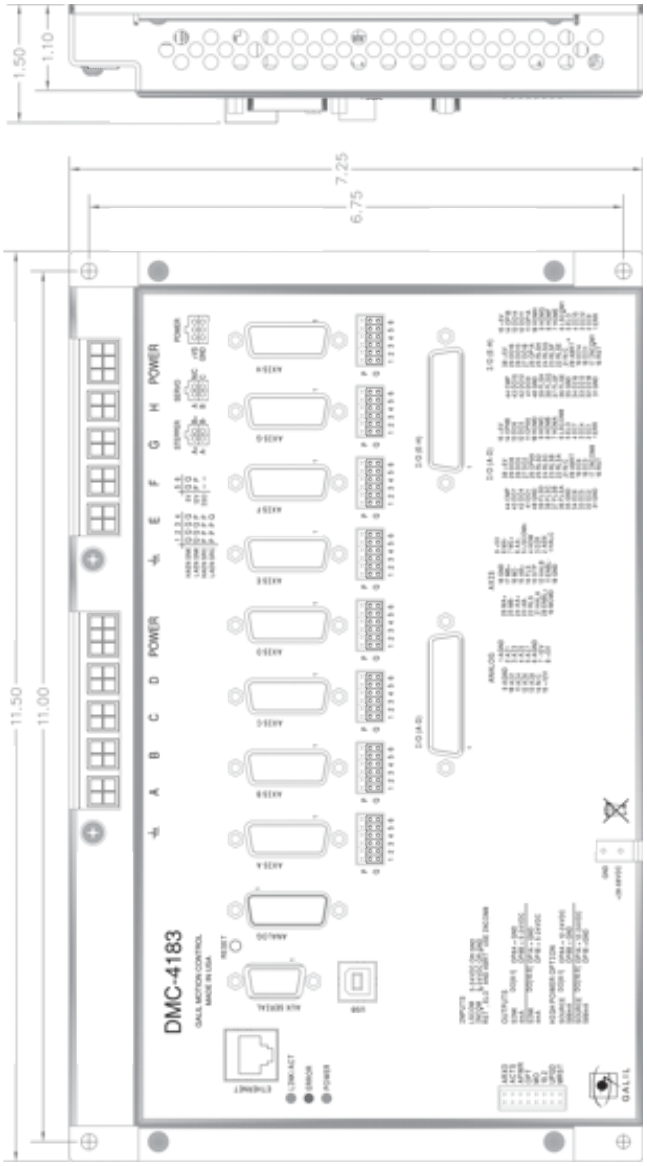

[1] Dimensions are subject to change. Contact the Galil factory for current dimensions of all products.

Electrical Specifications

NOTE	Electrical specifications are only valid once controller is out of reset.

Servo Control

Motor command line	±10 V analog signal Resolution: 16-bit DAC or 0.0003 volts 3 mA maximum. Output impedance – 500 Ω
Main and auxiliary encoder inputs	TTL compatible, but can accept up to ±12 volts Quadrature phase on CHA, CHB Single-ended or differential Maximum A, B edge rate: 15 MHz Minimum IDX pulse width: 39 nsec

Stepper Control

STPn (Step)	TTL (0-5 volts) level at 50% duty cycle. 3,000,000 pulses/sec maximum frequency
DIRn (Direction)	TTL (0-5 volts)

Input / Output

Opto-isolated Inputs: DI[16:1]*, Limit switches, home, abort, reset	2.2 kΩ in series with opto-isolator Active high or low requires at least 1mA to activate. Once activated, the input requires the current to go below 0.5mA. All Limit Switch and Home inputs use one common voltage (LSCOM) which can accept up to 24 volts. Voltages above 24 volts require an additional resistor. ≥ 1 mA = ON; ≤ 0.5 mA = OFF *[8:1] for 1-4 axes models, [16:1] for 5-8 axes models

Analog Inputs: AI[8:1]	±10 volts 12-Bit Analog-to-Digital converter 16-bit optional
Digital Outputs: DO[16:1]*	4mA sinking (25mA sinking/sourcing and 500mA sourcing options) *[8:1] for 1-4 axes models, [16:1] for 5-8 axes models
Auxiliary Inputs as Uncommitted Inputs: DI[96:81]*	The auxiliary pins can be used as uncommitted inputs and are assigned to the following bits: Axis A: DI81, DI82 Axis B: DI83, DI84 Axis C: DI85, DI86 Axis D: DI87, DI88 Axis E: DI89, DI90 Axis F: DI91, DI92 Axis G: DI93, DI94 Axis H: DI95, DI96 These inputs have the same specifications as listed above for encoder inputs. *The number of auxiliary inputs is dependent on the number of axes ordered

Power Requirements

20-80 V_{DC}	10 W at 25° C

+5, ±12V Power Output Specifications

Output Voltage	Tolerance	Max Current Output
+5V	±5%	1.1A
+12V	±5%	40mA
-12V	±5%	40mA

Performance Specifications

Minimum Servo Loop Update Time	
DMC-4113	125 µsec
DMC-4123	125 µsec
DMC-4133	250 µsec
DMC-4143	250 µsec
DMC-4153	375 µsec
DMC-4163	375 µsec
DMC-4173	500 µsec
DMC-4183	500 µsec
Position Accuracy	±1 quadrature count
Velocity Accuracy	
Long Term	Phase-locked, better than 0.005%
Short Term	System dependent
Position Range	±2147483647 counts per move
Velocity Range	Up to 15,000,000 counts/sec servo; 3,000,000 pulses/sec-stepper
Velocity Resolution	2 counts/sec
Motor Command Resolution	16 bit or 0.0003 V
Variable Range	±2 billion
Variable Resolution	1×10^{-4}
Number of Variables	510
Array Size	24000 elements, 30 arrays
Program Size	4000 lines x 80 characters

A.7 C-arm Fluoroscopy Units

OEC® Flexiview 8800 C-arm

Design
- Mobile C-arm
- Separate dual monitor cart

Generator
- 20 kHz high frequency
- 2.2 kW power
- Up to 110 kVp

X-Ray Tube
- Stationary Anode
- 0.5 mm and 1.5 mm focal spot
- Anode heat capacity: 74,200 HU
- Anode cooling rate: 39,960 HU/min

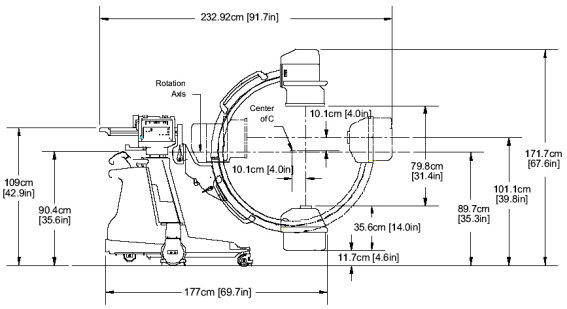

Video Imaging System & Processing
- Tri-mode 9"/6"/4.5" II
- 1k x 1k x 16 bit image processing
- 370° motorized camera rotation
- Touch screen system control
- Noise filter with on-screen indicator
- Optional DICOM 3.0 interface

Electrical
- Input power (60Hz or 50Hz)
- 100V @ 20A
- 120V @ 15A
- 200V, 220V, 230V, 240V @ 10A

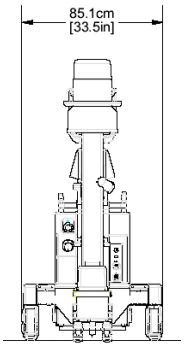

Dimensions

Mainframe

System length - 69.8" (177cm)
System height – 69.5" (176.5 cm)
System width - 33" (84cm)

C-arm

SID 39" (99cm)
Free space in arc 31" (79cm)
Depth in arc 26" (66cm)
Orbital rotation 135° (90°/45°)
Manual rotation 360° (180°/180°)
Wig/wag 20°
Horizontal travel 8" (20cm) 8" (20cm) 8" (20cm)
Vertical travel 18" (46cm)

Workstation

Height - 64" (163cm)
Width - 27" (69cm)
Depth - 27" (69cm)

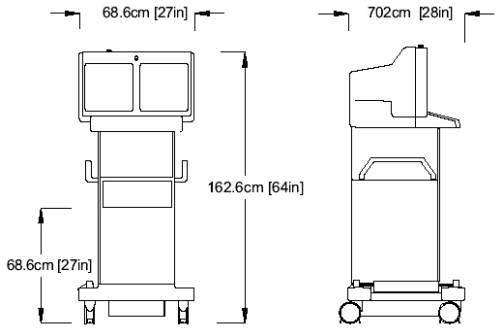

*OEC® is a registered trademark of GE Medical Systems. Specifications are subject to change.

HOLOGIC®
The Science of Sure

Fluoroscan® InSight™ 2

X-ray Specifications

X-Ray Source	Grounded tungsten anode x-ray tube 7.5 W high frequency
Focal Spot Size	0.045 mm
Tube kVp Range	40 to 75 kVp
Tube Current Range	0.020 to 0.100 mA
Maximum Output	0.1 mA @75 kVp
Laser Alignment Light	60 second timed on or full-time on IEC Class 1C

Image Receptor

Image Intensifier	High sensitivity Cesium Iodide Dual Mode 6 in./4 in.
Field of View	Full field - 6 in. diameter Limited field - 4 in. diameter
Image Matrix Size	1 k x 1 k

Control Modes

X-Ray	
Auto IQ	High resolution mode
Auto	Standard imaging mode
Manual	User override mode
Image Acquisition & Storage	
Standard Image	30 fps (frames per second)
Cine Video Recording	25 fps (framers per second)
Storage	Solid State Hard Drive (SSD) 10,000 Total images/500 per case
Imaging Modes	
Snapshot	Auto terminated single shot
Continuous	Fluoroscopy
Cine	Digital recorded fluoroscopy
Noise Suppression Options	
Ultra/Auto/High/Med/Low/Off	Selectable & configurable
Imaging Features	
Automated image processing	
Auto real-time noise reduction, edge enhancement and auto dose control	
Magnify-zoom-pan	
Brightness/contrast control	
Physician preference configurable	

Software/Connectivity

Operating System	Windows 7 Professional
Connectivity	Ethernet wired Wireless (optional)
DICOM Options	Store — with annotation Print, modality worklist and storage commitment
Removable Data Storage	USB Port & CD/DVD-RAM Drive Export file formats: JPEG, TIFF, DICOM, Fluoroscan or native

Display

Widescreen Multi-touch Color Monitor	Hi-Bright, PCAP touchscreen Hi-Definition 1920 x 1200 Digital DICOM compliant
Size	24 in. (61 cm)
Swing Mounting	Extendable with 350° swivel
Viewing Angle	178°
Primary “Live” Image	**Warp Correction Enabled** Standard view: Full Field 9.3 in. (23.5 cm), Limited Field 9.8 in. (25 cm) MegaView™ Image: Full Field 11 in. (28 cm), Limited Field 11.8 in. (30 cm)
	Warp Correction Disabled Standard view Full field/Limited field: 14.2 in. (26 cm) 12.2 in. (31 cm)

Structured Dose Report

Total Dose Area Product (DAP) (cGy*cm²), and Air Kerma (mGy)
Total exposure time (min:sec), and longest single exposure (min:sec)
Total images acquired and images saved
DICOM send and/or paper print options

Power Requirements

Input Line Voltage	100, 120, 220, 240 VAC selectable
AC Input Frequency	50/60 Hz
Frequency	750 watt (max)
Power Failure Protection	Images software protected

System Measurements

Base System	
Foot Print	28 in. x 32 in. (71.1 cm x 81.3 cm)
Door Clearance	30 in. (76.2 cm) minimum
C-Arm	
Depth	16 in. (40.6 cm)
Free Space	14 in. (35.5 cm)
Orbital Rotation	120°
Horizontal Travel	23°
Vertical Travel	23 in. (58.4 cm)
Pivot Rotation	380°
Panning Motion	320°

Options/Accessories

Footswitch Options	
Wired	Triple-function
Wireless	Triple-function RF
Pedal Configuration	Save and/or reference tag
Button Configuration	MegaView Image/print or print
Printer Options	
Standard Format	Sony Thermal Printer UP-898MD
Large Format	Sony Hybrid Graphic Printer UP-991AD Multi-print formats available

A.8 Machine Vision Camera

TECHNICAL DETAILS



Basler ace USB	
Product Group Specifications	
Interface	USB 3.0
Housing Size (L × W × H)	ace classic/ace U: 29.3 mm × 29 mm × 29 mm, ace L: 35.8 mm × 40 mm × 30 mm
Housing Temperature	0 °C - 50 °C[1]
Typical Weight	< 80 g
Power Requirements	Via USB 3.0 interface
Power Suspend Mode	Yes, less than 0.02 W, configurable
Synchronization	Via hardware trigger, via software trigger or free-run
Exposure Control	Via hardware trigger[2] or programmable via the camera API
Conformity	CE, RoHS, GenICam, USB3 Vision, IP30, UL[3], FCC
Driver	Basler pylon Camera Software Suite or 3rd party USB3 Vision Software
Operating System	Windows, Linux, macOS

[1] 0 °C - 60 °C for acA2040-90um/uc, acA2040-90umNIR
[2] not applicable for ace models with sensors of the MT line from ON Semiconductor
[3] UL in preparation for acA5472-17um/uc

Dimensions (in mm): **ace classic & ace U**

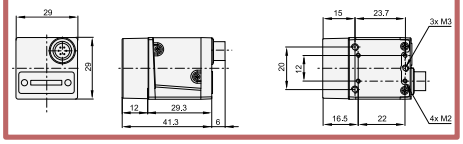

Dimensions (in mm): **ace L**

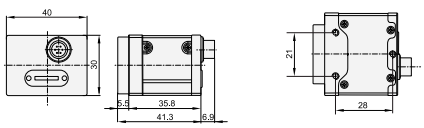

Basler ace classic	acA640-90um/uc	acA640-120um/uc	acA1300-30um/uc
Model Specifications			
Resolution (H×V pixels)	659 × 494	659 × 494	1296 × 966
Sensor	Sony ICX424	Sony ICX618	Sony ICX445
Sensor Size (optical)	1/3"	1/4"	1/3"
Sensor Technology	CCD, global shutter		
Pixel Size [µm²]	7.4 × 7.4	5.6 × 5.6	3.75 × 3.75
Frame Rate [fps]	90	120	30
Mono/Color	Mono/Color		
Pixel Format	Mono (8, 12, 12 Packed), Bayer BG (8, 12, 12 Packed), YCbCr422_8, RGB8, BGR8		
Lens Mount	C, CS*	C, CS	C
Digital I/O	1 opto-isolated input + 1 opto-isolated output + 2 Fast-GPIO (configurable as In/Out)		
Power Consumption	3.0 W	3.0 W	2.5 W

*only available for color model

TECHNICAL DETAILS

Basler ace U	acA1300-200um/uc	acA1440-220um/uc	acA1920-40um/uc
Model Specifications			
Resolution (H×V pixels)	1280×1024	1440×1080	1920×1200
Sensor	ON Semiconductor PYTHON 1300	Sony IMX273	Sony IMX249
Sensor Size (optical)	1/2"	1/2.9"	1/1.2"
Sensor Technology		CMOS, global shutter	
Pixel Size [µm²]	4.8×4.8	3.45×3.45	5.86×5.86
Frame Rate [fps]	203	227	41
Mono/Color		Mono/Color	
Pixel Format	Mono (8, 10, 10 Packed), Bayer BG (8, 10, 10 Packed), YCbCr422_8, RGB8, BGR8	Mono (8, 12, 12 Packed), Bayer BG (8, 12, 12 Packed), YCbCr422_8, RGB8, BGR8	Mono (8, 12, 12 Packed), Bayer RG (8, 12, 12 Packed), YCbCr422_8, RGB8, BGR8
Lens Mount		C	
Digital I/O	1 opto-isolated input + 1 opto-isolated output + 2 Fast-GPIO (configurable as In/Out)		
Power Consumption	3.3 W	3.3 W	2.9 W

Basler ace U	acA1920-150um/uc	acA1920-155um/uc	acA2040-55um/uc
Model Specifications			
Resolution (H×V pixels)	1920×1200	1920×1200	2048×1536
Sensor	ON Semiconductor PYTHON 2000	Sony IMX174	Sony IMX265
Sensor Size (optical)	2/3"	1/1.2"	1/1.8"
Sensor Technology		CMOS, global shutter	
Pixel Size [µm²]	4.8×4.8	5.86×5.86	3.45×3.45
Frame Rate [fps]	150	164	55
Mono/Color		Mono/Color	
Pixel Format	Mono (8, 10, 10 Packed), Bayer BG (8, 10, 10 Packed), YCbCr422_8, RGB8, BGR8	Mono (8, 12, 12 Packed), Bayer RG (8, 12, 12 Packed), YCbCr422_8, RGB8, BGR8	Mono (8, 12, 12 Packed), Bayer RG (8, 12, 12 Packed), YCbCr422_8, RGB8, BGR8
Lens Mount		C	
Digital I/O	1 opto-isolated input + 1 opto-isolated output + 2 Fast-GPIO (configurable as In/Out)		
Power Consumption	4.2 W	3.7 W	2.6 W

A.9 C-mount Lenses

computar

M1224-MPW2

f=12mm F2.4
for 2/3 type Cameras, 5 Megapixel
C-Mount

Model No.		M1224-MPW2		Effective	Front	φ19.5mm	
Focal Length		12mm		Lens Aperture	Rear	φ13.5mm	
Max. Aperture Ratio		1:2.4		Distortion	2/3 type	-0.05%(y=5.5)	
Max. Image Format		8.8mm x 6.6mm(φ11mm)			1/1.8 type	-0.34%(y=4.32)	
Operation Range	Iris	F2.4 - F16.0			1/2 type	-0.35%(y=4.0)	
	Focus	0.1m - Inf.		Back Focal Length		14.39mm	
Control	Iris	Manual		Flange Back Length		17.526mm	
	Focus	Manual		Mount		C-Mount	
Object Dimension at M.O.D.	2/3 Type	6.4cm x 8.5cm		Filter Size		M27.0 P=0.5mm	
	1/1.8 Type	5.0cm x 6.7cm		Dimensions		φ29mm x 42.68mm	
	1/2 Type	4.6cm x 6.2cm		Weight		72.0g	
Angle of View	D	2/3 Type	48.6°	1/1.8 Type	39.1°	1/2 Type	36.5°
	H		39.8°		31.7°		29.5°
	V		30.4°		24.0°		22.3°
Operating Temperature		-10℃ - +50℃					

M.O.D. : Minimum Object Distance

Dimensions

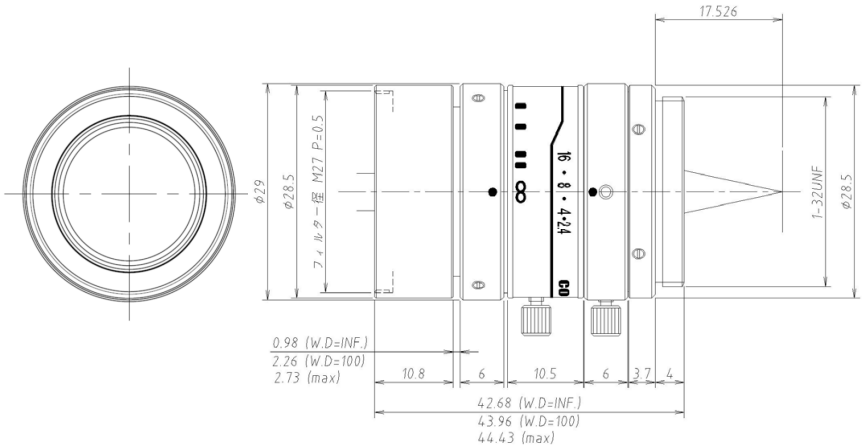

Specification is subject to change without any notice. 2014.08

computar

M2514-MP2

f=25mm F/1.4
for 2/3 type Megapixel Cameras
C-Mount

Model No.		M2514-MP2		Effective	Front	φ17.8mm	
Focal Length		25mm		Lens Aperture	Rear	φ12.0mm	
Max. Aperture Ratio		1:1.4		Distortion	2/3type	-0.3%(y=5.5)	
Max. Image Format		8.8mm x 6.6mm(φ11mm)			1/2type	-0.1%(y=4.0)	
Operation Range	Iris	F1.4 - F16C		Back Focal Length		13.1mm	
	Focus	0.3m - Inf.		Flange Back Length		17.526mm	
Control	Iris	Manual		Mount		C-Mount	
	Focus	Manual		Filter Size		M30.5 P=0.5mm	
Object Dimension	2/3 type	10.6cm x 7.9cm		Dimensions		φ33.5mm x 36mm	
at M.O.D	1/2 type	7.7cm x 5.8cm		Weight		71.2g	
Angle of View	D	2/3 type	24.9°	1/2 type	18.2°		
	H		20.0°		14.6°		
	V		15.1°		11.0°		
Operating Temperature		-10℃ - +50℃					

M.O.D : Minimum Object Distance

Dimensions

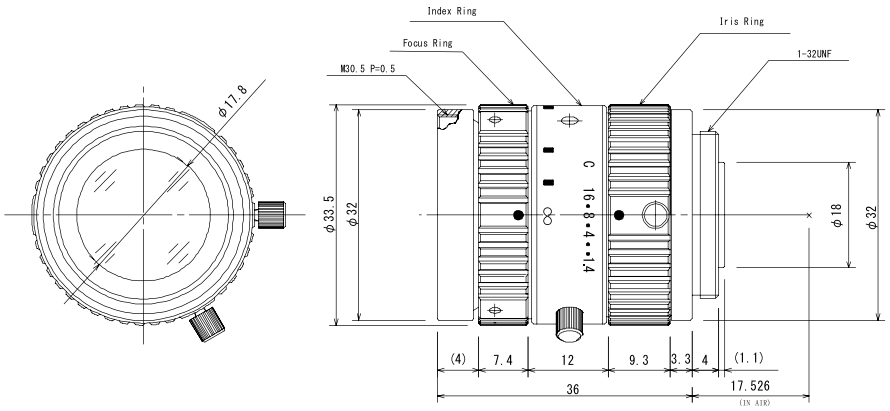

Specification is subject to change without any notice. 2008.05

A.10 Tekscan Pressure Mapping System

Evolution™ Standard USB

Used for standard applications, this system is lightweight and versatile. The Evolution scanning electronics consist of a handle that connects to a sensor and to the USB port of a PC. Multiple handles may be used simultaneously. Indicators on the handle show system status and allow some control of data collection.

Evolution Handle	
System Part #	IE1
Physical Characteristics	
Housing Material	Polycarbonate/ABS blend (Beige)
Size L x W x H	137.9 mm x 57.2 mm x 33.5 mm (5.43 in. x 2.25 in. x 1.32 in.)
Connection Type	USB 2.0
Weight	305 g (10.8 oz)
Power Source	USB Powered, 200mA, 1W
Standard Cable Length	4.57 m (15 ft)
Operating Characteristics	
Maximum Scanning Speed	Up to 100 Hz (speeds vary by sensor)
Pulse-Per-Frame Synchronization	No
Digital Pressure Resolution	8 Bit
Communication to PC	USB 2.0, 480 Mbps
Voltage: Current Consumption	200 mA, 1 W
Sensitivity Adjustment	x 3 to 1/7 of Sensor Pressure Rating
Operating Conditions	
Temperature	-20°C to 35°C (-4°F to 95°F)
Relative Humidity (%)	5-90 (non-condensing)
System Components (Part #)	
Evolution Handle (EH-2), System Carrying Case, Sensor Carrying Case, System Manual	

- Handle powered directly from PC via USB cable
- Up to 100 Hz scanning speed (speed varies by sensor)

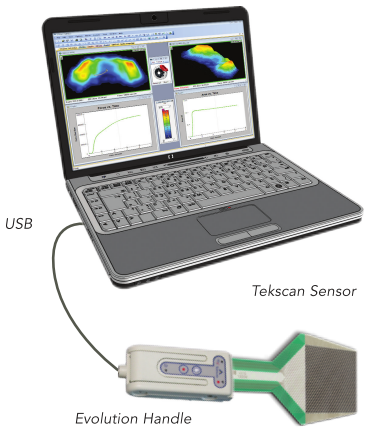

Evolution Handle Dimensions (mm)

Top View

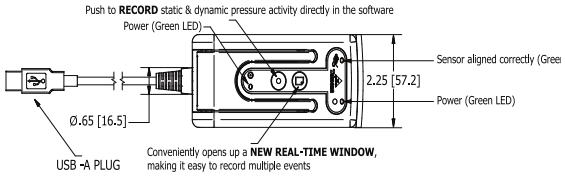

Side View

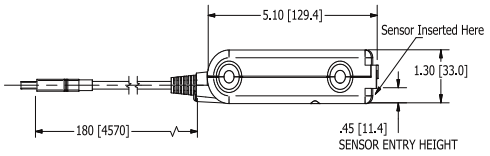

Bottom View

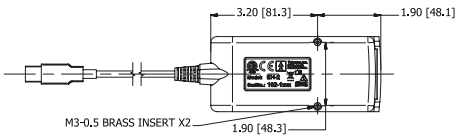

1.800.248.3669

Tekscan®

Medical Sensor 4000

PRESSURE MAPPING, FORCE MEASUREMENT, AND TACTILE SENSORS

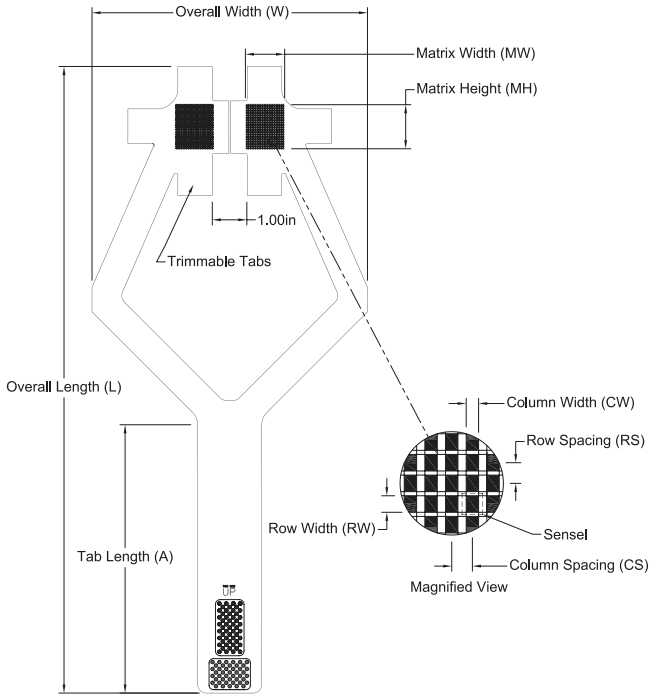

General Dimensions			Sensing Region Dimensions								Summary	
					Columns			Rows				
Overall Length *L*	Overall Width *W*	Tab Length *A*	Matrix Width *MW*	Matrix Height *MH*	*CW*	Pitch *CS*	*Qty.*	*RW*	Pitch *RS*	*Qty.*	Total No. of Sensels	Sensel Spatial Resolution
(mm)	(mm)	(mm)	(mm)	(mm)	(mm)	(mm)		(mm)	(mm)			(sensel per sq-cm)
462.0	203.2	198.1	27.9	33.0	0.8	1.3	22	1.0	1.3	26	572	62.0
(in)	(in)	(in)	(in)	(in)	(in)	(in)		(in)	(in)			(sensel per sq-in)
18.19	8.00	7.80	1.10	1.30	0.030	0.050	22	0.040	0.050	26	572	400.0

Pressure Ranges			
kPa	10,343	62,055	68,950
psi	1,500	9,000	10,000

A.11 Validation Plate

A. C. M. LABORATORY PTY. LTD.
NATA Accredited Laboratory No. 723
1 Kinwal Court, Moorabbin Vic., 3189 Australia Ph: 61 3 9555 0671
www.acmlab.com.au sales@acmlab.com.au Fax: 61 3 9555 6589

METROLOGY REPORT

TEST REPORT NO:	**723 2948/17**	ISSUED: 19.12.17	SHEET 1 OF 1

DESCRIPTION:	X-ray validation plate.
IDENTIFICATION:	ACML 723 2948/17 calibration label attached.
DESCR. OF TEST:	The coordinate position of each ball centre was measured as below. ACML traceably calibrated equipment used: 001.
DATE OF TEST:	19.12.17
CLIENT:	**MELBOURNE SCHOOL OF ENGINEERING**
ADDRESS:	Room 209 Building 170 Block E, Grattan St Parkville, VIC 3010
AUTHORITY OF TEST:	Xin Zhang

GENERAL INFORMATION: NATA Accreditation No. 723.
Reference temperature 20°C (68°F). ACML standard test method used unless otherwise stated. Uncertainty of Measurement has been estimated at a 95% confidence level with a coverage factor (k) = 2 unless otherwise stated. Results stated in this report refer to date of calibration. This report is issued free of any erasures or corrections and shall not be reproduced except in full.

Specified Dimension (mm)	Measured Size (mm) (X, Y)	U. of M. (mm)
Position A:	(-0.773, +39.847)	±0.005
Position B:	(0.000, 0.000)	±0.005
Position C:	(+29.504, 0.000)	±0.005

REMARKS:

AUTHORISED SIGNATORY

D. ZHAO

Accredited for compliance with ISO/IEC 17025.

The results of the tests, calibrations and/or measurements included in this document are traceable to Australian/National standards.

B

Intercarpal Kinematics

This appendix contains additional information about the intercarpal kinematics calculated for the scapholunate and lunocapitate joints.

B.1 Normal Physiological Wrist

Table B.1: Mean and standard deviation of the scaphoid kinematics measured relative to the lunate

Scaphoid (w.r.t Lunate)

Motion	Wrist Position		Intercarpal Rotation [deg]						Distance Between Centroids [mm]					
			Z		**X**		**Y**		**Z**		**X**		**Y**	
	Sagittal	Coronal	FL(+)/EX(-)	sd	UD(+)/RD(-)	sd	PR(+)/SU(-)	sd	RA(+)/UL (-)	sd	VO(+)/DO(-)	sd	PX(+)/DS(-)	sd
NEU			0.00	1.22	0.55	0.46	-0.20	0.38	0.10	0.20	0.00	0.14	-0.08	0.07
FEM	30FL		11.23	1.47	-0.15	3.45	0.92	1.43	-0.72	0.17	1.36	0.55	1.38	0.36
	25		9.60	1.56	-0.25	2.49	0.56	1.40	-0.56	0.14	1.08	0.51	1.17	0.28
	20		8.05	1.48	-0.13	1.99	0.27	1.20	-0.43	0.15	0.82	0.46	0.95	0.20
	15		6.31	1.33	0.02	1.47	0.15	1.10	-0.29	0.17	0.59	0.39	0.70	0.17
	10		4.37	1.16	0.07	1.08	0.04	0.93	-0.16	0.17	0.38	0.29	0.45	0.14
	5		2.30	1.15	0.22	0.63	-0.15	0.64	-0.03	0.18	0.19	0.20	0.20	0.09
	5		-2.76	1.63	0.73	0.59	-0.50	0.35	0.22	0.25	0.00	0.22	-0.26	0.18
	10		-5.43	1.98	1.02	0.62	-0.71	0.49	0.34	0.28	-0.25	0.27	-0.53	0.25
	15		-8.27	2.44	1.28	0.62	-0.95	0.67	0.45	0.31	-0.52	0.34	-0.79	0.32
	20		-10.78	2.82	1.50	0.77	-1.45	1.13	0.54	0.35	-0.80	0.40	-1.02	0.39
	25		-13.19	3.40	1.74	0.94	-1.85	1.34	0.59	0.39	-1.11	0.45	-1.26	0.46
	30EX		-15.40	3.87	2.01	1.29	-2.36	1.47	0.62	0.44	-1.45	0.49	-1.50	0.50
RUD		20UD	0.52	3.21	2.36	1.63	-0.57	2.34	-1.20	0.58	-0.19	0.64	-2.09	0.40
		15	-0.31	2.16	2.43	1.55	-0.80	1.66	-0.61	0.41	-0.24	0.54	-1.42	0.32
		10	-1.08	2.21	1.99	1.25	-0.90	1.11	-0.18	0.32	-0.13	0.42	-0.86	0.24
		5	-0.89	1.82	1.29	0.80	-0.63	0.64	0.04	0.26	0.00	0.30	-0.37	0.17
		5	2.23	1.40	-0.60	1.14	0.26	0.99	-0.08	0.17	0.06	0.39	0.36	0.17
		10	3.10	1.67	-1.12	1.77	0.39	1.10	-0.11	0.13	0.13	0.38	0.71	0.23
		15	3.83	1.95	-1.67	2.24	0.69	1.25	-0.16	0.14	0.20	0.47	0.99	0.30
		20RD	4.18	2.46	-2.45	2.66	1.45	1.89	-0.20	0.22	0.25	0.57	1.30	0.40
DTM	30FL	20UD	10.45	2.45	0.41	2.11	0.09	2.66	-1.55	0.56	1.86	0.62	-0.17	0.48
	24	16	8.61	2.02	0.29	1.40	-0.58	2.09	-1.05	0.39	1.26	0.49	-0.10	0.45
	18	12	6.49	1.55	0.44	0.86	-0.68	1.65	-0.62	0.25	0.77	0.39	-0.02	0.34
	12	8	4.33	1.48	0.43	0.65	-0.42	1.05	-0.32	0.21	0.41	0.30	0.01	0.21
	6	4	2.05	1.50	0.14	0.54	0.00	0.68	-0.09	0.20	0.13	0.24	0.02	0.11
	6	4	-1.21	1.76	-0.63	0.37	0.01	0.77	0.14	0.24	0.00	0.35	-0.04	0.17
	12	8	-3.41	2.32	-1.47	0.81	0.01	0.60	0.26	0.26	-0.21	0.40	-0.01	0.23
	18	12	-5.86	3.12	-2.95	1.85	-0.08	0.73	0.34	0.30	-0.42	0.47	0.05	0.31
	24	16	-7.78	3.58	-4.28	2.30	-0.23	0.95	0.39	0.37	-0.61	0.58	0.14	0.43
	30EX	20RD	-9.33	4.02	-6.02	2.72	-0.32	1.54	0.50	0.42	-1.01	0.89	0.38	0.62

Rotation: FL = flexion (+); EX = extension (-); UD = ulnar deviation (+); RD = radial deviation(+); PR = pronation (+); SU = supination (-).
Translation: RA = radial translation (+); UL = ulnar translation (-); VO = volar translation (+); DO = dorsal deviation (+); PX = proximal translation (+); DS = distal translation (-).

Table B.2: Mean and standard deviation of the capitate kinematics measured relative to the lunate

Capitate (w.r.t Lunate)

Motion	Wrist Position		Intercarpal Rotation [deg]						Distance Between Centroids [mm]					
			Z		**X**		**Y**		**Z**		**X**		**Y**	
	Sagittal	Coronal	FL(+)/EX(-)	sd	UD(+)/RD(-)	sd	PR(+)/SU(-)	sd	RA(+)/UL (-)	sd	VO(+)/DO(-)	sd	PX(+)/DS(-)	sd
NEU			0.18	0.80	0.79	0.36	-0.49	0.31	-0.07	0.13	-0.04	0.06	0.01	0.12
FEM	30FL		18.72	4.34	-0.95	0.65	1.05	2.32	-0.45	0.68	6.14	0.56	-0.20	0.52
	25		15.85	3.61	-0.43	0.86	0.79	2.18	-0.35	0.62	4.99	0.48	-0.34	0.38
	20		13.09	2.81	0.16	0.91	0.48	1.89	-0.28	0.52	3.90	0.41	-0.40	0.27
	15		10.11	1.93	0.52	0.99	0.27	1.70	-0.23	0.37	2.85	0.32	-0.40	0.19
	10		6.97	1.53	0.67	0.93	-0.14	1.31	-0.18	0.24	1.84	0.23	-0.33	0.10
	5		3.69	1.24	0.69	0.62	-0.45	0.84	-0.12	0.15	0.88	0.14	-0.19	0.07
	5		-5.97	1.74	0.98	0.68	0.60	0.93	0.18	0.32	-0.52	0.07	0.17	0.31
	10		-9.70	1.83	1.07	0.79	0.10	0.96	0.22	0.35	-1.35	0.10	0.45	0.40
	15		-13.58	2.03	1.04	0.80	-0.49	1.27	0.25	0.38	-2.13	0.16	0.78	0.48
	20		-17.46	2.37	0.85	0.80	-1.12	1.85	0.28	0.41	-2.87	0.22	1.17	0.55
	25		-21.06	2.87	0.64	0.99	-1.80	2.27	0.29	0.43	-3.58	0.29	1.60	0.59
	30EX		-24.48	3.50	0.37	1.33	-2.53	2.86	0.27	0.46	-4.28	0.34	2.08	0.61
RUD		20UD	11.93	7.31	10.09	1.73	4.39	2.80	-3.37	1.23	-1.39	0.16	-0.05	0.26
		15	8.90	6.29	9.13	1.70	3.66	1.84	-2.24	1.05	-1.04	0.12	-0.06	0.08
		10	4.93	4.89	7.28	1.39	2.58	1.18	-1.31	0.76	-0.55	0.09	-0.07	0.10
		5	1.34	2.72	4.71	1.17	1.49	0.69	-0.58	0.38	-0.10	0.07	-0.07	0.18
		5	-0.46	2.27	-3.85	0.74	-0.32	1.20	0.44	0.32	0.07	0.14	0.06	0.12
		10	-3.05	1.66	-8.02	0.59	-1.83	0.95	0.96	0.33	0.42	0.22	0.13	0.18
		15	-5.50	2.19	-12.54	0.60	-3.54	0.96	1.43	0.51	0.73	0.31	0.20	0.31
		20RD	-7.80	2.64	-17.24	0.52	-5.27	0.89	1.88	0.65	1.09	0.36	0.27	0.50
DTM	30FL	20UD	27.06	6.38	8.83	1.63	4.48	2.82	-3.71	0.90	5.19	0.68	-0.44	1.15
	24	16	22.91	5.65	8.11	1.54	3.34	2.24	-2.72	0.80	4.08	0.53	-0.52	0.85
	18	12	17.98	4.29	7.50	0.94	2.46	1.63	-1.88	0.70	2.91	0.37	-0.49	0.51
	12	8	12.43	3.11	5.99	0.75	1.53	1.31	-1.21	0.54	1.80	0.23	-0.40	0.29
	6	4	6.55	2.19	3.72	0.89	0.58	1.15	-0.64	0.38	0.79	0.11	-0.22	0.15
	6	4	-5.65	2.52	-3.03	0.41	-0.74	1.29	0.47	0.35	-0.79	0.13	0.28	0.21
	12	8	-11.84	1.95	-6.46	0.24	-2.37	1.35	0.92	0.32	-1.55	0.18	0.68	0.36
	18	12	-18.15	1.15	-10.17	0.23	-4.74	1.40	1.33	0.39	-2.21	0.23	1.14	0.50
	24	16	-24.47	0.87	-14.01	0.79	-7.72	1.36	1.69	0.47	-2.78	0.27	1.66	0.62
	30EX	20RD	-28.47	3.36	-18.24	2.05	-9.86	2.25	2.08	0.51	-3.36	0.27	2.15	0.80

Rotation: FL = flexion (+); EX = extension (-); UD = ulnar deviation (+); RD = radial deviation(+); PR = pronation (+); SU = supination (-).
Translation: RA = radial translation (+); UL = ulnar translation (-); VO = volar translation (+); DO = dorsal deviation (+); PX = proximal translation (+); DS = distal translation (-).

B.2 After Ligament Divisions and Reconstructive Surgeries

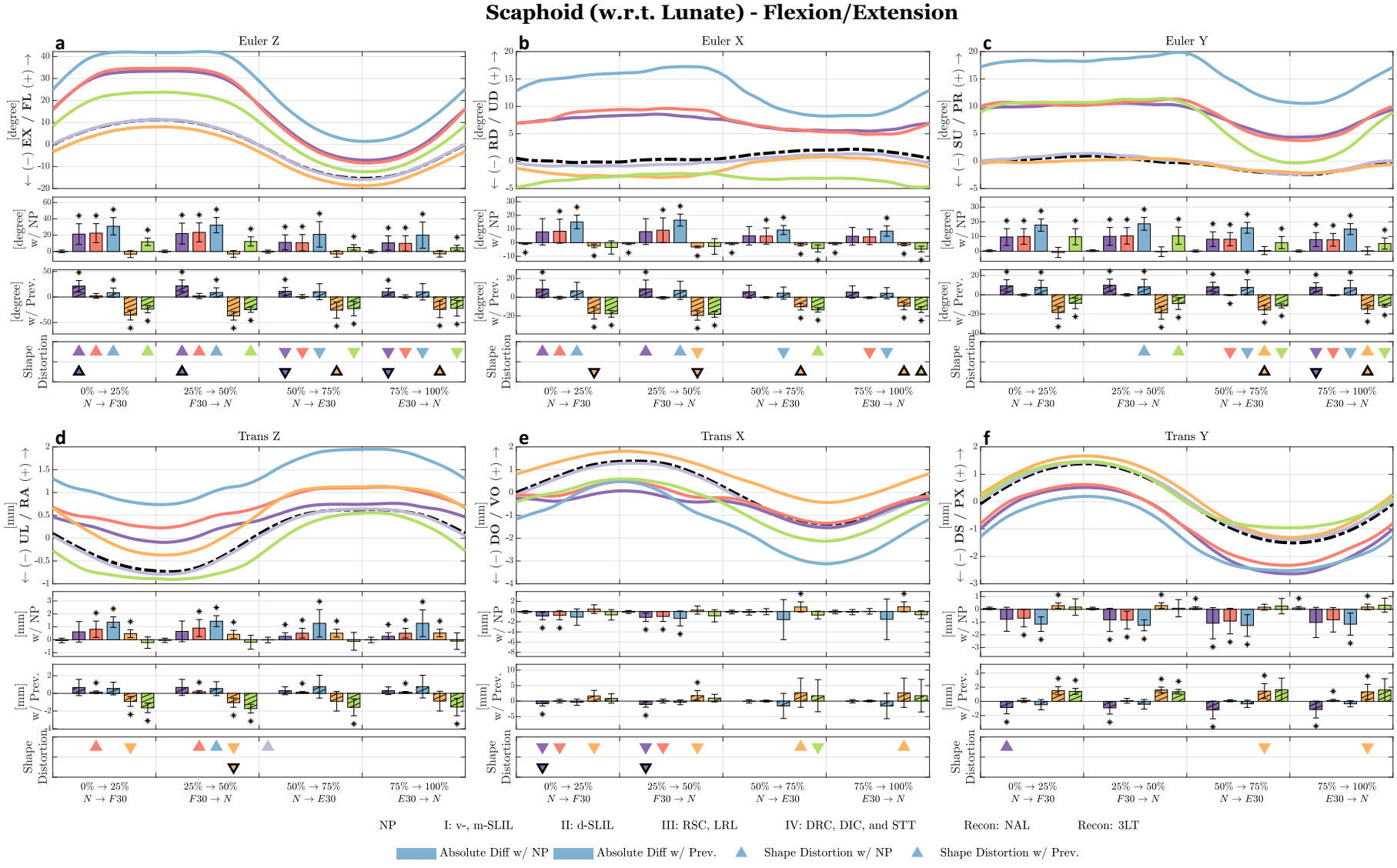

Figure B.1: Scaphoid kinematics (w.r.t the Lunate) measured during FEM following incremental ligament resection and two different SLIL reconstructions. * denotes a statistically significant difference. FL = flexion, EX = extension; UD = ulnar deviation, RD = radial deviation; PR = pronation, SU = supination.

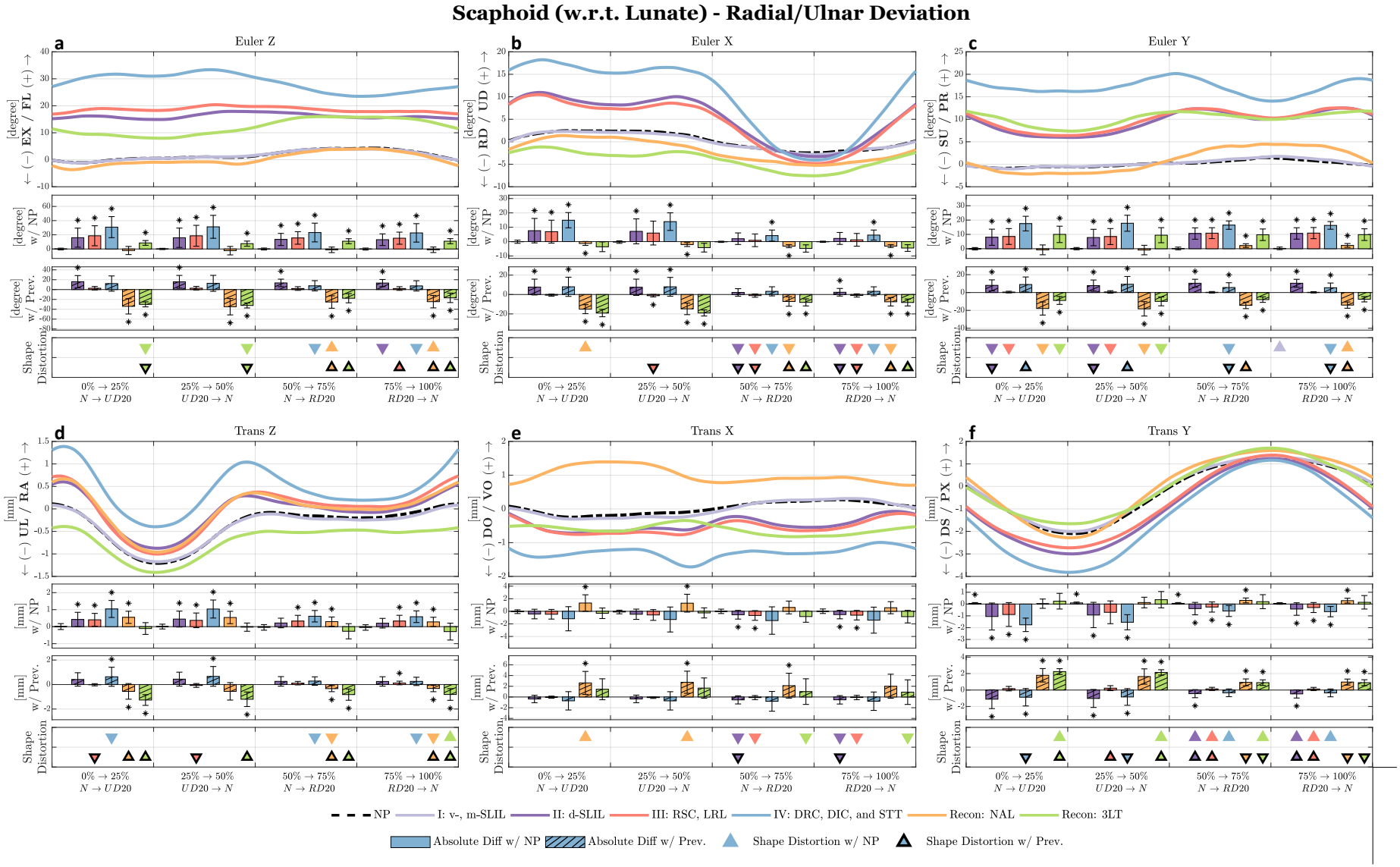

Figure B.2: Scaphoid kinematics (w.r.t the Lunate) measured during RUD following incremental ligament resection and two different SLIL reconstructions. * denotes a statistically significant difference. FL = flexion, EX = extension; UD = ulnar deviation, RD = radial deviation; PR = pronation, SU = supination.

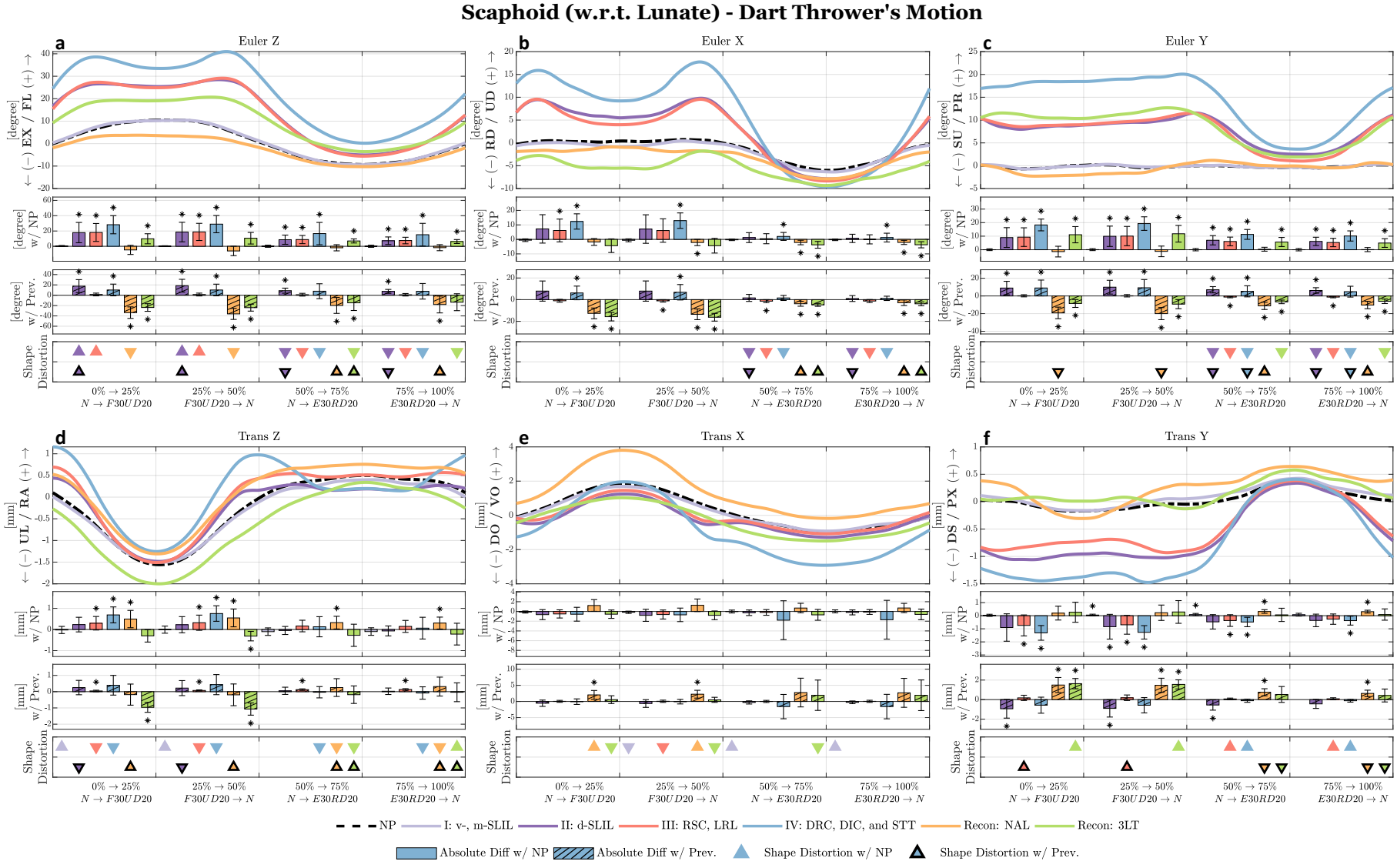

Figure B.3: Scaphoid kinematics (w.r.t the Lunate) measured during DTM following incremental ligament resection and two different SLIL reconstructions. * denotes a statistically significant difference. FL = flexion, EX = extension; UD = ulnar deviation, RD = radial deviation; PR = pronation, SU = supination.

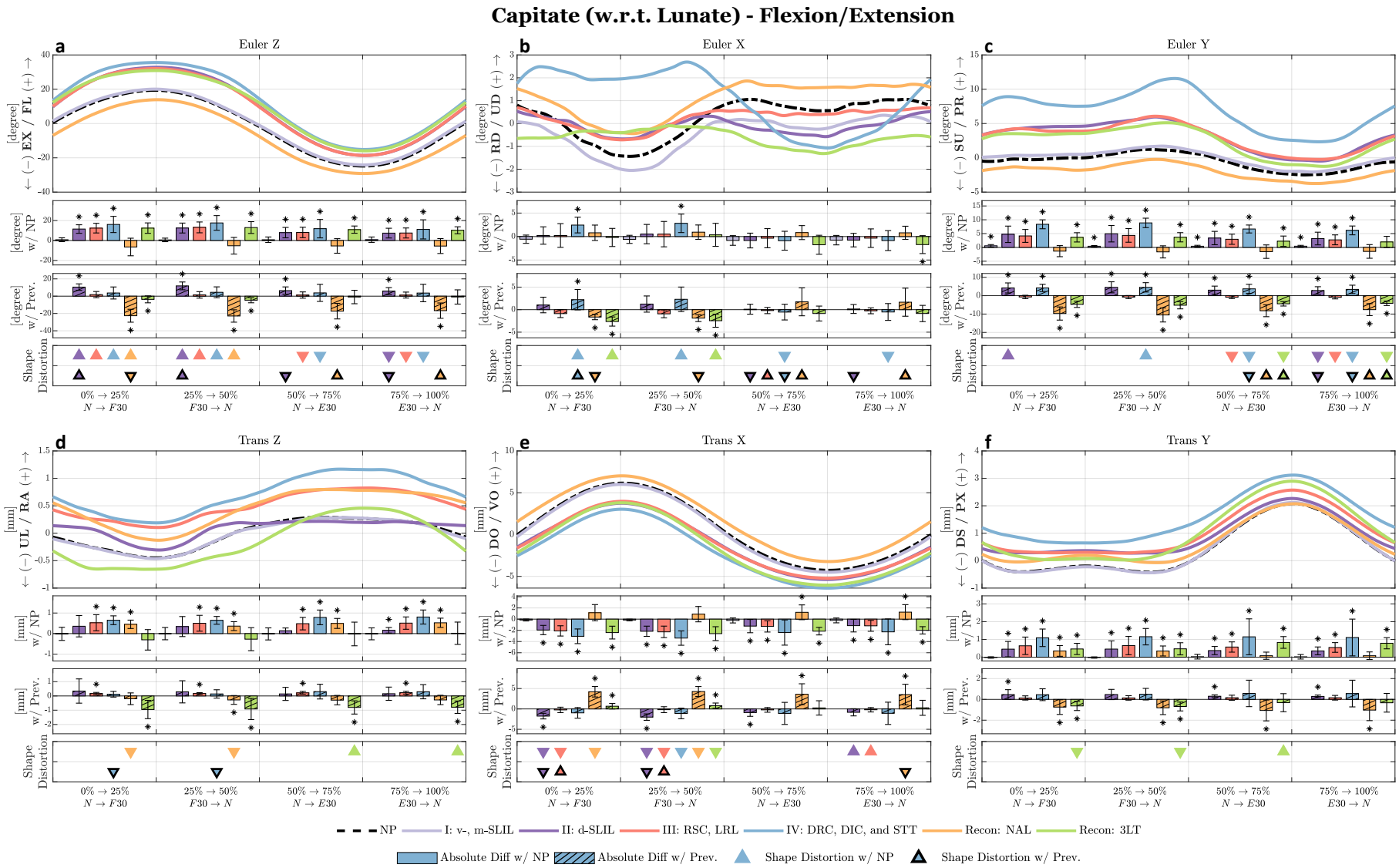

Figure B.4: Capitate kinematics (w.r.t the Lunate) measured during FEM following incremental ligament resection and two different SLIL reconstructions. * denotes a statistically significant difference. FL = flexion, EX = extension; UD = ulnar deviation, RD = radial deviation; PR = pronation, SU = supination.

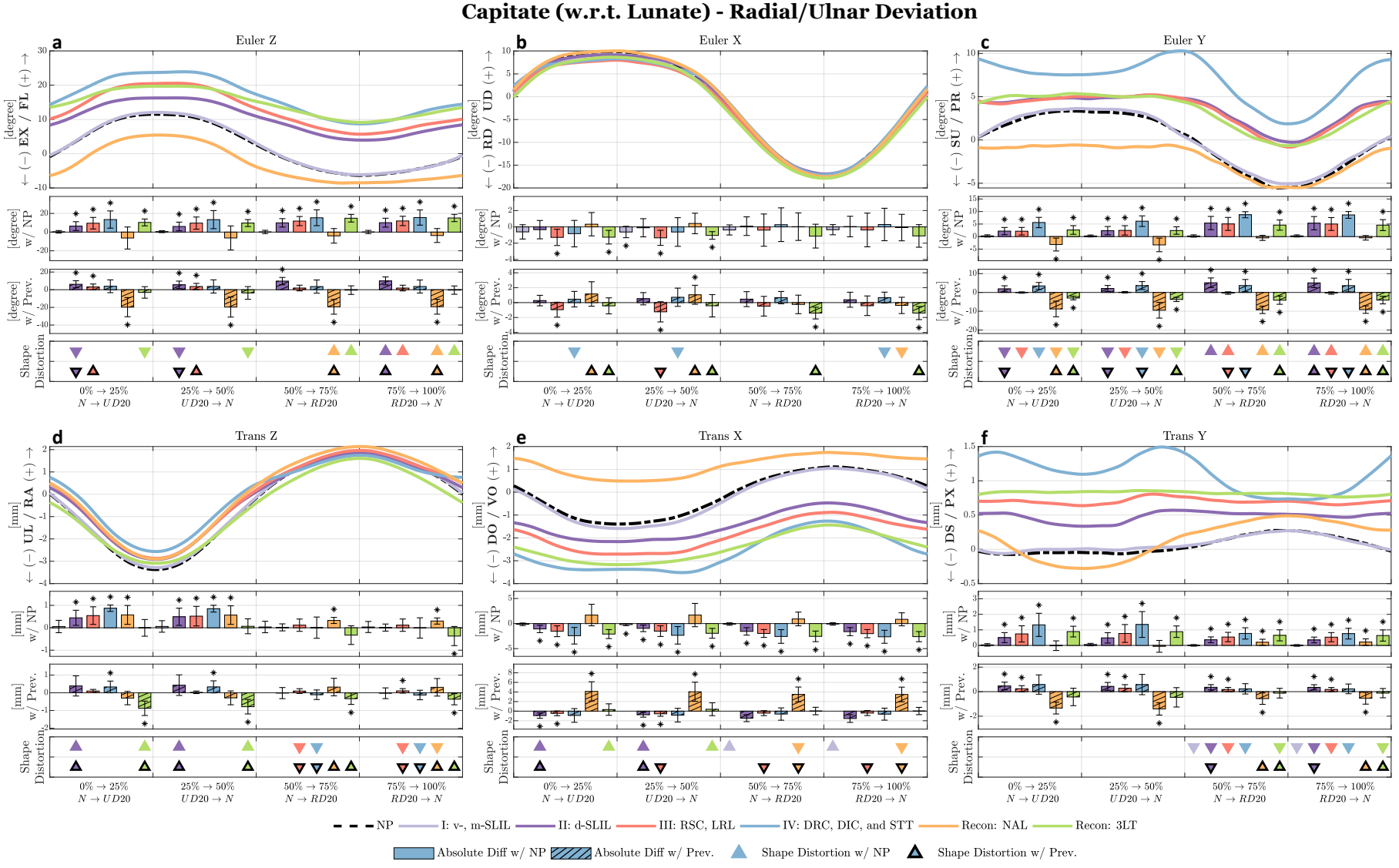

Figure B.5: Capitate kinematics (w.r.t the Lunate) measured during RUD following incremental ligament resection and two different SLIL reconstructions. * denotes a statistically significant difference. FL = flexion, EX = extension; UD = ulnar deviation, RD = radial deviation; PR = pronation, SU = supination.

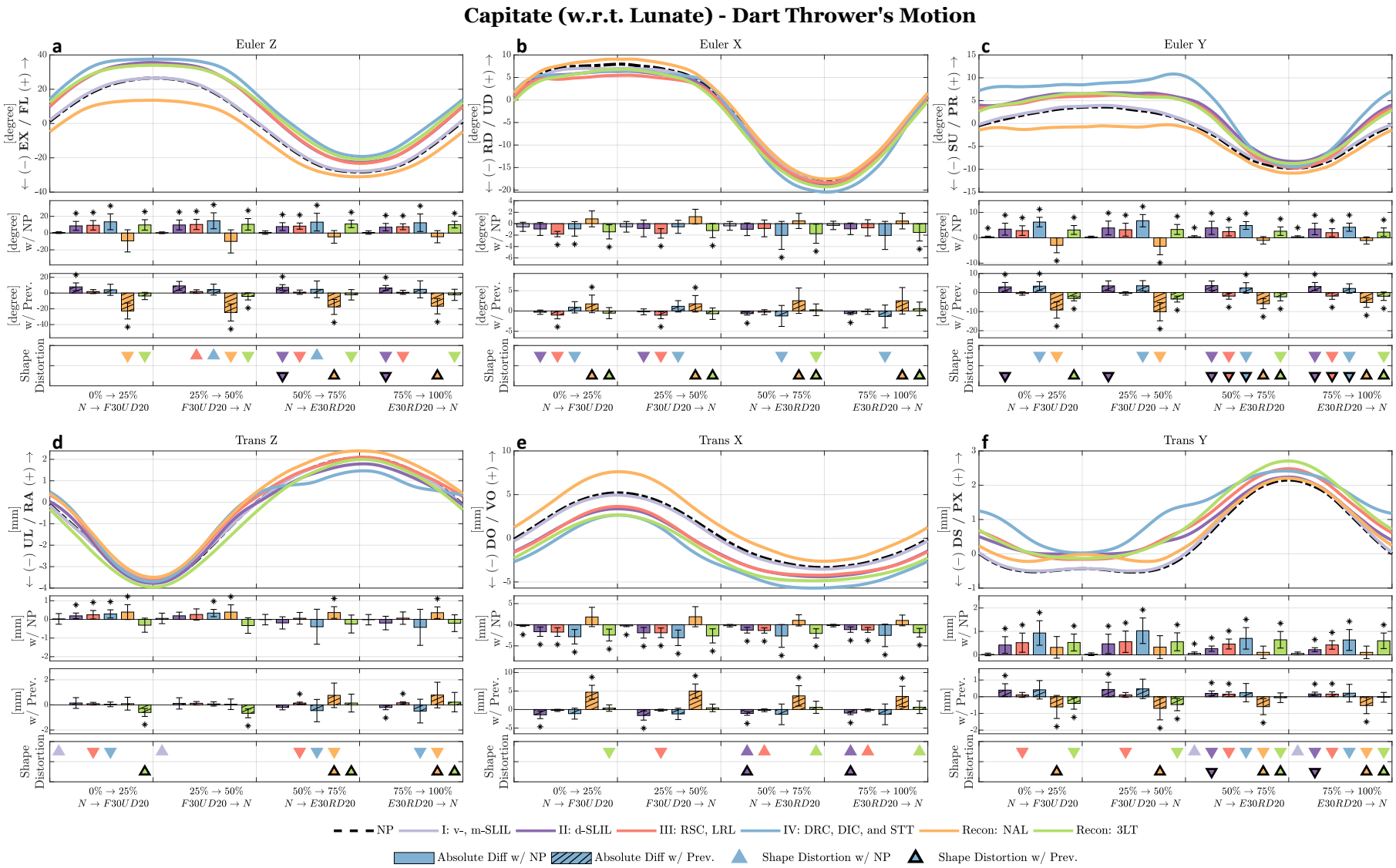

Figure B.6: Capitate kinematics (w.r.t the Lunate) measured during DTM following incremental ligament resection and two different SLIL reconstructions. * denotes a statistically significant difference. FL = flexion, EX = extension; UD = ulnar deviation, RD = radial deviation; PR = pronation, SU = supination.